UNIVERSITY OF
LINCOLN

Linking Shape and Sinking Speed in Planktonic Foraminifera

Matthew Walker

A thesis submitted in partial fulfilment of the requirements of the University of Lincoln for the degree of Doctor of Philosophy

July 2019

Acknowledgements

First, I would like to thank Stuart Humphries for his guidance over the entire project. His door has been (almost) always open. He has always been encouraging, even during the most difficult times, and his drive has been contagious. Of course, I thank Stuart for offering me the PhD; I hope he has enjoyed this time as much as I have. I would also like to thank Marcello Ruta for his stimulating conversations, and his knowledge and guidance through shape analysis and phylogenetic techniques. I also thank the Physical Ecology Lab members (Rudi Schuech, Òscar Guadayol i Roig, Fouad El Baidouri, Mariona Segura, Jackson Sage and Sei Suzuki-Teller) who have all provided me with a great deal of advice and discussion over the duration of my research. Rudi Schuech deserves special mention, without his indispensable knowledge of hydrodynamics this project would not have been possible. He also has been very helpful (and tolerant) with my many questions related to MATLAB; and his assistance writing much of the MATLAB code used is very much appreciated. Jackson has been a great friend, supporting me through all of the teething issues of starting a PhD. Tom Pike has provided advice on cameras, removal of distortion, statistics, and thought-provoking conversation, for which I am grateful. The PGR community in the School of Life Sciences has been of great support, as have the technical staff of both Joseph Banks Laboratories and the Science Building.

Outside of the University of Lincoln, thanks go to: Michael Kucera, Giles Miller and the micropaleontology department at the Natural History Museum (London) for supplying samples of planktonic foraminifera; Alex Blanke for taking foraminifera samples to Germany for synchrotron scanning; and Loren Petruny and colleagues at the American Museum of Natural History (New York), and the International School of Foraminifera (ISF) community for checking identification of foraminifera. Additionally, to Thorin Jonsson for demonstrating SPIERS software to me and, thanks to Emma Myers for translating Berthois and Le Calvez (1960). Special thanks go to Chris Venditti for his advice regarding MCMCglmm analyses and ancestral state reconstruction. I would also like to thank the Leverhulme Trust who funded my PhD, through the Research Leadership Award (RL-2012-022) awarded to Stuart.

With specific regard to chapter 2, I would like to thank Fernando Montealegre-Z, Tom Pike and Anna Wilkinson and members of the Physical Ecology Lab for reading and providing improvements to an early draft. I also thank Nigel Larkin, and Tim Shields for the information on uses of 3D printing in museums and conservation, respectively.

Over much of my research Tatjana Hoehfurtner has been extremely helpful, providing me with general assistance with 3D printing, synchrotron scan segmentation, R coding, graphics production, proof-reading and much more. Her support has made a huge difference to the project and to myself. I would also like to thank my Mum and Dad and my sister, Dawn, for their continued support, encouragement, enthusiasm and providing perspective that life is not just about science.

Contents

Chapter 1 Introduction

1.1 Introduction

Understanding the role of the oceans in the Earth's climate has never been more important as human-induced climate change becomes more apparent. A key part of the oceans' role is as a carbon sink. Carbon dioxide is absorbed by water, dissolving to form bicarbonate molecules. The dissolved carbon can be stored in a number of ways.

Firstly, there is the physical carbon pump. As warm ocean waters from low latitudes move towards higher latitudes, they cool and thus increasing the amount of dissolved CO_2 it holds. The cold dense water then sinks, taking the carbon to the deep ocean (Volk and Hoffert, 1985). The carbon dioxide stored in this way can be released when the water warms up.

Secondly, there is the biological (or soft-tissue) carbon pump (Volk and Hoffert, 1985). Carbon is captured and stored through primary production in phytoplankton via photosynthesis. Photosynthesis releases oxygen, and despite the small size of many marine primary producers (typically in the 1-100 µm range, with the notable exception of seaweeds and seagrasses), due to their numbers, their large biomass means that they account for ~50% of the oxygen production on Earth (Chapman, 2013). The phytoplankton are then either consumed by zooplankton, or other pelagic organisms, or die and slowly sink to the ocean floor. Any organism that is consumed has much of the carbon stored in its cell(s) converted back to carbon dioxide during the predators' respiration. However, those organisms which sink and reach the ocean floor have some of their carbon preserved in the sediment (Chapman, 2013).

Thirdly, carbon can be stored as carbonates (e.g.: magnesium and calcium carbonates, i.e. inorganic carbon) in the geobiological carbon pump. Carbon is stored as carbonates in the shells of organisms such as bivalves (e.g.: mussels), corals, and calcified plankton. The presence of carbonates in plankton makes them denser than water, and thus when the organisms die they sink rapidly to the ocean floor and (dependent on the depth, see below) can be stored for millions of years, eventually turning into sedimentary rocks. With the biological pump, the sinking rate of planktonic organisms is key to understanding the amount of carbon which is reaching and stored on the ocean floor. Faster sinking rates result in greater amount of carbon retching the ocean floor, compared to slower sinking rates. This is increasingly important as changes in the ocean's pH (due to carbon dioxide dissolving in the ocean) are resulting in reduced calcification in a range of planktonic organisms, including: petropods (Orr et al., 2005), coccolithophores (Meyer and Riebesell, 2015) and foraminifera (Russell et al., 2004; Davis et al., 2017). By quantifying sinking rates, the capacity of the ocean to act as a buffer to climate change, and the timescale at which this operates, can be better understood (De La Rocha and Passow, 2007). The production of calcium carbonate does, however, release carbon dioxide (see Equation 1-1).

Equation 1-1

$$Ca^{2+} + 2HCO_3^- \rightleftharpoons CaCO_3 + CO_2 + H_2O$$

The rate at which the shells of planktonic organisms sink has been the subject of laboratory based study (e.g.: Walsby & Holland 2006; Holland 2010; Bach et al. 2012; Caromel *et al*., 2014). Whilst in the ocean, studies use multinet sampling at different depths to sample the plankton populations as they sink towards the ocean floor (e.g.: Schiebel et al. 1995), this gives an understanding of the numbers of planktonic organisms present in the water column and the depths at which they live. The flux of plankton (and thereby carbon, for foraminifera predominantly inorganic carbon in the form of carbonate) reaching the ocean floor is calculated using the populations from the field and the sinking velocities determined in the laboratory.

The factors affecting the sinking rate of plankton are intertwined. Previous studies have tended to overlook the fact that size and shape can be interlinked. For example, the surface area perpendicular to sinking direction is affected by both size (i.e. the maximum dimensions) and shape. In order to untangle this relationship, one morphologically diverse phylum of plankton, planktonic foraminifera, are examined here to elucidate links between their shape and sinking velocity. Isolating the effect of shape on sinking velocities is complex and often overlooked. This could be due to: the technical difficulties of measuring the shapes of microscopic organisms, being unable to observe their orientation during sinking, or the lack of physics-based predictions for complex shapes. With larger objects, such as cars and planes (or in a more biological context; bird feathers, van Bokhorst *et al*. 2015), the shape of the object determines the amount of drag experienced. Such objects are said to operate at high Reynolds number (See Chapter 3). However, with smaller objects the drag experienced due to shape differences decreases and operate at low Reynolds numbers (see Chapter 3). The size of planktonic foraminifera is such that they fall in between high and low Reynolds numbers, where the hydrodynamic understanding of drag is less clear (see below and Chapter 3). This range, known as intermediate Reynolds number (Re, approximately 0.1 ≤ Re ≤ 50, Humphries, 2009), is difficult to make hydrodynamic-based predictions for, even for simple shapes such as a sphere. In this transitionary range the relative influence of fluid viscosity (stickiness, see Chapter 3) becomes less than at lower Re values, whilst the impact of the fluid's inertial properties increases (see Chapter 3). due to the departure from the purely viscosity dominated world of low (<0.1) Re. As the Re of a particle increases the flow around the particle transitions from viscous (laminar) flow to turbulent flow (see Figure 3-2), where the 'streams' of fluid separate more (Munson, Young and Okiishi, 1994). This is the range of Re with which we (humans) are familiar, and there are equations which predict the sinking velocities of particles within this range.

To add an additional layer of complexity to the problem, in the ocean there is turbulence. The physical, or mathematical, modelling of turbulence is a considerable technical challenge (Ecke, 2005). When a particle is settling in a quiescent (still) fluid, the orientation of the particle is

determined by the weight distribution. However, when (small-scale) turbulence is introduced to the ambient flow, this alters the wake structure and orientation of the particle (Bellani *et al.*, 2012). This change in orientation will affect the sinking velocity, as will changes in the wake structure (i.e. how the fluid moves around the particle, see Figure 3-2). Large scale turbulence also can affect sinking rates of particles, transporting particles (horizontally) over hundreds of kilometres as the particles sink vertically (Van Sebille *et al.*, 2015). Therefore, here the foraminifera are physically modelled sinking in a quiescent fluid to obtain a general understanding of the sinking velocities which might be obtained under natural conditions.

As such, the aims of this thesis are to:

1. Increase the sample size of species planktonic foraminifera for which sinking velocities have been measured. More, and more accurate, data on individual species will provide studies of climate change with better estimates of sinking velocities, allowing better measures of the flux of planktonic foraminifera to the ocean floor.

2. Develop a parameter (C_{DI}) which allows the prediction of sinking velocities within the intermediate Reynolds number range. The effect of size on sinking velocity has been determined by other studies (See Chapter 3) and as such this parameter will be less dependent on size than existing measures (e.g.: C_D).

3. Quantify the shape of planktonic foraminifera species. The measures of shape will then be compared to the parameters developed as Aim 2. This will result in a measure of shape which can be easily applied and directly linked to the sinking velocity of planktonic foraminifera. Finally, using the measure of shape, the interaction between shape and sinking velocity can be examined.

To achieve these aims a novel method of obtaining sinking velocities from planktonic foraminifera was developed using 3D printed models generated from existing micro-Computed-Tomographic (µCT) images, and new synchrotron-radiation tomographic microscopy.

1.2 Planktonic foraminifera

Planktonic foraminifera are a phylum of marine ameboid protists (B. K. Sen Gupta (ed.) , 2002; Schiebel & Hemleben, 2005) found at densities around 30 per cubic metre (Neil, Cooke and Northcote, 2005), or even higher (up to 500, Thiede 1975). The foraminifera produce a calcium carbonate shell, or test (Figure 1-1). Adult tests are usually between 200µm to 1500µm in diameter and are perforated (see some examples of ontogenetic sizes in Table 1-1). Through the perforations (or pores) the cell streams cytoplasm over the external surface of the test, gathering nutrients and capturing prey. There is also a large hole (or series of holes) called the aperture, through which cytoplasm streaming occurs. Once the cell dies or undergoes reproduction, the empty test sinks to the ocean floor. Their ubiquity means that the resultant sediment (comprised of millions of tests) covers approximately 70% of the sea floor (Neil, Cooke and Northcote, 2005) and oceanic sediments

contain substantial amounts of foraminifera tests. Due to their abundance and excellent fossilisation potential, foraminifera have been studied extensively within a stratigraphic and paleo-oceanographic context (e.g.: Prothero & Lazarus, 1980; Brummer *et al*., 1987; Universitaria & Herrero, 2002; Wade *et al*., 2011). Despite their ubiquity and scientific importance, foraminifera cannot be fully cultured in a laboratory (i.e. a full life cycle observed as the gametes do not fuse), nor is there a consensus on the purpose of the test. The test has been suggested to provide protection from predation (Lipps, 1979), by increasing handling time by a predator (Burke and Hull, 2017), despite no specific predators of foraminifera being known. Another suggestions for the tests' purpose is that it helps to maintain position within the water column (Caromel *et al.*, 2014).

Table 1-1: Some example lengths and heights for different ontogenetic stages in the foraminifera Globorotalia truncatulinoides Globigerinoides sacculifer, 'trilobus' form, Globigerinoides sacculifer, 'sacculifer' form, Globigerina bulloides (data from Caromel et al., 2015).

Chamber Number	*Globorotalia truncatulinoides*		*Globigerinoides sacculifer, 'trilobus' form*		*Globigerinoides sacculifer, 'sacculifer' form*		*Globigerina bulloides*	
	Length (µm)	Height (µm)	Length (µm)	Height (µm)	Length (µm)	Height (µm)	Length (µm)	Height (µm)
1	28.6	29.8	17.4	25.7	19.7	21.4	19.4	29.4
2	44.7	31.1	29.7	25.7	30.7	21.4	32.1	29.5
3	57	36.5	32.3	25.7	33.9	22.3	40	29.4
4	59.3	37.2	39.6	25.8	36.8	24.3	44.5	29.4
5	77.1	44.7	44.7	27.8	45	25.1	52.4	34.5
6	96.3	54.7	48.6	30.2	49.7	27.2	63.8	39.8
7	108.9	64.1	53.8	32.7	53	28.4	69.5	47.8
8	138.7	69.6	63	38.4	60.8	39.2	90.4	53.9
9	176.9	96.1	69.8	40.9	77.5	44	117.4	71.6
10	200	113	83.3	52.7	84.1	54.1	146.8	103.3
11	244.3	124.9	92.6	59.6	107.1	71.6	191.2	134.5
12	276.2	155.4	100.2	80.8	136.2	102.8	243.6	190.2
13	366.7	285.2	129.8	100.5	174.1	131.1	310.6	262.8
14	457.5	348.9	169.5	118.5	244.9	204	388.8	296.9
15	526.8	418.7	224.2	177.2	332.2	249.6		
16	571.8	445.7	337.1	249.6	458.4	366.5		
17	595.7	463.4	484.1	382.5	549.4	358.5		
18			697.2	495.4				

The adult tests of foraminifera have numerous chambers; however they initially consist of one chamber, with the foraminifera adding more as the cell grows. The formation of the test preserves the ontological changes from previous growth stages, resulting in a series of chambers often arranged in a spiral. Tests vary considerably in both size and shape, the reasons for which are mostly unknown, partly due to the scant knowledge of foraminiferal biology (B. K. Sen Gupta (ed.) , 2002). However, it is known that as sea surface temperature (SST) increases (with changes in latitude/geographic location), foraminifera test size increases (Figure 1-2, (Schmidt, Thierstein and Bollmann, 2004)). In addition, certain shapes repeatedly evolve through geological time (Cifelli, 2006) despite there being correlation with the depth at which the species lives (e.g.: Coxall *et al*., 2007).

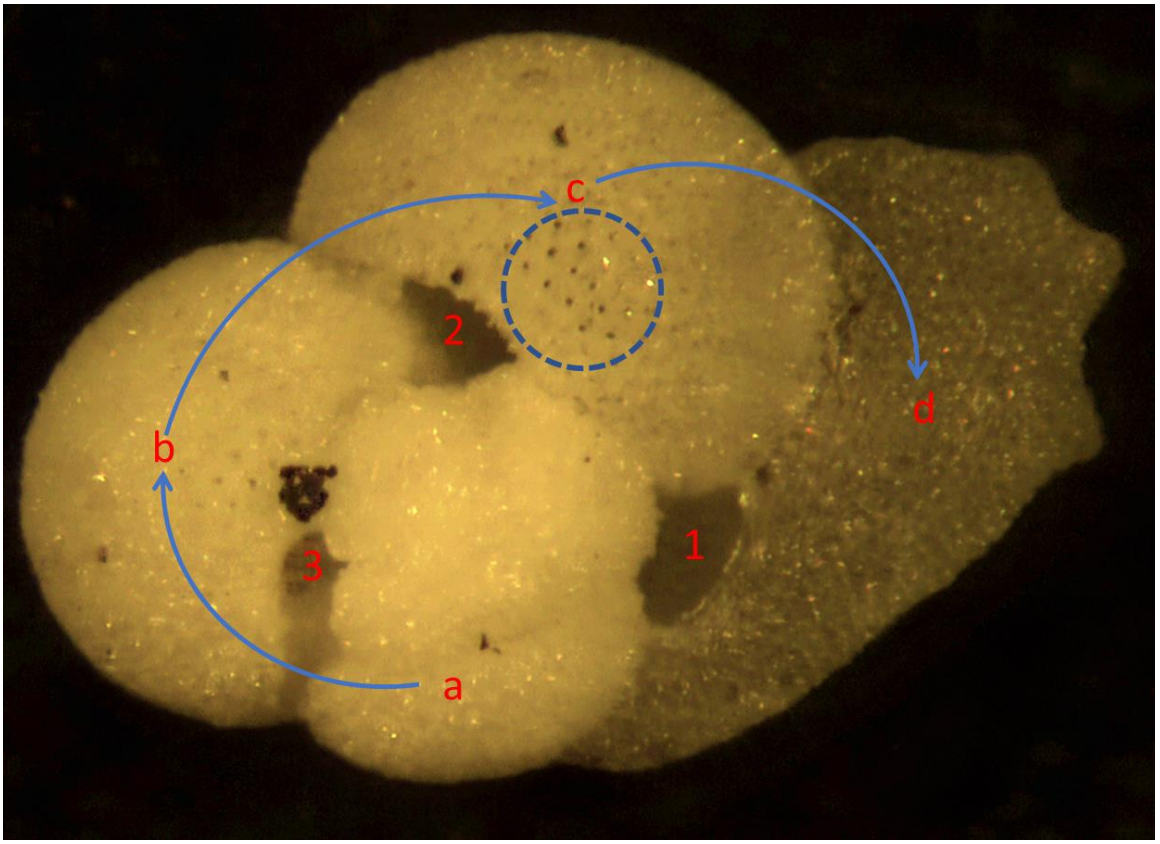

*Figure 1-1: A light micrograph of an example of a planktonic foraminifera (*G. sacculifer*). This species has a primary aperture (1) and supplementary apertures (2 and 3). The growth pattern is indicated for the chambers (a-d) outer whorl. In the dashed circle some particularly visible pores are highlighted. In the live foraminifera the cytoplasm is streamed out of the pores and aperture over the test surface (and along spines if present) for prey capture and exposing any symbionts to light.*

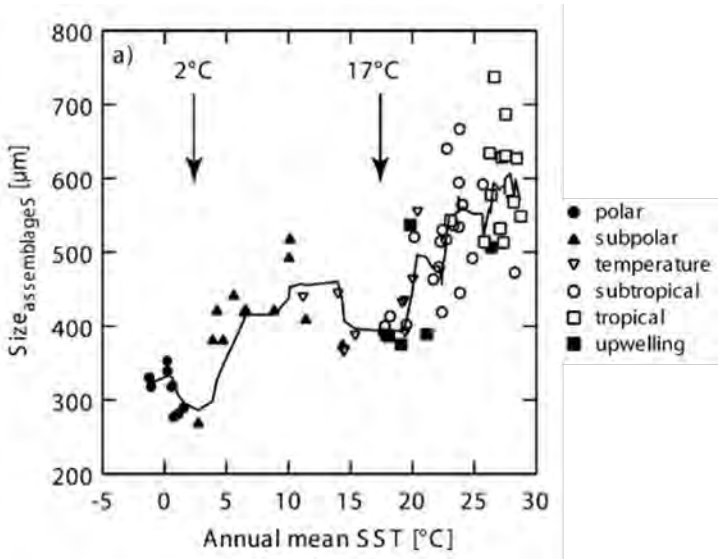

Figure 1-2: The trend between sea surface temperature (SST) and foraminifera test size which separates the smallest 95% of tests from the largest 5%. Samples of foraminifera were taken for different regions around the globe (indicated by point type) and their size measured. The line is a 5-point moving average, arrows indicate 2˚C and 17˚C the polar and the subtropical fronts, respectively. From (Schmidt *et al.*, 2004).

There are suggestions that the planktonic foraminifera are small enough to have been released from evolutionary pressures that would affect shape (Bonner, 2013). Other theories suggest that different morphologies influence sinking rates, which may be advantageous in the capture of prey (Furbish and Arnold, 1997), or simply increase prey encounter rate (Coxall *et al.*, 2007). Whatever

the causes of the shape variation, the morphology of the test has been the basis of foraminifera systematics for hundreds of years.

The majority of the expertise in foraminifera has, historically, been in the oil industry, as the tests of foraminifera can be used to identify the age of the rock. Sedimentary rocks can be dated by the presence or absence of different foraminifera species with known stratigraphic ranges (e.g.: Ross & Haman, 1989). As a result, the oil and gas industry have huge collections of foraminifera in their core samples from potential wells. Some of these collections (e.g.: British Petroleum, BP) have since been donated to museums, such as the Natural History Museum (NHM) in London, making them available for scientific study.

The prevalence of planktonic foraminifera in sediments was first highlighted by the Challenger expedition (1872-76). During this time, Murray (Murray, 1897) realised that the differences in the distribution of the planktonic foraminifera reflected the temperature of the ocean (for modern examples see Figure 1-3). Schott (Schott, 1935) found, using species counts, that there are changes in species compositions between glacial and inter-glacial periods (Kucera, 2007). Such works culminated in the development of Climate: Long range Investigation, Mapping, and Prediction, CLIMAP (CLIMAP Project Members, 1976). CLIMAP was a project based on sediment cores to estimate the historical climate of the Earth, predominately 18 thousand years ago (CLIMAP Project Members, 1976). Modern analyses rely on measuring the isotopes of oxygen, carbon, calcium as well as trace element isotopes to determine paleoclimates. The elements that are incorporated into the test during the cell's lifetime (generally thought to be around 20 to 30 days (B. K. Sen Gupta (ed.) , 2002), but potentially up to several months (Nigam, Saraswat and Mazumder, 2003)) are representative of the relative abundance of these elements and isotopes (mainly the ratios of: Calcium and Magnesium; Oxygen (^{18}O and ^{16}O); and Carbon (^{14}C and ^{12}C) in the ocean during the same time period (Pearson, Shackleton and Hall, 1993; Wolf-Gladrow, Bijma and Zeebe, 1999; Schiebel *et al.*, 2005; Fraile *et al.*, 2007, 2008; Sadekov *et al.*, 2009; Birch *et al.*, 2013). Using the ratios of elements and their isotopes, as well as the species composition, inferences can be made about the age of the rock (Lea *et al.*, 2002; Pearson and Wade, 2009) and the ocean temperatures at the time it was laid down (Bemis *et al.*, 1998; Mashiotta, Lea and Spero, 1999; Rosenthal and Lohmann, 2002; Barker *et al.*, 2005).

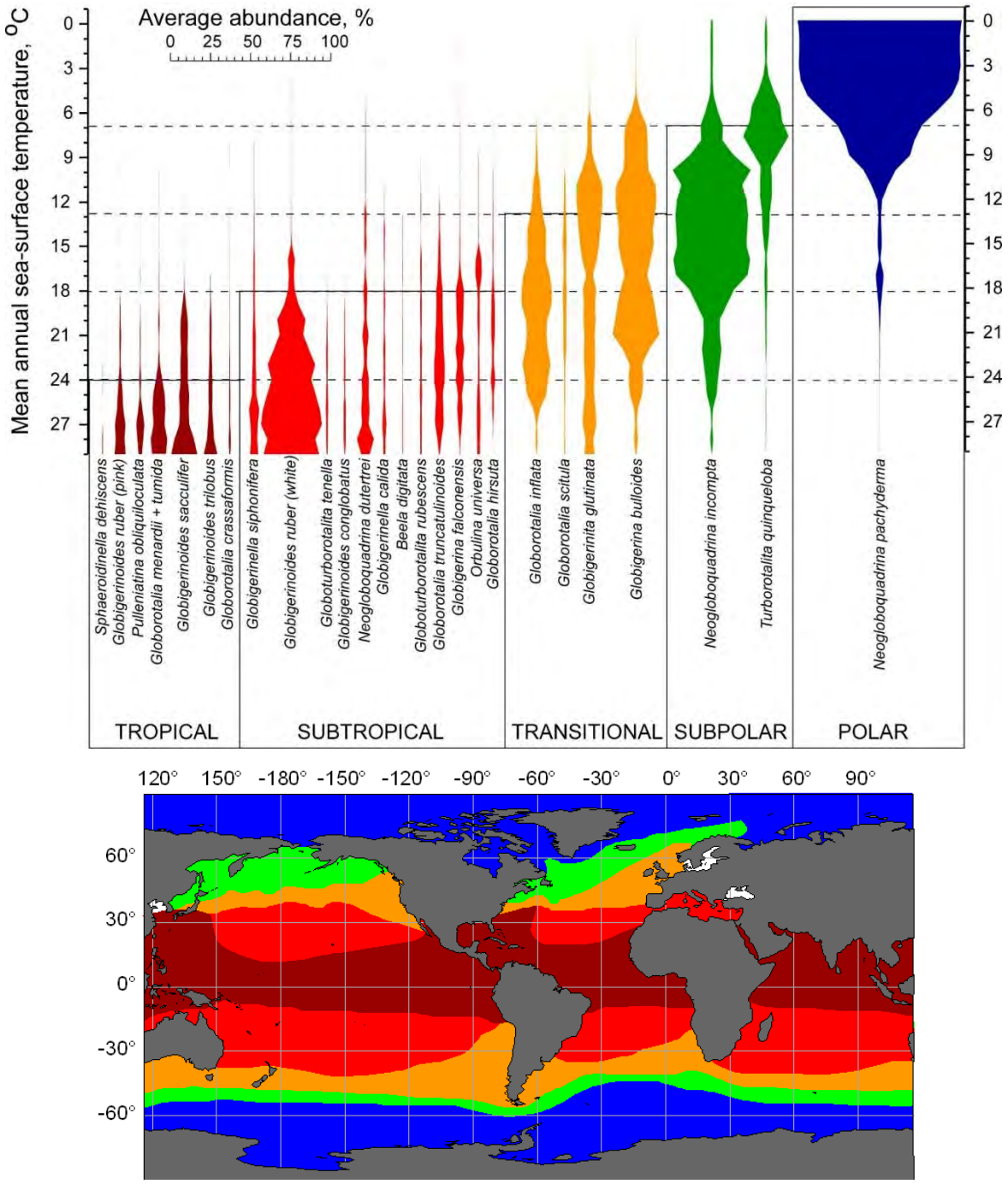

Figure 1-3: Foraminifera distributions across different oceans. From (Kucera, 2007). In the upper panel, the relative abundance of species is indicated by the width of the spindle. For example, Neogloboquadrina pachyderma is most abundant in waters with a cold average sea surface temperature (0-6˚C), whilst being mostly absent from warmer waters (12-18+ ˚C). Using the abundance of species the biogeographic regions can be mapped out (lower panel). Polar waters (blue) are indicated by a high abundance of Neogloboquadrina pachyderma. with only small percentages of Neogloboquadrina incompta, and Turborotalita quinqueliba. As can be seen different species are present in different abundances for subpolar (green), transitional (yellow), subtropical (light red) and tropical (dark red).

Furthermore, foraminifera account for 23-56% of the world's production of carbonate (CO_3, Schiebel, 2002) and transport the inorganic carbon out of the biological pump, to the deep ocean as part of the inorganic carbon cycle, the understanding of which is important for models of climate change (Passow and Carlson, 2012). As mentioned above the constant deposition of foraminifera tests provides a near complete record of various species and the changes in morphologies across time (Malmgren and Kennett, 1981). This makes foraminifera an excellent organism to study

evolutionary trends such as Cope's Rule (a general increase in body size over evolutionary time, Arnold *et al*. 1995; Schmidt *et al*. 2006), and speciation (e.g.: Arnold, 1983).

1.3 Planktonic foraminifera systematics

The first detailed descriptions of foraminifera were made by Leeuwenhoek, who drew them in sufficient detail that the species can be identified (Hemleben, Spindler and Anderson, 1989), but there are reports from the 17th century of the small foraminiferal tests being found in sands (Hemleben, Spindler and Anderson, 1989). Foraminifera were initially classified along with cephalopods (D'Orbigny, 1826), largely due the resemblance to *Nautilus* species that many benthic foraminifera show. Later attempts to classify foraminifera were based on the shell morphology and arrangement of chambers; this provides a useful guide to morphospecies to this day (Spezzaferri *et al.*, 2015). From the 1920s onwards, Cushman (Cushman, 1928) made huge changes to the classification of foraminifera, expanding on the classification of Brady (based on the findings of H.M.S Challenger expedition 1873 – 1876, Brady, 1884), from around 10 families to 50 by 1948. Cushman's classification changes where based on Brady's but considered the geological and ecological histories of the foraminifera (Schiebel and Hemleben, 2017). More recently a number of foraminifera phylogenies have been published. Most recently, Aze *et al.* (2011) published a complete phylogeney of cenozoic macro-perforate foraminifera (although there have been minor taxonomic changes, Spezzaferri *et al*., 2015).

1.3.1 Foraminifera morphology

As touched on above, traditional descriptions of foraminifera genera are based on a number of test characteristics: shape, coiling mode, chamber shape, apertures (number, position, modifications), spine morphology and any additional ornamentation (Figure 1-4). Planktonic species do not exhibit all test shapes, chamber shapes and coiling modes known for foraminifera (Figure 1-4), as some morphologies are restricted to benthic genera.

One of the most noticeable morphological differences between planktonic species is the presence or absence of spines. In living specimens, the spines extend the size of the test considerably (at least 3 times the maximum diameter of the test, Schiebel & Hemleben, 2017) and act as a support structure for the fine net-like streams of cytoplasm called pseudo- and rhizo-podia. Species without spines (non-spinose) are generally herbivorous (Anderson *et al.*, 1979; Hemleben *et al.*, 1985), whereas species with spines (spinose) are carnivorous. Spinose species often have symbiont algae, (Figure 1-5, Schiebel & Hemleben, 2017), which extend out via rhizopodial streaming during light periods and are retracted into the test during dark periods (Hemleben *et al.*, 1977). After the foraminifera dies or undergoes gametogenesis, the spines are either re-absorbed or fall off (B. K. Sen Gupta (ed.) , 2002). As such, most foraminifera in the sediment lack spines. The loss is increased by the dissolution (dissolving) of the spines. Dissolution occurs at different rates over different depths, dependent on the saturation of the water (Bostock *et al*., 2011). At lower depths the water

is undersaturated and so calcium carbonate dissolves into the water (Figure 1-7, Broecker and Peng, 1982, Bostock *et al*., 2011), causing damage to the tests of foraminifera, although the amount of dissolution is dependent on species (Berger, 1970; Bostock *et al.*, 2011). This could lead to bias sediments on the ocean floor as smaller, thinner-walled, spinose species dissolve and the larger, thicker-walled, non-spinose species remain (Nguyen, Petrizzo and Speijer, 2009).

Foraminifera build their test from secreted calcium carbonate (B. K. Sen Gupta (ed.) , 2002) and generally the growth pattern results in a spiral shape of the test, although there are a few exceptions to this in benthic species (e.g.: bi-serial growth). The direction of the spiral can be either sinistral (left-hand coiling) or dextral (right-hand coiling). Most species exhibit a preferred coiling direction (e.g.: the neogloboquadrinid clade, Darling *et al*., 2006) but, in some species, there is variation (Thiede, 1971). This variation appears to be under genetic control, for example, *Neogloboquadrina pachyderma* was thought to have two coiling modes which evolved from one another over several million years (Darling *et al.*, 2004), but this has now been identified to genetic differences and these are now referred to as two separate species (dextral coiling species is now called *N. incompta*, Darling *et al*. 2006). In some species (e.g.: *G. truncatulinoides*) the predominant coiling direction changes over time and had been linked with climate or environmental changes (e.g.: Ericson *et al*., 1954), but again these differences have now been found to be the result of genetic variation (Ujiié *et al.*, 2010).

In addition to coiling direction, the angle between the chambers affects the overall shape of the test. This angle is determined during the growth of the test. When the angle between the chambers is zero or very low the test is said to be planispiral (i.e. the spiral is in a single plane). Species with higher angles between chambers are described as trochospiral, supplementary descriptors can be added, for example: 'low' or 'high' trochospiral. Morphological features used to classify of all foraminifera (including benthic species) can be seen in Figure 1-4. As well as the coiling modes, the shape of the chamber can affect the overall shape. Some species have radially elongated chambers, resulting in an digitate morphology (e.g.: Figure 1-4, Shapes of Chambers, #10), whilst other species (e.g.: *G. truncatolinoides*) have angular conical chambers (e.g.: Figure 1-4, Shapes of Chambers, #9), this gives the species an overall cone-like shape.

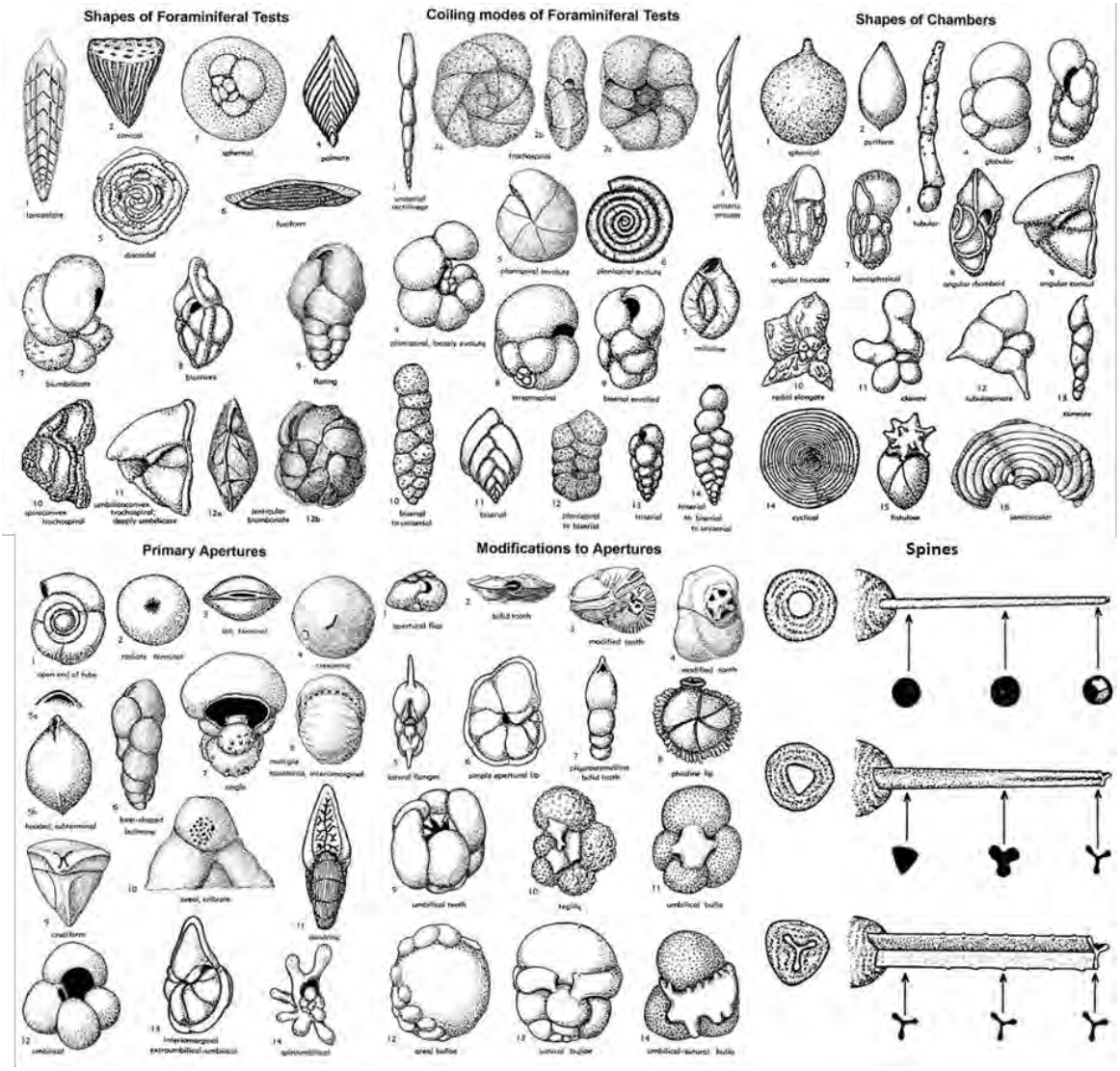

Figure 1-4: The characters traditionally used to classify foraminifera (both planktonic and benethic) genera. Images courtesy of M. Kaminiski.

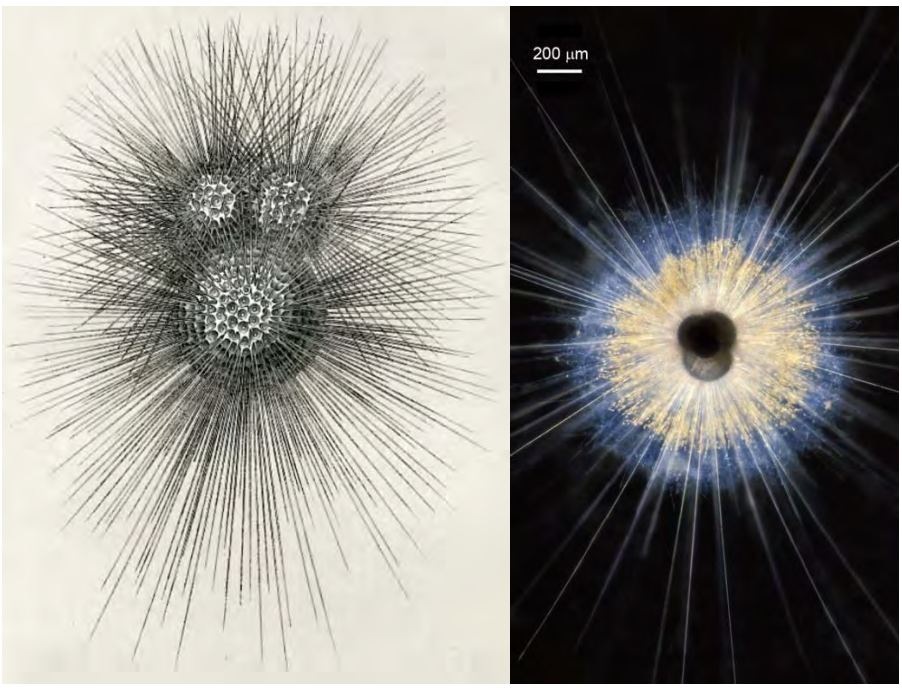

Figure 1-5: Left, Globigerina bulloides*, illustrating the size of the spines drawn by H.B. Brady, 1884. Right: a living specimen of* Globigerinoides ruber*. The test can be seen as the dark central area, the golden dots on the pseudopodia are symbionts which are extended out of the test during the day, whilst the whiteish cloud is the network of rhizopodia. Photograph by H. J. Spero (used with permission).*

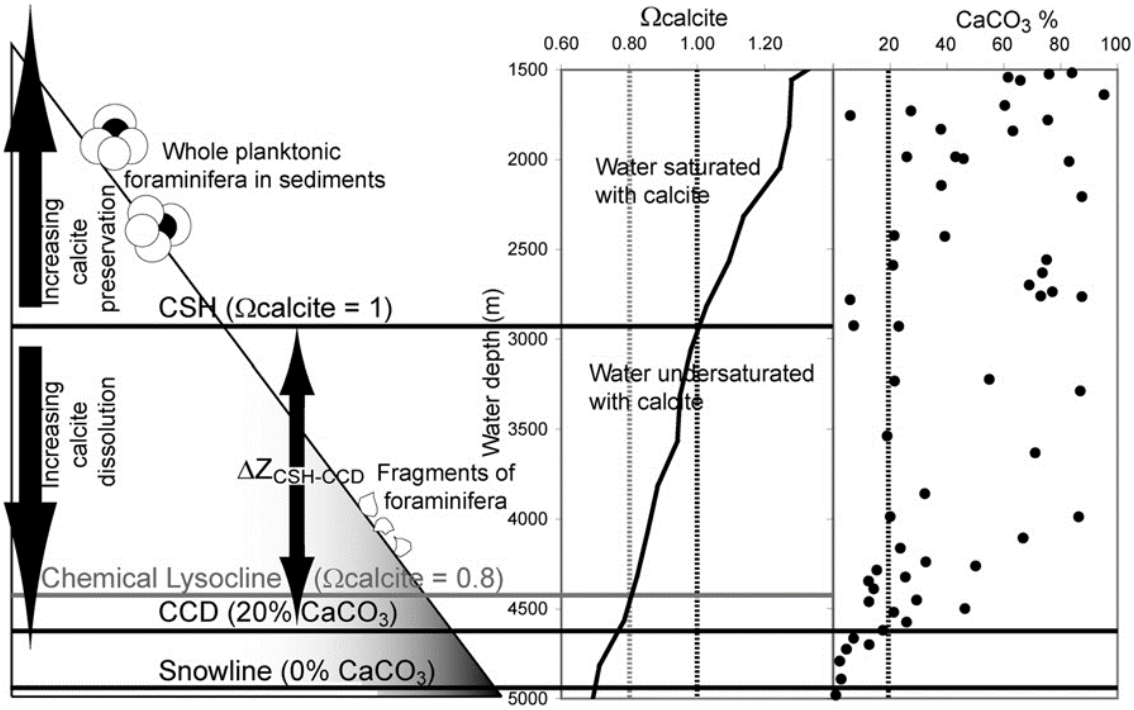

Figure 1-6: A simplified diagram illustrating the change in calcite concentration with depth. From Bostock et al. (2011).

There are general trends within the evolution of foraminifera, where certain morphologies or morphological characteristics repeatedly evolve (Figure 1-7, Cifelli, 1969; Norris, 1991b). One of these characters is the presence of a keel, a thickened ridge of calcite along the test edge (as seen in Figure 1-7). Whether the keel serves a biological purpose is unclear, with some authors suggesting keels help species migrate to, and maintain, specific depths (Hodell and Vayavananda, 1993; Norris, Corfield and Cartlidge, 1993). Coupled to this theory is the observation that foraminifera migrate to different depths during their life cycles (Fairbanks and Wiebe, 1980; Fairbanks *et al.*, 1980).

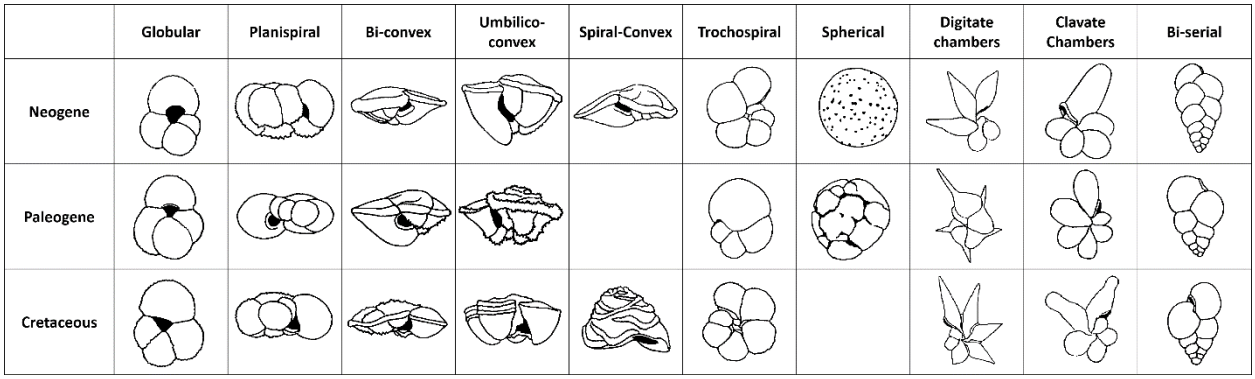

Figure 1-7: Re-occurring morphologies of planktonic foraminifera. Some morphologies are not present in certain time zones, marked as absent. Keels are present in bi-convex, umbilico-convex and spiral-convex morphologies. Adapted from (Norris, 1991a).

Indeed, the apparent relationship between the ocean's physical properties (e.g.: changes in density linked to changes in SST) and foraminifera test morphology has led to a number of hypotheses that changes in morphology are used to help maintain optimal position within the water column. These changes include: decreasing number of chambers, reduction and loss of keels, changes in aperture size and shape (Malmgren and Kennett, 1981), gaining of keels (Norris, Corfield and Cartlidge, 1993), increases in test size (Malmgren and Kennett, 1981; Wei, 1994) and how conical the test is

(Schneider and Kennett, 1999). All of these changes are hypothesised to alter the overall density of the test and some changes in morphology are linked to changes in depth (as measured by ^{18}O isotopes). Caromel *et al.* (Caromel *et al.*, 2014) tested these hypotheses with computer modelling, and found that flatter morphologies would be advantageous for species that inhabit deep, calm waters, where the lower temperatures would reduce their sinking velocity. As their findings are the opposite of what is seen in nature, they suggest that species which are non-spherical are not able to maintain a preferred orientation in the turbulent waters of the upper ocean, therefore natural selection favours for more spherical species. This could explain some of the ontogenetic changes in shape as species change depth during their life span, moving from deeper calmer waters to high more turbulent waters and *vice versa*. However, it should be noted that the gross morphology of the foraminiferal test may also serve some biological function. Tests that have elongate chambers could have higher prey encounter rates than other species (Coxall *et al.*, 2007). Whilst there are no known specific predators of planktonic foraminifera, some test morphologies (i.e. biconvex, keeled and conical forms) are significantly more resistant to crushing than others (i.e. spherical, Burke & Hull, 2017).

The cause of their morphological diversity is largely unexplained. In the fossil record there are three major diversifications of planktonic foraminifera: their origination in the mid-Jurassic; and following both the Cretaceous-Paleogene, and Eocene-Oligocene boundary extinction events (Leckie, 2009). During each of these events, the evolutionary paths taken appear similar as foraminifera follow similar *Bauplans* (Figure 1-8, Norris, 1991a). This apparent restriction to specific *Bauplans* suggests that there is either an inherent limitation of evolution, or a selective advantage to these forms (or a combination of both).

1.3.2 Naming

There is some debate over suitable terminology for foraminifera. Some authors prefer the use of foraminifer for the singular, reserving foraminifera (with some using foraminifers) for the plural; whereas others use foraminifera in both instances. In addition to these, there are other terms that appear in the literature such as foraminiferid (e.g.: Chapter One in Banner and Lord, eds., 1982). Furthermore, foraminiferal is sometimes used to denote items belonging to a foraminifera, e.g.: a foraminiferal test. The whole debate is given excellent coverage in Lipps, Finger and Walker (Lipps, Finger and Walker, 2011). Following their (Lipps, Finger and Walker, 2011) advice, foraminifera is used throughout this text.

Aside from the use of foraminifera, there is debate over the use of planktonic vs planktic, dependent on how the Greek derived words have been translated to English (Rodhe, 1974; Martinsson, 1979). Both terms are used in the literature, for both foraminifera and other organisms. Whilst this is a hotly debated topic in the literature, planktonic is used here by personal preference.

1.4 Current understanding of sinking velocity

Research incorporating the sinking velocity of foraminifera (e.g.: climate change models, understanding how accurate the fossil record is) have thus used only estimates from these 14 species. Of particular interest for climate predictions is calculating the flux of tests reaching the ocean floor (Schiebel, 2002; Jonkers *et al.*, 2015). Studies such as Schiebel (Schiebel, 2002) use species-specific sinking velocities and sinking velocities for a generalised size fraction as inputs to their calculations. Furthermore, much of paleo-oceanographic reconstruction relies on the idea that the species found on the ocean floor lived in the water column directly above. Van Sebille *et al*. (Van Sebille *et al.*, 2015) used estimates of sinking velocities to determine the drift of planktonic foraminifera. Van Sebille *et al*. (2015) found that drift of foraminifera is minimal during sinking, so the assemblages on the ocean floor will reflect those in the surface waters. Despite these findings, Van Sebille *et al*. also state that "A vital prerequisite to this application [using assemblages to understand paleoclimate], however, is a better understanding and quantification of the organism's ecology, including species-specific lifespans, depth habitats, calcification rates and sinking speeds" (van Sebille *et al*., 2015, page 5).

Thus, there is a disjunct between the existence of 30-40 extant morphospecies (and the 600+ in the fossil record (Aze *et al.*, 2011) and the 14 species for which sinking velocities have been measured. In addition, foraminifera fall within a Reynolds number (Re) range that makes theoretical predictions of their sinking velocities particularly difficult (see Chapter 4). Many phytoplankton which sink to the ocean floor, such as diatoms, are small enough (when sinking individually) for their sinking velocities to be predicted using established hydrodynamic theory (Stokes' Law, see Chapter 3), but the theoretical predictions are limited by the size (as an effect of Reynolds number) of the organism. Applying Stokes' Law to larger cells such as foraminifera results in increasingly inaccurate predictions that are overestimated with increasing size (Boggs, 2006). For this work, the sinking of dead (i.e. only the empty test) foraminifera will be modelled. This allows modelling of the empty test which is assumed to be the state which most adult tests are (having undergone reproduction, see above). It should be noted that as foraminifera grow, they will transition from low Reynolds number conditions, to intermediate Reynolds numbers at the full adult test size (see Table 1-1 for some size variations, sizes below ~100µm are likely to experience low Reynolds number conditions (i.e. laminar flow).

Furthermore, this study will not aim to model the living test, i.e. with spines and cytoplasm intact. The density of cytoplasm, both of foraminifera and cells in general, is not reported in the literature. As such, it is not possible to include cytoplasm in the modelling of the test. Inclusion of spines presents a technical difficulty due to the extremely small diameter of spines (~2 µm), this makes it difficult to visualise using micro-computed-tomography (see Chapter 4). If the spines are able to be

visualised, then 3D printing the spines would be extremely challenging even at the increased sizes which will be used in this study (see Chapter 4).

1.5 What is shape and how is it measured?

As this study aims to link sinking velocity with shape, it is important that shape is quantified in a meaningful way. Firstly, what is shape? Shape is the external form, contours or outline of an object (Oxford University Press, 2018). More explicitly, shape can be defined as the spatial relationships in three dimensions amongst the infinite geometric points of which an object is comprised, excluding size (Zelditch *et al.*, 2004). These relationships between points are such that they are maintained through rotation, translation or size changes of the object.

Understanding the shape of an organism (or parts of an organism) informs us of its function. Basic descriptions of shape can be made, e.g.: a bacterium might be spherical or reniform, while a phytoplankter might be cylindrical. However, whilst these are useful descriptions, for shapes to be effectively compared they must be quantified.

Quantifying and studying shape, which are the goals of morphometrics, has traditionally been achieved using measurements, such as lengths, ratios of lengths, or angles (Zelditch *et al.*, 2004). These measurements are taken between points, some of which can be anatomical (e.g.: the point where three sutures converge), or geometrically defined, e.g.: an object's widest point. Taking measurements between points results in large datasets. For example, working in 2D using 16 points yields a total of 120 measurements (Figure 1-8). This results in a dataset so large that to perform statistics with any meaningful results, a large number of replicates would be needed (i.e. many individuals would need to be measured, Zelditch *et al*., 2004). Ideally, the number of measurements should be reduced. To perform the reduction, a preliminary analysis of shape must be conducted; which would allow the statistically non-significant measurements to be identified for removal. However, this could still result in the loss of some information.

D'Arcy Thompson's "On Growth and Form" (Thompson, 1917) (specifically Chapter 17) explored how mathematical transformations could reproduce differences in shape between species (Figure 1-9). This is a key early example of using mathematical concepts to show variation in shape between organisms.

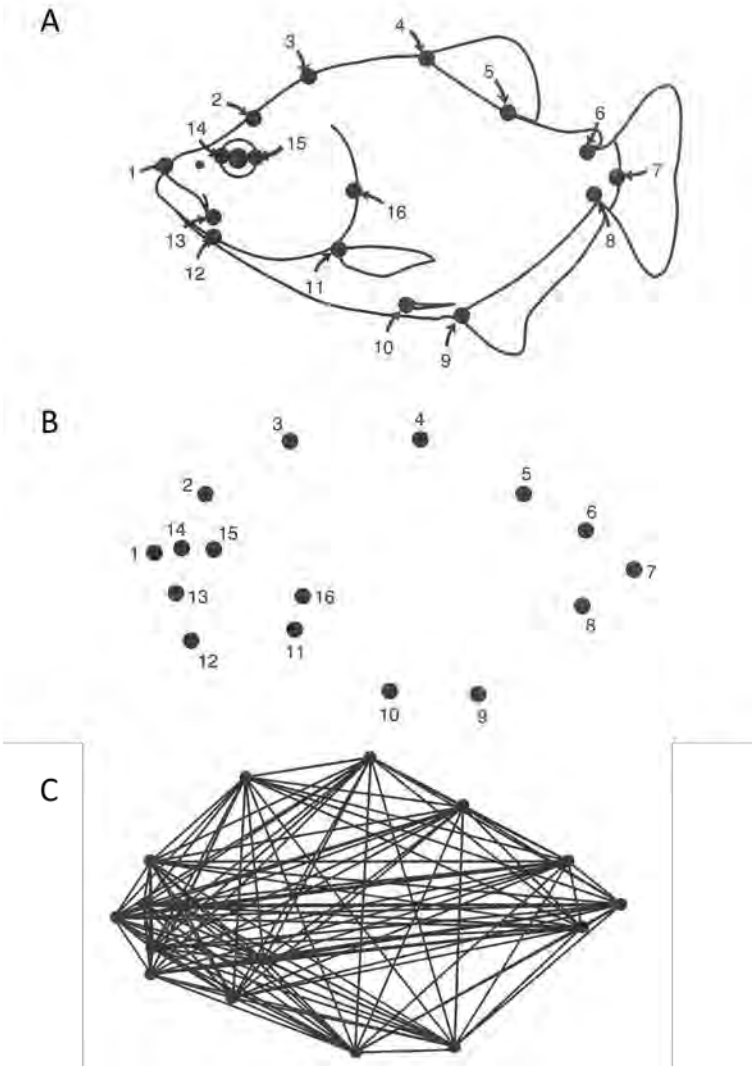

Figure 1-8: An example of landmarks on a teleost showing well-defined endpoints of measurements (A), the points themselves (B, which could be used as landmarks) and (C) the 120 measurements which could be used as linear measurements. From Zelditch et al. (2004).

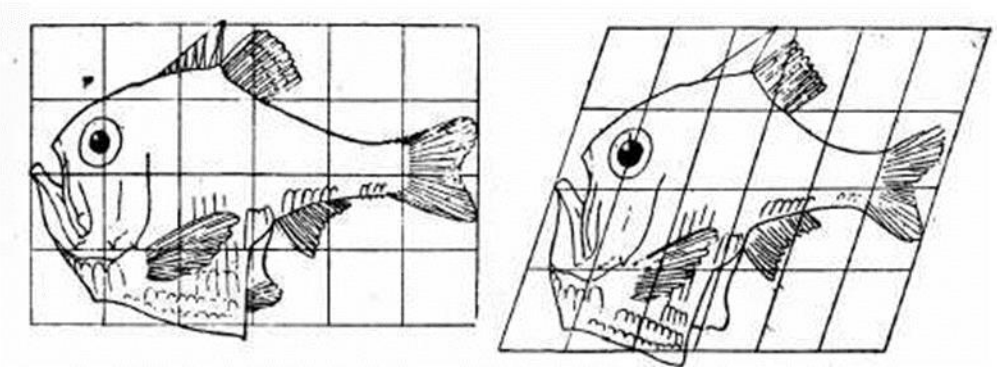

Figure 1-9: D'Arcy Thompson's transformation of Argyropelecus olfersi (left) into Sternoptyx diaphana (right). This is achieved by a mathematical transform (inclining the vertical axes at 70˚, as opposed to 90˚ on the left) applied across the whole grid system.

Advances in morphometrics (influenced by D'Arcy Thompson, (MacLeod, 2012)) have led to the development of new shape quantification methods, based upon mathematical principles. Many of these developments were originally published using planktonic foraminifera as examples. Different methods of shape quantification will be explored in Chapter 5.

1.6 Thesis summary

In Chapter 2, as a primer to the methods used in experimental chapters, the current applications of 3D printing in Ecology and Evolution are explored. By taking examples from a wide range of Ecological and Evolutionary studies, the advantages and pitfalls of this relatively novel technology are highlighted., Such as producing accurate models of organisms and organs for teaching and research, to producing mock-up experimental apparatus and laboratory equipment. This chapter demonstrates how 3D printing can be beneficial to ecological and evolutionary studies, such as this thesis.

Chapter 3 discusses our current understanding of factors controlling sinking velocities. Publications from the last ~125 years on the sinking velocities of planktonic foraminifera are reviewed and from these publications a dataset of 645 individual foraminifera, from 14 species, is generated. Using these data, the previous theories on which factors control sinking velocities are re-examined using linear models and simple measures of shape. Finally, comparisons between the sinking velocities of foraminifera and other plankton groups are made.

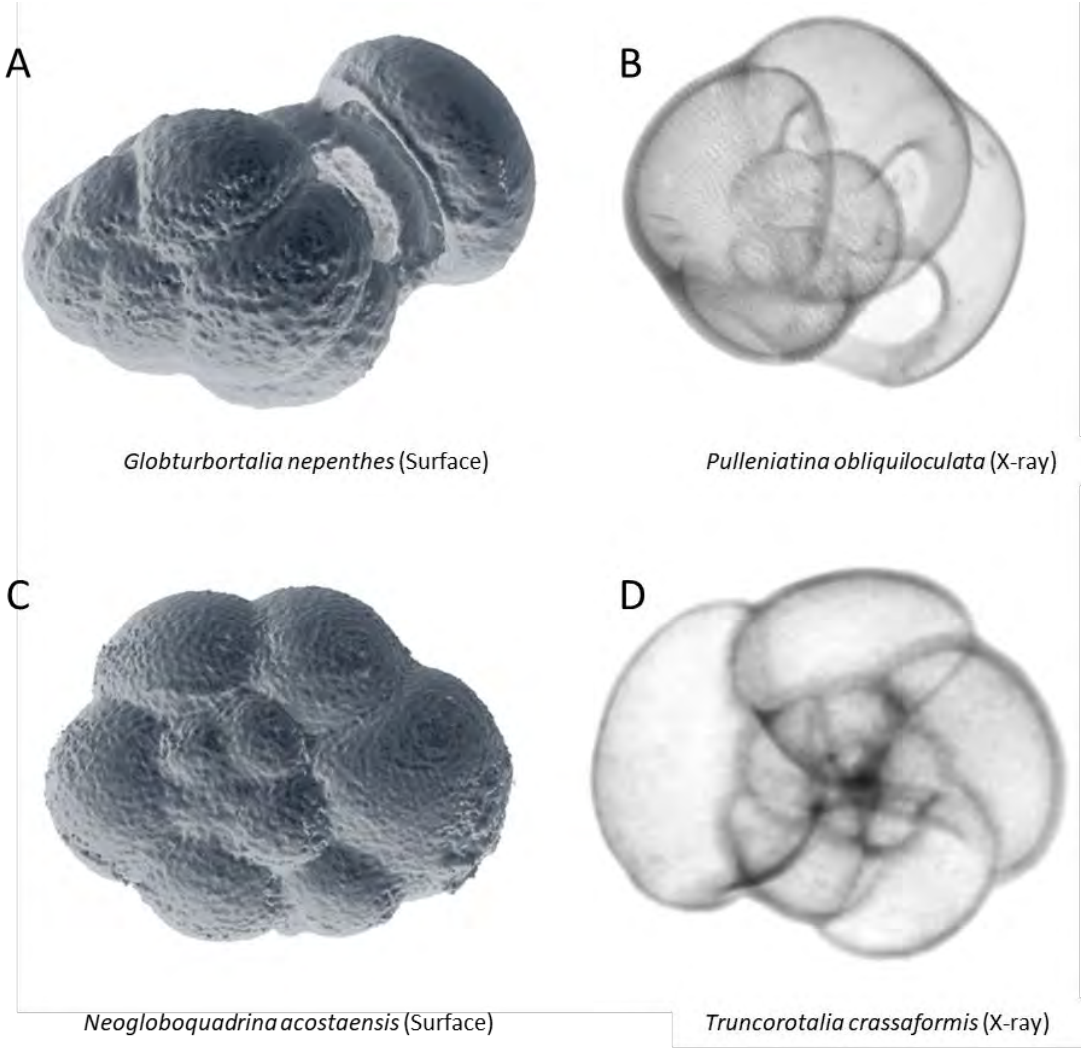

Figure 1-10: Some examples of the digital models of foraminifera from the eForam Stock (Tohoko University, Japan). Two examples have their surfaces rendered (A and C, labelled surface) and two are presented as X-ray views (B and D, labelled X-ray) showing the internal chambers. The specimens are scanned at a resolution of 2µm.

In Chapter 4 the development of a novel method used to determine the sinking velocities of 32 species of planktonic foraminifera, and the results from these experiments, are presented. The new method uses accurate 3D printed scale models to examine the sinking rates of planktonic foraminifera. The 3D printed models are based on micro-computer-tomography (µ-CT) images and synchrotron radiation x-ray imaging. The µ-CT data were obtained from eForam Stock, a digital resource provided by Tohoko University, Japan (e.g.: Figure 1-10). Synchrotron radiation x-ray images were obtained at the PETRA III synchrotron storage ring at DESY, Germany courtesy of A. Blanke. Using scale models permits sinking orientation to be easily measured and, using digital models, the functional surface area and test wall volume can be accurately measured in a manner not possible using real foraminifera tests. Based on our current understanding (summarised in Chapter 4) it is predicted that foraminifera with rounder test shapes will sink faster than those with flatter shapes. As a part of this method development, a new measure to allow predictions of sinking velocities within the intermediate Reynolds number range is developed.

Chapter 5 focuses on the quantification of test shape. Previous studies used linear measurements as a proxy for shape, and while these basic measurements give a general idea of the overall shape they lack specific details and are not always specific to differently shaped tests. Here, size-independent methods (Geometric Morphometrics and Elliptical Fourier Analysis) are used to improve on existing studies. To better capture shape variation, shape quantification is conducted from two different 2D orientations: the orientation used in the literature for identification of species, and the orientation in which each foraminifera sinks. From these two orientations, orthogonal views are taken and used for shape quantification. Using two viewpoints allows the shape of the foraminifera to be quantified in 3D, using 2D techniques. Geometric Morphometrics and Elliptical Fourier Analysis both quantify shape whilst removing the effect of size, allowing the aspects of size and shape to be separated.

Chapter 6 builds on the results from Chapters 3, 4 and 5, where statistics, which account for phylogeny, are used to link test shape and sinking speed of planktonic foraminifera. The combined dataset from Chapter 3 is re-examined within a phylogenetic statistical framework. This reanalysis accounts for the impact of shared ancestry on sinking speed to provide a better understanding of the interaction between this shared history and the physical variables influencing sinking speed. The data from Chapters 4 and 5 and then subjected to similar analyses. In addition, ancestral states are predicted for the foraminifera used in the study, providing an estimation of what the (hypothetical) ancestor to all the species used in this study looked like and how rapidly it may have sunk.

Chapter 7 will evaluate the findings of the preceding chapters, looking forward to how the results may affect the larger scientific community and suggesting the steps needed to further improve the understanding of sinking planktonic organisms.

Chapter 2 3D printing: Applications in Evolution and Ecology

2.1 Preface

The contents of this chapter have been published in Wiley's Ecology and Evolution (DOI: 10.1002/ece3.5050). The paper was conceived, researched and written by Matthew Walker, Stuart Humphries aided with the writing. Here the applications of 3D printing with Ecology and Evolution are explored, as the technique will be used in Chapter 4 for the creation of scale models of foraminifera.

2.2 Abstract

In the commercial and medical sectors, 3D printing is delivering on its promise to enable a revolution. However, in the fields of Ecology and Evolution we are only on the brink of embracing the advantages that 3D printing can offer. Here we discuss examples where the process has enabled researchers to develop new techniques, work with novel species, and to enhance the impact of outreach activities. Our aim is to showcase the potential that 3D printing offers in terms of improved experimental techniques, greater flexibility, reduced costs and promoting open science, whilst also discussing its limitations. By taking a general overview of studies using the technique from fields across the broad range of Ecology and Evolution, we show the flexibility of 3D printing technology and aim to inspire the next generation of discoveries.

2.3 Introduction

Studies of ecology and evolution often use equipment which has been made by the investigators, for a diverse range of applications and exhibits a high level of creativity. 3D printing offers an opportunity to produce equipment which can be shared with the scientific community, allowing other investigators to replicate studies with more accuracy than before, strengthening the open science movement (Pearce, 2013; Baden *et al.*, 2015). Furthermore, 3D printing offers timesaving over traditional manufacturing methods, as the process is largely automated. As well as simple models, 3D printing makes it possible to generate complex morphologies accurately, produce laboratory equipment and generate models for teaching and outreach. 3D printing also removes ethical concerns over using live animals for experimental manipulation.

Previous studies that have used models in one form or another, could be improved using 3D printing (e.g. in Fraisse *et al*. 2015). Many studies might simply benefit from the increased consistency of the technique, reduction in costs, and ease of production. For some studies, 3D printing would offer the opportunity to conduct the research using more life-like models, which may elicit more appropriate responses from the organisms involved.

The technique of 3D printing encompasses a range of manufacturing methods (see Table 2-1, Box 2-1 for an introduction and Figure 2-1 for a generalised workflow), which may be referred to as rapid prototyping, desktop-, additive-, or rapid-manufacturing. Originating with stereolithography

(SLA) using a specific photosensitive polymer (Wong and Hernandez, 2012), the technology now allows printing with a variety of materials with diverse properties (Berman 2012, see Table 2-1), including soft, flexible materials (Abdollahi *et al.*, 2018). Each 3D printing method has its own advantages and disadvantages (see Table 2-1), but overall the technique offers a method of creating objects in a way that is more like organic growth than traditional 'subtractive' methods. Rather than removing material to create an object, 3D printing builds layers up by adding material as a series of thin slices (Wong and Hernandez, 2012).

In many fields 3D printing is an established methodology. In medicine it has been used for almost 20 years to make surgical guides used to plan surgery (D'Urso *et al.*, 1999; Cohen *et al.*, 2009; Rengier *et al.*, 2010; Gerstle *et al.*, 2014). Technological developments now allow 3D printing of metals (Murr *et al.*, 2012), permitting prosthetics to be custom-made for the patient (Sing *et al.*, 2016). 3D printing is used in microbiology (Connell *et al.*, 2013), tissue culture, and the development of replacement (Duan *et al.*, 2013), and bionic (Mannoor *et al.*, 2013) organs. In all of these areas the technique has led to the development of new methods (D'Urso *et al.*, 1999; Herbert *et al.*, 2005; Cohen *et al.*, 2009; Ebert *et al.*, 2009; Rengier *et al.*, 2010; Connell *et al.*, 2013; Duan *et al.*, 2013; Mannoor *et al.*, 2013). With falling costs (Hoy, 2013) 3D printing has also become more common in Science and Engineering and, with falling costs its use is rapidly expanding.

There are also many instances where standard equipment does not meet the needs of the investigators (Lücking *et al.*, 2015). However, with some knowledge of CAD software, many bespoke items can be designed and printed in-house. Furthermore, the files can be easily sent to collaborators or included with publications. For example, microfluidic devices are commonly used for a range of experiments involving processes such as bacterial chemotaxis (Ahmed, Shimizu and Stocker, 2010), pollution monitoring, clinical diagnosis, drug discovery, and biohazard detection (Holmes and Gawad, 2010; Yazdi *et al.*, 2016). Where printing resolution allows, the use of 3D printing to create either moulds for Poly-dimethyl-siloxane (PDMS) chambers or to directly print the chambers is becoming increasingly popular (Bonyár *et al.*, 2010; Kitson *et al.*, 2012; Lee *et al.*, 2014; Ho *et al.*, 2015; Kamei *et al.*, 2015; Yazdi *et al.*, 2016) over the time-consuming and often expensive process of creating a mould using traditional techniques (Waldbaur *et al.*, 2011). The ability to quickly produce and test designs using the 3D printing process is also highly valuable, especially where new devices need to be developed.

3D printing can also significantly reduce the cost of standard lab equipment (e.g. lab jacks, retort stands, Eppendorf pipettes, and equipment holders), by up to 97% compared to vendors pricing (Zhang *et al.*, 2013). Despite the high initial cost of a 3D printer, the cost per unit in materials is low (Waldbaur *et al.*, 2011; Kitson *et al.*, 2012). In addition to financial benefits, time savings can be dramatic. Electronic files containing all the information needed to 3D print equipment can be obtained from a number of online sources (Baden, Chagas, G. J. Gage, *et al*. 2015; Willermet 2016,

as used by Brandley *et al*. 2016) and printed immediately. Thus, even with next day shipping from equipment vendors, downloading and 3D printing is far faster (Zhang *et al.*, 2013). As hardware reduces in cost 3D printing becomes accessible to individuals and small laboratory groups (Hoy, 2013). Additionally, there are now a number of commercial print-on-demand 3D printing companies, allowing researchers with more limited budgets to obtain printed models without the cost of buying hardware (e.g.: McDougal & Shepherd 2015).

Another blossoming application is the use of 3D models in teaching and learning, a key part of encouraging the next generation of scientists and engaging the public with research. Students with visual impairment, and members of the public can explore both large (Larkin, personal communication) and microscopic fossils (Teshima *et al.*, 2010; Rahman, Adcock and Garwood, 2012; Kaplan and Pyayt, 2015) which can be scaled to be easily held. This approach has been used to enable those with visual impairment to learn about microscopic planktonic organisms (Teshima *et al.*, 2010), as well as cells undergoing mitosis, striated muscle cells, and neuromuscular junctions (Kolitsky, 2014). Such models could also be used by students who are unable to use microscopes due to motor impairment. Furthermore, to make complex microscopic features accessible bacteria, viruses, proteins, enzymes (Gardner and Olson, 2016), molecules (Bara *et al.*, 2015), Natural Killer cells (from high-resolution micrographs, (Mace, Moon and Orange, 2015), and neurons (McDougal and Shepherd, 2015) have all been 3D printed. Compared to digital models and textbooks, models of complex anatomical structures, such as the human heart (Kaplan and Pyayt, 2015) and horses' feet (Preece *et al.*, 2013), provide the opportunity for the learner to interact with the subject, permitting physical exploration of the structures.

This review focuses on the advances within Ecology and Evolution, and related fields, which have been driven by 3D printing. Examples of how 3D printing could be used are provided throughout, with the hope of inspiring the reader.

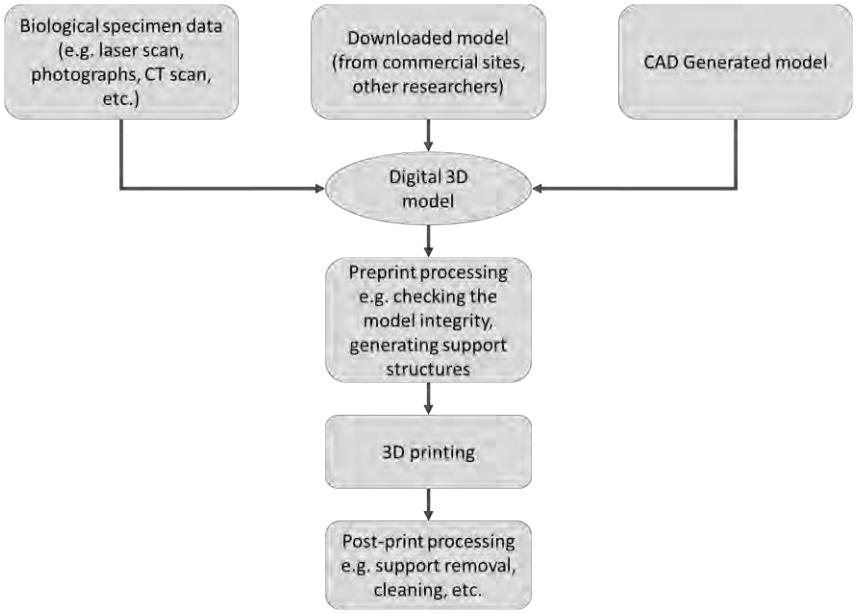

Figure 2-1: A generalised work flow of 3D printing. The digital model can be obtained from a biological specimen. If the model is laboratory equipment or does not need to be an exact replica of the structure of interest (e.g. Campos et al., 2015 see below) then the model can be generated using Computer Aided Design (CAD). Finally, either type of model (i.e. CAD or scan based) can be downloaded from commercial sites, collaborators or other researcher's publications.

Box 2-1: 3D printing: an introduction

Before 3D printing an object, the technique to be used needs to be chosen. Table 1 outlines some 3D printing methods and Table 2 outlines some costs and features of 3D printers. Important considerations include: the layer thickness; whether, if the object has cavities; and the minimum feature size required. For example, FFD 3D printers can print objects with cavities, but produce relatively thick layers and so the model will likely have a stepped appearance, especially on curved surfaces. SLA 3D printers have thinner layer thickness so curved surfaces are smoother, but they cannot create cavities. The first step of 3D printing is obtaining a digital model, this can be based on CT-scan, laser scan data, or it could be designed using a computer (Computer Aided Design, CAD). This model is digitally sectioned into thin layers, by the 3D printer software and these layers dictate the printer head's path. In the case of SLA the 'head' is a laser while, for FFD it is a nozzle extruding molten plastic filament. Once the 3D printer has produced the model there is often a level of post-print processing. The model may need to be cleaned in alcohol to remove excess resin in the case of SLA. Most 3D printers need a scaffold of material to support the model during printing, which needs to be removed after printing. In some cases, the support material is different from the final model (e.g. FFD) so can be dissolved, otherwise it needs to be cut (e.g. SLA). Powder based 3D printing technologies use the surrounding powder to support the model during printing. This means that the model will need to be removed and dusted, while, some powder-based models may need impregnating with binder (glue or similar) to solidify the object completely.

Table 2-1: A brief overview of 3D printing methods. Examples, from papers cited in the main text are provided to illustrate applications. Layer thicknesses are approximate as specific makes and models of 3D printers will vary. A guide of prices for different technology types can be found in Table 2-2.

Starting material		Method	Layer thickness (μm)	Method overview	Advantages	Disadvantages	Example of use in Ecology and Evolution
Solid	Plastic filament	Fused Filament Deposition (FFD)	300-1000	Plastic filament is melted and placed in layers by the print head.	Common plastics, such as ABS, can be used. Chemical properties retained.	Anisotropic (strength differs in Z-axis, to X-Y axis). Stepped surface, which lacks fine details.	Thermal ecology model lizards (Watson and Francis, 2015)
Powder	Metal	Laser melting	20-100	Thin layers of powder are spread over a bed which the laser selectively melts. Once solidified, a new layer of powder is spread.	>99% of the metal's density can be achieved, therefore good mechanical properties.	Expensive and slow, limited metals can be used, it is not suitable for reactive metals.	
		Electron beam	0.3-100	Powdered metals are selectively melted by electron beam in a vacuum.	As for Laser melting. Reactive metals (e.g. Titanium) can be used.	Expensive, slow and limited metals can be used.	
	Plastic Metal	Laser sintering	100-300	The laser selectively melts powdered plastics and the model is made in the powder bed.	Common plastics can be used. Cheap for small number of objects. Chemical properties of material are retained.	Poor surface finishes and tolerances are limited.	Ceramic filter holder (Lücking *et al.*, 2015)
	Any powder	Binder jetting	90-200	Powdered material is placed in layers over the build area and then glued together with a binding agent.	Any powdered material can be used. Relatively fast and cheap. Colour models are possible.	Produces fragile parts which need further treatment. Poor surface finish.	
Liquid	Photo-polymer	Stereolithography (SLA)	16-150	A laser selectively solidifies thin layers of photopolymer. The print bed moves down to allow a new layer of polymer to form.	Accurate with good surface finish that can capture fine details.	Expensive, and photopolymers are not stable long-term.	Model Neotropical bush-cricket (Jonsson *et al.*, 2017)
		Photopolymer jetting	16-500	Thin layers of photopolymer are jetted on to the build area. They are cured with UV light straight away.	Multiple materials can be used. Can be high precision.	Expensive and photopolymers are not stable long-term.	Models of black widow spiders (Brandley, Johnson and Johnsen, 2016) Mould for microfluidic devices (Kamei *et al.*, 2015)
	Wax	Material jetting	13-50	Inkjet printer heads drop hot wax on a bed, which cools and forms layers.	Accurate with good surface finish. Suitable for lost wax casting.	Slow process that produces fragile models.	Replicating delicate dinosaur bones (Bristowe *et al.*, 2004)

Table 2-2: A range of different 3D printers, their cost (as of February 2019) and features. Data from www.aniwaa.com, 3D printers with the highest customer rating for each technology were chosen. NS – not stated

Technology	Type	Manufacturer	Printer	Cost (USD)	Build Volume (mm)	Maximum Resolution (μm)	Connectivity
FFD	Desktop	Prusa Research	Original Prusa i3 MK3	$999	250 × 210 × 200	50	USB
	DIY/kit	Creality	Ender 5	$329	220 × 220 × 300	50	USB, SD card
	Desktop	Sindoh	3DWOX 1	$1499	210 × 200 × 195	50	USB, Ethernet, Wi-Fi
	Desktop	Qidi Tech	X-ONE 2	$279	140 × 140 × 140	50	NS
SLA	Desktop	ELEGOO	Mars	$349	120 × 68 × 155	50	USB
	Desktop	Photon	ANYCUBIC	$519	115 × 65 × 155	30	USB, SD card
	Professional	B9Creations	B9Creator v1.2	$4595	104 × 75 × 203	30	USB
	Professional	Formlabs	Form 2	$3499	145 × 145 × 175	30	USB, Ethernet, Wi-Fi
Binder Jetting	Industrial	3D systems	ProJet CJP 660Pro	$50000-$100000	254 × 381 × 203	10	Ethernet, Wi-Fi
Material Jetting	Industrial	Stratasys	Object Eden260VS	$50000-$100000	255 × 252 × 200	20	Ethernet
	Industrial	3D systems	ProJet 3500HD MAX	$50000-$100000	298 × 185 × 203	20	Ethernet, Wi-Fi
Powder binding	Industrial	EOS	P396	>$250000	340 × 340 × 600	60	Ethernet
	Industrial	EOS	Formiga P110	$100000-$250000	200 × 250 × 330	60	Ethernet

2.4 Evolution

2.4.1 Morphology and Colouration

Understanding both the inter- and intra-specific signals organisms convey to one another is a core aim for evolutionary, ecological and behavioural studies. Unpicking relationships between organisms and the signals that mediate them is often achieved through manipulative experiments (Krebs and Davies, 1993; Andersson, 1994). Here, 3D printed objects offer great benefit as they can be produced to specifications not possible with real organisms. An illustrative example is animal colouration. The communication of an individual's fitness through colouration is common, especially in males (Krebs and Davies, 1993; Andersson, 1994; Svensson and Wong, 2011). Testing the influence of colouration on mating success or other interactions is normally done through comparison between an individual's brightness and the rest of the population (Crothers and Cummings, 2015). However, this process is time consuming and may require the capture, and associated stress, of animals. Being able to produce 3D printed models of animals, that can be coloured to account for the species' visual system, allows direct manipulation of a visual signal, while maintaining (and controlling) morphology to encourage responses. This approach has been used to investigate the colouration of the poison frog*, Oophaga pumilio*, where brightness was found to be an indicator of more aggressive males (Crothers and Cummings, 2015). Similarly, Brandley *et al*. (Brandley, Johnson and Johnsen, 2016) investigated the evolution of the red 'hourglass' mark of the black widow spider (*Latrodectus spp.*), which is believed to be aposematic (a warning to deter predators). Hand-painted 3D printed models of the spiders received fewer

predation attempts when models exhibited the red hourglass marking (Brandley, Johnson and Johnsen, 2016).

While bright colouration is often considered an honest sexual signal, the presence of distinctive colours may result in high predation rates, reduced immune response and increased oxidative stress (Svensson and Wong, 2011), suggesting a trade-off between natural and sexual selection. For example, individuals in low risk environments are often more brightly coloured than those in high-risk environments (Endler and Jan, 1982). Heinen-Kay *et al*. (Heinen-Kay *et al.*, 2015) used 3D printing to investigate risk-moderated colouration in the Bahamas Mosquitofish (*Gambusia hubbsi*). In blue holes (large landlocked sinkholes) lacking predatory fish, male *G. hubbsi* have evolved a brighter orange colouration on their dorsal fin, compared to those in blue holes with predators. On the face of it the simplest method to investigate potential trade-offs would have been to translocate fish between blue holes, to observe the effect of colouration on mating success and predation. However, this is not only logistically challenging, but also ethically questionable. By using 3D printed models of males with and without colouration, the potential trade-off could be easily examined, and results indicated that signal diversity can be driven by the interaction of natural and sexual selection (Heinen-Kay *et al.*, 2015).

Another example is the colouration of brood-parasite eggs. Igic *et al* .(Igic *et al.*, 2015) used 3D printing to separate the effects of colouration on the rejection of brown-headed cowbird (*Molothrus ater*) eggs, by American robins (*Turdus migratius*). Igic *et al* .(2015) demonstrate how 3D printing can be used to remove human error when reproducing models that would otherwise have to be made by hand, whilst also allowing the flexibility for each batch of eggs to have a unique shape.

3D prints do not always need to be the final model - they can also be used to create a mould. This approach was used by Policha *et al*. (2016) to understand the visual and olfactory components of flower attraction. Silicone models from 3D printed moulds allowed the separation of visual and olfactory cues in the Dracula orchid (*Dracula lafleuri*). This species mimics mushrooms to attract flies, which then pollinate the plant. The authors used accurate scent-free silicone models (Figure 2d) to show that flies are attracted to both visual and olfactory cues, with a synergistic effect suggesting that it is driven by multimodal mimicry of the mushrooms by the plant (Policha *et al.*, 2016). Similarly, Campos *et al*. (Campos, Bradshaw and Daniel, 2015) used 3D printed flower analogues to investigate the effect of flower morphology on hawkmoth (*Manduca sexta*) feeding. Using flower mimics from a flat disk to a realistic trumpet shape (see Figure 2c), they found support for the theory that flower trumpets act as a mechanical guide, despite the printed 'flowers' lacking the colouration and flexural properties of the real flower (Campos, Bradshaw and Daniel, 2015). Both models produced for these studies would be difficult to fashion using traditional techniques,

and the studies show how CAD and 3D printing allow flexibility in design while facilitating the production of multiple identical units.

2.5 Biomechanics

Biomechanics allows researchers to link form to function, a key part of evolutionary biology. Here, 3D printing offers an opportunity to produce realistic models of whole or parts of organisms which can be used to test theories about shape and function of structures. As demonstrated by Policha *et al*. (2016) with the Dracula orchid, exploring organismal function with models using a reductionist approach, i.e. examining component parts, is often useful. Porter *et al*. (Porter *et al.*, 2015) produced 3D printed models to investigate the functional morphology of the seahorse (*Hippocampus spp.*) tail. Seahorses have a square cross-section tail, as opposed to the round cross-section tails which might be expected of fish. Hypothetical round cross-section tails were generated using CAD and compared to the square morphology of seahorse tails, which was obtained from CT scan data. To compare possible functional advantages of square cross-section tails Porter *et al*. (Porter *et al.*, 2015) then 3D printed both tail morphologies and subjected them to a series of tests. The authors found that square cross-section prototype tails (Figure 2-2f) performed better for grasping and are more resistant to crushing than round-section tails. Improved grasping ability of the square cross-section tail was likely an evolutionary advantage for seahorses, which use their tails to hold onto corals, algae and seagrasses (Porter *et al.*, 2015; Neutens *et al.*, 2016). By examining the tail in this way, Porter *et al*.'s work helps to explain some of the unusual morphology that seahorses have evolved.

In the neo-tropical bush cricket (*Acanthacara acuta*) the sound produced by the wings is amplified by an unusual extension of the pronotum (the dorsal covering of the thorax), which forms a chamber over the wings. To explore the function of this chamber, 3D printed models have been used to replicate the chamber, which is hypothesized to work as a Helmholtz resonator (Morris and Mason, 1995). By changing the material properties of the chamber (photopolymer resin in the 3D model, instead of insect cuticle), Jonsson *et al*. (Jonsson *et al.*, 2017) showed that the morphology of the structure alone is responsible for the amplification of sound. Surface texture can also be modelled well by 3D printing. In an examination of ice formation on surfaces, 3D printing was used to replicate surface textures of blue mussels, (*Mytilus edulis*), Antarctic sea urchin (*Sterechinus neumayeri*), and sub-polar butterclams (*Saxidomas nuttalli*) (Figure 2-2a).

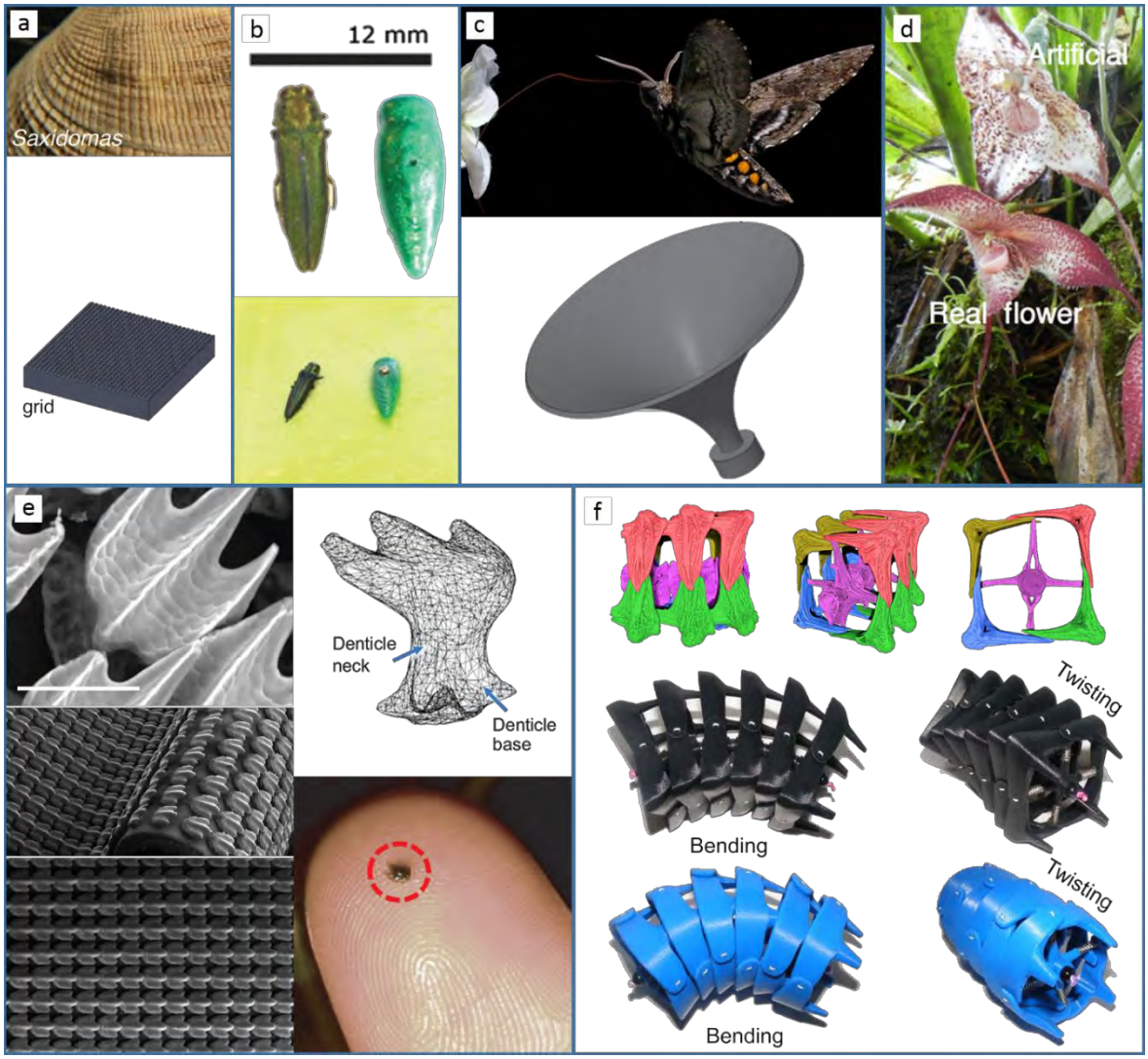

Figure 2-2: Examples of 3D printed objects from the studies described in the text.

a) *Top, Butterclam shell (*Saxidomas nuttalli*), and below textured 3D print replicating surface structure to test ice formation* (Mehrabani *et al.*, 2014). *Reproduced with permissions from PeerJ.*

b) *Left, a dead female Emerald Ash Borer (*Agrilus planipennis*) decoy used to bait traps and on the right a 3D printed model. Below, the real decoy and model mounted on a trap (Domingue et al. 2015). Reproduced with permissions from Journal of Pest Science.*

c) *) Top, a hawkmoth (*Manduca sexta*), using its proboscis to probe a flower, and below a CAD model of the 3D printed 'flowers' used by Campos et al.* (Campos, Bradshaw and Daniel, 2015). *Reproduced with permissions from Functional Ecology.*

d) *Flower of the Dracula Orchid (*Dracula lafleuri*) and silicone model used to separate visual and olfactory cues* (Policha *et al.*, 2016). *Reproduced with permissions from New Phytologist.*

e) *Top left, an Environmental Scanning Electron Microscope image of bonnethead shark (*Sphyrna tiburo*) skin. Scale bar 100µm. Top right, a digital model of a denticle. Bottom left, SEM images of 3D printed denticles embedded in membrane. Bottom Right, a single 3D printed denticle approximately 1.5mm in length* (Wen, Weaver and Lauder, 2014). *Reproduced with permissions from Journal of Experimental Biology.*

f) *Top, Micro-CT scan images of a seahorse (*Hippocampus spp.*) tail. Middle, a 3D printed model based on the micro-CT scan. Bottom, a 3D printed hypothetical tail structure. These models were used to assess how the square cross-section of the seahorse tail grips and resists crushing compared to the round cross-section* (Porter *et al.*, 2015). *Reproduced with permissions from Science.*

Mehrabani *et al*.(Mehrabani *et al.*, 2014) found that the ridges and bumps present on all tested surfaces reduced ice formation at -20°C, but the role of surface texture was limited to approximately 6%. Such 3D models have the advantage of having the same material properties, allowing only the variable under investigation to be modified.

Another use of 3D printing is to produce low cost, highly accurate objects for calibration. Many studies use cameras to record and facilitate later analysis, and cameras must be calibrated beforehand for measurement data to be meaningful. Koehler *et al*. (Koehler *et al.*, 2012) investigated deformation of dragonfly wings during flight to better understand the aerodynamics, structural dynamics, and control of the wing. By 3D printing their calibration rig (with a resolution of 25µm), the calibration points could be placed accurately, permitting the exacting calibration required for this study.

2.5.1 Fluid dynamics

Biological fluid dynamics is an area that is being changed dramatically with the use of 3D printing. The complex geometries of sponges and corals have been 3D printed to enable investigations of the fluid flow around organisms without the need to culture or remove them from their habitats (Kruszyński and Van Liere, 2009). 3D printed models could also be used to examine the flow of fluids through organisms, such as the machined steel models of sponges used by Vogel (1974), by offering more realistic and easily modified 3D models. Complex internal structures, e.g. sponge canals, or vertebrate nasal passages, can be replicated in clear plastics (or resins) for visualisation and Particle Image Velocimetry (PIV, Stamhuis 2006) can be used to quantify fluid flows to provide an understanding of form and function for both external and internal structures. In other instances, the size of an organism may present difficulties, both for the production of life-sized models and conducting research. Padisák *et al*. (Padisák *et al.*, 2003) used PVC-U and modelling material to create scaled-up models of microscopic planktonic organisms (real size 40 to 200µm, model sizes 5cm to 35cm) to investigate the effect of morphology on sinking rate. These construction methods resulted in greatly simplified models, much like Furbish and Arnold's (1997) use of beeswax and pins to produce models (2-6 cm) of foraminifera (real size ~150µm to 1200µm). As suggested by Fraisse *et al*. (Fraisse, Bormans and Lagadeuc, 2015), studies of microscopic plankton could be improved by using 3D printed, biologically realistic models, based on highly accurate CT or SEM images.

As well as enabling production of scaled models of microscopic structures, 3D printing can be used to recreate small structures whilst providing the opportunity to manipulate their shape. Shark skin has small tooth-like projections (denticles), which have been studied since the 1970s for applications in industry, as they are thought to reduce drag and have anti-fouling properties (Oeffner and Lauder, 2012; Pu, Li and Huang, 2016). Wen *et al*. (Wen, Weaver and Lauder, 2014) used 3D printed shark skin (Figure 2-2e) to examine water flow over denticles, finding that they reduce drag compared to a flat surface, leading to a predicted increase in swimming efficiency under certain conditions. In this instance, 3D printing allowed manipulation of the surface (i.e. denticle distribution and flexibility of the 'skin') and removed ethical issues of using real skin. Wen *et al*.'s (Wen, Weaver and Lauder, 2014) findings were echoed by Lauder *et al* .(Lauder *et al.*, 2016),

who also demonstrated the ability of 3D printing to accurately produce objects which are microscopic (10 by 15µm).

3D printed models can be used to test or ground-truth computational models and to perform experiments which would not be otherwise possible. An example is the re-creation of the airways of *Scincus scincus*. This species of skink spends its life below the sand, moving in a fish-like manner, hence its common name "sandfish lizard". Despite breathing whilst under the sand, Stadler *et al*. (Stadler *et al.*, 2016) found no evidence of sand inside dissected sections of the animals' airways. They theorised that the airways had morphological adaptations, possessing aerodynamic properties which limited sand ingress. To test this, Stadler *et al*. (Stadler *et al.*, 2016) used computational and 3D printed models. As the airways are small delicate structures they scaled the airways up (changing the working fluid to maintain the ratios of forces acting on the model) and used larger particles of sand. Whilst the 3D printed models were not able to fully recreate the inhalation and exhalation velocities seen *in vivo*, 50% of the tests resulted in no sand being present inside of the model airways, lending support to the computational models.

As evidenced above, 3D printing can be used to produce models that would simply not be possible using other methods. As we have seen 3D printing allows the production highly complex and detailed models that can be used for research. Printed models of extinct organisms, for example, can be used to measure efficiency of flight or swimming, helping us to understand behaviour and function of prehistoric creatures (e.g. swimming methods of plesiosaurs, Muscutt *et al*. 2017).

2.6 Paleobiology and Curation

Reproducing fossil material is traditionally achieved using moulds and casts (Hamilton Waters *et al.*, 1983), which often involves high temperatures (Benton and Walker, 1981) or chemicals (Spjeldnaes, 1963; Purnell, 2003), which can be harmful and may damage delicate specimens (Purnell, 2003; Bristowe *et al.*, 2004). In comparison, scanning and 3D printing of fossil material has far fewer risks. In an early example of 3D printing in this field Bristowe *et al*. (Bristowe *et al.*, 2004) created models of the thin bones of the dinosaur *Coelophysis rhodesiensis* to avoid damaging the fragile fossil. However, as the technology available at the time was limited to Fused Filament Deposition (FFD) 3D printing (Table 2-1) with paraffin wax, the prints were easily damaged. Such delicate paraffin wax bones could now be printed using alternative methods and materials to produce more robust models. In some instances, scanning and 3D printing has allowed non-destructive recreation of remains that only exist as cavities in a stone matrix, such as Clark *et al*.'s (2004) print of the negative space of a cavity to recreate the skull of a mammal-like reptile (dicynodont). Without Magnetic Resonance Imaging (MRI), there would be no way to visualise the complex skull from the inaccessible cavity, but from this scan 3D printing offers an opportunity to have a physical replica which can be held and observed.

Mitsopoulou *et al*. (Mitsopoulou *et al.*, 2015) used computational models and statistical methods to recreate missing bones from an incomplete skeleton of the extinct dwarf elephant (*Palaeoloxodon tiliensis*) using 3D printing. Another example is the Lapedo child's skull, which was broken into many pieces and had undergone taphonomic distortion in the 24,500 years since its burial (Almeida *et al.*, 2007). The skull was digitally reconstructed then 3D printed twice; one of the skulls was placed on display and the other used for facial reconstruction (Almeida *et al.*, 2007).

In the past, models have been a major point of interaction with both the public in museums and for teaching. These models are often expensive and can be fragile. 3D printed models are often robust and can be made in-house relatively quickly and cheaply. These models can be printed in colour, and dependent on the method a range of colours can be offered and prints can include multiple colours and transparent material (Begolo *et al.*, 2014; Sitthi-amorn *et al.*, 2015), so that internal details can be seen (Blackburn, 2017). These accurate models can be interactive, such as a model of a flint axe (Galvin, 2017), allowing people to understand more about an object (in this case how it was constructed).

Niven *et al*. (Niven *et al.*, 2009) envisaged the use of 3D printing as an opportunity for museum collections to expand the number of exhibits they hold by repairing skeletons, or by combining pieces of specimens already present in collections with 3D printed pieces. For example, the Quagga (*Equus quagga quagga*) skeleton on display in the Grant Museum of Zoology (University College London) has a 3D printed left leg replacing a missing limb, created by CT scanning the right leg and mirroring the data (Larkin and Porro, 2016). This approach is also being used to replace forelimb bones missing from a recently deceased Fin Whale, *Balaenoptera physalus* (Larkin, personal communication). By using a photogrammetric scan of the forelimb of a different specimen it has been possible to appropriately scale and print replacement bones for mounting with the real skeleton (Larkin, personal communication). Alternatively, scanned animals from other collections might be printed in a museum so that more locations have copies of specimens. By diversifying their natural history collections, museums can facilitate research and allow visitors to experience more (Niven *et al.*, 2009).

Using 3D printed models reduces damage to fossils by: not requiring climate (temperature and humidity) controlled display cases making them both easier and cheaper to display (Almeida *et al.*, 2007); the fossils do not have to be transported to and from mount-maker's studios; and 3D prints prevent over handling of the fossils, whilst allowing the creation of custom well-fitting support structures (Mallison, 2011). Instead of mounting the fossil material, lighter 3D printed replicas can be used, which require fewer mounts. As the 3D print can be drilled into, more aesthetically pleasing internal support structures can be built. 3D printing can also allow replicas of scientifically important but normally inaccessible parts of specimens such as the palate or inner ear bones to be placed on display (Larkin, personal communication) and for use in research.

As Koehl (Koehl, 2003) suggests, it is often quicker to make a physical model than to develop a computer simulation. The process of making physical models can now be even more accurate, as 3D printing based on CT scans allows increased realism, particularly as the use of models in research has traditionally been something of an art form. For example, physical modelling has been used in the assessment of how suitable feathers seen on preserved fossils of dinosaurs (*Microraptor gui*) could have been suitable for gliding or flight (Koehl, Evangelista and Yang, 2011). The models of *M. gui* used were originally made from foam with a wire skeleton, then updated to a steel and aluminium skeleton with polymer clay 'flesh', with feathers inserted to the foam or clay. By using 3D printing to create accurate skeletons it should be possible to build more realistic models that allow for more natural placement of feathers.

2.7 Ecology

Models of organisms or their parts are an excellent way to disentangle co-varying factors (Koehl, 2003). In some instances, 3D-printed models need not be biologically accurate. This has been exploited, for example, to isolate the influence of shape, colour, odour and chemical rewards in plant pollination. While flower nectar is an attractant and reward (Thomson, Draguleasa and Tan, 2015), some nectar also contains caffeine, which both a stimulant and toxic to most organisms. While flower nectar is an attractant and reward, many plants produce nectar that is toxic or repellent to some floral visitors (Adler, 2000). Investigating this counterintuitive pairing in nature had proved almost impossible and previous studies reported mixed results. However, Thomson *et al*. (Thomson, Draguleasa and Tan, 2015) used 3D prints to mimic the function of a flower's anther and stamen in collecting and depositing pollen. They printed small hoppers that deposited dye onto a bee when it brushed under the hopper to reach the nectar. By adding sticky tape, the hopper could also collect previously deposited dyes from the bees. Honeybees (*Bombus impatiens*) were presented with jars containing nectar with different caffeine concentrations. By measuring the amount of dye transferred, the authors found that the higher the caffeine content of the nectar the more bee visits (Thomson, Draguleasa and Tan, 2015), possibly due to the improvement in memory formation provided by caffeine (Wright *et al.*, 2013).

2.7.1 Conservation and monitoring

As we have shown, realistic models can be used in many areas of research, but they also have great potential for management and conservation. Current methods of capturing Emerald Ash Borers (*Agrilus planipennis*), an invasive species in North America, commonly use sticky traps baited with a dead female to attract males (Domingue *et al.*, 2014). To produce the bait, females must be caught, killed, and mounted with pins. Simplified 3D printed models of a female Ash Borer (Figure 2-2b) have now been successfully used to bait traps, and have the advantage of being cheaper, longer lasting, and are able to be mass-produced (Domingue *et al.*, 2014). While work is still needed

to look at the larger-scale efficacy of these traps, we can easily envisage the use of similar models to attract animals, for instance, to camera traps as a method of monitoring populations.

Watson and Francis (Watson and Francis, 2015) trialled the use of 3D printed ABS (Acrylonitrile Butadiene Styrene), a commonly used plastic, to produce models for studies of thermal ecology. Models are used to establish the distribution of environmental temperatures experienced by an organism, if it experiences no thermal regulation. Copper models are often used for this, but they are often poorly detailed, and are time consuming and difficult to construct. Copper models are produced using a paraffin wax mould of the animal, which is then electroplated, and the wax melted and drained. Copper tubing is often substituted for a detailed model but makes a poor substitute (Bakken and Angilletta, 2014). With reduced costs per model (albeit initial setup is more expensive), higher biological accuracy, reduced production times (1.55hrs compared to 29.83 hours for copper models) and robust nature of the models, Watson and Francis (Watson and Francis, 2015) suggest that 3D printed models for thermal studies have considerable advantages over traditional copper models, especially as the performance of both models is equal.

As of 2016, there has been a population explosion of ravens (*Corvus corax*) in the Mojave Desert. The increased numbers of predatory ravens are negatively impacting the populations of newly hatched Desert tortoises (*Gopherus agassizii*), a vulnerable species (IUCN, 2016). 3D-printed model tortoises that emit aerosol irritants when attacked are being used to condition the ravens not to eat the tortoises, thereby reducing predation (Shields, Personal Communication), this is a ground-breaking use of 3D printing in a conservation effort. 3D printing has also been used to help re-create coral reefs. The Great Barrier Reef is experiencing wide spread coral bleaching and coral death (Wolff *et al.*, 2018), but advances in 3D printing are enabling the production of coral shaped objects, 1 m in height (Sustainable Oceans International and International Sustainable Oceans, 2012). These large-scale 3D printed forms replicate the complexity of natural coral, providing organisms such as fish with suitable habitats whilst corals colonise the external surfaces.

In addition to producing items used directly in research or for teaching, 3D printing can also be used to create mock-ups of expensive or delicate equipment to test positioning or attachment methods. Chan *et al*. (Chan *et al.*, 2016), used 3D printed ABS models of GPS tags to test methods of attachment to Red Knots (*Calidirs canutus*). This allowed the authors to test attachment methods without the risk of losing expensive GPS tags. Whilst traditional methods can be used for mock-ups, 3D printing uses less material (due to the additive method, Gardner & Olson 2016) and can produce accurate replicas quickly and easily.

2.8 Limitations

There are limitations of using 3D printed models for research due to their static nature. These problems are no different to the limitations experienced by models made using traditional manufacturing techniques. Some of these problems could be overcome by employing 3D printed

shells into which robotics could be mounted. Robots are beginning to be used in studies of animal behaviour (see Frohnwieser *et al*. 2016 for a review), and this simple adaptation may yield interesting results. Using models in a manipulative experimental approach allows greater control over specific elements such as size of ornamentation, colouration, movement, or removal of olfactory cues (e.g. Heinen-Kay *et al*. 2015), but this is at the potential cost of realism. Therefore, a balance must be struck between absolute realism (which can only be achieved by using an organism), and manipulative control over specific elements important for the study. 3D printing can be of great benefit to such studies allowing models to be created with differences which would not be physically or ethically possible with live animals. There are, though, caveats to using models, including the potential that other factors are involved, e.g. signals, which are not manipulated through the use of models. As such, the observed responses may not be as "true" as when using an organism. However, by the same token, this method does provide the ability to precisely change only one element, which cannot be guaranteed with treatments or manipulations involving organisms. Observational or correlational studies can be used to address similar questions but rely only on natural variation. Observational studies may require more time and can suffer from confounding variables or reverse causation but do allow for testing in a biologically meaningful manner which might be lacking in the laboratory. For observational studies 3D printing can be used to produce equipment. One practical limitation of 3D printing, is the size of the object which can be printed. Most 3D printers have a relatively small print size. Objects larger than this print size can be made by incorporating joining features (e.g. sockets and pins) into the 3D prints or include positions for traditional fasteners (e.g. screws or nuts and bolts) to be used. These features can be added into the CAD drawings of parts, and some software allow for the inclusion of threaded holes to make assembly easier and faster. Large 3D prints often have lower resolution due to limitations of current scanning and printing methods, while smaller models can be printed at higher resolution but may be more expensive as a result.

Despite the advantages of 3D printing, many of the materials used in this process have not undergone testing for durability or toxicology. Where testing has occurred it often indicates leaching of chemicals from the materials. In one example, leached chemicals had a negative impact on the growth of zebra fish (*Danio rerio*) embryos (Oskui *et al.*, 2016). It seems prudent to suggest that materials likely to be in contact with living organisms need to be well researched first, given the release of chemicals from the 3D print may affect an animal's behaviour or even lead to death. Additional concerns centre on environmental impact, and while some feedstock used in 3D printing is recyclable (such as thermoplastic polymers used in FFD 3D printing, Table 2-1), others such as photopolymers (used in SLA 3D printing) are not. There are, however, continual developments, for example the toxicology of some models can be reduced with increased UV light treatment (Oskui *et al.*, 2016) and new printable plastics that are recyclable are in development (Mohammed, 2016). Additional problems with 3D printed equipment in the lab include the lack of guarantee and

possibility of a short lifespan, but if costs are low, this can be solved by re-printing the object. With sensible precautions, 3D printing can make many beneficial changes to the way we produce objects.

2.9 Take Home Messages

1. 3D printing enables the rapid production of items for low unit cost by commercial suppliers, or if many experimental pieces are to be printed then this can be done in-house. Printed items can be models of delicate bones, complex biological structures, microfluidic chambers, labware, or even hypothetical ancestral structures. 3D printed models can remove the reliance on the use of museum-preserved specimens.
2. A major limitation to the adoption of 3D printing is the initial cost of the printer, but this is falling. The cost of CT or laser scanning any structure to be modelled can also be high, but with suitable CAD software, many items can be approximated to a reasonable degree and custom items designed.
3. The impact of 3D printing on the environment is only just being studied. Many materials are not recyclable, and some plastics may release chemicals into the environment. The amount of chemicals released and the effects these may have is unknown.
4. Sharing of 3D models online is creating a large repository of objects that can be downloaded and printed, allowing anyone with a 3D printer to produce them. This can facilitate replication of experiments in a way never before possible.

The overarching advantage of 3D printing is the freedom given to researchers, allowing them to print custom objects, quickly and at relatively low cost. The application of 3D printing in Ecology and Evolution has begun but the technique offers many more opportunities for the future.

Chapter 3 Sinking Foraminifera: Analysis and Review of Current Knowledge

3.1 Introduction

3.1.1 Current Understanding

Outside of foraminifera, considerable research has been directed towards the sinking rates of planktonic organisms. The general motivation for such studies is estimating the rate at which material (especially carbon and carbon compounds) reaches the ocean floor (see Chapter 1). There is also substantial interest in the implications of widespread evidence that sinking velocities of many planktonic organisms can be modified by the cell, in order to maintain its position in the water column (Tappan and Loeblich, 1973). The largest daily migration of biomass occurs in the ocean; the movement of phytoplankton into the phototrophic zone is thought to be controlled by cell cytoplasm density changes (Schiebel and Hemleben, 2017). Nutrients (e.g.: phosphates and nitrates) are sparse in the photic zone, but more common in the deeper in ocean. Diurnal migration events thus allow phytoplankton to acquire these vital nutrients (Denny, 1993). It is thought that foraminifera may perform similar migrations on a longer time scale (Hemleben, Spindler and Anderson, 1989).

Current understanding of planktonic foraminiferal test sinking rates is based on a small number of studies, which are reviewed below. Currently it is known that the sinking velocities of planktonic organisms, including foraminifera, are determined by their size and density (see below). In addition, cell shape has been shown to have an effect on the sinking rates of plankton (Padisák *et al.*, 2003) including foraminifera (see below), and it is expected from theory that sinking velocity will be affected by shape (McNown and Malaika, 1950). Berthois and Le Calvez (Berthois and Calvez, 1960) found that spherical foraminifera sink at rates similar to a (theoretical) sphere of the same density and volume, however non-spherical foraminifera sink at slower rates from a sphere of the same density and volume. Their findings have been corroborated by Caromel *et al*. (Caromel *et al.*, 2014); that for a given size, flatter shaped foraminifera sink slower than spherical ones.

3.1.2 Aims

The objective of this chapter is to examine the accuracy of previous sinking speed estimates and where possible correct for differences between studies to provide more accurate estimates based on a larger, combined dataset. Once differences between datasets have been accounted for, the importance of length, volume and density in determining sinking velocities can be confirmed with the compiled dataset. Then, in section 3.3.1, using linear models, the amount of variation in sinking velocities determined by these parameters can be estimated. Finally, by accounting for most other parameters (e.g.: length, volume etc.), the role that shape plays in determining sinking velocities can also be explored.

In order to identify the role that shape plays, it has to be quantified. The Corey Shape Factor (CSF) is a measure of shape developed to quantify the shape of grains (e.g.: sand, pebbles, Komar and Reimers, 1978) and was used by Fok-Pun and Komar (1983). CSF can be easily calculated from three orthogonal measurements and here has been calculated for all specimens included in the compiled dataset (see Appendix 9.1.3). In addition, the morphogroups used by Aze *et al*. (Aze *et al.*, 2011) are included, and together these broad descriptors will be used to define shape. The parameters that are important in determining sinking velocity are identified in section 3.3.1, and are combined with the measures of shape (CSF and morphogroup) in linear models to explore the effect of shape on sinking velocities.

3.1.3 Hydrodynamics – What Predictions can be made from Physics?

The interaction of small particles with fluids is very different from the interactions that we (humans) are used to. The interaction or flow of the fluid around objects can be quantified by Reynolds number (Re) which is a measure of the ratio of inertial to viscous forces of a fluid (Vogel, 1994). Inertia is the resistance to change in motion. Inertial forces oppose changes in motion of a fluid, a fluid at rest is reluctant to start moving. However, once the fluid is in motion inertial forces continue to allow this movement, provided no external forces act on the fluid. Viscosity is mostly easily understood as the 'stickiness' of a fluid. Formally, viscosity is a measure of a fluid's resistance to deformation (i.e. flow) by sheer stress (bending or pushing) or tensile stress (pulling). To visualise viscosity, a fluid can be thought of as a stack of paper. Viscosity describes how well the individual sheets of paper stick together when the top page of the stack is pushed sideways (shear stress). If viscosity is high then all the sheets of paper would move, if viscosity is low then only the first few sheets would move (see Figure 3-1 and Equation 3-1). When Reynolds number is small, i.e. less than 1, viscous forces dominate, and as Re increases inertial forces become more important.

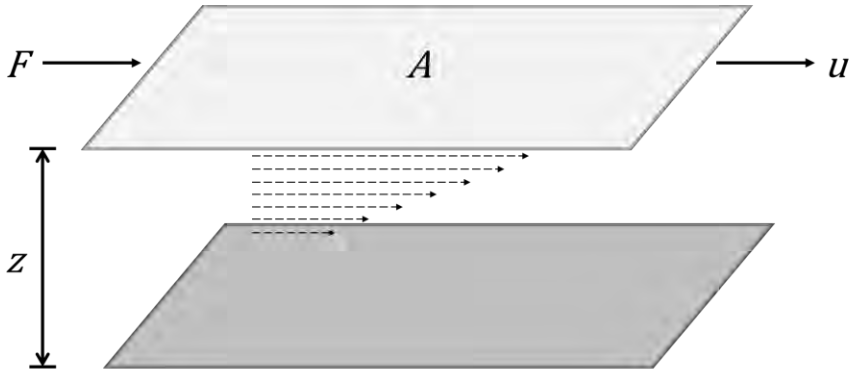

Figure 3-1: The dynamic viscosity of fluids (μ, in the units N·s·m^{-2}) can be measured using a plate viscometer. The fluid is placed between two plates, which are separated by distance z (in m) and the top plate moves with a force (F, in N) at a velocity of u (in m·s^{-1}). The amount of force required to move the plate is dependent on the surface area of the plate (A, m^{-2}) and the viscosity of the fluid. Dynamic viscosity of the fluid can then be found using Equation 3-1 (which uses the terms explained in this caption). Redrawn after Vogel (1996).

Equation 3-1

$$\mu = \frac{(F/A)}{(u/z)}$$

Re is calculated using Equation 3-2, where: ρ_{fluid} is density of the fluid (kg·m^{-3}); L is a characteristic length (m) of the object (see below); U is the sinking velocity (m·s^{-1}); and μ is the dynamic viscosity (N·s·m^{-2}, or Pa·s) of the fluid.

Equation 3-2

$$Re = \frac{\rho_{fluid} \cdot L \cdot U}{\mu}$$

From Equation 3-2, it is evident that Re will become larger if: the particle sinks faster; the fluid is less dense; the fluid is less viscous; or if the particle increases in size. The reverse is also true, Re will be smaller for small, slowly sinking particles in a dense, viscous fluid. Thus, Re can be used as an indicator of the flow around an object (Figure 3-2). In the case of low Re (conventionally <<1) there will be no sustained turbulence and the flow will be laminar (the flow streams are all parallel to each other), as Re values increase turbulence increases (See Figure 3-2). Table 3-1 provides some examples of Re in a biological context. It should be noted that the characteristic length used in the calculation of Re is somewhat arbitrary and must be chosen in accordance with the system being studied. However, Vogel (Vogel, 1994) states that it is common to use the longest length in the direction of flow for sinking objects.

Returning to the comparison of the sinking foraminifera and the swimming human, the swimmer has a Re on the order of 600,000 (Gettelfinger and Cussler, 2004), compared to the foraminifera which is likely to have an Re on the order of tens (i.e. 10-40). To draw a comparison, for a human (1.8m tall, swimming at 2 m·s^{-1}) to achieve a Re of 10-40 they would have to swim in molasses treacle (by substituting μ of water = 0.001 Pa·s in Equation 3-2, with μ of treacle = 20-80 Pa·s). As Vogel observed, “Reality is size dependent” (LaBarbera, 1989) and by using dimensionless numbers such as Re it is possible to quantify the relative importance of the various forces acting on an organism.

Table 3-1: Reynolds numbers of various organisms in fluids (From Vogel, 1994)

Organism and speed	**Reynolds number**
Large whale swimming at 10m s^{-1}	3,000,000,000
Tuna swimming at 10 m s^{-1}	30,000,000
A duck flying at 20 m s^{-1}	3,000,000
A large dragonfly flying at 7 m s^{-1}	30,000
A copepod at 0.2 m s^{-1}	300
Flapping wings of smallest flying insect	30
An invertebrate larva, 0.3 mm long, at 1 mm s^{-1}	0.3
A sea urchin sperm at 0.2 mm s^{-1}	0.03
A bacterium swimming at 0.01mm s^{-1}	0.00001

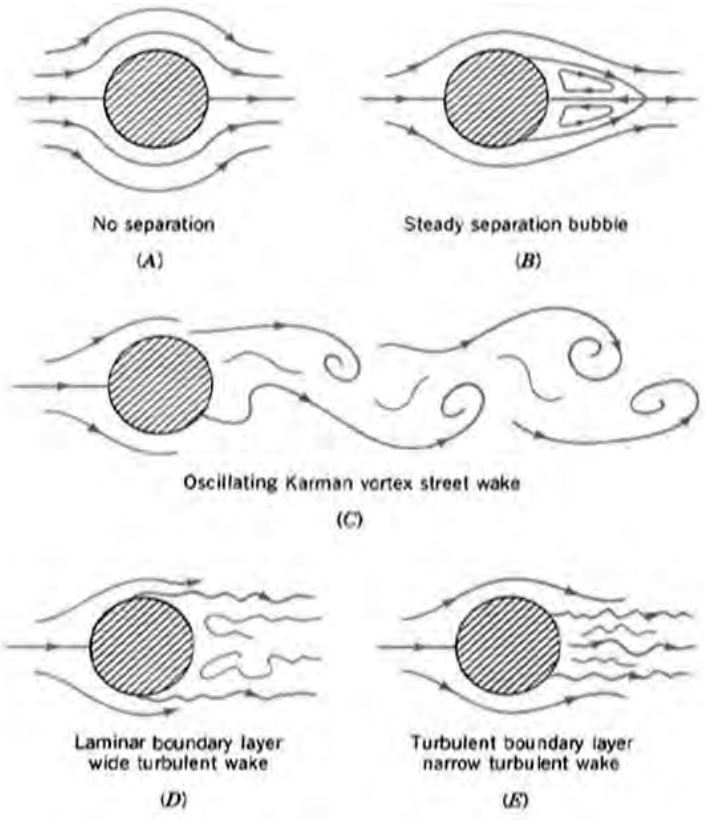

Figure 3-2: Diagrams of flow around smooth cylinders at varying Reynolds numbers. Reynolds number (A) = 10^{-1}, (B) = 100, (C) = 10^2, (D) = 2 x 10^4 and (E) = 3 x 10^5. From Munson et al. (Munson, Young and Okiishi, 1994)*. The separation of the turbulence occurs at the Re stated here only for smooth circular cylinders, for other shaped objects the separation of flow will occur at different Re values.*

In general, the physics of sinking for simple shapes, such as spheres, is well understood. The flow around spherical (Stokes, 1905) and cylindrical (White, 1946; Jones and Knudsen, 1961) particles as well as flat plates and other simple geometric shapes (McNown and Malaika, 1950) has been well characterised through theoretical and empirical studies. Specific formulae to predict sinking velocities for geometric particles in the same size range as foraminifera have been established (White, 1946; McNown and Malaika, 1950; Jones and Knudsen, 1961; Happel and Brenner, 1983). Using this knowledge, it is possible to make predictions about how fast a spherical particle will sink in a fluid if the properties of both the fluid and the particle are known. Sinking velocities of spherical particles can be predicted using Equation 3-3, where: $U_{terminal}$ is terminal velocity (m·s^{-1}); g is acceleration due to gravity (9.81 m· s^{-2}), Ø is particle diameter (m), C_D is drag coefficient (as calculated by Equation 3-6, Equation 3-7, Equation 3-8) and ρ is density (kg·m^{-3}).

Equation 3-3

$$U_{terminal} = \sqrt{\frac{4 \cdot g \cdot \emptyset}{3 \cdot C_D} \cdot \left(\frac{\rho_{particle} - \rho_{fluid}}{\rho_{fluid}}\right)}$$

To better understand Equation 3-3, knowledge of some variables commonly used in fluid dynamics is required. Once a particle reaches terminal velocity the net forces ($\sum F$) are equal to zero (i.e. Newton's Second Law, see Equation 3-4: where F is the force due to the subscript, e.g.: F_{drag} is force

due to drag). From here on, it is assumed that sinking velocity (U), is equal to terminal velocity ($U_{terminal}$). For low Re this is the case as terminal velocity is achieved in a short distance, but as Re increases so does the time taken to reach $U_{terminal}$ (see Appendix 9.1.1).

Equation 3-4

$$\sum \mathrm{F} = F_{drag} + F_{bouyancy} - F_{weight} = 0$$

The drag force ('drag') is the force opposing the movement of an object. The drag experienced by an object in a fluid is determined by properties of the fluid (ρ) and of the particle (U, A). Using these terms in Equation 3-5, along with C_D (drag coefficient), the drag experienced can be calculated.

Equation 3-5

$$F_{drag} = C_D \cdot {}^1/_2 \cdot \rho_{fluid} \cdot {U_{particle}}^2 \cdot A_{particle}$$

Comparison of drag forces allows predictions to be made for which shapes experience higher drag and therefore travel at lower velocities. However, the drag force (F_{drag}) is affected by surface area ($A_{particle}$) and so it is not possible to directly compare drag forces between different shapes, as different shapes have different surface areas. For example, a sphere, presenting a circular area to the fluid, presents less area than a cuboid (presenting a square area) with the same dimensions (Figure 3-3).

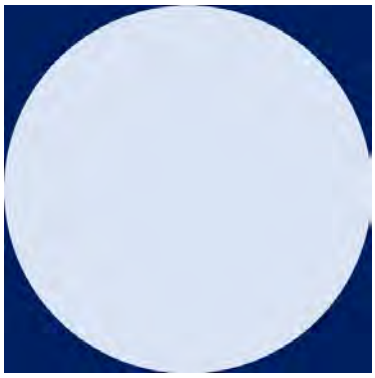

Figure 3-3: A circle and a square of the same length (i.e. diameter of the circle= length of the squares sides) showing the different areas presented to the fluid. Area of a square 10 units in length is 100 units^2 (area=length^2), the circle's area is 78.53 units^2.

To account for the influence of shape on surface area, C_D is commonly calculated. C_D provides a dimensionless number representing drag force per unit area (Equation 3-6), although definition of area (and thereby the actual measurement of area) used can differ (see below). At low Re (<<1) C_D is directly proportional to the velocity of the particle, but at higher Re regimes it is proportional to the square of the velocity, therefore the Re regime that is being investigated needs to be understood so that the correct equations can be used. For high Re regimes Equation 3-6 can be used but for low Re this would not be appropriate. The use of the incorrect equation can lead to substantial errors in the calculation of C_D (Vogel, 1994).

Equation 3-6

$$C_D = \frac{2 \cdot V \cdot (\rho_{particle} - \rho_{fluid}) \cdot g}{\rho_{fluid} \cdot U^2_{particle} \cdot A_{particle}}$$

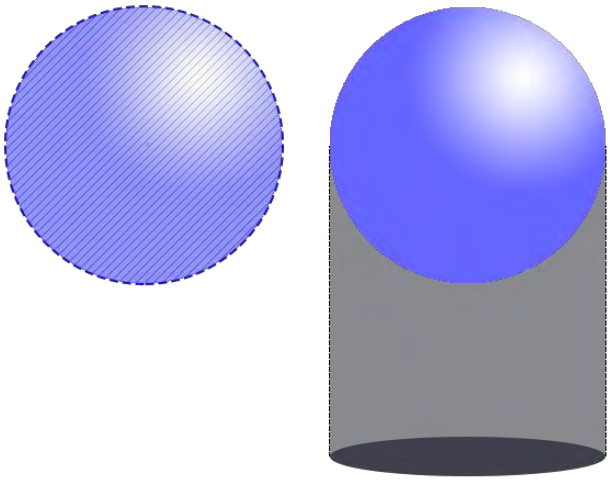

Figure 3-4: Different measurable areas of a sphere. On the left the wetted area (stripped) which includes the entire surface area. On the right the projected area (A_p), visualised as a shadow. Both these measures of area can be used in the calculation of C_D.

The use of C_D allows the direct comparison of drag experienced by differently shaped objects. When calculating C_D the choice of area is important, and there are three options: projected area; wetted surface area; and profile area (see Figure 3-4). Which is suitable depends on the Re regime and the object in question. Projected area is the area of an object presented to the flow. For intermediate (1-50) and high (> 50) Re the use of projected area (A_p, i.e. a shadow of an object, see Figure 3-4) is most common (Vogel, 1994), this is also the easiest of the areas to calculate (for more details see Chapter 5 in Vogel 1994). Wetted surface is the surface area of the object that is in contact with the fluid, in principle this is the best measure as it is independent of the object's orientation. However, in practice measuring the wetted area is challenging for irregular particles, so is rarely used beyond smooth streamlined shapes whose surface areas are relatively simple to estimate. For smooth streamlined shapes, the surface area can easily be divided into geometric shapes, whose surface areas can be calculated from known equations (e.g. the surface area of a sphere). For irregular shapes there are not established equations and using geometric shapes may results in serious over- or under-estimation of surface area. The final measure, profile area, is used predominantly for aero- and hydro- foils (e.g.: aircraft wings) and whilst relevant for a number of biological applications (e.g.: flight), profile area is not relevant here. The choice of area is often constrained by practicality in terms of ease of measurement and relevance to the question being asked. For non-spherical particles sinking in regimes with Re > 1, it is known that the particle will orientate itself so that the greatest possible projected surface area is presented to the fluid flow (referred to as the sinking orientation, Hutchinson, 1967; Vogel, 1994). Therefore, the area commonly used to calculate C_D is that which is presented to the fluid in the sinking orientation. There is an intrinsic link between Re and C_D as they share several terms; so whilst C_D may be calculated using Equation 3-6, it is also possible to calculate C_D using Re with either Equation 3-7 (known as Stokes' drag or Stokes' flow), or Equation 3-8 (derived from empirical data by Morrison, 2010). The use of Equation 3-7 should be limited to Re < 1 (Vogel, 1994), whereas Equation 3-8 can be used for all values of Re.

Equation 3-7

$$C_D = \frac{24}{Re}$$

Equation 3-8

$$C_D = \frac{24}{Re} + \frac{2.6 \cdot \left(\frac{Re}{5.0}\right)}{1 + \left(\frac{Re}{5.0}\right)^{1.52}} + \frac{0.411 \cdot \left(\frac{Re}{263{,}000}\right)^{-7.94}}{1 + \left(\frac{Re}{263{,}000}\right)^{-8.00}} + \left(\frac{Re^{0.80}}{461{,}000}\right)$$

However, the use of Equation 3-7 and Equation 3-8 to calculate C_D should be limited to spheres and spheroids only, as flow around different shaped bodies results in different relationships between Re and C_D (McNown and Malaika, 1950).

Now the link between area and C_D has been clarified (Equation 3-6), the relationship between C_D and sinking velocity can be explained using Equation 3-3 to Equation 3-9. As might be expected, increases in C_D (i.e. increases in area) will reduce sinking velocities (as C_D is a denominator in the equation). Following this, increases in length (as a numerator in Equation 3-8) will increase sinking velocity. Naturally, there is a trade-off between the increase in sinking velocity brought about by the increase in length, and the decrease in sinking velocity due to the increase in area (area $\approx$ length^2). From Equation 3-3, it is also possible to see that the density difference between the particle and fluid (also referred to as the specific gravity) is an important factor in determining sinking velocities. To summarise, the parameters effecting the sinking velocity of any particle can be divided into properties of the particle (i.e. the area, size (length) and density) and properties of the fluid (i.e. density and viscosity).

As outlined above, the manner in which the flow around sinking particles occurs is described by Re. For objects sinking at Re of less than one, the flow around the object is laminar and is sometime referred to as Stokes' or creeping flow (See Figure 3-2). Flow around a sphere in creeping flow was analytically addressed by Stokes (Stokes, 1905), and this mathematical description is often referred to as Stokes' Law (Equation 3-9 where: r is sphere radius in m). Whilst Stokes' Law is technically only applicable for Re << 1, experimental results are in agreement with Stokes' Law up to $Re \approx 1$ (Vogel, 1994).

Equation 3-9

$$F_{drag} = 6 \cdot \pi \cdot \mu \cdot U_{particle} \cdot r$$

In Stokes flow (Re <<1) the impact of inertia is negligible, and thus ignored in Stokes' Law, and viscous forces (of the fluid) dominate. Ignoring the effect of inertia results in a simpler solution to estimates of sinking velocities or drag, than for non-Stokesian flow, where inertia needs to be accounted for. At these lower Re ($\lesssim$1) the relationship between Re and C_D is linear, however as Re increases above 1 there is a departure from the predictions made by Stokes' Law (See Figure 3-5). Rearranging Equation 3-9, it is possible to predict the sinking velocity as well as the drag experienced by spheres at low Re. Since 1851, there have been numerous attempts at improving Stokes' Law to find a solution to C_D that is applicable across a range of Re. There have been

incremental improvements with the addition of terms, based on empirical data (for details see Happel and Brenner 1983). Morrison (Morrison, 2010) developed an empirically based equation for spheres, that uses Re to predict C_D over range of Re from Re = 0.1, to Re = 10^6 (Equation 3-8).

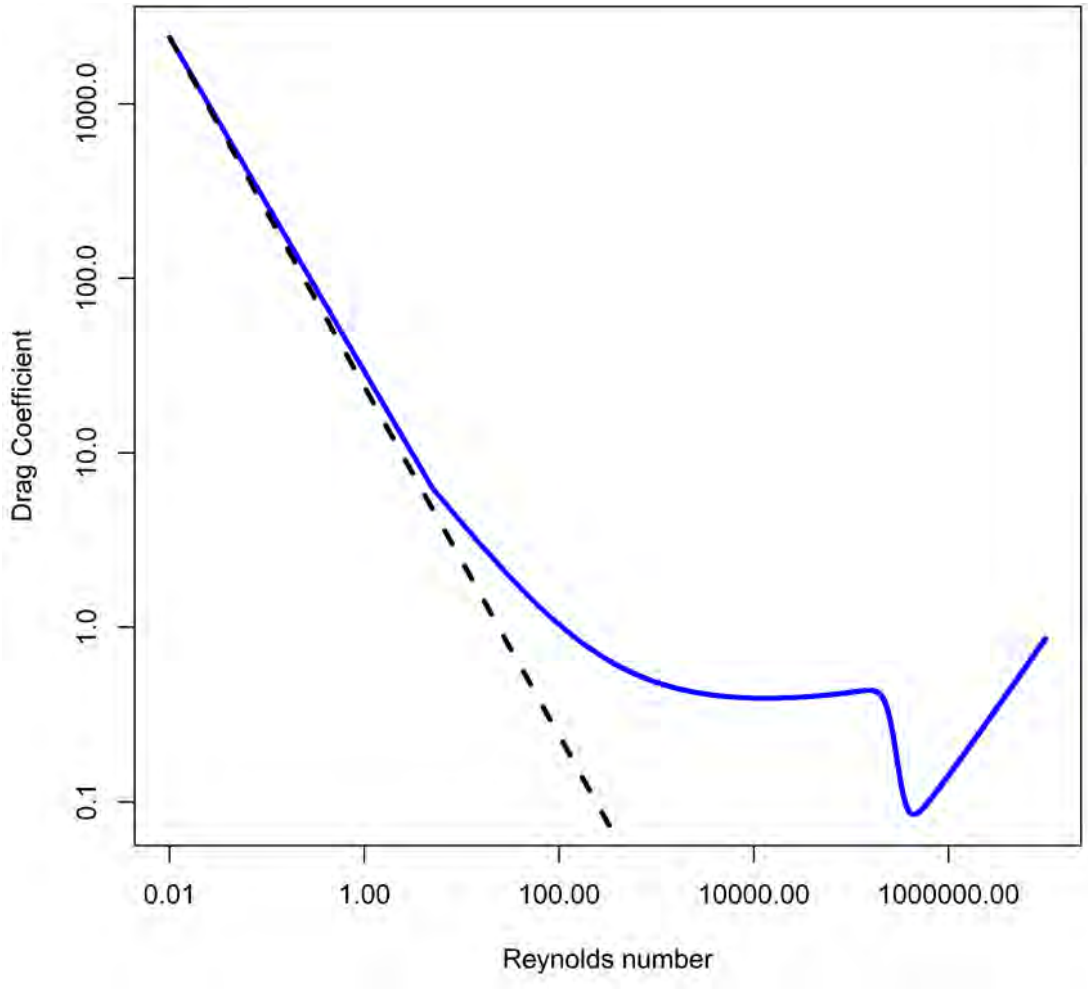

Figure 3-5: Drag coefficients of a smooth sphere. Black dashed line is Equation 3-7 (Stokes' Law) and blue solid line is Equation 3-9 (Morrison's Equation).

Based on the equations Equation 3-2 to Equation 3-8 it would appear reasonable to make some estimates of sinking velocities. However, this is not straightforward as many of the parameters are co-dependent (e.g.: C_D is dependent on Re, which is dependent on sinking velocity, which in turn is dependent on C_D, Le Roux, 2005). The actual relationship of sinking velocities of spherical particles at Re > 1 is non-linear (Goldstein and Coco, 2014), and so an iterative approach to solving this problem is developed in Chapter 4.

An additional consideration is that few particles are perfect spheres. Despite the fact that Stokes' Law can be applied to particles which are not spherical (White, 1991), non-spherical particles above the limits of Stokes' flow sink more slowly than spheres of the same diameter (McNown and Malaika, 1950). There have been many attempts to understand how non-spherical particles outside of Stokes' flow sink and how the departure from an ideal spherical particle can be measured (See: Rodriguez *et al*., 2013 for a review of shape factors). The first problem is to define the departure from sphericity, which can be considered equivalent to characterising the objects shape. The Corey

Shape Factor (CSF) is commonly used to quantify shape (Le Roux, 2005), and requires three orthogonal axial measurements to calculate deviance from a sphere (CSF=1, Equation 3-10, where ⌀ is diameter). This measure of linear deviation can then be used to adjust the sinking velocity prediction (See Le Roux ,2005 for a comprehensive review). CSF is discussed in more detail in 3.2.2.4. While there are a number of other shape measures in use, the CSF is used here as it is easily reconstructed from linear measurements available for foraminifera in the literature.

Equation 3-10

$$CSF = \frac{\varnothing_{shortest}}{\left(\varnothing_{longest} \cdot \varnothing_{intermediate}\right)^{0.5}}$$

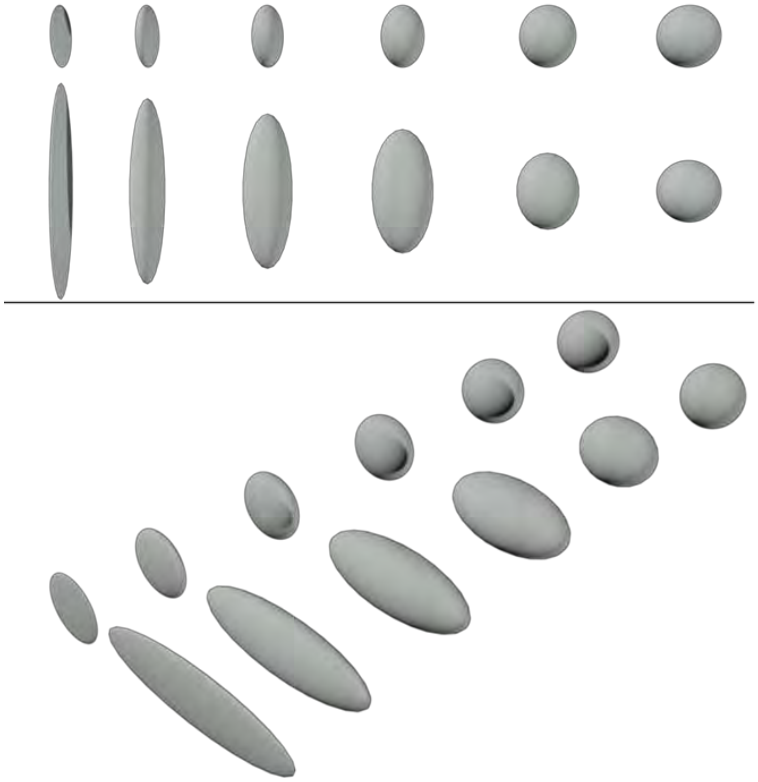

Figure 3-6: Examples of ellipsoids with different CSF values. A top view of the shapes, from left to right the CSF values are 0.1, 0.3, 0.5, 0.7, 0.9 and 1 (a sphere), both shapes in the upper and lower row have the same CSF value. Below a perspective view of the same shapes. For values and method see Appendix 9.1.2.

Now the basic hydrodynamic principles of sinking have been outlined, they must be viewed with foraminifera in mind. Sinking velocities are hard to predict as the parameters used to make the predictions are co-dependent (e.g.: length, area, volume, C_D, and Re are all co-dependent). It is not appropriate to apply Stokes' Law to sinking of foraminifera, as they are too large (Re > 1). Fok-Pun and Komar (1983) calculated that *Orbulina universa* would have to have a maximum diameter of 100µm for it to experience a Re of 1; where in real life this species has a maximum diameter of 830µm (Bé, Jongebloed and McIntyre, 1969) (the average diameter calculated from Fok-Pun and Komar, 1983; Takahashi and Bé, 1984; Caromel *et al*., 2014, is 560 µm). In addition, most modern foraminifera are not spherical (although *O. universa* approaches sphericity), and as previously mentioned, sinking objects that are not spherical differ in their sinking velocity compared to spheres

(McNown and Malaika, 1950). Therefore, it is expected there will be an effect of size and shape on sinking velocity of foraminifera, in line with the findings of previous studies (see section 3.2.2).

Table 3-2: The properties that determine sinking velocity of spheres, how to calculate them and the equation that shows their relationship to sinking velocity.

Property		Definition	For a sphere:	For a spheroid:	SI Units	Equation
Size	Length or diameter	Characteristic length, longest diameter or length			m	Equation 3-2 and Equation 3-3
	Area presented to the fluid	$A = \pi r^2$	$r = \frac{length_{max}}{2}$	$r^2 = \left(\frac{length_{max}}{2} \cdot \frac{length_{min}}{2}\right)$	m^2	Equation 3-5 and Equation 3-6
	Volume	$V = \frac{4}{3} \cdot \pi \cdot r^3$	$r = \frac{length_{max}}{2}$	$r^3 = \left(\frac{length_{max}}{2} \cdot \frac{length_{inter}}{2} \cdot \frac{length_{min}}{2}\right)$	m^3	Equation 3-6
Density		$\rho_{particle} = \frac{Mass}{Volume}$			$Kg \cdot m^{-3}$	Equation 3-3 and Equation 3-6

In summary, whilst foraminifera are not perfectly spherical it is possible to outline the main parameters that should determine sinking velocity, based on the equations developed for spheres and simple geometric shapes. Based on equations Equation 3-2 to Equation 3-8 some testable hypotheses can be formed. Sinking velocity will be predictable by: (1) foraminifera size, (2) the area presented to the fluid, and (3) specific gravity (difference in density between the test and the fluid) (see Table 3-2). In order to test these hypotheses, data from previously published studies investigating sinking velocities of planktonic foraminifera will be compiled and reanalysed. However, the studies suitable for use must first be identified. A summary of each study is set out below, with reasoning for inclusion or exclusion from the final dataset. Once the relationships between parameters predicting sinking velocity have been established, the parameters will be examined alongside basic measures of shape (CSF and morphogroup) to identified if there is a potential effect of shape.

3.2 Previous Studies

Sinking foraminifera have received attention for over 120 years, from Thoulet in 1891 to Caromel *et al.* (Caromel *et al.*, 2014). Below is a simple outline of a generalised experimental design, covering the basic apparatus, protocol and materials used in each study.

3.2.1 An Example Experiment

Whilst all of the studies considered here (Thoulet (1891), Berthois and le Calvez (Berthois and Calvez, 1960), Berger and Piper (Berger *et al.*, 1972), Fok-Pun and Komar (Fok-Pun and Komar, 1983), Takahashi and Bé (Takahashi *et al.*, 1984), Furbish and Arnold (Furbish and Arnold, 1997), Caromel *et al.* (Caromel *et al.*, 2014)) differ in their specifics, they all share a basic experimental design (Figure 3-7): the foraminifera are introduced to a fluid-filled tube and their sinking velocity is recorded. The specifics of the fluid used, the source of the foraminifera, the preparations of the foraminifera beforehand, diameter of the tube, how sinking time is measured and, definition and

calculation of various parameters (such as Re, C_D and density) differ from study to study and will be expanded on below.

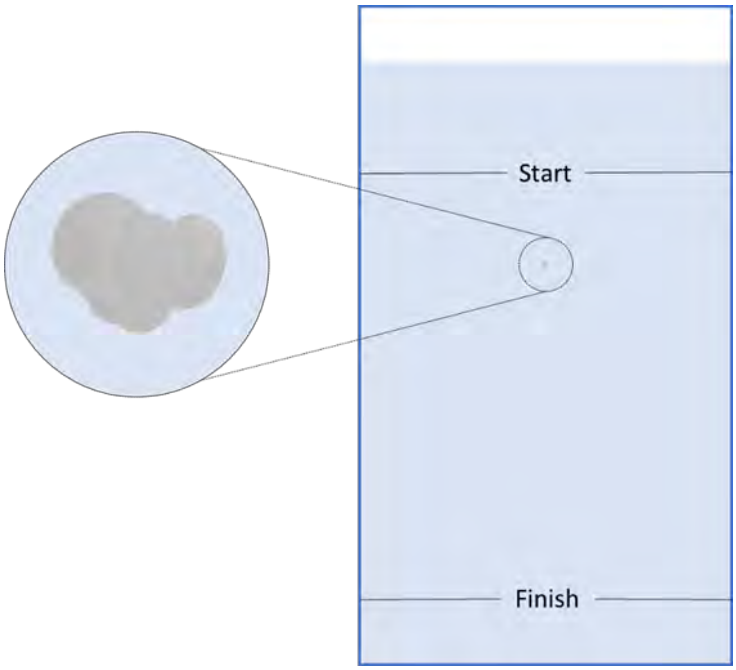

Figure 3-7: Schematic sketch of a generalised experimental setup. A foraminifera test sinking in a fluid filled tube. The time taken to sink from the start line to the finish line is recorded and used to calculate sinking velocity.

The first source of variation is the fluid that is used to fill the tube, which influences sinking velocities because of variation in density and viscosity. For example, seawater is denser (~1024Kg·m^{-3}), and more viscous (0.00108 Pa·S), than distilled water (998 Kg·m^{-3} and 0.001002 Pa·S respectively), at 20°C. Variation in water density and viscosity is also a function of temperature (IOC SCOR and IAPSO *et al.*, 2010), so the temperature at which the experiments are conducted is another source of variation, with colder water being more dense and viscous than warm water. Estimating the amount of variance (in sinking velocities) which might be expected due to differences in water temperature is a considerable challenge due to the interlinked nature of the factors controlling sinking velocities (see Chapter 4).

The source of the foraminiferal tests could also affect the rate at which they sink. There is debate over the amount of cytoplasm present in the test during its descent to the ocean floor. Bulk density is used here to describe the density of the water filled test, including the volume of calcite and of water present (see Appendix 9.1.3). In essence, the bulk density of the test is dependent on the origin of the test. If the test is from a plankton tow, there is likely to be cytoplasm present, which will slightly increase the bulk density as cytoplasm is denser than the water it displaces. Tests from sediment samples can contain finer sediment (resulting in a higher bulk density), or the test could have undergone dissolution thereby losing some of its calcite mass (resulting in a lower bulk density). As with differences in water temperature, the impact this increase in density would have on sinking velocities is difficult to estimate. However, for both test density and water temperatures, the changes are likely to be comparatively small.

Preparation of the foraminifera before they are sunk will affect their sinking velocities. Firstly, all bubbles must be removed from the test, as air will reduce the bulk density of the foraminifera. Cleaning techniques used may cause damage to the calcite (e.g.: the use of ultrasound can damage the thick gametogenic calcite crust of some foraminifera species Hodgkinson, 1991), again reducing the bulk density of the foraminifera. Not only the preparation, but the introduction of the foraminifera to the settling tube is important, the foraminifera should be placed into tube individually. This is because when particles sink in groups there are interactions between the sinking particles. These interactions alter the sinking velocities of the particles, in some cases there maybe increases in the sinking velocity of particles (if two particles are sinking along the same axis then the top one will 'chase' the bottom, increasing its sinking velocity, Vogel, 1994) and in other cases decrease the sinking velocity (particles interact with each other's flow, increasing drag, up to 400 diameters distance under low *Re* conditions. Happel and Brenner, 1983; Bach *et al*., 2012).

The diameter of the tube is also important, as if the size of the tube is too small relative to the diameter of the particle falling in the tube, wall effects (WE) will reduce its sinking velocity (Happel and Brenner, 1983). When a particle is sinking, the fluid must move to allow the particle passage. If the fluid is not able to move aside, for example if confined by the walls of a tube, then the sinking velocity of a particle will be retarded, as drag is increased when the fluid is unable to move. For instance, at very low Re (10^{-4}) the presence of boundaries 500 particle diameters away increases the drag by a factor of two (White, 1946). As the Re increases the presence of a wall has less of an effect (White, 1946). A rapid assessment of wall effects can be made using a normalised measure of wall effects (referred to here as a wall effects factor, WEF). This WEF (Equation 3-11) is derived from Vogel (1994) and White (1946), and uses the diameter of the particle (⌀), the distance from the edge of the particle to the wall, i.e. the radius of the tube minus the radius of the particle, (see Figure 3-8, l) and Re. When WEF is larger than one it can be assumed there will be no effect due to the presence of the wall.

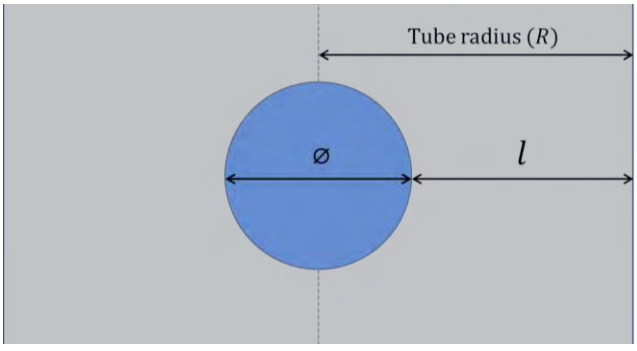

Figure 3-8: a section of a tube with a sinking particle, illustrating the measurements required for Equation 3-11. Dotted line is the centre line.

Equation 3-11

$$WEF = \left(\frac{\varnothing}{l}\right) \Big/ \left(\frac{20}{Re}\right)$$

The measurement of sinking times is another process that could influence the reliability of the sinking velocities reported. For example, if the sinking times are measured between two lines on the tube there could be artefacts due to parallax (the apparent change in position of an object from two different viewpoints). Few of the studies report the specific method they used (details in Section 3.2.2, below), but it would be reasonable to assume those that do not report a method use something akin to measuring the time taken for the foraminifera to travel between two lines.

To make comparison of sinking velocity and other variables, measurements of the foraminifera must be taken. These measurements are: size (longest, intermediate and shortest lengths), volume, weight, and density. It is hoped that the measurements of length within a study are conducted by the same person and therefore have reduced differences. However, between studies slight differences in orientation of the foraminifera when measuring lengths could result in different measurements being obtained for foraminifera of equal size (see Figure 3-9 for an example). The bulk volume of the test is calculated from these three orthogonal measurements using basic geometric shapes (see Appendix 9.1.3). The volume of the calcite walls is obtained by weighing the test, and then dividing this mass by the density of calcite. From these basic measurements, derived values such as Re and C_D can be calculated.

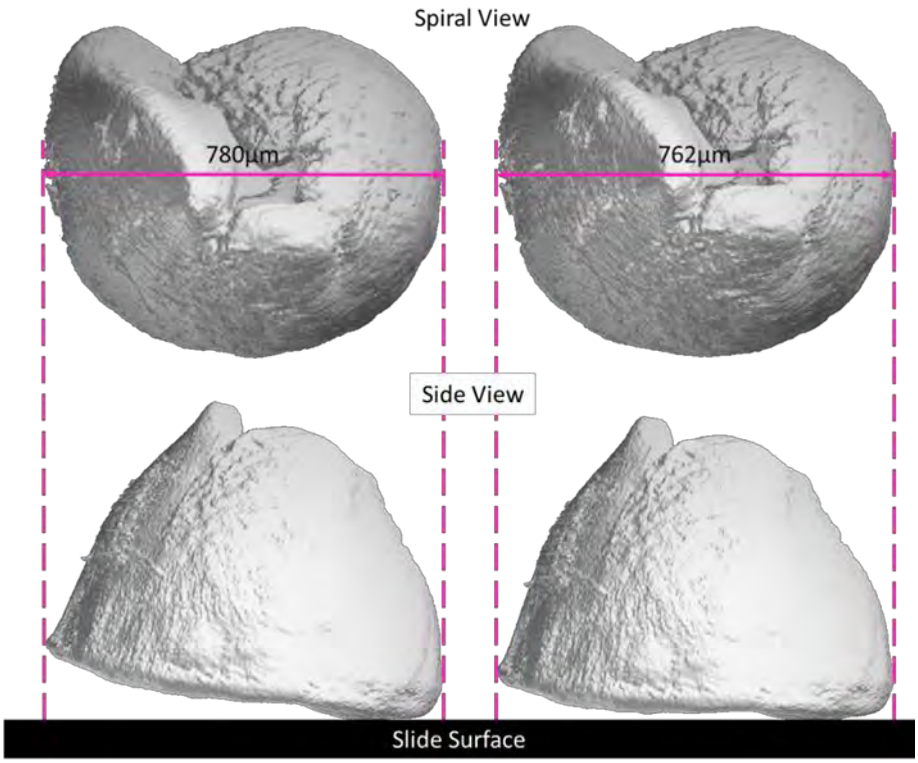

Figure 3-9: An illustrative example of how measurement error due to slight differences in foraminifera orientation could result in different measurements, despite the foraminifera being the same size. This example uses Truncorotalia truncatulinoides *from the Tohoko University dataset (see Chapter 4), visualised in Molcer. Measurements were taken using FIJI* (Schindelin *et al.*, 2012).

For the calculation of Re, as previously discussed, the choice of "characteristic length" is important (section 3.1.3). Ideally the characteristic length is the longest length measured in the direction of flow (Vogel, 1994). When sinking, this length is predicted by physics to be orientated perpendicular to the greatest projected area (see Figure 3-10). However, this length needs to be measured from an image of a sinking foraminifera. Instead, a number of different lengths have been used to calculate Re*:* the largest diameter by Fok-Pun and Komar (1983), and Caromel *et al*. (2014) average diameter by Takahashi and Bé (1984); Furbish and Arnold (1997) use the radius of a sphere which encompasses the protoplasm and test; and Berthois and La Calvez (1960) use a nominal diameter (the diameter of a sphere sinking at the same velocity). Consequently, Re values reported will be larger than the actual Re for most studies (see Figure 3-10 for an example). Similarly, the calculation of C_D relies on a suitable choice of area.

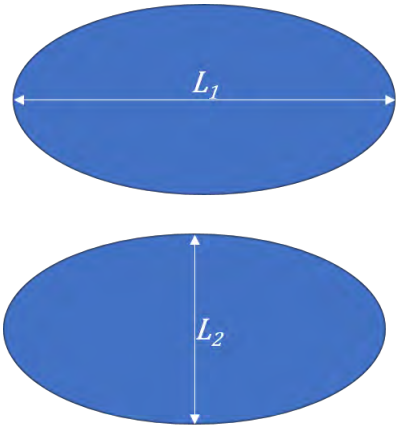

Figure 3-10: A simplified example of how the length used to calculate Re results in an overestimation of Re. In this example, L_1 is twice as long as L_2. Assuming the rest of the terms in Equation 3-2 are equal this would result in a Re value for the first particle (using L_1) being twice as large as for the second particle (using L_2), when actuality the two particles are the same size and therefore would experience the same Re.

Sinking velocities are affected by differences in water density and viscosity, one method of comparing studies is by using Re and C_D. Re and C_D account for differences in water density and viscosity (i.e. use of fresh or salt water) in their calculation (see Equation 3-3 and Equation 3-6). Despite the outlined problems in the calculation of these variables (above), it is helpful to examine relationships between Re and C_D to understand the drag experienced by the sinking foraminifera in comparison to a sphere.

3.2.2 Individual Experimental Details

Below is a summary of each study (see Table 3-3 for an overview), with its merits and demerits outlined. Unfortunately, there is no information in any of the papers as the geographic location in which the samples they used were taken. This means any physical variation in tests, due to differences in geographical location (e.g. porosity (Fisher *et al*., 2003) or coiling pattern (Quillévéré, *et al*. 2013) are not able to be quantified. For each study, the conclusions regarding the hydrodynamic parameters that predict sinking velocities (size, shape and density) are summarised, further details on the experiments can be found in Appendix 9.1.4. From these studies a dataset for further analysis was compiled following strict inclusion criteria. These criteria were:

1. Individual sinking velocities for each foraminifera were reported
2. Individual measurements (e.g.: size, volume) for each foraminifera were reported
3. The species must be present in Aze *et al*.'s (Aze *et al.*, 2011) phylogeny of macro-perforate planktonic foraminifera (to permit phylogenetic analysis, conducted in Chapter 6)

Table 3-3 Summary of the various studies in sinking velocities of foraminifera. Settling tank dimensions diameter (Ø) and height(H). Density values for Takahashi and Bé (1984) and Caromel et al. (2014) are calculated averages, using the datasets from the respective study.

Study	Settling tank dimensions (mm)	Fluid	Number of species	Size fractions (µm)	Reported Foraminifera Density ($kg \cdot m^{-3}$)	Method summary
Thoulet (1891)	Unknown	Unknown	Unknown	750, 500, 250, 125	N/A	Empty and broken *Globigerina* tests were sunk.
Berthois and le Calvez (1960)	Ø = 52 H = 500	Freshwater Seawater	>2	700, 400	1162	Sinking times over 500mm were recorded. Foraminifera placed on the water surface and allowed to gradually fill with water.
Berger and Piper (1972)	Ø =40 H = 1100	Demineralised water	18	62, 125, 177, 250	1500	Samples wetted with demineralised water (with a trace amount of ethyl alcohol). 100 to 1000 foraminifera introduced to the top of the tube at once. Foraminifera were collected from the bottom of the tube and the number of foraminifera were counted at 15 second intervals.
Fok-Pun and Komar (1983)	Ø =114 H = 2000	Demineralised water	4	>210 Individual foraminifera sizes reported (range: 300 - 800)	1480	Sinking velocity was measured over a central 1 m section of the tube, with an accuracy of 0.1s. Use of near spherical species to compare to sphere equations.
Takahashi and Bé (1984)	Ø =25 H = 160	Sargasso seawater (36.5‰ salinity)	10	Individual foraminifera sizes reported (range: 143 - 1423)	1301	Specimen was placed under the water surface on a brush and released. Sinking measured over 83mm descent in the tube.
Furbish and Arnold (1997)	Ø = 100 to 150 H = Unknown	Corn syrup, various shampoos	Representations of Spinose species	Scale models	N/A	Beeswax and pins used to make models of spinose species which were sunk in viscous fluids.
Caromel, Schmidt Phillips and Rayfield (2014)	Ø = 140 H = 155	Demineralised water	9	Individual foraminifera sizes reported (range: 254.8 - 1553.9)	1748	High speed video recordings used to measure sinking speeds from the lowest 30 mm of the settling tank.

3.2.2.1 *Thoulet* (1891)

Thoulet (1891) is the earliest reported study into the sinking velocities of planktonic foraminifera, the results are summarised in Table 3-4. Due to these uncertainties in the methodology and the small amount of data presented, this data is not included in this study. Based on the limited information available, it would be expected that sinking velocities obtained by Thoulet would have a larger range than expected, due to possible inclusion of sediment in the samples (increasing sinking velocities) and the use of fragments which would sink more slowly. As Thoulet does not remark on any method of removing air, so the presence of air may have caused whole specimens to sink slower.

Table 3-4: A summary of Thoulet's (1891) findings (Original data, headings translated from Thoulet, 1891).

Average Diameter (mm)	Sinking velocity ($cm \cdot s^{-1}$)	Time to reach 1850 m
0.75	3.78	13 h 35'
0.5	2.74	18h 45'
0.33	2.05	25h 3'
0.26	1.26	40h 5'
0.12	0.7	73h 25'

Table 3-5: Converted results of Thoulet (1891)

Average Diameter (µm)	Sinking velocity ($m \cdot s^{-1}$)
750	0.0378
500	0.0274
330	0.0205
260	0.0126
120	0.007

3.2.2.2 *Berthois and Le Calvez* (1960)

Berthois and Le Calvez (1960) compared sinking rates of planktonic foraminifera tests to the sinking rates of quartz grains (sand). They found that spherical foraminifera sink at rates similar to those predicted for a sphere of the same density and volume, however non-spherical foraminifera sink at different rates from those predicted for a sphere of the same density and volume.

However, the formulae authors use result in some inconsistencies; for example, an average density of the foraminiferal test was calculated using Stokes' law to be $1162 kg \cdot m^{-3}$, which is lower than most subsequent studies (see below, Table 3-3). Berthois and La Calvez (Berthois and Calvez, 1960) reported there may be inclusions of air bubbles in their samples, so is possible that their reported sinking velocities were lower than expected. Equally, there is no report of cleaning of the foraminifera prior to sinking, so sinking speeds may be increased compared to cleaned tests. They only report an average sinking velocity ($0.02009 m \cdot s^{-1}$) and no individual estimates, so their results will not be reanalysed as part of this work.

3.2.2.3 *Berger and Piper (1972)*

Berger and Piper (1972) address some of the issues that were present in the work of Berthois and Le Calvez (Berthois and Calvez, 1960). Two sample types were used, one from the sediment and another composed from plankton tows.

Berger and Piper (1972) found a positive relationship between sinking velocity and length of the foraminiferal shell. Much like Berthois and le Calvez (Berthois and Calvez, 1960), they found that foraminifera sink more slowly than quartz glass beads, for a bead to sink at the same rate as a foraminifera the bead needs to be 2.4 times smaller than the foraminifera. Despite using Stokes' Law to calculate density, their reported value of 1500 kg·m^{-3} is in close agreement with other studies (see above, Table 3-3). They report median sinking velocities for size fractions but no individual values, so their results are not included here. Based on the details provided, the use of demineralised water could result in slightly faster sinking velocities than would be observed in nature, due to the differences in density and viscosity of distilled water compared to seawater.

3.2.2.4 *Fok-Pun and Komar (1983)*

Fok-Pun and Komar (1983) sank foraminifera that were spherical (*Orbulina universa*) or near spherical (*Globigerinoides ruber, G. sacculifer* and *Globorotalia hirsuta*) in shape to allow easier comparison with the predictions from equations for the sinking speed of a sphere (see above).

Diameters of each foraminifera were measured along three orthogonal axes, with the longest used to calculate Re. As most species of foraminifera are not spherical, they have at least one axis which is shorter than the rest. Fok-Pun and Komar (1983) were the first to numerically quantify test shape, using the Corey Shape Factor (CSF, see Equation 3-10). The three measured diameters were used to calculate a CSF value for each foraminifera. The authors found that CSF values <<1.0 (a perfect sphere) resulted in decreased sinking velocities compared to CSF values closer to 1. Furthermore, "a good [positive] trend" between sinking velocity and length was found, which is in accordance with the predictions made using Equation 3-12 (Fok-Pun and Komar's (1983) equation 4). It should be noted that Equation 3-12 is derived from Stokes' Law (Equation 3-9). Density was calculated using sinking velocity, using Equation 3-12, and their value of 1480 kg·m^{-3} is in line with other studies (see above, Table 3-3). They concluded that sinking velocities of non-spherical species are lower than *O. universa* (almost spherical) due to reduced densities and departure from sphericity. These data are included for further analysis in this chapter. As Fok-Pun and Komar (1983) used demineralised water at room temperature, it would be expected that the sinking velocities they observed would be faster than in nature, due to the increase in density and reduced viscosity of water at room temperature.

Equation 3-12

$$\rho_{foraminifera} = \frac{3}{4} \cdot \rho_{fluid} \cdot C_D \cdot \left(\frac{U^2_{particle}}{g \cdot \emptyset} \right) + \rho_{fluid}$$

3.2.2.5 *Takahashi and Bé (1984)*

As outlined above (section 3.1) it is not clear if sinking foraminifera still have intact cytoplasm. To address this Takahashi and Bé (1984) used samples taken from a plankton tow and from sediment to investigate the potential effect of the presence of cytoplasm on sinking. A subset of the foraminifera from the plankton tow were heated in a furnace at 150°C to remove all organic matter, resulting in three sample types, 'ashed' (planktonic specimens which have been heated to remove organic matter), 'planktonic' (taken from the plankton tow, assumed to have cytoplasm intact) and 'sediment' (from the ocean floor, presumed not to have cytoplasm). The use of a lower temperature for ashing, compared to Berger and Piper (1972), should have maintained the structure of the calcium carbonate. The sinking velocities of the different sample types were then compared to see if cytoplasm has an effect on sinking velocities.

Takahashi and Bé (1984) found that using a nominal foraminifera diameter that accounts for weight improves the prediction of sinking velocities compared to the real test diameter, which might be expected based on the equations discussed in section 3.1.3 (as weight is used in the calculation of density). However, they did not find a strong correlation between sinking velocity and density, which hydrodynamic theory (see Equation 3-3, in section 3.1.3) predicts would have an effect (the average density is reported in Table 3-3). The data used for the published work (Takahashi and Be 1984) are reported along with various other measurements taken in a Scripps Institute of Oceanography (SIO) report (Takahashi, 1984), it is these data from the SIO report that are included for further analysis in this chapter. The most likely source of variation in this data is the origin of the material (planktonic, ashed, sediment). Material obtained from the sediment could still have fine sediments within the test that would be difficult to remove entirely. Particles within the test would make the sediment sample specimens heavier, and sink faster, than the specimens from the planktonic and the ashed sample types (see Appendix 9.1.8 , for testing of this theory).

3.2.2.6 *Furbish and Arnold (1997)*

Furbish and Arnold (1997) examined the possible evolutionary advantage to foraminifera having spines. To do this, they modelled foraminifera using beeswax and added spines made from entomological pins to some of the models. These enlarged models were then sunk in a range of viscous fluids (Table 3-3) to cover a range of Re numbers, which might be relevant to foraminifera. They found that the presence of spines increased the amount of drag for any given shape. This increase in drag is sufficiently large that the exact shape of the test does not have any effect on sinking speed when spines are present.

This study differs considerably from previous works on sinking foraminifera, firstly the use of shampoo, a non-Newtonian fluid (Gorla *et al.*, 2014), may affect the results. Secondly there is no attempt to model the foraminifera in a realistic manner. Basic shapes were formed using a bullet

mould and there is no attempt to replicate specific species morphologies. If more complex shape were modelled, then perhaps there would be an effect of shape. Additionally, the pins used to replicate spines were metal (entomological pins) and so considerably denser than the calcite of real spines. The use of metal pins would result in a distribution of mass that differs compared to a real foraminifera, despite the pins being positioned in "predetermined quasispherical pattern". However, their insights are interesting as they suggest that living foraminifera may use the presence of spines to reduce sinking rates, as well as a support structure for the pseudopodia. Further to the methodological issues highlighted above, Furbish and Arnold (1997) provide no settling velocities for their models. For these reasons their data are not included here.

3.2.2.7 *Caromel, Schmidt, Phillips and Rayfield (2014)*

Caromel *et al*. (2014) used a mixture of computational fluid dynamics (CFD) and experimental approaches to explore evolutionary possibilities available to planktonic foraminifera when faced with changing environments. As mentioned in section 3.1, and Chapter 1, there are arguments that living foraminifera use spines, and in non-spinose species, their morphology, to regulate their position in the water column. Under changing environments (i.e. warming or cooling of the water, resulting in changes in viscosity and density of the water) Caromel *et al*. (2014) suggest that different shapes may confer an evolutionary advantage. For the experimental methods foraminifera were classified into four groups of species with similar morphologies, referred to here as morphotypes (near-spherical, conical, discoidal and globular, see Figure 3-11).

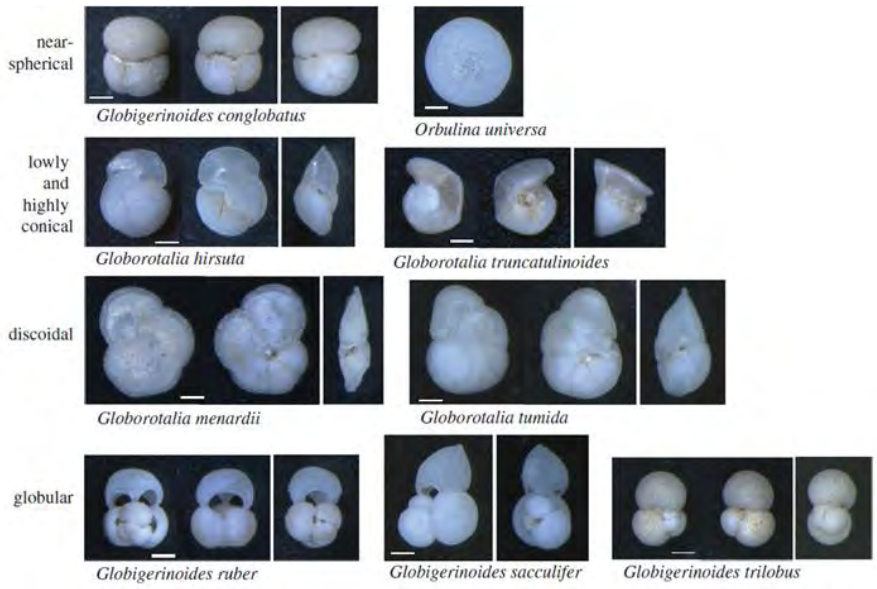

Figure 3-11: The groupings used by Caromel et al. (2014). From Caromel et al. (2014)

In addition to the experimental methods, CFD was also used to independently vary parameters such as calcite volume, water density and viscosity to examine the effects these variables have upon sinking velocities. Caromel *et al*. (2014) found that for a given size (maximum diameter) flatter shapes sink more slowly. They also found, in agreement with predictions from Equation 3-3, that lower density foraminifera sink more slowly than high density species. From the CFD, they found that changes in water viscosity (but not density) affect sinking velocity - this is interesting as if

foraminifera operate in lower Re ranges then viscosity would probably be the predominating force. However, foraminifera operate in the poorly understood intermediate Re range (although as discussed earlier the reported Re values in all studies may be overestimations), where the interactions between inertial and viscous forces cause effects that are less intuitive and not fully understood (Humphries, 2009). The data from Caromel *et al*. (2014) are included in the analysis here. The use of demineralised water is likely to increase the observed sinking velocities compared to those seen in nature.

3.2.2.8 *Summary*

The main parameters that control sinking speed have been found repeatedly in the previously published studies. These are:

1. Size - (Thoulet, 1891; Berthois and Calvez, 1960; Berger *et al.*, 1972; Fok-Pun and Komar, 1983; Takahashi *et al.*, 1984; Caromel *et al.*, 2014). Size is generally defined as maximum diameter. Berthois and le Calvez (Berthois and Calvez, 1960) also measured the projected area, which both encompasses size and shape.
2. Shape - (Thoulet, 1891; Berthois and Calvez, 1960; Fok-Pun and Komar, 1983; Caromel *et al.*, 2014). Shape is only numerically quantified by Fok-Pun and Komar (1983) using CSF, which provides a broad description, defined as departure from a sphere. Caromel *et al*. (2014), sort the species into morphotypes (as opposed to Aze *et al*'s (2011) morphogroups) which do not measure individual shape variations. As noted above, Berthois and Le Calvez's (1960) measure of area also includes some aspect of shape.
3. Density –(Berthois and Calvez, 1960; Fok-Pun and Komar, 1983; Takahashi *et al.*, 1984; Caromel *et al.*, 2014). Takahashi and Bé (1984) found a nominal diameter that accounts for weight (the diameter of a sphere with the same density and mass), which they found to be a better predictor of sinking velocity than maximum length. As their nominal diameter includes volume (as lengths) and mass they are effectively including density ($kg \cdot m^{-3}$) in their predictions. The calculation of density is a common pitfall in all studies, with the use of Stokes Law (Equation 3-9) by Berthois and la Calvez (1960) and the use of bulk volume measurements by Takahashi and Bé (1984) and Caromel *et al*. (2014).

3.3 Current Work

3.3.1 Confirming Findings and Identifying Measures of Size and Shape

3.3.1.1 *Introduction*

Since most of the studies were conducted, there have been considerable advances in both statistics and computational power which now permit more complex statistical analyses to be performed on the data. In order to conduct statistical analysis, all of the data was compiled into a single dataset.

To control for differences between studies (i.e. in calculation of variables such as C_D) the calculations were standardised and 'missing' variables calculated.

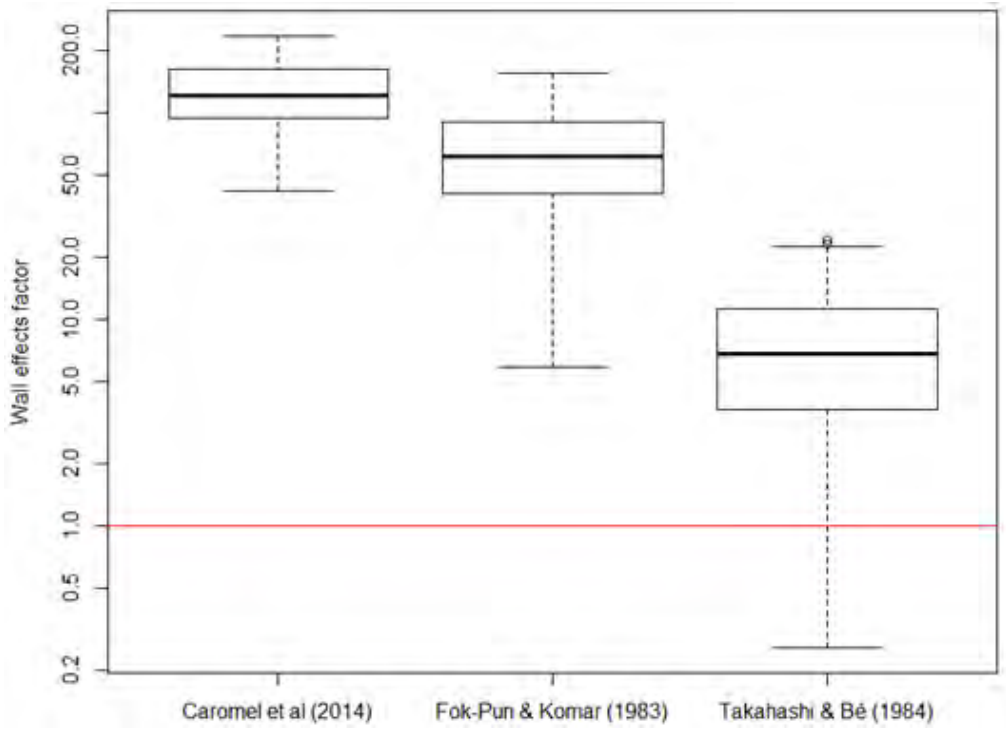

Figure 3-12: Potential for wall effects in three previous studies. For wall effects factors > 1 (calculated using Equation 3-11, above) it can be assumed there is no effect of the wall. (White, 1946; Vogel, 1994). *Only two specimens in Takahashi and Bé* (Takahashi *et al.*, 1984) *crossed the wall effects threshold (red line).*

As acknowledged above, one possible source of variation in sinking velocities is the different diameters of the settling tubes used. Whilst the authors of two of the studies (Fok-pun and Komar 1983; Caromel *et al*. 2014) state that wall effects were minimal (confirmed in Figure 3-12), the application of a wall effects correction factor (WECF, α in Equation 3-14) accounts for the variation in diameters of settling tube relative to the particle and sinking speed. Equation 3-14, modified from Ristow (Ristow, 1997), takes the measured sinking velocity ($U_{measured}$) of a sphere and adjusts this value to give the sinking velocity of the same particle in an unbounded fluid (U_{true}), i.e. the ocean. Equation 3-14 uses the ratio of particle radius (r) and tube radius (R) along with the value of α calculated from Equation 3-13, which also uses r and R. Equation 3-13 was empirically derived by Haberman and Sayre (Haberman and Sayre, 1958), accounting for wall effects up to particle-to-tube ratios of 0.6 (i.e. the particle diameter is two-thirds of the tube diameter), and assuming an infinite tube. Although foraminifera are not perfect spheres, this method allows variation due to different settling tubes to be minimised by calculating a standardised sinking velocity (U_{true}). Therefore, all sinking velocities were converted for analysis in this study to U_{true}.

Equation 3-13

$$\alpha = \frac{1 - 0.75857 \cdot \left(\frac{r}{R}\right)^5}{1 - 2.1050 \cdot \left(\frac{r}{R}\right) + 2.0865 \cdot \left(\frac{r}{R}\right)^3 - 0.72603 \cdot \left(\frac{r}{R}\right)^6}$$

Equation 3-14

$$U_{true} = \frac{U_{measured}}{\left(1 - \frac{1}{\alpha} \cdot \frac{r}{R}\right)}$$

Once the reoccurring predictors of sinking velocity were identified from the published literature, namely length, volume and density, the data were combined into a large dataset which was examined for relationships between these variables and sinking velocity. If there is a relationship between sinking velocity and volume, it is expected there will be a similar relationship with density as density relies on volume.

3.3.1.2 *Methods*

Sinking Velocity and Foraminifera Data

Published data from three studies, Fok-Pun and Komar (1983), Takahashi and Bé (1984) and Caromel *et al.* (2014) were compiled and compared, resulting in sinking velocities and other measurements (see Appendix 9.1.3, for full list of parameters) for 645 individual foraminifera from 14 species. Where possible, values that were absent from individual studies were calculated (see Appendix 9.1.3, Table 9-2Table 9-2). All species names were cross-checked for synonyms with the World Register of Marine Species (Horton *et al.*, 2018) and adjusted to match the names used in Aze *et al.* (2011).

WECF (Equation 3-14) was applied to sinking velocities using longest length as the particle diameter. Following the suggestion of Vogel (1994) that sinking particles have a preferred orientation, i.e. presenting the maximum projected area to the fluid. Therefore, the longest length is a reasonable approximation of the particle diameter when in the sinking orientation (i.e. ⌀ in Figure 3-8). This was converted to a radius for use in Equation 3-14. Tank radius (R in Equation 3-14) was calculated for each study using reported tank diameter.

Here, maximum length is used as a measure of size. In all the datasets it was measured directly from the specimen, rather than being estimated or calculated (e.g.: average diameter). Furthermore, length is an independent measure of size as it does not include other variables, for example nominal diameter (as calculated by Takahashi and Bé, 1984) introduces mass as a confounding factor (i.e. a factor which has a relationship between the dependent (sinking velocity) and the independent factors (parameters influencing sinking velocity)).

While length is an adequate proxy for size, volume is also included here because it measures size in more than one axis. However, for all studies the bulk volume is calculated here using three orthogonal measurements and a basic 3D shape geometric equation (see Appendix 9.1.3, Table 9-2). This is not the most accurate method of quantifying the volume of the test and will result in an overestimation of volume, but the same method of calculation was used for all data sources and, thus, allows for trends to be observed. Volume is also a component of density, another variable

which is included here (see below), along with mass. By including both volume and mass, the different aspects of density can be individually examined with relation to sinking velocity.

Density is included as it is predicted to be an important determinant of sinking velocity (See Equation 3-3), and it has been found to correlate with sinking velocity in a number of studies (Berthois and Calvez 1960; Fok-pun and Komar 1983; Takahashi and Be 1984; Caromel *et al*. 2014). The calculation of density is for a water-filled test (see Table 9-2) and uses the bulk volume and an assumed density for calcite of 2700 Kg·m^3 (as only the dead organism is being considered here, no consideration of cytoplasm needs to be made), the water density used in the calculation is as reported in each specific study.

As previously mentioned, C_D and Re are dimensionless, so they can be used to remove the effect of differences in fluid viscosity and density. In this work Re and C_D will not be used to predict sinking velocity (as sinking velocity is used in the calculation of Re (see Equation 3-2) and C_D (see Equation 3-6). However, both will be examined in light of Stokes' Law and compared to empirically derived solutions for spheres across all Re regimes.

Takahashi and Bé (1984) examined foraminifera from different sampling locations. This is the only study, for which individual foraminifera data are available, that used foraminifera of different sample types. Therefore, differences in a number of variables (sinking velocity, length, mass, density, Re and C_D) between the different sample types was investigated using ANOVA and Tukey HSD *post hoc* test.

The two measures of shape that will be used to look for an effect on sinking velocity are CSF and Morphogroup. CSF allows the capturing of individual morphology and difference from a sphere, which has shown to influence sinking speed (Fok-pun and Komar, 1983). Morphogroup allows a more complete but qualitative description of morphology which is not defined by three linear measurements (i.e. CSF), but morphogroups which are very similar in overall shape are present (i.e. morphogroup 2 (spinose globular) and 3 (non-spinose globular), see Figure 3-13 and Table 3-6). Once potential variables had been identified (section 3.3.1.5) regression statistics were performed (3.3.2).

Table 3-6: Morphogroups described by Aze et al. (2011).

Aze *et al.* morphogroup	Aze *et al.* definition
2	Spinose, globular
3	Spinose, globular with supplementary apertures
4	Spinose, spherical
6	Spinose, planispiral
7	Non-spinose, globular
14	Non-spinose, globorotaliform, keeled
15	Non-spinose, globorotaliform, angluconical

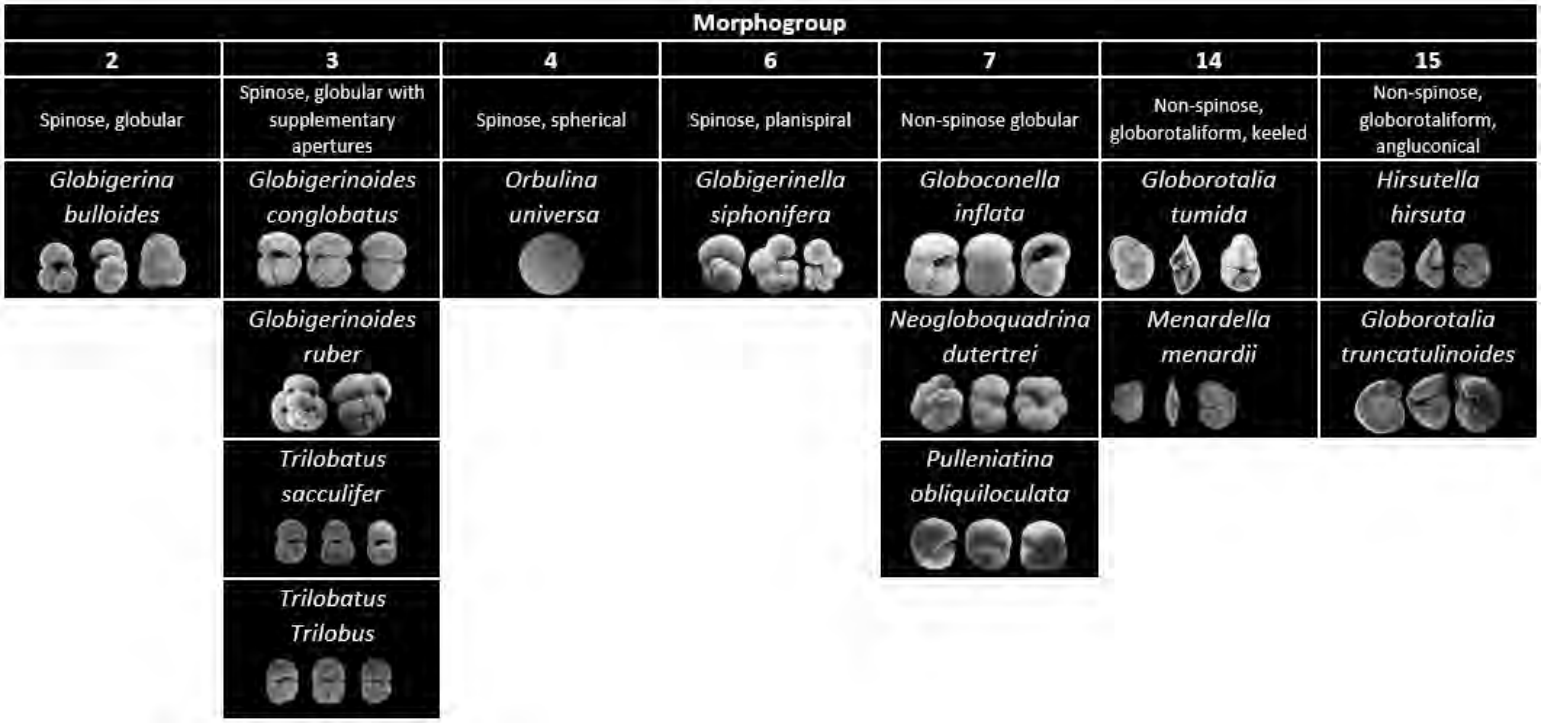

Figure 3-13: Species used in (Fok-Pun and Komar (1983), Takahashi and Bé (1984) and Caromel et al. (2014)), and classified under the morphogroups defined by Aze et al. (2011). Images from http://www.mikrotax.org/pforams/index.html.

3.3.1.3 *Statistical Analyses*

Chapter 4 All statistical analyses were conducted in R (version 3.4.2, R Core Team, 2018) using the 'stats' base package. Initial investigation of parameters was conducted on only the single variables, to mimic the previous studies. Sinking velocities, lengths and densities were log transformed (Log_{10}) to reduce skew and homogenise variance (Box and Cox, 1964; LaBarbera, 1989). Furthermore, the effect of increases in length results in a multipliable effect on volume and density (and the inverse is true), and as such these data are suitable for log-transformation (Quinn and Keough, 2002; O'Hara and Kotze, 2010). Linear models were used to examine relationships between sinking velocity and the parameters identified above. Analyses of variance (ANOVA) were performed with a Tukey Honest Significant Differences (HSD) *post-hoc* test to find differences in sinking velocity, and CSF, between morphogroups. Differences between the sources, for each variable, were also tested. This was achieved using ANOVA and Tukey HSD *post-hoc* test.

3.3.1.4 *Results*

In the dataset compiled from Fok-Pun and Komar (1983), Takahashi and Bé (1984) and Caromel *et al.* (2014), henceforth *compiled dataset*, when each parameter is examined individually sinking velocity correlates significantly with maximum length ($F_{1,643}$=550.4, p<0.001, adjusted R^2=0.460), volume ($F_{1,643}$=494.7, p<0.001, adjusted R^2= 0.434), density ($F_{1,643}$=331, p<0.001, adjusted R^2=0.339) and mass ($F_{1,643}$=3336, p<0.001, adjusted R^2= 0.838), (see Figure 3-14 left hand side and Table 3-8). However, the strength of the correlation varies when the data are examined by study (see Figure 9-1 and Table 9-6).

When adjusting the sinking velocity (to account for the differing diameters of settling tank i.e. U_{true}) in place of reported sinking velocity, the amount of variation in the data explained by the models is very slightly increased for: maximum length ($F_{1,643}$=555.3, p<0.001, adjusted R^2=0.463), volume ($F_{1,643}$=499.8, p<0.001, adjusted R^2= 0.437) and mass ($F_{1,643}$=3350, p<0.001, adjusted R^2= 0.839), but the increase in the R^2 values is fairly small (a maximum increase in R^2 of 0.003, or 0.3%), confirming that the effect of the settling tube diameter is minimal (See Figure 3-14, right hand side). However, there is a slight decrease in the amount of variation explained by the models for density ($F_{1,643}$=328.8, p<0.001, adjusted R^2= 0.337). The relationships between predictor variables and sinking velocities between studies differ in their strength (Table 9-6 and Figure 9-1).

The sinking velocity of all species can be predicted using the maximum length (Figure 9-2), although the strength of the correlation differs between species. For the other predictor variables (volume, density and mass) there are also differences between species (see Appendix 9.1.5)

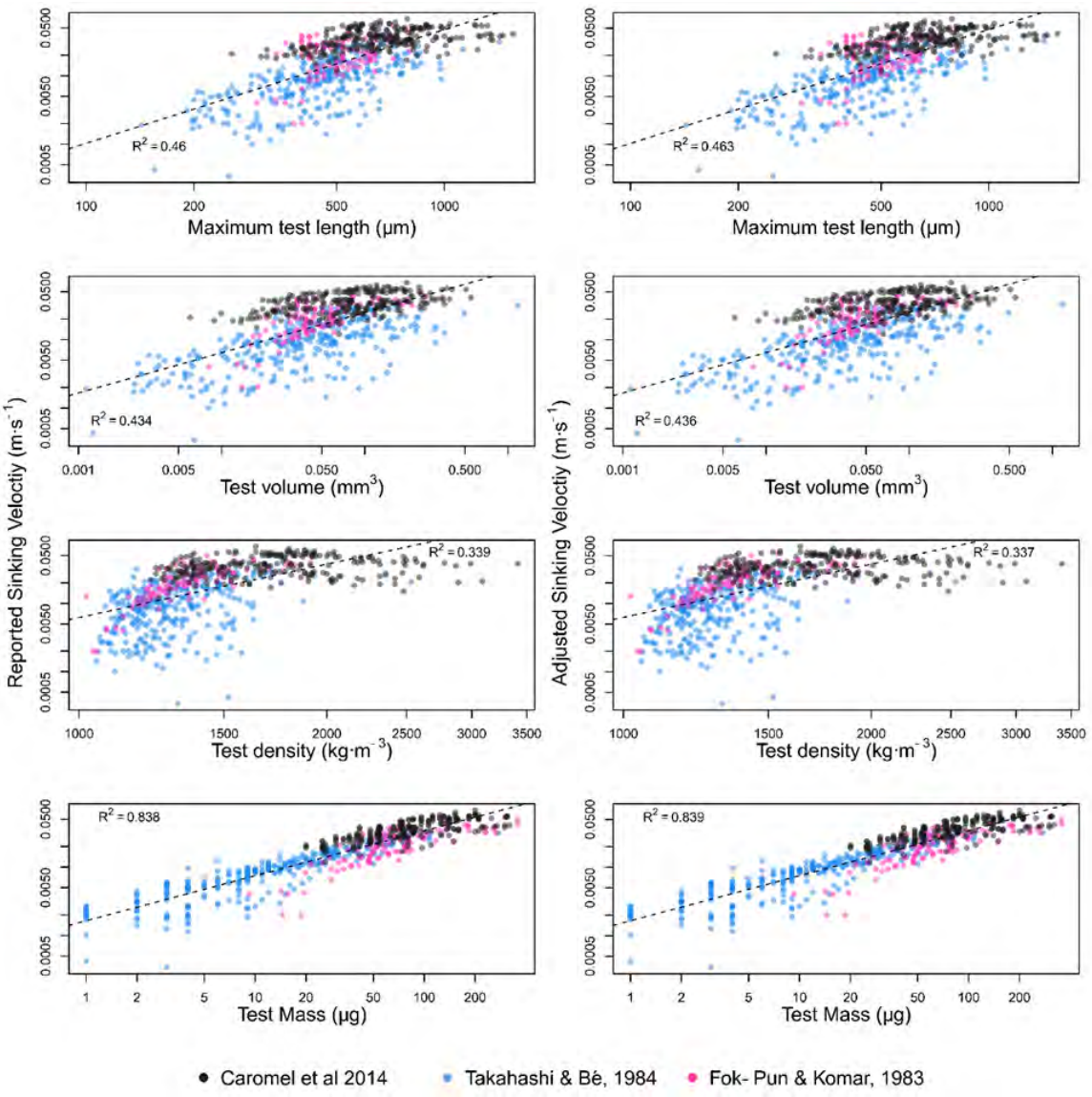

Figure 3-14: Pooled data from Fok-Pun and Komar (1983)*, Takahashi and Bé* (1984)*, and Caromel et al.* (2014) *of reported (left), adjusted (right) sinking velocities and length, volume density and test weight. In each panel a dotted line shows a linear regression of the relative sinking velocity and predictor variable with R^2 values reported.*

Using ANOVA, there are significant differences between studies (Fok-Pun and Komar, 1983; Takahashi and Bé, 1984; and Caromel *et al.*, 2014) for all variables: sinking velocity ($F_{2,642}$ = 344, p<0.001, see Figure 3-16), length ($F_{2,642}$ = 99.66, p<0.001, Figure 3-15A), mass ($F_{2,642}$ = 332.2, p<0.001, Figure 3-15B), density ($F_{2,642}$ = 212.9, p<0.001, Figure 3-15C), volume ($F_{2,642}$ = 48.65, p<0.001, Figure 3-15D), Re ($F_{2,642}$ = 508.4, p<0.001, Figure 3-15E) and C_D ($F_{2,642}$ = 182.9, p<0.001, Figure 3-15F). When examining the pair-wise differences, there are differences between all studies (i.e. each study is different from the other two studies) for sinking velocity, length, volume, Re and C_D (Table 3-7). For mass there are no significant differences (i.e. the variances of the two are the same) between Fok-Pun and Komar (1983) – Caromel *et al.* (2014), but all other pairwise comparisons are significantly different (Table 3-7).

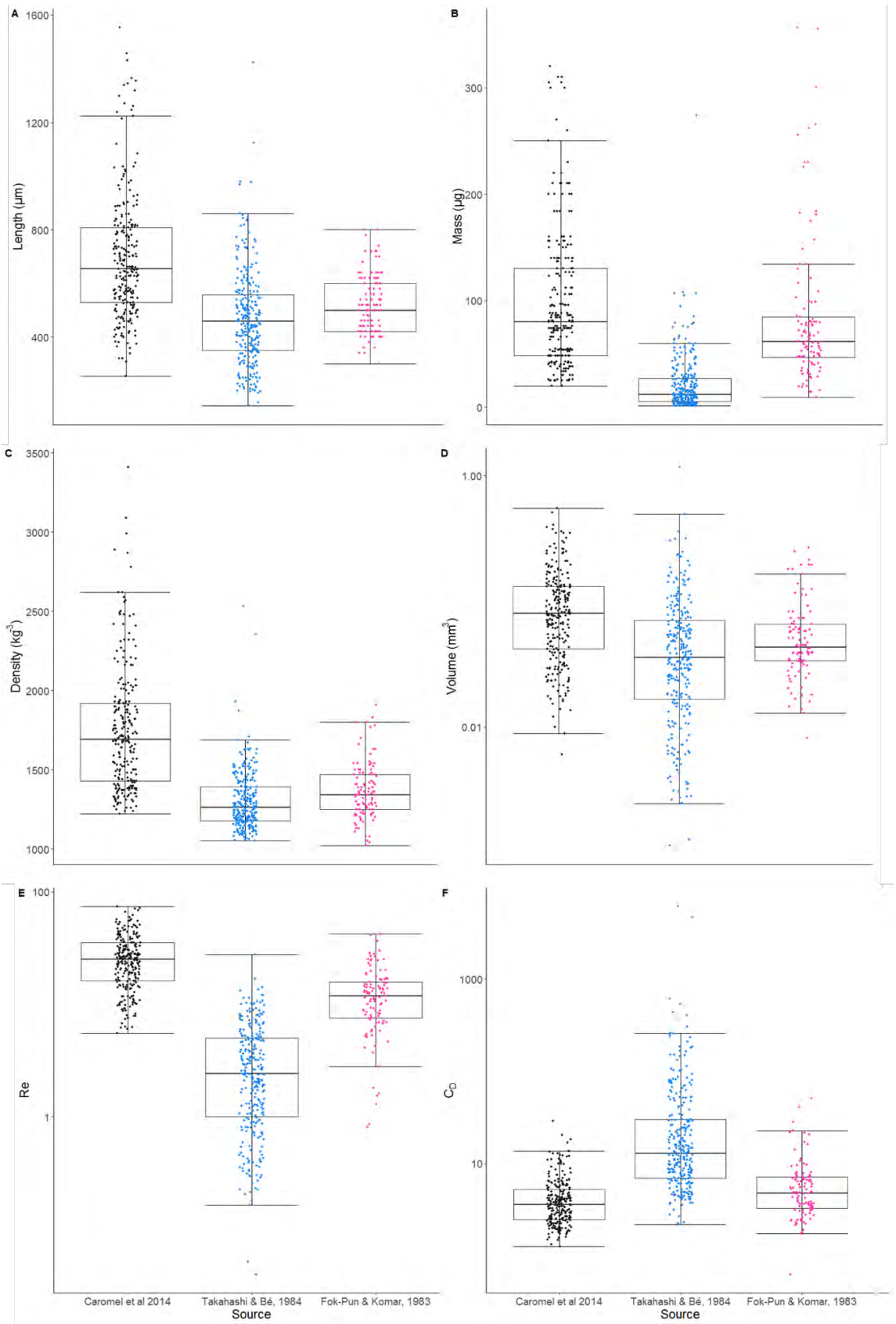

Figure 3-15: Differences in length (A, $F_{2,642}$ = 99.66, p<0.001), mass (B, $F_{2,642}$ = 332.2, p<0.001), density (C, $F_{2,642}$ = 212.9, p<0.001), volume (D, $F_{2,642}$ = 48.65, p<0.001), Re (E, $F_{2,642}$ = 508.4, p<0.001) and C_D (F, $F_{2,642}$ = 182.9, p<0.001) between studies. Note volume and C_D (D and F) are plotted with a logged y axis to allow better visualisation. Pairwise comparisons presented in Table 3-7.

Table 3-7: Pairwise comparison of each variable (sinking velocity, length, mass, density, Re and C_D) between each data source.

Comparison	Difference in means	Lower CI	Upper CI	Adjusted p value
Sinking Velocity				
Fok-Pun and Komar (1983) – Caromel *et al.* (2014)	-0.247	-0.323	-0.171	<0.001
Takahashi and Bé (1984) – Caromel *et al.* (2014)	-0.633	-0.69	-0.576	<0.001
Takahashi and Bé (1984) – Fok-Pun and Komar (1983)	-0.386	-0.46	-0.312	<0.001
Length				
Fok-Pun and Komar (1983) – Caromel *et al.* (2014)	-0.112	-0.151	-0.073	<0.001
Takahashi and Bé (1984) – Caromel *et al.* (2014)	-0.176	-0.205	-0.146	<0.001
Takahashi and Bé (1984) – Fok-Pun and Komar (1983)	-0.064	-0.102	-0.025	<0.001
Mass				
Fok-Pun and Komar (1983) – Caromel *et al.* (2014)	-0.089	-0.195	0.018	0.124
Takahashi and Bé (1984) – Caromel *et al.* (2014)	-0.829	-0.91	-0.749	<0.001
Takahashi and Bé (1984) – Fok-Pun and Komar (1983)	-0.741	-0.845	-0.637	<0.001
Density				
Fok-Pun and Komar (1983) – Caromel *et al.* (2014)	-0.102	-0.121	-0.083	<0.001
Takahashi and Bé (1984) – Caromel *et al.* (2014)	-0.122	-0.137	-0.108	<0.001
Takahashi and Bé (1984) – Fok-Pun and Komar (1983)	-0.021	-0.039	-0.002	0.026
Volume				
Fok-Pun and Komar (1983) – Caromel *et al.* (2014)	-0.199	-0.313	-0.085	<0.001
Takahashi and Bé (1984) – Caromel *et al.* (2014)	-0.36	-0.446	-0.274	<0.001
Takahashi and Bé (1984) – Fok-Pun and Komar (1983)	-0.161	-0.272	-0.05	0.002
Reynolds number				
Fok-Pun and Komar (1983) – Caromel *et al.* (2014)	-0.344	-0.447	-0.241	<0.001
Takahashi and Bé (1984) – Caromel *et al.* (2014)	-1.037	-1.115	-0.96	<0.001
Takahashi and Bé (1984) – Fok-Pun and Komar (1983)	-0.693	-0.794	-0.592	<0.001
C_D				
Fok-Pun and Komar (1983) – Caromel *et al.* (2014)	0.13	0.019	0.241	0.017
Takahashi and Bé (1984) – Caromel *et al.* (2014)	0.658	0.574	0.742	<0.001
Takahashi and Bé (1984) – Fok-Pun and Komar (1983)	0.529	0.419	0.638	<0.001

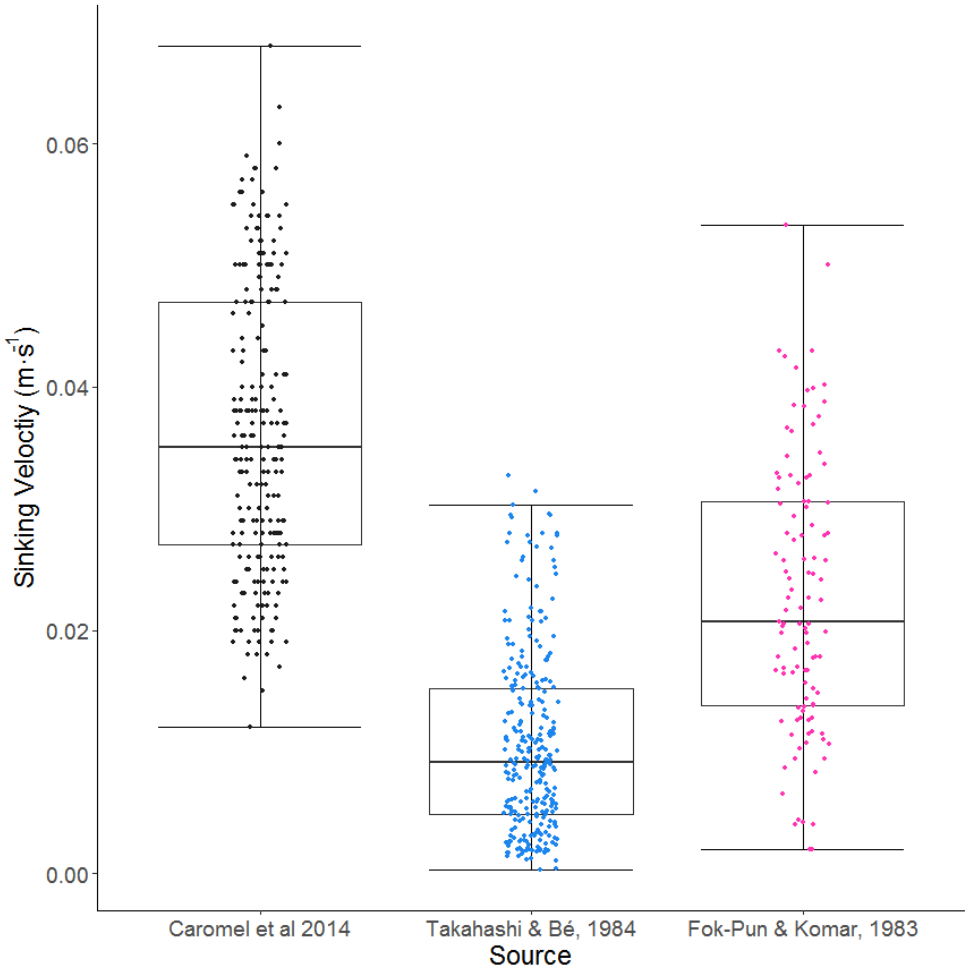

Figure 3-16: Comparisons of sinking velocities between sources. There are significant differences between the studies ($F_{2,642}$ = 344, p<0.001), see Table 3-7 for pairwise comparisons. Error bars are 1.5 times the inter quartile range (IQR).

When comparing the C_D values of the foraminifera, to those expected under Stokes Law (for low Re) and with Morrison's equation (for a sphere over all values of Re), the data do not fit well with either (R^2 = 0.181 for both Stokes' Law and Morrison's (2010) equation, Figure 3-17). When examining the C_D values by broad morphotypes as defined by Caromel *et al.* (2014), the different morphotypes have different relationships with C_D (see Figure 3-18, and R^2 values therein), so the more spherical species fit closer to the empirically derived equation (Morrison's (2010) equation, which calculates C_D) for a sphere than the less spherical (e.g.: discoidal) species.

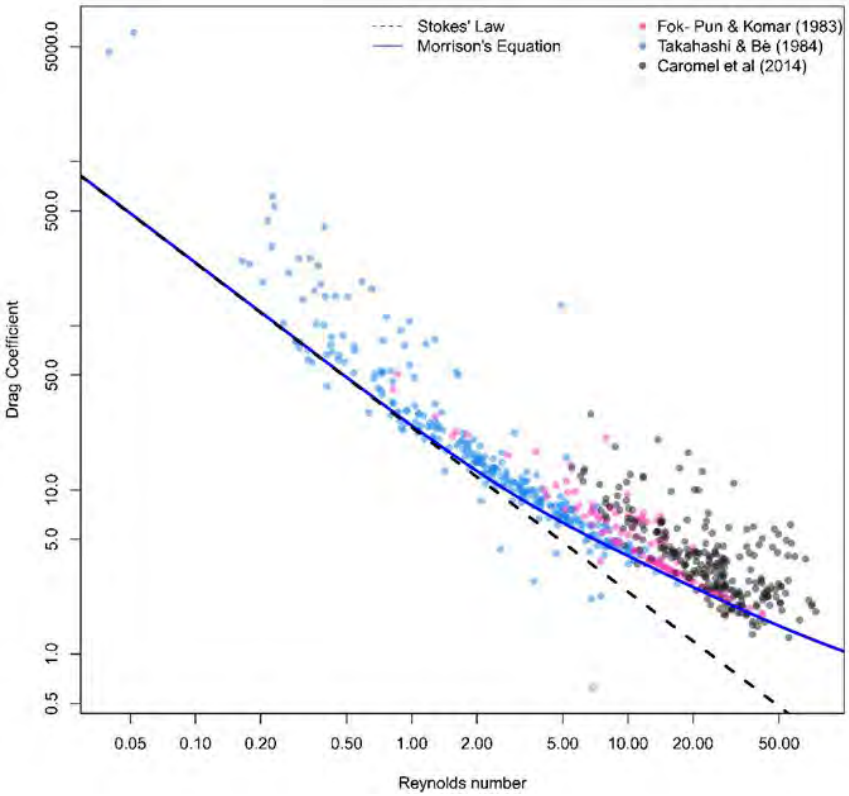

Figure 3-17: Re (calculated using adjusted sinking velocity values) and C_D (calculated using adjusted sinking velocity values). C_D values are calculated assuming an area of $A = \pi \cdot (\frac{L_{max}}{2}) \cdot (\frac{L_{min}}{2})$. Black line is Stokes Law (Equation 3-7) for C_D at low Re (R^2 = 0.181). Blue line uses Equation 3-8 for the C_D of a sphere across all Re values (R^2 = 0.181).

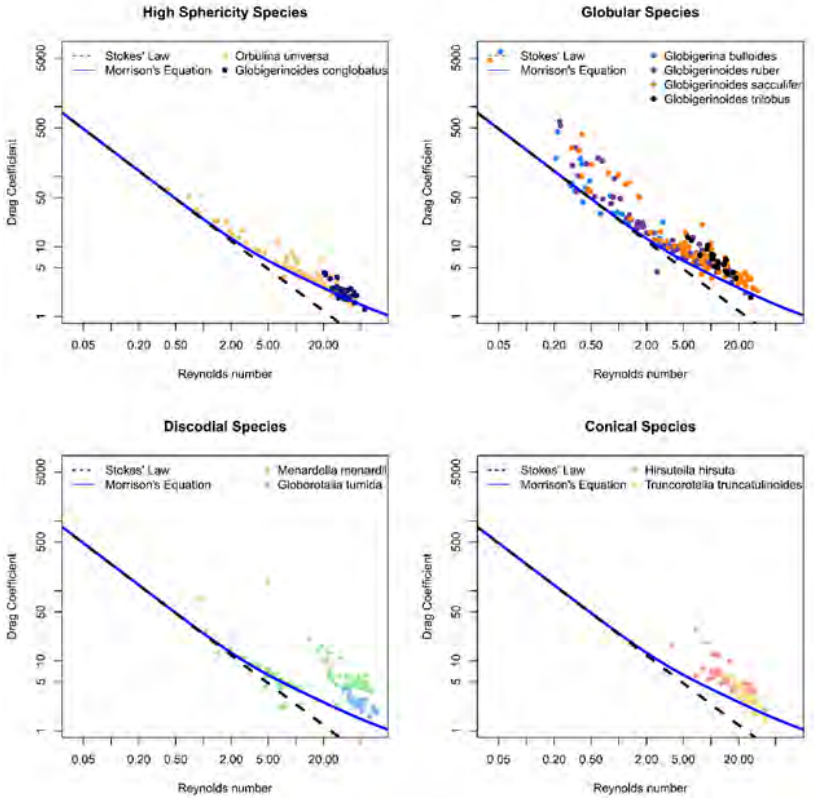

Figure 3-18: Corrected Re and C_D values for the different morphotypes (following Caromel et al's definitions; Highly spherical, globular, discoidal and conical) in comparison to Stokes' Law (dashed black line, Equation 3-7) and Morrison's Equation for a sphere (Equation 3-8). R^2 values with Morrison's equation for: Highly spherical, 0.865; globular, 0.168; discoidal, -0.210; and conical, -0.001. R^2 values with Stokes Law for: Highly spherical, 0.817; globular, 0.168; discoidal, -0.252; and conical, -0.498

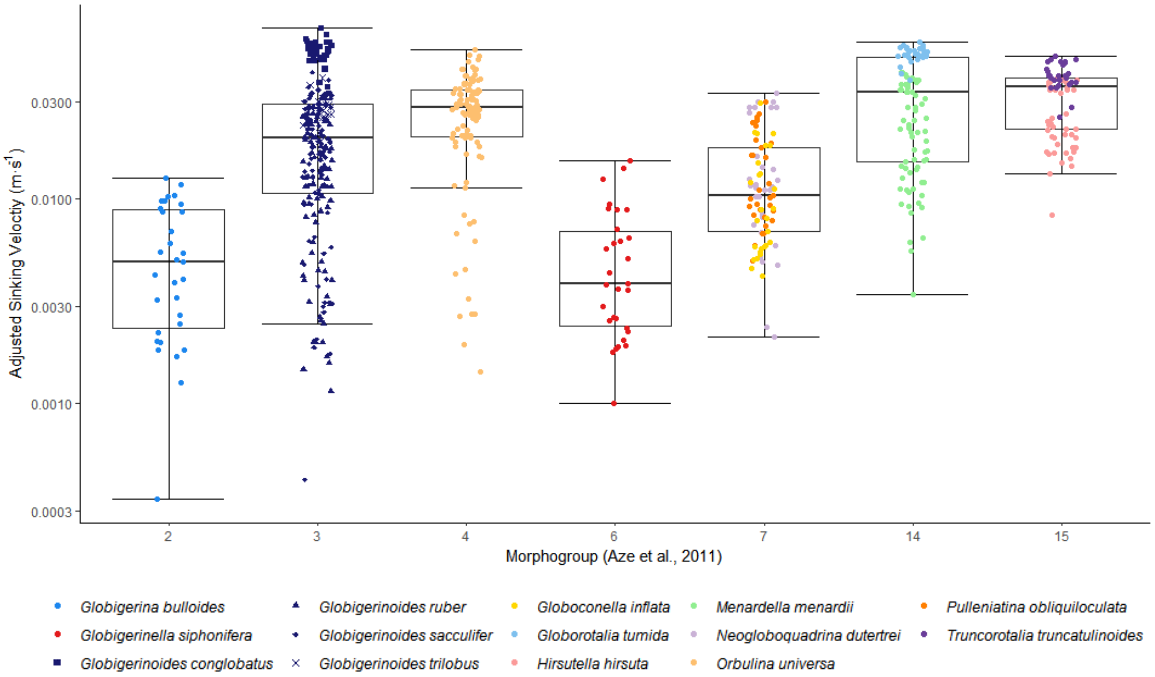

Figure 3-19: Sinking Velocity differ between morphogroup (F6,638 = 40.98, p<0.001). Morpho-groups are, 2 = spinose and globular, 3 = spinose and globular with supplementary apertures, 4 = spinose and spherical, 5 = spinose, clavate (club-shaped), 6 = spinose, planispiral (flatly coiled), 7 = non-spinose, globular, 14 = non-spinose, keeled globorotaliform (disc-like shape, narrower at the edges than the centre), 15 = non-spinose, globorotaliform, anguloconical (cone-shaped). Note some 'jitter' has been introduced to the data in the x axis to prevent over-plotting.

Sinking velocity (U_{true}) varies significantly between morphogroups (Figure 3-19, $F_{6,638}$ = 40.98, p<0.001). When making pairwise comparisons of sinking velocities across morphogroups using Tukey HSD, there is significant separation of sinking velocities between groups. Morphogroups which have sinking velocities that are not significantly different are: Spinose and planispiral and spinose globular (6 and 2); non-spinose globular and spinose globular (7 and 2); non-spinose globorotaliform (keeled) and spinose spherical (14 and 4); non-spinose globorotaliform anguloconical and spinose spherical (15 and 4); and non-spinose globorotaliform (keeled) and spinose globorotaliform anguloconical (14 and 15). Apart from these all morphogroup combinations have significantly different sinking velocities (Tukey HSD results in Table 3-8).

Table 3-8: Tukey HSD pairwise comparisons morphogroups for sinking velocities. Morphogroups with sinking velocity which are significantly different are underlined.

Morphogroup Comparison	Difference in mean sinking velocity ($m \cdot s^{-1}$)	Lower CI	Upper CI	Adjusted p value
3-2	0.017	0.009	0.024	<0.001
4-2	0.022	0.014	0.029	<0.001
6-2	0	-0.01	0.01	>0.99
7-2	0.008	-0.001	0.016	0.086
14-2	0.026	0.018	0.034	<0.001
15-2	0.026	0.018	0.035	<0.001
4-3	0.005	0	0.009	0.035
6-3	-0.017	-0.024	-0.009	<0.001
7-3	-0.009	-0.014	-0.004	<0.001
14-3	0.009	0.004	0.014	<0.001
15-3	0.01	0.004	0.015	<0.001
6-4	-0.022	-0.03	-0.014	<0.001
7-4	-0.014	-0.02	-0.008	<0.001
14-4	0.004	-0.001	0.01	0.264
15-4	0.005	-0.001	0.011	0.179
7-6	0.008	0	0.016	0.078
14-6	0.026	0.018	0.034	<0.001
15-6	0.027	0.018	0.035	<0.001
14-7	0.018	0.013	0.024	<0.001
15-7	0.019	0.013	0.025	<0.001
15-14	0.001	-0.005	0.007	>0.99

Table 3-6: Morphogroups described by Aze et al. (2011)

Aze *et al.* morphogroup	Aze *et al.* definition
2	Spinose, globular
3	Spinose, globular with supplementary apertures
4	Spinose, spherical
6	Spinose, planispiral
7	Non-spinose, globular
14	Non-spinose, globorotaliform, keeled
15	Non-spinose, globorotaliform, angluconical

As sinking velocity and length closely correlate, the differences in length between morphogroup were also compared. Morphogroups with lengths which are not significantly different are: Spinose, planispiral and Spinose, globular (6 and 2); Non-spinose globular and Spinose, globular (7 and 2); Spinose, planispiral and Spinose globular with supplementary apertures (6 and 3); Non-spinose, globorotaliform, angluconical and Spinose spherical (15 and 4); and Non-spinose globular and Spinose, planispiral (7 and 6, see Table 3-9).

From these results (above) it can be seen that some morphogroups that have lengths that do not differ significantly also have sinking velocities that do not differ significantly: Spinose, planispiral and Spinose, globular (6 and 2); Non-spinose globular and Spinose, globular (7 and 2); Non-spinose, globorotaliform, angluconical and Spinose spherical (15 and 4); and Non-spinose globular and

Spinose, planispiral (7 and 6). However, some morphogroups which have non-significantly different lengths have significantly different sinking velocities (6 spinose, globular; and 3 spinose globular with supplementray apertures; 15, non-spinose, globorotaliform, angluconical; and 14, Non-spinose, globorotaliform, keeled) and conversely one pair of morphogroups have significantly different lengths but not sinking velocities (15, Non-spinose, globorotaliform, angluconical; and 14, Non-spinose, globorotaliform, keeled). It should be noted that *P. obliquiloculata* (morphogroup 7, Non-spinose, globular) and *Gs*. *Conglobatus* (morphogroup 3, Spinose, globular with supplementary apertures) both have thicken walls, due to a thick layer of calcite crust. This will substantially increase the mass and density of these species, and thereby their sinking velocities, which may explain some of these results.

There are significant differences in density ($F_{6,638}$ = 34.38, p<0.001), mass ($F_{6,638}$ = 47.4, *p*<0.001) and volume ($F_{6,638}$ = 55.6, *p*<0.001) between morphogroups. However, there are some morphogroup pairs that do not differ significantly in density (2 from 4,6 and 7; 3 from 14; 4 from 7 and 14; 6 from 7; and 7 from 14), mass (2 from 7 and 6; 4 from 15 and 6 from 7) and volume (2 from 3, 6,7 and 15; 3 from 6,7 and 15; 6 from 7 and 15 and 7 from 15) (See Appendix 9.1.6 for full pairwise comparison).

Table 3-9: Pairwise comparisons of length between morphogroups. For both length and sinking velocity there are no differences between morphogroups 2-6 and 15-4 (see Table 3-8). Significant p values are underlined.

Morphogroup Comparison	Difference in mean length (µm)	Lower CI	Upper CI	Adjust p value
3-2	150.315	63.108	237.521	<0.001
4-2	207.642	114.622	300.661	<0.001
6-2	66.16	-50.26	182.581	0.629
7-2	77.632	-17.171	172.434	0.191
14-2	551.813	457.786	645.839	<0.001
15-2	262.141	165.266	359.016	<0.001
4-3	57.327	3.233	111.421	0.03
6-3	-84.154	-172.626	4.317	0.074
7-3	-72.683	-129.788	-15.577	0.003
14-3	401.498	345.691	457.305	<0.001
15-3	111.827	51.343	172.31	<0.001
6-4	-141.481	-235.688	-47.275	<0.001
7-4	-130.01	-195.65	-64.369	<0.001
14-4	344.171	279.657	408.685	<0.001
15-4	54.499	-14.1	123.098	0.222
7-6	11.472	-84.496	107.439	>0.99
14-6	485.652	390.452	580.853	<0.001
15-6	195.981	97.966	293.995	<0.001
14-7	474.181	407.122	541.24	<0.001
15-7	184.509	113.511	255.507	<0.001
15-14	-289.672	-359.629	-219.714	<0.001

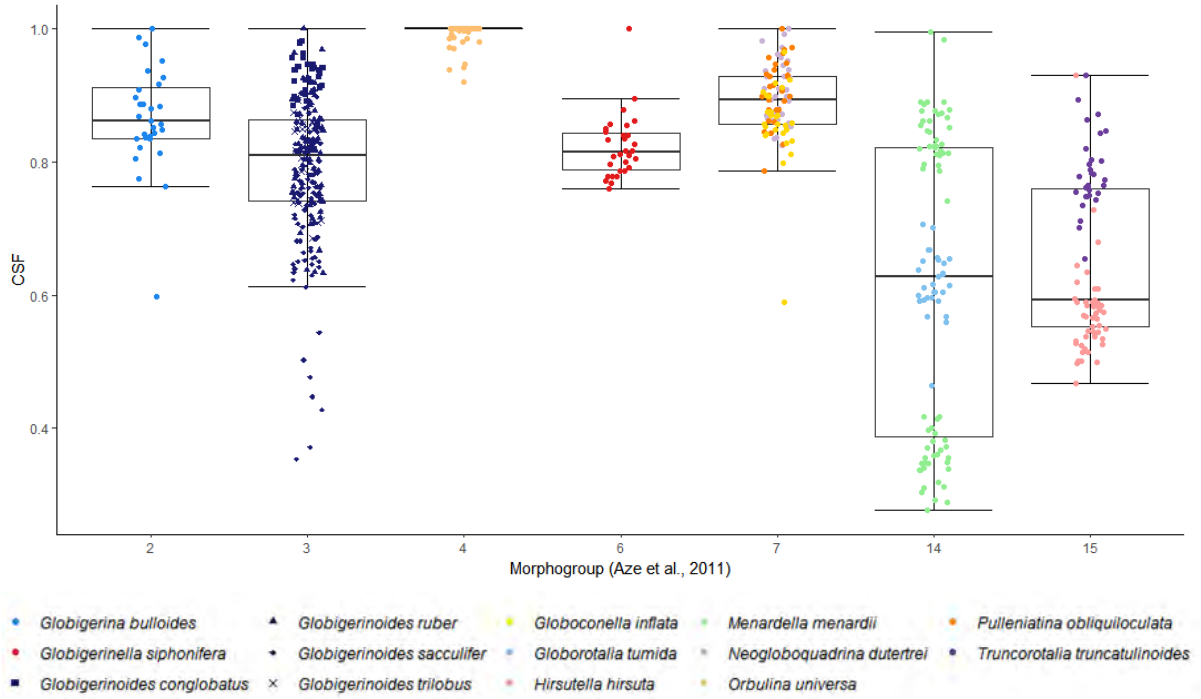

Figure 3-20: Overlap between CSF values and morphogroup, showing that foraminifera with different shapes (morphogroup) can have the same CSF values. Note some 'jitter' is introduced to the data in the x axis to prevent over-plotting. Morpho-groups are, 2 = spinose and globular, 3 = spinose and globular with supplementary apertures, 4 = spinose and spherical, 5 = spinose, clavate (club-shaped), 6 = spinose, planispiral (flatly coiled), 7 = non-spinose, globular, 14 = non-spinose, keeled globorotaliform (disc-like shape, narrower at the edges than the centre), 15 = non-spinose, globorotaliform, anguloconical (cone-shaped). Note some 'jitter' has been introduced to the data in the x axis to prevent over-plotting.

There is overlap in CSF values between morphogroups (using ANOVA with Tukey HSD, see Figure 3-20), but CSF can be predicted by morphgroup ($F_{6,638}$ = 122.5, p<0.001). Pairwise comparisons (Table 3-10) show that the morphogroups which are not separated are: 6-2, 7-2, 6-3, 7-6 and 15-14.

Table 3-10: Pairwise comparisons of CSF between morphogroups. Significant p values are underlined.

Morphogroup Comparison	Difference in mean CSF	Lower CI	Upper CI	Adjust p value
3-2	-0.07262	-0.13763	-0.00762	0.017337
4-2	0.127272	0.057932	0.196611	<0.001
6-2	-0.04584	-0.13263	0.04094	0.706417
7-2	0.022563	-0.04811	0.093231	0.965132
14-2	-0.24991	-0.32	-0.17982	<0.001
15-2	-0.21518	-0.28739	-0.14296	<0.001
4-3	0.199895	0.159572	0.240218	<0.001
6-3	0.02678	-0.03917	0.092729	0.893739
7-3	0.095186	0.052618	0.137754	<0.001
14-3	-0.17729	-0.21889	-0.13569	<0.001
15-3	-0.14255	-0.18764	-0.09747	<0.001
6-4	-0.17311	-0.24334	-0.10289	<0.001
7-4	-0.10471	-0.15364	-0.05578	<0.001
14-4	-0.37718	-0.42527	-0.32909	<0.001
15-4	-0.34245	-0.39358	-0.29131	<0.001
7-6	0.068405	-0.00313	0.139942	0.071529
14-6	-0.20407	-0.27503	-0.1331	<0.001
15-6	-0.16933	-0.2424	-0.09627	<0.001
14-7	-0.27247	-0.32246	-0.22248	<0.001
15-7	-0.23774	-0.29066	-0.18481	<0.001
15-14	0.034733	-0.01742	0.086881	0.434921

Table 3-6: Morphogroups described by Aze et al. (2011)

Aze *et al.* morphogroup	Aze *et al.* definition
2	Spinose, globular
3	Spinose, globular with supplementary apertures
4	Spinose, spherical
6	Spinose, planispiral
7	Non-spinose, globular
14	Non-spinose, globorotaliform, keeled
15	Non-spinose, globorotaliform, angluconical

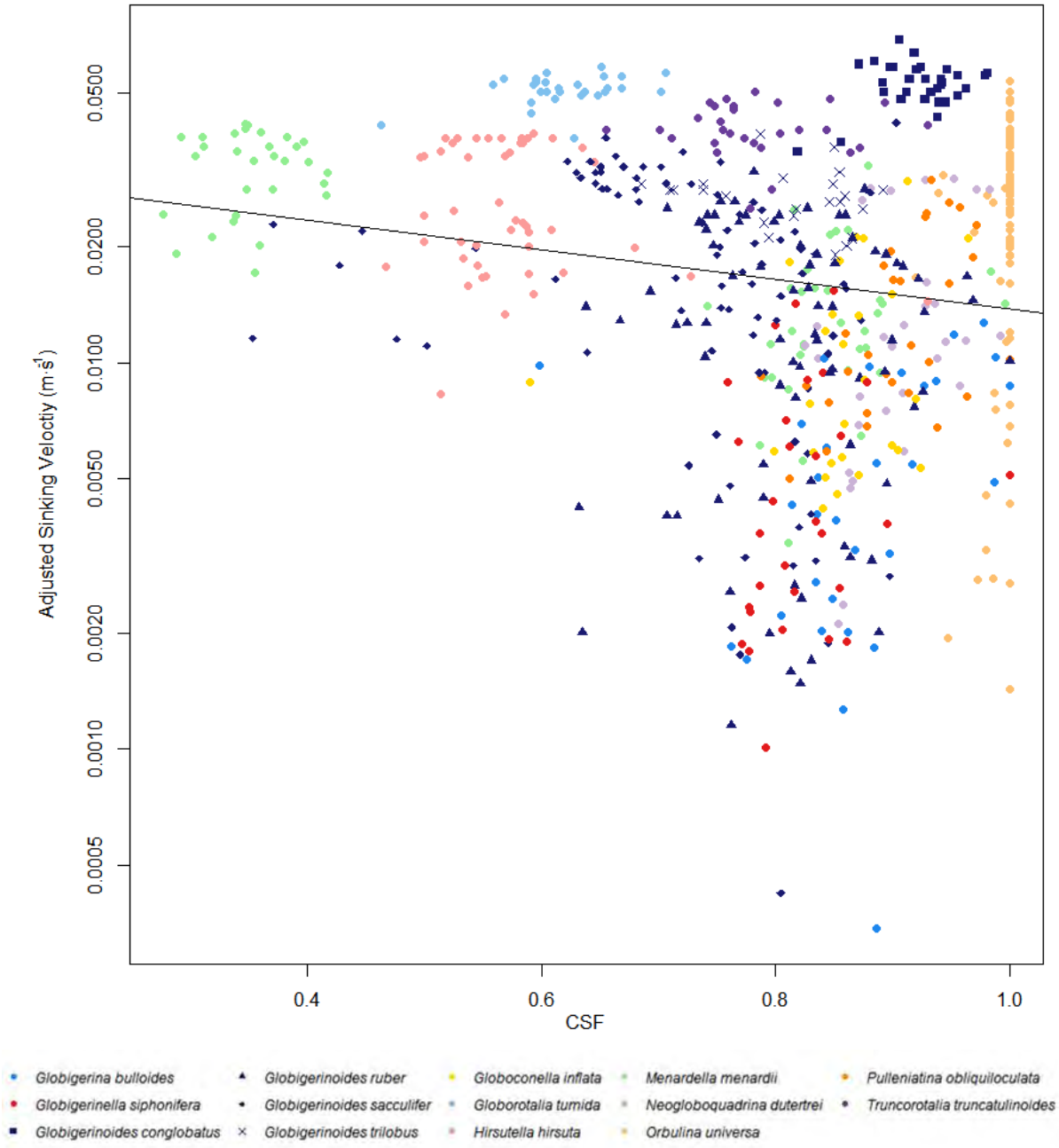

Figure 3-21: Sinking velocity ($m \cdot s^{-1}$) and CSF. There is no significant relationship between sinking velocity and CSF

Examining the relationship between sinking velocity and CSF finds no significant relationship ($F_{1,356}$=2.846, p=0.09249, Adjusted R^2= 0.005143, Figure 3-21). Some species have limited ranges in sinking velocity (e.g.: *G. tumida*), whilst some species have a larger range (e.g.: *O. universa*).

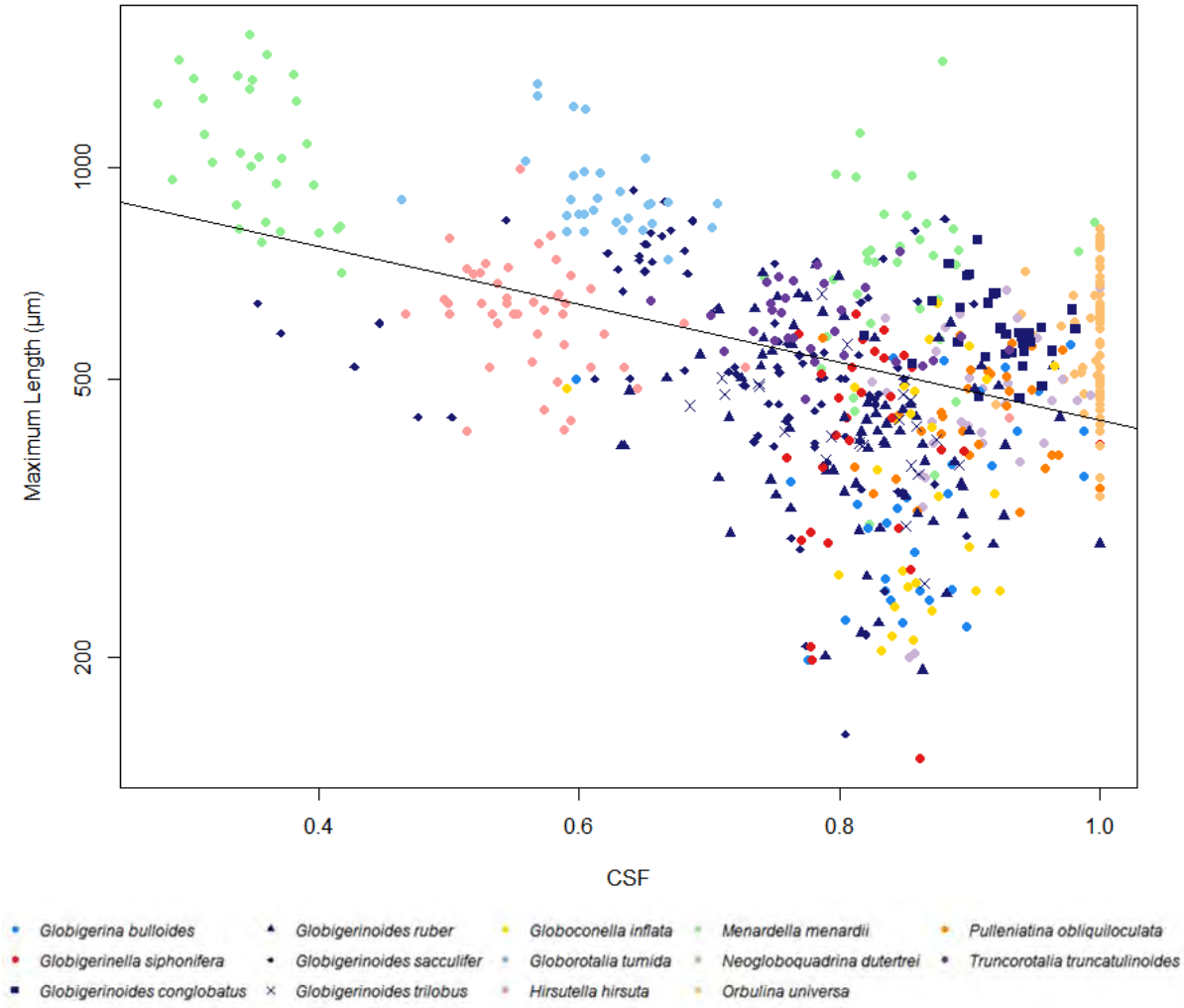

Figure 3-22: CSF and maximum length, coloured by species

There is a significant, negative relationship between maximum length and CSF ($F_{1,643}$=220.3, p<0.001, Adjusted R^2= 0.254), as maximum length decreases sphericity (CSF) increases (see Figure 3-22). Making comparisons between Figure 3-22 and Figure 3-21, species which have high sinking velocities are not the longest species.

3.3.1.5 *Parameters to be Explored Further*

From previous studies, the important parameters in determining sinking velocities are: Size, shape and density (see above, 3.2.2). Using the pooled data from previous studies, the relationship between sinking velocity and these variables has been confirmed here (see Appendix 8.1)

Sinking velocity (U_{true}) and maximum test length has a relatively strong positive correlation (R^2 = 0.463 for the pooled data (see Figure 3-14, Appendix 9.1.7 Figure 9-1, and Appendix Figure 9-2 and accompanying tables Appendix 9.1.7 **Error! Reference source not found.** and Appendix 9.1.7 Table 9-7). Although the specific relationship varies between species (see Appendix 9.1.7 Figure 9-2 and Table 9-7).

Mass is a strong predictor of sinking velocity (see Figure 3-14, R^2 = 0.839 for the pooled data). However, mass and volume are interconnected, foraminifera with larger volumes have larger

masses. Density accounts for both mass and volume, providing a mass per unit of volume (i.e. $kg \cdot m^{-3}$), and shows a positive relationship with sinking velocity ($R^2 = 0.337$ for pooled data).

Sinking velocity was found to differ between morphogroups (Figure 3-19), suggesting that this measure of shape maybe be able to help understand how shape effects sinking velocity. There is not a significant relationship between CSF and sinking velocity, however CSF does provide a numerical quantification of shape, as opposed to the categorical approach of morphogroup. Furthermore, different morphogroups have different CSF values (Table 3-10), showing that different morphogroups have different sphericity, which Fok-Pun and Komar (1983) found to be an important variable in determining sinking velocity. This difference in sphericity coupled with other features which are captured by the morphogroups (but missed by the tri-axial linear measurements of CSF) could explain the differences seen in sinking velocities between morphogroups.

There are significant differences between both sinking velocities and the variables (e.g.: length, density etc.), which are shown both here and elsewhere (Thoulet, 1891; Berthois and Calvez, 1960; Berger *et al.*, 1972; Fok-Pun and Komar, 1983; Takahashi *et al.*, 1984; Caromel *et al.*, 2014) to be important in determining sinking velocities, between data sources. These differences could be due to different species being used by each study, as different species have different sinking velocities and sizes (see Appendix 9.1.7 Figure 9-1 and Appendix 9.1.7 Figure 9-2). Regardless of the reason this shows that source needs to be controlled for in the phylogenetic analyses. Furthermore, there are differences between the different samples, used by Takahashi and Bé (1984), for all variables. Again, this needs to be controlled for in the phylogenetic statistics, which will be addressed in Chapter 6.

In summary, from these analyses we can determine that parameters that should be included in linear models to predict sinking velocity from are: length (as a measure of size), density (as a volume-less measure of mass), CSF (as a continuous measure of shape) and morphogroup (as a discrete measure of shape).

3.3.2 Linear models

3.3.2.1 *Methods*

Linear models were specified (in R, using the base function “lm”) to investigate the relationship between the important variables identified above (length and density), shape and sinking velocity. Three models were specified each using different measures of shape. Model One used both CSF and morphogroup as shape descriptors, Model Two uses only morphogroup, and Model Three uses only CSF. Model reduction was conducted using the function “stepAIC” from the R package “MASS” (Version 7.3-50, Venables & Ripley 2002). Variables were both removed and added to the model (using directionality specified as “both”) during the model reduction. In the models which used morphogroup, morphogroup is specified as a factor, using morphogroup 4 (spinose, spherical) as

the reference level. The linear models are presented as Type III ANOVA tables which were generated using the "car" (Version 3.0-0, Fox & Weisberg 2011) package's "Anova" function.

Interaction plots allow visualisation of two-way interactions between continuous variables. When one of the variables is a factor (i.e. morphogroup) this can be plotted as separate lines for each level of the factor (morphogroup 2, morphogroup 3, etc). This means that three-way interactions can be plotted on a single graph, if one of the variables is a factor. Four-way interactions (i.e. those with three continuous interactions and a fourth categorical variable) cannot be visualised easily. For the interaction plots, with continuous variables, lines are produced for a range of values (e.g.: minimum, mean and maximum). However, for interaction plots with CSF and morphogroup as variables, only values of CSF observed within the specified morphogroup are used. For example, an interaction plot of density interacting with CSF and morphogroup 4 (i.e. spinose, spherical), the lines are provided for minimum and maximum CSF values within morphogroup 4. This is because it would not be possible for a foraminifera to be morphogroup 4 and have a low CSF (e.g.: 0.4), as shapes with a CSF value of 0.4 are flattened spheroids (see Figure 3-6; for reference the species with the lowest average CSF is *Menardella menardii*, with CSF = 0.27). If a variable is not being plotted, but is present in the model, then the value is specified as the mean for that variable.

3.3.2.2 *Results*

Table 3-11: The linear models, formulae and AIC values.

Model Number	Model Formulation	AIC
1	Sinking Velocity ~ Length*Density*CSF*Morphogroup	-2496.77
2	Sinking Velocity ~ Length*Density*Morphogroup	-2443.68
3	Sinking Velocity ~ Length*Density*CSF	-2200.27

Model 1

Removing any of the variables or interactions in model one did not improve the fitness of the model, therefore the final model is as presented in Table 3-11. The full model result is presented in Table 3-12, and the model is significant ($F_{55,589}$= 88.49, p<0.001, adjusted R^2 = 0.882). The significant fixed effect (morphogroup) can be seen in Figure 3-19, significant interactions are visualised below (Figure 3-23 to Figure 3-28).

Table 3-12: Model results from model 1. Significant terms and interactions are underlined

	Sum of Squares	Degrees of freedom	F value	p value
(Intercept	0.002	1	0.114	0.736
Length	0.002	1	0.079	0.779
Density	0.002	1	0.116	0.734
CSF	0.002	1	0.12	0.729
Morphogroup	0.265	6	2.301	0.033
Length : Density	0.002	1	0.081	0.776
Length : CSF	0.002	1	0.087	0.769
Density : CSF	0.002	1	0.124	0.725
Length : Morphogroup	0.261	6	2.268	0.036
Density : Morphogroup	0.272	6	2.36	0.029
CSF : Morphogroup	0.308	6	2.677	0.014
Length : Density : CSF	0.002	1	0.09	0.764
Length : Density : Morphogroup	0.268	6	2.327	0.031
Length : CSF : Morphogroup	0.304	6	2.642	0.015
Density : CSF : Morphogroup	0.317	6	2.757	0.012
Length : Density : CSF : Morphogroup	0.313	6	2.722	0.013

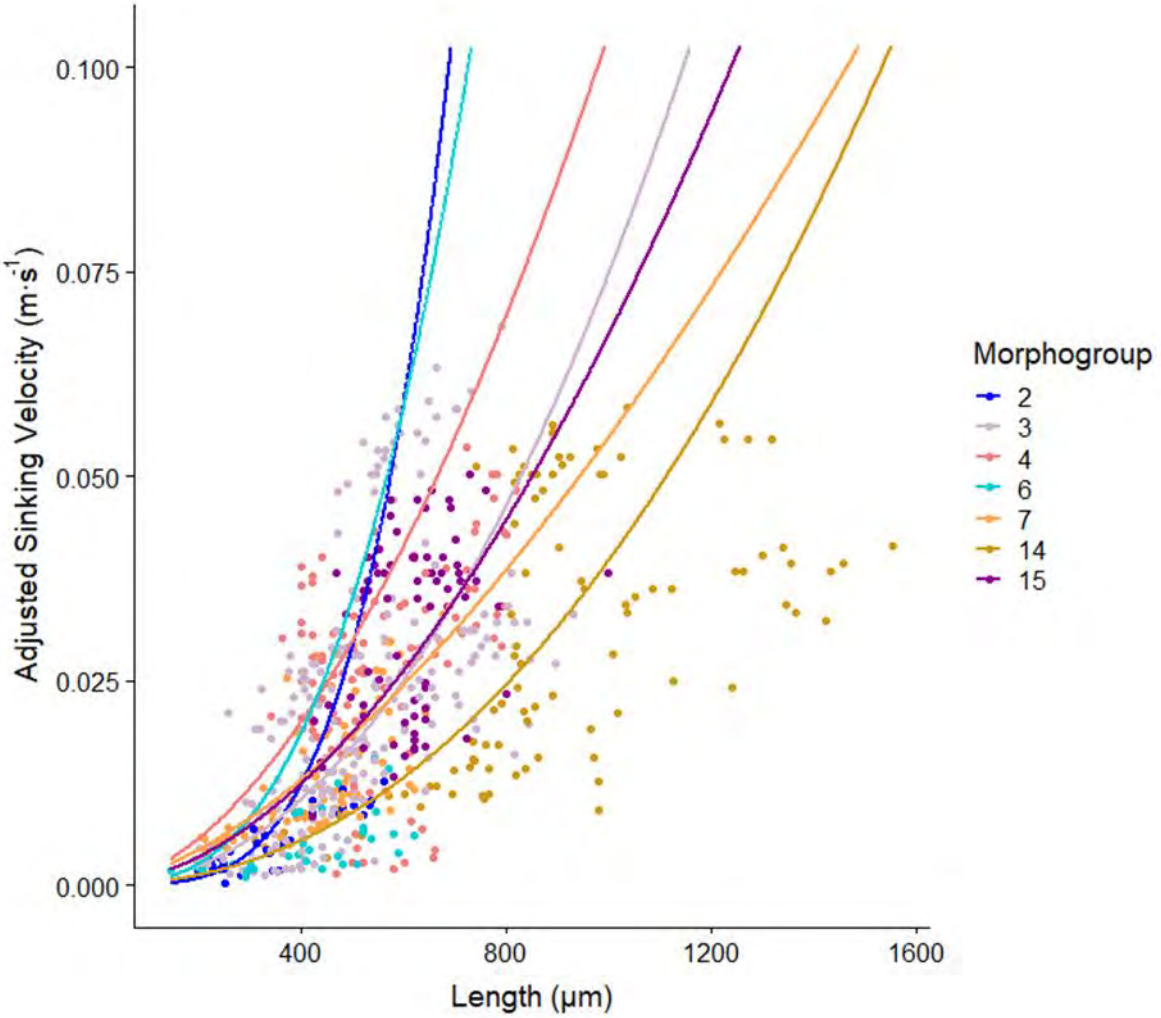

Figure 3-23: The significant two-way interaction between maximum length and morphogroup when predicting adjusted sinking velocity (Table 3-12). Points and lines coloured by morphogroup. Morphogroups are 2, Spinose, globular; 3, Spinose, globular with supplementary apertures; 4, Spinose, spherical; 6, Spinose, planispiral; 7, Non-spinose, globular; 14, Non-spinose, globorotaliform, keeled; and 15, Non-spinose, globorotaliform, angluconical.

When examining the relationship between sinking velocity and the significant two-way interaction of length and morphogroup (Figure 3-23), it is positive for all morphogroups, as expected based on the hydrodynamic predictions. The effect of length on adjusted U, varies across morphogroups, but is always increasing. Morphogroup 14 (Non-spinose, globorotaliform, keeled) has the gentlest slope and morphogroup 2 the steepest (Spinose, globular).

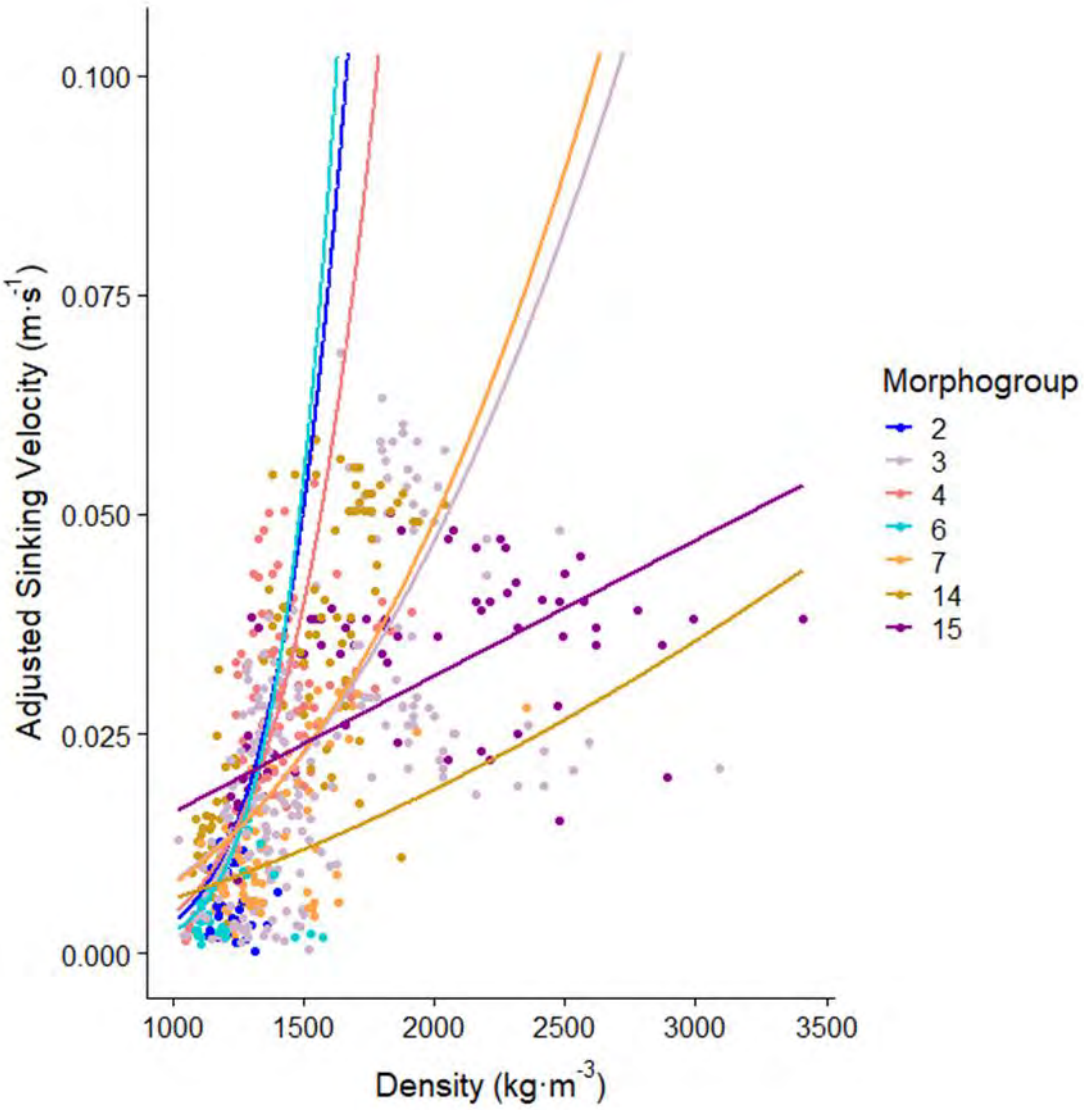

Figure 3-24:The significant two-way interaction between density and morphogroup, when predicting adjusted sinking velocity (Table 3-12). Points and lines coloured by morphogroup. Morphogroups are 2, Spinose, globular; 3, Spinose, globular with supplementary apertures; 4, Spinose, spherical; 6, Spinose, planispiral; 7, Non-spinose, globular; 14, Non-spinose, globorotaliform, keeled; and 15, Non-spinose, globorotaliform, angluconical.

The significant interaction between density and morphogroups, when predicting sinking velocity, is positive for all morphogroups (Figure 3-24), as expected based on the hydrodynamic predictions (as per 3.1.3). Slope of the lines are similar for morphogroups 2 (spinose, globular), 4 (spinose, spherical) and 6 (spinose, planispiral) which have the steepest slope. Morphogroups 3 (spinose, globular with supplementary apertures) and 7 (non-spinose, globular) have similar slopes, and 14 (non-spinose, globorotaliform, keeled) and 15 (non-spinose, globorotaliform, angluconical) have similar slopes but the intercept differs.

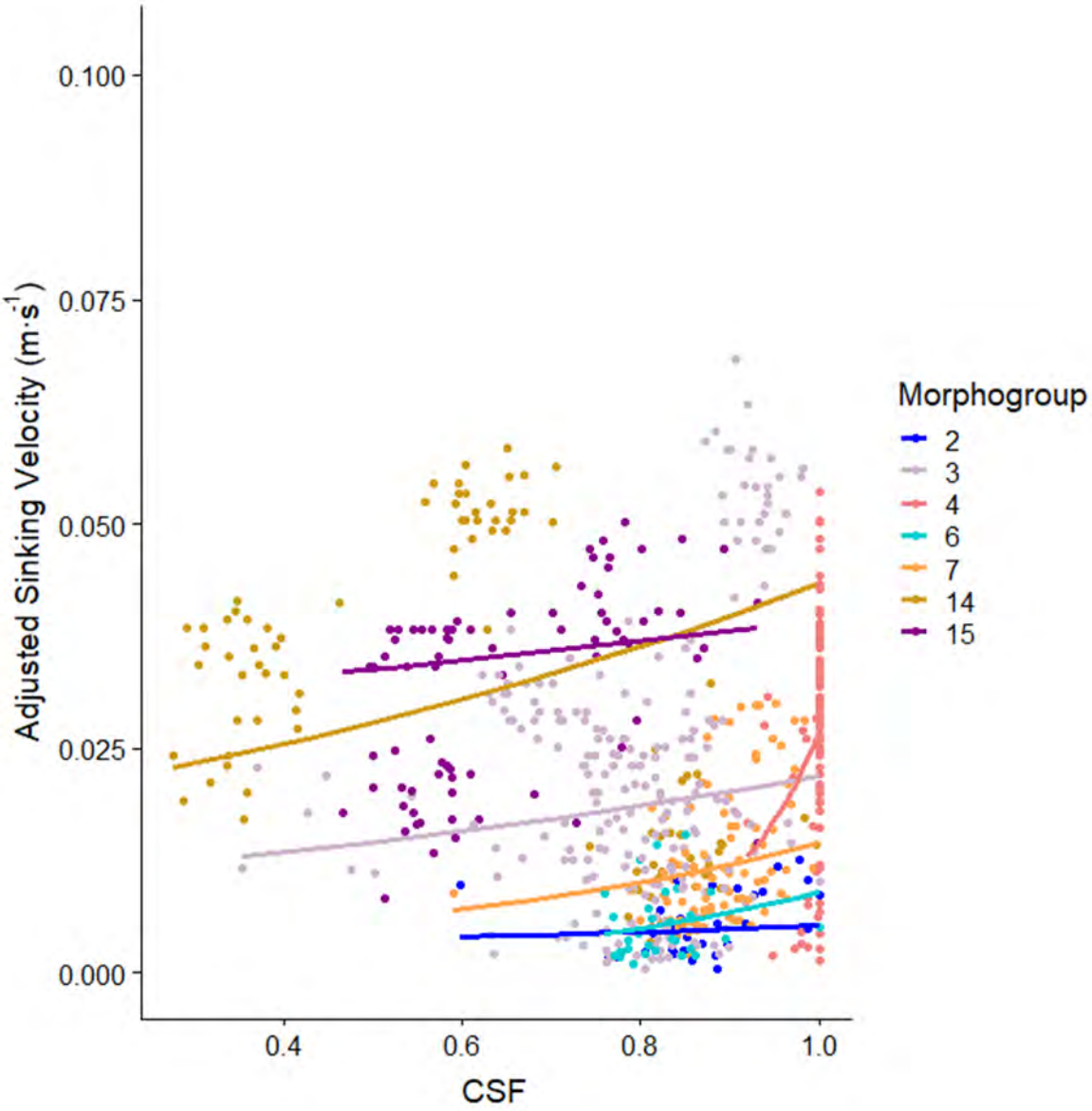

Figure 3-25: The significant two-way interaction between CSF and morphogroup (Table 3-12). Lines and points coloured by morphogroup. Morphogroups are 2, Spinose, globular; 3, Spinose, globular with supplementary apertures; 4, Spinose, spherical; 6, Spinose, planispiral; 7, Non-spinose, globular; 14, Non-spinose, globorotaliform, keeled; and 15, Non-spinose, globorotaliform, angluconical.

For all morphogroups there is a positive trend with sinking velocity as predicted by the interaction between CSF and morphogroup (Figure 3-25). This means that the more spherical the species are the faster they sink. Morphotype 2 (spinose, globular) has the shallowest slope, so as CSF increases the increase in sinking velocity is smallest. Morphotype 4 (spinose, spherical) has the steepest slope, as CSF increases sinking velocity increases proportionally more, than for other morphogroups.

The relationship between sinking velocity and the three-way interaction of density, length and morphogroup (Figure 3-26) is positive. The slopes differ with shorter lengths (pink) having shallower slopes, and longer lengths (blue) having the steepest slopes.

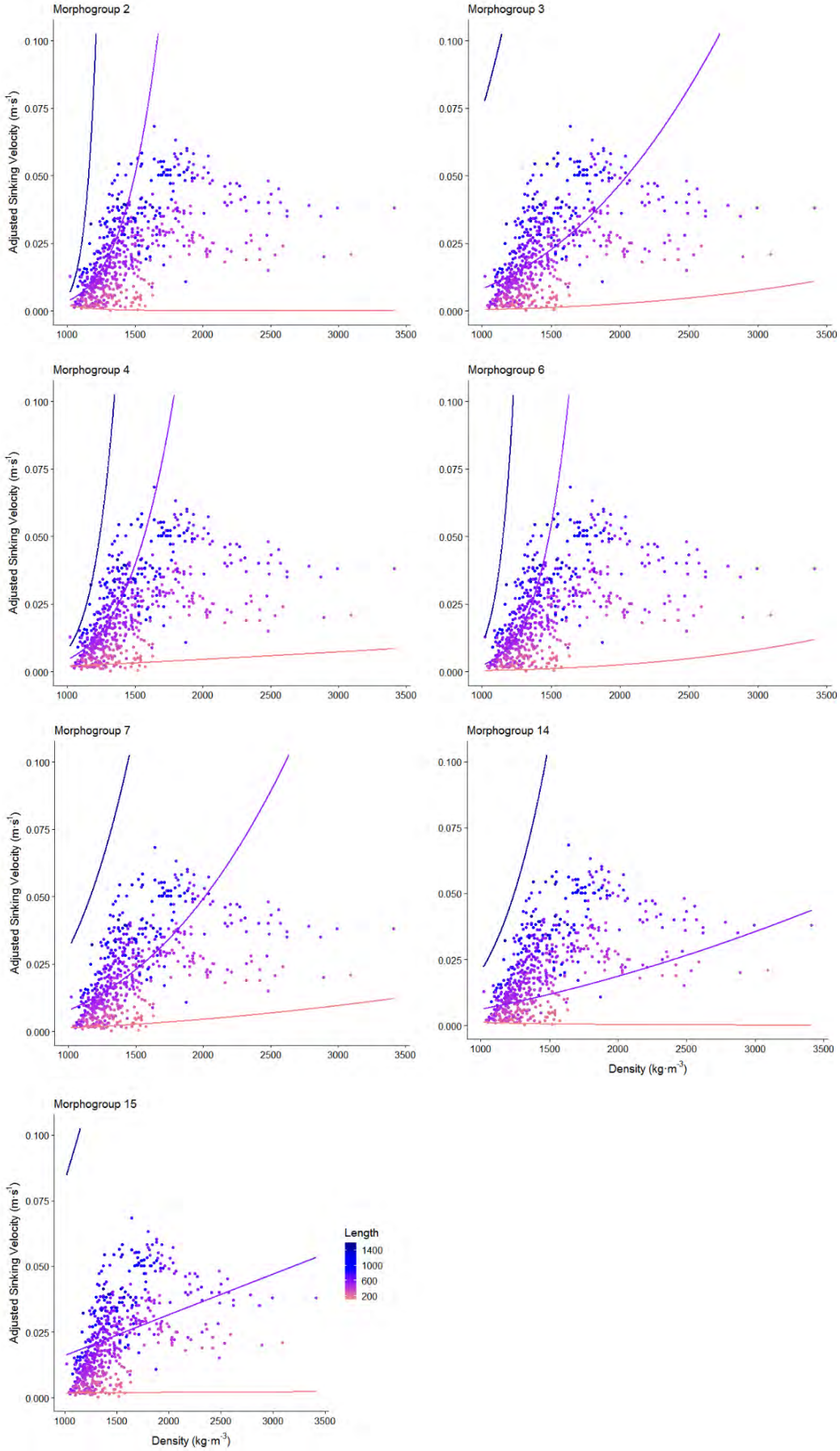

Figure 3-26: The significant three-way interaction of density, length and morphogroup. Lines are plotted for minimum, mean and maximum lengths for that morphogroup. Lines and points coloured by length.

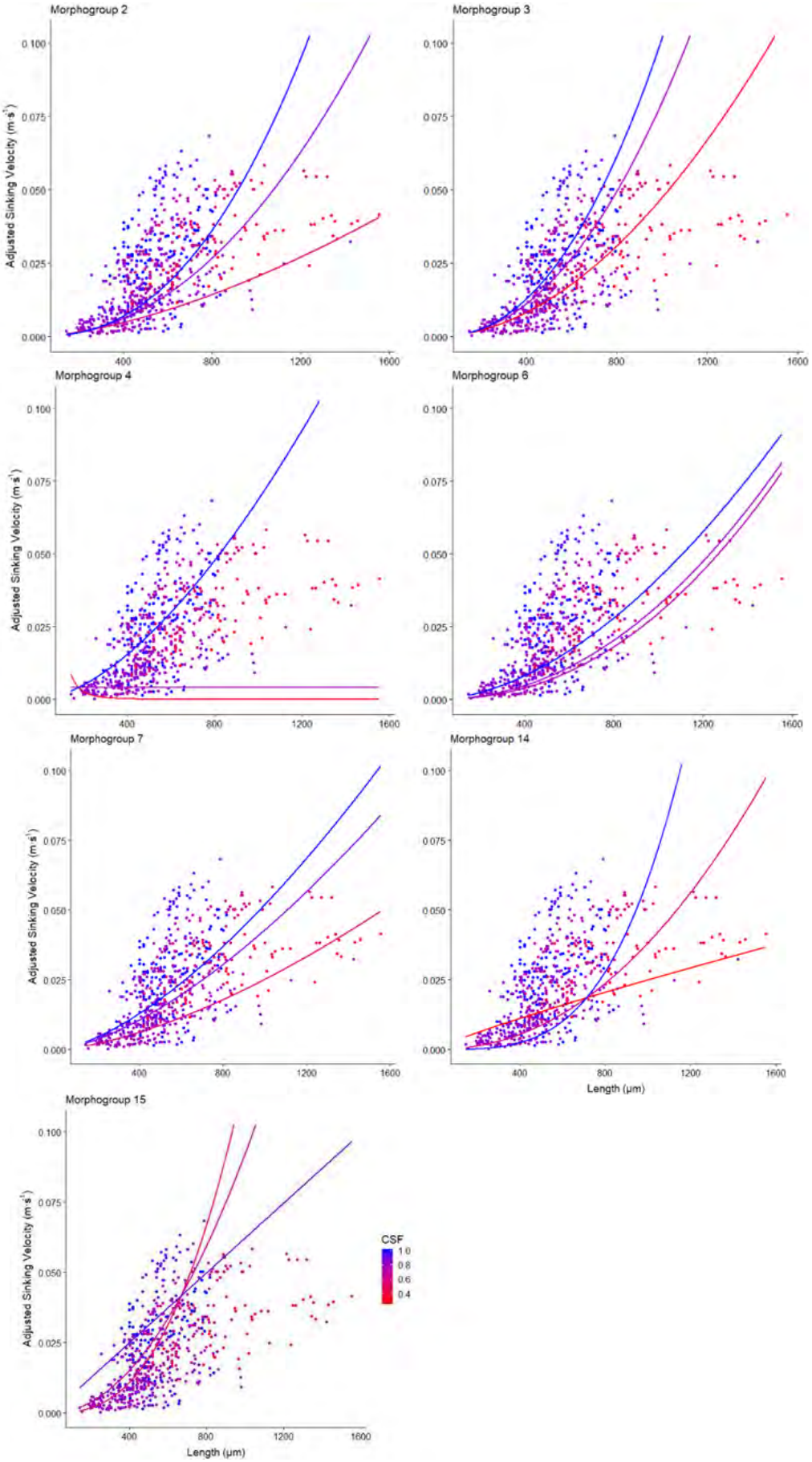

Figure 3-27: The significant three-way interaction of length, CSF and morphogroup. Lines are plotted for minimum, mean and maximum CSF values for that morphogroup. Lines and points coloured by CSF. Morphogroups are 2, Spinose, globular; 3, Spinose, globular with supplementary apertures; 4, Spinose, spherical; 6, Spinose, planispiral; 7, Non-spinose, globular; 14, Non-spinose, globorotaliform, keeled; and 15, Non-spinose, globorotaliform, angluconical.

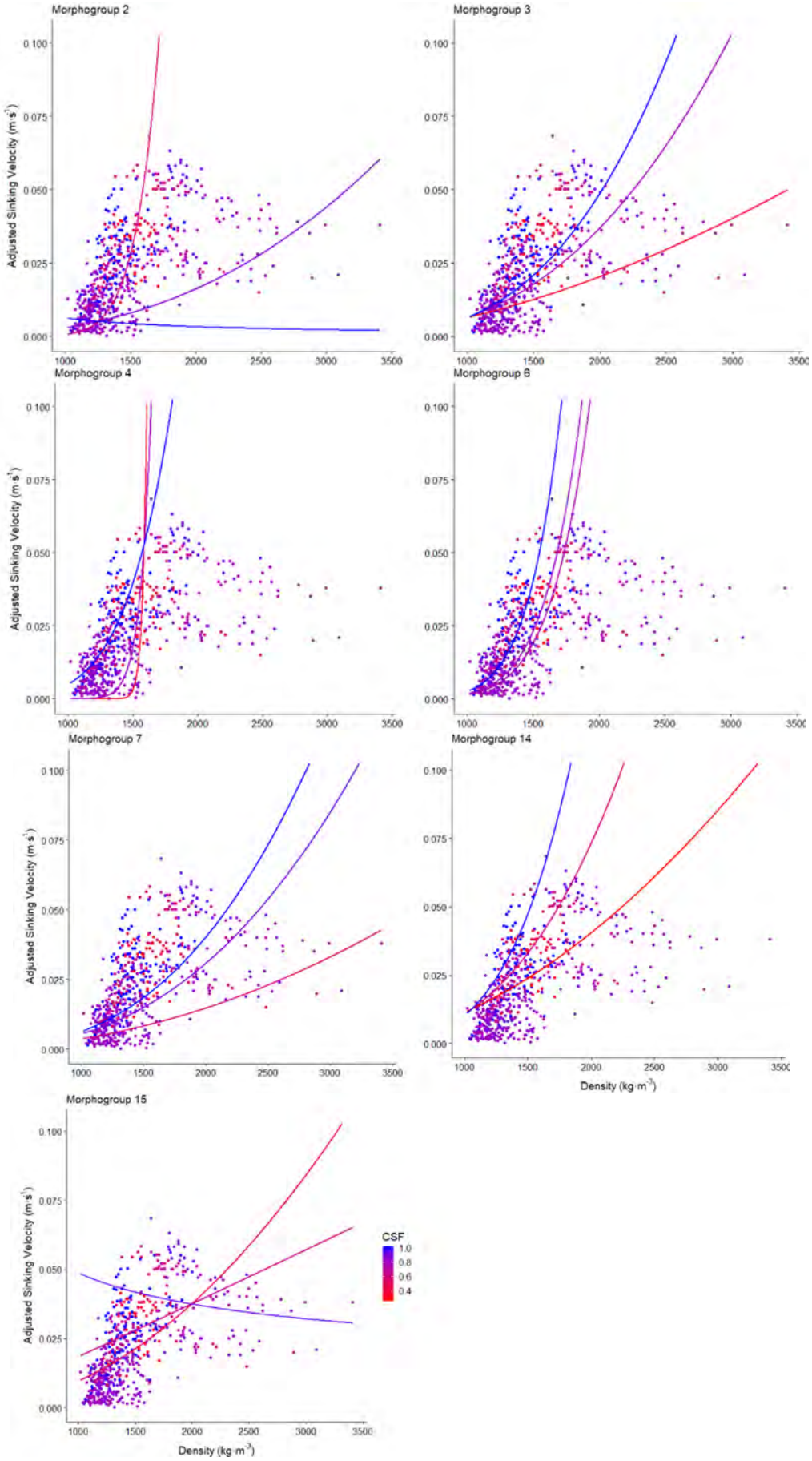

Figure 3-28: The significant three-way interaction of density, CSF and morphogroup. Lines are plotted for minimum, mean and maximum values for that morphogroup. Lines and points coloured by CSF. Morphogroups are 2, Spinose, globular; 3, Spinose, globular with supplementary apertures; 4, Spinose, spherical; 6, Spinose, planispiral; 7, Non-spinose, globular; 14, Non-spinose, globorotaliform, keeled; and 15, Non-spinose, globorotaliform, angluconical.

The relationship between sinking velocity and the three way interaction of length, CSF and morphogroup (Figure 3-27) is positive. Broadly, high CSF values (i.e. bluer coloured lines in Figure 3-27) have a steeper trend line, meaning that more spherical foraminifera have a higher increase in sinking velocity per unit of length increase, compared to those with lower CSF values (i.e. redder coloured lines in Figure 3-27). Morphogroups 14 and 15 below ~700µm have a different trend, the lowest CSF has the steepest slope, so less spherical foraminifera have a higher increase in sinking velocity per unit of length increase than foraminifera with a high CSF. Above ~700µm the trend reverts to the general trend seen in other morphogroups.

The three-way interaction between density, CSF and morphogroup (Figure 3-28), has a positive relationship with sinking velocity for all morphogroups. The exceptions being morphogroups 2 and 15, when CSF is high the trend is negative for those morphogroups.

Model 2

The reduced version of model 2 is significant ($F_{21,623}$= 198.6, p<0.001, adjusted R^2 = 0.87, AIC = -2445.17), and is presented in Table 3-13. The final model took the form of:

$$Sinking\ velocity \sim length + density + morphogroup\ + \\ length{:}\,density\ +\ length{:}\,morphogroup + density{:}\,morphogroup$$

Table 3-13: Results of the reduced model 2.

	Sum of Squares	Degrees of freedom	F value	p value
(Intercept)	0.026	1	1.188	0.276
Length	0.077	1	3.508	0.062
Density	0	1	0.006	0.94
Morphogroup	2.706	1	20.662	<0.001
Length : Density	0.152	6	6.98	0.008
Length : Morphogroup	1.162	1	8.871	<0.001
Density : Morphogroup	4.588	1	35.025	<0.001
Residuals	13.6	1	-	-

The significant fixed effect of morphogroup can be seen in Figure 3-19. The significant interactions are presented graphically below (Figure 3-29 to Figure 3-31).

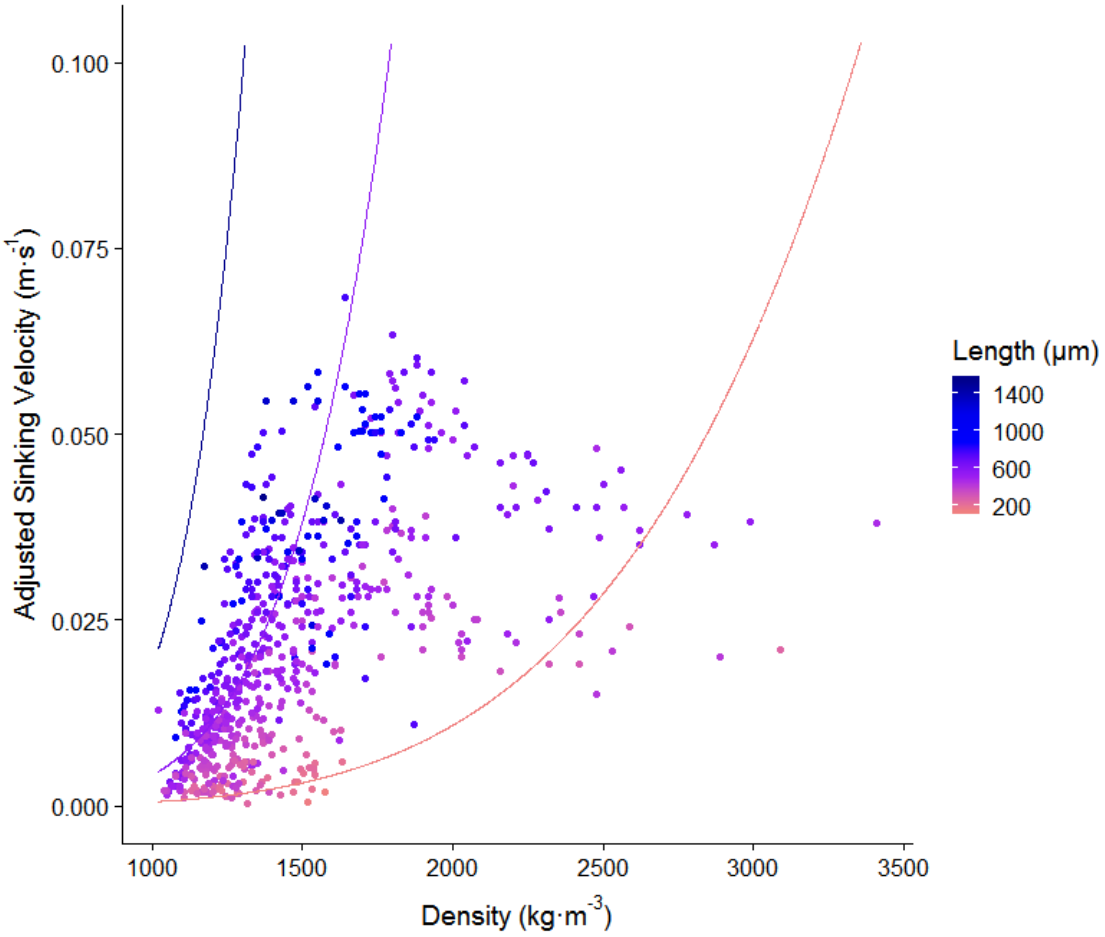

Figure 3-29 The significant two-way interaction between density and length, when predicting adjusted sinking velocity. For this interaction, morphogroup is not included, therefore for the graph above morphogroup is specified as 4 (spherical). Lines show the fit of the model for: minimum length (pink), mean length (purple) and maximum length (blue).

The relationship between sinking velocity and density interacting with length (Figure 3-29) is such that the longest foraminifera have the steepest slope, so as density increases sinking velocity increases rapidly. For the shortest foraminifera the slope is much less steep. Intermediate sized foraminifera have a relationship more similar to the largest foraminifera, than to smaller foraminifera.

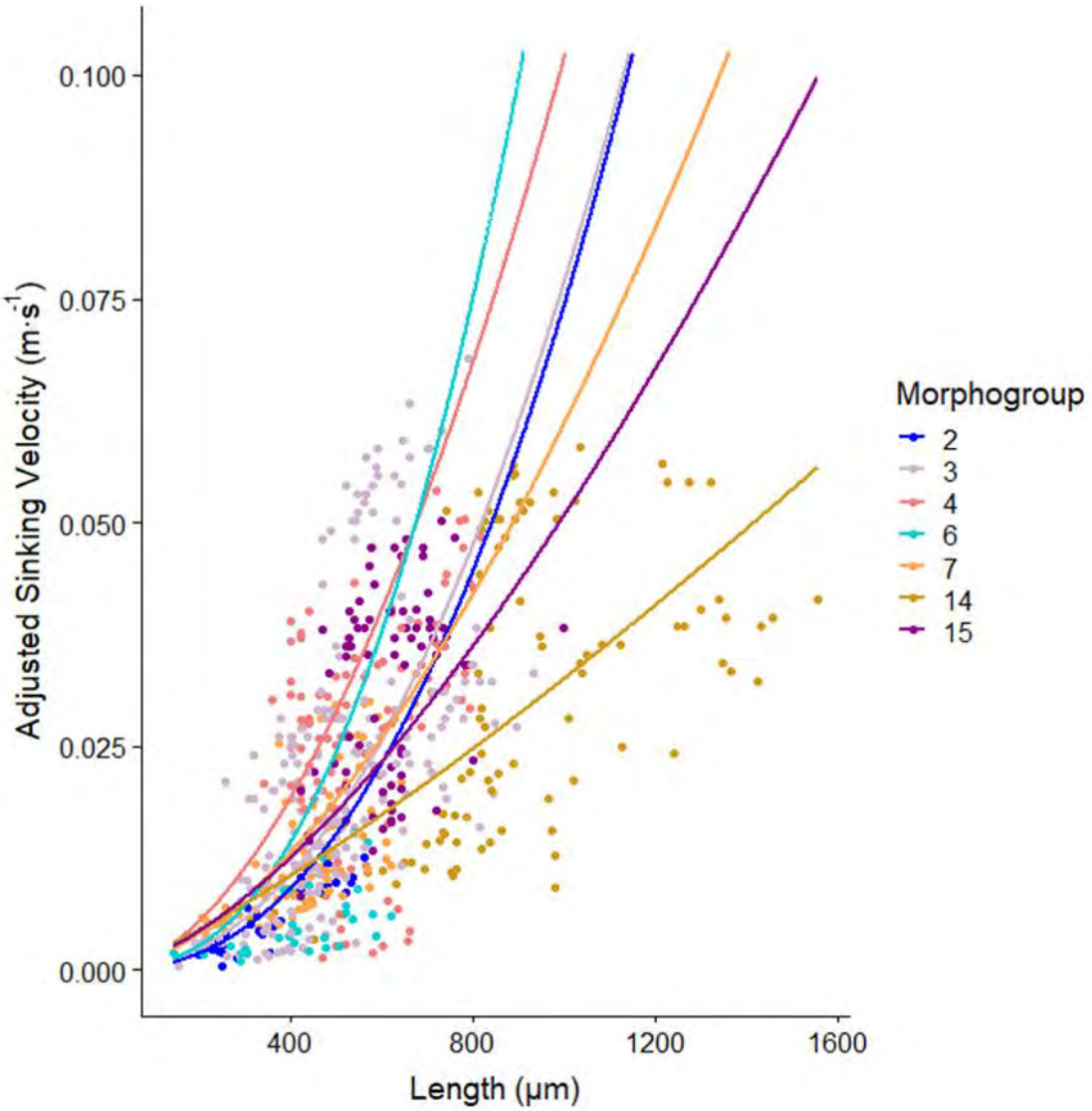

Figure 3-30: The significant two-way interactions between length and morphogroups, when predicting adjusted sinking velocity. The lines and points are coloured by morphogroup morphogroups are 2, Spinose, globular; 3, Spinose, globular with supplementary apertures; 4, Spinose, spherical; 6, Spinose, planispiral; 7, Non-spinose, globular; 14, Non-spinose, globorotaliform, keeled; and 15, Non-spinose, globorotaliform, angluconical.

The relationship between sinking velocity and the interaction of length and morphogroup is positive for all morphogroups. Therefore, as the foraminifera become longer, they sink faster. Morphogroup 6 has the steepest relationship between sinking velocity and length (Figure 3-30) and steeper than morphogroup 4's relationship for foraminifera <~600-700µm range, however foraminifera larger than this in morphogroup 6 will sink slower than equally sized foraminifera in morphogroup 4. For morphogroup 14 the relationship between length and sinking velocity is also positive, but the slope much less steep than any other morphogroup.

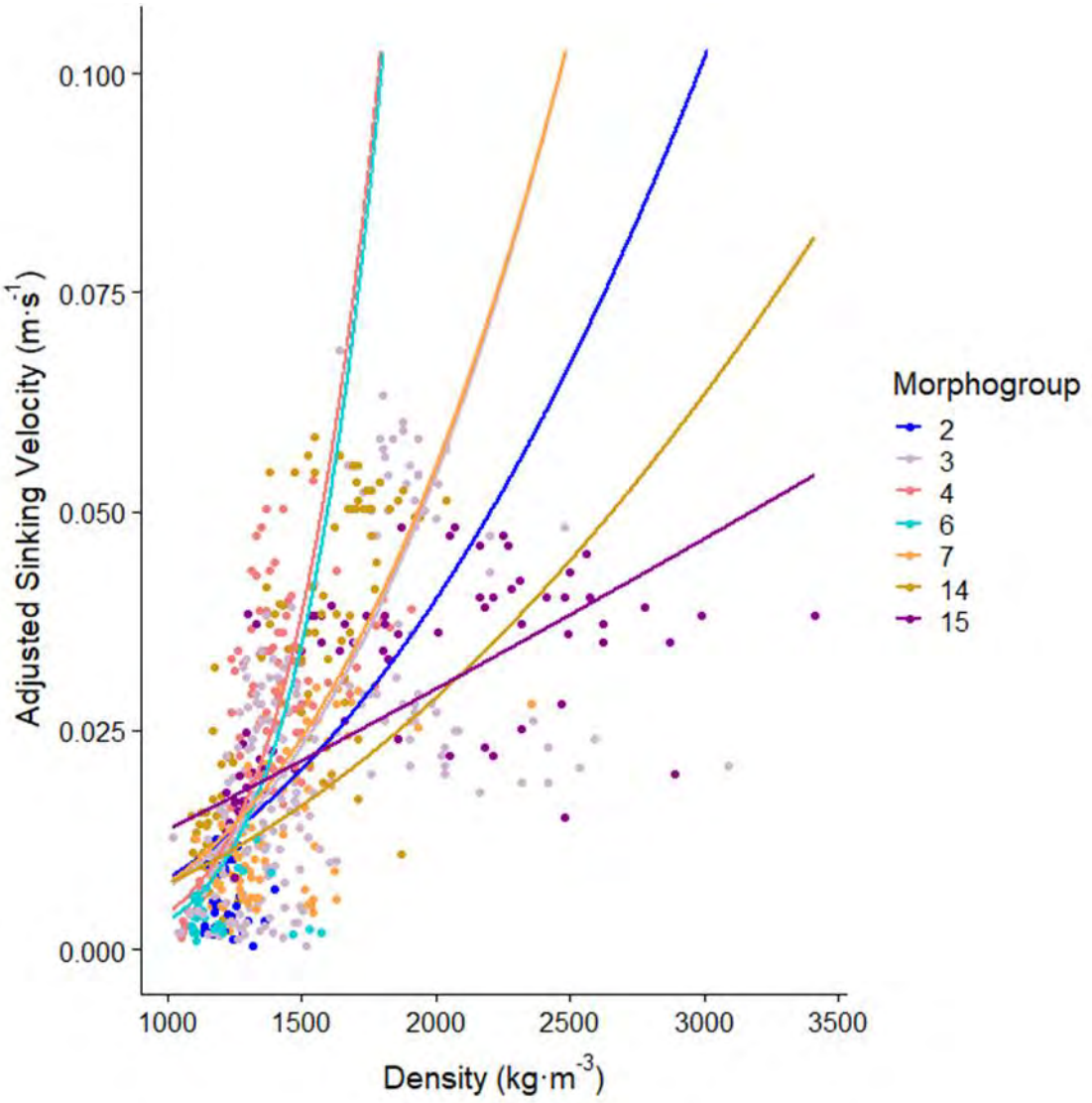

Figure 3-31: The significant two-way interactions between density and morphogroups, when predicting adjusted sinking velocity. Points and lines are coloured by morphogroup. Morphogroups are 2, Spinose, globular; 3, Spinose, globular with supplementary apertures; 4, Spinose, spherical; 6, Spinose, planispiral; 7, Non-spinose, globular; 14, Non-spinose, globorotaliform, keeled; and 15, Non-spinose, globorotaliform, angluconical.

Sinking velocity increases with increasing density for all morphogroups (which have a significant interaction with density, Figure 3-31). The relationship between sinking velocity and morphogroup with the steepest slope is morphogroup 4, and the least steep is morphogroup 15. Morphogroups 3 (Spinose globular with supplementary apertures) and 7 (Non-spinose globular) have an almost identical relationship, as do morphogroups 6 (Spinose, planispiral) and 4 (spherical).

Model 3

The reduced model 3 took the form of:

$$Sinking\ velocity \sim length + \ density + CSF + \ density{:}\,CSF$$

and is significant ($F_{4,640}$= 645.4, p<0.001, adjusted R^2 = 0.80, AIC = -2205.40). The reduced model results are presented in Table 3-14.

Table 3-14: The results of the reduced model 3, significant values are underlined

	Sum of Squares	Degrees of freedom	F value	p value
(Intercept)	0.019	1	0.585	0.445
Length	47.625	1	1466.018	<0.001
Density	0.345	1	10.635	0.001
CSF	1.794	1	55.209	<0.001
Density : CSF	1.921	6	59.133	<0.001
Residuals	20.791	1	-	-

The significant relationship between sinking velocity and the fixed effects can be seen in a graphical format in Figure 3-14, the significant interaction is presented below (Figure 3-32).

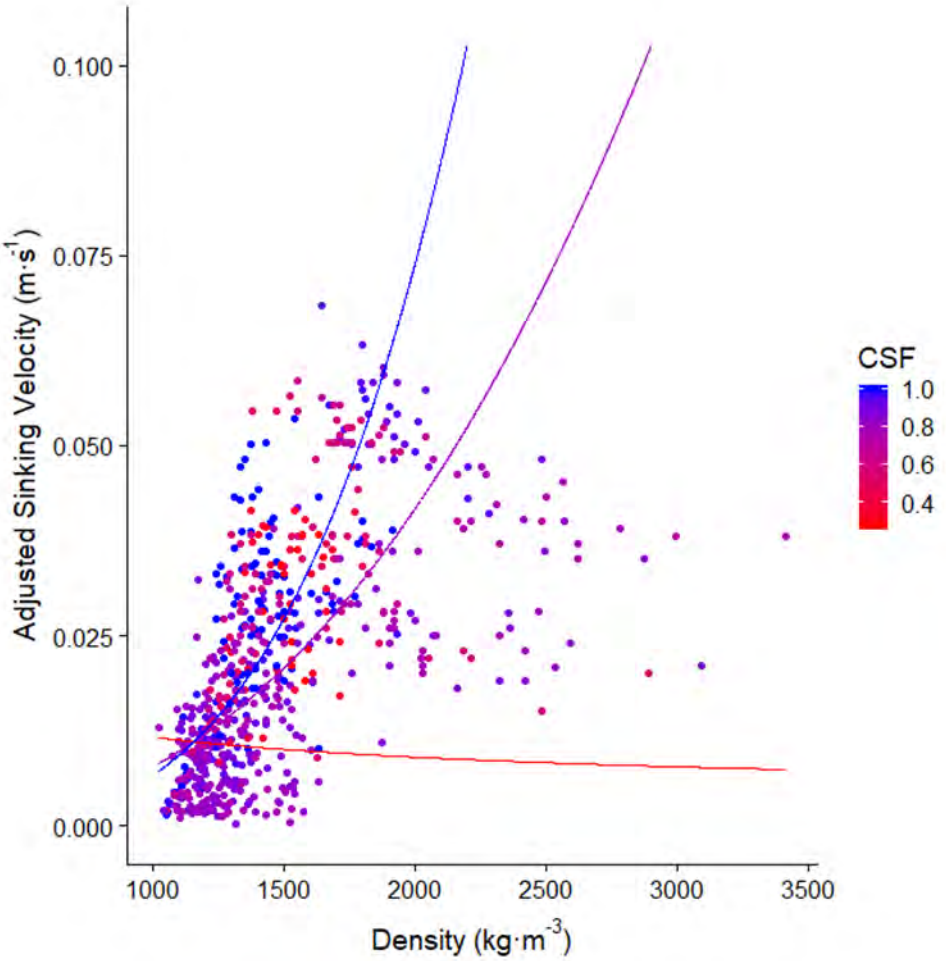

Figure 3-32: The interaction between, density and CSF, when predicting adjusted sinking velocity. Lines are shown for low (red), intermediate (purple) and high (blue) CSF (CSF = <0.4, ~0.6 and 1 respectively).

The relationship between sinking velocity and density interacting with CSF is positive for intermediate and high CSF values (CSF = ~0.6 and 1 respectively), with high CSF having the steeper trend. For low CSF (<0.4) the relationship is negative, as density increases sinking velocity decreases.

3.4 Discussion

3.4.1 Summary of Findings

Based on visual examination (Figure 3-17) and the R^2 values comparing the fit of Stokes' Law and Morrison's equation, there appears to be substantial deviation in C_D values of sinking foraminifera from the predictions of Stokes' Law and Morrison's equation. This is to be expected as foraminifera experience Re values that are >1. As Stokes Law is a function of Re (Equation 3-7), the only way to change the Stokes C_D value is to change the Re. The only property of the particle that changes Re is its length (and sinking velocity, which are co-dependent). The rest of the terms in the Re equation (Equation 3-2) are determined by the fluid. Therefore, deviation from Stokes Law is arguably an indication of the effect of size on sinking velocity. However, Morrison's equation is applicable to spheres across all ranges of Re. The data are an imperfect fit to this equation too. As foraminifera are not spherical, it is reasonable to argue that the deviation from Morrison's equation (Equation 3-8) is due to shape. In addition, in Figure 3-18 differently shaped foraminifera have different relationships with Stokes Law and Morrison's equation. Therefore, we would expect that sinking velocity would be influenced by size and shape.

Based on individual linear models (i.e. those where sinking velocity is predicted by only one variable) the important variables in predicting sinking velocity are: length, volume, density and mass (Figure 3-14). This agrees with the physics-based predictions outlined in section 3.1.3. When linear models are used to analyse relationships between sinking velocity and these variables, both the intercept and slope of each model differ for each species (Appendix 9.1.7 Figure 9-2). This suggests there is, minimally, an effect of species. Given that foraminifera are morphospecies (Pawlowski and Holzmann, 2014), it is reasonable to assume part of this difference in sinking velocity is due to shape. That is to say, morphospecies have different shapes and here it is shown they have different sinking velocities. Therefore, some element of the differences in sinking velocity could be due to differences in shape. However, it should be noted that that differences in morphologies have been attributed to genetic variation, (see Chapter 1, e.g. Ujiié et al., 2010) and as such the differences in shape is likely to be due to hidden (genetic) or cryptic species. As can be seen in Figure 3-19 there are some differences in sinking velocity between most morphogroups (see Table 3-8). Some of the groups that do have similar sinking velocities, also have similar lengths (see Table 3-9). This would suggest that factors other than the aspects of shape used to define morphogroups also play a role in determining sinking velocity, as species with similar lengths and sinking velocities are in different morphogroups.

When examining the pair-wise comparisons of mean CSF value and sinking velocities (i.e. Table 3-8 and Table 3-10), most morphogroups which have differences in sinking velocity also have different CSF values. The exceptions (i.e. those that are not significantly different, Table 3-10) in terms of CSF are 6-3 (Spinose planispiral and Spinose Globular with supplementary apertures) and 7-6 (Non-

spinose globular and Spinose planispiral), showing that these morphogroups have the same mean CSF. However, these groups do have significantly different sinking velocities. This would suggest that the shape information captured by morphogroup is more hydrodynamically relevant than that captured by CSF. Morphogroups which have significantly different CSF values, but not significantly different sinking velocities, are: 14-4 (non-spinose, globorotaliform, keeled and spinose spherical) and 15-4 (non-spinose, globorotaliform, angluconical and spinose spherical). Despite the differences in average shape (CSF) these morphogroups, on average, sink at the same velocity. This suggests that factors other than shape are more important in determining sinking velocities for these morphogroups.

The findings presented here (section 3.3.2.2: Model 1, Model 2, Model 3) suggest that length and density are major parameters in determining sinking velocity, and are in line with the predictions made based on hydrodynamics (section 3.1.3). In the best model (measured by AIC), Model 1, all morphogroups have a positive relationship between sinking velocity and maximum length (Figure 3-23), density (Figure 3-24) and CSF (Figure 3-25). Sinking velocity appears to be determined by length and density, with an effect of shape as measured by both morphogroup and CSF. These measures of shape are significant (independently or as interactions) in all three models (see Table 3-12, Table 3-13, and Table 3-14). However, the measures of shape available are far from adequate. Morphogroup is a more general descriptor of the species overall shape compared to the individual variation that can be captured by CSF. CSF uses linear measurements in an arbitrary orientation, which can be the same for differently shaped foraminifera (Figure 3-20). The overlap in CSF values between morphogroups simply re-iterates the problems with using linear measures in the definition of shapes, especially in a biological context (Zelditch *et al.*, 2004; Deeming and Ruta, 2014). Additionally, the specific orientation used is dependent on the person taking the measurements. Morphogroup, however, is less subjective than the orientation of linear measurements, but is not a continuous variable so there is no continuum of shape. In addition to this, whilst there is a weak (but significant) relationship between maximum length and CSF, there is an intrinsic link between the two as maximum length is used in the calculation of CSF. This link could mean the relationship is an artefact of the methodology, as using ratios (such as CSF) in statistics can sometimes provide false correlations (Atchley *et al*. 1976; Atchley & Anderson 1978; cf. Albrecht 1978). Ideally a size independent method of quantifying shape should be used, such as Fourier analysis or Geometric morphometrics. Sinking orientation determines the area of the foraminifera test that is presented to the fluid, which is expected (from Equation 3-3 and Equation 3-6) to be an important measure of shape. The method used by Berthois and Le Calvez (1960) is the only currently published study to use a method which measures an area that could be similar to the area presented to the fluid as the foraminifera falls.

3.4.2 Reasons for the Trends

When examining the relationship between CSF and maximum length, where the larger foraminifera (as defined by maximum length) tend to be less spherical (see Figure 3-22), has also been seen in a number of phytoplankton taxa (Stanca *et al.*, 2013) and follows the findings of Caromel *et al.* (2014). There are number of possible reasons for this. Deviation from sphericity causes an increase in the surface to volume ratio of the cell. In phytoplankton (which may be up to two orders of magnitude smaller than foraminifera) non-sphericity is thought to be for increased nutrient uptake (Chisholm, 1992). As Reynolds (Reynolds, 1997) outlines, increases in size are best paired with a departure from a spherical form to maintain a constant surface to volume ratio. However, Caromel *et al.* (2014) suggest that in planktonic foraminifera sinking velocity can be maintained more easily by more spherical species during periods of species size increase (on evolutionary scales) than by those species with a flatter morphology. Indeed, the spherical species (*O. universa*) shows a large range in size compared to other species (Figure 3-22), which could be due to differences in temperature during calcification (Schmidt *et al.*, 2004; Lombard *et al.*, 2009). This species is known to modify its density (via differences in wall thickness, due to depth at which calcification occurs, Marshall et al., 2015) and number of pores dependent on ocean temperature (Bijma, Faber and Hemleben, 1990), which has also been seen in other species of planktonic foraminifera (Frerichs *et al.*, 1972; Naidu and Malmgren, 1996). Over evolutionary time there have been noted changes in planktonic foraminifera morphology which coincide with changes in global temperature (and thereby ocean temperature and water properties (Norris, Corfield and Cartlidge, 1993). These changes are assumed to be related to maintaining a sinking velocity (to stay in position in the water column, whilst the foraminifera cell is alive) and thereby depth (Malmgren and Kennett, 1981; Wei, 1994), or to permit movement to a new habitat (e.g.: cooler waters more similar to the species 'original' range, (Schneider and Kennett, 1999).

The sinking velocities of the foraminifera are similar to sinking velocities of planktonic organisms from other studies, when predicted by diameter (see Figure 3-33), which is interesting given that the shape of the organisms will differ. Both here and elsewhere (Padisák *et al.*, 2003) shape has been shown to be an influential factor in determining sinking velocity. It should be noted that foraminifera are some of the largest sinking matter and sink at the fastest rates, this means that foraminifera experience different interactions (i.e. Re and C_D) with the fluid compared to other sinking matter. As previously discussed, this relatively large size places foraminifera in the range of Re known as "Intermediate Reynolds numbers" where theoretical predictions are of limited use. An experimental approach to finding sinking velocities, and how particles interact with the fluid environment, in the intermediate Re regime is fundamental to validating any theoretical predictions.

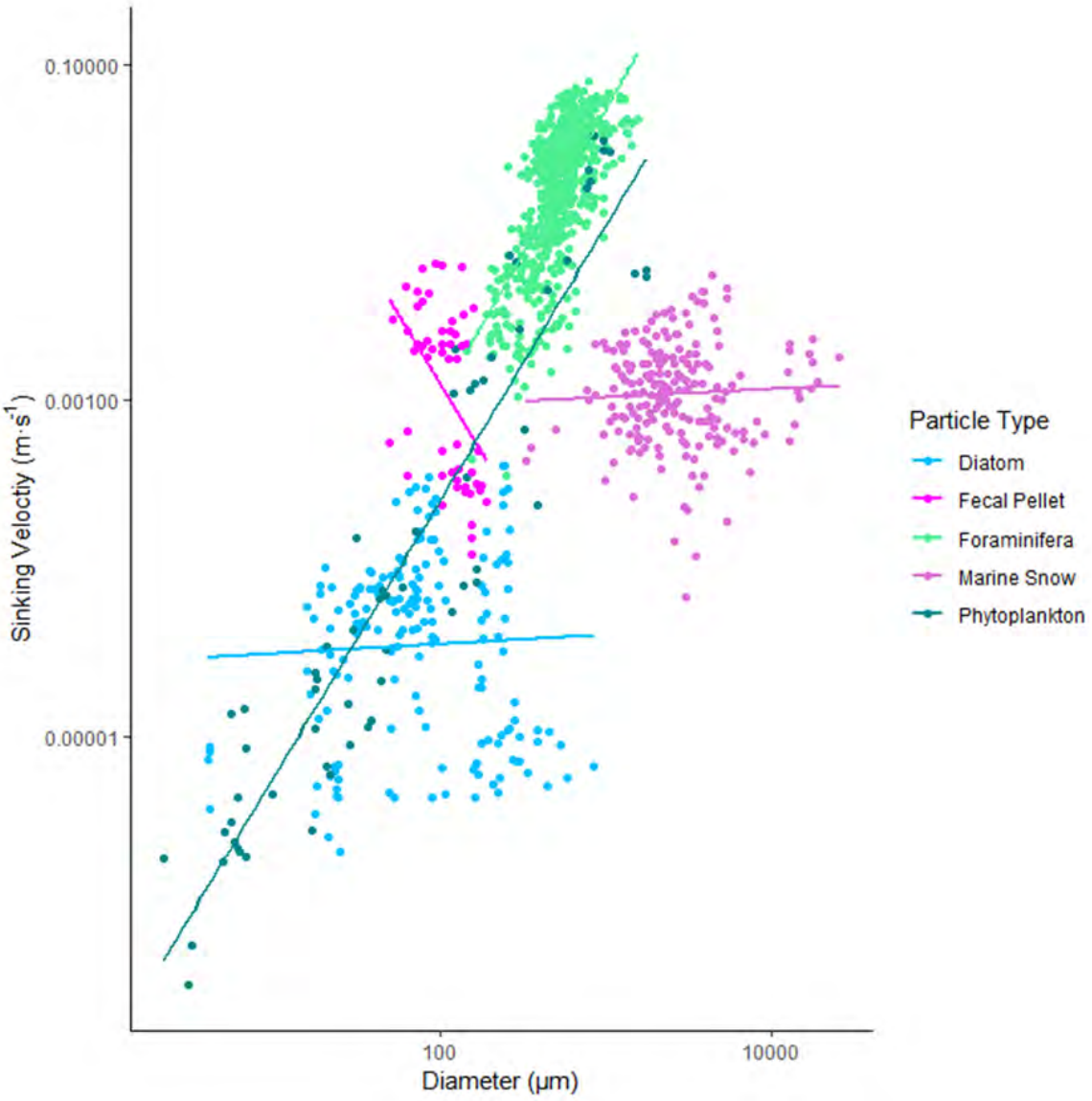

Figure 3-33: Sinking velocity and longest length of diatoms, fecal pellets, foraminifera, marine snow and phytoplankton. See Appendix 9.1.9 for data origins. Data from Alldredge & Gotschalk, 1988; Davey, 1986; Iversen & Ploug, 2010; Miklasz & Denny, 2010; Smayda, 1971.

Based on the previous works, their data, and these new analyses, several considerations for the experimental phase of the current work were made. Firstly, the 2D quantification of shape needs to be made in the sinking orientation and using a method which is not sensitive to size. Secondly, the length and areas measured for use in the calculation of Re and C_D should be taken in the sinking orientation, to make them physically relevant. In addition, the sinking tests must be free of air bubbles, and not contain any additional material that is not foraminiferal test, e.g.: sediment, smaller foraminifera, etc. Measures of volume used in previous studies have been based on a weight measurement and the calculation of a basic shape, which resulted in a bulk volume. Volume will need to be more accurately quantified in this study. Finally, to improve the statistical testing power the sample size should be increased from the 14 species presented here.

3.5 Take Home Messages

1. Sinking foraminifera deviate from Stoke's Law, demonstrating that sinking within the intermediate Re regime is dependent on the size of the particle. Deviation from Morrison's equation suggests that there is an effect of shape on sinking velocities within the intermediate Re regime.
2. Maximum length and density of the foraminifera test both have the largest impact on sinking velocities, which was predicted from hydrodynamics.
3. Foraminifera in different morphogroups sink at different velocities, which is also the case for species with different CSF values. Species which have similar sinking velocities are similar in maximum length. This suggests that the effect of shape (as measured by morphogroup and CSF) is relatively small compared to size.
4. The trends seen with parameters (such as length and density) can be explored within a biological framework, with changes in these parameters being used to mediate sinking velocity of the test. However, it should be noted that only the empty test is being sunk (in most cases, excluding Takahashi and Bé, 1984) therefore implying biological relevance to the finds should be done with caution.
5. Using morphogroup as a measure of shape is limited to a generalised gross morphology, lacking the individual variation which is present. CSF captures some of this individual variation, but some differently shaped species can have similar CSF values, so a better measure of shape needs to be used to capture individual variation and better quantify shape.

Chapter 4 Sinking experiments

4.1 Aims

This chapter aims to quantify the sinking velocity of planktonic foraminifera using 3D printed, accurately scaled models. The main aim is to determine accurate sinking velocities for more planktonic foraminifera species than are currently present in the literature. This approach captures some of the inter-specific morphological variation which is exhibited by this diverse group.

In addition, it aims to provide a quantification of hydrodynamically relevant measures of foraminifera length and projected area and accurate volume measurements of the calcite test wall (V_{wall}). These measurements are then examined, and their relative importance determined. By accurately quantifying and measuring these various hydrodynamically-relevant parameters, a better general understanding can be gained of the factors which govern the sinking velocities of particles within the intermediate Reynolds number regime. The parameters gathered for foraminifera will be explored to hypothesis the function of the morphological variation seen and relate this to the literature, whilst acknowledging that only the dead, empty, test is modelled here.

Then a comparison will be drawn from the obtained sinking velocities and the parameters identified Chapter 3 as important in determining sinking velocities. Finally, the data generated here are compared to the previously published data, with the aim of validating the results obtained here with studies using actual foraminifera.

4.2 Introduction

To attempt to link shape and sinking velocity of planktonic foraminifera, both need to be quantified from the same specimen. The published data examined in Chapter 3 provides sinking velocities and basic linear measurements taken from specimens but does not offer the opportunity to employ new methods of shape quantification as the original specimens cannot be viewed. Therefore, based on the conclusions at the end of 3.4, some recommendations were made for the sinking experiments: the foraminifera need to be empty of additional material and air upon sinking; the test volume needs to be accurately estimated; and more species need to be examined. This will allow any potential increase in sinking velocities due to increased density (due to the presence of additional material) or decrease in sinking velocities due to air being present within the test. Ensuring that the test is both empty of additional material and air, provides sinking velocities which (theoretically) should have reduced variation and have less associated variation.

Further considerations include how to measure the length and area used in the calculation of Reynolds number (*Re*) and drag coefficient (C_D) respectively. For example, area could be measured as the total surface area, frontal area or projected area in a plane. Both length and area need to be measured in the sinking orientation, to make them hydrodynamically relevant, which requires clear imaging of the foraminifera during sinking. As in Chapter 3, there are some problems with using

actual planktonic foraminifera, so instead in this chapter a novel method of using scale models is adopted.

The production of model foraminifera has a long history (See Miller, 2013, for an overview), but these models are simply reconstructions of the external surface and structures of the foraminifera. Within the context of this study, empty foraminifera tests need to be recreated in such a manner that they can accurately represent the original (as dead foraminifera are being modelled here, they will not include protoplasm, or spines), and both the external and internal structures must be reproduced. Models which only replicate the external morphology would not behave the same during sinking due to differences in mass distribution (if the chambers are filled and not hollow). Therefore, the models used to measure the sinking velocities need to be exact scaled versions, both internally and externally, of real foraminifera.

The first step in creating scale models is imaging the tests. This can be achieved by several methods. Photomicroscopy using light or electron microscopes would produce models of the external surfaces, but not the internal surfaces. To reproduce both internal and external morphologies serial grinding, and photography could be used. This method would involve setting the test inside a block of hard material and successively grinding off thin layers of this material and test. Photographs could be taken, from which a model of the test could be made. This approach, however, destroys the test. By using computed tomography (CT) the test is preserved after imaging. This method uses X-rays to image rotating specimens. The differences in the absorption and scattering of the X-rays by the object are used to generate a series of cross-sectional (tomographic) greyscale images. The 2D slices can then be stacked and combined in software to produce a 3D image. The differences in absorption produce varying intensity in the greyscale images, so parts that absorb more X-rays (dense structures such as bone and foraminifera tests) are displayed as white, whilst more X-ray transparent material appears darker (see Figure 4-1). For materials that are similar in density the X-rays will be absorbed at similar rates and so the materials will appear similar in intensity on the slices, which can present a problem with imaging some specimens (e.g.: bones embedded in rock, Clark *et al*., 2004). To overcome this issue, and to only include the desired material in the final image, segmentation is performed on the slices. Image segmentation is a method of digitally portioning an image (each 2D slice) into segments or groups of pixels which share similar properties or are part of the structure of interest (Shapiro and Stockman, 2000) in this case the internal and external chamber walls of the foraminifera. This process may be automated using threshold values to remove imaging artefacts and unwanted material, but in the case of similar materials this must be performed manually, highlighting the parts of the image that will be kept for the final image or 3D rendering (Figure 4-1 b & c, Rahman *et al*., 2012), the process of selecting which pixels to be kept and which are removed is based on the experience of the person reproducing the image.

MicroCT-scanning (µCT-scanning) is a high-resolution version of CT-scanning, capable of producing images with µm or sub-µm levels of resolution, used to image small objects in 3D. Tomographic datasets can also be generated using other X-ray sources, such as synchrotrons, which typically offer still higher resolutions (typically in the range of 0.1 – 0.5µm). The use of synchrotrons has allowed detailed studies of onotogenetic stages of foraminifera (e.g. Caromel et al., 2015b), linking of development and evolution (Schmidt *et al.*, 2013) and examining the deposition of Mg and Ca within the test wall (e.g. Branson et al., 2013).

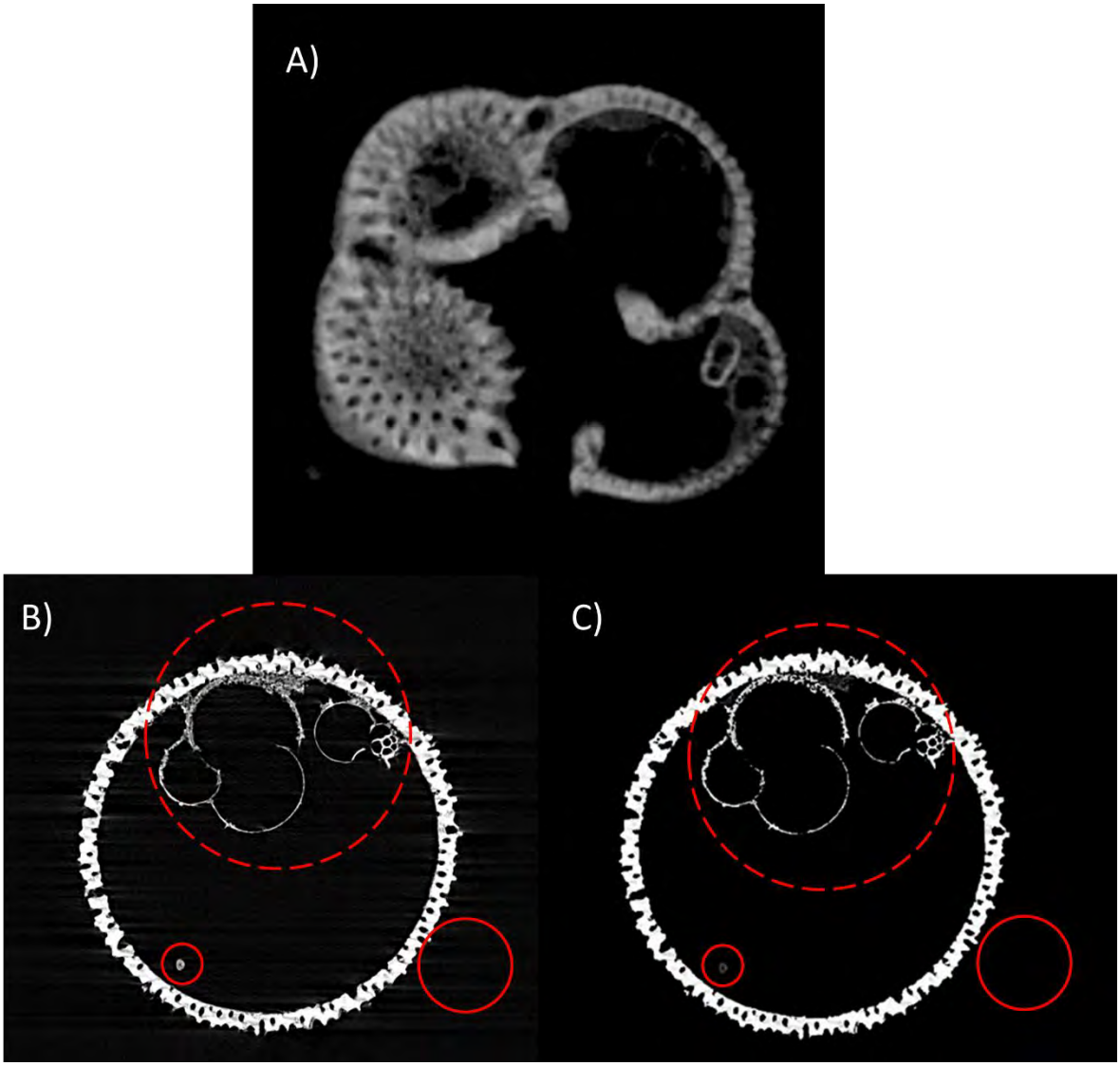

Figure 4-1: A) slice from a µCT-scan of Sphaeroidinellopsis kochi*, the brighter the white colouration of the image the less X-rays have reached the detector. B) a slice from a high resolution (synchrotron x-ray source) scan of* Orbulina universa*, C) segmentation of same slice as in B). In the bottom left red circle in B) there is an un-wanted object in the scan (i.e. not part of the foraminifera), which was removed manually removed as can be seen in C) the object is grey not white. In the top dashed circle are parts of the foraminifera test wall which are removed during automated segmentation (are grey in B) and were manually added back in to the final version (are white in C). In B in the bottom right circle there are scan artefacts (beam-hardening, where the test refracted the X-rays, seen as thin lines at the edge of the foraminifera test). These were removed during automatic segmentation. The final renderings of both foraminifera are presented in Figure 4-2.*

From tomographic data, it is possible to generate a 3D model (Figure 4-2), which can then be exported for 3D printing (See Chapter 2 for an overview). Using these techniques accurate models of organisms can be made at larger scales (e.g.: Teshima *et al.*, 2010 (the Radiolaria: *Svinitzium*

pseudopuga Dumitrica and *Pantanellium riedeli Pessagno*; and the benthic foraminifera: *Elphidium spp.*); Rahman *et al*., 2012 (the trigonotarbid arachnid: *Eophrynus prestvicii*)).

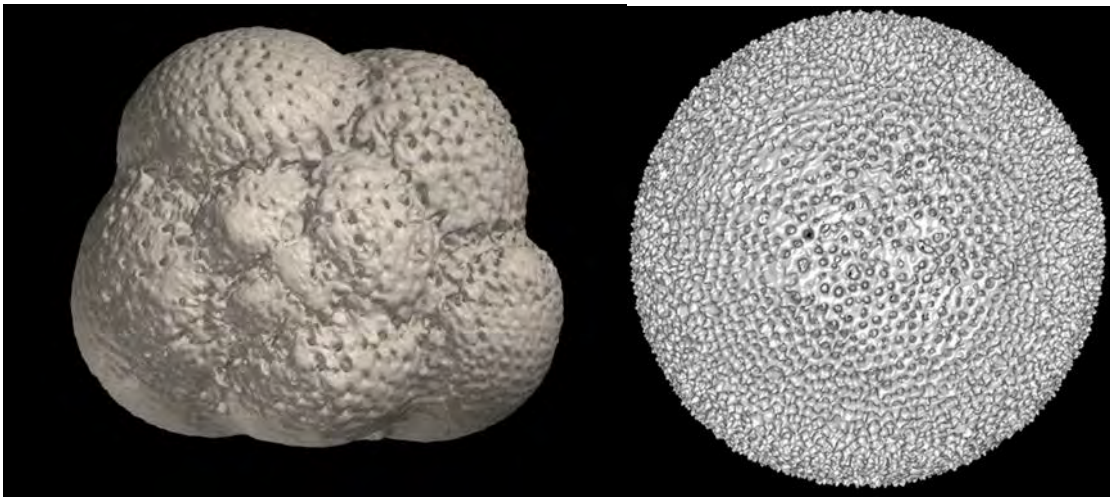

Figure 4-2: 3D rendered models of Sphaeroidinellopsis kochi *(Tohoko University) and* Orbulina universa *(this study, original specimen courtesy of M. Kucera)*

However, simply 3D printing scale versions of foraminifera does not allow sinking velocities of the real tests to be determined. This is because an enlarged model will behave differently when sinking in water to the life size foraminifera. To overcome this, dynamic scaling (Zohuri, 2015), a technique common in engineering, was used. An example in which this method is commonly used is the production of aircraft, where scale models are made and airflow around them is tested in a wind tunnel. Such testing allows the aerodynamic characteristics of an aircraft to be identified, providing validation to theory and providing data in areas where theory is lacking (Wolowicz and Bowman, 1979).

Dynamic scaling, or similitude, requires the model and the real object to have kinematic, dynamic, and geometric similarities (Zohuri, 2015). In other words, the model and the real object must have the same: fluid flow around them (kinematic similitude), ratios of forces acting upon them (dynamic similitude), and shape (geometric similitude). To return to the aircraft example, this would mean that the model should experience the same flow around it as the real aircraft, the ratio of forces (e.g.: drag and lift) should be the same and the model should be the same shape as the final aircraft. Dynamic scaling will be discussed in more detail in section 4.3.1.

4.3 Method Development

Before sinking scale models of foraminifera, several tests had to be conducted to determine a suitable fluid, modelling resin, settling tank dimension, particle release mechanism, as well as visualisation and tracking methods. This method development process is detailed below.

Enlarged scale models allow the precise sinking orientation to be captured (Fraisse, Bormans and Lagadeuc, 2015), without the use of high speed cameras. Additionally, the use of CT scan data allows segmentation of material from the internal cavities of the test, ensuring that only the test

walls are reproduced. Furthermore, the digital model generated from the CT scan data can be measured with high accuracy and precision (Schmidt *et al.*, 2013). This includes accurately measuring the volume of the test wall (V_{wall}). In addition to this, the use of 3D printing allows access to specimens that might otherwise be difficult, as explained for other (non-foraminiferal) species in Chapter 2.

For clarity, in the following sections "particle" is used to refer generically to the object being sunk in the tank, which may be a sphere or a model foraminiferal test.

4.3.1 Dynamic Scaling

The most technically challenging part of the project is the dynamic scaling. To produce an accurately scaled model, the model and the foraminifera must have geometric, kinematic and dynamic similitude.

Geometric similitude implies that the ratio of any length in the real foraminifera is shared by the corresponding length in the model. The ratio $\frac{Length_{model}}{Length_{real}}$ is used to describe how the model differs in size to the real foraminifera. This ratio is known as scale factor (scale from here on) and is the number of times larger than life the model is, so a model that is scale 10 will be ten times longer than a real foraminifera and have one hundred times the area, and one thousand times the volume. This is because area and volume scale to the power of two and three respectively. In summary, geometrically similar objects are similar in shape but not in size. In this study 3D printing is used to produce an exactly scaled foraminifera, thereby matching geometry (i.e. geometric similitude is achieved).

Kinematic similarity is the similarity of motions (i.e. speed, acceleration), which are described using length and time. As the relative lengths of kinematically similar systems must match, geometric similarity is implied. To achieve kinematic similarity the model and the real foraminifera must experience the same relative change in fluid flows. Returning to the example of the aircraft in the wind tunnel, to understand the changes in flow between a real airspeed of 10 $m{\cdot}s^{-1}$ and 50 $m{\cdot}s^{-1}$, a scale model must experience a change in flow rate of the same relative magnitude. In this example, five times the original speed (for example, the model could be tested at 1 $m{\cdot}s^{-1}$ and 5 $m{\cdot}s^{-1}$). Kinematic similarity can be achieved by matching Re. When Re under the model and real-life conditions are equal, the fluid flow from the model's perspective (i.e. the flow streams around the model) will be the same as that experienced by the real foraminifera, but may happen on different timescales.

If both geometric and kinematic similitude have been met, then dynamic similitude (the balance of forces acting upon the object and the fluid) ought to be achieved. When dynamic similitude is achieved, the model and the real foraminifera behave in the same manner in the fluid flow. To obtain kinematic and dynamic similitude, it is important that both Re and C_D of the model and the

real foraminifera are the same. In addition, the model needs the same distribution of mass as in real life, which will also ensure the same sinking orientation.

In order to achieve similitude Buckingham π (pi) theory was used. Buckingham π theory states that any physical problem which can be formulated as an equation can be rewritten as a series of dimensionless groups called π terms or π groups. According to Buckingham π theory for the experimental models and the real foraminifera to be similar, both must share the same dimensionless π terms (and these terms must be equal).

As previously mentioned (Chapter 3) when an object is sinking at its terminal velocity the forces acting upon it are balanced, that is the net force is equal to zero (Equation 3-4).

Equation 3-4

$$\Sigma \mathrm{F} = F_{Drag} + F_{bouyancy} - F_{weight} = 0$$

Again, drag force (F_{Drag}) is classically defined, for high Re, as the interactions between Drag Coefficient (C_D), density of the fluid (ρ_{fluid}), the velocity of the particle (U) and the area of the particle (A):

Equation 3-5

$$F_{drag} = C_D \cdot {}^1/_2 \cdot \rho_{fluid} \cdot U_{particle}^2 \cdot A_{particle}$$

F_{drag} is not commonly used in hydrodynamics as a measure of drag, as explained in Chapter 3, as it is dependent on area. Instead C_D is used, which can be used to compare drag between shapes of different areas. C_D is a dimensionless measure of drag and therefore has no units or more properly no physical dimension (hence dimensionless). This lack of dimensions can be verified by writing out the equation in terms of the units used (known as factor-labelling, e.g.: volume is measured in m^3 so V in the equation can be replaced with the unit m^3), thus:

$$C_D = \frac{2 \cdot V_{wall} \cdot \left(\rho_{fluid} - \rho_{particle}\right) \cdot g}{\rho_{fluid} \cdot {U_{particle}}^2 \cdot A_{particle}} = \frac{m^3 \cdot kg \cdot m^{-3} \cdot m \cdot s^{-2}}{kg \cdot m^{-3} \cdot (m \cdot s^{-1})^2 \cdot m^2}$$

Expand sinking velocity squared (U^2):

$$\frac{m^3 \cdot kg \cdot m^{-3} \cdot m \cdot s^{-2}}{kg \cdot m^{-3} \cdot (m \cdot s^{-1})^2 \cdot m^2} = \frac{m^3 \cdot kg \cdot m^{-3} \cdot m \cdot s^{-2}}{kg \cdot m^{-3} \cdot m^2 \cdot s^{-2} \cdot m^2}$$

Cancelling terms, e.g.: $m^{-3} \cdot m^3 = 0$

$$\frac{kg \cdot m^{-3} \cdot m \cdot s^{-2} \cdot m^3}{kg \cdot m^{-3} \cdot m^2 \cdot s^{-2} \cdot m^2} = \frac{kg \cdot m \cdot s^{-2}}{kg \cdot m \cdot s^{-2}} = \frac{\cancel{kg \cdot m \cdot s^{-2}}}{\cancel{kg \cdot m \cdot s^{-2}}} = 0 \; units$$

It is readily verified that C_D is a dimensionless number, since all units in the numerator and denominator cancel. This is a vital requirement when calculating similitude problems, as the problem should be reduced to dimensionless measures which contain all the variables of interest.

In this case, C_D contains the sinking velocity (U), the volume of the particle (V), the density of the fluid (ρ_{fluid}), the area (see section 3.1.3 for discussion on choice of area) of the particle (A) and the density of the particle ($\rho_{particle}$), as well as acceleration due to gravity (g). All of these parameters are important in determining the scale required to accurately replicate the sinking of real foraminifera. In this study, the exact volume of the test walls are known, and so can be used in place of the particle volume. Therefore, Equation 3-6 is modified slightly thus replacing the particle volume (V) with the volume of the wall (V_{wall}). Additionally, the equation can now include the term for scale (S). Under real life conditions S will be equal to 1, whereas under experimental conditions S has to be determined. Once adjusted to accept these terms, Equation 3-6 can be rewritten as:

Equation 4-1

$$C_D = \frac{2 \cdot (V_{wall} \cdot S^3) \cdot (\rho_{fluid} - \rho_{particle}) \cdot g}{\rho_{fluid} \cdot U_{particle}^2 \cdot (A_{particle} \cdot S^2)}$$

Therefore, C_D is the first dimensionless quantity (π term). It is also known that there is a relationship between C_D and Re (see Chapter 3), where C_D can be described as a function of Re:

Equation 4-2

$$C_D = \mathbb{f}(Re)$$

To recap from Chapter 3, Re is a dimensionless measure of the ratio of inertial and viscous forces acting upon a particle. Re is determined by the density of the fluid (ρ), a characteristic length (L, referred to as length from here on in) of the object (see below), sinking velocity (U), and dynamic viscosity (μ) of the fluid:

Equation 3-2

$$Re = \frac{\rho_{fluid} \cdot L \cdot U}{\mu}$$

Therefore, Re is the second π term. Under each of the two conditions (the experimental tank and real life), Re and C_D have to be matched between the real foraminifera test and the model test to achieve similitude. All of the variables in the equations for real life are fixed, therefore only the variables in Equation 4-1 and Equation 3-2 for the model can be adjusted (See Table 4-1).

*Table 4-1: The variables in Equation 4-1 and Equation 3-2 and their values for a real foraminifera test (*Neogloboquadrina acostaensis*, chosen as an example foraminifera to provide illustrative length, projected area and wall volume) with their potential for change under the tank conditions. Values that are To Be Determined (TBD) in the study through either theoretical and computational or experimental methods are marked as TBD. The values in this table will be updated, as the methodology is developed, such that Table 9-12 contains the same example species but with more values for the tank conditions.*

Variable		**Real Life**	**Tank**
Foraminifera & Foraminifera model	Density ($\rho_{foraminifera}$)	Calcite: 2700 kg·m^3	TBD: Fixed
	Volume$_{wall}$ (V_{wall})	1.6 · 10^7 µm^3	TBD: Adjustable
	Length (characteristic, L)	543 µm	TBD: Adjustable
	Projected Area (A_P)	Unknown	TBD: Adjustable
	Sinking Velocity (U)	Unknown	TBD: dependent on other variables
Gravity		Fixed: 9.81 m·s^{-1}	Fixed: 9.81 m·s^{-1}
Fluid	Density (ρ_{fluid})	Seawater: 1028 kg·m^3	TBD: Fixed
	Dynamic Viscosity (µ)	Seawater: 0.00108 Pa·s	TBD: Fixed

By inspection of the previous three equations (Equation 4-1, Equation 4-2 and Equation 3-2), it is possible to derive the following:

Equation 4-3

$$0 = \frac{\frac{1}{2} \cdot C_D \cdot A_P \cdot (Re^2) \cdot (\mu^2)}{\rho_{fluid} \cdot L^2 \cdot V_{wall} \cdot g \cdot (\rho_{model} - \rho_{fluid})}$$

The real solution (i.e. root) of this equation gives a value for the scale at which to print the models to achieve similitude. To solve this equation, the values for all of the variables must be known. This is complicated by the fact that many of them are interdependent. For example:

- The Re of both the model and real test (as these should be equal) is dependent on the sinking velocity (U) of the model or test and their characteristic lengths (L), which are dependent on sinking orientation.
- The C_D is dependent on sinking velocity, area presented to the fluid, and V_{wall} of the model (Equation 3-3).
- The area presented to the fluid (Projected area, A_P) depends on sinking orientation and the scale of the model.
- Length and Volume of the test wall (L and V_{wall}), both of which are dependent on the scale (and geometry) of the model.

The terms in Equation 4-3 that are known are the density and viscosity of the fluid (ρ_{fluid} and μ respectively), the density of the model (ρ_{model}), and acceleration due to gravity (g). The remaining

variables (Re, C_D, L, A_P and V_{wall}) are unknown and interlinked. Therefore, a solution to Equation 4-3 had to be found in a computationally iterative process. For the first time, when no previous versions of that species had been sunk, some initial guesses based on literature values were provided for the values of Re, L, and A_P, and theoretical predictions for a sphere for the value of C_D. Using these estimated values (for Re C_D, L, A_P and V_{wall}) and the known variables (ρ_{fluid} and μ) Equation 4-3 was solved for S. A model was then printed at this scale (i.e. original dimensions · S).

Once the model had been printed it was weighed as the 3D printing and cleaning process was found to always print a slightly larger volume than a direct scaling of the computer model (see Figure 4-3), presumably due to excess material being printed, or a thin layer of material being left on the surfaces of the model. The additional volume of material on the model was typically in the region of $0.5 – 1 \cdot 10^{-7}$ m^3 or approximately 0.03 – to 0.05 grams of additional material (approximately 10% increase in mass). The volume of the wall (V_{wall}) was found using the known density of the resin and the model's mass, thereby accounting for this additional material in the computation of the $Re - C_D$ (see below). It should be noted that the model tests lacked pores due to limitations of low resolution µCT scans and 3D printer resolutions capabilities in the case of high-resolution synchrotron scans, therefore the V_{wall} measurements would be higher than for the actual foraminifera test. The foraminifera model was then sunk, its orientation observed (from which the projected area (A_P) was found using the computer-generated model, see section 4.4.8 and Figure 4-8), and the sinking velocity (U) measured. Re and C_D for the sinking model were then calculated using Equation 4-1 and Equation 3-2, respectively.

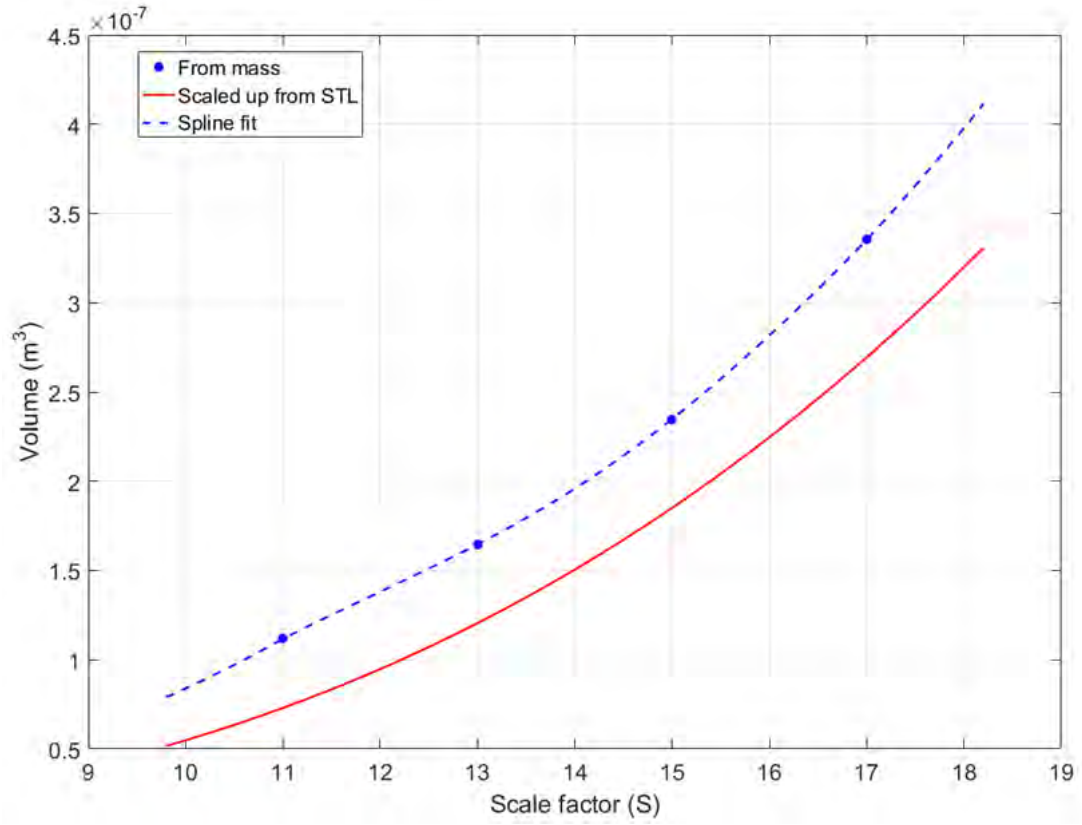

Figure 4-3: Differences in actual and expected model volumes. Model expected V_{wall}, based on scaled V_{wall} from the .stl file (Red line, scaled from STL file) and actual 3D printed V_{wall} (blue dots with dashed interpolated cubic spline fit, from mass measurements) for C. dissimilis 3D printed at different scale factors.

Therefore, from the experiment values for Re C_D, L, A_P and V_{wall} for the model were obtained, and were then entered into the scale prediction equation (Equation 4-3) and a new scale was predicted. This predicted scale is an improvement over the previous estimated scale but will still not be the 'true' scale factor needed to achieve similitude. The process of printing a new model at the new predicted scale, measuring its sinking velocity and calculating Re and C_D was repeated several times. The data points from the experiments for each species produced an experimental Re-C_D curve for each species.

In addition to the values derived from the experimental data, C_D values of both the real foraminifera and the model can be calculated using the force balance equation (i.e. Newton's Second Law, Equation 3-4). When the force balance equation is solved for the foraminifera under real life conditions, with a range of Re values, a series of values are produced. When plotted, these real-life values form a second curve (the first being obtained from the experimental data). The exact point along this second curve at which the foraminifera operates (i.e. it's true Re-C_D) is unknown. The experimental data allow the location on the real-life curve of Re-C_D values to be identified. Once a number of experimental data points have been collected, a spline may be drawn through these points (e.g.: Figure 9-19 and Figure 4-9). The place where the force balance curve and the experimental splines intersect is the real operating point of the foraminifera (Figure 4-9). This method is expanded upon in section 4.4.8 and see Figure 4-4 for full method. For an overview of dynamic scaling theory see Chapter 2 in Zohuri (Zohuri, 2015).

4.4 Material and Methods – Sinking Experiments

Using the dynamic scaling techniques outlined above (section 4.3) the aim was to determine the sinking velocities of 35 species of planktonic foraminifera. More details on the choice of 3D printer, 3D printed resin, tank choice, and model visualisation during sinking can be found in Appendix 9.2. The species were chosen based on their availability in the eforam Stock (see below). This selection of foraminifera was intended to be supplemented with an additional 5 species of commonly occurring foraminifera (e.g. *O. universa*), as detailed below it was not possible to determine sinking velocities for all of these additional foraminifera.

4.4.1 Low resolution CT scans

The University of Tohoko museum's database, eforam Stock, contains electronic models of 133 individual foraminifera based on CT scan data, with a scan resolution between 2.5 and 3.6 pixels per µm. These models represent 53 separate species and are freely available under Creative Commons Attribution-NonCommercial-NoDerivs 2.1 Japan License. Electronic models of all the forams in the eforam stock database were downloaded, in the propriety file format ".mol" from http://webdb2.museum.tohoku.ac.jp/e-foram/. Molcer (Version 1.35, White Rabbit Corp., 2016) was then used to import these models and save them as ".stl" files (STereoLithograph files). The scan resolution, and therefore actual size, was not known for several specimens, and along with species not present in the phylogeny of macro-perforate planktonic foraminifera (Aze *et al.*, 2011), were removed from the dataset. This resulted in a dataset of 30 species for which complete information was available. For species where more than one scan was available, the scan that contained the best-preserved specimen was chosen. This approach, unfortunately, removes phenotypic plasticity which is demonstrated in planktonic foraminifera, by only providing one specimen per species.

4.4.2 High resolution scans

To supplement the eforam dataset seven species of planktonic foraminifera were scanned, at the PETRA III synchrotron storage ring at DESY in Germany, with a scan resolution of 0.721 µm per pixel, by A. Blanke and the technicians on-site. These scans were segmented and rendered using SPIERS (Sutton *et al.*, 2012), and the resulting 3D mesh was exported as an ".stl" file, and checked in Meshlabs (Callieri *et al.*, 2012) for integrity, by myself and T. Hoehfurtner.

4.4.3 Tank and oil

For details on the choice of tank see section 9.2.1.6. The tank measured 0.9 m in diameter and 1.239 m in height (Figure 9-13). The tank was filled with "Carnation" white mineral oil (Tennants Distribution Limited, Cheetham, Manchester, UK) to a depth of 1.18m (approximately 750 L). The tank was placed on a custom fabricated steel platform, atop a 1000L bunding to contain any accidental spillages. The tank was fitted with a custom net and net retrieval system (Figure 9-13) to

allow easy retrieval of the models after their descent. Integrated to the net retrieval system was the release mechanism, which was held centrally over the tank, with the grasping parts submerged below the oil level. To minimise reflections, the tank was surrounded by a black fabric tent-like structure. This also served as a dark background to facilitate visualisation of the model during descent.

4.4.4 3D Printing

All the computer-generated models of the foraminifera were imported into Preform (Versions 1.8.2 onwards, Formlabs, Somerville, Massachusetts, USA) software, which prepare the models for printing on a FormLabs Form1+ (Formlabs, Somerville, Massachusetts, USA) 3D printer. Preform computes optimal orientation for highest quality printing results and automatically adds support structures. All models were printed using FormLabs Clear Resin Version 2 (Formlabs, Somerville, Massachusetts, USA) with a layer thickness of 50 µm. Preform software can only create and load preform files of a certain complexity (3 million vertices), as such the models were printed in small groups (approximately six models). The high-resolution scans had to be printed in smaller groups, due to the larger file size.

The external surfaces were cleaned as recommended by Formlabs (see 9.2.1.1). Whilst, the internal chambers of the foraminifera model were cleaned as per the spheres above. The support structures were removed with side cutters and any excess hardened resin from the support structures removed using 400-grit “wet-&-dry” abrasive paper. A final rinse of the model was performed with propan-2-ol to remove any remaining particles or residue from the support removal process. The model was then allowed to air dry.

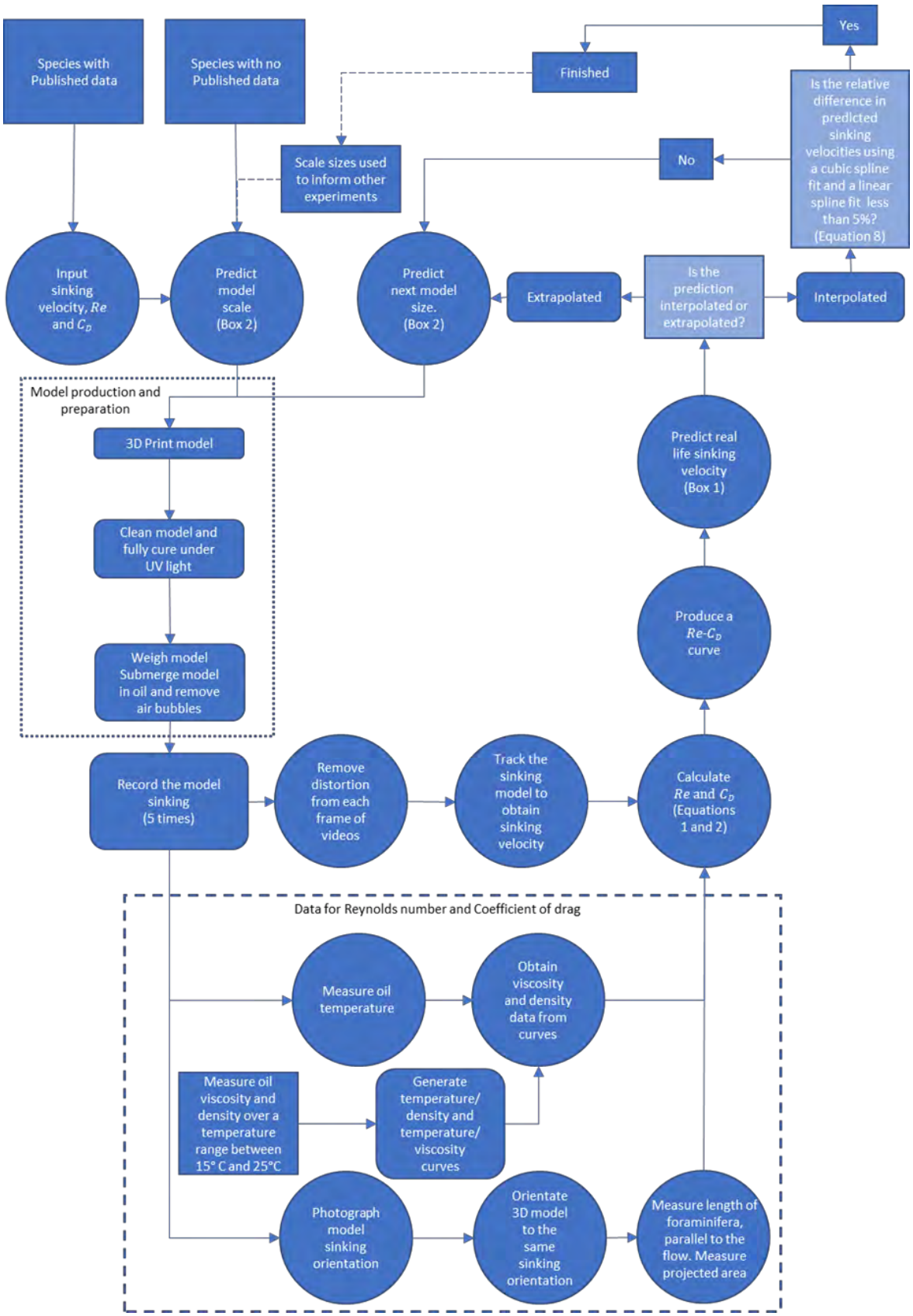

Figure 4-4: A flow chart of the dynamic scaling process. This is a summary of the full method; the details are discussed below. Lighter shades represent a decision, square boxes are data inputs, rounded square boxes are manual processes, and circles are computational steps. (Equations and boxes continue below, note equation numbering applies to this figure only).

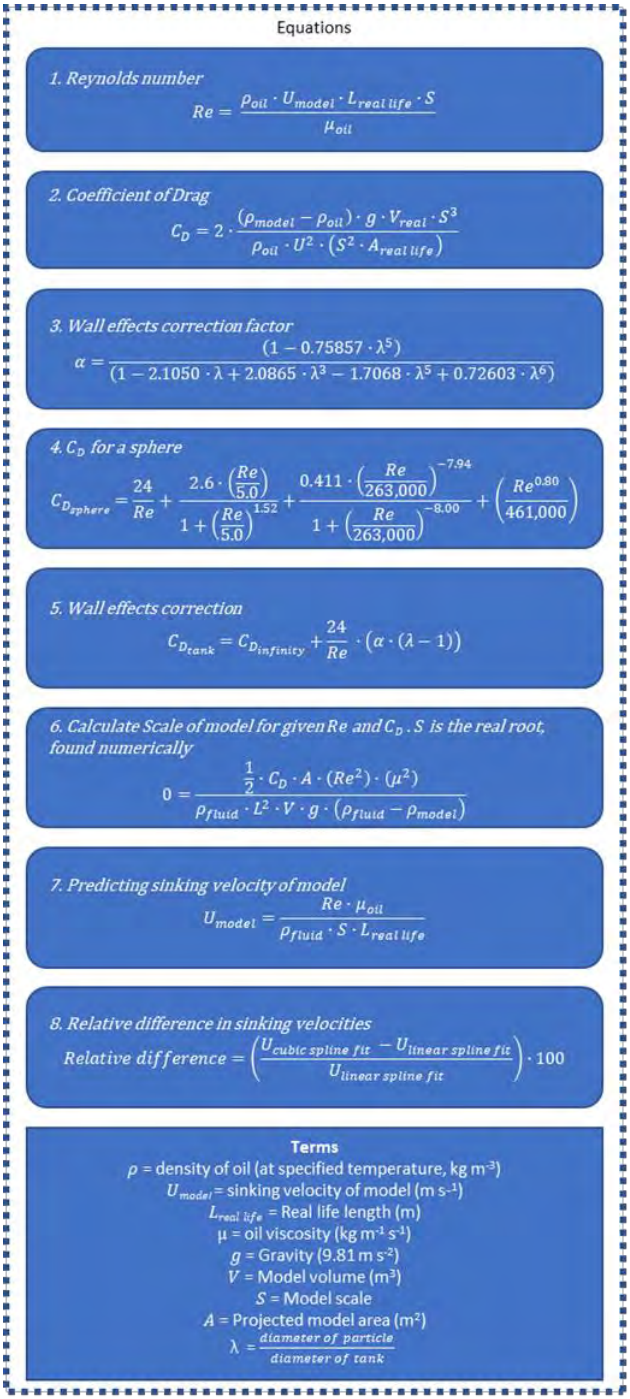

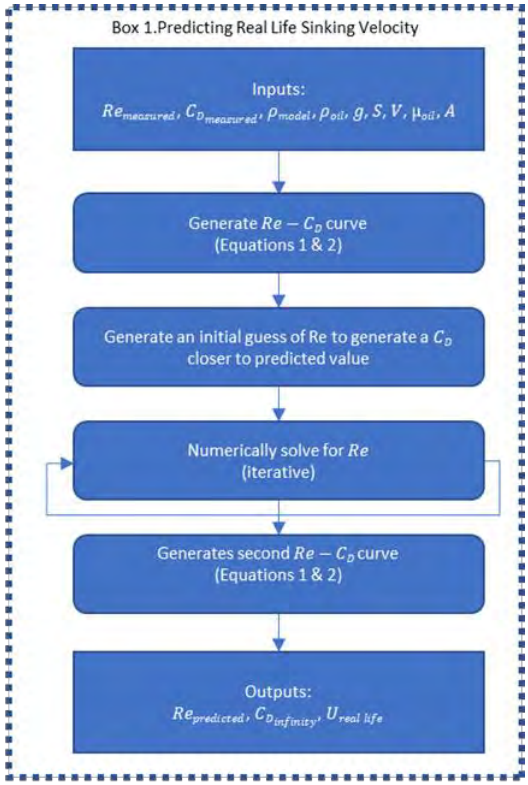

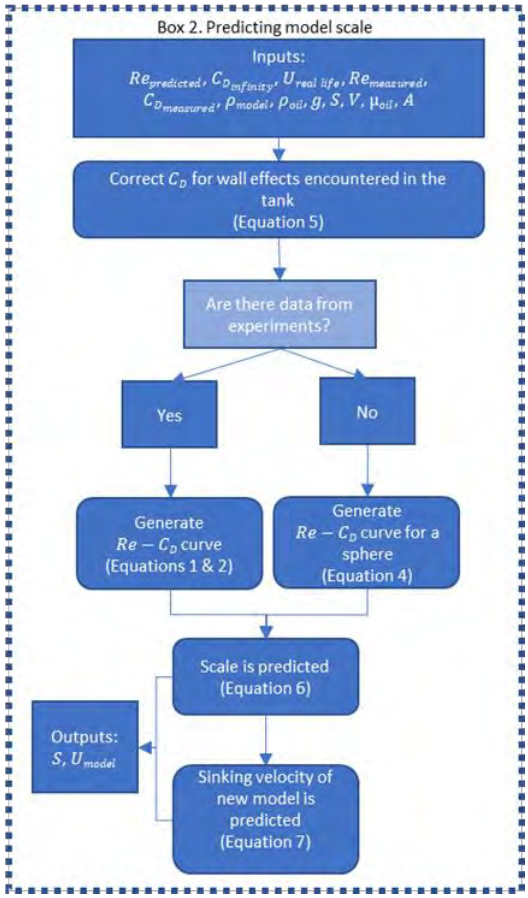

Figure 4-4 (continued)

4.4.5 Submersion in mineral oil

The finished models were left for at least 12 hours to ensure all propan-2-ol had evaporated. Then the models were weighed using an electronic balance (Entris 224-1S), accurate to 0.001g. Masses were measured five times and an average mass calculated. Despite thorough cleaning, there was always more resin than predicted by scaling of the ".stl" V_{wall}, i.e. the model was heavier than expected (Figure 4-3, and section 4.3). To account for this the average model mass was a parameter for both the calculation of the sinking velocity of the actual foraminifera and for the prediction of the next scale (see Figure 4-4). Once the model mass had been determined, the model was submerged in mineral oil in a small screw top container (Sarstedt Ltd, Leicester, UK) and air bubbles removed from the internal cavities using a 30-gauge needle and syringe (see section 9.2.1.5). The model was then stored in oil until it was used in experiments. The time between 3D printing and sinking the model was less than the 6 weeks test period for the beams (section 9.2.1.3).

4.4.6 Sinking the models

3D printed models were removed from the screw top jar while the entire jar was submerged in the tank, preventing air from entering the model. The model was then mounted in the release mechanism, which was submerged below the surface. Each model was dropped five times, and each descent was recorded. One model of each species was dropped an additional time and photographed using a Canon 1200D DSLR camera (Tokyo, Japan) mounted on a tripod close to the tank, to obtain high resolution (18 megapixels) images Figure 4-8a), using a remote trigger to avoid camera shake. These higher resolution images were used to align the computer-generated models in the sinking orientation, from which the measurements of projected area were measured.

As the viscosity of oil changes with temperature, its temperature was measured for each descent using a digital temperature probe (Digitron model 2024T, Buje, Croatia), accurate to 0.1°C. Using a viscometer (Brookfield DV2T, Middleboro, Massachusetts, USA) with a temperature-controlled water-bath (Brookfield TC 550, Middleboro, Massachusetts, USA), the viscosity of the mineral oil across a range of temperatures was measured. These measurements and the temperatures recorded during the experiments were then used to match the value used for the viscosity of the oil in the calculations of sinking velocity. This ensured any changes in viscosity of the oil due to temperature changes in the tank were accounted for. After sinking, the model was replaced in the container filled with oil for future use. This prevented air from re-entering the model.

4.4.7 Model tracking and velocity calculation

Models were tracked from distortion-corrected frames (Section 9.2.1.7) using a modified version of Trackbac (Guadayol, 2016; Guadayol, Thornton and Humphries, 2017). The per-frame centroid coordinates obtained were then paired with the timestamp values recorded to calculate sinking velocities in 2D for each camera. A linear regression slope was fitted to the time-position data (Figure 4-5) for both horizontal and vertical movement for both cameras. The slope of the

regression line (vertical and horizontal for each camera, see Figure 4-5) gives the velocity of a given camera and plane, which can be combined using Equation 4-4 to give a 3D velocity from each camera, which was then averaged to give a single velocity for a given particle.

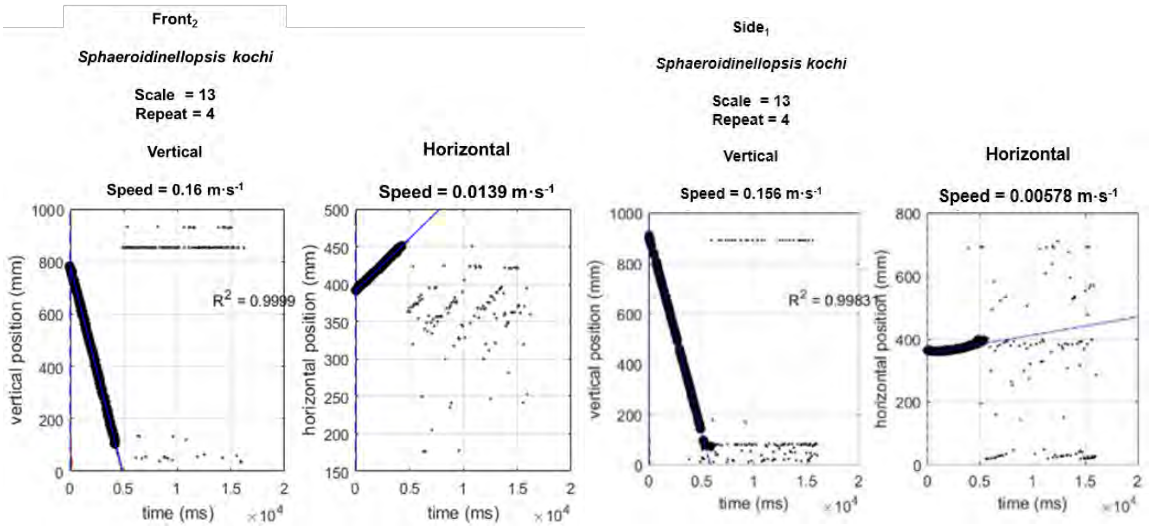

Figure 4-5: An example of the centroid position over time plots, from camera 1 (Side$_1$) and camera 2 (Front$_2$) (See Figure 9-14 for camera placement). In this example plot the centroid positions are for a model of Sphaeroidinellopsis kochi *at scale 13 during the fourth sinking. The blue line is a linear fit used to determine velocity using Equation 4-4. The small circles are points identified by the tracking code, which were subsequently removed using the "data-sorting" code (see 9.2.1.7 - Image Processing and particle tracking).*

The horizontal speeds from both cameras were then combined with the vertical velocities to calculate a 3D speed. To do this, the horizontal speed from camera one (U_x) and camera two (U_y) were combined with the vertical speed from camera one ($U_{z,1}$) using Equation 4-4a. This procedure was repeated using the same horizontal speeds and the vertical speed from camera two ($U_{z,2}$), i.e. Equation 4-4b. From these two 3D sinking velocities, an average was calculated (Equation 4-4c). The co-ordinate system is demonstrated in Figure 4-6.

Equation 4-4

a.

$$3D_1\ U = \sqrt{{U_x}^2 + {U_y}^2 + {U_{z,1}}^2}$$

b.

$$3D_2\ U = \sqrt{{U_x}^2 + {U_y}^2 + {U_{z,2}}^2}$$

c.

$$3D_{total}\ U = \frac{3D_1\ U + 3D_2\ U}{2}$$

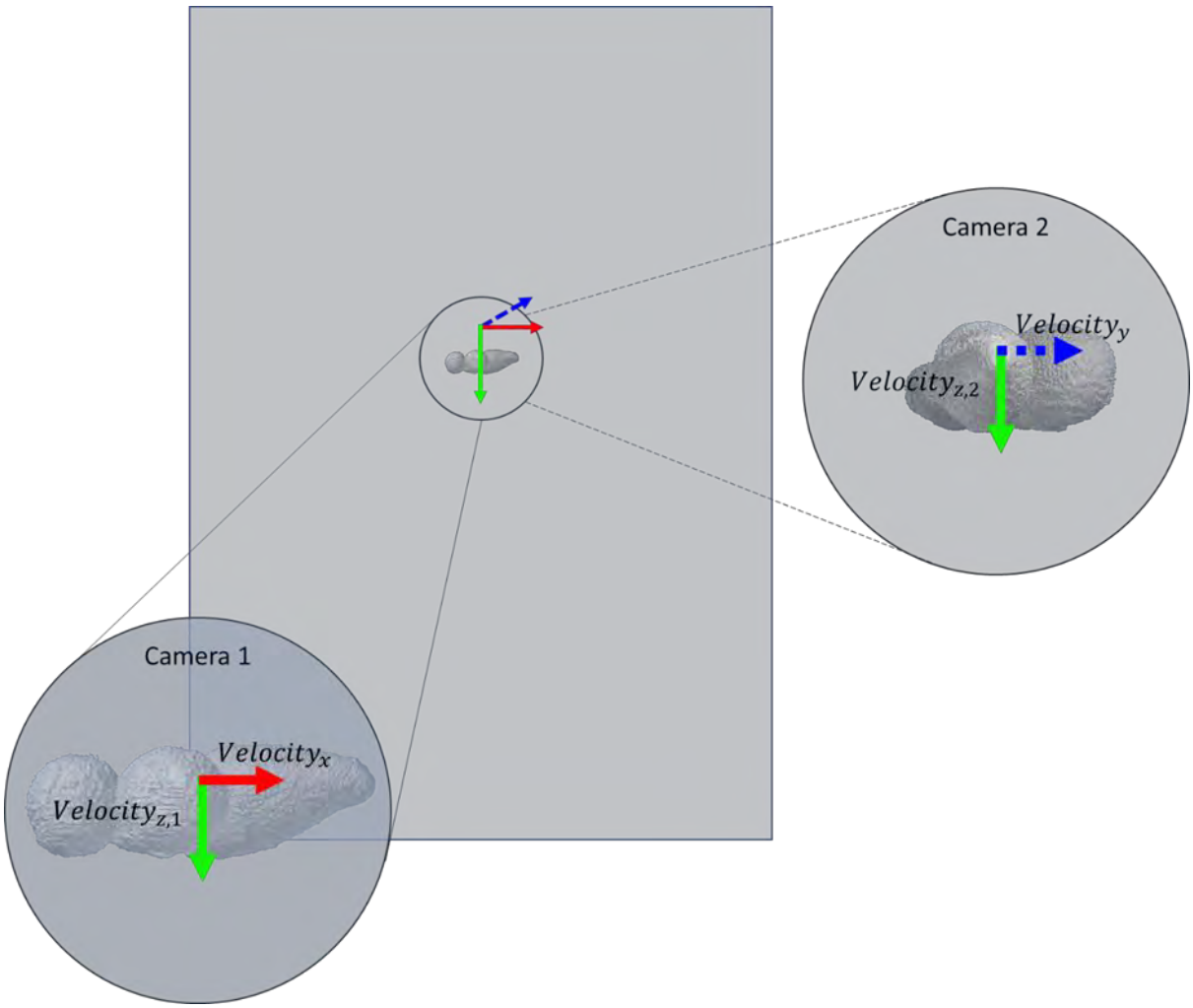

Figure 4-6: An example sinking foraminifera with the views from cameras one and two, at 90˚ to each other (see Figure 9-14), illustrating the velocities used to calculate the 3D sinking velocity. 3D co-ordinate system is used where the x-axis is solid red line, y-axis is dashed blue, and z-axis (vertical) is green.

Each model was sunk five times (see Figure 4-4 and Figure 4-7) and an average 3D velocity obtained. A threshold of ±5% of the median sinking velocity, for a given scale, was applied to include a run's 3D speed in the calculation of the average sinking velocity for that scale. That is, if the sinking velocity of a run deviated more than 5% of the median speed from the repeats for that scale, it was not included in that calculation of the average sinking velocity for that scale.

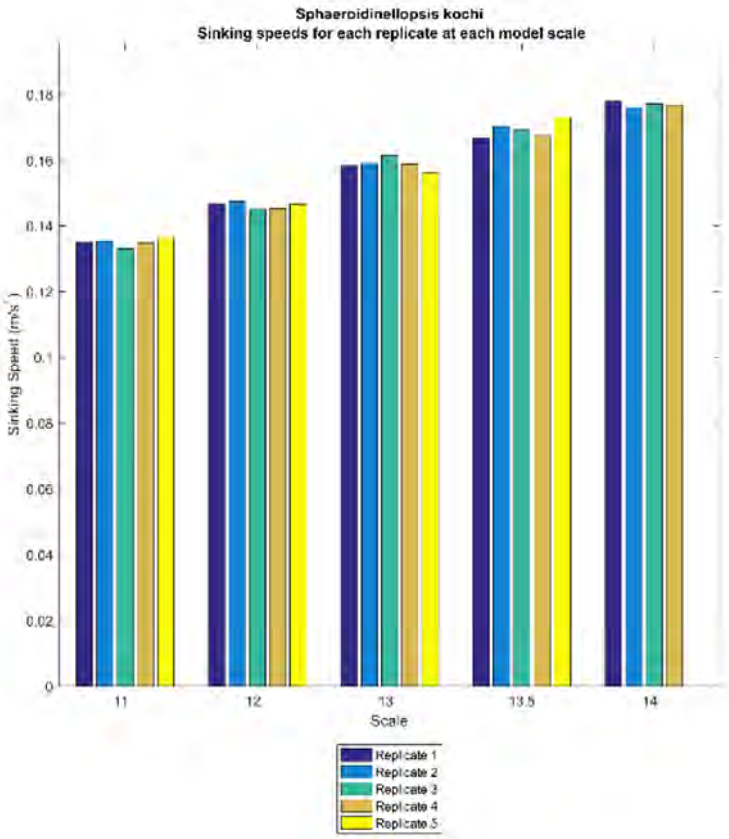

Figure 4-7: An example of the sinking velocities for each replicate at each scale. Shown are 3D sinking velocities of each scale of model for Sphaeroidinellopsis kochi*. Note that Replicate 5 for scale 14 was removed as it does not meet the criteria for average speed calculation for that model size.*

4.4.8 Generating Reynolds Number and Drag Coefficient Curves

Each scanned foraminifera was rotated in 3D (using Molcer, Version 1.35, White Rabbit Corp., 2016) to match the sinking orientation of the printed model from high resolution still image (See Figure 4-8a and section 4.3.1). From this computer-generated model, measurements of length parallel to the flow (L_S) and projected area (area of the model presented to the fluid on a 2D plane, A_P) were taken in FIJI (Schindelin *et al*. 2012, see Figure 4-8b and c). These measurements were then scaled by the same factor as the printed model.

Re and C_D curves were then generated (for an example see Figure 4-9) using custom MATLAB code and used to estimate the sinking velocity of the real foraminifera. The next model scale to be printed was also predicted using these curves, as previously discussed (see method in Figure 4-4 and section 4.3.1). With each new 3D printed model, the estimation gets closer to the real Re and C_D (and therefore sinking velocity) of the foraminifera.

To see if there were sufficient data points close to the predicted operating point of the foraminifera, a linear spline was also fitted to the data points from the experiments (obtained thus far), this resulted in straight lines between the data points, instead of a smoothed curve. This linear-fit spline removed any effect of fitting a smoothed spline through the data points (e.g.: if the data points were too far apart the fitting of the cubic spline would generate a predicted point, which could have been too far from the real Re-C_D, and therefore sinking velocity, of the foraminifera). To test if

more 3D printed models were required, the difference in the estimated sinking velocity of the cubic-fit (model sinking velocity$_{cubic}$) and the linear-fit (model sinking velocity$_{linear}$) splines were calculated (Equation 4-5). If the difference between the two estimated sinking velocities (generated by the linear- and cubic-fit splines) was small (less than 5%) then the iterative experimental process could be stopped. If the difference was large (greater than 5%) then another model was 3D printed at the predicted scale and sunk. These new data from this latest experiment were added to the graph and the fit of the linear and cubic splines were re-calculated. This process was repeated for all species until the difference between the linear- and cubic-fit splines was less than 5%.

Equation 4-5

$$Percentage\ Relative\ difference = \left(\frac{Model\ Sinking\ Velocity_{cubic} - Model\ Sinking\ Velocity_{linear}}{Model\ Sinking\ Velocity_{linear}}\right) \cdot 100$$

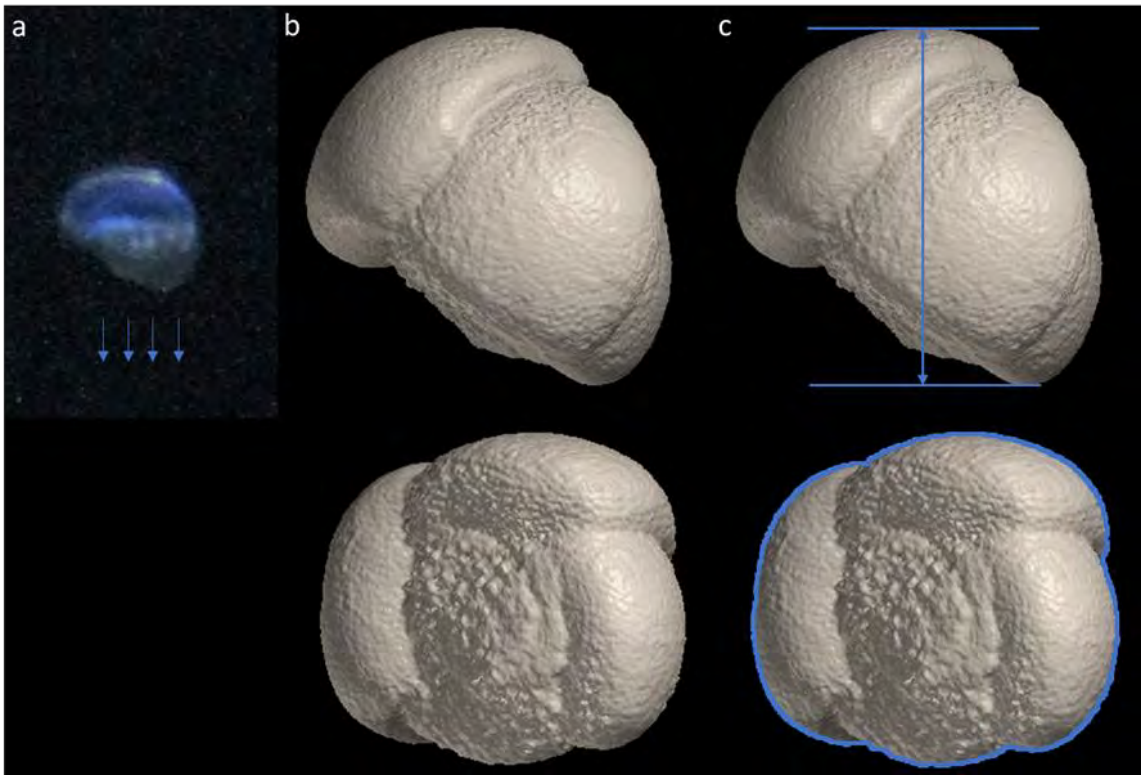

Figure 4-8: a) An example high resolution image of a model sinking foraminifera (Globoconella inflata).

b) Top: The computer-generated model of the same specimen rotated to the sinking orientation. Bottom: underside view of the foraminifera, i.e. the projected area to the fluid as the foraminifera sinks.

c) Measurements taken from the electronic model. Top: the sinking orientation length, parallel to the flow (L_S). Bottom: The projected area (A_P, within the outline in blue)

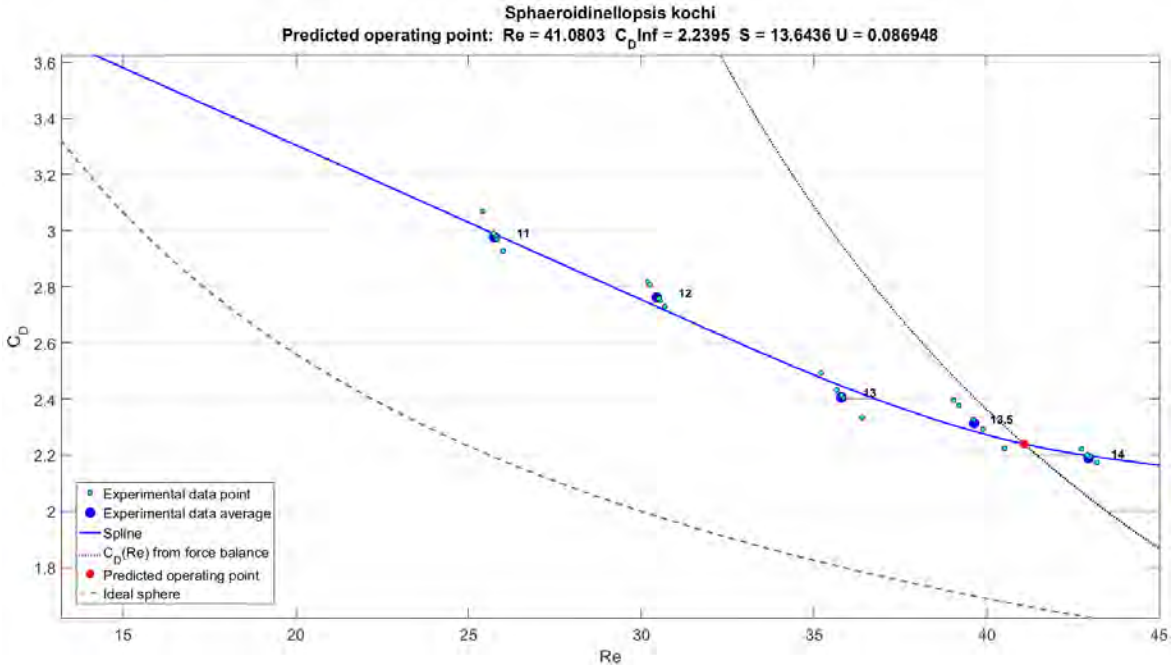

Figure 4-9: An example Re-C_D curve, the small cyan points are each data point and the large blue circles are the average for that model scale (scale indicated). The solid blue line is a constrained (i.e. to be monotonically decreasing) cubic spline through the mean values. The point of intersection (red circle) between this spline and the C_D and Re line obtained from the force balance equation (Equation 3-4, dotted line) is the predicted operating point of the foraminifera in real life. The values at this predicted operating point can be seen at the top of the figure, where: Re is Reynolds number, $C_{D_{inf}}$ is the drag coefficient (C_D) in an unbounded fluid, S is the predicted scale factor needed to exactly replicate this operating point in the experimental tank and U is the sinking velocity of the real foraminifera under natural conditions. For reference the figure also included the Re-C_D curve for a sphere (grey dashed line, Equation 3-8).

Equation 3-5

$$\Sigma \mathrm{F} = F_{Drag} + F_{bouyancy} - F_{weight} = 0$$

Equation 3-8

$$C_D = \frac{24}{Re} + \frac{2.6 \cdot \left(\frac{Re}{5.0}\right)}{1 + \left(\frac{Re}{5.0}\right)^{1.52}} + \frac{0.411 \cdot \left(\frac{Re}{263{,}000}\right)^{-7.94}}{1 + \left(\frac{Re}{263{,}000}\right)^{-8.00}} + \left(\frac{Re^{0.80}}{461{,}000}\right)$$

Equation 3-6

$$C_D = \frac{2 \cdot V \cdot (\rho_{fluid} - \rho_{particle}) \cdot g}{\rho_{fluid} \cdot U_{particle}^2 \cdot A_{particle}}$$

4.4.9 Developing a Novel Measure of Drag

C_D has classically been defined (see Equation 3-6) assuming that the drag force (F_{Drag}) scales with particle velocity squared (U^2). This equation results in a nearly constant C_D value over a Re range of ~1,000 – ~80,000, which encompasses highly turbulent flows. This Re range is suitable for a number of applications such as automobile and aircraft design and allows the straightforward comparison of drag on different bodies across these Re values. However, at low Re (≤10), there is a strong decrease in C_D with Re (see Figure 3-5). This is because low Re describes the creeping flow regime in which the drag force is linearly proportional to U, as seen in Stokes Law (Equation 3-5). As foraminifera experience intermediate Re regimes, between the extremes represented by creeping flow and fully turbulent flow, a different C_D was required that would yield approximately equal values over the Re range of interest here (*Re ≈10-75*). Such behaviour allows the separation

of the effects of shape on drag, from the effects of the flow regime on drag. Constant C_D values over the range of Re experienced by the foraminifera would also permit more reliable extrapolation of C_D at an Re slightly beyond the experimentally measured range to allow comparison of many different species at the same Re value. Again, this helps to isolate the effect of shape from the confounding effect of flow regime on the drag force being experienced by the foraminifera. In this case a new C_D for intermediate Re was formulated for which drag force scales with U^n, where n is ≥1 and ≤2. If n = 1 this is equivalent to Stokes' Law and when n = 2, this is equivalent to Equation 4-6. This novel C_D for intermediate Re (henceforth C_{DI}) was defined as follows.

Classically, C_D appears in dimensional analyses of fluid drag problems as one of two dimensionless groups that completely describe the problem (the other dimensionless group being Re). That is to say by using C_D and Re the drag experienced by a body in a fluid may be described. C_D is calculated using Equation 4-6, with drag force (F_{Drag}), the density of the fluid (ρ_{fluid}), the sinking velocity (U), the area of the object (A), the characteristic length (L) and the kinematic viscosity (υ, as defined by Equation 4-7).

Equation 4-6

$$C_D = \left(\frac{F_{Drag}}{\frac{1}{2} \cdot \rho_{fluid} \cdot U^2 \cdot A} \right) = \mathbb{f}\left(\frac{U \cdot L}{\upsilon} \right)$$

Equation 4-7

$$\upsilon = \frac{\rho}{\mu}$$

Equation 4-2

$$C_D = \mathbb{f}(Re)$$

By combining the several variables involved in the problem into C_D and Re there is now only one unknown functional relationship, $\mathbb{f}$, that must be determined from experiments (Equation 4-2).

While the definition of C_D in Equation 4-6 is typically used, a different combination of variables may be chosen, as long as the resulting group is still dimensionless. Since drag force should scale as U^n, Equation 4-6, where the relationship between drag force and U is $\frac{F_{Drag}}{\mathbb{f}(U^n)}$. However, for Stokes' Law the relationship is $F_{Drag} = \mathbb{f}(U)$. With this in mind, the other variables' exponents need to be varied such that the dimensions still cancel. It should be noted Equation 4-6 implicitly contains υ^0, despite its absence in the equation, as $\upsilon^0 = 1$. By inspection, C_{DI} can be defined as:

Equation 4-8

$$C_{DI} = \frac{F_{Drag}}{\frac{1}{2} \cdot \rho_{fluid} \cdot U^n \cdot A_{particle}^{\frac{n}{2}} \cdot \upsilon^{2-n}} = \mathbb{f}(Re)$$

Here, as above $\mathbb{f}$ is used to indicate that C_{DI} is a function of Re. However, as can be seen (in Equation 4-8) the exact functional relationship between $C_{DI}$and Re will depend on the choice of n. A choice of n = 2 yields C_{DI}= C_D, while n = 1 yields a linear dependence of C_{DI} on U and also introduces a linear dependence of the drag coefficient on viscosity as expected at low Re (i.e. as under Stokes flow).

Finally, it is convenient to obtain a relationship between C_D and C_{DI} to facilitate conversion between the two. So Equation 4-8 is divided by Equation 4-6, to obtain:

Equation 4-9

$$\frac{C_{DI}}{C_D} = \frac{\left(\frac{F_{Drag}}{\frac{1}{2}\cdot\rho\cdot U^n\cdot {A_{particle}}^{\frac{n}{2}}\cdot \upsilon^{2-n}}\right)}{\left(\frac{F_{Drag}}{\frac{1}{2}\cdot\rho\cdot U^2\cdot A_{particle}}\right)} = \frac{\frac{1}{2}\cdot\rho\cdot U^2\cdot A_{particle}}{\frac{1}{2}\cdot\rho\cdot U^n\cdot {A_{particle}}^{\frac{n}{2}}\cdot \upsilon^{2-n}}$$

$$= U^{2-n}\cdot {A_{particle}}^{1-\frac{n}{2}}\cdot \upsilon^{n-2}$$

Which can be solved for C_{DI} in terms of C_D:

Equation 4-10

$$C_{DI} = C_D\cdot U^{2-n}\cdot {A_{particle}}^{1-\frac{n}{2}}\cdot \upsilon^{n-2}$$

The choice of area (A) used in Equation 4-6 and Equation 4-8-Equation 4-10 deserves some attention. In typical situations, the projected area (A_P) is used as at very high Re the pressure drag due to flow separation behind the body is the dominant source of drag (Vogel, 1994). However, at low Re the dominant source of drag is form drag (i.e. drag over the surface, form, of a particle) that depends on viscous stress acting over the entire surface of the body (Vogel, 1994). At intermediate Re some combination of these is expected to be important, as previously described. However, even with computer-generated models of the foraminifera measuring the total surface area is technically possible but time consuming, so the projected area is used. C_{DI} could possibly be improved with the use of a total surface area.

Drag force (F_{Drag}) should logically depend on both the shape and size of an object, amongst other variables. Both shape and size are partially encoded by the object's surface area. Since it is desirable to have a C_D that is only dependent on shape and not size, A should contain as much information on size and as little information on shape as is possible. The least shape dependent area would be volume$^{2/3}$ which would result in different shapes of the same volume, having the same area. However, the volume available from the dataset is that of the calcite wall, while in this case it would

be beneficial to have a volume for the whole test, including internal spaces. Instead, in an attempt to approximate such a volume, Equation 4-11 was used. The new measure of area (Calculated area, A_{calc}) was obtained using the projected area (A_P) and stream-wise length (L_s).

Equation 4-11

$$A_{calc} = (A_P \cdot L_s)^{\frac{2}{3}}$$

Indeed, using A_{calc} in Equation 4-6-Equation 4-10 as per Equation 4-11 instead of simply as $A = A_P$ resulted in a reduced dependence of C_{DI} on Re indicating a better isolation of the effects of shape alone.

Using the sinking data from the models, the most suitable value of n was determined using Equation 4-10 by plotting C_{DI} as a function of n. Coefficients of linear models for each species' C_{DI} as a function of Re were calculated. An average of the square of these coefficients ("mean squared coefficient") was taken so that negative coefficients of some species do not cancel positive coefficients of other species, Equation 4-12. The value for n was chosen at the point where the mean squared coefficient average was closest to zero. The results of the n values and coefficient were then plotted (Figure 4-10), a spline was fitted through these data and then the "predict" function (R base package: "stats") was used to predict the value of n where the mean coefficient was equal to 0. This 'best' n was 1.23, which was then refined using a finer sequence of n (increasing by 0.01, between 1.2 and 1.3). This yielded the result of n = 1.232, where the mean squared coefficient was equal to 0.

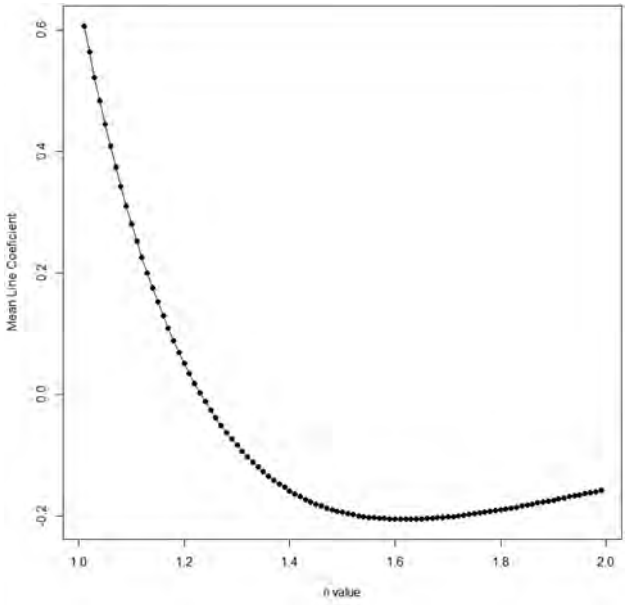

Figure 4-10: Mean squared coefficient (as defined in Equation 4-12) obtained from varying n values.

Equation 4-12

$$Mean\ squared\ coefficient = \frac{\sum(coefficient\ of\ each\ species\ line^2)}{number\ of\ coefficents}$$

Once a value of n that flattened the curves plotted through the relationship of C_{DI} and Re (i.e. the mean squared coefficient was equal to 0) had been found, C_{DI} was determined for all species using this value of n. Visual inspection of a plot of C_{DI} as a function of Re (Figure 4-11) showed that most species Re ranges included Re = 13. Therefore Re = 13 was chosen as the operating point to obtain the single C_{DI} value for each species, which would be used for the statistical analysis.

For some species, the curves plotted through the relationship of C_{DI} on Re included values at Re = 13. However, this was not the case for all species, for those species where the relationship between C_{DI} and Re is flat, extrapolations made beyond the data points are more reliable. To make these extrapolations, the "predict" function was used on the linear models for each species ($C_{DI} \sim Re$), Re was specified at 13 and the value for C_{DI} was predicted. *Globorotalia flexuosa* and *Sphaeroidinellopsis kochi* both do not contain any data points close to Re = 13. These species have either steep slopes (Figure 4-11) which would make extrapolations unreliable or their data lie far from Re = 13. As such they are removed from subsequent analyses using C_{DI}.

4.4.10 Data for Statistical analysis

The final predicted sinking velocities, along with genera, species, length parallel to the direction of travel, projected area, volume of the real foraminifera test (V_{wall}) and an estimated mass, were exported from MATLAB to a text file. Estimated mass was calculated using the density of calcite (2700kg·m^3) and V_{wall}. These were then paired with measurements of longest, intermediate and shortest lengths, measured using FIJI (Schindelin *et al.*, 2012) from the 3D scans. CSF values were then calculated and the morphogroups of Aze *et al.* (2011, Table 4-2) were added.

As mass was determined to be an important factor in determining sinking velocities (Chapter 3), normalisation of sinking velocity by mass (U_{mass}) was conducted (Equation 4-13) to account for mass when making comparisons of sinking velocities across species.

Equation 4-13

$$U_{mass} = \frac{U}{mass}$$

Table 4-2: Aze et al. (2011) morphogroups, also see Figure 4-12 below.

Aze *et al.* morphogroup	Aze *et al.* definition
2	Spinose, globular
3	Spinose globular with supplementary apertures
4	Spinose spherical
5	Spinose, clavate
7	Non-spinose globular
12	Non-spinose, turborotaliform, keeled
13	Non-spinose, turborotaliform, non-keeled
14	Non-spinose, globorotaliform, keeled
15	Non-spinose, globorotaliform, angluconical

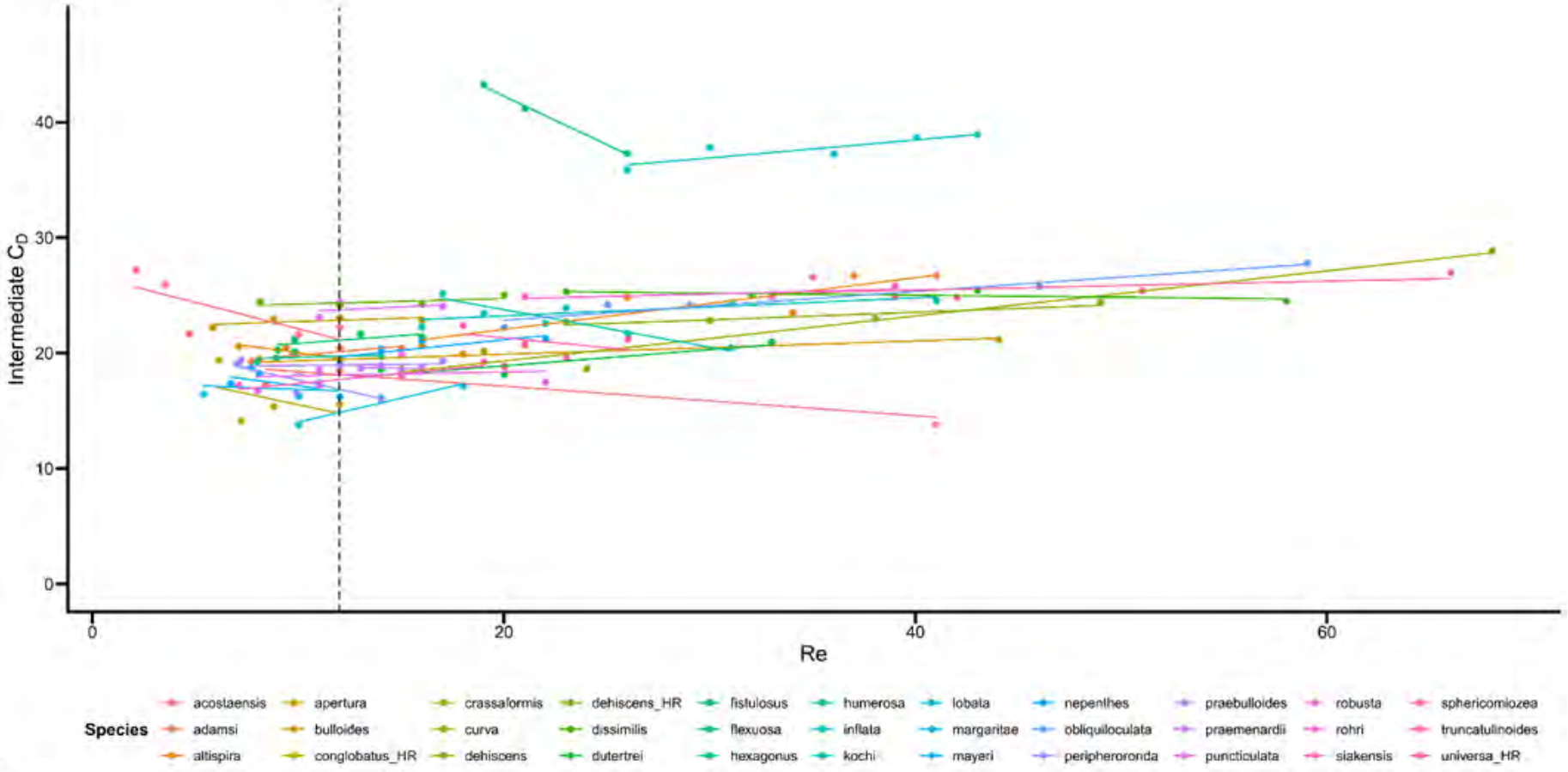

Figure 4-11: Intermediate C_D (C_{DI}) as a function of Re for all species. The vertical dashed line at Re = 13 is the point at which a single value for C_{DI} was calculated for each species (see text for details).

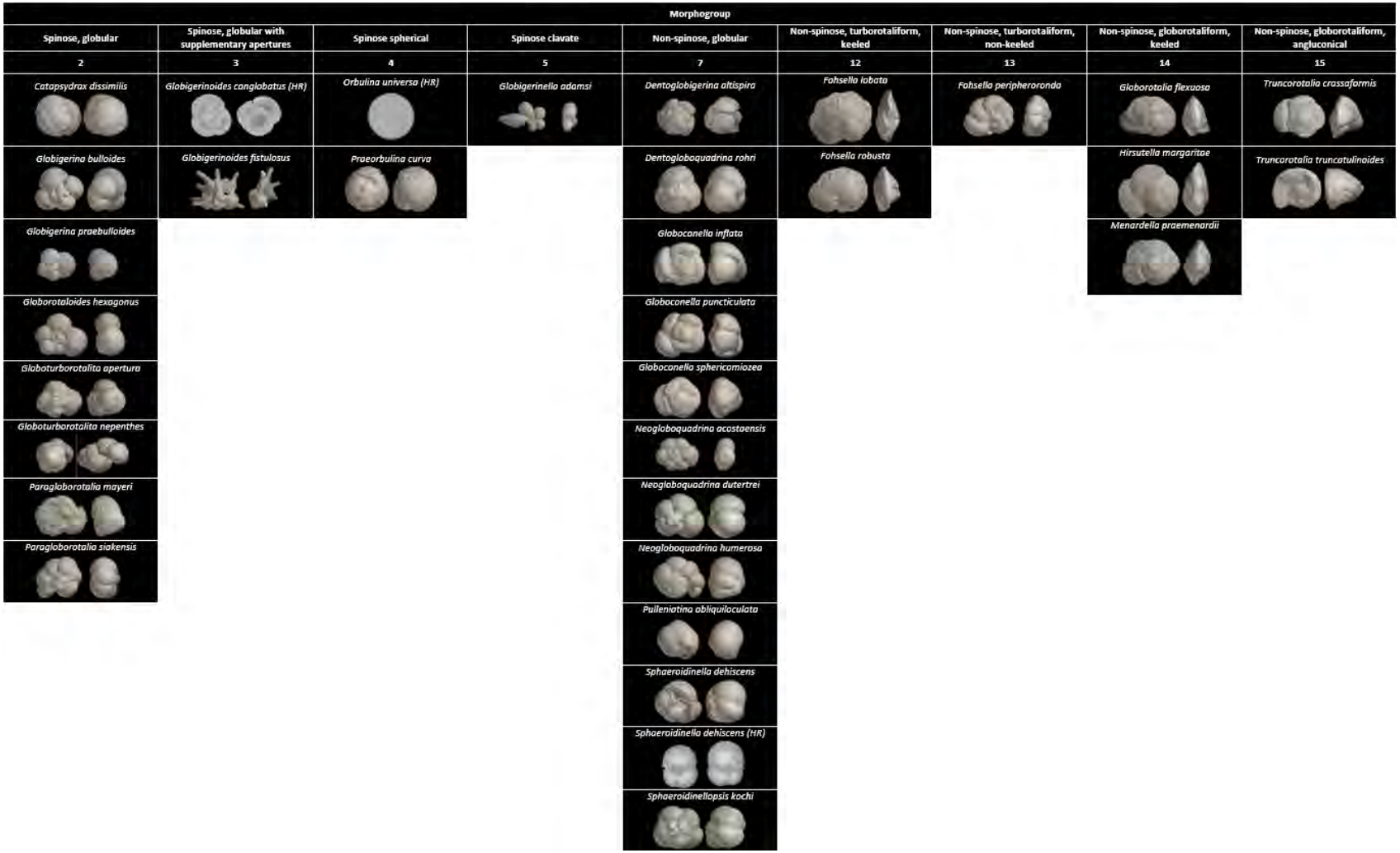

Figure 4-12: The species in this work sorted by Aze et al's morphogroups, shown in both spiral view and 90˚ rotation (so that the spiral view is facing to the left of the page). (HR) denotes species scanned at high resolution

4.4.11 Statistics

Statistical tests were conducted in R (version 3.4.2, R Core Team, 2018). Longest length, L_s, V_{wall}, density, mass, A_P, and mass-controlled sinking velocity (U_{mass}, Equation 4-13) were log transformed (Log_{10}) for the same reasons given in Chapter 3.

To examine how similar the data obtained from the dynamic scaling method are to the previously published data (Fok-Pun and Komar (1983), Takahashi and Bé (1984) and Caromel *et al.* (2014), see Chapter 3), comparisons were carried out using ANOVA, with Tukey HSD *post-hoc* tests, to produce pairwise comparisons between each study for: sinking velocity, maximum length, mass, and CSF. These variables were chosen as mass and length were both shown in Chapter 3 to have a strong relationship with sinking velocity. The comparison of sinking velocities between the different sources is important to show that the values obtained here are valid. CSF is compared to facilitate comparisons between the results of Chapter 3, where there is no significant relationship between sinking velocity and CSF. Comparisons could not be made for volume, as the volumes used in the previously published data are the volume of the entire foraminifera, whereas in this study the volume is V_{wall}. Likewise, comparisons of Re and C_D are not possible as they use different methods to calculate them; C_D in this dataset uses V_{wall} in its calculation and Re uses L_s (compared to those calculated in Appendix 9.1.3).

The relationships between sinking velocity and: longest length, V_{wall}, density, mass, A_P and L_s were individually examined using linear models (as per Chapter 3). Individual linear models were also conducted for U_{mass} and longest length, V_{wall}, density, A_P, and L_s.

ANOVA and Tukey HSD *post hoc* tests were conducted to compare: sinking velocities, U_{mass}, A_P, and V_{wall}, between morphogroups. For the ANOVAs and linear models, morphogroup categories were specified as un-ordered factors. Comparisons of C_D values obtained from the experiments to those expected using Morrison's equation (Equation 3-8) and Stokes Law (Equation 3-7) were conducted by calculating R^2 values using Equation 9-24. Individual linear models were used to examine the relationships between sinking velocity and U_{mass} with CSF.

Linear models were conducted to examine the relationships between C_{DI} and measures of shape, CSF and morphogroup. Additionally, a linear model was used to analyse the relationship between C_{DI} and Re when including CSF as an interaction.

Linear models were conducted to examine the relationship between sinking velocity, V_{wall}, A_P and shape, as measured by CSF, and their interactions. Model quality was tested using AIC and models were reduced using "stepAIC", a "MASS" package (Venables and Ripley, 2002) function, which reduces the model based on AIC score. AIC scores for the model with interactions were obtained using the

"extractAIC" function of the R package base "stats". Constructing models with morphogroup as a predictor was not possible as these models lacked sufficient degrees of freedom.

Interaction plots allow visualisation of the interactions between variables and are used here to examine the interaction terms in models, as per Chapter 3. Interaction plots allow two-way interactions to be visualised, but three-way interactions between continuous variables would require a 4-dimensional plot. Instead, three-way interactions are plotted here as a series of two-way interaction plots, with the third variable varying between each graph.

4.5 Results

4.5.1 Sinking Velocities determined using dynamic scaling

The sinking velocities of 32 of the 35 species (33 of 37 individuals) could be determined using dynamic scaling (Table 4-3). Three of the species scanned at high resolution were removed from the study (*Globigerinoides trilobus*, *Globigerinoides ruber* and *Neogloboquadrina dutertrei*) as the final scale required to match the Re was ultimately too small to allow the foraminifera model to be 3D printed. One *menardii*-type (i.e. planispiral in shape resemblance to the species *G. menardii*) species (also scanned at high resolution) was also removed from the study as the walls were too thin to be printed, as it was not possible to print the specimen an identity was not confirmed. As the specimens were scanned at high resolution, the test wall was thinner and was composed of less material as the pores were present in the model (see Discussion 4.6 for possible effects of this on the study).

A number of species did not exhibit completely vertical sinking paths, with planispiral species (e.g.: *Hirsutella margaritae*) often having helical sinking paths. All species showed a preferred sinking orientation. Species in the genus *Truncorotalia* appear to have more than one preferred orientation, either with the spiral side upwards or downwards at 45˚ from vertical. The orientation of these species varied between each sinking repetition. However, when the projected area in both orientations was measured from the digital model, the area was found to be equal. For all other species, orientation was consistent during sinking and was obtained within 1 s of release (Figure 4-13).

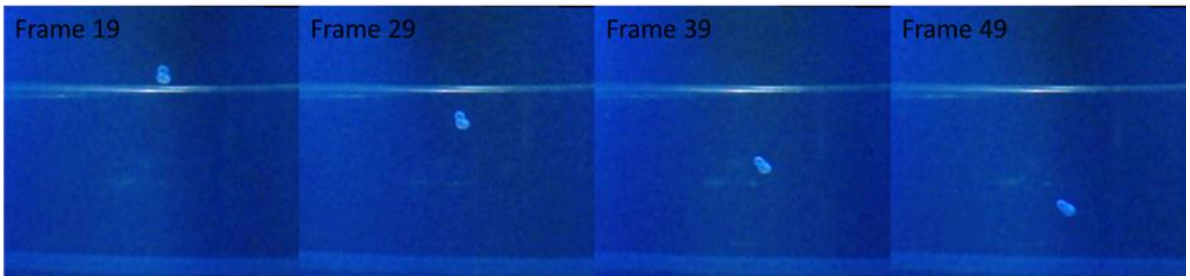

Figure 4-13: A foraminifera model re-orientating during sinking recorded at ~30FPS

Table 4-3: Final estimated sinking velocities of each species. Those with "(HR)" were scanned at high resolution.

Genus	Species	Sinking velocity ($m \cdot s^{-1}$)
Catapsydrax	*dissimilis*	0.062
Dentoglobigerina	*altispira*	0.061
Dentogloboquadrina	*rohri*	0.057
Fohsella	*lobata*	0.042
	peripheroronda	0.036
	robusta	0.035
Globigerina	*bulloides*	0.033
	praebulloides	0.028
Globigerinella	*adamsi*	0.03
Globigerinoides	*conglobatus (HR)*	0.018
	fistulosus	0.026
Globoconella	*inflata*	0.039
	puncticulata	0.04
	sphericomiozea	0.043
Globorotalia	*flexuosa*	0.06
Globorotaloides	*hexagonus*	0.027
Globoturborotalita	*apertura*	0.028
	nepenthes	0.042
Hirsutella	*margaritae*	0.029
Menardella	*praemenardii*	0.039
Neogloboquadrina	*acostaensis*	0.036
	dutertrei	0.04
	humerosa	0.05
Orbulina	*universa (HR)*	0.01
Paragloborotalia	*mayeri*	0.031
	siakensis	0.034
Praeorbulina	*curva*	0.048
Pulleniatina	*obliquiloculata*	0.041
Sphaeroidinella	*dehiscens*	0.051
	dehiscens (HR)	0.025
Sphaeroidinellopsis	*kochi*	0.087
Truncorotalia	*crassaformis*	0.033
	truncatulinoides	0.063

4.5.2 Comparison with published data

When the sinking velocities determined using dynamic scaling, and the mean sinking velocities measured from sinking actual planktonic foraminifera (Figure 4-14) are compared, an ANOVA shows that there are significant differences in the variances in sinking velocity between sources ($F_{3,674}$=307.5, p<0.001). Tukey HSD showed that there were significant differences between all datasets, apart from this study and Caromel *et al.* (2014) (Table 4-4Table 4-4).

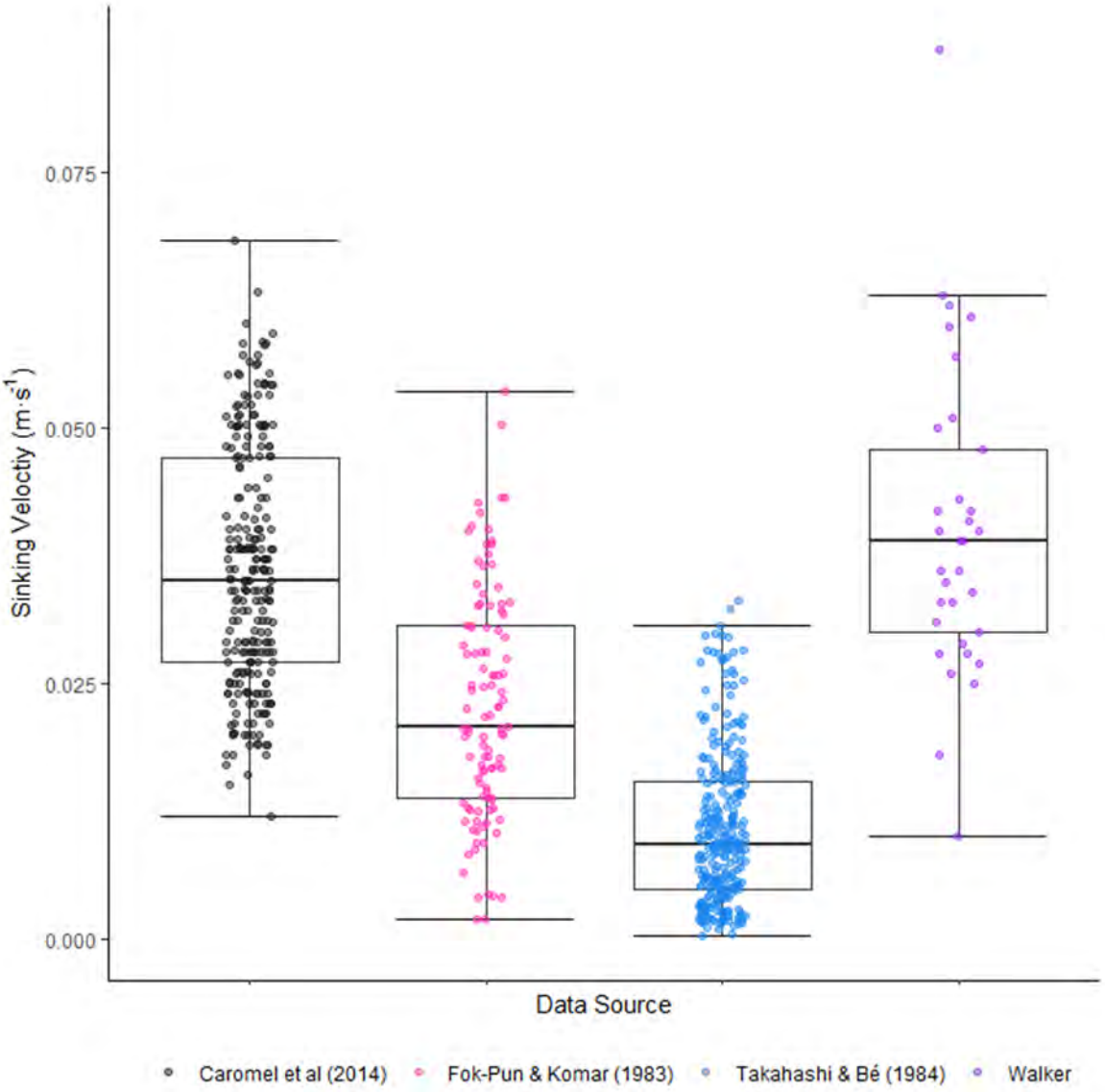

Figure 4-14: Comparison of Sinking velocities between the published data and the data from this study (Walker). There are significant differences between all data sources, apart from this study and Caromel et al. (2014), see Table 4-4.

Table 4-4: Tukey HSD results on the ANOVA of sinking velocities from different studies.

Comparison	Difference in means	Lower CI	Upper CI	Adjusted p value
Walker – Caromel *et al.* (2014)	0.003756	-0.00114	0.00865	0.198
Walker – Fok-Pun & Komar (1984)	0.017334	0.012085	0.022582	<0.001
Walker – Takahashi & Bé (1983)	0.029375	0.024519	0.034231	<0.001

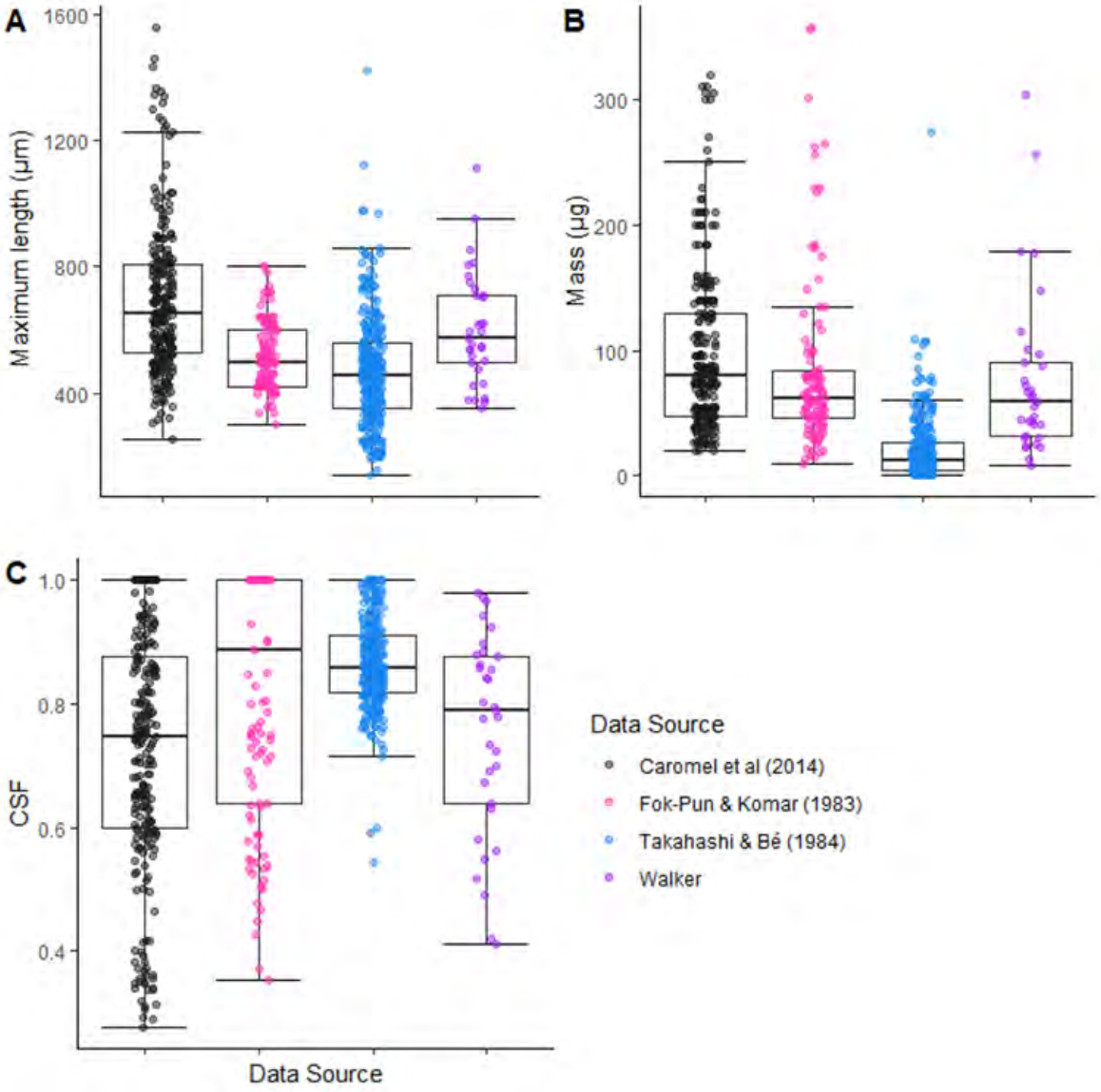

Figure 4-15: Comparison of my data and published data for A) maximum test length, B) test mass and C) CSF value. For each variable there are significant differences between some sources (see text and Table 4-5 for details).

Comparison of variance between the datasets from each study shows that length, mass, and CSF are all significantly different (length: $F_{3,674}$=63.12, p<0.001; mass: $F_{3,674}$=99.88, p<0.001; and CSF: $F_{3,674}$=38.51, *p*<0.001, Figure 4-15). Tukey HSD results are reported in Table 4-5, there are significant differences in all variables between this study and Takahashi and Bé (1984).

Table 4-5: Tukey HSD pairwise comparisons for Length, Mass and CSF. Significant differences are underlined.

Comparison	Difference in means	Lower CI	Upper CI	Adjusted p value
Length				
Walker – Caromel *et al.* (2014)	-87.77	-179.31	3.76	0.07
Walker – Fok-Pun & Komar (1984)	86.43	-11.74	184.6	0.11
Walker – Takahashi & Bé (1983)	135.48	44.66	226.31	<u><0.001</u>
Mass				
Walker – Caromel *et al.* (2014)	-19.42	-44.67	5.83	0.2
Walker – Fok-Pun & Komar (1984)	-6.27	-33.35	20.81	0.93
Walker – Takahashi & Bé (1983)	56.22	31.17	81.27	<u><0.001</u>
CSF				
Walker – Caromel *et al.* (2014)	0.03	-0.05	0.1	0.75
Walker – Fok-Pun & Komar (1984)	-0.07	-0.15	0.01	0.14
Walker – Takahashi & Bé (1983)	-0.11	-0.19	-0.04	<u><0.001</u>

4.5.3 Linear Models – Sinking Velocity and Other Variables

When each of the parameters was investigated individually with sinking velocity there was a significant positive relationship with maximum length ($F_{1,31}$=16.18, p<0.001, adjusted R^2=0.32), V_{wall} ($F_{1,31}$=174.7, p<0.001, adjusted R^2=0.84), and test mass ($F_{1,31}$=174.7, p<0.001, adjusted R^2=0.84), while the relationship with test density was weaker ($F_{1,31}$=8.12, p<0.001, adjusted R^2=0.182). When using U_{mass} the relationship between sinking velocity and length is significant but negative ($F_{1,31}$=139, p<0.001, adjusted R^2=0.81). As the relationship is negative increases in length result in a decrease in U_{mass}. When comparing V_{wall} and mass-adjusted sinking velocity there is again a stronger relationship than for V_{wall} and sinking velocity ($F_{1,31}$=231.2, p<0.001, adjusted R^2=0.88). There was no relationship between test density and mass adjusted sinking velocity ($F_{1,31}$=0.15, p=0.6931, adjusted R^2=-0.027, Figure 4-16).

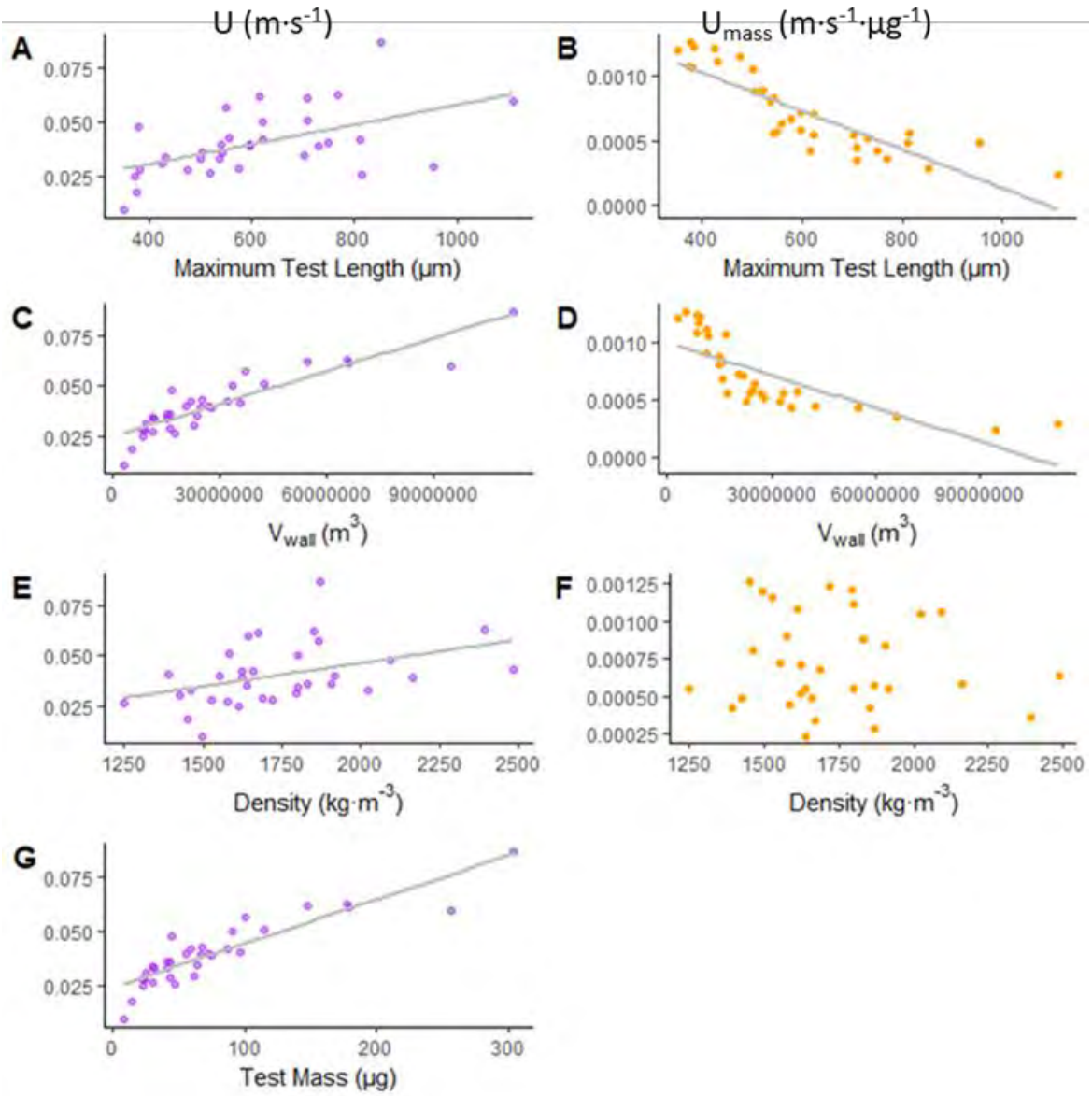

Figure 4-16: Left: Sinking Velocity (in purple) with the key parameters from Chapter 3 (maximum length, a measure of volume (test wall volume, V_{wall}) density and mass) in determining sinking velocities. On the right the same parameters (not including mass) plotted with sinking velocity per unit of mass (U_{mass}, in orange).

The relationship between L_s and sinking velocity is significant ($F_{1,31}$=16.83, p<0.001, adjusted R^2=0.33). When accounting for mass in sinking velocity, the trend between U_{mass} and L_s is also significant ($F_{1,31}$=22.01, p<0.001, adjusted R^2=0.40, Figure 4-17). A_P and sinking velocity positively correlate and the relationship is significant ($F_{1,31}$=16.33, p<0.001, adjusted R^2=0.32), as above (Figure 4-16) when accounting for the mass of the test, the relationship is stronger but negative (i.e. as area increases sinking velocity per unit mass decreases, $F_{1,31}$=102.6, p<0.001, adjusted R^2=0.76).

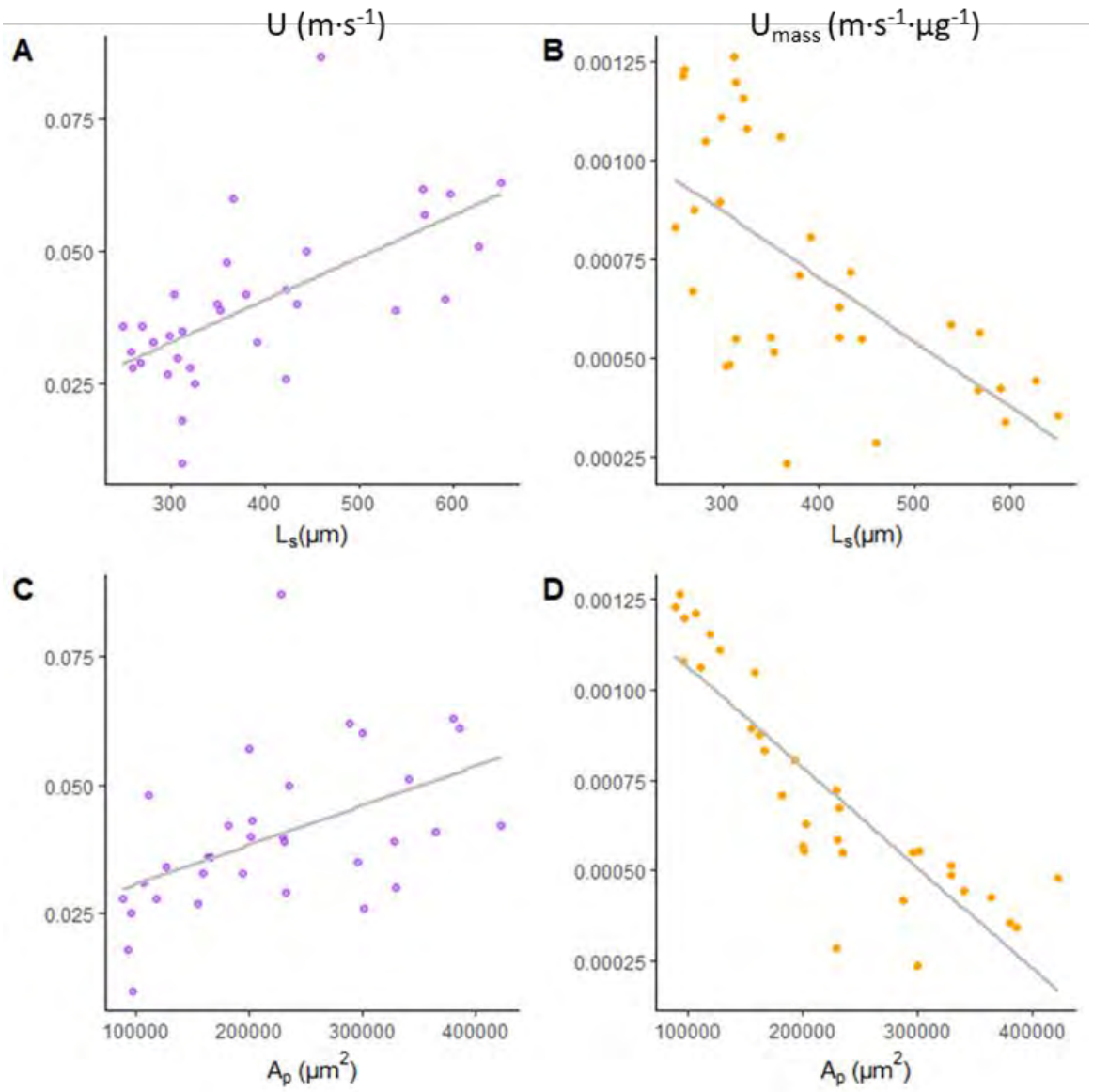

Figure 4-17: Both sinking velocity (U), and sinking velocity per unit of mass (U_{mass}), with length in the direction of sinking (L_S) and projected area (A_P). In A and B the relationship of L_S is shown, the relationship when accounting for mass (U_{mass}) is stronger than sinking velocity alone. The relationship between the A_P and sinking velocity in the C suggests that as the area presented to the fluid increases so does sinking velocity. Intuitively this does not make sense, when a parachutist opens their parachute their velocity does not increase. When mass is accounted for (D), sinking velocities decrease as area presented to the fluid increases as expected, showing the influence of mass.

Comparison of the Re and C_D values determined for the 32 species of planktonic foraminifera shows they deviate from the values expected for Stokes' Law (where Re>1) and Morrison's Equation (valid over all ranges of Re but only for spheres, see Figure 4-18). R^2 values were calculated using Equation 9-24, using C_D values generated from Stokes Law and Morrison's equation. The data fit slightly better to Morrison's equation (R^2 = 0.627) than Stokes Law (R^2 = 0.543).

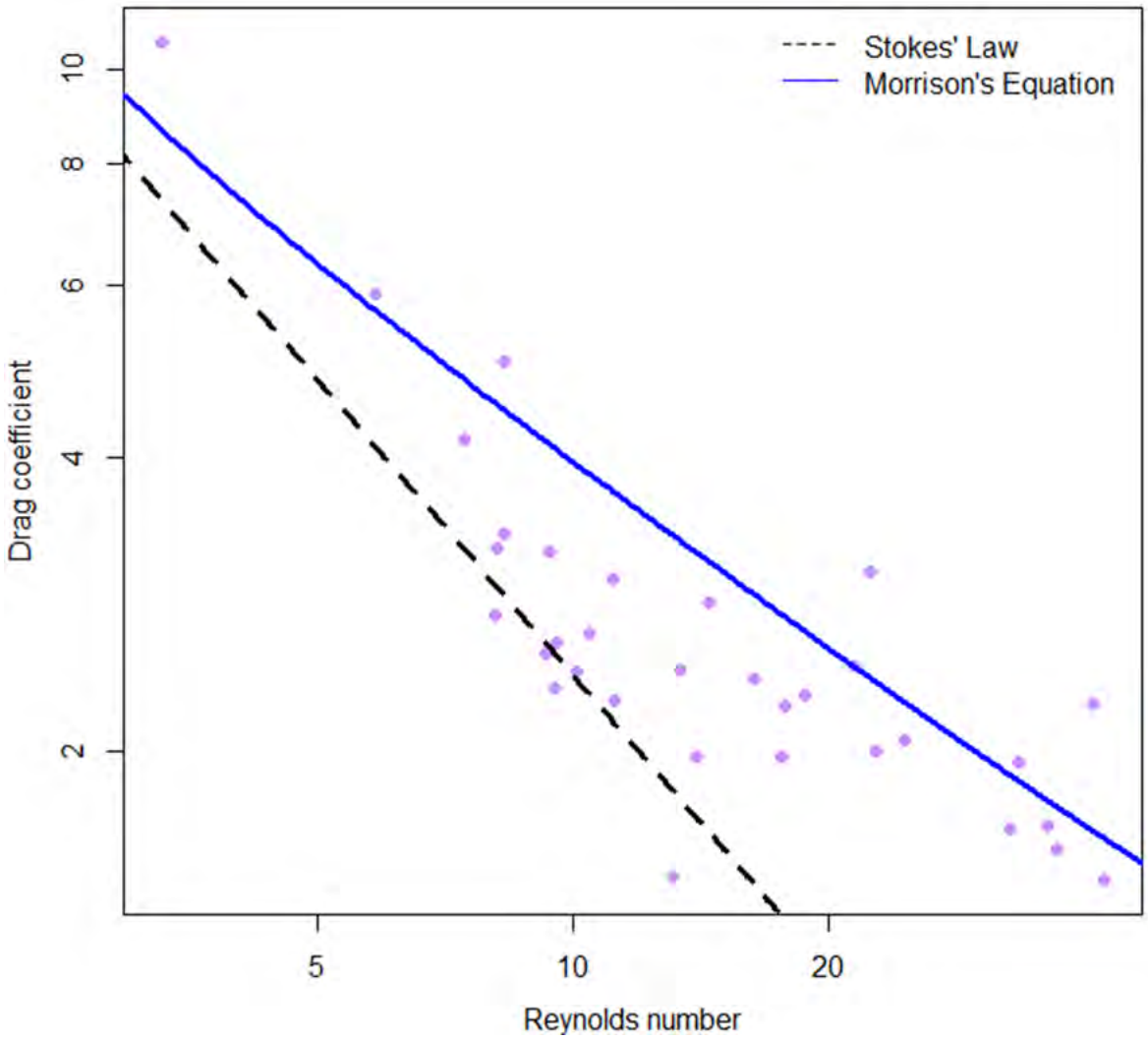

Figure 4-18: Reynolds number and drag coefficient for the 33 individuals. Reynolds number is calculated using Equation 3-2, where the length used is L_s measured vertically in the sinking orientation. The data are better described by Morrison's equation (R^2 = 0.627) than by Stokes Law (R^2 = 0.543).

4.5.4 Comparisons between morphogroups

When examining sinking velocities by Aze *et al*'s (2011) morphogroups using an ANOVA, overall the different morphogroups did not differ significantly ($F_{8,24}$=1.099, p=0.398, Figure 4-19A). There are significant differences in U_{mass} between morphogroups ($F_{8,24}$=2.406, p=0.046, Figure 4-19B), but no significant differences when making pairwise comparisons using Tukey HSD (see Appendix 9.2.2).

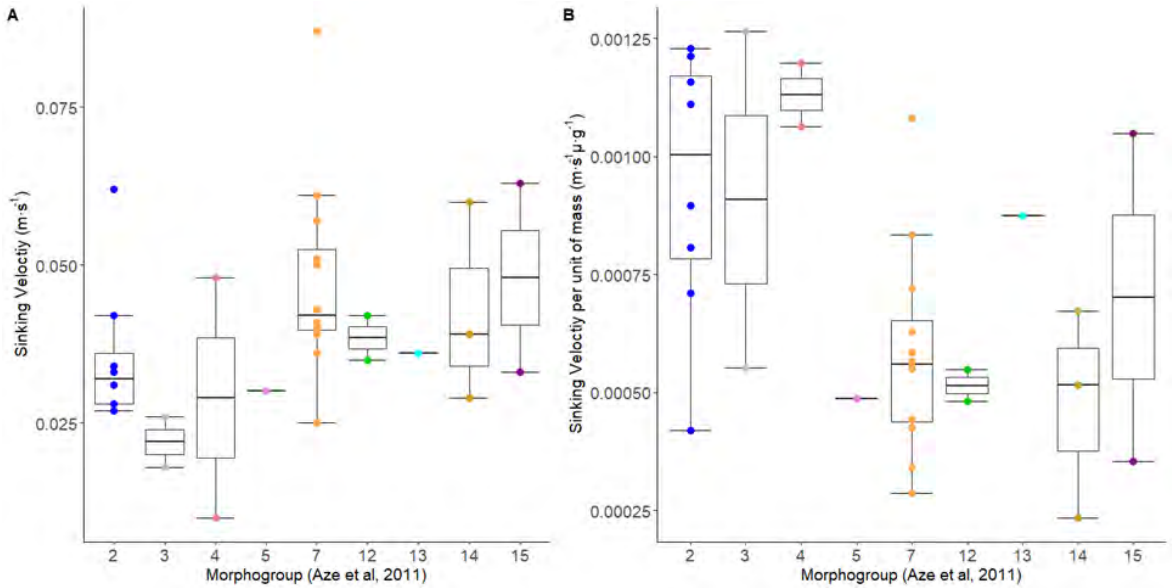

Figure 4-19: Sinking velocity (A) and sinking velocity per unit of mass (U_{mass}) (B) across Aze et al.'s (2011) morphogroups, points are coloured by morphogroup for clarity. There are no significant differences.

Table 4-2: Aze et al. (2011) morphogroups, also see Figure 4-12 below.

Aze *et al.* morphogroup	Aze *et al.* definition
2	Spinose, globular
3	Spinose globular with supplementary apertures
4	Spinose spherical
5	Spinose, clavate
7	Non-spinose globular
12	Non-spinose, turborotaliform, keeled
13	Non-spinose, turborotaliform, non-keeled
14	Non-spinose, globorotaliform, keeled
15	Non-spinose, globorotaliform, angluconical

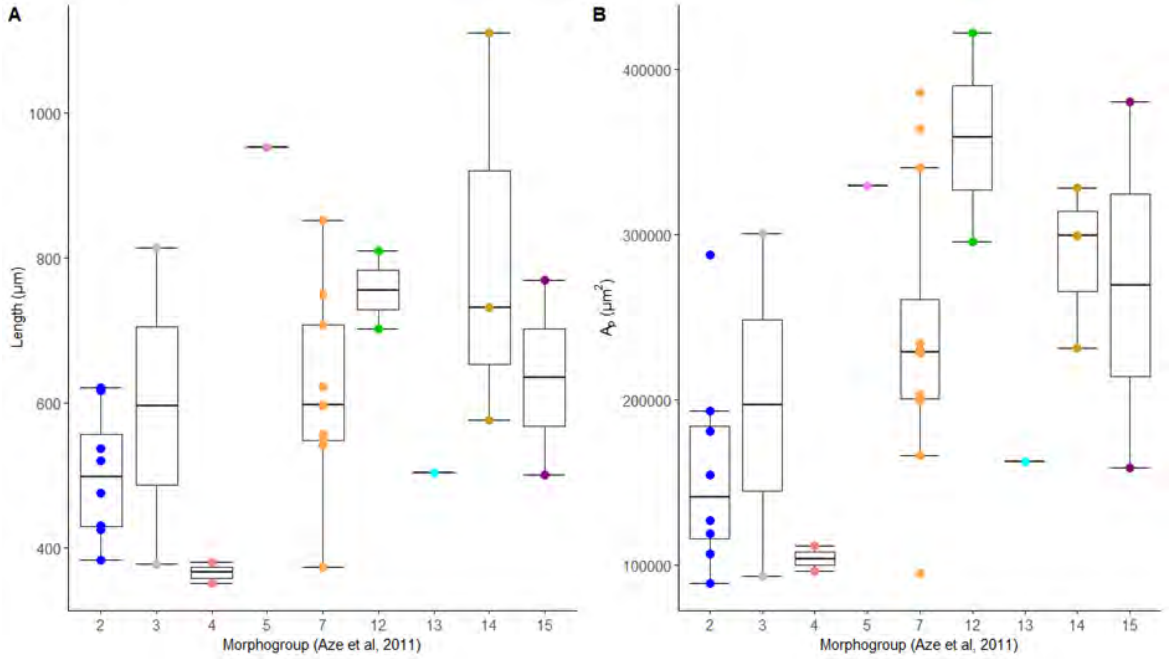

Figure 4-20: maximum test length (A) and A_P (B) across Aze et al.'s (2011) morphogroups, points are coloured by morphogroup for clarity.

An ANOVA shows there are significant differences in the variance for: length ($F_{8,24}$=2.937, p= 0.0194, Figure 4-20B) and A_P ($F_{8,24}$= 2.459, p=0.0421, Figure 4-20B), between morphogroups, but no significant differences were found in a Tukey HSD comparison (see 9.2.2 Comparisons between morphogroups). There are no significant differences between any of the other variables (volume, density, mass, and L_S, see 9.2.2 Comparisons between morphogroups).

4.5.5 Intermediate Reynolds number C_D (C_{DI})

Values for C_{DI} for each species are presented in Figure 4-21, showing that the values are similar (as expected), apart from *G. flexuosa* and *S. kochi* which were removed (as stated above) from further analyses which use C_{DI}. *G. flexuosa* and *S. kochi* are included in the graph below to illustrate the deviation from the rest of the data.

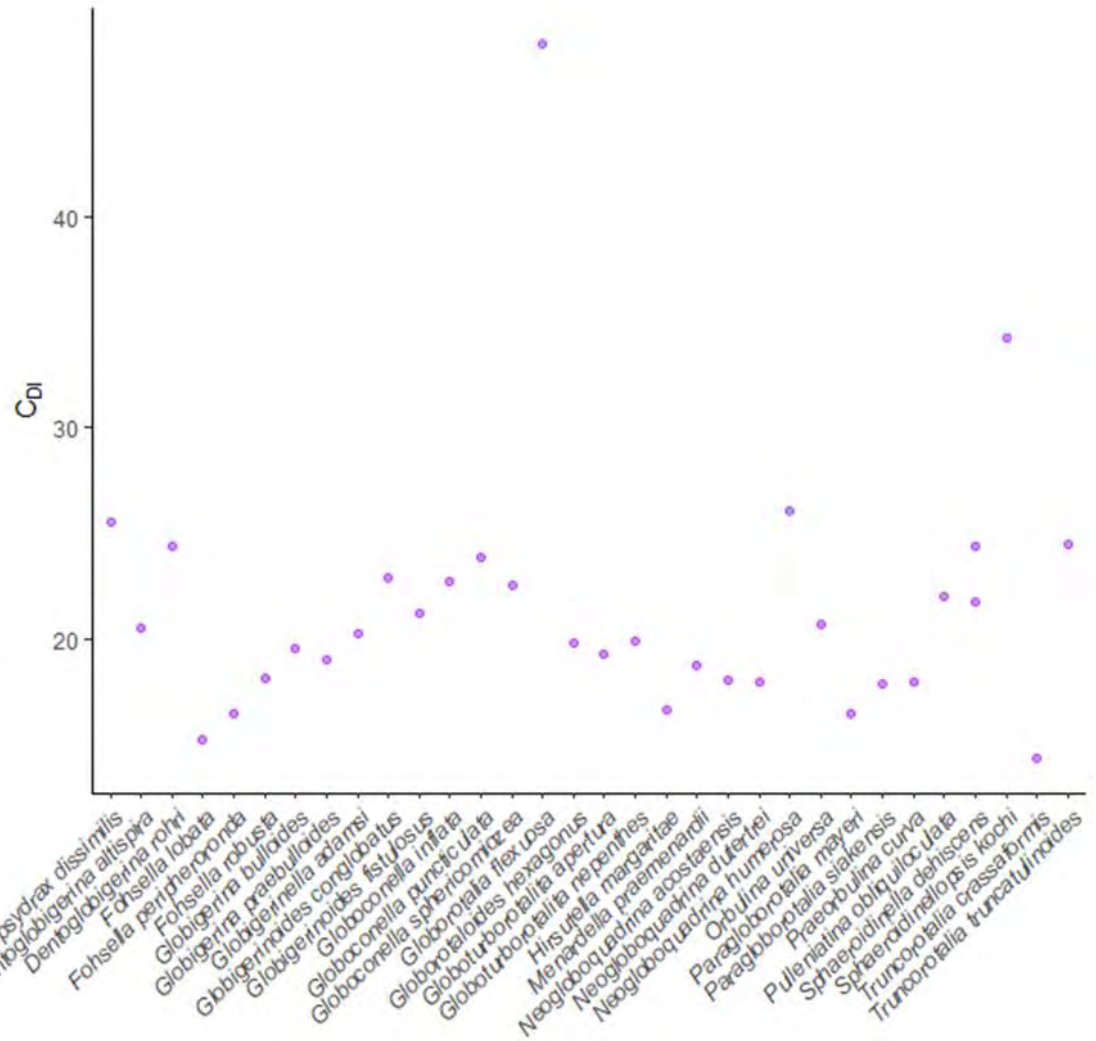

Figure 4-21: C_{DI} for each species. Note that Globorotalia flexuosa and Sphaeroidinellopsis kochi have higher than expected values, as discussed in 4.4.9.

When examining C_{DI} and CSF (shape) we see that more spherical species (i.e. those with higher CSF values) have higher C_{DI} values ($F_{1,29}$=11.63, p=0.0019, adjusted R^2= 0.262, Figure 4-22).

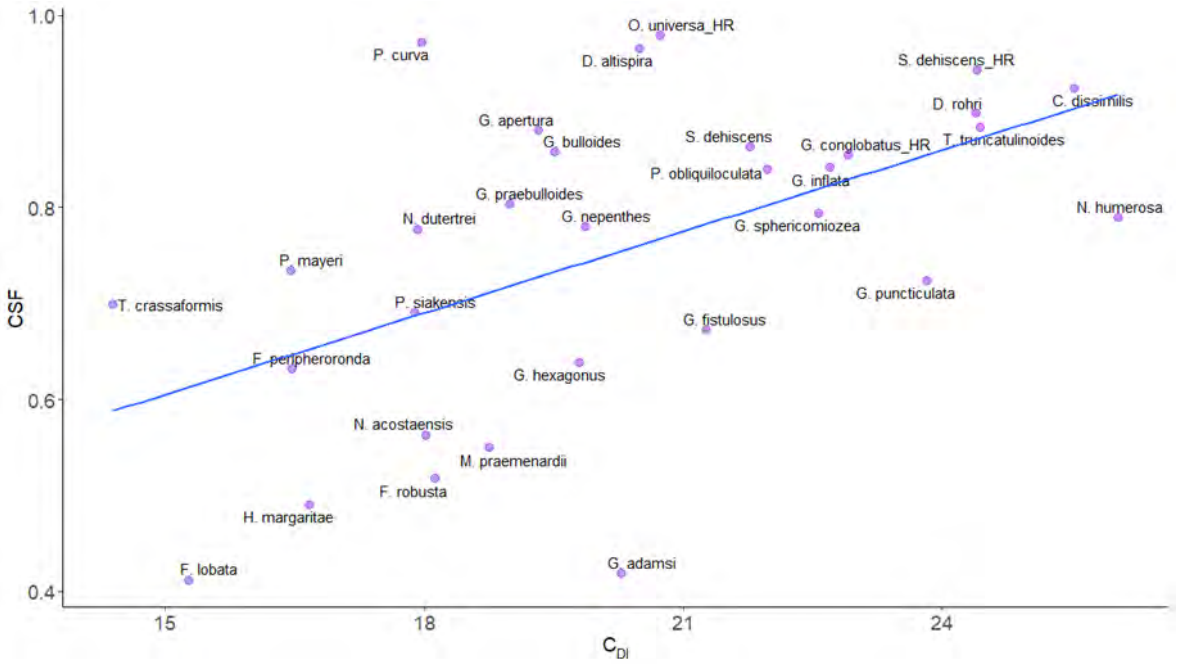

Figure 4-22: There is a positive trend between C_{DI} and CSF ($F_{1,29}$=11.63, p=0.0019, adjusted R^2= 0.262). Species with HR after then names denotes the high-resolution scans.

When examining the C_{DI} and the operating Re for each species there is a general trend that species experiencing higher C_{DI} have higher operating Re ($F_{1,29}$=11.47, p=0.0020, adjusted R^2= 0.259, Figure 4-23). As evidenced by a linear model with the formula:

$$C_{DI} \sim Re * CSF$$

there is also a trend that species with lower operating Re and C_{DI} tend to be less spherical than those with higher operating Re and C_{DI} ($F_{3,27}$ = 7.262, adjusted R^2 = 0.3851, p = 0.001, Table 4-6).

Using an interaction plot reveals the relationship between C_{DI}, Re and CSF (Figure 4-23). When CSF is low, the increase in Re results in a large increase in C_{DI}, when CSF is intermediate increases in Re are smaller. However, when CSF is high, there is a decrease in C_{DI} as Re increases. Therefore, more spherical species will have lower drag as Re increases. As mentioned previously, the factors in Re which are linked to the particle (and not the fluid) are the size of the particle (i.e. the foraminifera) and the speed at which it is sinking. It is possible to infer from these results that larger, faster sinking foraminifera (i.e. those at higher Re) experience less drag (C_{DI}) when they are spherical than when they are less spherical.

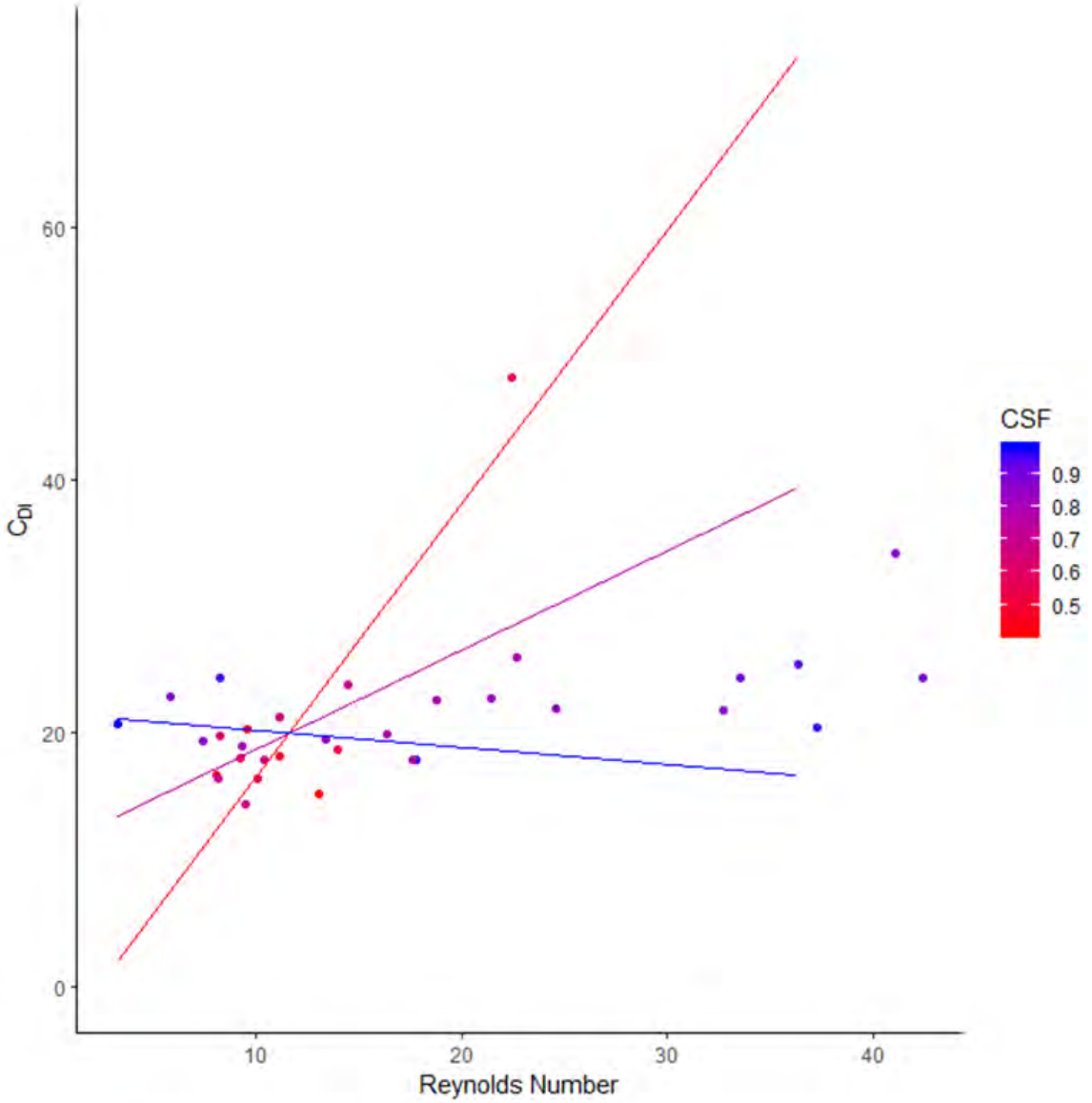

Figure 4-23: C_{DI} and Re for all species, coloured by CSF with more blue colours being more spherical species and more red colours being less spherical (lower CSF). Three lines are plotted, in red the relationship between C_{DI} and Re with CSF is low, in purple mean CSF values, and in blue the highest CSF value.

*Table 4-6: Model results for C_{DI} ~ Re * CSF. Significant p values underlined*

	Estimate	**Standard Error**	**T – value**	**P value**
(Intercept)	3.6364	6.52	0.558	0.5816
Re	0.9709	0.5619	1.728	0.0954
CSF	17.6502	7.4941	2.355	<u>0.026</u>
Re : CSF	-0.9624	0.6261	-1.537	0.1359

4.5.6 Linear Models – With interactions

A model was specified where CSF was included as a measure of shape (model 1 in Table 4-7).

Table 4-7: LM with interaction terms, with morphogroup as defined by Aze et al. (2011).

Model	Formula	AIC (full model)
1	Sinking velocity $\sim L{*}V_{wall}{*}A_P$ *CSF	-227.7809

Upon reduction the model had the following interaction terms removed: $L{:}\ A_P{:}\ CSF$ and $L{:}\ V_{wall}{:}\ A_P{:}\ CSF$, and results in the lower AIC value of -230.9107. The reduced model took the form of:

$$log10(U) \sim log10(L) + log10(V_{wall}) + log10(A_P) + CSF +){:}\ log10(V_{wall}) + log10(L){:}\ log10(A_P) + log10(V_{wall}){:}\ log10(A_P) + log10(L){:}\ CSF + log10(V_{wall}){:}\ CSF + log10(A_P){:}\ CSF + log10(L){:}\ log10(V_{wall}){:}\ log10(A_P) + log10(L){:}\ log10(V_{wall}){:}\ CSF + log10(V_{wall}){:}\ log10(A_P){:}\ CSF$$

The reduced model is significant ($F_{13,19}$= 110.2, p<0.001, adjusted R^2= 0.9779), full results are presented in Table 4-8. To understand the effect of the interactions in the model, interaction plots are presented below, for significant interactions (Figure 4-24, Figure 4-25 and Figure 4-26).

Table 4-8: Reduced model results, significant p values underlined.

	Sum of Squares	Degrees of freedom	F value	p value
(Intercept)	0.002	1	2.98	0.101
log10(L)	0.004	1	6.58	<u>0.019</u>
log10(V_{wall})	0.002	1	3.012	0.099
log10(A_P)	0.001	1	1.601	0.221
CSF	0.003	1	4.87	<u>0.04</u>
log10(L):log10(V_{wall})	0.005	1	6.735	<u>0.018</u>
log10(L):log10(A_P)	0.004	1	5.693	<u>0.028</u>
log10(v):log10(A_P)	0.001	1	1.659	0.213
log10(L):CSF	0.002	1	2.739	0.114
log10(v):CSF	0.003	1	4.977	<u>0.038</u>
log10(A_P):CSF	0.004	1	5.736	<u>0.027</u>
log10(L):log10(V_{wall}):log10(A_P)	0.004	1	5.828	<u>0.026</u>
log10(L):log10(V_{wall}):CSF	0.002	1	2.835	0.109
log10(v):log10(A_P):CSF	0.004	1	6.135	<u>0.023</u>
Residuals	0.013	19		

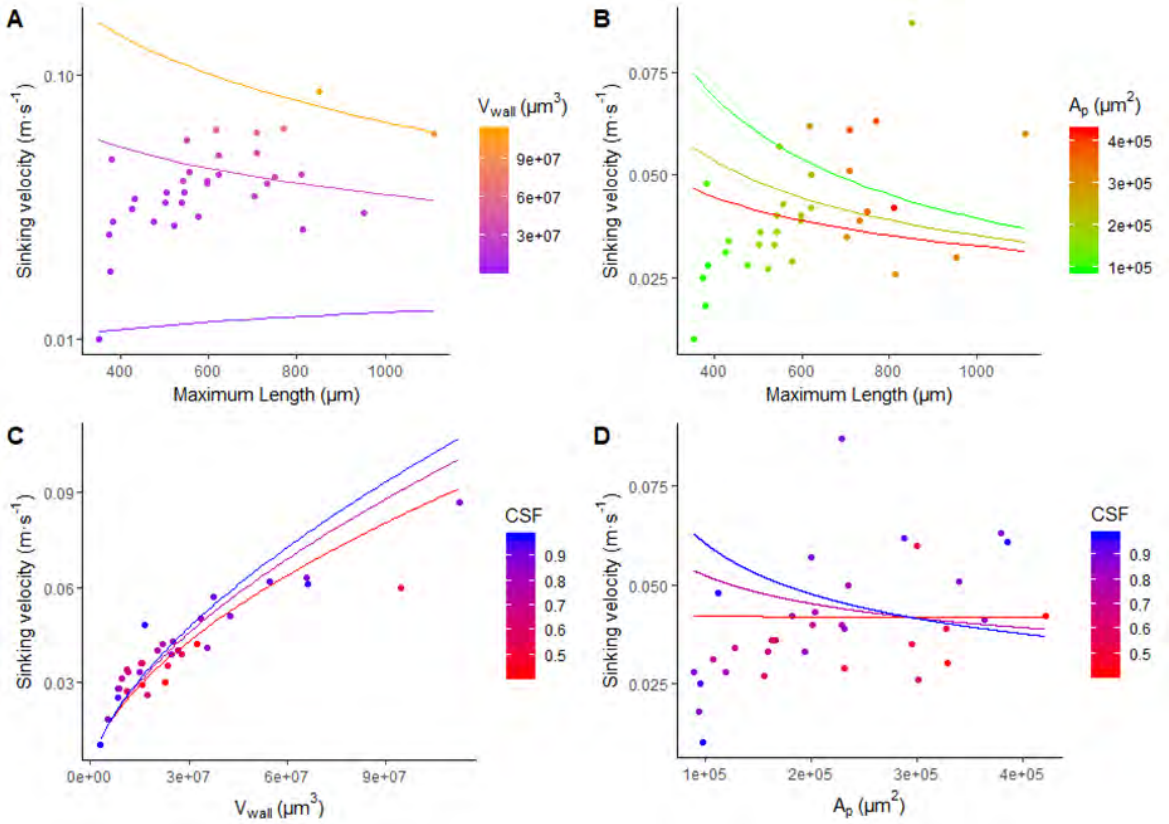

Figure 4-24. The two-way interactions in model 1. Each graph shows the effect of a pair of interactions on sinking velocity, the first term is on the x-axis with the second term (with which the first interacts) shown as the colouration. The lines present on the graph are the trends when the second term is at its maximum, mean and minimum values. A) shows the effect of the interaction between length and volume on sinking velocity, with lines plotted for the maximum, mean and minimum volumes present within the data. B) is the interaction between length and area. C) is the interaction between volume and CSF. D) is the interaction between area and CSF. The curvature of the lines is due to the use of logged values in the model.

In Figure 4-24A, the relationship between sinking velocity and the interaction of volume and length can be seen. When volume is high, as size increases sinking velocities decrease. When volume is intermediate increases in length result in much less steep reduction of sinking velocity, compared to high volume. For low V_{wall} values, increases in length have very little effect on sinking velocity.

Figure 4-24B shows the relationship of sinking velocity with the interactions between length and A_P. When A_P is high, increases in length result in a decrease in sinking velocity. As area reduces the negative relationship with sinking velocity and length becomes steeper.

The relationship between the interaction of V_{wall} and CSF and sinking velocity (Figure 4-24C) is positive. When CSF is high, the relationship between V_{wall} and sinking velocity is steepest, as CSF decreases the steepness of the relationship decreases.

When looking at the relationship between sinking velocity and the interaction between CSF and A_P (Figure 4-24D) more spherical species (high CSF) experience relatively steep decreases in sinking velocity, species with a CSF of ~0.7 experience less steep decreases in sinking velocity as A_P increases. Species with lower CSF (~0.5) experience very little change in sinking velocity regardless in A_P.

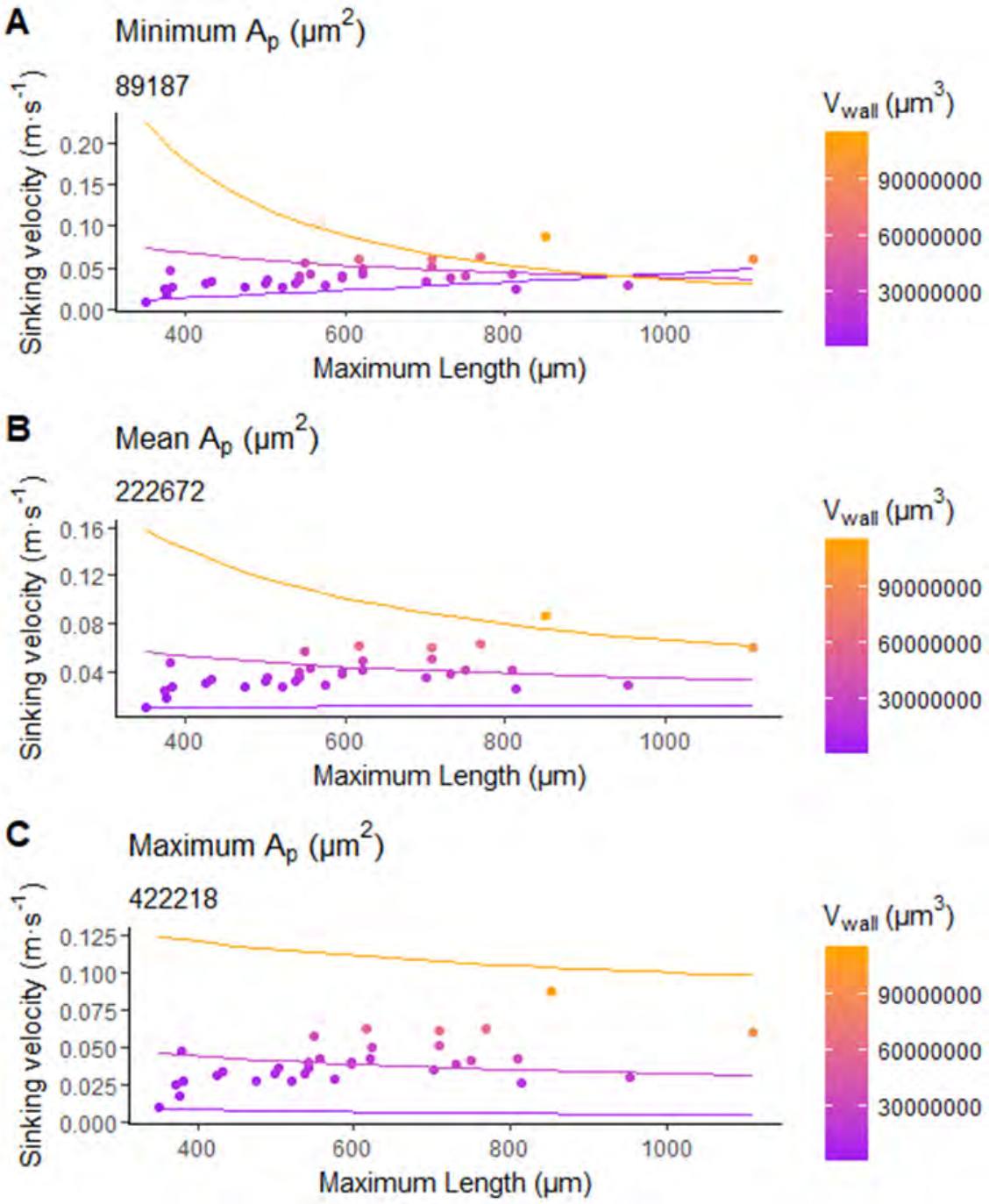

Figure 4-25: The three-way interaction plot of : A_P : V_{wall} from model 1. A) the interaction between L and V_{wall} when A_P the A_P is specified as the minimum value present in the dataset, B) the same interaction (L : A_P) when A_P is set as the mean A_P value, and C) when the A_P is specified as the maximum A_P present in the dataset. Values for the A_P used are presented below the title for each graph.

When length increases at small V_{wall}, and small A_P, this results in slow increases in sinking velocity. At intermediate V_{wall} with small A_P, there are moderate decreases in sinking velocity, as length increases. At high V_{wall}, with small A_P, increases in length result in a larger decrease in sinking velocity (Figure 4-25A).

For low V_{wall}, intermediate A_P foraminifera, increases in length results in very little increases in sinking velocity. For intermediate V_{wall}, with intermediate A_P, increases in length result in small decreases in velocity. For high V_{wall} foraminifera with intermediate A_P, increases in length results in a large decrease in sinking velocity (Figure 4-25B).

For foraminifera with a small V_{wall} but large A_P, increases in length results in a small decrease in sinking velocity. Foraminifera with a large A_P and an intermediate V_{wall} experience larger decreases in sinking velocity, but foraminifera with a large V_{wall} and large A_P experience the greatest decrease in sinking velocity (Figure 4-25C).

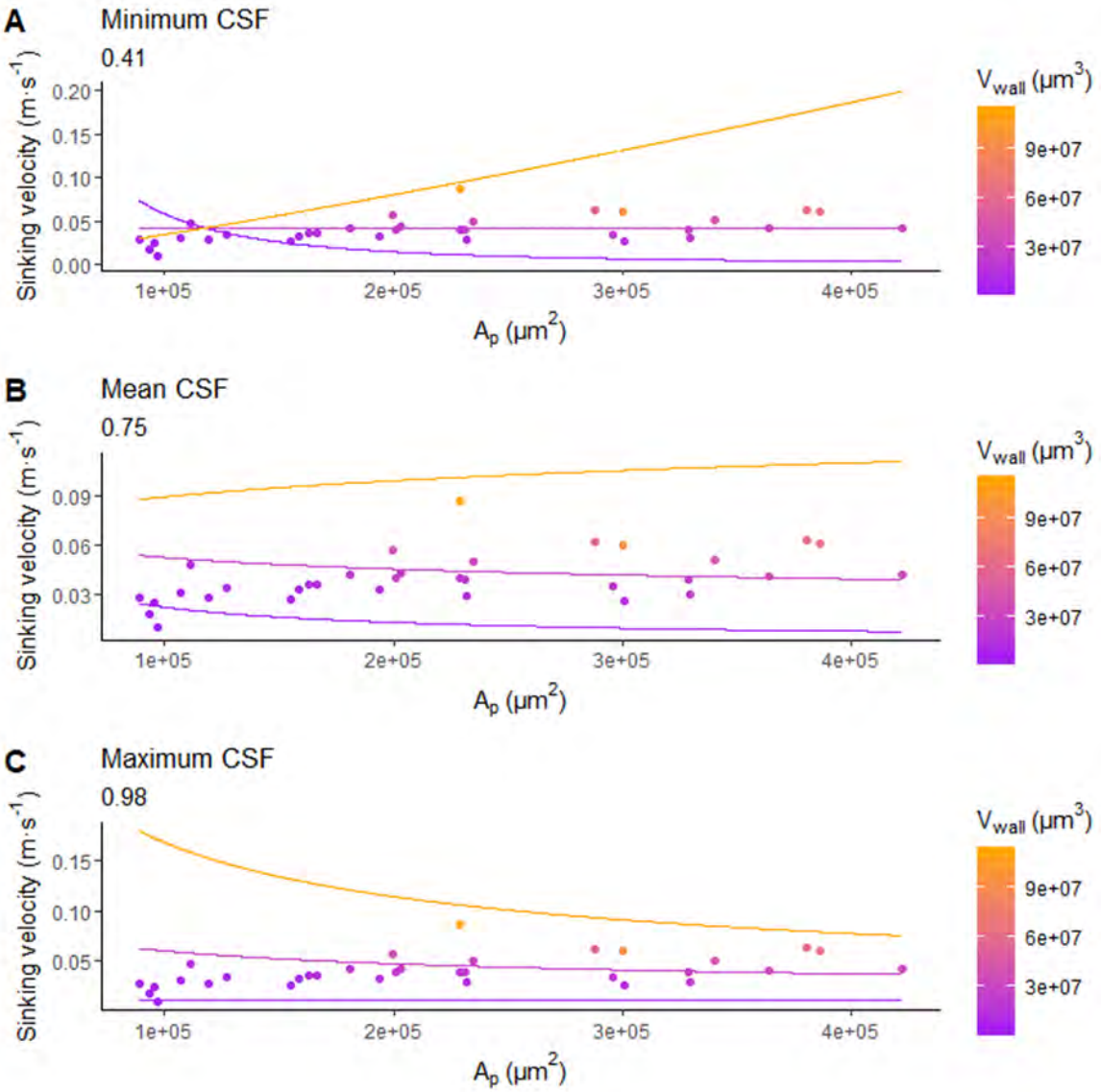

Figure 4-26: Graphs of the three-way interaction between A_P: V_{wall} : CSF. Each graph shows the interaction between A_P and V_{wall} when CSF is at: A) the minimum value; B) the mean value; and C) maximum value.

In Figure 4-26 the relationship between sinking velocity and the three-way interaction of CSF, A_P and V_{wall} is explored. When CSF is at a minimum (for the species observed in this study, Figure 4-26A) changes in A_P when V_{wall} is high, have a relatively steep positive slope with sinking velocity. As V_{wall}

decreases to intermediate values, the slope is horizontal. For low V_{wall} values sinking velocity decreases as $\mathrm{A_P}$ increases. In Figure 4-26B, there are increases in sinking velocity when V_{wall} is high, and decreases in sinking velocity when V_{wall} is intermediate and low. When CSF is specified as the maximum observed value (Figure 4-26C), sinking velocity decreases with increases in area regardless of the V_{wall} value. The slope of the line becomes less steep as V_{wall} becomes smaller, with the lowest observed V_{wall} values having constant sinking velocities regardless of increases in A_P.

4.6 Discussion

In summary, this study found there are positive correlations between sinking velocity and: length, volume, mass, density, projected area, and length parallel to the flow. There were significant relationships between sinking velocity and CSF, when used in conjunction with other variables (length, A_P, V_{wall}). Despite the relationships in Chapter 3 using density and not V_{wall}, the results between Chapter 3 and this chapter are comparable. In some respects, the use of V_{wall} is a more direct measure of the size of the foraminifera. However, the density as calculated in Chapter 3 includes the (approximate) volume of the wall and also the (approximate) volume of the water filled chambers, something which V_{wall} cannot account for.

Despite the general trends being similar, the data obtained in this study are significantly different to some of the previously published work, specifically all variables compared differ from Takahashi and Bé (1984, Figure 4-14 and Figure 4-15, and Table 4-4 and Table 4-5). Sinking velocities measured here are similar to Caromel *et al.* (2014). As explored in the discussion of Chapter 3, some of these differences could be due to the inherent differences in the sinking velocities of the species used, and the sample type (See section 3.4). The differences observed in length, mass and CSF could be due to the species used, too. Unlike the other studies, here only one value per species was obtained (with the exception of *Sphaeroidinella dehiscens*, discussed below). This would limit the variance of the values for all variables and might explain some of the differences seen. One similarity between Caromel *et al.* (2014) and this study is the use of camera to accurately quantify the sinking velocities. The use of cameras means that the time taken between two-points can be measured after the recording, thus the foraminifera can be tracked during its entire descent ensuring the sinking velocity obtained is as accurate (and repeatable) as possible. As highlighted in Chapter 3, there are associated problems of human error from reaction speeds for the activation of a stop watch and ensuring there is no parallax distortion, if cameras are not being used to record the sinking velocities.

It is of interest that the sinking velocities obtained by Fok-Pun and Komar (1983) and this study differ (Table 4-4), when the rest of the variables (length, mass and CSF) investigated here do not (Table 4-5). As the variables (which do not differ) determine sinking velocities (which do differ). Fok-Pun and Komar

(1983) report values that are, on average, lower than the sinking velocities obtained here (Table 4-4 and Figure 4-14). This could be due to differences in sample origins, which could influence the amount of calcium carbonate in the test wall (i.e. test density, which if lower reduces sinking velocity) and morphology of the test thereby effecting sinking velocities.

In section 3.3.1.4, Table 3-8 there are differences in the variance of sinking velocities between morphogroups. However, no such differences were found using the experimental data in this chapter. This could be due to the differences in sample sizes, as in this study there are only a limited number of species per morphogroup (the lowest being 1 species in morphogroups 5 and 13, and the most being 12 in morphogroup 7).

Using mass to normalise parameters has been used in a number of studies (e.g.: Gillooly *et al*., 2001 and Schmidt, 2018). Investigating the important parameters in determining sinking velocity identified in Chapter 3, and in this Chapter (length, V_{wall} and density), sinking velocity per unit of mass (U_{mass}) helped to illuminate some interesting trends. When U_{mass} is compared to these parameters, there are significant, negative relationships with length, V_{wall}, projected area and length parallel to the flow.

There is no significant relationship between U_{mass} and density. Accounting for mass in sinking velocity, shows that length and V_{wall} are important factors (i.e. have strong significant relationships) in determining sinking velocities even when mass is accounted for. These results also follow from the understanding of hydrodynamics laid out in this chapter and Chapter 3. When examining the equation for C_D (Equation 3-6 below), V_{wall} is present as a term and length is implicit in both V_{wall} and area. As the drag experienced (therefore C_D) by an object is a determining factor of sinking velocity, it follows that the parameters which have been shown to determine C_D (i.e. that are terms in Equation 3-6) would have a significant relationship with sinking velocity.

Equation 3-6

$$C_D = \frac{2 \cdot V_{wall} \cdot (\rho_{fluid} - \rho_{particle}) \cdot g}{\rho_{fluid} \cdot U_{particle}^2 \cdot A_{particle}}$$

As stated above, U_{mass} decreases as size (length, A_P and V_{wall}) increases. This is in agreement with Equation 3-6, as V_{wall} and projected area in contact with the fluid increases the drag will increase too, thereby causing the foraminifera to sink more slowly. These findings are in agreement with Caromel *et al.* (2014) and lends support to the hypothesis that (living) foraminifera in warmer conditions (i.e. during periods of global warming, and the tropical oceans) have increased surface area. This trend has been seen over geological time, as species size increases with sea surface temperature (Schmidt *et al*., 2004, see Figure 1-2). By having a larger projected area, the foraminifera will sink more slowly as the

drag experienced increases (much as a parachute increases a sky-divers drag). Of course, the inference drawn from the data obtained here must be taken with some scepticism as only the dead foraminifera test was modelled, and the living organisms may have other measure which they use to compensate for changes in sea surface temperature. If (living) foraminifera want to maintain their position (which might be assumed especially for those with photosynthetic symbionts, but for which there is no evidence) in the water column they have to do so by achieving neutral buoyancy, by the use cell contents (e.g. fats, lipids, gases) which are less dense than the water they live in (to counter the density of the test). In warmer oceans the viscosity of the water is lower, meaning that foraminifera of the same size and shape would sink faster than in cooler waters. Changing their test size to present a greater area, may help foraminifera maintain location in the water column (Caromel *et al.*, 2014). However, there may be additional factors at play, warmer seas are generally less productive than colder oceans (Denny, 1993). Tappan and Loeblich (Tappan and Loeblich, 1973) suggest that foraminifera in warmer oceans might have larger test area to support the pseudopodia over a larger area, thereby increasing the possibility of capturing relatively sparse prey items, which may be the case in less productive oceans. Therefore, the increase in test area could be an effect obtaining prey items, rather than a response to water temperature. There have also been links made with test size and the presence and activity of symbionts (Bé, Spero and Anderson, 1982); with species that have symbionts (and if those symbionts are active) being larger.

Much like the data in Chapter 3, when examining Re and C_D with respect to Stokes' Law (Equation 3-6) and Morrison's Equation (Equation 3-8) the deviations from these empirical calculations suggest there is an effect of size (as per the findings that length is important even when accounting for mass) and shape (Figure 4-17, See section 4.5.3 for more details). Both Re and C_D are calculated differently to the methods used by previous works on sinking foraminifera. Here efforts have been made to use measurements which are hydrodynamically relevant and clearly defined, to help provide a clearer understanding of the Re regimes which foraminifera experience.

The effect of shape on sinking speed is hinted at with comparison of sinking velocities per unit of mass between morphogroups, where the spherical species (morphogroup 4; *Orbulina universa*) has a significantly different U_{mass} from non-spinose globular species (morphogroup 7). However, for both sinking velocity and U_{mass}, there is no significant relationship between CSF and sinking velocity. This may be due to the use of linear measurements used in these particular quantifications of shape, the problems with which are outlined in section 3.4. Additionally, there is some overlap in the shapes between morphogroups. For example, morphogroup 12 and 14 (non-spinose, turborotaliform, keeled and non-spinose, globorotaliform, keeled, respectively) are similar in morphology. Equally, the groupings with and without spinse (i.e. spinose and non-spinose), whilst biologically relevant, are of

less use here due to the lack of spines on the physical models. The differences in morphogroups are relevant for their original purpose (i.e. for the construction of the phylogeny), however here their applicability is questionable. As previously stated, the method of shape quantification needs improvement and is the focus of Chapter 5.

Further evidence of the effect of shape can be seen in Figure 4-22 which suggests that more spherical species experience more drag than less spherical species. This is contrary to expectations, as spherical objects generally experience less drag and thus sink faster (Vogel, 1994). This effect was investigated further (Figure 4-23), and it was found that larger, more spherical, faster sinking foraminifera (e.g. morphogroup 4, spinose, spherical, *O. universa*) experience higher drag compared to less spherical species (e.g. morphogroups 14, non-spinose, globorotaliform, keeled and 15, non-spinose, globorotaliform, angluconical). This is in agreement with previous investigations into shape effects in sinking particles (McNown & Malaika, 1950), which found that double-cone shapes (similar to morphogroup 14, non-spinose, globorotaliform, keeled) experience more drag than comparable ellipsoids.

There could be an additional effect of using a 3D sinking velocity. The relative sinking velocity of a particle taking a longer, spiral path must be faster than a particle travelling the same vertical distance in completely vertically manner, to cover the distance in the same time. Flatter species are known to exhibit longer spiral paths than more round species (This study, section 4.5.1 and Takahashi & Bé, 1984). Previous studies have only used a point to point approach to measure sinking velocities, compared to the 3D sinking velocity of this study. This difference in the measurement of the sinking velocities could explain some of the differences between the data of Takahashi and Bé (1984) and this study. However, other studies used the same point-to-point measurement that Takahashi and Bé (1984) used and there are no significant differences between those and this work.

When examining the linear model with interactions (Model 1) a large percentage of the variance within the dataset (97.8%) is explained using length, A_P, V_{wall} and CSF. Looking at the results of model 1 (Figure 4-24 to Figure 4-26), there are interesting trends. Firstly, sinking velocity changes as length interacts with volume and area (i.e. the size) of the foraminifera (Figure 4-25). The lowest sinking velocity is theoretically obtained by foraminifera with a large maximum length, a large volume and small projected area (Figure 4-25A). Small increases in length over the 400-600µm range result in a large decrease in sinking velocity (from ~0.17 $m \cdot s^{-1}$ at 400µm in length to ~0.09 $m \cdot s^{-1}$ at 600µm in length), if the volume is large (Figure 4-25A). Indeed, for all projected areas, larger volumes experience lower sinking velocity with longer lengths (Figure 4-25). The effect of shape is indicated in (Figure 4-26), where the relationship between sinking velocity and the interaction of A_P, V_{wall} and CSF is steepest for

foraminifera with the lowest CSF, but highest V_{wall} values. This means for foraminifera with low CSF values and large V_{wall} values they experience an increase in sinking velocity as the projected area (A_P) increases. Whilst these analyses contain no information on sinking orientation, the only logical way to achieve a high volume with a small A_P and CSF would be a disc shape object sinking with the edge facing downwards, which is not an orientation which was observed in this study. The decrease in sinking velocity seen in Figure 4-26C with increasing A_P, when V_{wall} and CSF are high is the result which is predicted under the hydrodynamic understanding outlined in Chapter 3. Both of these results (visualised in Figure 4-25 and Figure 4-26) are in agreement with Caromel *et al.* (2014), who found that to maintain sinking velocity whilst increasing volume, it was better to be flatter in shape.

Species do show preferential orientation during sinking, as is expected based on Vogel's (1994) discussion of low and intermediate Re objects. Many species of phytoplankton are also known to have a preferred orientation (Hutchinson, 1967), which is assumed to maintain the largest area for photosynthesising. Whilst this is not a concern for foraminifera themselves, it may be a consideration for some species which contain photosynthetic symbionts (e.g. *O. universa* Bijma et al., 1992). However, this is of little importance when the cell is dead and only the empty test is sinking to the ocean floor. Differences in orientation could be caused by uneven distribution of weight within the test, i.e. the areas where the spiralling of the chambers is more compact will be of a higher density compared to the final chamber. At higher Reynolds numbers uneven distribution of mass gives sinking objects a side-to-side sinking motion, seen characteristically in a falling leaf (Albertson, 1953), but at low Re these motions are not seen due to the greater effect of viscous forces.

An interesting observation is the difference in sinking velocity of the two specimens of *Sphaeroidinella dehiscens*. The high-resolution scan has a better quantification of the test wall volume. The high resolution of the scan is detailed enough to image the pores, therefore measuring the volume of the scan ensures it is only the calcite wall being measured. For the low-resolution scan, the scanning resolution is lower meaning that individual pores are not resolved. Therefore, the volume of the same specimen scanned at both high and low resolutions, would have a lower volume at higher resolutions. However, in this case the difference in sinking velocity is also accompanied by differences in length, simply the specimen scanned at high resolution was smaller than the specimen scanned at lower resolution (Table 4-9, Figure 4-27).

Table 4-9: Measurements of the two specimens of S. dehiscens*, showing the differences between them.*

Specimen	Length (µm)	Projected Area (µm^2)	V_{wall} (µm^3)	C_D	Re	Sinking Velocity (m·s^{-1})
Low resolution	627.1	340288	42692100	1.669	32.763	0.051
High Resolution	325.0	95143.1	8562120	5.031	8.283	0.025

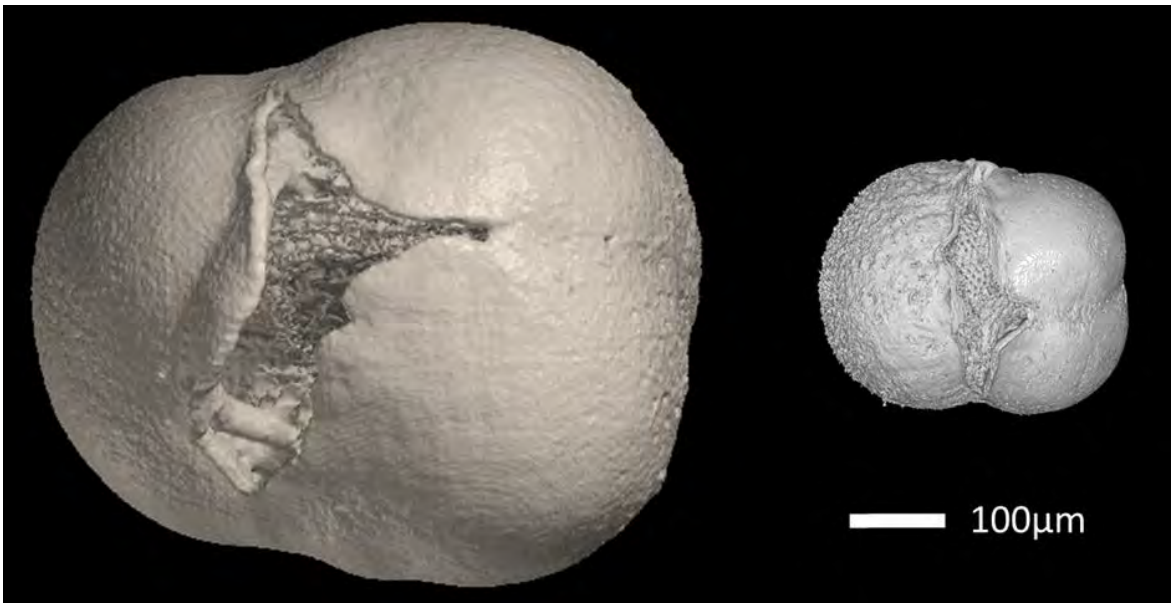

Figure 4-27: S. dehscens in low resolution (left) and high resolution (right).

In this study sources of error are also considered. The important consideration is how closely the tank is able to match the Re values which would be obtained in a boundless fluid. Testing the tank's Re regime was conducted using spheres, for which the relationship between Re and C_D is theoretically and empirically well known. The nonlinear relationship between the predicted values for the C_D of the spheres and the observed values exhibited R^2 = 0.85, with all of the measurements lying above the predicted values. This would suggest there is some (~15%) systematic error in the measurements of the C_D values for all the models, and also systematic error in variables derived from C_D such as absolute sinking velocity. However, relative differences (e.g.:, ratios between C_D, C_{DI}, and sinking velocities) across different species do not suffer from this systematic error, so trends seen with other variables will be maintained.

The novel measure C_{DI} presented here encompasses as much variance in drag with as little dependence on size as possible. This, theoretically, leaves only variation in shape to explain the C_{DI} value.

Equation 4-10

$$C_{DI} = C_D \cdot U^{2-n} \cdot A^{1-\frac{n}{2}} \cdot \upsilon^{n-2}$$

By finding other measures of shape which are more intuitive than C_{DI} as physical shape descriptors, the link between shape and sinking velocity can be understood.

Whilst the data from the dynamic scaling experiments has produced values which are congruent with the previously published data, it should be noted that there is only one value per species. As can be seen in Appendix 9.1.7 (Figure 9-1) there is variation in sinking velocities within a species (e.g. *Globigerina bulloides* shows variation between ~0.0005 and ~0.01 $m \cdot s^{-1}$, Appendix 9.1.7 Figure 9-2). This highlights a limitation of this method; it relies on the CT-scanning of multiple specimens. This limitation presents an issue regarding phenotypic variation of planktonic foraminifera within (morpho)species. Foraminifera are known to have considerable variation in morphologies over their geographic ranges (e.g. *Truncorotalia truncatulinoides,* Lohmann, 1983; Morard et al., 2013). This morphological variation is not captured in this study, however an initial insight into the sinking orientations and velocities in ways that have not been previously possible is gained using this method.

Moving forward, shape needs to be quantified in a manner which is independent of size and easy to calculate. Chapter 5 is focused on two methods of shape quantification, the results from which will be analysed in a phylogenetic context with the sinking velocities determined in this chapter, in Chapter 6.

4.7 Take Home Messages

1. Previous literature found that size (Thoulet, 1891; Berthois and Calvez, 1960; Berger *et al.*, 1972; Fok-Pun and Komar, 1983; Takahashi *et al.*, 1984; Caromel *et al.*, 2014), shape (Thoulet, 1891; Berthois and Calvez, 1960; Fok-Pun and Komar, 1983; Caromel *et al.*, 2014) and density (Berthois and Calvez, 1960; Fok-Pun and Komar, 1983; Takahashi *et al.*, 1984; Caromel *et al.*, 2014) are important in determining sinking velocity. Here, the effect of length, density and shape were confirmed. Additionally, volume, mass, projected area, and length parallel to the flow have been shown to be important in determining the sinking velocities of foraminifera test.
2. As with Chapter 3, foraminifera have been shown to conform to neither Stoke's law, nor Morrison's equation, suggesting an effect of size and shape, respectively, on sinking velocity.
3. The relationships between the predictors of sinking velocity have been explored, showing how interactions between length, volume and test wall volume (V_{wall}) contribute to sinking velocity when accounting for the mass of the particle (U_{mass}).
4. These interactions might explain some of the morphologies for foraminifera which are observed. However, these findings do come with the caveat that such inferences are based on dead, empty tests, and the living organism might employ other methods, such as lipids, to regulate buoyancy.

Chapter 5 Shape Analysis of Planktonic Foraminifera

5.1 Aims

The aim of this chapter is to quantify the shape of the planktonic foraminifera in my dataset. The measures of shape explored in this chapter will be used in the analyses in Chapter 6 to determine the effect of shape on sinking velocities. Shape appears to play a role in determining the sinking velocity of foraminifera, as suggested by the departure from Morrison's equation (see Chapter 4), and the findings of previous works (Thoulet, 1891; Berthois and Calvez, 1960; Fok-Pun and Komar, 1983; Caromel *et al.*, 2014). These studies have not quantified shape in a hydrodynamically relevant way (i.e. from a sinking orientation) or quantified shape using in a size independent method. As such, this chapter aims to capture the shape variation between the specimens which were 3D printed and sunk in Chapter 4, using two views from a standard orientation reported in the literature and two views from the sinking orientation. In theory, the sinking orientation views should capture more hydrodynamically relevant shape than the standard orientation views. This theory will be explored in Chapter 6.

Size independent shape quantification can be obtained from outlines of shapes using geometric morphometrics (GM) or Elliptical Fourier Analysis (EFA). Historically, EFA has been more frequently used for shape analysis of foraminifera, as such comparisons between the results of GM and EFA are presented in Appendix 9.3.3. Finally, PC scores from GM will be compared to other shape descriptors such as Aze *et al.*'s (Aze *et al.*, 2011) morphogroups and Corey Shape Factor (CSF, see Chapter 3 for an overview), to see how well these other methods (morphogroup and CSF) describe more detailed descriptions of shape (GM).

5.1 Shape and Planktonic Foraminifera

Planktonic foraminifera are divided into species based upon morphological characters, such as the number of chambers in the outer whorl (Schiebel and Hemleben, 2017). Therefore, there is a great deal of literature on the shape of individual species and of their lineages, where morphometrics has been used to delineate both species and chronospecies (i.e. a species which has evolved continually and uniformly from an extinct ancestor Schiebel & Hemleben, 2017). However, novel approaches have recently been introduced to automate planktonic foraminifera species identification based on morphometric criteria (Schmidt, Thierstein and Bollmann, 2004; Macleod, 2010; Hsiang, Elder and Hull, 2016).

Traditional morphometrics of foraminifera have focused on linear measurements of chamber size, angles between chambers, and aperture shape and size (e.g.: Wei, 1987; Biolzi, 1991), following the techniques that Raup (Raup, 1966) used in molluscs and first used for foraminifera by Arnold (Arnold,

1983). However, outlining techniques (EFA) were first applied to foraminifera earlier than these traditional morphometrics (Healy-Williams and Williams, 1981). There are several problems with traditional morphometrics. One is that the relationship between size and shape is implicit in these measurements. Therefore, separating the size and shape components that constitute form can be difficult, especially because size is likely to overwhelm the effect of shape (Zelditch *et al.*, 2004). Another problem is that the relative location of the points between which the measurement is taken is not known from the measurements themselves. To make comparisons between shapes (as is the point of morphometrics), the relative position of the points needs to be known. In addition, measurements often miss true shape variation as different morphologies may share distances (e.g.: Figure 5-1).

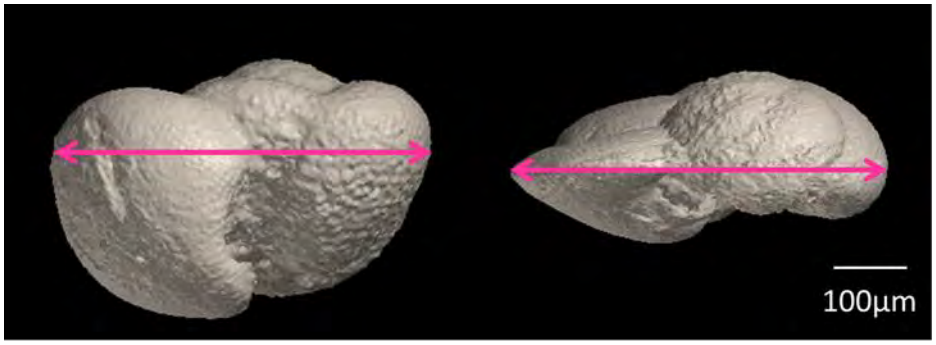

Figure 5-1: Two foraminifera (left: Globoconella puncticulata *and right:* Hirsutella margaritae*) showing measurements of equal maximum length but are different shapes.*

5.1.1.1 *Geometric Morphometrics*

To overcome the issues with linear measurements a new branch of shape analysis, Geometric Morphometrics (GM), was developed (see Zelditch *et al*. (2004) and Cooke & Terhune (2015) for a primer, and Viscosi & Cardini (2011) for a more technical introduction). GM is technically a suite of methods that rely on the same underlying principle: using the Cartesian coordinates of 2D or 3D points, called landmarks, to study the differences (and similarities) between objects. These landmarks are essentially equivalent to the measurement points in traditional morphometrics. A set of landmarks (specifically their positions) then act as a proxy for the shape of the objects. As with measurement points, landmarks may be biologically relevant (i.e. at the suture of chambers) or mathematically defined (e.g.: at the point of maximum curvature). By using landmark locations (in 2D or 3D), scale, translation and rotation can be mathematically eliminated, resulting in a quantification of shape alone. Continuing with the example of using 16 landmarks from the traditional morphometrics example in Chapter 1: Introduction (Figure 1-8), using GM results in a list of 16 pairs of numbers (if quantifying shape in 2D, if quantifying shape in 3D there are 16 triples), which are cartesian (x-y, or x-y-z respectively) coordinates of the landmarks. These landmarks can still be used to reconstruct the 120 measurements which could be used in traditional morphometrics. As such, GM results in a smaller dataset (i.e. the list of cartesian coordinates) from which: the geometric position of each landmark is

known relative to each other landmark; the 120 distances can be reconstructed; there is no loss of shape information; and (after performing a Procrustes fit, see below) variance in size is not the predominating variation in the dataset (unlike with linear measurements, Zelditch *et al.*, 2004). Landmarks may be of three types (Zelditch *et al.*, 2004):

Type I. Landmarks placed at specific, homologous, locally defined, anatomical points. Dependent on the organism being studied, and the purpose of the study, this point could be determined by histology, development or a structure being studied. An example of Type I landmarks would be sutural joints, which are determined by development.

Type II. Landmarks placed at points, determined by structures of the organism. For example, Type II landmarks could be placed at the point of maximum or minimum curvature, e.g.: the tip of a chamber, and are defined by their position relative to specific local features or points along a structure.

Type III. Landmarks that are placed at extremities, in relation to another point. Type III landmarks are not defined by local anatomical structures.

As the choice of landmark position influences the result of GM, the landmarks chosen should be relevant to the question being asked. In situations where, discrete landmarks cannot be placed, or do not provide information about the specific shape between them, then outlining of the object (or section of the object) can be carried out. One important advantage that GM methods have over traditional morphometrics is that they do not require the a priori choice of angles or lengths to be measured (Stayton and Ruta, 2006).

Once placed the landmarks are subjected to a series of mathematical transformations. To explain the mathematic processes behind GM, an example using triangles is used (Figure 5-2). The first stage of GM after obtaining the landmarks (or outlines) is conducting a Procrustes fit, this removes the effect of translation, rotation and scale. The resulting (newly aligned) co-ordinates for each landmark are then used to produce a variance-covariance matrix, upon which a Principle Component Analysis (PCA) is conducted. This gives a metric of the direction in which shape changes occur, with PC axis 1 (PC1) explaining the most variance.

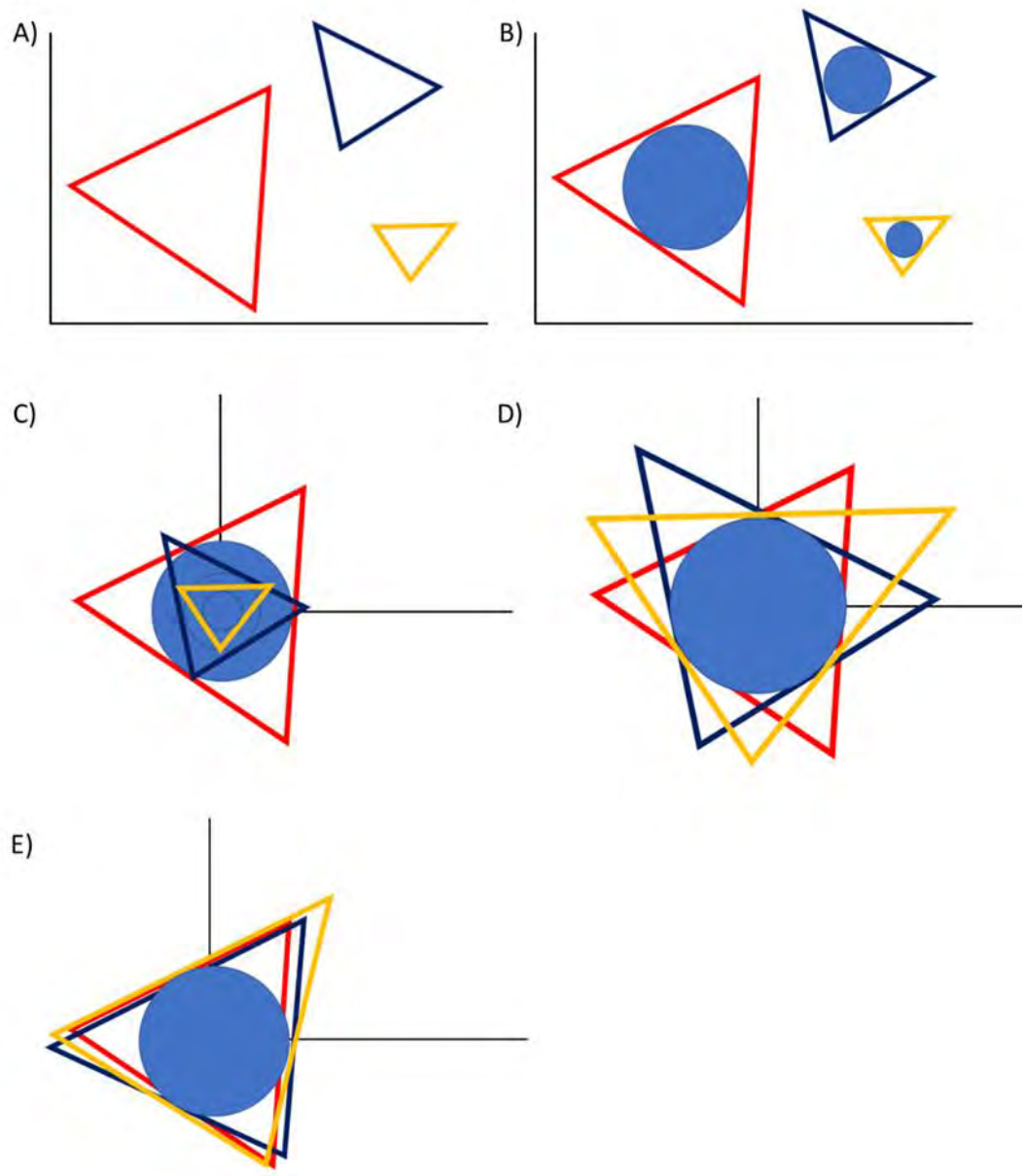

Figure 5-2:An example of Procrustes fit, using three triangles. First (in A) the triangles are different sizes, rotated differently and are in different locations within the 2D space. B) The centroid size (blue circle) is calculated, this is the square root of the sum of the squared distances from each landmark to the centroid. Note the blue circle is for illustrative purpose only. C) The triangles are re-located to the origin of 2D space. D) The triangles are resized to have a centroid size of 1 (Kendall, 1984; Bookstein, 1989, 1991). *Then finally, (in E) the triangles are rotated to minimise the distance between the same landmarks on different triangles (Webster & Sheets, 2010).*

When trying to quantify shape, foraminifera present a number of challenges. For example, there are differences in chamber configuration (e.g.: number of chambers, coiling direction, etc., see Figure 1-4). Despite this, foraminifera present some options for the placement of landmarks, with the suture between chambers (Type I and II) and extremes of the chambers (Type III) all suitable to use when making comparison within a species or between similar species.

However, the aim in this chapter is to make comparisons between species. To employ (Type I) landmarks on the sutures, for example, would require species to have the same number of chambers.

In the varied species studied here, this is not the case (see Figure 5-3 for some examples). To overcome these difficulties imposed by, e.g.: the selection of Type I landmarks, an outline analysis was conducted (details in Appendix 9.3). Whilst outline analysis sacrifices the direct and exact one-to-one correspondence among landmarks, from different foraminifera (which would be obtained using a homologous landmark-based approach), outline analysis quantifies the shape of homologous curves, capturing a smoother and continuous range of variation. Outlines consist of semi-landmarks (Gunz and Mitteroecker, 2013), which are a series of landmarks placed around the periphery of the object, but that share no homologous points (apart from the starting location of the outline), however the orientation of the foraminifera must be consistent. These semi-landmarks can then be subjected to the same analyses as traditional landmarks. Outlining techniques present a computationally cheap method of quantifying shape, which are well established (e.g.: Lohmann, 1983). There are, however, other alternatives for quantifying shape from outlines of objects, such as Elliptical Fourier Analysis (Healy-Williams and Williams, 1981). EFA uses a similar method for quantifying shape, details of EFA can be found in Appendix 9.3.5.

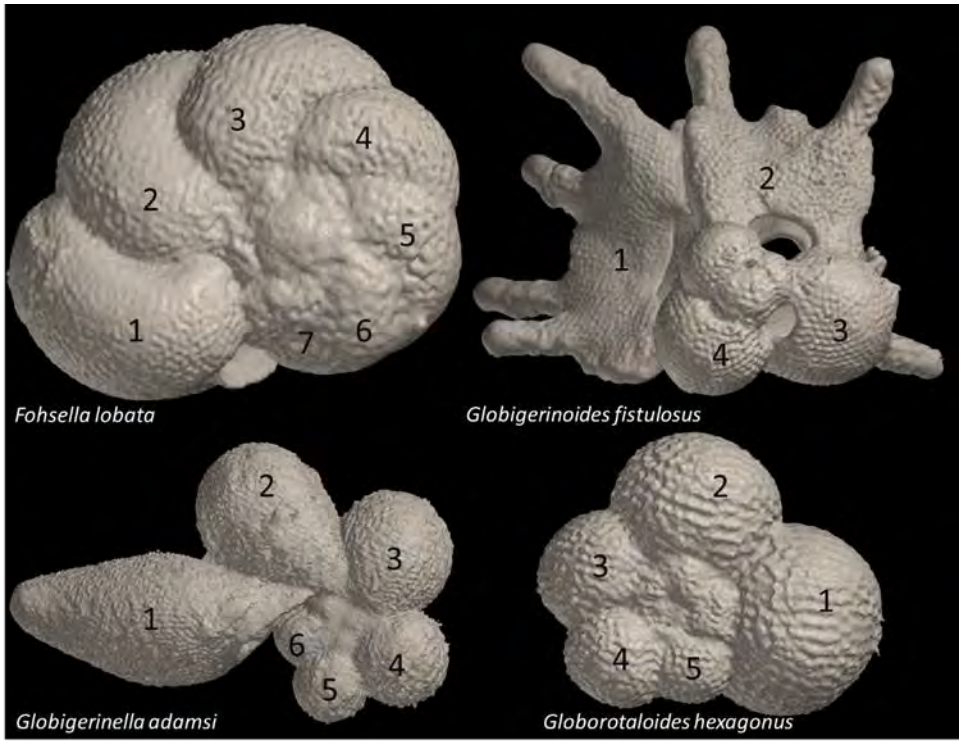

Figure 5-3: Some examples of the species used in this study, visualised using Molcer (White Rabbit Corp, 2016) *to illustrate the different numbers of chambers present, which makes landmark-based comparison difficult. Chambers are numbered starting at the final chamber and ending at the first chamber of the outer whorl. In the top row* Fohsella lobata *has seven chambers in the outer whorl,* Globigerinoides fistulosus *has four chambers. On the bottom row,* Globigerinella adamsi *has six chambers and* Globorotaloides hexagonus *has five chambers.*

5.1.1.2 *Problems with Outlining Approaches*

However, as highlighted by Webb and Swann (Webb and Swan, 1996), the relationship between the outline (analysed using either GM or EFA) and the 3D morphology is uncertain. Webb and Swann argue

that the outlines of foraminifera are “an indirect consequence of the pattern of chamber accretion, the three-dimensional shape of the chambers and the viewing direction”. To solve this, Webb and Swann (1996) suggest the use of linear measurements and angles between chambers in three dimensions, but this approach suffers from the same problems as outlined above for traditional linear measurements. To address the problems with using outlines (i.e. only capturing shape in 2D) new methods for quantifying shape in 3D have been developed, for instance spherical harmonics (Shen, Farid and McPeek, 2009). Briefly, spherical harmonics is a 3D version of Elliptical Fourier analysis. The object whose shape is to be quantified is represented digitally as a ‘cloud’ of co-ordinates. This cloud is composed of vertexes of triangles that form a mesh of the object. Spherical harmonics still require the placement of landmarks, which are used to align the cloud of one object with the cloud of another object. Therefore, spherical harmonics has the same problems of finding homologous points between different species, and as such was not used in the quantification of shape in this study. To attempt to overcome these problems this study will quantify shape in 2 different planes, see Appendix 9.3 for details.

5.1 Methods

Data were downloaded from the University of Tohoko (Japan) eforam stock (as per Chapter 4) and obtained from synchrotron scans (see Chapter 4 for details). From the digital models of the foraminifera maximum extensions in 2 views from 2 orientations were obtained. Maximum extensions can be thought of as projections or shadows of an object, providing a clear outline of the shape but no details of the shape variation within the outline. As the specimens are the same as those used in Chapter 4, the same caveats apply regarding the lack of phenotypic diversity within the species, as only one specimen per species is being analysed (excluding *Sphaeroidinella dehiscens*).

Dependent on the source of the material (i.e. University of Tohoko or synchrotron) the maximum extensions were obtained by slightly different methods (see below, section 5.1.1). To address the problem highlighted by Swann and Webb (1996) above, with using 2D outlines to quantify 3D shape, outlining was conducted on two orientations. The first orientation is used in the literature and is assumed to provide maximum shape variation, to permit identification of species. From this “standard” orientation two perspectives or views are taken: the spiral view and aperture view. The second orientation is the sinking orientation and provides two views. The first view, the projected area (A_p in Chapter 4) of the sinking foraminifera as viewed from underneath (underneath view). Secondly, an arbitrary side view of the sinking orientation, perpendicular to the underneath view (side view). The sinking orientation provides views which are functionally relevant (i.e. the shape of the projected area,

important in determining drag, see Chapter 4). Therefore, the sinking orientation might better explain the effect of shape on sinking velocity than the standard orientation.

5.1.1 Standard Orientation

For those data from eforam, the shadow projection was obtained by orientating the digital model, in Molcer (Version 1.35, White Rabbit Corp., 2016), so that a 2D view matched the orientation used in the literature. For the synchrotron data, rendering of the images from the image stacks was performed in SPIERS (Sutton *et al.*, 2012). This rendering was then aligned in the suitable orientation and an image of the rendered foraminifera was captured. The images, regardless of source, were then subjected to thresholding which generated a white foraminifera 'shadow' on a black background image (Figure 5-4a). The process was repeated for the aperture view.

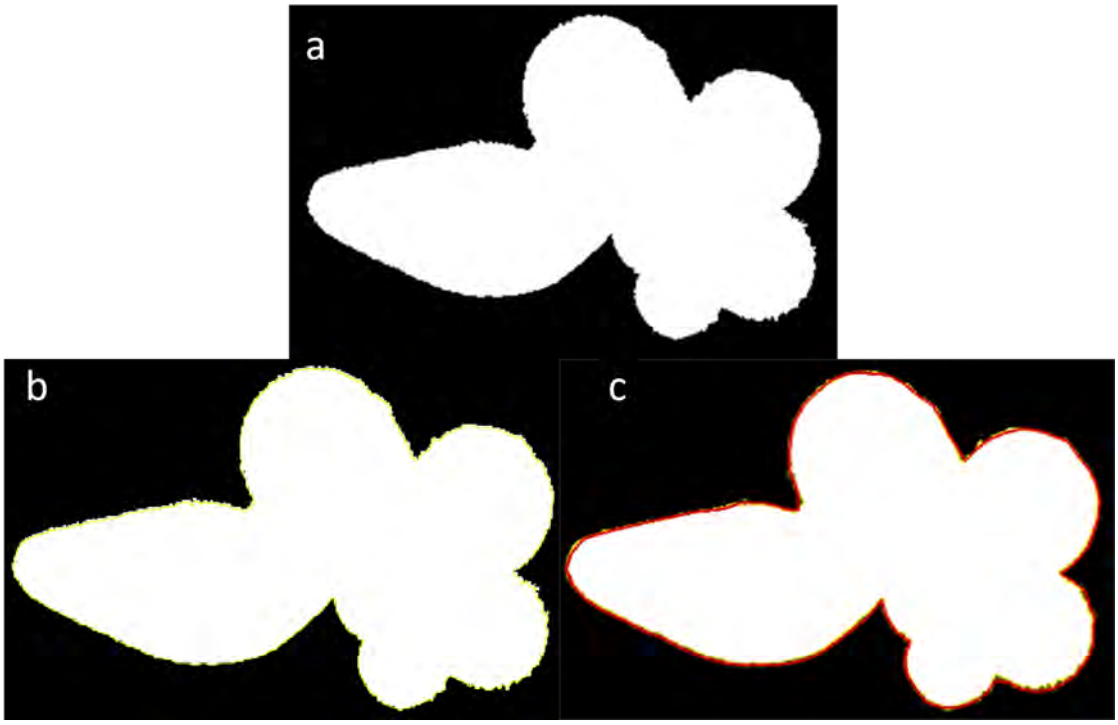

Figure 5-4 Example spiral view of Globigerinella adamsi ***a****:thresholded image*, ***b****: outline (in yellow), and* ***c****: the outline formed from the 100 landmark points (in red).*

5.1.2 Sinking Orientation

For the sinking orientation outlines, the digital model of the foraminifera was orientated (in either Molcer or SPIERS, as above) to match the orientation during sinking using the high definition images (See section 4.4.8, Figure 4-8) taken during the sinking experiments as a reference (each species has a consistently preferred orientation, see section 4.5.1). The digital model was then rotated (about the z-axis) to orientate the largest chamber to the left of the image, providing a side view of the sinking orientation. The foraminifera model was then rotated 90˚ relative to the x-y axis to provide a viewpoint as if the test was descending directly towards the viewer, providing the underneath view. These images

(the underneath and side views) were then subjected to the same thresholding procedure as the spiral and aperture views.

5.1.3 Geometric Morphometrics

GM outline analysis was used in this study, specifically a Relative Warps Analysis of Procrustes-fitted coordinates or in slightly more general terms, a Coordinate Point Eigenshape Analysis. For simplicity the method shall be referred to as GM.

Using tpsDig2 (Rohlf, 2015) an outline of 100 landmarks was placed around the shadow of the test (Figure 5-4b and c), in the four views described above. In the spiral view the suture between the penultimate and final chambers of the outer whirl was used as a starting point. Species that coiled sinsitrally were mirrored so that the suture was on the right of the image. For the sinking orientation the suture between the penultimate and final chamber of the outer whorl was also used, however for the side view of the sinking orientation the outlining was conducted from the furthest left of the outline.

The R package "geomorph" (Version 3.0.6, Adams *et al*., 2018) was used to perform a Procrustes Fit. A variance-covariance matrix was generated across all species, upon which a PCA was performed resulting in a unique PC score for each species, for each PC axis. PC axes explaining more than 10% of variance were included. Higher PC axes represent negligible aspects of shape variation, which probably have their source in stochastic error or image imperfection (Stayton and Ruta, 2006).

Analysis and visualisation of results was conducted using the R package "geomorph" and code used in Olsen (Olsen, 2017) to produce Back-transformed PCA plots (i.e. taking PC scores and back-transforming these values to a shape which can be plotted). Shape changes were visualised using transformation grids.

5.1.4 Phylomorphospace

A phylomorphospace uses PC scores to place species in morphospace, and superimposes the phylogeny showing how species are related. Using the 'phylomorphospace' function from the R package "phytools" (version 0.6-44, Revell, 2012), allowing visual inspection of magnitude and direction of shape changes along branches of the tree (Sidlauskas, 2008). The nodes on the tree were estimated morphologies of ancestral species, based on ancestral state reconstruction. In a phylogeny the length of the branches is equivalent to the time since the bifurcation (node) in the tree. However, in a phylomorphospace, the branch lengths between the nodes instead represent distance in morphospace. Ancestral states were reconstructed using maximum likelihood approaches, these reconstructed states were used to position the nodes of the phylogeny. In summary, a phylomorphospace plot represents the changes in shape within the phylogeny and permits visual examination of if closely related species

are similar shapes. To permit both the low-resolution and high-resolution scans of *S. dehiscens* to be included in these phylomorphospace plots, a new branch was inserted to the phylogeny with minimal branch length using "phytools".

5.1.5 Comparison of Measures of Shape

Comparisons between the PC scores generated by GM were compared to the morphogroups of Aze *et al.* (2011) and to the CSF values (as calculated in section 3.1.3). These comparisons will identify if the morphogroup are significantly separated in morphospace (i.e. there are true differences in shape, in the orientations used here, between the different morphogroups).

As EFA and GM use different methods to quantify shape, a comparison of the PC scores from each method was conducted to identify differences between them. As previously mentioned, EFA is commonly used in the literature to examine differences in shape within a species (or groups of closely related species), and therefore served as a comparison for the GM analyses. Comparisons of GM and EFA results can be found in Appendix 9.3.3.

5.1.6 Statistics

Linear models (regressions) were used to examine potential relationships between PC scores and CSF. Comparison of GM and EFA PC scores were achieved using Spearman's Correlation Coefficient, as the PC scores are neither independent, nor normally distributed. Both comparisons were performed in R (version 3.4.2, R Core Team, 2018) Relationships between PC scores and morphogroups were performed using multinomial logistic regressions (MLR), using the R package "mlogit" version 0.3-0 (Croissant, 2018). MLR was used as it allows for relationships between data where the dependent variable is a non-ordered categorical value (i.e morphogroup) with more than two possible values. PC scores are not correlated, by definition, but are not statistically independent. MLR does not require the independent variables (i.e. PC scores) to be statistically independent from one another. Finally, comparisons between the distances of species within morphospace where compared to phylogenetic distances (i.e. how closely related species are). This was achieved using two matrices, the first being a matrix of morphospace (PC score) distances and the second being branch length distances. PC score matrices were composed for all views (i.e. spiral, aperture, underneath and side) using the base "stats" package's "dist" function in R. The branch length matrix was composed using the function "cophenetic", also from the base package "stats". These matrices were then compared using a Mantel test, using the function "MantelCor" from the package "evolqg" Version 0.2-5 (Melo *et al.*, 2016). The Mantel test evaluates for correlations between the two matrices by randomly permutating the rows and columns of the matrices and the correlation is tested. The observed correlation is then compared to these

hypothetical matrices, with the significance result being a proportion of the permutations equal to the observed correlation from the actual input matrices. Here, 1000 permutations were used.

5.1 Results and Discussion

Shape changes along PC axes occur in both directions, for example in the results presented here, as PC1 increases stretching may occur horizontally and compression vertically, as PC1 decreases stretching would occur vertically, and compression horizontally. Here, the shape changes will generally be described as PC scores increase, unless otherwise stated. Morphospace and phylomorphospace plots which follow have all 32 species displayed, which are numbered for convenience as per Table 5-1.

Table 5-1: The 32 species of planktonic foraminifera whose shape was quantified in this study. The numbering provided is used throughout this chapter in figures to identify species.

Number	Species	Number	Species
1	*Neogloboquadrina acostaensis*	**18**	*Sphaeroidinellopsis kochi*
2	*Globigerinella adamsi*	**19**	*Fohsella lobata*
3	*Dentoglobigerina altispira*	**20**	*Hirsutella margaritae*
4	*Globoturborotalita apertura*	**21**	*Paragloborotalia mayeri*
5	*Globigerina bulloides*	**22**	*Globoturborotalita nepenthes*
6	*Globigerinoides conglobatus*	**23**	*Pulleniatina obliquiloculata*
7	*Truncorotalia crassaformis*	**24**	*Fohsella peripheroronda*
8	*Praeorbulina curva*	**25**	*Globigerina praebulloides*
9	*Sphaeroidinella dehiscens*	**26**	*Menardella praemenardii*
10	*Sphaeroidinella dehiscens (HR)*	**27**	*Globoconella puncticulata*
11	*Catapsydrax dissimilis*	**28**	*Fohsella robusta*
12	*Neogloboquadrina dutertrei*	**29**	*Dentoglobigerina rohri*
13	*Globigerinoides fistulosus*	**30**	*Paragloborotalia siakensis*
14	*Globorotalia flexuosa*	**31**	*Globoconella sphericomiozea*
15	*Globorotaloides hexagonus*	**32**	*Truncorotalia truncatulinoides*
16	*Neogloboquadrina humerosa*	**33**	*Orbulina universa*
17	*Globoconella inflata*		

5.1.1 Geometric Morphometrics

To gain a general overview of the outlines, the aligned coordinates for the standard orientation and the sinking orientation are displayed in Figure 5-5 and Figure 5-6 respectively.

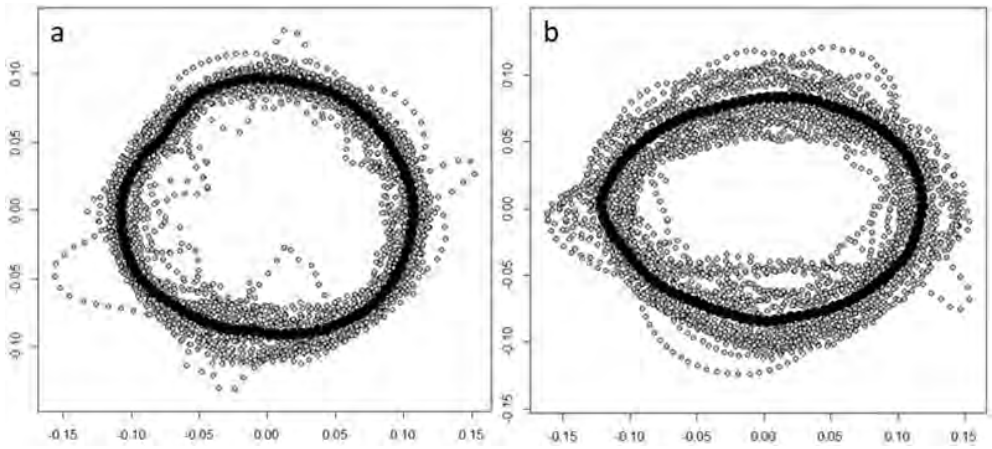

Figure 5-5: The aligned landmarks for the standard orientation (with the axes being non-dimensional distance), a. the spiral view and b. the aperture view. The black points are the average shape, whilst the grey points are the 100 landmarks from the outlines of each foraminifera used in this study.

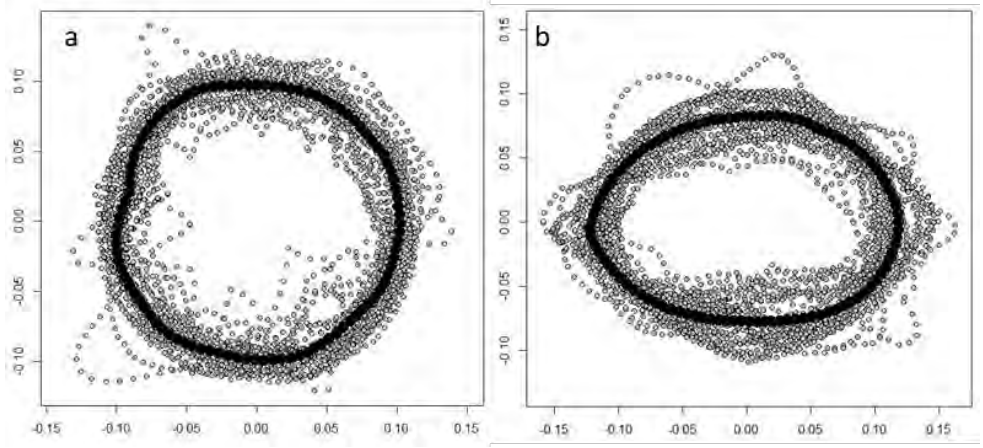

Figure 5-6: The aligned landmarks for the sinking orientation, a. the underneath view and b. side view. The black points are the average shape, whilst the grey points are the landmarks from the outlines of each foraminifera used in this study.

In the morphospace plot generated by data on the spiral view (i.e. spiral view morphospace, Figure 5-7), PC1 explains 33.13% of the shape variation in that orientation, PC2 explains 20.27% and PC3 explains 15.87%. Meaning the 3 axes account for 69.27% of the shape variation. There is a general clustering of species in the low (±0.1) positive and negative values for PC1, 2, and 3, with two species (*G. adamsi*, 2 and *G. fistulosus*, 13) which lie outside of this cluster. Based on visual inspection, it is not unexpected that *G. fistulosus* has extreme PC scores given its unusual shape and, the high levels of curvature of the outline. The changes in morphology along PC axes in the spiral orientation morphospace suggests that the majority of the shape changes are due to the spiralling pattern of growth. In the aperture orientation shape changes are due to changes in the chamber coiling angle, for a low PC1 value the angle between chambers is very low (i.e. planispiral, or very lowly trochospiral) as PC1 values become higher the chambers are at greater angles to one another (i.e. highly trochospiral). The results of the other views and orientations are presented below, for the morphospace plots see Appendix 9.3.1.

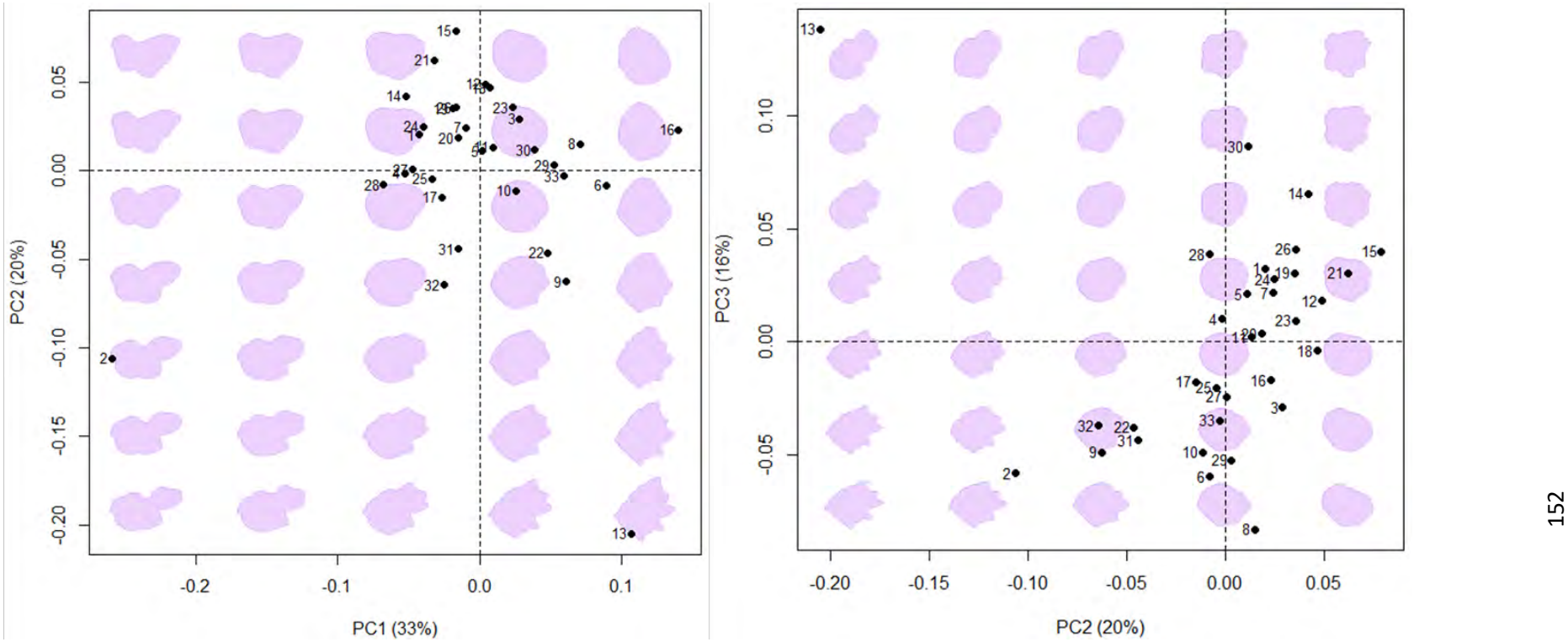

Figure 5-7: An example of PC scores in spiral orientation, with representative shapes in purple, these are the shapes a species would be if they occurred at that point in morphospace and are present in all figures from here on in. Percentage of shape variation (rounded to the nearest one percent) explained by each axis is included. Numbering as per table below.

N°	Species	N°	Species	N°	Species	N°	Species	N°	Species	N°	Species
1	*Neogloboquadrina acostaensis*	7	*Truncorotalia crassaformis*	13	*Globigerinoides fistulosus*	19	*Fohsella lobata*	25	*Globigerina praebulloides*	31	*Globoconella sphericomiozea*
2	*Globigerinella adamsi*	8	*Praeorbulina curva*	14	*Globorotalia flexuosa*	20	*Hirsutella margaritae*	26	*Menardella praemenardii*	32	*Truncorotalia truncatulinoides*
3	*Dentoglobigerina altispira*	9	*Sphaeroidinella dehiscens*	15	*Globorotaloides hexagonus*	21	*Paragloborotalia mayeri*	27	*Globoconella puncticulata*	33	*Orbulina universa*
4	*Globoturborotalita apertura*	10	*Sphaeroidinella dehiscens (HR)*	16	*Neogloboquadrina humerosa*	22	*Globoturborotalita nepenthes*	28	*Fohsella robusta*		
5	*Globigerina bulloides*	11	*Catapsydrax dissimilis*	17	*Globoconella inflata*	23	*Pulleniatina obliquiloculata*	29	*Dentoglobigerina rohri*		
6	*Globigerinoides conglobatus*	12	*Neogloboquadrina dutertrei*	18	*Sphaeroidinellopsis kochi*	24	*Fohsella peripheroronda*	30	*Paragloborotalia siakensis*		

In the aperture view (Figure 9-22), PC1 and PC2 explain 61.98% and 19.75% of shape variation, respectively, cumulatively explaining 81.73%. As PC1 increases there is lateral shortening and dorso-ventral stretching, as PC2 increases the lowest point of the test shifts from left to right, with PC2 = 0 being approximately flat. Overall species are more spread in morphospace compared to the spiral view, but with no specific patterns or clusters. *G. fistulosus* is, again, isolated but not as distant from the rest of the species, instead *G. nepenthes* (22) is more separated, due to the elongated final chamber.

In the underneath view morphospace (Figure 9-23), PC1 explains 41.92%, PC2 explains 18.47% and PC3 explains 15.90% of shape variation, a total of 76.29% across the three axes. Shapes changes along PC1 show the elongation of the foraminifera at ~45° to horizontal, PC2 describes the lateral compression and PC3 describes the smoothness of the foraminifera, with lower PC3 values having more projections. There is a general clustering, with species being low in PC1, with only *G. adamsi* (2) and *G. nepenthes* (22) having higher PC1 values. Both species have an extremely pronounced final chamber. In PC2 there is a wide spread of species. PC3 shows clustering with most species falling below 0.1. *G. fistulosus* is the exception, due to the finger-like protrusions. In the sinking orientation shape changes are less dependent on the arrangement of the chambers, compared to the spiral and aperture orientations, as the orientation is dependent on the area presented to the fluid. Despite this the changes seen in PC1 and 2 in this orientation are generally due to the chamber patterns (i.e. position, coiling mode) of the foraminifera.

In the side view of the sinking orientation PC1 and PC2 (Figure 9-24) explain 58.63% and 24.21% respectively. Combined, PC1 and 2 explain 82.84% of the shape variation in this view. There is a general spread of species across the range of PC1. In PC2 most species are found between 0.1 and -0.1, with the exceptions being *G. fistulosus* (13), *G. nepenthes* (22) and *T. crassaformis* (7). In the side view of the sinking orientation the changes seen in PC1 are due to the height and width of the foraminifera, whereas the changes in PC2 mostly reflect the orientation combined with the arrangement of the chambers relative to one-another.

5.1.1.1 *Phylomorphospace*

No general trends emerge from visual inspection of the phylomorphospaces (for an example see Figure 5-8) for all orientations, that is, species that are closely related are not also necessarily similar in shape, i.e. are divergent, within morphospace. Mantel test results in Table 5-2 confirm that species that are closely related are not close to one-another in morphospace. If the branch lengths and the PC scores from the analysis were the same (i.e. position of species in morphospace directly correlates with the position of species in the phylogeny) then the R^2 would be equal to one. All of the R^2 values obtained for the Mantel test, are below 0.25. Phylomorphospaces for other views are in Appendix 9.3.2.

Table 5-2: Mantel test R^2 and p values for comparison between the branch length matrix and the PC score distances matrix. Significant p values are underlined.

	R^2	p values
PC1 spiral	0.225	<u>0.010</u>
PC2 spiral	0.201	<u>0.028</u>
PC3 spiral	0.144	0.065
PC1 aperture	0.144	0.054
PC2 aperture	0.135	<u>0.048</u>
PC1 underneath	0.15	0.072
PC2 underneath	0.056	0.222
PC3 underneath	0.183	<u>0.044</u>
PC1 side	-0.025	0.603
PC2 side	0.011	0.421

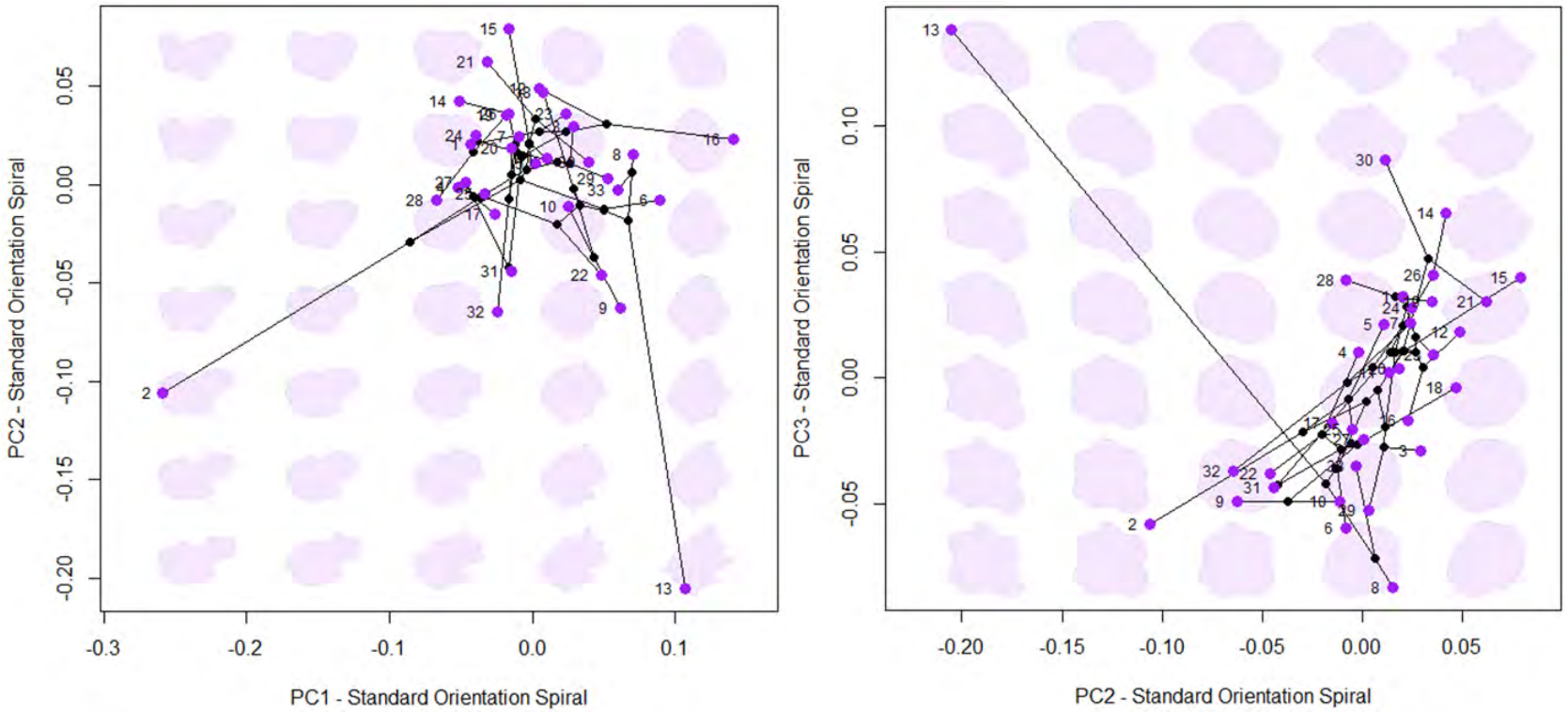

Figure 5-8: Phylomorphospace using PC axes 1 - 3 in the spiral orientation. The premise of a phylomorphospace plot is that it shows the distribution of species in morphospace, with the phylogeny superimposed. Now instead of branch length, the branches of the phylogeny represent distance in morphospace. In these plots the terminal taxa are shown in purple and numbered in accordance with table below. Nodes are coloured black; their position being calculated using Ancestral State Reconstruction (ASR).

Nº	Species	Nº	Species	Nº	Species	Nº	Species	Nº	Species	Nº	Species
1	*Neogloboquadrina acostaensis*	**7**	*Truncorotalia crassaformis*	**13**	*Globigerinoides fistulosus*	**19**	*Fohsella lobata*	**25**	*Globigerina praebulloides*	**31**	*Globoconella sphericomiozea*
2	*Globigerinella adamsi*	**8**	*Praeorbulina curva*	**14**	*Globorotalia flexuosa*	**20**	*Hirsutella margaritae*	**26**	*Menardella praemenardii*	**32**	*Truncorotalia truncatulinoides*
3	*Dentoglobigerina altispira*	**9**	*Sphaeroidinella dehiscens*	**15**	*Globorotaloides hexagonus*	**21**	*Paragloborotalia mayeri*	**27**	*Globoconella puncticulata*	**33**	*Orbulina universa*
4	*Globoturborotalita apertura*	**10**	*Sphaeroidinella dehiscens (HR)*	**16**	*Neogloboquadrina humerosa*	**22**	*Globoturborotalita nepenthes*	**28**	*Fohsella robusta*		
5	*Globigerina bulloides*	**11**	*Catapsydrax dissimilis*	**17**	*Globoconella inflata*	**23**	*Pulleniatina obliquiloculata*	**29**	*Dentoglobigerina rohri*		
6	*Globigerinoides conglobatus*	**12**	*Neogloboquadrina dutertrei*	**18**	*Sphaeroidinellopsis kochi*	**24**	*Fohsella peripheroronda*	**30**	*Paragloborotalia siakensis*		

5.1.2Comparison of GM with CSF

Visual inspection of spiral orientation morphospace with CSF mapped by colour (Figure 5-9) suggests a general trend towards higher CSF values (more spherical) towards PC1 = 0.075 and PC2 = -0.02. Assuming this as a "central point", the CSF values then reduce (shapes become less spherical) further from this point. There is a similar, but less dominating, trend presented in PC2 and 3. There is a significant relationship between CSF and: PC1, 2 and 3 in the spiral view (Figure 5-9, $F_{7,25}$= 5.763, p<0.001, adjusted R^2=0.510), PC1 and 2 in aperture view (Appendix 9.3.4 Figure 9-29, $F_{3,29}$= 40.13, p<0.001, adjusted R^2= 0.786), and the side view (Appendix 9.3.4 Figure 9-31, $F_{3,29}$= 83.67, p<0.001, adjusted R^2= 0.886). The relationship between CSF and the underneath view is not significant (Appendix 9.3.4 Figure 9-30, $F_{7,25}$= 1.637, p=0.171, adjusted R^2=0.122).

In the aperture view, there are increasing CSF values towards higher PC1 values, with the most spherical species found around PC1 = 0.15 and PC2 = 0.01 and the least spherical species being found at PC1 = -0.25 and PC2 = -0.08 (Appendix 9.3.4 Figure 9-29).

In the underneath view (Appendix 9.3.4 Figure 9-30), there are increasing CSF values towards PC1 and PC2 = 0, moving away from the origin, shapes decrease in CSF value (becoming less spherical). In PC2 and 3 there is less of a trend. In the side view, CSF values are highest at PC1 = 0.15 and PC2 = -0.025 (Appendix 9.3.4 Figure 9-31).

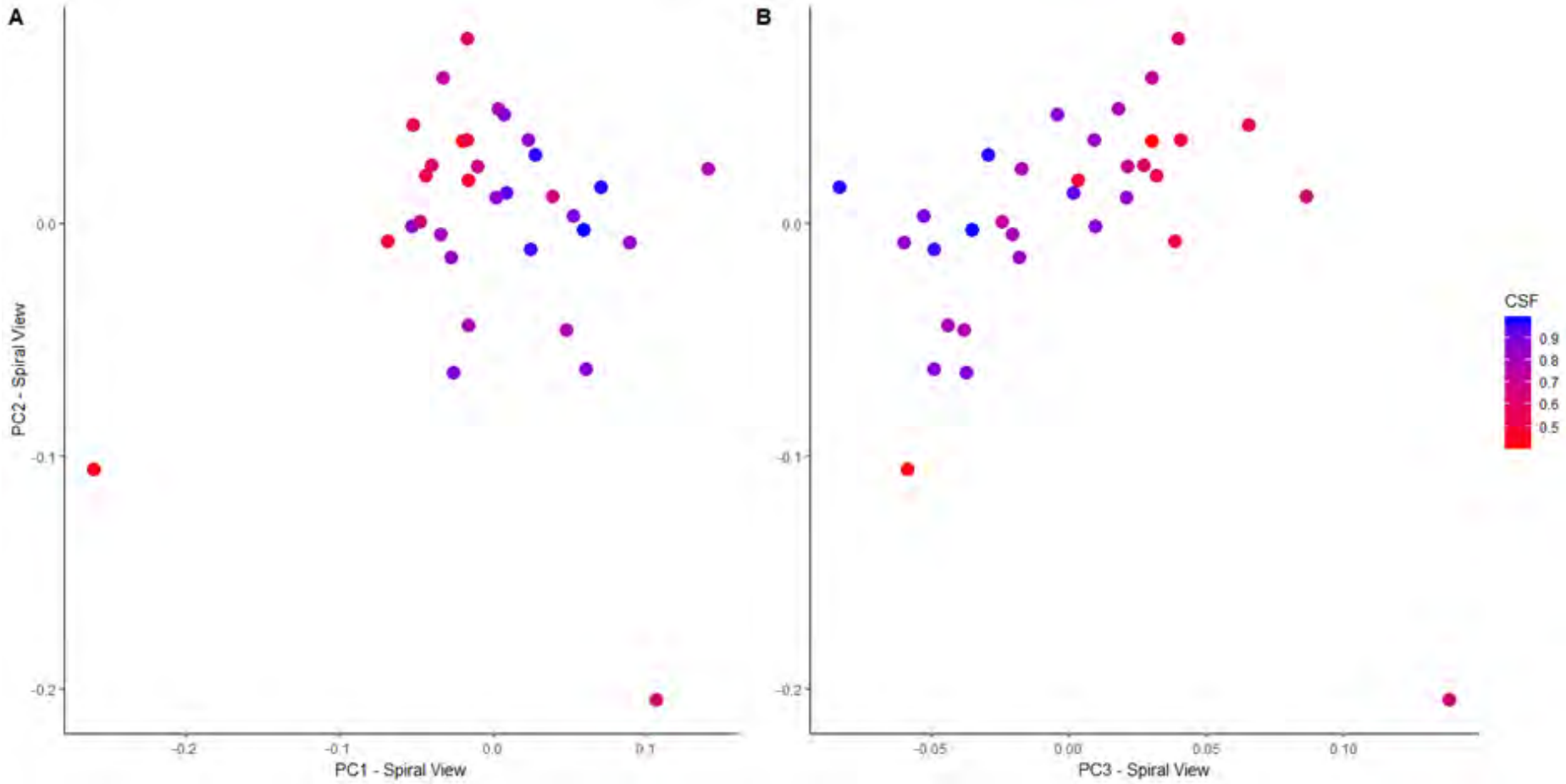

Figure 5-9: PC1, 2, & 3 in spiral view, with the data points coloured by CSF value, with bluer colours being more spherical shapes and the redder the colour the less spherical.

5.1.3 Comparison of GM and Morphogroups

5.1.3.1 *GM*

When visually comparing spiral view PC scores with morphogroup there is overlap between morphogroups (see Figure 5-10). 68% of variation in morphogroup is explained by PC scores in the spiral view (McFadden R^2=0.68, X^2=82.20, p = 0.013). An ANOVA revealed significant differences in the variance of PC scores between morphogroups in PC1 ($F_{8,24}$ = 7.847, p<0.001) and PC2 ($F_{8,24}$ = 2.535, p = 0.037), but not for PC3 ($F_{8,24}$ = 1.88, p = 0.111). *Post hoc* Tukey HSD test show significant differences between morphogroup 5 (spinose, clavate) and all other morphogroups, and between morphogroups 12 (non-spinose, turborotaliform, keeled) and 3 (spinose, globular with supplementary apertures) in PC1, between Morphogroups 2 (spinose, globular) and 3 (spinose, globular with supplementary apertures) in PC2 (see Table 5-3), that is the most extreme morphologies are significantly different from the other morphogroups.

Table 5-3: Significant results from the TukeyHSD pairwaise comparison between morphogroups for spiral view.

	Morphogroup pair	Difference	Lower Interval	Upper Interval	Adjusted p value
PC1	5-2	-0.254	-0.403	-0.106	<0.001
	5-3	-0.357	-0.528	-0.185	<0.001
	5-4	-0.324	-0.496	-0.152	<0.001
	5-7	0.276	0.131	0.422	<0.001
	5-12	0.216	0.044	0.387	0.007
	5-13	0.219	0.021	0.417	0.022
	5-14	0.231	0.069	0.393	0.002
	5-15	0.242	0.07	0.413	0.002
	3-12	-0.141	-0.281	-0.001	0.047
PC2	2-3	-0.122	-0.243	-0.001	0.047

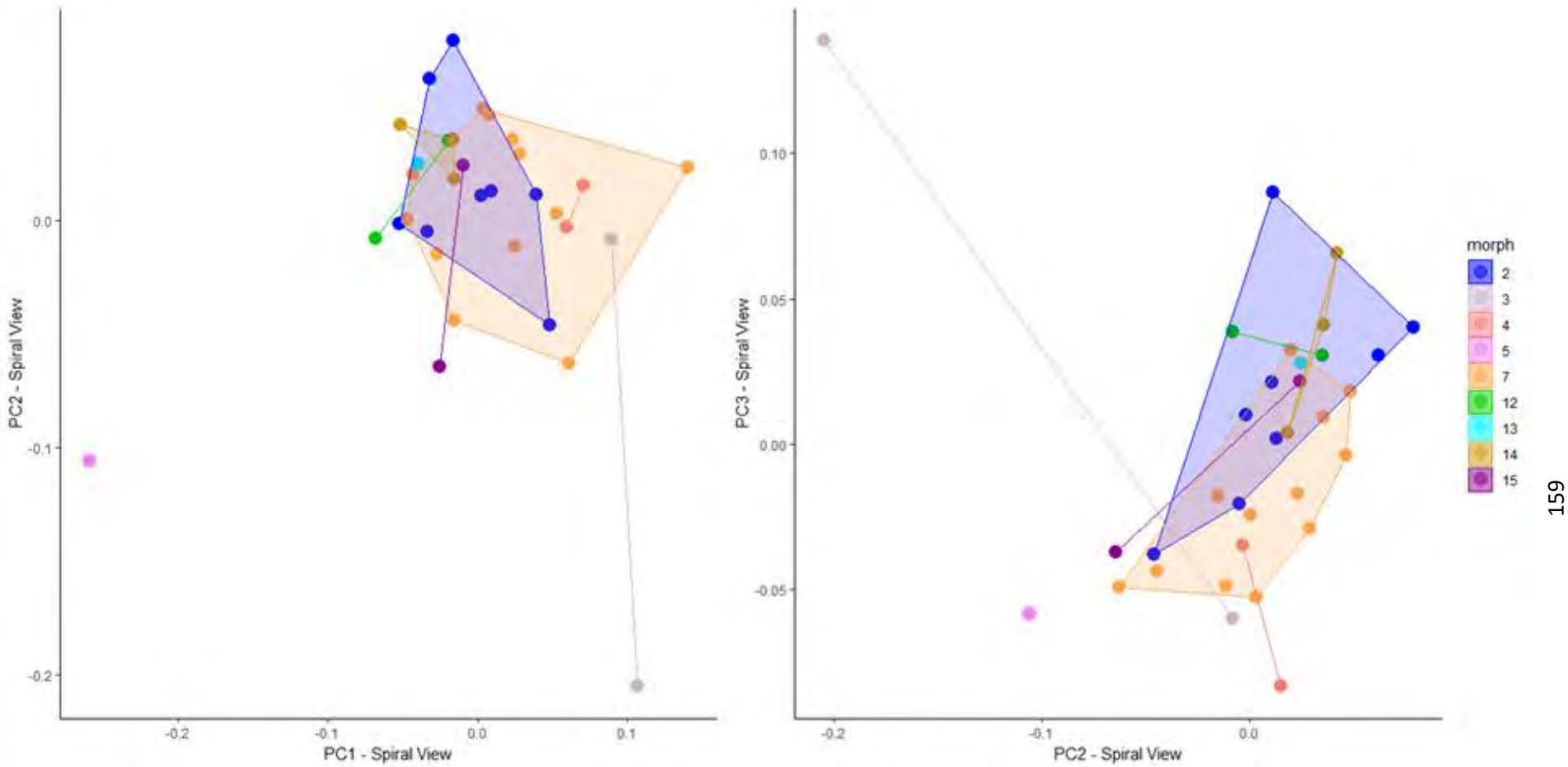

Figure 5-10: PC1 & 2 in the spiral view, coloured by morphogroup. Note that G. adamsi, morphogroup 5 sits to the far left of PC axis 1. This is reflected in the Tukey HSD pairwise comparison (see Table 5-3).

In the aperture view, 57% of variation in morphogroups is explainable by differences in PC score (McFadden R^2=0.57, X^2=68.36, p< 0.001), but morphogroups overlap in morphospace (see Appendix 9.3.2). ANOVA showed a significant difference in the variance of PC scores between morphogroups in PC1 ($F_{8,24}$ = 3.981, p = 0.004) but is not significant for PC2 ($F_{8,24}$ = 1.326, p = 0.278). Tukey HSD pairwise comparisons of morphogroups in PC1 found only one significant difference, between morphogroup 7 (non-spinose globular) and 14 (non-spinose, globorotaliform, keeled, Appendix 9.3.2).

Table 5-4: Significant result from the Tukey HSD pairwise comparison between morphogroups for aperture view.

	Morphogroup pair	Difference	Lower Interval	Upper Interval	Adjusted p value
PC1	7-14	-0.247	-0.49	-0.005	0.043

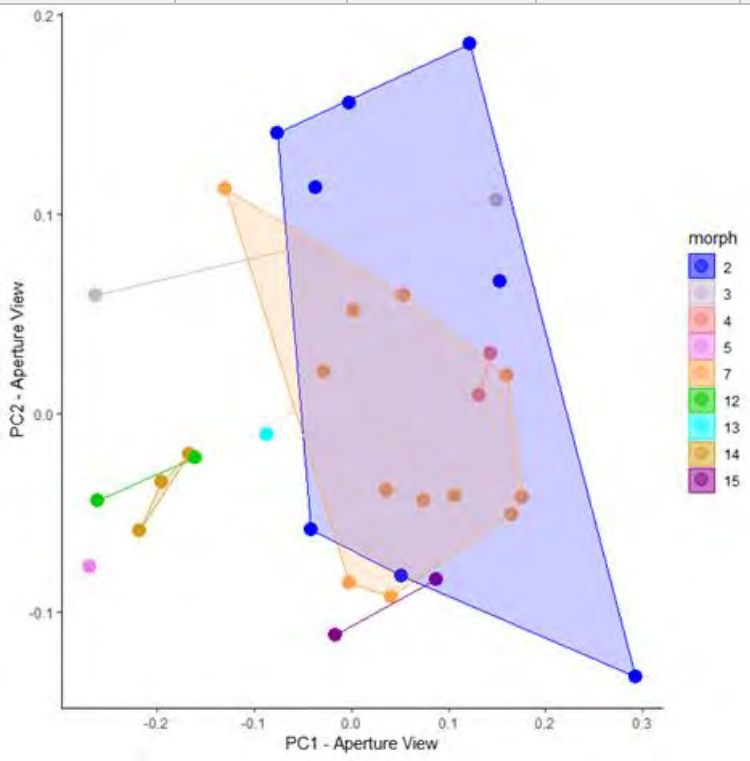

Figure 5-11: PC1 and 2 in the aperture orientation, coloured by morphogroup (see morphogroup definitions Table 4-6, below).

Table 4-2: Aze et al. (2011) morphogroups, also see Figure 4-12 below.

Aze *et al.* morphogroup	Aze *et al.* definition
2	Spinose, globular
3	Spinose globular with supplementary apertures
4	Spinose spherical
5	Spinose, clavate
7	Non-spinose globular
12	Non-spinose, turborotaliform, keeled
13	Non-spinose, turborotaliform, non-keeled
14	Non-spinose, globorotaliform, keeled
15	Non-spinose, globorotaliform, angluconical

Overlap between morphogroups in PC scores is repeated in the underneath view (Figure 5-12) with 75% of variation explained (McFadden R^2=0.75, X^2=89.90, p< 0.001). ANOVA testing showed there is a

significant difference in the variance of PC1 and 3 scores between morphogroups (PC1, $F_{8,24}$ = 4.191, p = 0.003; and PC3, $F_{8,24}$ = 5.304, p<0.001) but not for PC2 (PC2, $F_{8,24}$ = 0.789, p = 0.617). Tukey HSD found significant differences in pairwise comparisons between morphogroup 5 (spinose, clavate) and all other morphogroups apart from morphogroup 13 (non-spinose, turborotaliform, non-keeled) in PC1 (Table 5-5). In PC3 Tukey HSD showed significant differences between morphogroup 3 and all other morphogroups apart from 5 (Table 5-5).

Table 5-5: Significant results from the Tukey HSD pairwise comparison between morphogroups for underneath view.

	Morphogroup Pair	Difference	Lower Interval	Upper Interval	Adjusted p value
PC1	5-2	0.259	0.025	0.492	0.022
	5-3	0.359	0.09	0.629	0.004
	5-4	0.303	0.033	0.572	0.02
	5-7	-0.309	-0.538	-0.08	0.003
	5-12	-0.373	-0.643	-0.104	0.002
	5-14	-0.356	-0.611	-0.102	0.002
	5-15	-0.348	-0.618	-0.078	0.005
PC3	3-2	-0.156	-0.256	-0.056	0.001
	3-4	-0.163	-0.29	-0.037	0.005
	3-7	0.172	0.076	0.268	<0.001
	3-12	0.184	0.058	0.31	0.001
	3-13	0.172	0.017	0.326	0.022
	3-14	0.174	0.058	0.289	0.001
	3-15	0.179	0.053	0.305	0.002

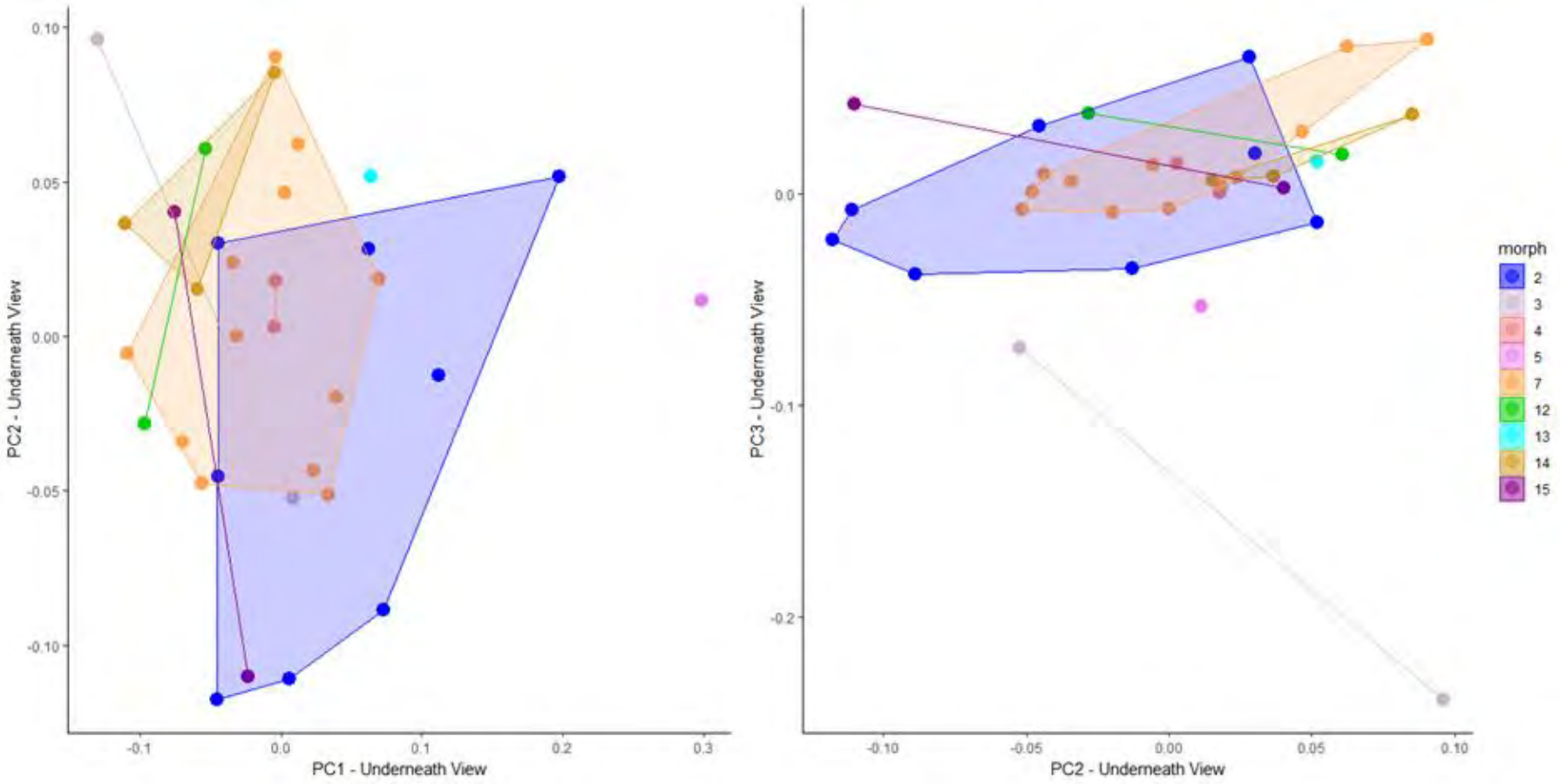

Figure 5-12: PC1, 2 and 3 in underneath view, coloured by morphogroup

In the side view, 69% of variation in morphogroups is explained by PC scores (McFadden R^2=0.69, X^2=83.4, p< 0.001). ANOVA showed significant differences in variance of PC scores between morphogroup ($F_{8,24}$ = 7.802, p<0.001), for PC1. Significant Tukey HSD pairwise comparison for PC1 are shown in Table 5-6. For PC2, ANOVA did not find any significant differences.

Table 5-6: Significant results from the Tukey HSD pairwise comparison between morphogroups for side view.

	Morphogroup pair	Difference	Lower Interval	Upper Interval	Adjusted p value
PC1	5-3	-0.345	-0.667	-0.023	0.029
	5-4	-0.411	-0.733	-0.089	0.006
	5-7	0.311	0.037	0.584	0.018
	5-15	0.349	0.027	0.671	0.027
	12-2	-0.217	-0.425	-0.009	0.036
	12-3	-0.288	-0.551	-0.025	0.024
	12-4	-0.355	-0.617	-0.092	0.003
	12-7	-0.254	-0.455	-0.053	0.006
	12-15	0.292	0.029	0.555	0.022
	14-2	-0.198	-0.376	-0.02	0.021
	14-3	-0.27	-0.51	-0.03	0.019
	14-4	-0.336	-0.576	-0.096	0.002
	14-7	-0.235	-0.405	-0.066	0.002
	14-15	0.274	0.034	0.514	0.017

Using MLR, morphogroup cannot be significantly differentiated, using any PC score in any orientation, from morphogroup 4 (i.e. spherical). In the cases where Tukey HSD did not find any significant differences between morphogroups, this is possibly an effect of the sample size (N = 33) and the number of groups (N=9).

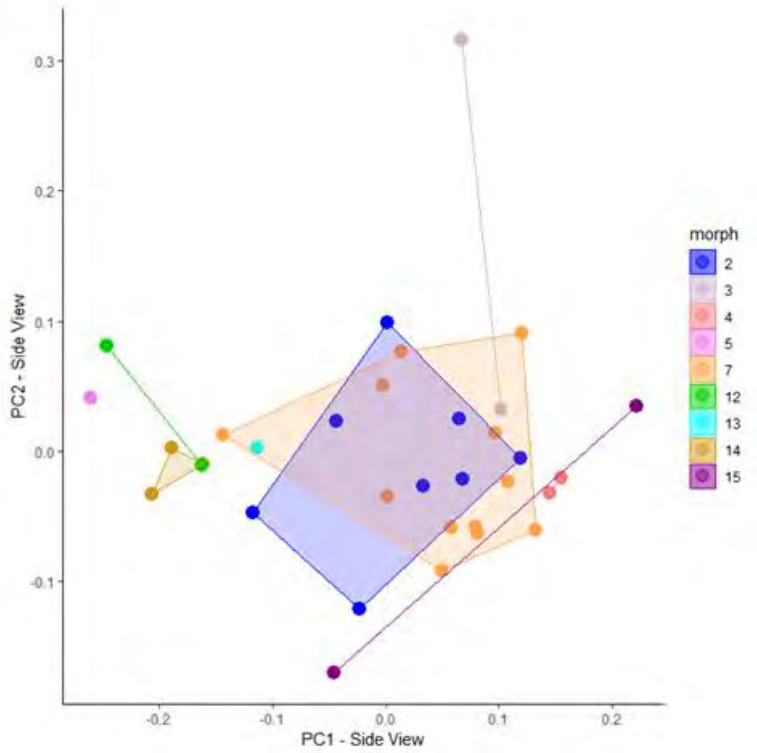

Figure 5-13: PC1 and 2 in sinking orientation viewed from a side, coloured by morphogroup.

Table 4-2: Aze et al. (2011) morphogroups, also see Figure 4-12 below.Figure 4-12

Aze *et al.* morphogroup	Aze *et al.* definition
2	Spinose, globular
3	Spinose globular with supplementary apertures
4	Spinose spherical
5	Spinose, clavate
7	Non-spinose globular
12	Non-spinose, turborotaliform, keeled
13	Non-spinose, turborotaliform, non-keeled
14	Non-spinose, globorotaliform, keeled
15	Non-spinose, globorotaliform, angluconical

When examining the pairwise comparisons in both the underneath view PC1 and the spiral view PC1 morphogroup 5 (spinose, clavate), the sole species *G. adamsi*, has significantly different variance in PC score compared to all other morphogroups. This is likely due to the unusual shape of *G. adamsi* and that it is the only species in morphogroup 5. Morphogroup 5 is also separated from morphogroups 3,4,7,15 (spinose globular, spinose globular with supplementary apertures, non-spinose globular, Non-spinose, globorotaliform, angluconical respectively) in the side view PC1. This difference could be due to the protrusion of the final chamber of *G. adamsi* or alternatively the angle at which the foraminifera sinks. In the spiral view PC1 morphogroup 3 is separated from morphogroup 12 (Non-spinose, turborotaliform, keeled), this suggests that in the spiral view the spinose globular species are different shapes to the keeled turborotaliforms. As with morphogroup 5, morphogroup 12 only has one species representing it (*F. lobata*). Morphogroup 3 has two species present, one of which is *G. fistulosus*, which is found at the extremes of spiral view PC1. Observing

the back-transformed PC plots (e.g.: Figure 5-7) it is possible to see that variance in the PC1 axis equates to how rounded the shape is overall. Morphogroup 12 species tend to be tear-drop shaped, whereas species belonging to morphogroup 3 tend to be more compact and rounded (Examples in Figure 5-14).

Figure 5-14: F.lobata and G.conglobatus, examples from morphogroup 12 and 3 respectively.

In the spiral view PC2, morphogroups 2 and 3 differ from one another, which is surprising given that the major difference between the two groups is the presence of supplementary apertures. Morphogroup 2 is spread over a large range of PC scores. *G. nepenthes* (13) is probably responsible for this significant difference due to its low PC2 value of <-0.2. The low PC2 value of *G. nepenthes* is attributable to the large final chamber. The species has a high trochospiral growth pattern, so most earlier chambers are in a tight coil, but the final chamber protrudes beyond this, producing a snail-shell-like silhouette (Figure 5-15).

Figure 5-15: Spiral view of G. nepenthes*, showing the enlarged final chamber (far right) giving the species a snail-shell-like silhouette*

In underneath view PC2, there are significant differences between morphogroup 3 and all other morphogroups (2, 4, 7, 12, 13, 14, 15). PC2 of the underneath view of sinking, shows whether the foraminifera is more or less rounded and if the movement away from round is towards an elongated or flattened form. Again, this difference in variance could be due to the presence of *G. fistulosus* in morphogroup 3.

In the aperture view PC1, only morphogroups 7 and 14 had sufficiently different variance in PC scores that they were separated from each other. This separation is due to the short tapering disc like shape of morphogroup 14 compared to the rounded form of morphogroup 7. This leads to the two morphogroups occupying different areas in morphospace. Ultimately this difference is due to a difference in the coiling pattern, with morphogroup 14 having a very low trochospiral, whereas morphogroup 7 has a higher trochospiral pattern (i.e. the angle between chambers in the z axis is relatively high, e.g.: Figure 5-16).

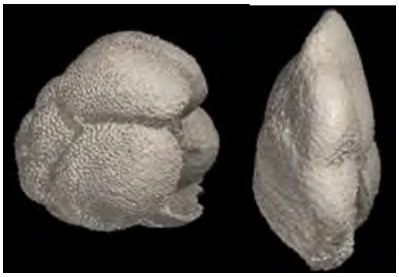

Figure 5-16: D. altispira and H. margaritae highlighting how the differences in coiling pattern result in different shapes. For more examples see Figure 4-12.

In the side view morphogroup 12 is separated from morphogroups 2, 3, 4, 7 and 15. Much like morphogroup 14, which is separated from morphogroups 2, 3, 7 and 15, this appears to be that these two groups occupy different regions of morphospace. As with the differences in aperture view, this is due differences in the coiling patterns between these morphogroups (12 and 14) and all other morphogroups.

In summary, GM and morphogroups do not show much agreement. There is limited separation between different morphogroups within morphospace, with species in the same morphogroup being far apart in morphospace. This is likely due to the nature of the morphogroups, which are qualitative character-based quantifications of shape, whereas GM is a continuous quantitative quantifications of shape.

5.1.4Comparison of GM, EFA, and other measures of shape – summary

Assuming that GM and EFA produce a reliable shape description of the foraminifera in each orientation, the morphogroups of Aze *et al.* (2011) do not describe the species' shape well. There is limited separation of morphogroups in morphospace, using both GM and EFA PC scores. This is likely due to the broad nature of the morphogroup categories. This limited separation is expected for morphogroups 2 and 7 (spinose globular and non-spinose globular), which might be expected to not be separated from the spherical species (morphogroup 4). However, it might be expected that morphogroups 14 and 15 (keeled and anguloconical globorotaliforms respectively) would be separated from the rest of the morphogroups in some orientation, yet this is not the case (Figure 5-10and Appendix 9.3.7 Figure 9-43 and Figure 9-44).

When comparing PC scores to CSF there are some general trends, but as previously expressed there are issues with using CSF, as it relies on the use of linear measurements which may be equal for differently shaped species. Additionally, not only could the linear measurements be similar, but the overall CSF value could be equal for different shapes (see examples in Figure 3-6). It should be noted that CSF correlates better with EFA PC scores than with GM PC scores.

Previous studies have suggested that EFA is the best technique for identifying members of species (Bocxlaer and Schultheiß, 2010) from other species in unornamented gastropods. However, Van Bocxlaer and Schultheiß (2010) found that semi-landmark approaches, such as the one used here, is better for more ornamented species as these approaches do not suffer from a loss of detail during

the alignment procedure unlike EFA. For the species used in this analysis, the differences between EFA and GM are relatively limited with the exception of the underneath view of the sinking orientation. Additionally, *G. adamsi* is an outlier in both sets of analyses in the spiral view, where the ornamentation of this species is most prominent suggesting that any loss of detail in the EFA is relatively small.

5.2 Conclusions

Both GM and EFA quantify shape, the methods in which they do this is slightly different but has similar underlying principles. In this study, the shape of different species varies considerably from the near spherical *O. universa*, to the elongated *G. adamsi* and wide spread *G. fistulosus*. EFA has the advantage that it captures these broad differences and requires general alignment of specimens to be similar, but not exactly the same. However, EFA fails to capture the subtle changes in morphology (Van Bocxlaer & Schultheiß, 2010), which could be important in determining sinking velocities, the ultimate reason for performing shape analysis. GM requires shapes to be correctly aligned and assumes there is homology between semilandmarks (i.e. landmark 10 is in the same place on all specimens). In this study the semilandmarks are place from the same starting point and then equidistant around the outline. Whilst this may not provide strict biological/functional homology (a problem associated with all outline GM based methods), the landmarks are mathematically homologous. Therefore, in subsequent analyses involving shape it would be prudent to test the effect of shape on sinking velocities using GM PC scores, as these capture all of the variation achievable using EFA but also the more understated variation which could be important in influencing sinking velocities.

Chapter 6 Phylogenetic Comparative Analyses

6.1 Aims for the chapter

The relationships between sinking velocity and various parameters (e.g. length, density, shape etc.) have thus far been explored with statistics which do not account for the fact that the data points are not truly statistically independent, as the data are collected from species which have a shared phylogenetic history. As such, in this chapter the findings from Chapter 3, 4 and 5 will be re-analysed within a phylogenetic context. This allows the identification of trends, which are not seen simply due to shared ancestry. Here, parameters have been measured from the empty dead tests of foraminifera, which does not replicate the state of the living organism, upon which evolutionary selection takes place. Therefore, the inferences made here should be viewed with the view point that living foraminifera may experience selection on traits which have not been included in the work conducted within this thesis.

First, the dataset compiled from the previously published studies (as used in Chapter 3) will be subjected to phylogenetic comparative analysis. In this chapter, two Phylogenetic Comparative Methods (PCM) are used: Phylogenetic Generalised Least Squares (PGLS) and Markov Chain Monte Carlo Generalised Linear Mixed Models (MCMCglmm). Then, the influence of shape on sinking velocities obtained in Chapter 4 is examined, but instead of examining the effect of sinking velocity directly, C_{DI} is used. C_{DI} was developed in Chapter 4 as a novel drag coefficient which includes sinking velocity in its calculation.

In order to identify the influence of shape on sinking velocity, the most appropriate orientation to quantify the shape of the foraminifera has to be found first. As in Chapter 5 this chapter considers two orientations (with each view leading to several PC axes (see Chapter 5): Sinking orientation, (giving two views: below and from a side); and 'standard' orientation (with spiral and aperture views). These PC axes are then used as independent variables in MCMCglmm, using C_{DI} as the dependent variable. These models can then be compared to find the orientation and PC axes that best quantify C_{DI}. The use of MCMCglmm also permits phylogenetic relationships between the species to be accounted for. Considering phylogenetic relationships in this way shows if a relationship between, in this case, C_{DI} and shape is due to shared ancestry or to separate evolutionary processes.

6.2 Introduction

Phylogenetic Comparative Methods (PCM) are a framework for studying species, populations or individuals within an evolutionary context (i.e. accounting for relatedness) (Grafen, 1989, 1992; Joy *et al.*, 2016). PCM aim to elucidate the mechanisms behind the diversity of life. Whilst PCM are a separate field of study to phylogenetics (the reconstruction and study of relationships between species), the two are intertwined (Joy *et al.*, 2016). With newer generations of DNA sequencing

producing more accurate, higher resolution phylogenies the relationships between species are becoming better understood (Joy *et al.*, 2016) and therefore the driving mechanisms behind the diversity of life can be explored in a more meaningful manner. Increasingly PCM are being applied to a variety of statistical methods to account for shared ancestry, including approaches such as phylogenetic regressions (O'Meara, 2012). Here, phylogenetic regressions are used to assess the relationship between shape and C_{DI}.

Most traditional statistical tests assume that each of the data points within the test group are independent of one another. However when considering species, it is important to remember that they have shared history (i.e. a phylogenetic relationship) and are therefore non-independent (Revell, 2010). For example, the distribution of a character amongst species could be due to shared ancestry or due to evolutionary processes, such as convergent evolution (Figure 6-1). The use of phylogenetically controlled methods allows for the true correlations between data to be found.

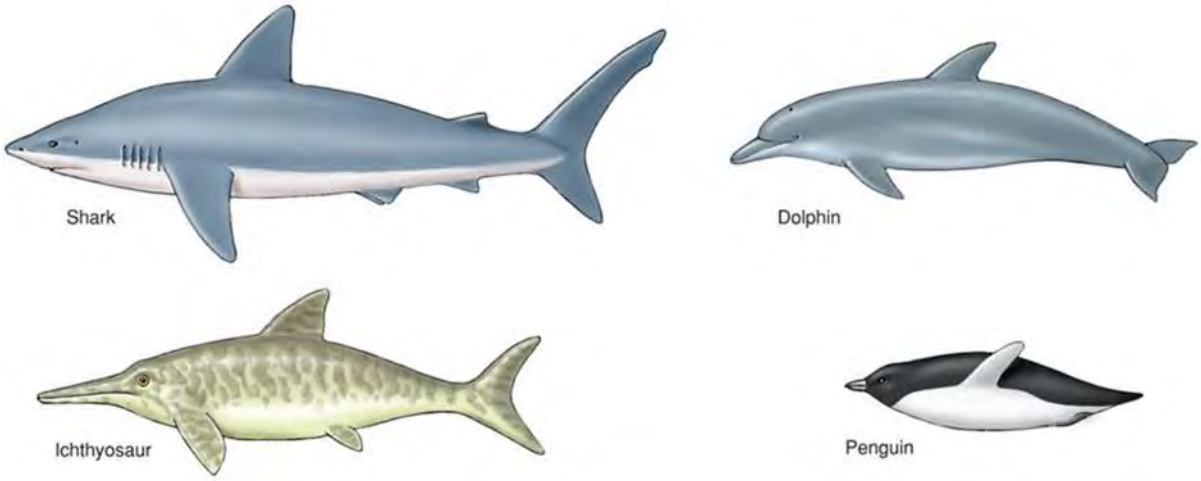

Figure 6-1: An example of convergent evolution of streamlining across distantly related taxa. Large aquatic fish, mammals, reptiles, and birds independently evolved a torpedo-like body shape to minimise drag while swimming.

To illustrate phylogenetic statistics, a simulated foraminifera phylogeny (or tree, Figure 6-2) will be used. This tree is composed of twenty (t1-t20) taxa and the phylogeny shows their relationships. Each taxon has two characters, one continuous (length of a chamber) and one discrete (presence or absence of spines). In this (hypothetical) example, the hypothesis that is being tested is that the presence of spines will result in longer chambers. As can be seen in Figure 6-3, the taxa with spines have longer chambers than those without spines. This result is confirmed with an ANOVA, which shows the difference is significant ($F_{1,18}$= 4.608, p =0.0457).

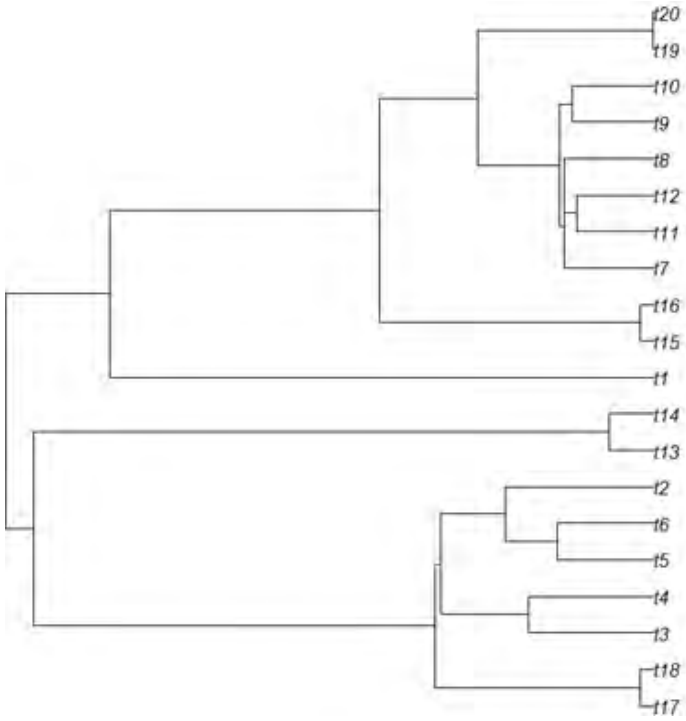

Figure 6-2: An example phylogeny with twenty taxa (t1 – t20)

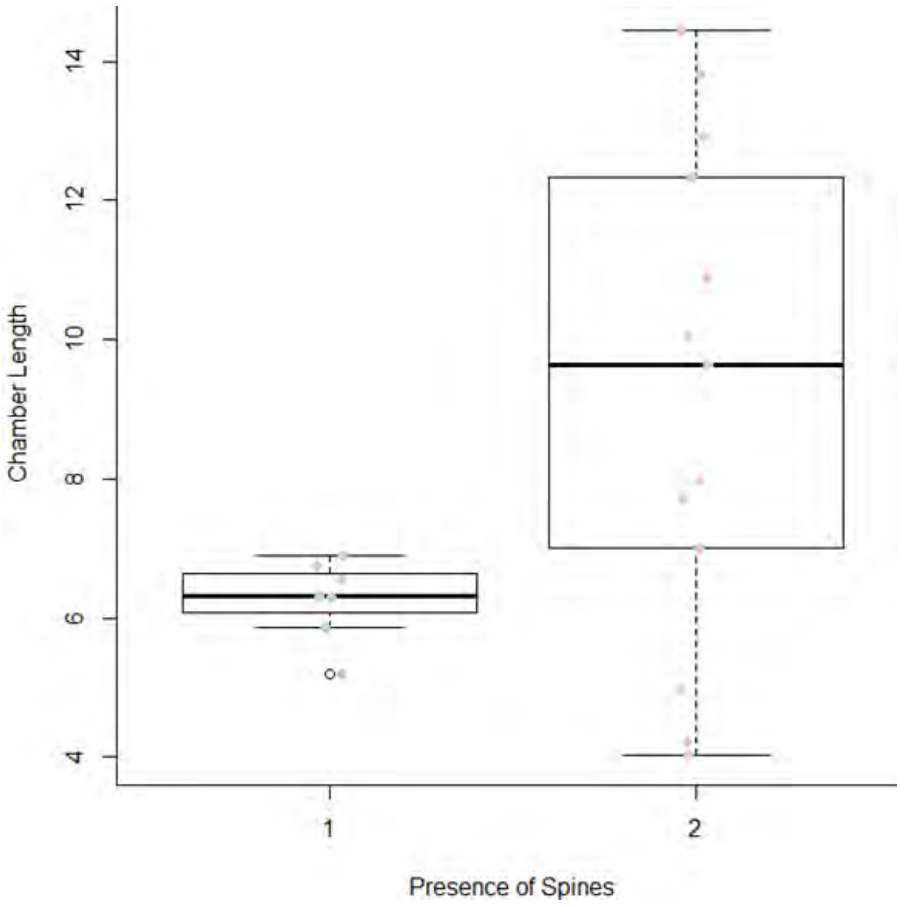

Figure 6-3: Chamber length and absence (1) or presence (2) of spines.

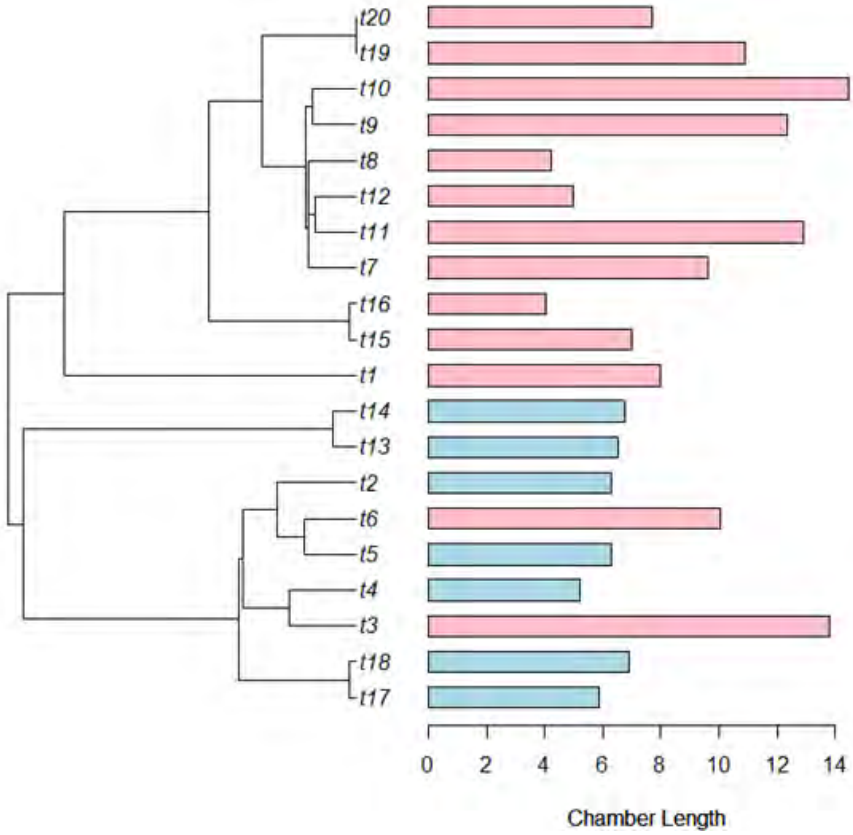

Figure 6-4: The phylogeny with the absence (light blue) and presence (pink) of spines and with each taxa's chamber length (µm) plotted next to it. There is a tendency for shorter chambers to not have spines, but there is no trend with the presence or absence of spines when phylogeny is accounted for due to the clustering of the spines within closely related taxa.

However, when a phylogenetically controlled analysis (a Phylogenetic Generalised Least Squared regression, PGLS) is performed, it becomes clear that the presence of spines does not affect the length of the chamber ($F_{1,18}$= 0.9601, p=0.3401) and, in fact, the presence of spines is simply due to shared ancestry (Figure 6-4). So, an ancestor to the lower branch (containing t14, t13, t2, t6, t5, t4, t3, t4, t18, t17) did not have spines whereas the ancestor to the upper branch did while taxa t6 and t3 have independently evolved spines.

6.2.1 PGLS

PGLS is an adaptation of Generalised Least Squares modelling, which can be used for continuous dependent variables (Nunn, 2011). PGLS allows testing under different modes of evolution, by fitting different distributions of explained variance, for example using a Brownian motion mode of evolution (a random path), or Ornstein-Uhlenbeck (OU) i.e. evolution towards one or more adaptive peaks (Nunn, 2011; Freckleton, Harvey and Pagel, 2016)

Whilst using PGLS allows for similarity due to relatedness to be accounted for in the statistical testing (Grafen, 1989; Nunn, 2011) only one value per variable per species can be used. This requires species averages (e.g.: a species average sinking velocity) to be generated from the dataset. MCMCglmm can also be used to control for phylogeny (Hadfield, 2010a, 2010b), but allows for the testing of more than one value of a trait per species.

6.2.2 MCMCglmm

An MCMCglmm (Monte Carlo Markov Chain generalised linear mixed model) is a Bayesian approach to generalised linear mixed models that can incorporate nested correlations between datapoints (i.e. phylogenies) making it equivalent to phylogenetic regressions (Hadfield, 2010a, 2010b, 2015). Crucially for this study, MCMCglmm can conduct PGLS-like analysis, but allows the inclusion of more than one data point per species, so within-species effects can be included. This permits more of the variation to be explained, compared to the averages used for PGLS. In addition, MCMCglmm allows for the inclusion of random effects. This is useful for the data obtained in Chapter 3, so that the source of the data (i.e. which study the data comes from) and the sample type (i.e. if the foraminifera test was a planktonic specimen, ashed-planktonic or picked from a sediment sample) is controlled for.

6.2.2.1 *What are Bayesian Statistics?*

In contrast to frequentist methods which consider the probability of an outcome, Bayesian methods instead examine the probability of parameter values conditional on observing the data. For instance, if phenomenon X is seen then Y and Z must have occurred. Bayesian statistics assesses the probability that Y and Z could have occurred. To find the probability, distributions of probabilities from previously observed events from previous cases (prior distributions) are included, thereby allowing current knowledge to inform the process. The whole process is summarized as updating prior beliefs, $P(A)$, after considering new evidence. This is formalised by Bayes' Theorem:

$$P(A|B) = \frac{P(B|A) \cdot P(A)}{P(B)}$$

A represents a proposition (e.g.: a coin lands on tails 50% of the time) and B is the evidence or new data which needs to be included (e.g.: a record of the previous coin flips). $P(A)$ is the prior probability of A; this indicates the beliefs of A before evidence is taken into account. $P(B|A)$ is the likelihood function, which quantified the extent which the evidence (B) supports the observation (A). $P(A|B)$ is the posterior probability, i.e. the probability that the proposition A occurs (e.g.: the coin landing on heads) after accounting for the evidence (B).

A Bayesian Statistician building a model begins with a prior distribution. For example, this could be a probability distribution of foraminifera sinking velocity *before* the collection of any data in a new study. For example, it is known that the sinking velocity (U) of *species A* must be between 0.5m·s^{1} and 0.01m·s^{-1} (due to physical constraints, as explored in previous chapters), and it is more likely to lay somewhere in the middle of this range, based on knowledge from other studies. This distribution of possible sinking velocities (which are normally distributed) is the prior distribution. After collecting the sinking velocities of some foraminifera (e.g.: a sinking velocity of a random sample of *species A*), the prior distribution can be updated to include this new information, creating

a posterior distribution. Using the posterior distribution there can be a Bayesian probability estimate of the value of *species A*'s sinking velocity which could be:

$$P(0.06\,m \cdot s-1 \leq U \leq 0.1\,m \cdot s-1) = 95\%$$

That is to say, the probability of the sinking velocity being between 0.06 $m \cdot s^{-1}$ and 0.1 $m \cdot s^{-1}$ could be 95%. In summary, Bayesian statistics allows the understanding of a statistical problem to be updated according to the new data that is collected. By changing the information added (i.e. altering the prior distribution) the estimates are improved.

In contrast, a Frequentist statistician can only make probability statements about sampled data, i.e. a confidence interval, which describes how likely it is that the value obtained is the 'true' value. Using Bayesian statistics allows not only for a credible interval (equivalent to a confidence interval) to be applied to the estimate but also allows for the associated error to be included.

6.2.3 Details of MCMCglmm

Monte Carlo (MC), the first "MC" of MCMC, is a method of estimating a distribution by drawing random samples from it and calculating their mean (van Ravenzwaaij, Cassey and Brown, 2018) These means of random samples are used to inform the next random choice (this is the second C, the "chain" in MCMC), so the current choice is informed by the *only* previous choice (denoted by the second M: "Markov). Generalised Linear Mixed Models (glmm) allow analysis of data that is not normally distributed and allow inclusion of random effects into their analyses (Bolker *et al.*, 2009). By using MCMCglmm it is possible to account for phylogeny (Hadfield, 2015), in which none of the variables are truly independent as they have shared history. This makes MCMCglmm a useful tool to investigate the data which have been collected in this work.

More specifically, MCMCglmm uses pre-set Bayesian framework parameter estimates (priors) generated from a *prior* distribution and the fit of the data is assessed using model likelihood. This process is repeated using a different set of parameter estimates (drawn from the same distribution of priors as the first set), the parameters that fit best are then recorded. This process is repeated for the number of iterations specified, so that the models which fit the data better are visited more than the models which fit the data less well. A posterior distribution of the models visited is then generated, this shows the number of visits in proportion to the fit of each model. During the "burn-in" phase with each iteration the models 'explain' the data increasingly well, until the chain converges to a stable set of values and a distribution of values is determined (for an example, Figure 6-5). The burn-in data are then discarded, and using the models chosen during this period the process is repeated. The posterior chain is sampled at specified intervals to reduce autocorrelation and to generate an effective sample size of posterior values.

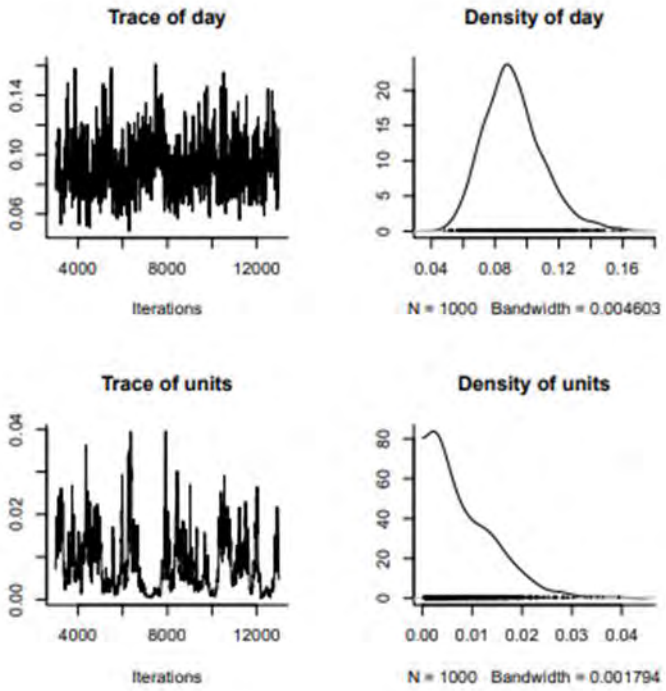

Figure 6-5: From Hadfield (2010b) *at the top an example showing convergence of a chain, whilst at the bottom, the residual variance shows strong autocorrelation (evidenced by the peaks and troughs), indicating more iterations are required.*

6.3 Phylogenetic analysis of the previously published data

6.3.1 Material and Methods

6.3.1.1 *Material*

The same dataset as in Chapter 3 (see section 3.3.1) is used, with average values calculated for each species for the PGLS, while for the MCMCglmm all the data were used. As before, all continuous variables except CSF were log transformed (Log_{10}) for analysis.

Phylogeny

The phylogeny of macroperforate foraminifera constructed by Aze *et al.* (Aze *et al.*, 2011) is used in this study and for consistency their taxonomy is followed. Aze *et al.*'s (Aze *et al.*, 2011) phylogeny is built from the large amount of paleontologically orientated work on planktonic foraminifera. The phylogeny is calibrated using paleomagnetic (changes in the earth's magnetic field) and astronomic (changes in the earth's tilt, detectable in depositions of micro- and nano-fossils) timescales.

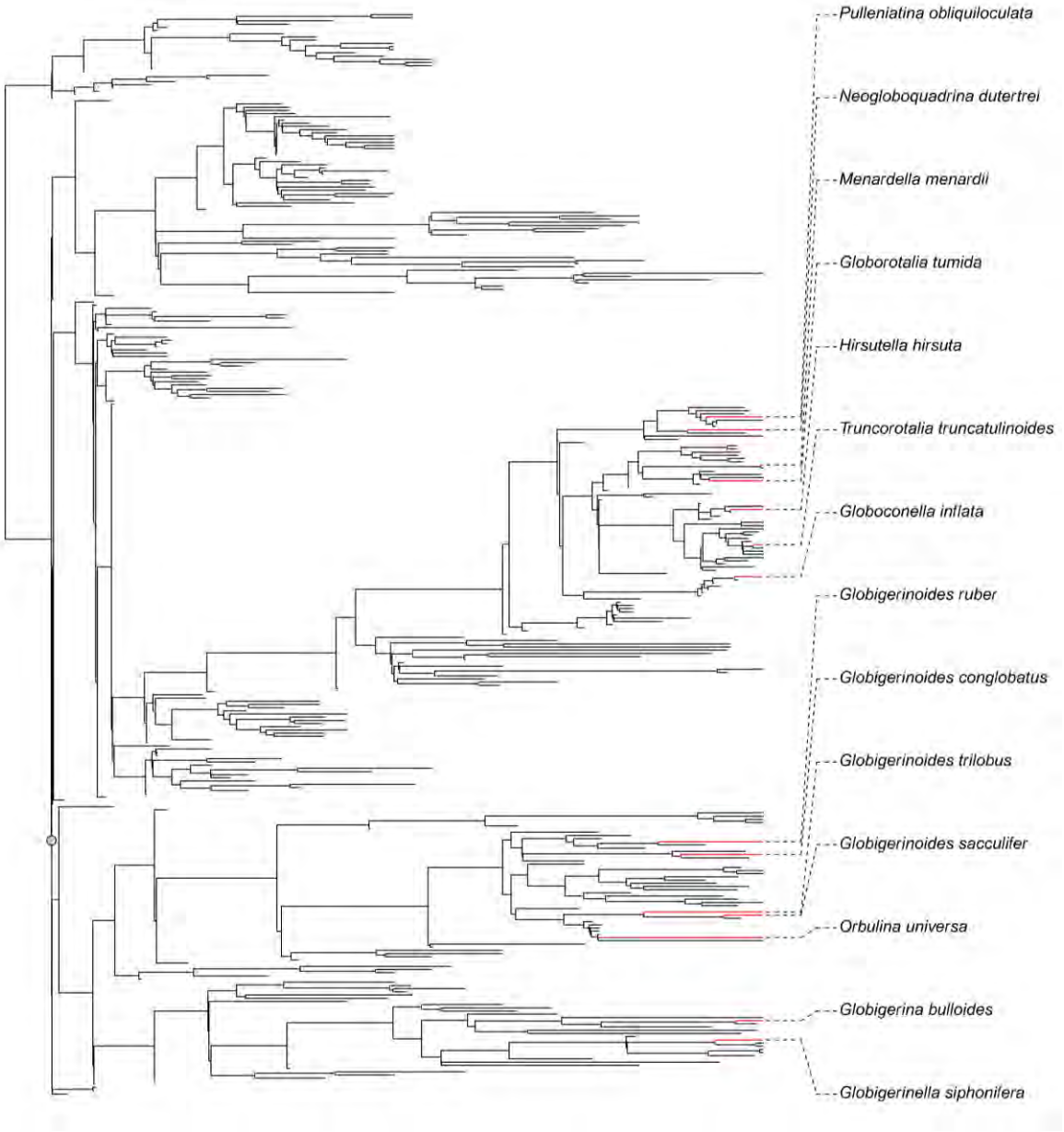

Figure 6-6: Aze et al's phylogeny, with species which are present in the published data labelled and highlighted in red. For ease of viewing, species not used in this analysis are not labelled. On the left of the phylogeny, the most recent common ancestor of the species used is indicated with a pink circle.

Figure 6-7: The trimmed version of Aze et al. (2011) containing only the species for which sinking velocities are reported in the literature.

Since the publication of this phylogeny some adjustments have been made, especially the genus *Globigerinoides*, which has been amended. A new genus was erected, *Trilobatus*, to resolve the polyphyletic nature of *Globigerinoides* (Spezzaferri *et al.*, 2015), but consists only of changes in the species names. As such, the phylogeny was used as published in Aze *et al.* (2011) and trimmed to include only the species of interest using the "drop.tip" function of the R package "ape" (Version 5.1, Paradis *et al*. 2004). The final phylogeny can be seen in Figure 6-7. The sampling of species within the phylogeny are dependent on the species present in previous studies and can be seen in Figure 6-6.

6.3.1.2 *Statistical Analyses*

All analyses were conducted in R using "geiger" (version 2.0.6, Harmon *et al*. 2008), "caper" (version 1.0.1, Orme 2013), "ape" (version 5.1, Paradis *et al*. 2004), and "MCMCglmm" (version 2.26, Hadfield 2010a) packages. Variables included in the models are the same as for the non-phylogenetic tests (Length, density, CSF and morphogroup) for the reasons outlined previously (3.3.1.5).

The fit of PGLS models was assessed using the Akaike Information Criterion (AIC), which considers the relative quality of each statistical model, accounting for both the fit and the simplicity of each, with lower AIC scores being better. The fit of the MCMCglmm's was assessed using the Deviance Information Criterion (DIC) values, which is the Bayesian equivalent to AIC. As with AIC, lower DIC values indicate a better model. The number of degrees of freedom available in the models is not

sufficient to permit examination of interactions between the terms, so here only fixed effects were used.

MCMCglmms were performed using 5.3 million iterations, with a burnin of 300,000 iterations and thinning interval of 1000, to produce a set of ~5000 independent values. The priors for the models run here consist of the variance structures for the error terms (R-structure) and for the random effect (G-structure). Both the R- and G- structures contain the expected covariances (V) between the fixed and random effects, and the degree of belief in the value of V (nu). For both the R- and G-structures V was set to unity and nu to 0.002 following Hadfield (Hadfield, 2010b) to obtain an inverse matrix for shared phylogenetic history. As species was the only random effect specified, only one G-structure value is needed and for this G-structure the prior mean (alpha.mu) and prior covariance matrix (alpha.V) were specified as 0 and 25^2 respectively. In summary, the priors used were: R=list(V=1, nu=0.002), G=list(G1 = list(V = 1, nu = 1, alpha.mu = 0, alpha.V = 25^2)), which are non-informative (Hadfield, 2010b).

Model reduction was conducted for both PGLS models and MCMCglmm models. For PGLS and MCMCglmm manual model reduction was conducted using AIC and DIC respectively; individual terms were removed, and the model fitness measured using AIC/DIC. If the model AIC/DIC was lower (i.e. a better model) then the variable was removed from the model, if the AIC/DIC was higher (i.e. the model was worse) then the variable was re-inserted, and the next variable removed.

MCMCglmm does not provide R^2 values, so pseudo-R^2 values were calculated using the R package "MuMIn" with the function "r.squaredLR". To generate the pseudo-R^2 values a null model with no fixed effects is required. This model is also presented in the results for comparison to the final models for each orientation. As the null model included no fixed effects, only the random effects were present (i.e. species identity). To check that the models had fully converged plots of the estimates of the posterior distribution against iteration number were observed for convergence patterns (i.e. the graph should appear as white noise with no trends).

6.3.2 Results

6.3.2.1 *PGLS*

When phylogenetic relatedness is included in the analysis, there is a significant relationship between sinking velocity and length ($F_{1,12}$= 7.317, p= 0.01913, adjusted R^2= 0.327, AIC = 0.7398). Including measures of shape (CSF, morphogroup) and density results in a significant relationship and a better model ($F_{9,4}$= 9.12, p= 0.0240, Adjusted R^2= 0.849, AIC= -19.5605). Model reduction was used to determine the best fitting model (see Table 6-1 for all models tested). The best model is the full model (see Table 6-2 for a summary of the model).

Table 6-1: Summary of all the PGLS models.

	Model	Model statistics	AIC
1	Sinking Velocity ~ Length + Density + CSF + Morphogroup	$F_{9,4}$= 9.12, p= 0.0240, Adjusted R^2= 0.849	-19.5605
2	Sinking Velocity ~ Length + Density + CSF	$F_{3,10}$= 20.89, p< 0.001, Adjusted R^2= 0.8211	-16.3621
3	Sinking Velocity ~ Length + Density + Morphogroup	$F_{8,5}$= 8.11, p= 0.0169, Adjusted R^2= 0.8139	-15.5094
4	Sinking Velocity ~ Length + CSF + Morphogroup	$F_{8,5}$= 1.65, p= 0.302, Adjusted R^2= 0.2849	3.3332
5	Sinking Velocity ~ Density + CSF + Morphogroup	$F_{8,5}$= 2.602, p= 0.1536, Adjusted R^2= 0.4964	-1.5747

Table 6-2: Summary of the best PGLS model (i.e. lowest AIC score), significant p values are underlined.

	Estimate	Standard Error	t value	p value
(Intercept)	-14.9615	2.386853	-6.2683	0.003305
Length	2.187112	0.614347	3.5601	0.023585
Density	2.558506	0.576807	4.4356	0.011372
CSF	-0.88053	0.598752	-1.4706	0.215351
Morphogroup 3	-0.04623	0.257419	-0.1796	0.866193
Morphogroup 4	0.247797	0.256647	0.9655	0.388962
Morphogroup 6	-0.20518	0.169219	-1.2125	0.292041
Morphogroup 7	0.079721	0.226976	0.3512	0.743134
Morphogroup 14	-0.58366	0.426619	-1.3681	0.243091
Morphogroup 15	-0.43329	0.374662	-1.1565	0.311847

6.3.2.2 *MCMCglmm*

Table 6-3 details the MCMCglmms and their DIC scores. Based on these DIC scores the best model was one with length, density, CSF and morphogroup (see Model 1, Table 6-3). Using this model pMCMC values (equivalent to p values) for longest length (pMCMC $<5\cdot10^{-5}$), density (pMCMC $<5\cdot10^{-5}$) and CSF (pMCMC $<5\cdot10^{-5}$, see Table 6-4), were all significant. Including morphogroup (a non-significant term), in Model 1, improved the model over Model 2.

Table 6-3: The MCMCglmm models, their DIC scores and pseudo-R^2 values.

	Model	DIC	Pseudo-R^2
1	Corrected sinking velocity ~ longest length + density + CSF + morphogroup	-850.0185	0.996
2	Corrected sinking velocity ~ longest length + density + CSF	-849.6558	-0.995
3	Corrected sinking velocity ~ longest length + density + morphogroup	-700.2086	-0.811
4	Corrected sinking velocity ~ longest length + CSF + morphogroup	-570.5454	-0.616
5	Corrected sinking velocity ~ density + CSF + morphogroup	-314.0829	-0.057

Table 6-4: MCMCglmm output from the model with the lowest DIC value, Model 1.

	Posterior mean	Lower 95% Confidence Limit	Upper 95% Confidence Limit	Effective sample size	pMCMC
(Intercept)	-12.6042	-15.0758	-10.3922	1876	0.003
Longest Length	1.54902	1.44339	1.66	2000	<0.0005
Density	1.88425	1.69243	2.10542	2000	<0.0005
CSF	0.72892	0.62184	0.85082	1889	<0.0005
Morphogroup 3	0.02304	-0.68249	0.66508	1785	0.922
Morphogroup 4	-0.04219	-0.7485	0.72168	1819	0.929
Morphogroup 6	-0.04922	-0.53424	0.47952	2000	0.802
Morphogroup 7	0.17179	-0.49582	0.96266	2000	0.576
Morphogroup 14	0.01474	-0.73802	0.81252	2000	0.982
Morphogroup 15	-0.05681	-0.75971	0.76482	2000	0.852

6.3.3 Discussion

From the phylogenetic analyses, the relationship between sinking velocity and length is weaker when using the phylogenetic statistics (R^2= 0.327), than when not accounting for phylogeny (R^2 = 0.463). This would suggest that some of the variance (~13.6%) seen in the relationship between length and sinking velocity is due to closely related species being a similar length and sinking at a similar velocity. It should be noted that the lengths used for these analyses matches with the sinking velocities which are measured in the individual studies (see Chapter 3). Here, the longest length is used for the analyses, as per Chapter 3.

The results from the PGLS and MCMCglmms both indicate that length and density are important factors in determining sinking velocities. It would appear that sinking velocity is predominately determined by length and density, with only a small effect of shape. The findings presented here are in line with the predictions made based on hydrodynamics (section 3.1.3).

One of the limiting factors of this study is the relatively small sample size - ideally there should be a larger number of species included (Freckleton *et al.*, 2002). Freckleton *et al.* (2002), found that log-likelihood ratio increases with increasing number of species, and phylogenetic regression models with fewer taxa/tips gave more ambiguous results, although no suggestions are given for a minimum sample size. In addition to improving the statistical power of the tests, this would allow examination of the evolution of traits and more robust examination of the effect of relatedness in determining the parameters which affect sinking velocity. Another limiting factor is missing data (such as intermediate length in Takahashi & Bé, 1984) and the possible reproducibility problems of different workers specifying orientation for length measurement. Although it should be noted that the specimen of each species is not selected to be representative in terms of length, or any other parameter. This means that the results determined below are valid for these specific specimens and whilst the general finds are likely applicable across foraminifera in general caution should be applied when making generalisations. Whilst an attempt to minimise the differences between

studies was made, this is difficult to do for parameters such as water temperature and salinity which are known to affect sinking velocities (Caromel *et al.*, 2014). Other differences which may introduce more variation to the data are the sample type, source of the sample and how well the sample was cleaned. However, the MCMCglmms included the study from which the data originated as a random effect, which should account for some of this variation. It is not possible to account for the cleanliness of the tests.

When accounting for phylogeny the results agree with the findings from Berthois & le Calvez (Berthois and Calvez, 1960), Fok-Pun & Komar (1983), Takahashi & Bé (1984) and Caromel *et al.* (2014) that length and density are important in determining sinking velocity. The results from PGLS analyses agree with Berger & Piper (1972) and Takahashi & Bé (1984) that shape is not of significant importance. Conversely, MCMCglmm results support the findings of Thoulet (1891), Berthois & la Calvez (1960), Fok-Pun & Komar (1983) and Caromel *et al.* (2014) that shape may be important (as discussed in 3.4.2). MCMCglmm has a greater degree of control over the effects which differ between studies (e.g.: the sample type, the source of the data etc), suggesting that the relationships found using MCMCglmm might be more robust than those found using PGLS.

6.4 Phylogenetic analysis of C_{DI} and shape

6.4.1 Material and Methods

The C_{DI} values for 31 individuals across 30 species of planktonic foraminifera that were calculated as part of this work (Chapter 4) were combined with the geometric morphometric data (i.e. PC scores) for each species (see Chapter 5 for details). Two species (*Globorotalia flexuosa* and *Sphaeroidinellopsis kochi*), for which C_{DI} had been calculated initially, were removed as per Chapter 4. The phylogeny was then trimmed (as above section 6.3.1.1 – Phylogeny) to leave only those species that are present in the current experimental and morphometric work (See Chapters 4 and 5, Figure 6-9).

The 30 species do not give even, nor complete coverage of the phylogeny. As can be seen in Figure 6-8 some branches have reasonable sampling, whilst most branches lack any coverage. This does present further implactions of findings, as the diversity of planktonic foraminifera is not covered by the species which are sampled here. Unfortunately, species for which sinking velocities could be determined was limited by the availability of µCT-scans.

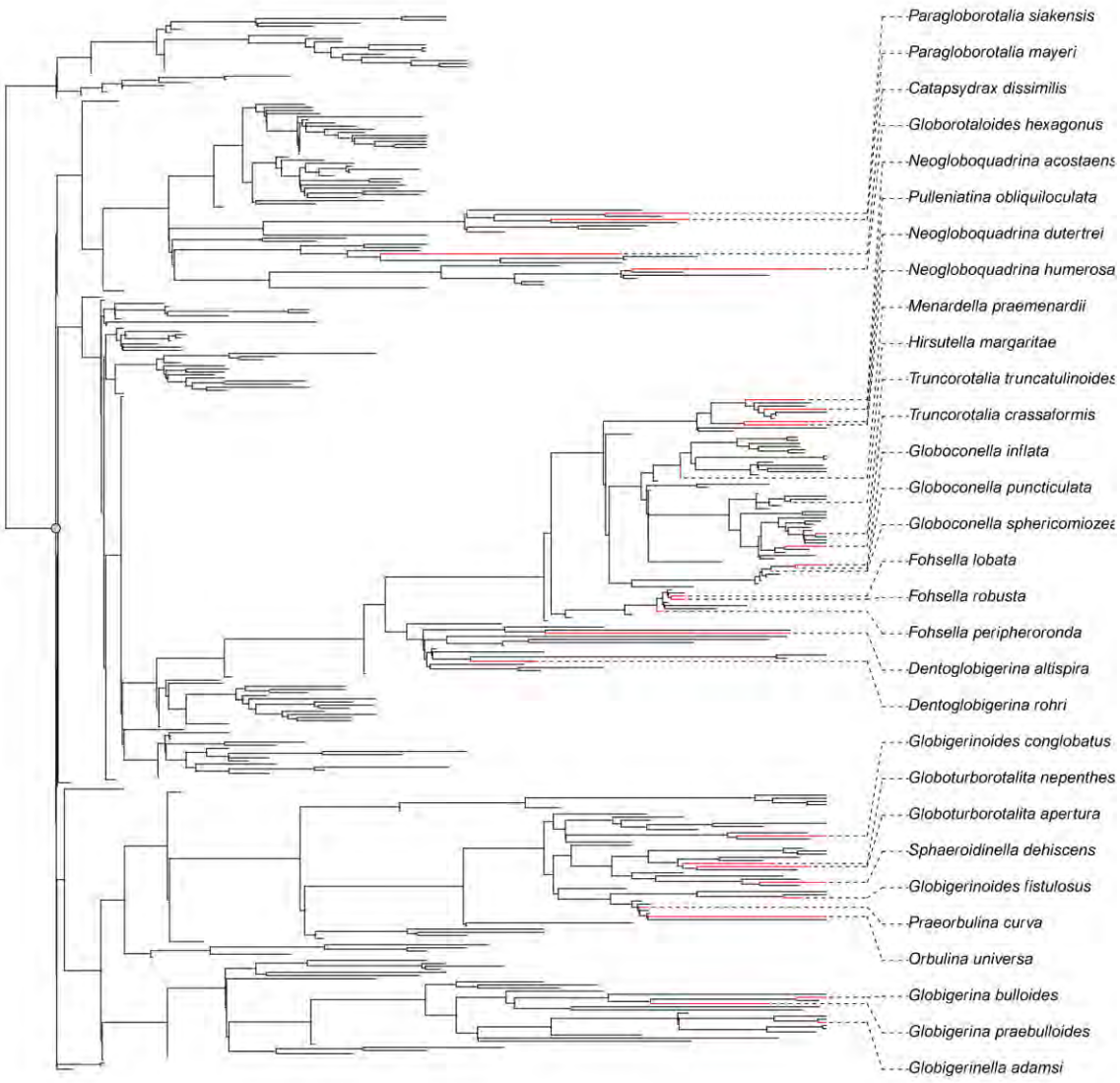

Figure 6-8: Aze et al's phylogeny, with species used in this phylogenetic analysis labelled and highlighted in red. For ease of viewing, species not used in this analysis are not labelled. On the left of the phylogeny, the most recent common ancestor of the species used is indicated with a pink circle.

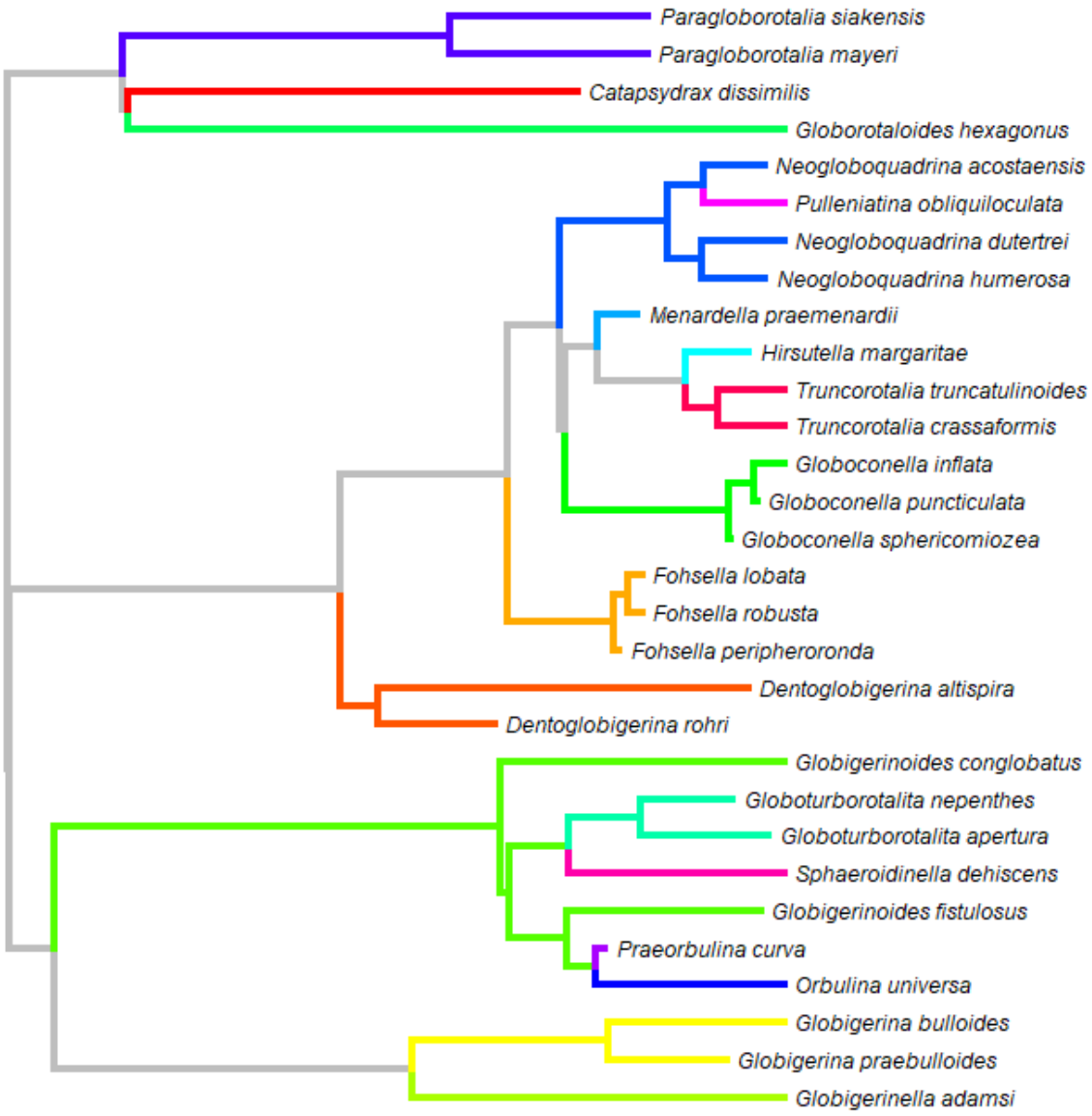

Figure 6-9: The trimmed version of Aze et al's (2011) phylogeny used in the MCMCglmm analyses, for sections 6.4 and 6.4.3. Branches are coloured by genera.

MCMCglmm settings were specified as above (section 6.3.1.2). All models conducted took the form of:

$$CDI \sim shape\ descriptor$$

with more advanced models containing multiple shape descriptors, i.e.:

$$CDI \sim shape\ descriptor\ 1 * shape\ descriptor\ 2$$

Where the shape descriptors were either continuous variables such as PC scores or CSF or the categorical morphogroupings of Aze *et al.* (2011). Models used PC axes from multiple orientations (e.g.: spiral and aperture) as predictor variables. As discussed in Chapter 5, such models are being used as a proxy for the quantification of shape in 3D, whilst only using 2D data.

A model selection process was conducted for the MCMCglmms. There were two base models: the first used the PC scores obtained from the standard orientation, to give five scores in total, two from the aperture orientation and three from the spiral orientation. The second base model used the PC scores from the sinking orientation and, again, five PC scores were used: two from the side view, and three from the underneath view. Model fitness was assessed using DIC (as above), with lower DIC values indicating a better-quality model. Terms to be removed were selected based on interaction level and pMCMC value and DIC compared. If removing a term did not reduce the DIC value then the term was replaced, and the next term removed. This process was continued until no further terms were removed.

6.4.2 Results

6.4.2.1 *MCMCglmm results*

CSF and Morphogroups

Table 6-5: MCMCglmm models, formulae, DIC values and pseudo-R^2.

Model	Orientation	Formula	DIC	Pseudo-R^2
1	N/A	C_{DI} ~CSF	152.24	0.21
2		C_{DI} ~ Morphogroup	163.00	0.08
3		C_{DI} ~ CSF + Morphogroup	150.94	0.40
4		C_{DI} ~ CSF * Morphogroup	153.37	0.42

Models 1, 3 and 4 (Table 6-5) are slight improvements over the null model's DIC of 159.2, but model 2 has a higher DIC value. This suggests that C_{DI} can be better predicted using only species (as a random effect) than by including only morphogroup. The best model includes both CSF and morphogroup but with no interaction between them (Table 6-6, Figure 6-10).

Table 6-6: Results of Model 3, which has the lowest DIC value.

	post.mean	l-95%	CI	u-95%	p
(Intercept)	6.569	-2.979	15.99	5000	0.168
csf	16.753	4.732	28.284	4783	0.005
morph3	3.042	-1.963	7.661	5000	0.192
morph4	-3.419	-8.646	1.517	5000	0.163
morph5	7.026	-0.386	15.387	5000	0.066
morph7	1.811	-1.942	5.595	5000	0.282
morph12	2.107	-3.821	8.32	5000	0.474
morph13	-0.911	-6.948	5.426	5000	0.762
morph14	2.152	-3.256	8.018	5000	0.428
morph15	-0.667	-6.015	4.884	4788	0.803

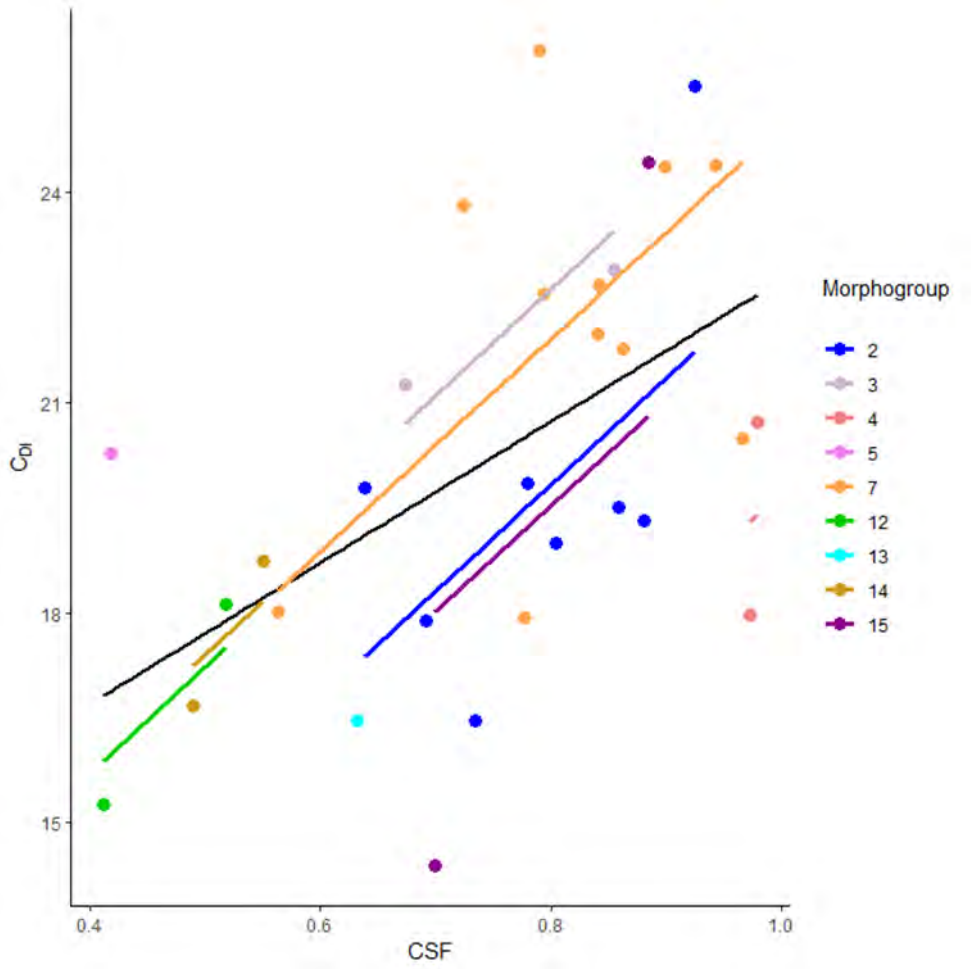

Figure 6-10: The relationship between C_{DI}, CSF and Morphogroup from Model 3 (see Table 6-5). The black line is the relationship between C_{DI} and CSF (i.e. Model 1 in Table 6-5), whilst the relationships between C_{DI}, CSF and each morphogroup (Model 3 in Table 6-5) are coloured appropriately.

Standard orientation

The most complex model took the form:

$$C_{DI} \sim PC1_{spiral} * PC2_{spiral} * PC3_{spiral} * PC1_{aperture} * PC2_{aperture}$$

Meaning that the fixed effects are: $PC1_{spiral}, PC2_{spiral}, PC3_{spiral}, PC1_{aperture}$ and $PC2_{aperture}$ and includes the interactions between all of these variables (resulting in a total of 26 interactions).

The final (reduced) model took the form of:

$$\begin{aligned} C_{DI} \sim\ & PC1_{spiral} + PC2_{spiral} + PC3_{spiral} + PC1_{aperture} + PC2_{aperture} \\ & + PC1_{spiral}{:}\,PC2_{aperture} + PC2_{spiral}{:}\,PC2_{aperture} + PC3_{spiral}{:}\,PC2_{aperture} \\ & + PC1_{aperture}{:}\,PC2_{aperture} + PC1_{spiral}{:}\,PC2_{spiral}{:}\,PC3_{spiral} \\ & + PC1_{spiral}{:}\,PC2_{spiral}{:}\,PC1_{aperture} + PC1_{spiral}{:}\,PC3_{spiral}{:}\,PC1_{aperture} \\ & + PC2_{spiral}{:}\,PC3_{spiral}{:}\,PC1_{aperture} + PC1_{spiral}{:}\,PC2_{spiral}{:}\,PC2_{aperture} \\ & + PC1_{spiral}{:}\,PC1_{aperture}{:}\,PC2_{aperture} \end{aligned}$$

The model results can be found in Table 6-7 and some example traces (showing the model is fully converged) are shown in Figure 6-11. All of the traces are given in 9.4 Chapter 7 Appendices

MCMCglmm traces from Standard Orientation.

Table 6-7: Results for the reduced standard orientation MCMCglmm, significant values are underlined.

	Posterior mean	Lower 95% CI	Upper 95% CI	Effective Sample size	pMCMC
(Intercept)	22.277	19.65	24.749	5204	<0.001
$PC1_{spiral}$	31.282	11.251	52.418	5414	0.0064
$PC2_{spiral}$	-101.434	-142.512	-61.497	5180	0.0004
$PC3_{spiral}$	30.815	-8.757	67.704	5000	0.1144
$PC1_{aperture}$	9.951	2.372	17.183	5000	0.0096
$PC2_{aperture}$	44.413	26.528	61.495	5000	0.0004
$PC1_{spiral}$:$PC2_{aperture}$	1420.447	979.997	1849.448	5000	0.0004
$PC2_{spiral}$:$PC2_{aperture}$	-1119.601	-1613.959	-647.815	5252	0.0008
$PC3_{spiral}$:$PC2_{aperture}$	931.323	413.021	1429.195	4883	0.0028
$PC1_{aperture}$:$PC2_{aperture}$	-253.715	-387.899	-129.524	5000	0.0044
$PC1_{spiral}$:$PC2_{spiral}$:$PC3_{spiral}$	44703.324	21925.579	67669.976	6065	0.0028
$PC1_{spiral}$:$PC2_{spiral}$:$PC1_{aperture}$	12017.452	5992.211	17831.158	5595	0.0032
$PC1_{spiral}$:$PC3_{spiral}$:$PC1_{aperture}$	-4284	-9665.731	1808.214	5417	0.1324
$PC2_{spiral}$:$PC3_{spiral}$:$PC1_{aperture}$	-8727.448	-13319.792	-4449.089	4755	0.002
$PC1_{spiral}$:$PC2_{spiral}$:$PC2_{aperture}$	-30873.509	-46485.587	-14239.5	5000	0.0012
$PC1_{spiral}$:$PC1_{aperture}$:$PC2_{aperture}$	-8945.206	-13103.464	-4945.68	5602	0.0028

This reduced model has a pseudo-R^2 of 0.996 and a DIC score of -47.8, which is an improvement over the null model's DIC of 159.2, and is also an improvement over the model which uses CSF and morphogroup (DIC = 150.94, pseudo-R^2 = 0.400).

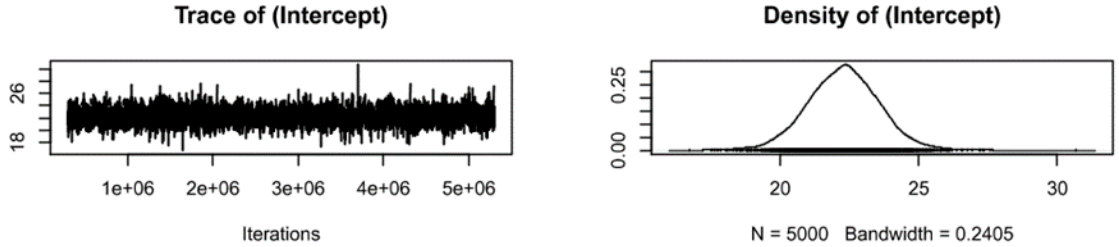

Figure 6-11: The trace of the intercept from the fully reduced model, showing good mixing of the model, as the trace resembles white noise. The graphs for all of the variables are presented in 9.4 Chapter 7 Appendices

MCMCglmm traces from Standard Orientation.

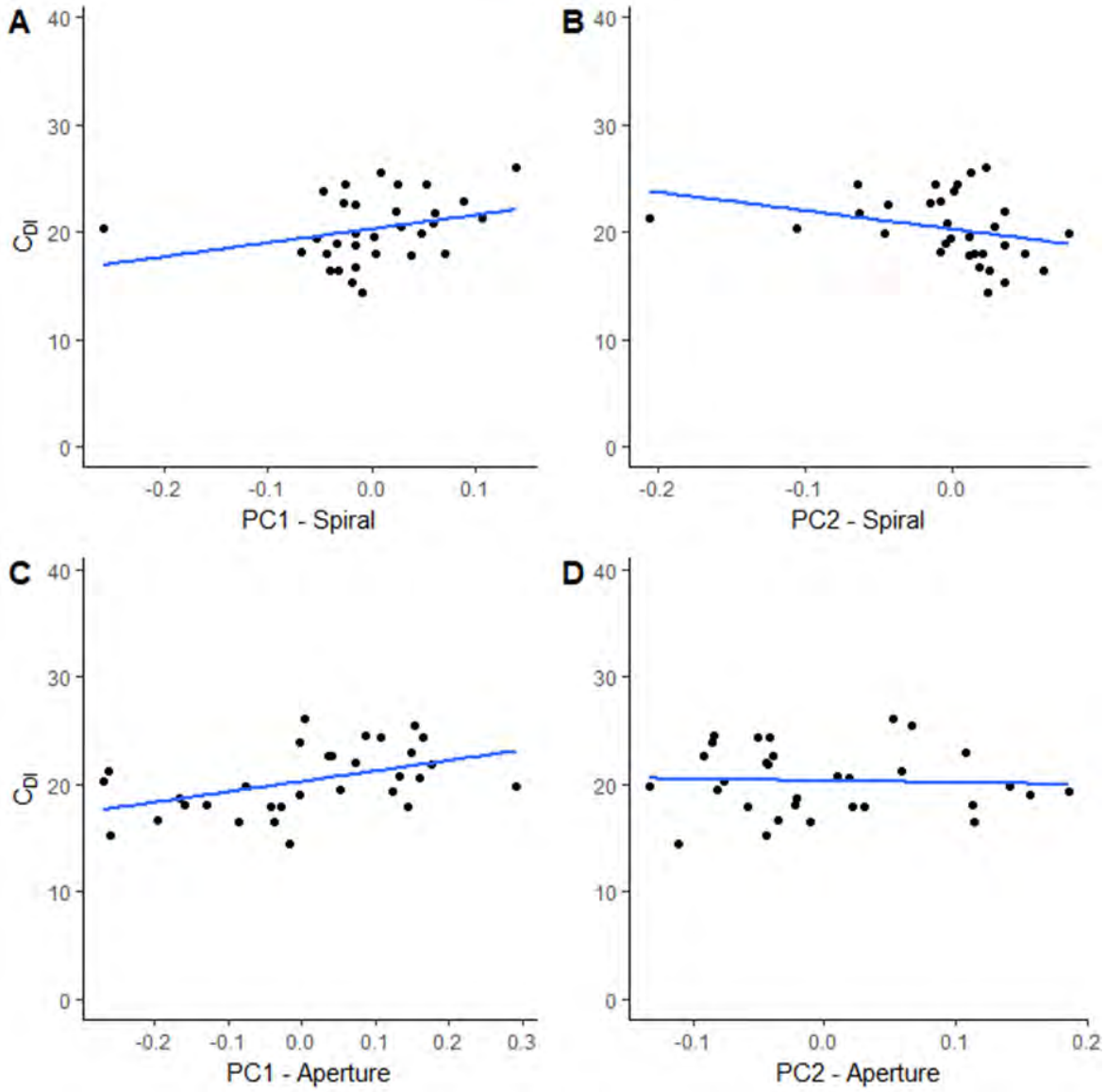

Figure 6-12:The relationships between C_{DI} and the significant PC scores (fixed effects) in the standard orientation model, both spiral and aperture view.

When looking at the fixed effects only (Figure 6-12), there is a positive relationship with C_{DI} and $PC1_{spiral}$ and $PC1_{aperture}$, but a negative relationship with $PC2_{spiral}$ and $PC2_{aperture}$. This means as PC1 values increase so do the C_{DI} values, whilst when PC2 values increase C_{DI} decreases.

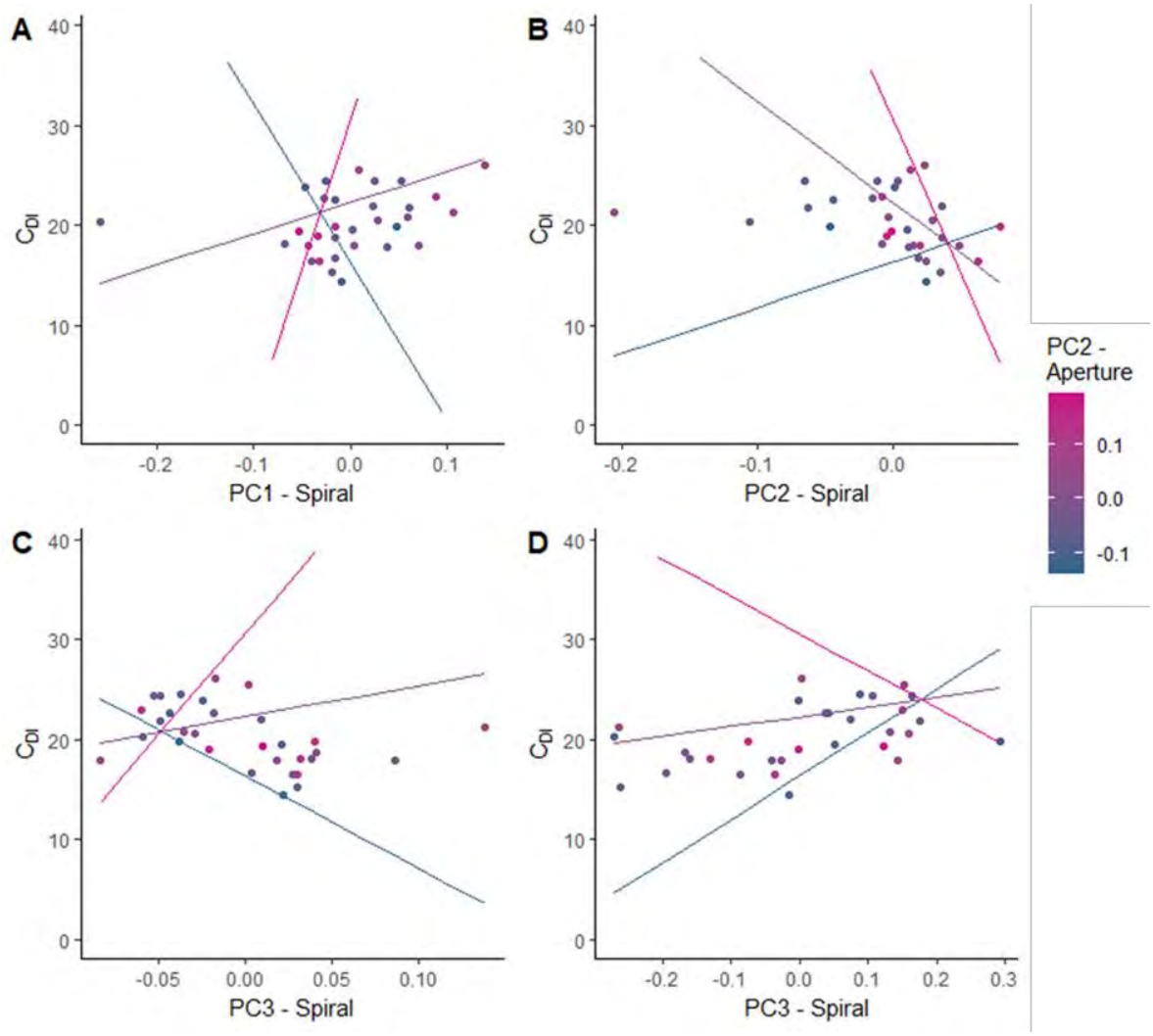

Figure 6-13: Graphs of the significant two-way interactions from the best model using Standard orientation PC scores. Each panel shows C_{DI} plotted with: **A)** *$PC1_{spiral}$* **B)** *$PC2_{spiral}$* **C)** *$PC3_{spiral}$* **D)** *$PC1_{aperture}$. In all graphs the points are coloured by $PC2_{aperture}$ value and lines for high, average and low $PC2_{aperture}$ values are shown. These lines show how the PC on the x-axis interacts with $PC2_{aperture}$ (at the minimum, mean and maximum values observed in the data) to produce the distribution of C_{DI} values seen.*

When looking at the interaction plots (Figure 6-13), increases in $PC1_{spiral}$ when $PC2_{aperture}$ is high, result in a sharp increase in C_{DI} values. When $PC2_{aperture}$ is intermediate in value the increases in $PC1_{spiral}$ result in less dramatic increases in C_{DI} and when $PC2_{aperture}$ is low increases in $PC1_{spiral}$ result in decreases in C_{DI} value (Figure 6-13A). The same general pattern is repeated for $PC3_{spiral}$ (Figure 6-13C). However, the pattern is reversed for $PC2_{spiral}$ with high $PC2_{aperture}$ values resulting in sharp decreases in C_{DI} as $PC2_{spiral}$ increases, moderate decreases when $PC2_{aperture}$ is intermediate and increases in C_{DI} when $PC2_{aperutre}$ is low (Figure 6-13B). This general pattern is repeated for $PC1_{aperture}$ (Figure 6-13D).

Sinking orientation

The most complex model took the form of:

$$CDI \sim PC1_{underneath} * PC2_{underneath} * PC3_{underneath} * PC1_{side} * PC2_{side}$$

And includes the interactions between all of these variables (resulting in a total of 26 interactions).

The final (reduced) model took the form of:

$$C_{DI} \sim PC1_{underneath} + PC2_{underneath} + PC3_{underneath} + PC1_{side} + PC2_{side}$$
$$+ PC1_{underneath}:PC2_{underneath} + PC1_{underneath}:PC3_{underneath}$$
$$+ PC2_{underneath}:PC3_{underneath} + PC2_{underneath}:PC1_{side} + PC3_{sink}:PC1_{side}$$
$$+ PC1_{underneath}:PC2_{side} + PC3_{underneath}:PC2_{side} + PC1_{side}:PC2_{side}$$
$$+ PC1_{underneath}:PC2_{underneath}:PC3_{underneath}$$
$$+ PC1_{underneath}:PC2_{underneath}:PC1_{side}$$
$$+ PC1_{underneath}:PC3_{underneath}:PC1_{side}$$
$$+ PC1_{underneath}:PC3_{underneath}:PC2_{side}$$
$$+ PC2_{underneath}:PC3_{underneath}:PC2_{side} + PC2_{underneath}:PC1_{side}:PC2_{side}$$
$$+ PC3_{underneath}:PC1_{side}:PC2_{side}$$

This reduced model has a pseudo-R^2 = 0.998 and DIC = -35.4738, an improvement over the null model's DIC of 159.2 and to the most complex sinking orientation model (pseudo-R^2 = 0.9767081 and DIC = -8.09922). The significant terms can be seen in Table 6-8 and significant fixed effect and two-way interactions are visualised in Figure 6-15 and Figure 6-16, respectively. The model reached convergence (an example trace presented in Figure 6-14, for all traces from the model see 9.4.2 MCMCglmm traces from Sinking Orientation).

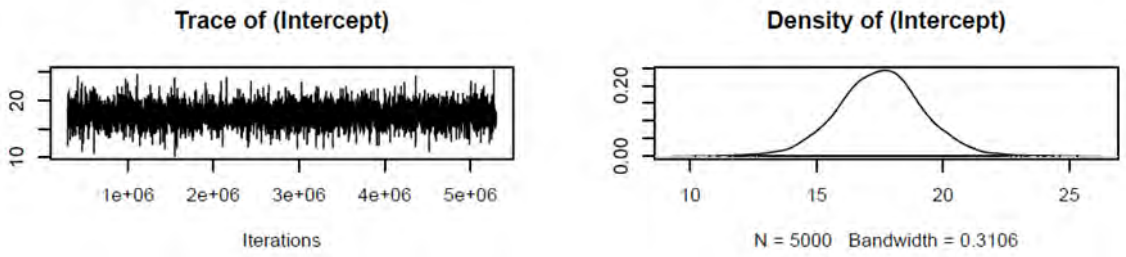

Figure 6-14: Trace of the intercept values from the MCMCglmm model, showing that the model is well mixed. See 9.4.2 MCMCglmm traces from Sinking Orientation for trace graphs of this model.

Table 6-8: The MCMCglmm results of the fully reduced model for the sinking orientation.

	Post mean	Lower 95% CI	Upper 95% CI	Eff. Sample	pMCMC
(Intercept)	17.523	14.19	20.979	5000	<0.001
$PC1_{underneath}$	-25.53	-55.24	3.453	4509	0.0848
$PC2_{underneath}$	-16.542	-53.339	23.038	5000	0.3452
$PC3_{underneath}$	40.957	-22.229	108.162	4798	0.2028
$PC1_{side}$	13.872	-1.436	28.209	5000	0.0564
$PC2_{side}$	28.972	3.106	54.274	4658	0.0396
$PC1_{underneath}$:$PC2_{underneath}$	-252.948	-770.324	255.266	5000	0.274
$PC1_{underneath}$:$PC3_{underneath}$	-1442.264	-2600.081	-216.023	5000	0.0268
$PC2_{underneath}$:$PC3_{underneath}$	1087.418	409.695	1785.15	4801	0.0084
$PC2_{underneath}$:$PC1_{side}$	-261.425	-478.138	-22.264	5000	0.034
$PC3_{underneath}$:$PC1_{side}$	802.165	184.445	1406.606	4793	0.0244
$PC1_{underneath}$:$PC2_{side}$	123.251	-133.627	379.525	5000	0.3124
$PC3_{underneath}$:$PC2_{side}$	-2348.032	-4096.408	-569.096	5000	0.0236
$PC1_{side}$:$PC2_{side}$	-292.921	-502.418	-63.673	4261	0.028
$PC1_{underneath}$:$PC2_{underneath}$:$PC3_{underneath}$	-33170.499	-58992.06	-4196.634	5000	0.0372
$PC1_{underneath}$:$PC2_{underneath}$:$PC1_{side}$	-10939.051	-17247.15	-4227.622	5000	0.014
$PC1_{underneath}$:$PC3_{underneath}$:$PC1_{side}$	-6483.179	-11955.92	-1267.184	4228	0.0368
$PC1_{underneath}$:$PC3_{underneath}$:$PC2_{side}$	33296.78	9937.386	56832.997	5049	0.0228
$PC2_{underneath}$:$PC3_{underneath}$:$PC2_{side}$	31283.544	6331.316	55524.135	5000	0.0304

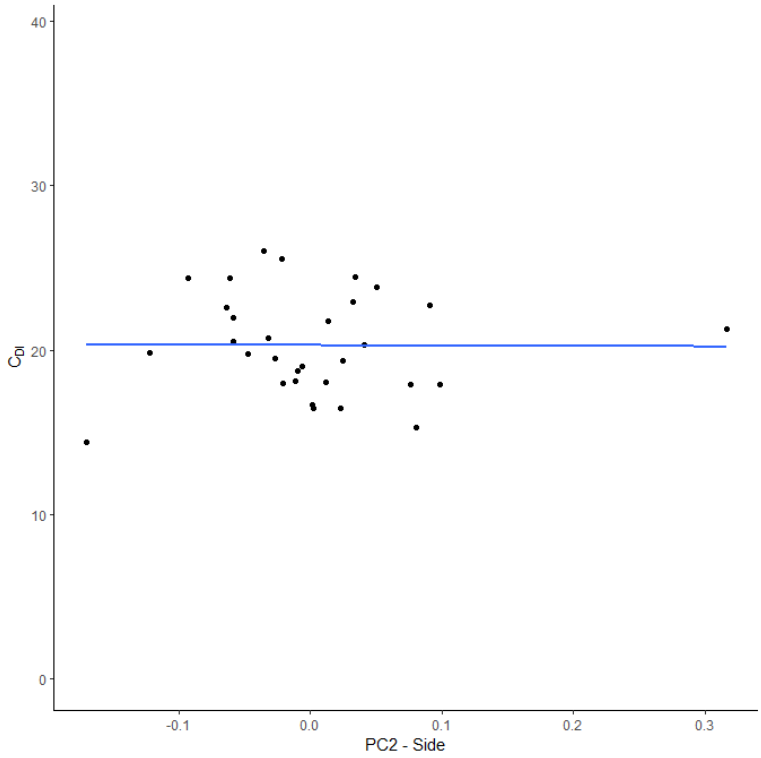

Figure 6-15: The significant relationship (from the reduced sinking orientation model, see Table 6-8) between C_{DI} and $PC2_{side}$ in the reduced model for sinking orientation.

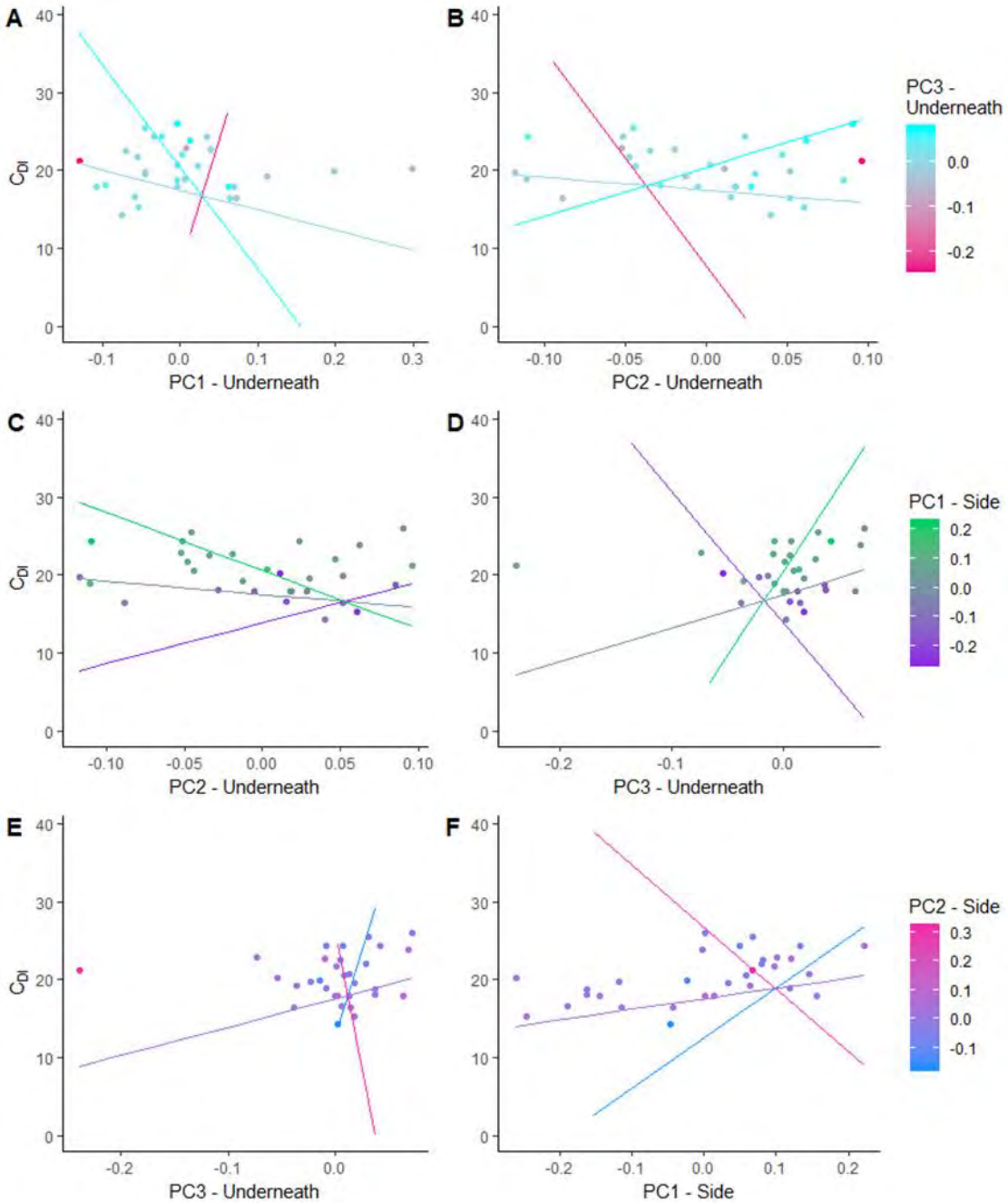

Figure 6-16: Interaction plots for the significant two-way interactions for the reduced sinking orientation model (see Table 6-8): A) $PC1_{underneath}$:$PC3_{underneath}$, B) $PC2_{underneath}$:$PC3_{underneath}$, C) $PC2_{underneath}$:$PC1_{side}$, D) $PC3_{underneath}$:$PC1_{side}$, E) $PC3_{underneath}$:$PC2_{side}$, F) $PC1_{side}$:$PC2_{side}$, for the reduced sinking orientation model. Points are coloured by the PC value as follows Top row, $PC3_{underneath}$; middle row, $PC1_{side}$; bottom row, $PC2_{side}$. Fitted lines are also coloured by the same PC value and are plotted for the maximum, average and minimum PC scores.

When looking at the interactions between $PC1_{underneath}$ and $PC3_{underneath}$ (Figure 6-16A) the following behaviours are seen: when $PC3_{underneath}$ is low, small increases in $PC1_{underneath}$ results in large increases in C_{DI}. The relationship flips from positive to negative as $PC3_{underneath}$ moves from low to intermediate, at which point increases in $PC1_{underneath}$ correlate with decreases in C_{DI}. When $PC3_{underneath}$ is high the relationship becomes still steeper and a given increase in $PC1_{underneath}$ results in a greater decrease in C_{DI} compared to intermediate $PC3_{underneath}$.

The trends seen for the relationship between C_{DI} and the interaction between $PC2_{underneath}$ and $PC3_{underneath}$ (Figure 6-16B) are the opposite of $PC1_{underneath}$ and $PC3_{underneath}$; when $PC3_{underneath}$ is low increases in $PC2_{underneath}$ correlate with decreases in C_{DI}. When $PC3_{underneath}$ is intermediate increases

in $PC2_{underneath}$ correlates with decreases in C_{DI}. When $PC3_{underneath}$ is high, the relationship between $PC2_{underneath}$ and C_{DI} is even steeper.

The changes in C_{DI} as a result of the interaction between $PC1_{side}$ and $PC2_{underneath}$ (Figure 6-16C) can be summarised as: when $PC2_{underneath}$ increases and $PC1_{side}$ is low, C_{DI} increases. As $PC1_{side}$ values become larger, increasing $PC2_{underneath}$ values result in decreases in C_{DI}, with larger $PC1_{side}$ values having a larger effect (i.e. the same increase in $PC2_{underneath}$ results in greater decreases in C_{DI} when $PC1_{side}$ is higher). Changes in $PC3_{underneath}$ and $PC1_{side}$ (Figure 6-16D) cause C_{DI} values to change in the opposite direction to the interaction of $PC1_{side}$ and $PC2_{underneath}$.

At intermediate values of $PC2_{side}$ the interaction with $PC3_{underneath}$ results in increases in C_{DI} values (Figure 6-16E). However, for high $PC2_{side}$ there are large decreases in C_{DI} value and when $PC2_{side}$ is high there are large increases in C_{DI} values, for the same increase in $PC3_{underneath}$. This trend is repeated for the interaction between $PC1_{side}$ and $PC2_{side}$ (Figure 6-16F).

6.4.3 Discussion

From the results of the MCMCglmm model reduction, the best model (using DIC as a metric) is that which uses the standard orientation PC axes. In some respects, this is an expected result - the standard orientation is the one used in the literature and, presumably, has been chosen to display as much variation in the foraminifera test shape as possible in an orientation comparable among species. As discussed in Chapter 4, in this thesis C_{DI} has been developed to include the effects of shape with as little effect of size as possible. With the effect of size removed, the remaining variation in C_{DI} values between species should be due to differences in shapes. It would follow that the sinking orientation would be determined by the entire shape of the foraminifera.

However, when examining the results from the MCMCglmm that used the sinking orientation PC axes, whilst the DIC value is lower than the standard orientation model, the pseudo-R^2 value is slightly higher (0.998 compared to 0.996). This shows that the sinking orientation PC axes capture the variation in C_{DI} slightly better than the standard orientation PC axes. However, the slightly higher pseudo-R^2 value (of the sinking orientation model) is obtained using more interaction terms, hence is penalised in the calculation of DIC. Obtaining the sinking orientation is a substantial amount of work, even if real foraminifera tests are being used. The test must be prepared, sunk, photographed and the images subjected to shape analysis. Comparatively, standard orientation photographs are readily available for most species of foraminifera, and shape analysis is relatively rapid to conduct. Although the aim is to estimate C_{DI} as well as possible, the gain of 0.2% explanation of C_{DI} when using sinking orientation is probably inefficient compared to the use of the standard orientation.

For the standard orientation model, the significant fixed effects are PC1 and PC2 in both the spiral and the aperture views. This suggests that the overall morphology captured in these views is

important in determining C_{DI}. In the spiral orientation changes in the roundness of the outline are described by PC1 and PC2. $PC1_{spiral}$ describes shape changes in the lateral and dorsal-ventral axes, whilst PC2 describes the presence of projections from the outline (see Chapter 5). Based on the hydrodynamic predictions (spheres experience less drag than less spherical objects), it is expected that the roundest shapes ($PC1_{sprial}$ and $PC2_{spiral}$ = 0) will experience least drag. These predictions are supported, as $PC1_{spiral}$ becomes larger (i.e. less wide but taller shapes) the C_{DI} experienced increases and with increasing $PC2_{spiral}$ (i.e. fewer projections, a rounder outline) C_{DI} decreases. This result ties in with the formulation of CSF (Equation 3-10).

Equation 3-10

$$CSF = \frac{diameter_{shortest}}{\left(diameter_{longest} \cdot diameter_{intermediate}\right)^{0.5}}$$

As can be seen, the shortest length is the numerator, placing more importance on this length in the determination of CSF compared to the longest and the intermediate lengths (see Komar & Reimers, 1978). The shortest length is generally assumed to be the height of the object in its sinking orientation. However, this thesis has demonstrated that the effect of the height of the particle extends beyond the basic measurement of length, to an effect of shape (i.e. changes in $PC1_{aperture}$), as the effect of size is removed in the quantification of shape. Within a hydrodynamic context this makes some sense, as the overall drag experienced by a sinking object is affected by the total surface exposed to the fluid and by the shape of the object. This effect varies dependent on size (i.e. the Re regime), with greater influence at lower Re, the presence of this effect in foraminifera shows that the total surface area is important for intermediate Re sinking particles.

Comparing the findings of the shape analysis and the sinking velocities from this study, the weak relationship found between sinking velocity and CSF found in Chapter 3 is echoed here with the pseudo-R^2 of 0.21 for the model including C_{DI} (C_{DI} contains sinking velocity in it calculation) and CSF. As the models containing GM PC scores perform better (i.e. have lower DIC values), this suggest that CSF captures shape variation, but (perhaps unsurprisingly) GM PC scores do so in a way that is more meaningful in this context.

In this study, when the shape of the sinking test is narrower and taller the upper section interferes with the fluid flow as the flow fields come together after the particle passes through it, affecting the formation of the wake behind the particle. This theory is supported by numerical modelling of infinite cylinders with elliptical cross section of varying aspect ratio (AR). Sen *et al.* (Sen, Mittal and Biswas, 2012) found that separation of the recirculating region behind the particle occurs at different Re for ellipses with different ARs. Taller ellipses show separation sooner than ellipses which are shorter (in the direction of flow, Figure 6-17). This separation region reduces the drag experienced by the particle, thereby the C_D (and therefore C_{DI}) would be lower for particles which have this separation region than particles (sinking at the same velocity) which lack a separation

region (Vogel, 1994). It should be noted the models were cylinders (extending perpendicular to the page in Figure 6-17) and thus flows around ellipsoids would differ.

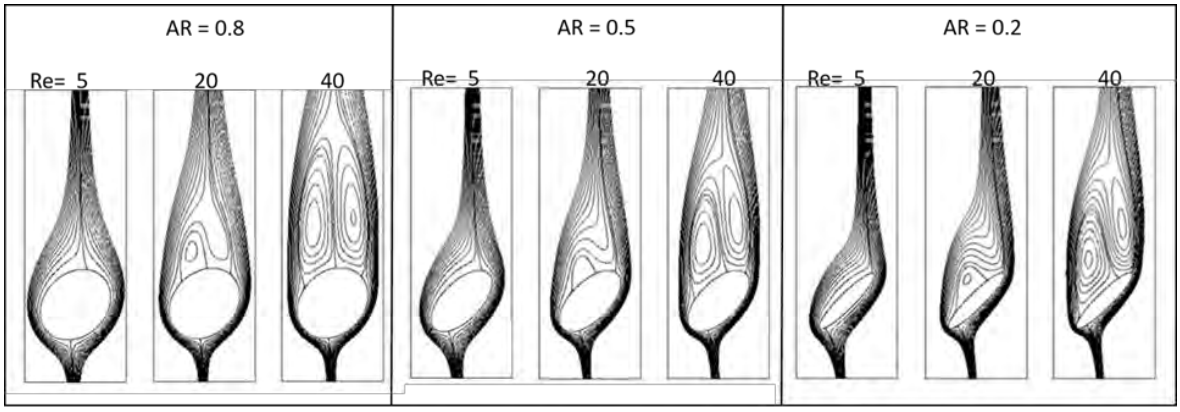

Figure 6-17: The flow patterns from numerical simulations of flow around cylinders of different cross-sectional aspect ratios (from left to right 0.8, 0.5, 0.2) at different Re (from left to right 5, 20, 40). Adapted from Sen et al. (Sen, Mittal and Biswas, 2012).

However, the fixed effects in these models are only part of the picture, individual views and PC axes need to be used with other views and PC axes to describe the total shape of the test. Indeed, the interactions of PC axes help to explain the patterns in C_{DI} values. There is a significant interaction between $PC2_{aperture}$ and $PC1_{spiral}$. In terms of shape changes this means species which are rounder ($PC1_{spiral}$ is close to 0) and have a flat base in the aperture view ($PC2_{aperture}$), experience lower C_{DI} than species at the extremes of $PC1_{spiral}$ and $PC2_{aperture}$. GM analyses remove all elements of size, as does C_{DI}, thus it is possible to see that the shape of the foraminifera in the sinking orientation is important and this effect is independent of size. This result suggests that the entire shape of the foraminifera is important in determining sinking velocity, not just the shape of the projected area. The factors that were determined to be important in determining sinking velocity in Chapter 3 (3.3.2.2) are still accounted for in this new method, as C_{DI} encompasses all of these variables (Equation 4-10).

Chapter 7 General Discussion

7.1 Summary

A review of the literature on sinking foraminifera (Chapter 3) found that foraminifera sink at an intermediate Re. Descriptions of how sinking particles behave are well established for low Re (e.g.: Happel & Brenner, 1983) but for non-spherical particles at intermediate Re theoretical predictions are uncertain at best. Therefore, experimental approaches provide a method to evaluate the relationships between different parameters. When revaluating the literature, relationships between sinking velocity and length, density, volume, and mass were confirmed. There were also some differences in sinking velocity between morphogroups, e.g. Morphogroup 15 (spinose globorotaliform anguloconical, mean sinking velocity is ~0.011) and Morphogroup 2 (spinose globular, mean sinking velocity ~0.008) differ significantly in sinking velcoities. Only some (80% when including density and length in Model 3) of the differences in sinking velocity might be explained using CSF as a measure of shape. By examining linear models predicting sinking velocity from the parameters identified (length, density, volume, mass and shape), length and density appeared to be the most important. These findings fit with the hydrodynamic theory outlined at the start of Chapter 3. The effect of shape (as measured by CSF and morphogroup) was significant, both as a fixed effect and as an interaction term, highlighting that shape does influence sinking velocity.

In Chapter 4 a novel method of measuring sinking velocity of foraminifera was developed, permitting 32 species' sinking velocities to be determined. 3D printing was used to produce scale models, coupled with digital models this allowed the projected area (A_P) of sinking foraminifera to be easily measured *in silico*. By quantifying the projected area in a sinking orientation (as opposed to using an estimated projected area based on maximum and intermediate test lengths) allows better comparisons to be made between species, as the projected areas being compared are hydrodynamically functional. Additionally, the use of µCT scans allowed the precise volume of the test wall (V_{wall}) to be measured. This volume measure is an improvement over the estimates of total test volume generated using formulae for generic geometric shapes. Once again using linear models, significant relationships were found between sinking velocity and shape (as measured by CSF), a relationship which is still present when accounting for mass. Linear models with interactions found that shape interacts with A_P and V_{wall}. However, morphogroup and CSF are limited shape descriptors (as discussed in Chapters 3 and 4). So, to identify the role which shape plays in determining sinking velocity, C_{DI} was developed. While C_{DI} includes only the effects of shape (and not the effects of size, as variables which contain measures of size have been accounted for in the formulation of C_{DI}) on drag (and therefore sinking velocity), it is a dimensionless measure and does not describe the shape of a foraminifera, therefore shape needed to be quantified.

Chapter 5 focused on obtaining shape quantifications using GM and EFA. Most species were found to cluster together with no discernible pattern. Using phylomorphospaces it was possible to see that some species that are (relatively) closely related are very distant in morphospace (e.g.: *Paragloborotalia mayeri, Paragloborotalia siakensis)* Statistical testing confirms that species are more separated than expected given their phylogenetic relationships. These results were the same using either GM- or EFA-based PC scores. Comparisons between CSF and PC scores showed that the variance seen in CSF values could be best explained by GM PC scores in the side view (of the sinking orientation). GM was chosen as the method of shape quantification as it is more able to capture the subtle variations in shape which are lost when using EFA. Most morphogroups overlap in morphospace, suggesting the morphogroup, whilst helpful for systematics, is not a useful measure of shape in this context. Those morphogroups that were significantly separated in morphospace were represented by a limited number of species.

In Chapter 6, the relationships identified between sinking velocity and length, density, CSF, and morphogroup (in Chapter 3) were tested using phylogenetic comparative methods. Two different methods were employed, PGLS using species-averaged values and MCMCglmm using each individual specimens' data. Length and density were confirmed as significant predictors of sinking velocity using PGLS, while MCMCglmm results suggested that CSF is significant in determining sinking velocity, and whilst morphogroup is not significant, including it improved the model. Next the GM PC scores from Chapter 5 were compared to the C_{DI} values obtained in Chapter 4. As C_{DI} is a dimensionless number, to link sinking velocity and shape it is important to find a shape descriptor which explains C_{DI}. The relationship between C_{DI} and the GM PC scores was investigated using MCMCglmm, accounting for phylogeny, by including species as a random effect (with a distribution determined by branch length). It was found that C_{DI} is best described using GM PC scores from the standard orientation, as used in the literature. These results show that the sinking velocity of the foraminifera is affected by the total (i.e. 3D) test shape as shape variation was captured in two orthogonal planes. As the precise relationship between C_{DI} and sinking velocity is known (from its formulation), the way that shape effects sinking velocity can be seen. These findings reflect the findings in Chapters 3 and 4, where the linear models including CSF were able to predict sinking velocity and showed the importance of CSF interacting with other variables. However, in Chapter 5 it was determined that the side view GM PC scores best predict CSF. Thus, it is reasonable to conclude that the effect of 'height' (or more properly; the shape of the foraminifera parallel to the sinking direction) is captured by CSF, but CSF contains limited information regarding the shape of A_P.

7.2 Future Outlook

One potential avenue of research is to examine the sinking velocities of ancestral species to gain a better understanding of the deposition of foraminifera tests over geological time. To this end, using

the admittedly small sample size presented in this work, ancestral state reconstruction was conducted. Here, the results from this speculative work are presented. In the future a large number of species and larger number of specimens from within a species would enable such analyses to be conducted with much more robust results.

7.2.1 Ancestral State Reconstruction

7.2.1.1 *Material and Methods*

Ancestral states were reconstructed in BayesTraits (Meade and Pagel, 2016). The models specified were for continuous variables (e.g.: length) in an independent contrasts variable rates model, utilising MCMC, with the default priors. Independent contrasts effectively use the branch length and an assumed rate of evolution to turn each of the terminal taxa into independent data points. Variable rates models detect varying rate of evolution along branches (Venditti, Meade and Pagel, 2011). For categorical variables (e.g.: morphogroup) the models were multistate with reverse jump MCMC and an exponential prior with a mean of 10.

Model convergence was achieved for all models with a burn-in of 500,000 and two million iterations. To check that the models had fully converged plots of the predicted value against sample number were observed for convergence patterns (i.e. the graph should appear as white noise with no trends). Each model was run at least twice (as per Meade and Pagel's (2016) recommendation) and the check (plots of alpha appear to be white noise) was repeated. The phylogeny used is the same as for the analyses above (Section 6.4, Figure 6-9). For all models of evolution, the root was reconstructed.

7.2.1.2 *Results*

Random Walk

The results for the ASR using a random walk model of evolution can be found in Table 7-1. The PC scores are visualised as back-transformed shapes (as per Chapter 5) in Figure 7-1.

Table 7-1: The results of the ASR using a random walk model of evolution

Variable	Mean (± Standard Deviation)	Median
Longest Length (µm)	536.6 ±1.3	536.3
Intermediate Length (µm)	468.5 ±1.3	470.3
Shortest Length (µm)	379.9 ±1.3	379.0
Spiral PC1	0.00026 ±0.00001	0.000253
Spiral PC2	0.00022 ±0.00001	0.000217
Spiral PC3	0.00016 ±0.00001	0.000159
Aperture PC1	0.00143 ±0.00008	0.001401
Aperture PC2	0.00052 ±0.00003	0.000511
Sinking Underneath PC1	0.00076 ±0.00004	0.000746
Sinking Underneath PC2	0.00058 ±0.00003	0.000573
Sinking Underneath PC3	0.00029 ±0.00002	0.000281
Sinking Side PC1	0.00151 ±0.00007	0.001486
Sinking Side PC2	0.00088 ±0.00004	0.000859
C_{DI}	20.71 ±3.10	20.74

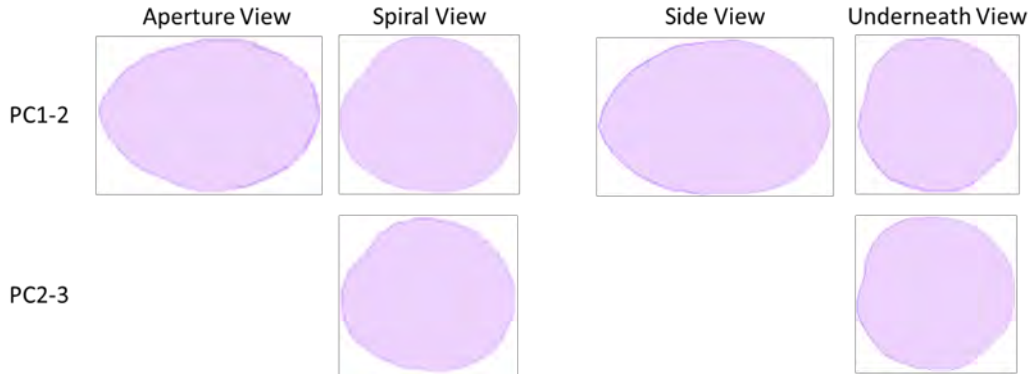

Figure 7-1:Ancestral shape under a random walk assumption

Directional

The results for the ASR using a directional model (OU) of evolution can be found in Table 7-2. The reconstructed PC scores are visualised as back-transformed shapes in Figure 7-2.

Table 7-2: Results of ASR using a directional model of evolution

Variable	Mean (± Standard Deviation)	Median
Longest Length (µm)	269.4 ±1.77	273.3
Intermediate Length (µm)	267.3 ±1.74	268.8
Shortest Length (µm)	240.6 ±1.81	235.6
Spiral PC1	0.00027 ±0.00002	0.00026
Spiral PC2	0.00022 ±0.00002	0.000211
Spiral PC3	0.00015 ±0.00001	0.000146
Aperture PC1	0.00147 ±0.00012	0.001432
Aperture PC2	0.00054 ±0.00005	0.000528
Sinking Underneath PC1	0.00078 ±0.00006	0.000765
Sinking Underneath PC2	0.0006 ±0.00005	0.000589
Sinking Underneath PC3	0.00029 ±0.00002	0.000279
Sinking Side PC1	0.00157 ±0.00011	0.001537
Sinking Side PC2	0.00084 ±0.00006	0.000822
C_{DI}	16.24 ±7.31	16.14

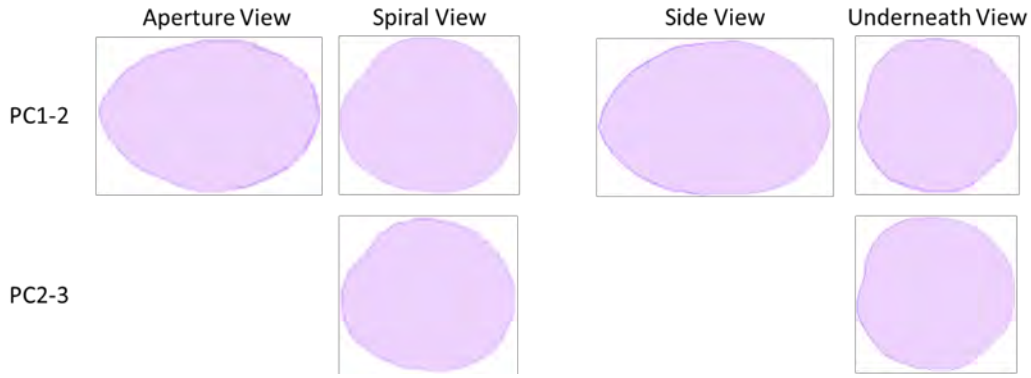

Figure 7-2:Ancestral shape under a directional walk assumption

Independent Contrasts

The results for the ASR using independent contrasts can be found in Table 7-3. The PC scores are visualised as back-transformed shapes in Figure 7-2.

Table 7-3: Results for the ASR using independent contrasts

Variable	Mean (± Standard Deviation)	Median
Longest Length (µm)	556.5 ±1.3	561.8
Intermediate Length (µm)	474.2 ±1.3	475.3
Shortest Length (µm)	389.7 ±1.3	388.9
Spiral PC1	0.02499 ±0.04342	0.000287
Spiral PC2	0.00012 ±0.00007	0.000108
Spiral PC3	0.00009 ±0.00004	8.19E-05
Aperture PC1	0.00121 ±0.00059	0.001148
Aperture PC2	0.0004 ±0.00017	0.000366
Sinking Underneath PC1	0.0005 ±0.00023	0.000469
Sinking Underneath PC2	0.00029 ±0.00019	0.00024
Sinking Underneath PC3	0.0032 ±0.0048	0.000114
Sinking Side PC1	0.00057 ±0.00044	0.000412
Sinking Side PC2	0.00044 ±0.00141	0.000192
C_{DI}	20.74 ±3.19	20.82

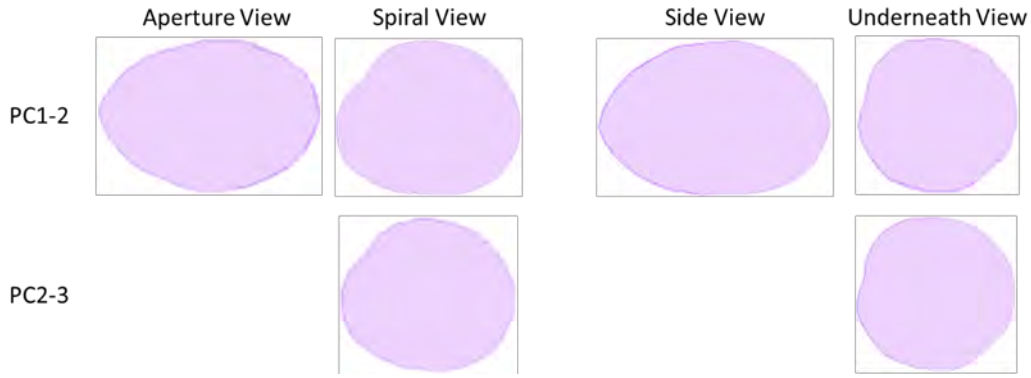

Figure 7-3:Ancestral shape under an independent contrasts model

Discussion

The ASR of PC scores suggests that the ancestor of all the species present in the study was most likely a flattened spheroid. Using Aze *et al*'s (2011) phylogeny, there are two ancestral species from which all planktonic foraminifera arose at the start of the Paleocene, 66 million years ago (MYR, these are *Hedbergella monmouthensis* and *Hedbergella holmdelensis* (see Figure 7-4). Whilst both of these species are flattened in the aperture views (seen in the centre of each panel in Figure 7-4), their outlines in the spiral view are less rounded than those predicted with the ASR (Figure 7-5).

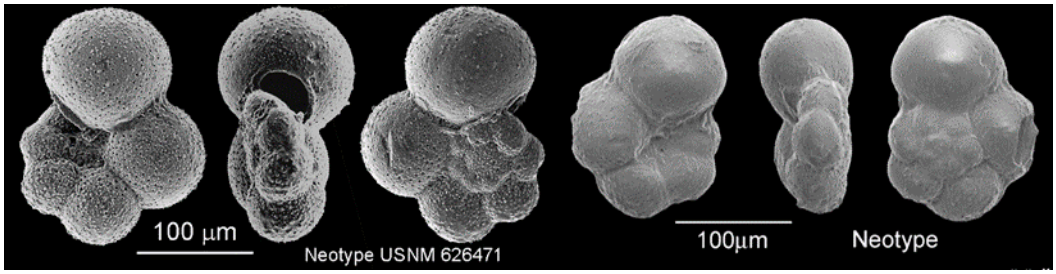

Figure 7-4: Three views (umbilical, aperture and spiral) of Hedbergella monmouthensis (left) and Hedbergella holmdelensis (right) the two species of planktonic foraminifera from ~73 to ~69 MYA. From these two species all known planktonic foraminifera arose, based on the Aze et al. (2011) phylogeny. Source: http://www.mikrotax.org/pforams/index.html

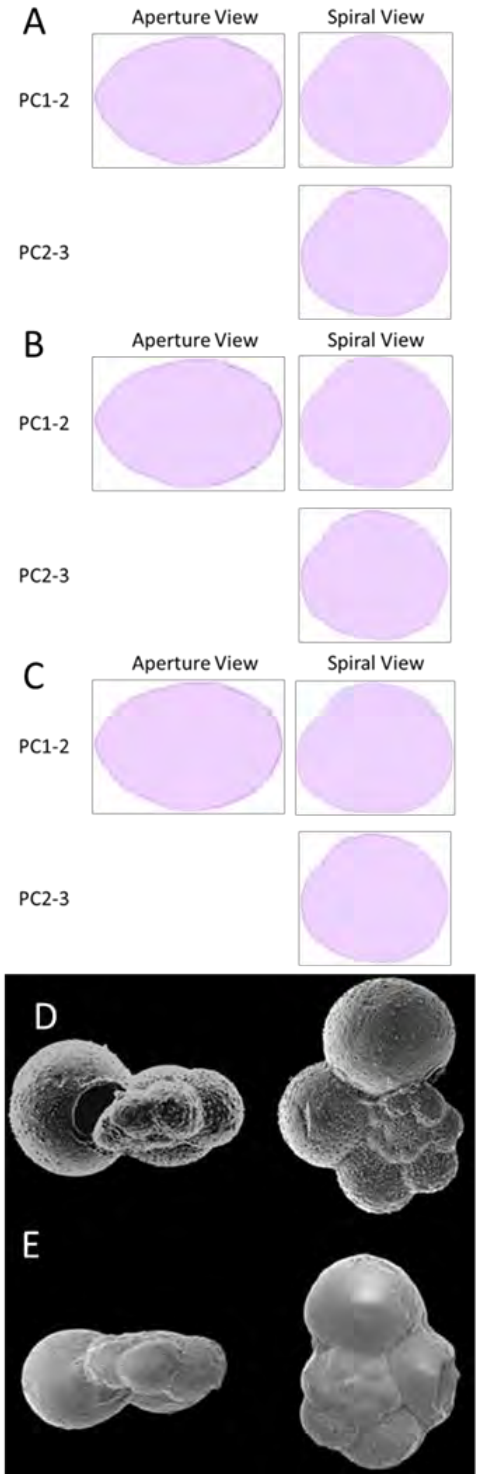

Figure 7-5: The reconstructed Ancestral form in the aperture and spiral views from random walk (A); directional (B); and independent contrasts(C); ASR. For comparison with Hedbergella monmouthensis (D) and Hedbergella holmdelensis (E), the known ancestors to all planktonic foraminifera (as per Figure 7-4), in the same views.

The results of the random walk and independent contrasts suggest that the ancestor was approximately 530-550µm (maximum length), ~470µm (intermediate length) and ~380-390µm (shortest length). *H. holmdelensis* measures approximately 173µm, 126µm and 78µm and *H. monmouthensis* measures 201µm, 158µm and 114µm (longest, intermediate and shortest lengths respectively, based on the neotype and holotype in Figure 7-4). It should be noted that these results, as discussed above, are based on a small sample size which is not evenly distributed across the phylogeny. This small sample size almost certainly biases the results seen here for all the models

regardless of the mode of evolution used. However, the results from the ASR using the directional model of evolution are much closer to the values seen for *H. holmdelensis* and *H. monmouthensis* (~270µm, ~267µm and ~240µm). This result suggests that foraminifera have been under directional selection for larger size. This does not fit with the overall trend of decreasing temperatures over the last 65 million years (Figure 7-6), as lower sea-surface temperatures result in smaller foraminifera (Schmidt *et al.*, 2004). However, there have been periods of warming which could have placed selective pressures on species to increase their test size, as larger tests would sink at slower in the less viscous seawater. These trends could also be due to local variations in the regions in which species have arisen. For example, species within a body of water which experiences warming (due to the retreat of ice shelves, for example), could undergo selection pressures for increases in size, explaining the trend seen in the ASR. Such effects have not been investigated in this study but warrant further examination, for example using data for species known to live in polar waters. It should also be noted that species living in tropical oceans will have seen less dramatic changes of temperature compared to the foraminifera living in higher latitudes.

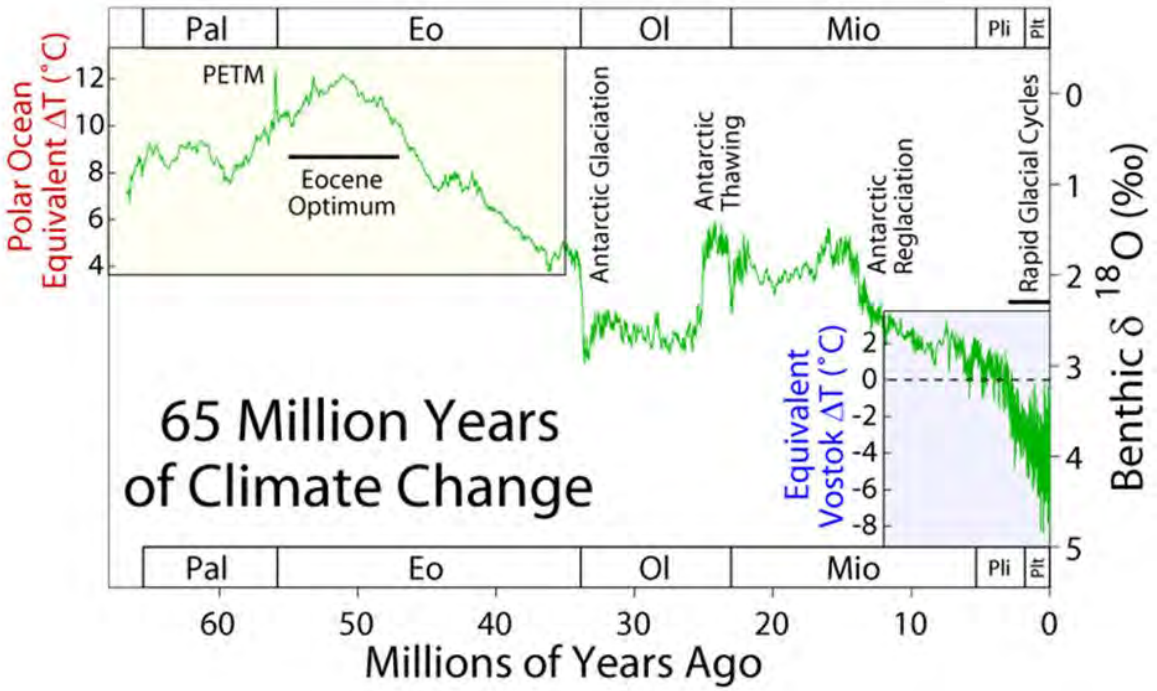

Figure 7-6: Decreasing global temperatures over the past 65 million years. Image by R. A. Rohde.

Clearly the ASR and the actual ancestors to planktonic foraminifera differ in their shapes. As the species used in this work are not sampled evenly across the phylogeny, this could explain the lack of full agreement with the observed ancestral foraminifera.

When examining the results of the ASR for C_{DI} value, the directional model and independent contrasts both agree that the ancestral C_{DI} was ~20 and the random evolutionary model suggests a C_{DI} of ~16. The ASR C_{DI} values are in agreement with the results of the ASR PC scores, as foraminifera with similar PC scores have similar C_{DI} values. These results suggest there has been selection (again, these results are based on the dead empty test, so this is speculation as to possible

selection pressures) for higher drag, which would be required to maintain position in the water column in warmer waters.

However, all of these ASR findings should be viewed with some caution due to the limited sampling of the phylogeny. Recent findings by Si *et al.* (Si, Berggren and Aubry, 2018) have found that *Fohsella* linages have undergone a myriad of different evolutionary trends including periods of stasis and punctuated changes. These changes may be detectable within the phylogeny of planktonic foraminifera but will most likely require a more in-depth study which focuses on all available taxonomic levels to better understand the evolution of the planktonic foraminifera.

Ancestral states for the root of the phylogeny used here were calculated and compared with the known ancestral species to all planktonic foraminifera. These ASR results suggested that the ancestor was a slightly differently shape and a larger size than the observed ancestor species. This is likely an effect of the species combination used in the reconstruction. Though it should be noted that directional model of evolution used in ASR provided sizes closer to the observed states, suggesting planktonic foraminifera have been under some selection pressure. This method could be used to estimate the sinking velocities of planktonic foraminifera for which it is not possible to experimentally determine (e.g.: fossil species for which it is not possible to obtain clean specimens).

7.3 Synthesis

Making comparisons with other planktonic organisms is difficult as foraminifera are much larger than most phytoplankton (for which much data have been accrued, e.g. size ranges in (Marañón *et al.*, 2012). This increased size means foraminifera experience different ranges of Re than most other plankton. Despite some of the largest diatom species approaching foraminifera sizes (~225µm) they reportedly sink at Re = 0.1 (Miklasz and Denny, 2010). While this Re value (0.1) should mean that predictions of sinking velocities made using Stokes' Law are a true reflection of the sinking velocities observed, this does not appear to be the case (Miklasz and Denny, 2010). Miklasz & Denny (2010) determined, as found here for foraminifera, that density is important for diatom sinking velocities, which fits with the hydrodynamic theory outlined in Chapter 3. Padisak, Soróczki-Pintér and Rezner (Padisák *et al.*, 2003) investigated the sinking of different shaped phytoplankton using models made of PVC-U or a PVC-based modelling material and increased viscosity fluid. They found that phytoplankton show differences in sinking velocity dependent on their shape. These differences in sinking velocity can be predicted using the form resistance (ϕ) of the phytoplankter. Form resistance is a measure of the factor by which sinking velocity differs between the particle and a sphere of identical volume and density, to which Stokes' Law can appropriately be applied. However, Holland (2010) suggests that some of the Re values of Padisak *et al.* (2003)'s models exceeded the threshold for Stokes' Law (with Re potentially exceeding 20). Holland argues this would lead to an underestimate of sinking velocities of similar shapes and an overestimation of Φ. All of these studies (Padisák *et al.*, 2003; Holland, 2010; Miklasz and Denny,

2010) found that there is an effect of shape in determining sinking velocities within the low Re regime. However, none of these studies go beyond the comparison of the sinking particles to the sinking velocities of equivalent spheres.

Faecal pellets of various plankton species (e.g.: copepods, salps, etc.) approach similar sizes to foraminifera (e.g.: ~250 – 2270 µm, Yoon *et al*., 2001 Figure 3-33) and are different shapes dependent on the organism producing them. Whilst sinking velocities of faecal pellets have been experimentally measured (e.g.: Alldredge & Gotschalk 1988; Davey 1986; Iversen & Ploug 2010; Miklasz & Denny 2010; Smayda 1971), theoretical predictions made using Stokes' Law or other formulae (e.g.: Komar & Reimers, 1978) differ from these predictions. Yoon, Kin and Han (Yoon, Kim and Han, 2001) found that Stokes' Law and Komar and Reimers' (Komar and Reimers, 1978) equation over-estimated sinking velocities for faecal pellets. Newton's second law (Equation 3-4; when sinking at $U_{terminal}$ all forces are balanced) provided the best estimate, despite the use of the same C_D value for all faecal pellets. This result suggests a minimal effect of shape upon sinking velocities as the generic C_D yielded results similar to the measured sinking velocities. Echoing the results found here for planktonic foraminifera, Taghon *et al.* (Taghon, Nowell and Jumars, 1984) found that accounting for shape in the prediction of sinking velocities for faecal pellets improved the fit of trend lines compared to regressions that did not account for shape.

From these studies (above and the present work) it is possible to make a general claim that planktonic organisms (including foraminifera) sink at rates proportional to their density and size. Additionally, there is an effect of shape which causes deviations from predictions made by equations derived for use with a sphere. Based on the findings of this thesis, shape influences sinking velocity; resulting in the C_D experienced by a foraminifera being different to the C_D experienced by a sphere, confirming previous findings (see Chapter 3).

Whilst the work presented in this thesis fills a gap in knowledge of sinking velocities (of empty tests) for a number of species, it should be remembered that this study was conducted in quiescent fluid. The ocean has levels of turbulence from large scale currents (Belcher *et al.*, 2012) to micro-scale eddies (Lazier and Mann, 1989). Turbulence is hard to model computationally (Ecke, 2005). The effect of turbulence is not intuitive, one might expect turbulence to reduce sinking velocity by effectively re-suspending particles. However, the opposite is true for phytoplankton (Ruiz, Macias and Peters, 2004), but this is dependent on the size of the particle and the size of the turbulence. To gain a better understanding of sinking foraminifera, models or real foraminifera need to be sunk under conditions replicating the continuous motions of the ocean, which is a considerable technical challenge.

8. References

Abdollahi, S. et al. (2018) 'Expert-guided optimization for 3D printing of soft and liquid materials', PLOS ONE, 13(4), p. e0194890. doi: 10.1371/journal.pone.0194890.

Adams, D. C., Collyer, M. L. and Kaliontzopoulou, A. (2018) 'Geomorph: Software for geometric morphometric analyses. R package'.

Adler, L. S. (2000) 'The ecological significance of toxic nectar', Oikos, 91(3), pp. 409–420. doi: 10.1034/j.1600-0706.2000.910301.x.

Ahmed, T., Shimizu, T. S. and Stocker, R. (2010) 'Microfluidics for bacterial chemotaxis.', Integrative biology, 2(11–12), pp. 604–629. doi: 10.1039/c0ib00049c.

Albertson, M. L. (1953) 'Effect of Shape on the Fall Velocity of Gravel Particles', Proceedings of the Fifth Hydraulics Conference, p. 308. Available at: http://ir.uiowa.edu/uisie/34.

Albrecht, G. H. (1978) 'Some Comments on the Use of Ratios', Systematic Zoology, 27(1), p. 67. doi: 10.2307/2412815.

Alldredge, A. L. and Gotschalk, C. (1988) 'In situ settling behavior of marine snow', Limnology and Oceanography, 33(3), pp. 339–351. doi: 10.4319/lo.1988.33.3.0339.

Almeida, F. et al. (2007) 'The Lapedo Child Reborn : Contributions of CT Scanning and Rapid Prototyping for an Upper Paleolithic Infant Burial and Face Reconstruction. The Case of Lagar Velho Interpretation Centre, Leiria, Portugal', in VAST 2007: Furture Technologies To Empower Heritage Professionals: Short and Project papers from VAST 2007, pp. 69–73. doi: 10.1.1.627.3900.

Anderson, O. R. et al. (1979) 'Trophic Activity of Planktonic Foraminifera', Journal of the Marine Biological Association of the United Kingdom, 59(3), pp. 791–799. doi: 10.1017/S002531540004577X.

Andersson, C. (1994) Sexual Selection. 1st edn. Princeton, N.J., N.J., USA: Princeton University Press.

Arnold, A. (1983) 'Phyletic evolution in the Globorotalia crassaformis (Galloway and Wissley) linage: a preliminary report', Paleobiology, 9(4), pp. 390–397.

Arnold, A. J., Kelly, D. C. and Parker, W. C. (1995) 'Causality and Cope's Rule: evidence from the planktonic foraminifera', Journal of Paleontology, 69(02), pp. 203–210. doi: 10.1017/S0022336000034557.

Atchley, W. R. and Anderson, D. (1978) 'Ratios and the Statistical Analysis of Biological Datas', Systematic Zoology, pp. 71–78.

Atchley, W. R., Gaskins, C. T. and Anderson, D. (1976) 'Statistical Properties of Ratios. I. Empirical Results', Systematic Zoology, 25(2), p. 137. doi: 10.2307/2412740.

Autodesk.com (2017) 'AutoCAD'. Available at: http://www.autodesk.com/solutions/cad-software.

Aze, T. et al. (2011) 'A phylogeny of Cenozoic macroperforate planktonic foraminifera from fossil data.', Biological Reviews, 86(4), pp. 900–27. doi: 10.1111/j.1469-185X.2011.00178.x.

Bach, L. T. et al. (2012) 'An approach for particle sinking velocity measurements in the 3-400 µm size range and considerations on the effect of temperature on sinking rates', Marine Biology, 159(8), pp. 1853–1864. doi: 10.1007/s00227-012-1945-2.

Baden, T. et al. (2015) 'Open Labware: 3-D Printing Your Own Lab Equipment', PLoS Biology, 13(3), pp. 1–12. doi: 10.1371/journal.pbio.1002086.

Bakken, G. S. and Angilletta, M. J. (2014) 'How to avoid errors when quantifying thermal environments', Functional Ecology. Edited by M. Konarzewski, 28(1), pp. 96–107. doi: 10.1111/1365-2435.12149.

Banner, F. T. and Lord, A. R. (1982) Aspects of Micropalaeontology. First, Statewide Agricultural Land Use Baseline 2015. First. Edited by F. T. Banner and A. R. Lord. London: George Allen & Unwin. doi: 10.1007/ 978-94-011-6841-0.

Bara, J. E. et al. (2015) 'Tangible visualization of molecular dynamics simulations using 3-D printing', Education for Chemical Engineers. Institution of Chemical Engineers, 13, pp. 9–16. doi: 10.1016/j.ece.2015.07.001.

Barker, S. et al. (2005) 'Planktonic foraminiferal Mg/Ca as a proxy for past oceanic temperatures: A methodological overview and data compilation for the Last Glacial Maximum', Quaternary Science Reviews, 24(7-9 SPEC. ISS.), pp. 821–834. doi: 10.1016/j.quascirev.2004.07.016.

Bé, A. W. H., Jongebloed, W. L. and McIntyre, A. (1969) 'X-ray microscopy of Recent planktonic Foraminifera', Journal of Paleontology, 43(6), pp. 1384–1396.

Bé, A. W. H., Spero, H. J. and Anderson, O. R. (1982) 'Effects of symbiont elimination and reinfection on the life processes of the planktonic foraminifer Globigerinoides sacculifer', Marine Biology, 70(1), pp. 73–86. doi: 10.1007/BF00397298.

Begolo, S. et al. (2014) 'The pumping lid: Investigating multi-material 3D printing for equipment-free, programmable generation of positive and negative pressures for microfluidic applications', Lab on a Chip. Royal Society of Chemistry, 14(24), pp. 4616–4628. doi: 10.1039/c4lc00910j.

Belcher, S. E. et al. (2012) 'A global perspective on Langmuir turbulence in the ocean surface boundary layer', Geophysical Research Letters, 39(18), pp. 1–9. doi: 10.1029/2012GL052932.

Bellani, G. et al. (2012) 'Shape effects on turbulent modulation by large nearly neutrally buoyant particles', Journal of Fluid Mechanics, 712, pp. 41–60. doi: 10.1017/jfm.2012.393.
Bemis, B. E. et al. (1998) 'Reevaluation of the oxygen isotopic composition of planktonic foraminifera: Experimental results and revised paleotemperature equations', Paleoceanography, pp. 150–160. doi: 10.1029/98PA00070.
Benton, M. J. and Walker, A. D. (1981) 'The use of flexible synthetic rubbers for casts of complex fossils from natural moulds', Geological Magazine, 118(05), p. 551. doi: 10.1017/S0016756800032921.
Berger, W. H. (1970) 'Planktonic Foraminifera: Selective solution and the lysocline', Marine Geology, 8(2), pp. 111–138. doi: 10.1016/0025-3227(70)90001-0.
Berger, W. H. et al. (1972) 'Planktonic Foraminifera: Differential Settling, Dissolution, and Redeposition', Limnology and Oceanography, 17(2), pp. 275–287. doi: 10.4319/lo.1972.17.2.0275.
Berman, B. (2012) '3-D printing: The new industrial revolution', Business Horizons. 'Kelley School of Business, Indiana University', 55(2), pp. 155–162. doi: 10.1016/j.bushor.2011.11.003.
Berthois, L. and Calvez, L. E. (1960) 'Etude de la vitesse de chute des coquilles de foraminifères planctoniques dans un fluide comparativement a celle des grains de quartz', Revue des travaux de l'Institut des pêches maritimes, 24(2), pp. 293–301.
Bijma, J. et al. (1992) 'The effects of increased water fertility on tropical spinose planktonic foraminifers in laboratory cultures', The Journal of Foraminiferal Research, 22(3), pp. 242–256. doi: 10.2113/gsjfr.22.3.242.
Bijma, J., Faber, W. W. and Hemleben, C. (1990) 'Temperature and salinity limits for growth and survival of some planktonic foraminifers in laboratory cultures', The Journal of Foraminiferal Research, pp. 95–116. doi: 10.2113/gsjfr.20.2.95.
Biolzi, M. (1991) 'Morphometric analysesof the Late Neogene planktonic foraminiferal lineage Neogloboquadrina dutertrei', Atlantic, 18, pp. 129–142.
Birch, H. et al. (2013) 'Planktonic foraminifera stable isotopes and water column structure: Disentangling ecological signals', Marine Micropaleontology, 101, pp. 127–145. doi: 10.1016/j.marmicro.2013.02.002.
Blackburn, D. C. (2017) Check out the next generation of 3D printing of museum specimens. Thanks to the @Stratasys team for the demo and @DrScanley for the CT work!, Twitter. Available at: https://twitter.com/davidcblackburn/status/858042278035718145 (Accessed: 28 April 2017).
Bocxlaer, B. Van and Schultheiß, R. (2010) 'Comparison of morphometric techniques for shapes with few homologous landmarks based on machine-learning approaches to biological discrimination', Paleobiology, 36(03), pp. 497–515. doi: 10.1666/08068.1.
Boggs, S. J. (2006) Princplies of Sedimentology and Stratigraphy. Fourth, Princplies of Sedimentology and Stratigraphy. Fourth. London: Pearson Education, Inc. doi: 10.1017/CBO9781107415324.004.
van Bokhorst, E. et al. (2015) 'Feather roughness reduces flow separation during low Reynolds number glides of swifts', Journal of Experimental Biology, 218(20), pp. 3179–3191. doi: 10.1242/jeb.121426.
Bolker, B. M. et al. (2009) 'Generalized linear mixed models: a practical guide for ecology and evolution', Trends in Ecology and Evolution, 24(3), pp. 127–135. doi: 10.1016/j.tree.2008.10.008.
Bonhomme, V. et al. (2013) 'Momocs: outline analysis using R', Journal of Statistical Software, 56(13), pp. 1–24. doi: 10.18637/jss.v056.i13.
Bonner, J. T. (2013) Randomness in Evolution. Oxford: Princeton University Press.
Bonyár, A. et al. (2010) '3D Rapid Prototyping Technology (RPT) as a powerful tool in microfluidic development', Procedia Engineering. Elsevier, 5, pp. 291–294. doi: 10.1016/j.proeng.2010.09.105.
Bookstein, F. L. (1989) '"Shape and size": A comment on semantics', Systematic Zoology, 38(2), pp. 173–180.
Bookstein, F. L. (1991) Morphometric tools for landmark data: Geometry and biology. Cambridge: Cambridge University Press.
Bostock, H. C. et al. (2011) 'Deep-water carbonate concentrations in the southwest Pacific', Deep-Sea Research Part I: Oceanographic Research Papers. Elsevier, 58(1), pp. 72–85. doi: 10.1016/j.dsr.2010.11.010.
Box, G. E. P. and Cox, D. R. (1964) 'An Analysis of Transformations', Journal of the Royal Statistical Society. Series B (Methodological), 26(2), pp. 211–252.
Brady, H. B. (1884) 'Report on the Foraminifera dredged by H.M.S. Challenger, during the years 1873 - 1876', in Report on the scientific results of the voyage of H.M.S. Challenger during the years 1873-76 : under the command of Captain George S. Nares, R.N., F.R.S. and Captain Frank Turle Thomson, R.N. / prepared under the superintendence of Sir C. Wyville Thomson. Edinburgh: Neill, pp. 1–858. doi: 10.5962/bhl.title.6513.

Brandley, N., Johnson, M. and Johnsen, S. (2016) 'Aposematic signals in North American black widows are more conspicuous to predators than to prey', Behavioral Ecology, 00(4), pp. 1–9. doi: 10.1093/beheco/arw014.
Branson, O. et al. (2013) 'The coordination of Mg in foraminiferal calcite', Earth and Planetary Science Letters. Elsevier B.V., 383, pp. 134–141. doi: 10.1016/j.epsl.2013.09.037.
Bristowe, A et al. (2004) 'A non-destructive investigation of the skull of the small theropod dinosaur, Ceolophysis rhodesiensis, using CT scans and rapid prototyping. BT - Palaeontologia Africana', Palaeontologica Africana, 40(December), pp. 31–36.
Broecker, W. S. and Peng, T.-H. (1982) Tracers in the Sea. Palisades, NY: Lamon-Doherty Geological observatory, Coumbio University.
Brummer, G. J. A., Hemleben, C. and Spindler, M. (1987) 'Ontogeny of extant spinose planktonic foraminifera (Globigerinidae): A concept exemplified by Globigerinoides sacculifer (Brady) and G. Ruber (d'Orbigny)', Marine Micropaleontology, 12(C), pp. 357–381. doi: 10.1016/0377-8398(87)90028-4.
Burke, J. E. and Hull, P. M. (2017) 'Effect of gross morphology on modern planktonic foraminiferal test strength under compression', Journal of Micropalaeontology, 2, pp. jmpaleo2016-007. doi: 10.1144/jmpaleo2016-007.
Callieri, M. et al. (2012) 'Meshlab as a Complete Open Tool for the Integration of Photos and Colour with High- Resolution 3D Geometry Data', Computer Applications and Quantitative Methods in Archaeology, pp. 406–416.
Campos, E. O., Bradshaw, H. D. and Daniel, T. L. (2015) 'Shape matters: corolla curvature improves nectar discovery in the hawkmoth Manduca sexta', Functional Ecology. Edited by A. Brody, 29(4), pp. 462–468. doi: 10.1111/1365-2435.12378.
Caple, J., Byrd, J. and Stephan, C. N. (2017) 'Elliptical Fourier analysis: fundamentals, applications, and value for forensic anthropology', International Journal of Legal Medicine. International Journal of Legal Medicine, 131(6), pp. 1675–1690. doi: 10.1007/s00414-017-1555-0.
Caromel, A. G. M. et al. (2015) 'Morphological Change During The Ontogeny Of The Planktic Foraminifera', Journal of Micropalaeontology, pp. 2014–017. doi: 10.1144/jmpaleo2014-017.
Caromel, A. G. M. M. et al. (2014) 'Hydrodynamic constraints on the evolution and ecology of planktic foraminifera', Marine Micropaleontology, 106, pp. 69–78. doi: 10.1016/j.marmicro.2014.01.002.
Chan, Y.-C. et al. (2016) 'Testing an attachment method for solar-powered tracking devices on a long-distance migrating shorebird', Journal of Ornithology. Springer Berlin Heidelberg, 157(1), pp. 277–287. doi: 10.1007/s10336-015-1276-4.
Chapman, R. L. (2013) 'Algae: the world's most important "plants"—an introduction', Mitigation and Adaptation Strategies for Global Change, 18(1), pp. 5–12. doi: 10.1007/s11027-010-9255-9.
Chisholm, S. W. (1992) 'Phytoplankton Size', in Primary Productivity and Biogeochemical Cycles in the Sea. Boston, MA, MA: Springer US, pp. 213–237. doi: 10.1007/978-1-4899-0762-2_12.
Cifelli, R. (2006) 'Radiation of Cenozoic Planktonic Foraminifera', Systematic Zoology, 18(2), p. 154. doi: 10.2307/2412601.
Clark, N. D. L. L. et al. (2004) 'The Elgin marvel: Using magnetic resonance imaging to look at a mouldic fossil from the Permian of Elgin, Scotland, UK', Magnetic Resonance Imaging, 22(2), pp. 269–273. doi: 10.1016/j.mri.2003.09.006.
CLIMAP Project Members (1976) 'The Surface of the Ice-Age Earth', Science, 191(4232), pp. 1131–1137. doi: 10.1126/science.191.4232.1131.
Cohen, A. et al. (2009) 'Mandibular reconstruction using stereolithographic 3-dimensional printing modeling technology', Oral Surgery, Oral Medicine, Oral Pathology, Oral Radiology and Endodontology. Elsevier Inc., 108(5), pp. 661–666. doi: 10.1016/j.tripleo.2009.05.023.
Connell, J. L. L. et al. (2013) '3D printing of microscopic bacterial communities', Proceedings of the National Academy of Sciences, 110(46), pp. 18380–18385. doi: 10.1073/pnas.1309729110.
Cooke, S. B. and Terhune, C. E. (2015) 'Form, Function, and Geometric Morphometrics', Anatomical Record, 298(1), pp. 5–28. doi: 10.1002/ar.23065.
Coxall, H. K. et al. (2007) 'Iterative evolution of digitate planktonic foraminifera', 33(4), pp. 495–516. doi: 10.1666/06034.1.
Croissant, Y. (2018) 'mlogit: Multinomial Logit Models. R package'. Available at: https://cran.r-project.org/package=mlogit.
Crothers, L. R. and Cummings, M. E. (2015) 'A multifunctional warning signal behaves as an agonistic status signal in a poison frog', Behavioral Ecology, 26(2), pp. 560–568. doi: 10.1093/beheco/aru231.
Cunningham, J. A. et al. (2014) 'A virtual world of paleontology', Trends in Ecology and Evolution. Elsevier Ltd, 29(6), pp. 347–357. doi: 10.1016/j.tree.2014.04.004.
Cushman, J. A. (1928) Foraminifera; Their Classification and Economic Use. Sharon, Massachusetts, USA.

D'Urso, P. S. et al. (1999) 'Biomodelling of skull base tumours', Journal of Clinical Neuroscience, 6(1), pp. 31–35. doi: 10.1016/S0967-5868(99)90599-4.
Darling, K. F. et al. (2004) 'Molecular evidence links cryptic diversification in polar planktonic protists to Quaternary climate dynamics', Proceedings of the National Academy of Sciences, 101(20), pp. 7657–7662. doi: 10.1073/pnas.0402401101.
Darling, K. F. et al. (2006) 'A resolution for the coiling direction paradox in Neogloboquadrina pachyderma', Paleoceanography, 21(2), p. n/a-n/a. doi: 10.1029/2005PA001189.
Davey, M. C. (1986) 'The Relationship Between Size, Denisty and Sinking Velocity Through the Life Cycle of <i>Melosira granulata<i> (<i>Bacillariophyta<i>)', Diatom Research, 1(1), pp. 1–18. doi: 10.1080/0269249X.1986.9704954.
Davis, C. V. et al. (2017) 'Ocean acidification compromises a planktic calcifier with implications for global carbon cycling', Scientific Reports. Springer US, 7(1), pp. 1–8. doi: 10.1038/s41598-017-01530-9.
Deeming, D. C. and Ruta, M. (2014) 'Egg shape changes at the theropod–bird transition, and a morphometric study of amniote eggs', Royal Society Open Science, 1(3), p. 140311. doi: 10.1098/rsos.140311.
Denny, M. (1993) Air and Water. Princeton University Press.
Domingue, M. J. et al. (2014) 'Detecting emerald ash borers (Agrilus planipennis) using branch traps baited with 3D-printed beetle decoys', Journal of Pest Science. Springer Berlin Heidelberg, 88(2), pp. 267–279. doi: 10.1007/s10340-014-0598-y.
Duan, B. et al. (2013) '3D Bioprinting of heterogeneous aortic valve conduits with alginate/gelatin hydrogels', Journal of Biomedical Materials Research Part A, 101A(5), pp. 1255–1264. doi: 10.1002/jbm.a.34420.
Ebert, J. et al. (2009) 'Direct Inkjet Printing of Dental Prostheses Made of Zirconia', Journal of Dental Research, 88(7), pp. 673–676. doi: 10.1177/0022034509339988.
Ecke, R. (2005) 'The Turbulence Problem', Los Alamos Science, (29), pp. 124–141. doi: 10.1007/978-94-007-0117-5.
Endler, J. A. and Jan, N. (1982) 'Convergent and Divergent Effects of Natural Selection on Color Patterns in Two Fish Faunas', Evolution, 36(1), p. 188. doi: 10.2307/2407979.
Ericson, D. B., Wollin, G. and Wollin, J. (1954) 'Coiling direction of Globorotalia truncatulinoides in deep-sea cores', Deep-Sea Research, 2(2), pp. 152–158. doi: 10.1016/0146-6313(55)90018-6.
Fairbanks, R. G. et al. (1980) 'Vertical Distribution and Isotopic Composition of Living Planktonic Foraminifera in the Western North Atlantic', Science, 207(4426), pp. 61–63. doi: 10.1126/science.207.4426.61.
Fairbanks, R. G. and Wiebe, P. H. (1980) 'Foraminifera and chlorophyll maximum: Vertical distribution, seasonal succession, and paleoceanographic significance', Science, 209(4464), pp. 1524–1526. doi: 10.1126/science.209.4464.1524.
Fisher, C. G. et al. (2003) 'Planktic foraminiferal porosity analysis as a tool for paleoceanographic reconstruction, mid-Cretaceous Western Interior sea', Palaios, 18(1), pp. 34–46. doi: 10.1669/0883-1351(2003)018<0034:PFPAAA>2.0.CO;2.
Fok-Pun, L. and Komar, P. D. (1983) 'Settling Velocities of Planktonic Foraminifera : Density Variations and Shape Effects', Journal of Foraminiferal Research, 13(1), pp. 60–68. doi: 10.2113/gsjfr.13.1.60.
Fox, J. and Weisberg, S. (2011) An R Companion to Applied Regression. Second. Thousand Oaks, CA, CA: Sage.
Fraile, I. et al. (2007) 'A dynamic global model for planktonic foraminifera', Biogeosciences Discussions, 4(6), pp. 4323–4384. doi: 10.5194/bgd-4-4323-2007.
Fraile, I. et al. (2008) 'Predicting the global distribution of planktonic foraminifera using a dynamic ecosystem model', Biogeosciences, 5(3), pp. 891–911. doi: 10.5194/bg-5-891-2008.
Fraisse, S., Bormans, M. and Lagadeuc, Y. (2015) 'Turbulence effects on phytoplankton morphofunctional traits selection', Limnology and Oceanography, 60(3), pp. 872–884. doi: 10.1002/lno.10066.
Freckleton, R. P., Harvey, P. H. and Pagel, M. (2016) 'Phylogenetic Analysis and Comparative Data', The American Naturalist, 160(6), pp. 712–726.
Frerichs, W. E. et al. (1972) 'Latitudal variations in planktonic foraminiferal test porosity; Part 1, Optical studies', The Journal of Foraminiferal Research, 2(1), pp. 6–13. doi: 10.2113/gsjfr.2.1.6.
Frohnwieser, A. et al. (2016) 'Using robots to understand animal cognition', Journal of the Experimental Analysis of Behavior, 105(1), pp. 14–22. doi: 10.1002/jeab.193.
Furbish, D. J. and Arnold, A. J. (1997) 'Hydrodynamic strategies in the morphological evolution of spinose planktonic foraminifera', Bulletin of the Geological Society of America, 109(8), pp. 1055–1072. doi: 10.1130/0016-7606(1997)109<1055:HSITME>2.3.CO.

Galvin, E. (2017) 3D scan &printed Acheulean handaxe shows the flakes and knapping with magnets to make the stone tool #CAAAtlanta, Twitter. Available at: https://twitter.com/LisaGalvin_BM/status/841722935232589824 (Accessed: 14 March 2017).
Gardner, A. and Olson, A. (2016) '3D Printing of Molecular Models', The Journal of Biocommunication, 40(1), pp. 15–21. doi: 10.5210/jbc.v40i1.6626.
Gerstle, T. L. L. et al. (2014) 'A Plastic Surgery Application in Evolution', Plastic and Reconstructive Surgery, 133(2), pp. 446–451. doi: 10.1097/01.prs.0000436844.92623.d3.
Gettelfinger, B. and Cussler, E. L. (2004) 'Will humans swim faster or slower in syrup?', AIChE Journal, 50(11), pp. 2646–2647. doi: 10.1002/aic.10389.
Gillooly, J. F. et al. (2001) 'Effects of size and temperature on metabolic rate', Science, 293(September), pp. 2248–2251. doi: 10.1126/science.1061967.
Goldstein, E. B. and Coco, G. (2014) 'A machine learning approach for the prediction of settling velocity', Water Resource Research, 50, pp. 3595–3601. doi: 10.1002/2013WR015116.Received.
Gorla, R. S. R. et al. (2014) 'Heat and mass transfer in non-newtonian fluids', Advances in Mechanical Engineering, 2014, pp. 1–2. doi: 10.1155/2014/104392.
Grafen, A. (1989) 'The Phylogenetic Regression', Philosophical Transactions of the Royal Society B: Biological Sciences, 326(1233), pp. 119–157. doi: 10.1098/rstb.1989.0106.
Grafen, A. (1992) 'The uniqueness of the phylogenetic regression', Journal of Theoretical Biology, 156(4), pp. 405–423. doi: 10.1016/S0022-5193(05)80635-6.
Guadayol, Ò. (2016) 'Trackbac'. doi: 10.5281/zenodo.45559.
Guadayol, Ò., Thornton, K. L. and Humphries, S. (2017) 'Cell morphology governs directional control in swimming bacteria', Scientific Reports, 7(1), pp. 1–13. doi: 10.1038/s41598-017-01565-y.
Gunz, P. and Mitteroecker, P. (2013) 'Semilandmarks: A method for quantifying curves and surfaces', Hystrix, 24(1), pp. 103–109. doi: 10.4404/hystrix-24.1-6292.
Gupta, B. K. Sen (ed.) (2002) Modern Foraminifera. Kluwer Academic Publishers.
Haberman, W. L. and Sayre, R. M. (1958) 'Motion of Rigid and Fluid Spheres in Stationary and moving liquids inside cylindrical tubes', David Taylor Model Basin Report No. 1143. Washington D.C.
Hadfield, J. (2010a) 'MCMC methods for multi-response generalized linear mixed models: the MCMCglmm R package', (Brown). Available at: http://ftp5.gwdg.de/pub/misc/cran/web/packages/MCMCglmm/vignettes/Overview.pdf.
Hadfield, J. (2010b) 'MCMCglmm : Markov chain Monte Carlo methods for Generalised Linear Mixed Models', . org/web/packages/MCMCglmm/vignettes/Tutorial. pdf, pp. 1–25. Available at: http://citeseerx.ist.psu.edu/viewdoc/download?doi=10.1.1.160.5098&rep=rep1&type=pdf.
Hadfield, J. D. (2015) 'Increasing the efficiency of MCMC for hierarchical phylogenetic models of categorical traits using reduced mixed models', Methods in Ecology and Evolution, 6(6), pp. 706–714. doi: 10.1111/2041-210X.12354.
Hamilton Waters, P. et al. (1983) 'A review of the moulding and casting materials and techniques in use at the palaeontology laboratory , British museum (natural history)', The Conervator, 7(1), pp. 37–43. doi: 10.1080/01410096.1983.9994977.
Happel, J. and Brenner, H. (1983) Low Reynolds number hydrodynamics with special applications to particulate media. Third. The Hague: Martin Nijhoff Publishers a member of Kluwer Academic Publishers Group.
Harmon, L. J. et al. (2008) 'GEIGER: Investigating evolutionary radiations', Bioinformatics, 24(1), pp. 129–131. doi: 10.1093/bioinformatics/btm538.
Healy-Williams, N. and Williams, D. F. (1981) 'Fourier analysis of test shape of planktonic foraminifera', Nature, 289, pp. 485–487.
Heinen-Kay, J. L. et al. (2015) 'A trade-off between natural and sexual selection underlies diversification of a sexual signal', Behavioral Ecology, 26(2), pp. 533–542. doi: 10.1093/beheco/aru228.
Hemleben, C. et al. (1977) 'Test morphology, organic layers and chamber formation of the planktonic foraminifer Globorotalia menardii (d'Orbigny)', The Journal of Foraminiferal Research, 7(1), pp. 1–25. doi: 10.2113/gsjfr.7.1.1.
Hemleben, C. et al. (1985) 'Field and Laboratory Studies on the Ontogeny and Ecology of some Globorotaliid species from the Sargasso Sea off Bermuda', Journal for Foraminiferal Research, 15(4), pp. 254–272. doi: 10.2113/gsjfr.15.4.254.
Hemleben, C., Spindler, M. and Anderson, O. R. (1989) Modern Planktonic Foraminifera. London: Springer-Verlag.
Herbert, N. et al. (2005) 'A preliminary investigation into the development of 3-D printing of prosthetic sockets', Journal of Rehabilitation Research and Development, 42(2), pp. 141–146. doi: 10.1682/JRRD.2004.08.0134.

Hills, A. W. D. (1968) 'The mechanism of the thermal decomposition of calcium carbonate', Chemical Engineering Science, 23(4), pp. 297–320. doi: 10.1016/0009-2509(68)87002-2.
Ho, C. M. B. et al. (2015) '3D printed microfluidics for biological applications', Lab On A Chip, 15(18), pp. 3627–3637. doi: 10.1039/C5LC00685F.
Hodell, D. A. and Vayavananda, A. (1993) 'Middle Miocene paleoceanography of the western equatorial Pacific (DSDP site 289) and the evolution of Globorotalia (Fohsella)', Marine Micropaleontology, 22(4), pp. 279–310. doi: 10.1016/0377-8398(93)90019-T.
Hodgkinson, R. L. (1991) 'Microfossil Processing: A Damage Report', Micropaleontology, 37(3), p. 320. doi: 10.2307/1485894.
Holland, D. P. (2010) 'Sinking rates of phytoplankton filaments orientated at different angles: Theory and physical model', Journal of Plankton Research, 32(9), pp. 1327–1336. doi: 10.1093/plankt/fbq044.
Holmes, D. and Gawad, S. (2010) 'Microengineering in Biotechnology', in Hughes, M. P. and Hoettges, K. F. (eds) Microengineering in Biotechnology. Totowa, NJ, NJ, USA: Humana Press (Methods in Molecular Biology), pp. 55–80. doi: 10.1007/978-1-60327-106-6.
Horton, T. et al. (2018) World Register of Marine Species. Available at: http://www.marinespecies.org.
Hoy, M. B. (2013) '3D Printing: Making Things at the Library', Medical Reference Services Quarterly, 32(1), pp. 93–99. doi: 10.1080/02763869.2013.749139.
Hsiang, A. Y., Elder, L. E. and Hull, P. M. (2016) 'Towards a morphological metric ofassemblage dynamics in the fossil record a test case using planktonic foraminifera.pdf', Philosophical transactions of the Royal Society of London. Series B, Biological sciences, 371(1691), pp. 20150227-. doi: 10.1098/rstb.2015.0227.
Humphries, S. (2009) 'Filter feeders and plankton increase particle encounter rates through flow regime control.', Proceedings of the National Academy of Sciences of the United States of America, 106(19), pp. 7882–7887. doi: 10.1073/pnas.0809063106.
Hutchinson, G. E. (1967) A Treatise on Limnology. Volume II. Introduction to lake biology and the limnoplankton. London: John Wiley and Sons, Inc.
Igic, B. et al. (2015) 'Using 3D printed eggs to examine the egg-rejection behaviour of wild birds', PeerJ, 3, p. e965. doi: 10.7717/peerj.965.
IOC SCOR and IAPSO et al. (2010) 'The international thermodynamic equation of seawater – 2010: Calculation and use of thermodynamic properties', Intergovernmental Oceanographic Commission, Manuals and Guides No. 56, (June), p. 196.
IUCN (2016) The IUCN Red List of Threatened Species. Version 2016-3.
Iversen, M. H. and Ploug, H. (2010) 'Ballast minerals and the sinking carbon flux in the ocean: Carbon-specific respiration rates and sinking velocity of marine snow aggregates', Biogeosciences, 7(9), pp. 2613–2624. doi: 10.5194/bg-7-2613-2010.
Jones, A. M. and Knudsen, J. G. (1961) 'Drag coefficients at low Reynolds numbers for flow past immersed bodies', American Institute of Chemical Engineers Journal, 7(1), pp. 20–25. doi: 10.1002/aic.690070107.
Jonkers, L. et al. (2015) 'Global analysis of seasonality in the shell flux of extant planktonic foraminifera', Biogeosciences, 12(7), pp. 2207–2226. doi: 10.5194/bg-12-2207-2015.
Jonsson, T. et al. (2017) 'Chamber music: an unusual Helmholtz resonator for song amplification in a Neotropical bush-cricket (Orthoptera, Tettigoniidae)', The Journal of Experimental Biology, 220(16), pp. 2900–2907. doi: 10.1242/jeb.160234.
Joy, J. B. et al. (2016) 'Ancestral Reconstruction', PLoS Computational Biology, 12(7), pp. 1–20. doi: 10.1371/journal.pcbi.1004763.
Kamei, K. ichiro et al. (2015) '3D printing of soft lithography mold for rapid production of polydimethylsiloxane-based microfluidic devices for cell stimulation with concentration gradients', Biomedical Microdevices, 17(2), p. 36. doi: 10.1007/s10544-015-9928-y.
Kaplan, H. and Pyayt, A. (2015) 'Tactile Visualization and 3D Printing for Education', in Encyclopedia of Computer Graphics and Games. Cham: Springer International Publishing, pp. 1–8. doi: 10.1007/978-3-319-08234-9_57-1.
Kendall, D. G. (1984) 'Shape manifolds, procrustean metrics, and complex projective spaces', Bulletin of the London Mathematical Society, 16(2), pp. 81–121. doi: 10.1112/blms/16.2.81.
Kitson, P. J. et al. (2012) 'Configurable 3D-Printed millifluidic and microfluidic "lab on a chip" reactionware devices', Lab on a Chip, 12(18), p. 3267. doi: 10.1039/c2lc40761b.
Koehl, M. A. R. (2003) 'Physical modelling in biomechanics', Philosophical Transactions of the Royal Society B: Biological Sciences, 358(1437), pp. 1589–1596. doi: 10.1098/rstb.2003.1350.
Koehl, M. A. R. R., Evangelista, D. and Yang, K. (2011) 'Using physical models to study the gliding performance of extinct animals', Integrative and Comparative Biology, 51(6), pp. 1002–1018. doi: 10.1093/icb/icr112.

Koehler, C. et al. (2012) '3D reconstruction and analysis of wing deformation in free-flying dragonflies', Journal of Experimental Biology, 215(June), pp. 3018–3027. doi: 10.1242/jeb.069005.
Kolitsky, M. A. (2014) '3D Printed Tactile Learning Objects: Proof of Concept', Journal of Blindness Innovation and Research, 4(1). doi: 10.5241/4-51.
Komar, P. D. and Reimers, C. E. (1978) 'Grain Shape Effects on Settling Rates', The Journal of Geology, 86(2), pp. 193–209. doi: 10.1086/649674.
Krebs, J. R. and Davies, N. B. (1993) An Introduction to Behaviour Ecology. 3rd edn. London: Blackwell Science Ltd.
Kruszyński, K. J. and Van Liere, R. (2009) 'Tangible props for scientific visualization: Concept, requirements, application', Virtual Reality, 13(4), pp. 235–244. doi: 10.1007/s10055-009-0126-1.
Kucera, M. (2007) 'Chapter Six Planktonic Foraminifera as Tracers of Past Oceanic Environments', Developments in Marine Geology. London: Elsevier, 1(07), pp. 213–262. doi: 10.1016/S1572-5480(07)01011-1.
De La Rocha, C. L. and Passow, U. (2007) 'Factors influencing the sinking of POC and the efficiency of the biological carbon pump', Deep-Sea Research Part II: Topical Studies in Oceanography, 54(5–7), pp. 639–658. doi: 10.1016/j.dsr2.2007.01.004.
LaBarbera, M. (1989) 'Analyzing Body Size as a Factor in Ecology and Evolution', Annual Review of Ecology and Systematics, 20(1), pp. 97–117. doi: 10.1146/annurev.es.20.110189.000525.
Larkin, N. R. and Porro, L. B. (2016) 'Three legs good, four legs better: Making a quagga whole again with 3D printing', Collection Forum, 30(1–2), pp. 73–84. doi: 10.14351/0831-4985-30.1.73.
Lauder, G. V. et al. (2016) 'Structure, biomimetics, and fluid dynamics of fish skin surfaces', Physical Review Fluids, 1(6), p. 060502. doi: 10.1103/PhysRevFluids.1.060502.
Lazier, J. R. N. and Mann, K. H. (1989) 'Turbulence and the diffusive layers around small organisms', Deep Sea Research Part A, Oceanographic Research Papers, 36(11), pp. 1721–1733. doi: 10.1016/0198-0149(89)90068-X.
Lea, D. W. et al. (2002) 'Reconstructing a 350 ky history of sea level using planktonic Mg/Ca and oxygen isotope records from a Cocos Ridge core', Quaternary Science Reviews, 21(1–3), pp. 283–293. doi: 10.1016/S0277-3791(01)00081-6.
Leckie, R. M. (2009) 'Seeking a better life in the plankton', Proceedings of the National Academy of Sciences, 106(34), pp. 14183–14184. doi: 10.1073/pnas.0907091106.
Lee, K. G. et al. (2014) '3D printed modules for integrated microfluidic devices', RSC Advances, 4(62), pp. 32876–32880. doi: 10.1039/C4RA05072J.
Lipps, J. H. (1979) 'Ecology and Paleoecology of Planktic Foraminifera', in Foraminiferal Ecology and Paleocology. SEPM (Society for Sedimentary Geology), pp. 62–104. doi: 10.2110/scn.79.06.0062.
Lipps, J. H., Finger, K. L. K. L. and Walker, S. E. S. E. (2011) 'What should we call the Foraminifera?', The Journal of Foraminiferal Research, 41(4), pp. 309–313. doi: 10.2113/gsjfr.41.4.309.
Lohmann, G. P. (1983) 'Eigenshape analysis of microfossils: A general morphometric procedure for describing changes in shape', Journal of the International Association for Mathematical Geology, 15(6), pp. 659–672. doi: 10.1007/BF01033230.
Lombard, F. et al. (2009) 'Modelling the temperature dependent growth rates of planktic foraminifera', Marine Micropaleontology. Elsevier B.V., 70(1–2), pp. 1–7. doi: 10.1016/j.marmicro.2008.09.004.
Lücking, T. H. et al. (2015) '3D-printed individual labware in biosciences by rapid prototyping: A proof of principle', Engineering in Life Sciences, 15(1), pp. 51–56. doi: 10.1002/elsc.201400093.
Mace, E. M., Moon, J. and Orange, J. S. (2015) 'Three-Dimensional Printing of Super-Resolution Microscopy Images', Microscopy Today, 23(04), pp. 26–29. doi: 10.1017/S1551929515000607.
Macleod, N. (2010) 'Alternative 2D and 3D form characterization approaches to the automated identification of biological species', Tools for identifying biodiversity: progress and problems, pp. 225–229.
MacLeod, N. (2012) 'Going around the bend: Eigenshape analysis I', Palaeontology Newsletter, 80, pp. 32–48.
Mallison, H. (2011) 'Digitizing Methods for Paleontology: Applications, Benefits and Limitations', in Elewa, A. M. T. (ed.) Computational Palentology. Berlin, Heidelberg: Springer, pp. 7–38. doi: 10.1007/978-3-642-16271-8_2.
Malmgren, B. A. and Kennett, J. P. (1981) 'Phyletic Gradualism in a Late Cenozoic Planktonic Foraminiferal Lineage; DSDP Site 284, Southwest Pacific', Paleobiology, 7(2), pp. 230–240. Available at: http://www.jstor.org/stable/2400475.
Mannoor, M. S. et al. (2013) '3D Printed Bionic Ears', Nano Letters, 13(6), pp. 2634–2639. doi: 10.1021/nl4007744.
Marañón, E. et al. (2012) 'Temperature, resources, and phytoplankton size structure in the ocean', Limnology and Oceanography, 57(5), pp. 1266–1278. doi: 10.4319/lo.2012.57.5.1266.

Marshall, B. J. et al. (2015) 'Morphometric and stable isotopic differentiation of Orbulina universa morphotypes from the Cariaco Basin, Venezuela', Marine Micropaleontology. Elsevier B.V., 120, pp. 46–64. doi: 10.1016/j.marmicro.2015.08.001.
Martín-Polvillo, M., Márquez-Ruiz, G. and Dobarganes, M. C. (2004) 'Oxidative stability of sunflower oils differing in unsaturation degree during long-term storage at room temperature', JAOCS, Journal of the American Oil Chemists' Society, 81(6), pp. 577–583. doi: 10.1007/s11746-006-0944-1.
Martinsson, A. (1979) 'Planktonic Once More', 12, p. 19791.
Mashiotta, T. a., Lea, D. W. and Spero, H. J. (1999) 'Glacial–interglacial changes in Subantarctic sea surface temperature and δ18O-water using foraminiferal Mg', Earth and Planetary Science Letters, 170(4), pp. 417–432. doi: 10.1016/S0012-821X(99)00116-8.
McDougal, R. A. and Shepherd, G. M. (2015) '3D-printer visualization of neuron models.', Frontiers in neuroinformatics, 9(June), p. 18. doi: 10.3389/fninf.2015.00018.
McNown, J. S. and Malaika, J. (1950) Effects of particle shape on settling velocity at low Reynolds numbers., Transactions, American Geophysical Union. doi: 10.1029/TR031i001p00074.
Meade, A. and Pagel, M. (2016) 'BayesTraits V3', (November), p. 81. Available at: http://www.evolution.rdg.ac.uk/BayesTraitsV3/Files/BayesTraitsV3.Manual.pdf.
Mehrabani, H. et al. (2014) 'Bio-inspired design of ice-retardant devices based on benthic marine invertebrates: the effect of surface texture', PeerJ, 2, p. e588. doi: 10.7717/peerj.588.
Melo, D. et al. (2016) 'EvolQG - An R package for evolutionary quantitative genetics', F1000Research, 4, p. 925. doi: 10.12688/f1000research.7082.3.
Meyer, J. and Riebesell, U. (2015) 'Reviews and syntheses: Responses of coccolithophores to ocean acidification: A meta-analysis', Biogeosciences, 12(6), pp. 1671–1682. doi: 10.5194/bg-12-1671-2015.
Miklasz, K. A. and Denny, M. W. (2010) 'Diatom sinking speeds : Improved predictions and insight from a modified Stokes ' law', Limnology and Oceanography, 55(6), pp. 2513–2525. doi: 10.4319/lo.2010.55.6.2513.
Miller, C. G. (2013) 'A brief history of modelling Foraminifera : from d ' Orbigny to Zheng Shouyi', in Bowden, A. J., Gregory, F. J., and Henderson, A. S. (eds) Landmarks in Foraminiferal Micropalaeontology: History and Development. London: The Micropalaeontological Society, Special Publications, Geological Society, pp. 337–349.
Mitsopoulou, V. et al. (2015) 'Digitizing, modelling and 3D printing of skeletal digital models of Palaeoloxodon tiliensis (Tilos, Dodecanese, Greece)', Quaternary International. Elsevier Ltd, 379, pp. 4–13. doi: 10.1016/j.quaint.2015.06.068.
Mohammed, J. S. (2016) 'Applications of 3D printing technologies in oceanography', Methods in Oceanography. Elsevier B.V., 17(3), pp. 97–117. doi: 10.1016/j.mio.2016.08.001.
Morard, R. et al. (2013) 'Ecological modeling of the temperature dependence of cryptic species of planktonic Foraminifera in the Southern Hemisphere', Palaeogeography, Palaeoclimatology, Palaeoecology. Elsevier B.V., 391, pp. 13–33. doi: 10.1016/j.palaeo.2013.05.011.
Morris, G. K. K. and Mason, A. C. C. (1995) 'Covert stridulation: Novel sound generation by a South American Katydid', Naturwissenschaften, 82(2), pp. 96–98. doi: 10.1007/BF01140151.
Morrison, F. A. F. (2010) 'Data correlation for drag coefficient for sphere', Michigan Technology University, Houghton, MI, 6(April), pp. 1–2. Available at: http://www.chem.mtu.edu/~fmorriso/DataCorrelationForSphereDrag2013.pdf.
Munson, B. R., Young, D. F. and Okiishi, T. H. (1994) Fundamentals of Fluid Mechanics. Second. New York: John Wiley and Sons, Inc.
Murr, L. E. et al. (2012) 'Fabrication of Metal and Alloy Components by Additive Manufacturing: Examples of 3D Materials Science', Journal of Materials Research and Technology. Elsevier, 1(1), pp. 42–54. doi: 10.1016/S2238-7854(12)70009-1.
Murray, J. (1897) 'On the distribution of pelagic Foraminifera at the surface and on the floor of the ocean', Natural Science (ecology), 1, pp. 17–27.
Muscutt, L. E. et al. (2017) 'The four-flipper swimming method of plesiosaurs enabled efficient and effective locomotion', Proceedings of the Royal Society B: Biological Sciences, 284(1861), p. 20170951. doi: 10.1098/rspb.2017.0951.
Naidu, P. D. and Malmgren, B. a. (1996) 'Relationship between late Quaternary upwelling history and coiling properties of Neogloboquadrina pachyderma and Globigerina bulloides in the Arabian Sea', The Journal of Foraminiferal Research, 26(1), pp. 64–70. doi: 10.2113/gsjfr.26.1.64.
Neil, H., Cooke, P. and Northcote, L. (2005) 'The life and death of planktonic foraminifera', 13(1), pp. 18–19.
Neutens, C. et al. (2016) 'Prehensile and non-prehensile tails among syngnathid fishes: what's the difference?', Zoology. Elsevier GmbH., pp. 1–11. doi: 10.1016/j.zool.2016.11.002.
Nguyen, T. M. P., Petrizzo, M. R. and Speijer, R. P. (2009) 'Experimental dissolution of a fossil foraminiferal assemblage (Paleocene-Eocene Thermal Maximum, Dababiya, Egypt): Implications for

paleoenvironmental reconstructions', Marine Micropaleontology. Elsevier B.V., 73(3–4), pp. 241–258. doi: 10.1016/j.marmicro.2009.10.005.
Nigam, R., Saraswat, R. and Mazumder, a (2003) 'Life spans of planktonic foraminifers: New sight through sediment traps', Journal of The Palaeontological Society of India, 48, pp. 129–133.
Niven, L. et al. (2009) 'Virtual skeletons: using a structured light scanner to create a 3D faunal comparative collection', Journal of Archaeological Science. Elsevier Ltd, 36(9), pp. 2018–2023. doi: 10.1016/j.jas.2009.05.021.
Norris, R. D. (1991a) 'Biased Extinction and Evolutionary Trends', Paleobiology, 17(4), pp. 388–399.
Norris, R. D. (1991b) 'Parallel evolution in the keel structure of planktonic foraminifera', The Journal of Foraminiferal Research, 21(4), pp. 319–331. doi: 10.2113/gsjfr.21.4.319.
Norris, R. D., Corfield, R. M. and Cartlidge, J. E. (1993) 'Evolution of depth ecology in the planktic foraminifera lineage (Globorotalia (Fohsella)', Geology, 21(11), pp. 975–978. doi: 10.1130/0091-7613(1993)021<0975:EODEIT>2.3.CO.
Nunn, C. (2011) The Comparative Approach in Evolutionary Anthropology and Biology. Chicago: Chicago University Press.
O'Hara, R. B. and Kotze, D. J. (2010) 'Do not log-transform count data', Methods in Ecology and Evolution, 1(2), pp. 118–122. doi: 10.1111/j.2041-210X.2010.00021.x.
O'Meara, B. C. (2012) 'Evolutionary Inferences from Phylogenies: A Review of Methods', Annual Review of Ecology, Evolution, and Systematics, 43(1), pp. 267–285. doi: 10.1146/annurev-ecolsys-110411-160331.
Oeffner, J. and Lauder, G. V. (2012) 'The hydrodynamic function of shark skin and two biomimetic applications', Journal of Experimental Biology, 215(5), pp. 785–795. doi: 10.1242/jeb.063040.
Olsen, A. M. (2017) 'Feeding ecology is the primary driver of beak shape diversification in waterfowl', Functional Ecology, 31(10), pp. 1985–1995. doi: 10.1111/1365-2435.12890.
D'Orbigny, A. (1826) 'Tableau methodique de la classe des Cephalopodes', Ann. Sci. Nat. Paris: Crochard, 7, pp. 245–314.
Orme, D. (2013) 'The caper package : comparative analysis of phylogenetics and evolution in R', R package version 0.5, 2, pp. 1–36. doi: 1.
Orr, J. C. et al. (2005) 'Anthropogenic ocean acidification over the twenty-first century and its impact on calcifying organisms', Nature, 437(7059), pp. 681–686. doi: 10.1038/nature04095.
Oskui, S. M. et al. (2016) 'Assessing and Reducing the Toxicity of 3D-Printed Parts', Environmental Science & Technology Letters, 3(1), pp. 1–6. doi: 10.1021/acs.estlett.5b00249.
Oxford University Press (2018) OED Online. Available at: http://www.oed.com/viewdictionaryentry/Entry/11125.
Padisák, J. et al. (2003) 'Sinking properties of some phytoplankton shapes and the relation of form resistance to morphological diversity of plankton - An experimental study', Hydrobiologia, 500(1–3), pp. 243–257. doi: 10.1023/A:1024613001147.
Paradis, E., Claude, J. and Strimmer, K. (2004) 'APE: Analyses of phylogenetics and evolution in R language', Bioinformatics, 20(2), pp. 289–290. doi: 10.1093/bioinformatics/btg412.
Passow, U. and Carlson, C. a. (2012) 'The biological pump in a high CO2 world', Marine Ecology Progress Series, 470(2), pp. 249–271. doi: 10.3354/meps09985.
Pawlowski, J. and Holzmann, M. (2014) 'A plea for DNA barcoding of Foraminifera', Journal for Foraminiferal Research, (1), pp. 62–67. doi: 10.2113/gsjfr.44.1.62.
Pearce, J. M. (2013) Open-source lab: How to build your own hardware and reduce research costs. London: Elsevier.
Pearson, P. N., Shackleton, N. J. and Hall, M. a. (1993) 'Stable isotope paleoecology of middle Eocene planktonic foraminifera and multi-species isotope stratigraphy, DSDP Site 523, South Atlantic', (2), pp. 123–140. doi: 10.2113/gsjfr.23.2.123.
Pearson, P. N. and Wade, B. S. (2009) 'Taxonomy and stable isotope paleoecology of well-preserved planktonic foraminifera from the uppermost oligocene of Trinidad', (3), pp. 191–217. doi: 10.2113/gsjfr.39.3.191.
Policha, T. et al. (2016) 'Disentangling visual and olfactory signals in mushroom-mimicking Dracula orchids using realistic three-dimensional printed flowers', New Phytologist, 210(3), pp. 1058–1071. doi: 10.1111/nph.13855.
Porter, M. M. et al. (2015) 'Why the seahorse tail is square', Science, 349(6243), pp. 46-. doi: 10.1126/science.aaa6683.
Preece, D. et al. (2013) '"Let's Get Physical": Advantages of a physical model over 3D computer models and textbooks in learning imaging anatomy', Anatomical Sciences Education, 6(4), pp. 216–224. doi: 10.1002/ase.1345.

Prothero, D. R. and Lazarus, D. B. (1980) 'Planktonic microfossils and the recognition of ancestors', Systematic Zoology, 29(2), pp. 119–129. doi: 10.1093/sysbio/29.2.119.
Pu, X., Li, G. and Huang, H. (2016) 'Preparation, anti-biofouling and drag-reduction properties of a biomimetic shark skin surface', Biology Open, 5(4), pp. 389–396. doi: 10.1242/bio.016899.
Purnell, M. A. (2003) 'Casting, replication, and anaglyph stereo imaging of microscopic detail in fossils, with examples from conodonts and other jawless vertebrates', Palaeontologia Electronica, 6(December 2003), pp. 1–11. Available at: http://www.nhm.ac.uk/hosted_sites/pe/2003_2/rubber/rubber.pdf.
Quillévéré, F. et al. (2013) 'Global scale same-specimen morpho-genetic analysis of Truncorotalia truncatulinoides: A perspective on the morphological species concept in planktonic foraminifera', Palaeogeography, Palaeoclimatology, Palaeoecology. Elsevier B.V., 391, pp. 2–12. doi: 10.1016/j.palaeo.2011.03.013.
Quinn, G. P. and Keough, M. J. (2002) 'Experimental Design and Data Analysis for Biologists', Journal of Experimental Marine Biology and Ecology, 277(2), p. 537. doi: 10.1016/S0022-0981(02)00278-2.
R Core Team (2018) 'R: A Language and Environment for Statistical Computing'. Vienna, Austria, Austria: R Foundation for Statistical Computing. Available at: https://www.r-project.org.
Rahman, I. A., Adcock, K. and Garwood, R. J. (2012) 'Virtual Fossils: a New Resource for Science Communication in Paleontology', Evolution: Education and Outreach, 5(4), pp. 635–641. doi: 10.1007/s12052-012-0458-2.
Raup, D. M. (1966) 'Geometric Analysis of Shell Coiling : General Problems', Journal of Paleontology, 40(5), pp. 1178–1190.
van Ravenzwaaij, D., Cassey, P. and Brown, S. D. (2018) 'A simple introduction to Markov Chain Monte–Carlo sampling', Psychonomic Bulletin and Review, 25(1), pp. 143–154. doi: 10.3758/s13423-016-1015-8.
Reidenbach, M. A., George, N. and Koehl, M. A. R. (2008) 'Antennule morphology and flicking kinematics facilitate odor sampling by the spiny lobster, Panulirus argus', Journal of Experimental Biology, 211(17), pp. 2849–2858. doi: 10.1242/jeb.016394.
Rengier, F. et al. (2010) '3D printing based on imaging data: review of medical applications', International Journal of Computer Assisted Radiology and Surgery, 5(4), pp. 335–341. doi: 10.1007/s11548-010-0476-x.
Revell, L. J. (2010) 'Phylogenetic signal and linear regression on species data', Methods in Ecology and Evolution, 1(4), pp. 319–329. doi: 10.1111/j.2041-210X.2010.00044.x.
Revell, L. J. (2012) 'phytools: An R package for phylogenetic comparative biology (and other things)', Methods in Ecology and Evolution, 3(2), pp. 217–223. doi: 10.1111/j.2041-210X.2011.00169.x.
Reynolds, C. S. (1997) Vegetation Processes in the Pelagic: A Model for Ecosystem Theory Vol. 9. Oldendorf/Luhe, Germany, Germany: Ecology Institute.
Ristow, G. H. (1997) 'Wall correction factor for sinking cylinders in fluids', Physical Review E, 55(3), pp. 2808–2813. doi: 10.1103/PhysRevE.55.2808.
Rodhe, W. (1974) 'Plankton, planktic, planktonic', Limnology and Oceanography, 19(2), pp. 360–360. doi: 10.4319/lo.1974.19.2.360.
Rodriguez, J. M., Edeskär, T. and Knutsson, S. (2013) 'Particle shape quantities and measurement techniques-A review', Electronic Journal of Geotechnical Engineering, 18 A, pp. 169–198. doi: https://pure.ltu.se/portal/files/41279547/shape_report_november_2012_A4.pdf.
Rohlf, F. J. (2015) 'The tps series of software', Hystrix, 26(1), pp. 1–4. doi: 10.4404/hystrix-26.1-11264.
Rosenthal, Y. and Lohmann, G. P. (2002) 'Accurate estimation of sea surface temperatures using dissolution-corrected calibrations for Mg/Ca paleothermometry', Paleoceanography, 17(3), pp. 1–6. doi: 10.1029/2001PA000749.
Ross, C. A. and Haman, D. (1989) 'Suprageneric ranges of Foraminiferida', The Journal of Foraminiferal Research, 19(1), pp. 72–83. doi: 10.2113/gsjfr.19.1.72.
Le Roux, J. P. (2005) 'Grains in motion: A review', Sedimentary Geology, 178(3–4), pp. 285–313. doi: 10.1016/j.sedgeo.2005.05.009.
Ruiz, J., Macias, D. and Peters, F. (2004) 'Turbulence increases the average settling velocity of phytoplankton cells', Proceedings of the National Academy of Sciences, 101(51), pp. 17720–17724. doi: 10.1073/pnas.0401539101.
Russell, A. D. et al. (2004) 'Effects of seawater carbonate ion concentration and temperature on shell U, Mg, and Sr in cultured planktonic foraminifera', Geochimica et Cosmochimica Acta, 68(21), pp. 4347–4361. doi: 10.1016/j.gca.2004.03.013.
Sadekov, A. et al. (2009) 'Surface and subsurface seawater temperature reconstruction using Mg/Ca microanalysis of planktonic foraminifera Globigerinoides ruber , Globigerinoides sacculifer , and Pulleniatina obliquiloculata', Paleoceanography, 24(3), p. PA3201. doi: 10.1029/2008PA001664.

Schiebel, R. (2002) 'Planktic foraminiferal sedimentation and the marine calcite budget', Global Biogeochem. Cycles, 16(4), p. 1065. doi: 10.1029/2001gb001459.
Schiebel, R. et al. (2005) 'Modern planktic foraminifera', Palaontogische Zeitschrift, 79(1), pp. 135–148. doi: 10.1007/BF03021758.
Schiebel, R. and Hemleben, C. (2017) Planktic Foraminifers in the Modern Ocean. Berlin, Heidelberg, Heidelberg: Springer Berlin Heidelberg.
Schiebel, R., Hiller, B. and Hemleben, C. (1995) 'Impacts of storms on Recent planktic foraminiferal test production and CaCO3flux in the North Atlantic at 47 °N, 20 °W (JGOFS)', Marine Micropaleontology, 26(1–4), pp. 115–129. doi: 10.1016/0377-8398(95)00035-6.
Schindelin, J. et al. (2012) 'Fiji: An open-source platform for biological-image analysis', Nature Methods, 9(7), pp. 676–682. doi: 10.1038/nmeth.2019.
Schmidt, D. N. et al. (2004) 'Size distribution of Holocene planktic foraminifer assemblages: biogeography, ecology and adaptation', Marine Micropaleontology, 50(3–4), pp. 319–338. doi: 10.1016/S0377-8398(03)00098-7.
Schmidt, D. N. et al. (2006) 'Biogeography and evolution of body size in marine plankton', Earth-Science Reviews, 78(3–4), pp. 239–266. doi: 10.1016/j.earscirev.2006.05.004.
Schmidt, D. N. et al. (2013) 'Linking evolution and development: Synchrotron Radiation X-ray tomographic microscopy of planktic foraminifers', Palaeontology, 56(4), pp. 741–749. doi: 10.1111/pala.12013.
Schmidt, D. N. (2018) 'Determining climate change impacts on ecosystems: the role of palaeontology', Palaeontology. Edited by A. Smith, 61(1), pp. 1–12. doi: 10.1111/pala.12335.
Schmidt, D. N., Thierstein, H. R. and Bollmann, J. (2004) 'The evolutionary history of size variation of planktic foraminiferal assemblages in the Cenozoic', Palaeogeography, Palaeoclimatology, Palaeoecology, 212(1–2), pp. 159–180. doi: 10.1016/j.palaeo.2004.06.002.
Schneider, C. E. and Kennett, J. P. (1999) 'Segregation and speciation in the Neogene planktonic foraminiferal clade Globoconella', Paleobiology, 25(3), pp. 383–395. doi: 10.1017/S0094837300021345.
Schott, G. (1935) 'Geographie des Indischen und Stillen Ozeans', Die Naturwissenschaften, 23(49), pp. 830–832. doi: 10.1007/BF01491916.
Van Sebille, E. et al. (2015) 'Ocean currents generate large footprints in marine palaeoclimate proxies', Nature Communications. Nature Publishing Group, 6(Ivm), p. 6521. doi: 10.1038/ncomms7521.
Sen, S., Mittal, S. and Biswas, G. (2012) 'Steady separated flow past elliptic cylinders using a stabilized finite-element method', CMES - Computer Modeling in Engineering and Sciences, 86(1), pp. 1–26.
Shapiro, L. and Stockman, G. (2000) Computer Vision. New Jersey: Prentice-Hall.
Shen, L., Farid, H. and McPeek, M. a. (2009) 'Modeling three-dimensional morphological structures using spherical harmonics', Evolution, 63(4), pp. 1003–1016. doi: 10.1111/j.1558-5646.2008.00557.x.
Si, W., Berggren, W. A. and Aubry, M. P. (2018) 'Mosaic evolution in the middle Miocene planktonic foraminifera Fohsella lineage', Paleobiology, 44(2), pp. 263–272. doi: 10.1017/pab.2017.23.
Sidlauskas, B. (2008) 'Continuous and arrested morphological diversification in sister clades of characiform fishes: A phylomorphospace approach', Evolution, 62(12), pp. 3135–3156. doi: 10.1111/j.1558-5646.2008.00519.x.
Sing, S. L. et al. (2016) 'Laser and electron-beam powder-bed additive manufacturing of metallic implants: A review on processes, materials and designs', Journal of Orthopaedic Research, 34(3), pp. 369–385. doi: 10.1002/jor.23075.
Sitthi-amorn, P. et al. (2015) 'MultiFab: A Machine Vision Assisted Plaform for Multi-material 3D Printing', ACM Transactions on Graphics, 34(4), pp. 129:1-129:11. doi: 10.1145/2766962.
Smayda, T. J. (1971) 'Normal and accelerated sinking of phytoplankton in the sea', Marine Geology, 11(2), pp. 105–122. doi: 10.1016/0025-3227(71)90070-3.
Spezzaferri, S. et al. (2015) 'Fossil and genetic evidence for the polyphyletic nature of the Planktonic foraminifera "Globigerinoides", and description of the new genus Trilobatus', PLoS ONE, 10(5), pp. 1–20. doi: 10.1371/journal.pone.0128108.
Spjeldnaes, N. (1963) 'Some Upper Tremadocian graptolites from Norway', Palaeontology, 6(1), pp. 121–131.
Stadler, A. T. et al. (2016) 'Adaptation to life in aeolian sand: how the sandfish lizard, Scincus scincus , prevents sand particles from entering its lungs', The Journal of Experimental Biology, 219(22), pp. 3597–3604. doi: 10.1242/jeb.138107.
Stamhuis, E. J. (2006) 'Basics and principles of particle image velocimetry (PIV) for mapping biogenic and biologically relevant flows', Aquatic Ecology, 40(4), pp. 463–479. doi: 10.1007/s10452-005-6567-z.
Stanca, E. et al. (2013) 'Phytoplankton composition in the coastal magnetic island lagoon, western pacific ocean (Australia)', Transitional Waters Bulletin, 7(2), pp. 145–158. doi: 10.1285/i1825229Xv7n2p145.

Stayton, C. T. and Ruta, M. (2006) 'Geometric morphometrics of the skull roof of stereospondyls (Amphibia: Temnospondyli)', Palaeontology, 49(2), pp. 307–337. doi: 10.1111/j.1475-4983.2006.00523.x.
Stokes, G. G. (1905) 'On the Effect of the Internal Friction of Fluids on the Motion of Pendulums', Mathematical and Physical Papers, 9, pp. 1–10. doi: 10.1017/CBO9780511702266.002.
Sustainable Oceans International and International Sustainable Oceans (2012) 'Worlds First 3D Printed Reef', pp. 1–2. Available at: http://www.sustainableoceans.com.au/images/stories/Media_releases/SOI_Worlds_FIRST_3D_printed_reef_MEDIA_RELEASE_2012.pdf.
Sutton, M. D. et al. (2012) 'SPIERS and VAXML; A software toolkit for tomographic visualisation and a format for virtual specimen interchange', Paleontologica electronica, 15(2), pp. 1–15.
Svensson, P. A. A. and Wong, B. B. M. B. M. (2011) 'Carotenoid-based signals in behavioural ecology: a review', Behaviour, 148(2), pp. 131–189. doi: 10.1163/000579510X548673.
Taghon, G. L., Nowell, A. R. M. and Jumars, P. A. (1984) 'Transport and breakdown of fecal pellets: Biological and sedimentological consequences', Limnology and Oceanography, 29(1), pp. 64–72. doi: 10.4319/lo.1984.29.1.0064.
Takahashi, K. (1984) Measured and computed data for dimensions and sinking speeds of planktonic foraminifera from plankton tows and sediments. San Diego.
Takahashi, K. et al. (1984) 'Planktonic foraminifera: factors controlling sinking speeds', Deep Sea Research Part A. Oceanographic Research Papers, 31(12), pp. 1477–1500. doi: 10.1016/0198-0149(84)90083-9.
Tappan, H. and Loeblich, A. R. (1973) 'Evolution of the oceanic plankton', Earth Science Reviews, 9(3), pp. 207–240. doi: 10.1016/0012-8252(73)90092-5.
Teshima, Y. et al. (2010) 'Enlarged Skeleton Models of Plankton for Tactile Teaching', in Miesenberger, K. et al. (eds) Computers Helping People with Special Needs: 12th International Conference, ICCHP 2010, Vienna, Austria, July14-16, 2010, Proceedings, Part II. Berlin, Heidelberg, Heidelberg: Springer Berlin Heidelberg, pp. 523–526. doi: 10.1007/978-3-642-14100-3_78.
The Mathworks, I. (2016) 'MATLAB Release 2016a'. Natick, Massachusetts, United States of America, Massachusetts, United States of America.
Thiede, J. (1971) 'Variations in coiling ratios of Holocene planktonic foraminifera', Deep-Sea Research and Oceanographic Abstracts, 18(8), pp. 823–831. doi: 10.1016/0011-7471(71)90049-0.
Thiede, J. (1975) 'Distribution of foraminifera in surface waters of a coastal upwelling area', Nature, 253(5494), pp. 712–714. doi: 10.1038/253712a0.
Thompson, Da. W. (1917) On Growth and Form. Edited by J. T. Bonner. Cambridge: Cambridge University Press. doi: 10.1017/CBO9781107589070.
Thomson, J. D., Draguleasa, M. A. and Tan, M. G. (2015) 'Flowers with caffeinated nectar receive more pollination', Arthropod-Plant Interactions, 9(1), pp. 1–7. doi: 10.1007/s11829-014-9350-z.
Thoulet, J. (1891) 'Expériences sur la Sédimentation', Annales des Mines, 8th Series, 19, pp. 5–35. Available at: https://patrimoine.mines-paristech.fr/items/viewer/239#page/Image+36/mode/2up/.
Ujiié, Y. et al. (2010) 'Coiling dimorphism within a genetic type of the planktonic foraminifer Globorotalia truncatulinoides', Marine Micropaleontology. Elsevier B.V., 77(3–4), pp. 145–153. doi: 10.1016/j.marmicro.2010.09.001.
Universitaria, C. and Herrero, C. (2002) 'Taphonomic Processes in Selected Lower and Middle Jurassic Foraminifera From the Iberian Range and Basque-Cantabrian Basin (Spain)', The Journal of Foraminiferal Research, 32(1), pp. 22–42. doi: 10.2113/0320022.
De Vargas, C. et al. (2001) 'Pleistocene adaptive radiation in Globorotalia truncatulinoides: genetic, morphologic, and environmental evidence', Paleobiology, 27(1), pp. 104–125. doi: 10.1666/0094-8373(2001)027<0104:PARIGT>2.0.CO;2.
Venables, W. N. and Ripley, B. D. (2002) Modern Applied Statistics with S. Fourth. New York: Springer.
Venditti, C., Meade, A. and Pagel, M. (2011) 'Multiple routes to mammalian diversity', Nature. Nature Publishing Group, 479(7373), pp. 393–396. doi: 10.1038/nature10516.
Viscosi, V. and Cardini, A. (2011) 'Leaf morphology, taxonomy and geometric morphometrics: A simplified protocol for beginners', PLoS ONE, 6(10), pp. 667–669. doi: 10.1371/journal.pone.0025630.
Vogel, S. (1974) 'Current-induced flow through the sponge, Halichondria.', Biological Bulletin, 147(2), pp. 443–456. doi: 10.2307/1540461.
Vogel, S. (1994) Life in Moving Fluids. Second. Princeton, N.J., N.J.: Princeton University Press.
Volk, T. and Hoffert, M. I. (1985) 'Ocean carbon pumps: Analysis of relative strength and efficiencies in ocean-driven atmospheric CO2 changes', in Geophysical Monograph Series, pp. 99–110. doi: 10.1029/GM032p0099.

Wade, B. S. et al. (2011) 'Review and revision of Cenozoic tropical planktonic foraminiferal biostratigraphy and calibration to the geomagnetic polarity and astronomical time scale', Earth-Science Reviews. Elsevier B.V., 104(1–3), pp. 111–142. doi: 10.1016/j.earscirev.2010.09.003.
Waldbaur, A. et al. (2011) 'Let there be chip—towards rapid prototyping of microfluidic devices: one-step manufacturing processes', Analytical Methods, 3(12), p. 2681. doi: 10.1039/c1ay05253e.
Walsby, A. E. and Holland, D. P. (2006) 'Sinking velocities of phytoplankton measured on a stable density gradient by laser scanning.', Journal of the Royal Society, Interface / the Royal Society, 3(8), pp. 429–439. doi: 10.1098/rsif.2005.0106.
Watson, C. M. and Francis, G. R. (2015) 'Three dimensional printing as an effective method of producing anatomically accurate models for studies in thermal ecology', Journal of Thermal Biology. Elsevier, 51, pp. 42–46. doi: 10.1016/j.jtherbio.2015.03.004.
Webb, L. P. and Swan, a. R. H. A. R. H. (1996) 'Estimation of parameters of foraminiferal test geometry by image analysis', Palaeontology, pp. 471–475. Available at: http://eprints.kingston.ac.uk/14364/.
Wei, K.-Y. Y. (1987) 'Multivariate morphometric differentiation of chronospecies in the late Neogene planktonic foraminiferal lineage Globoconella', Marine Micropaleontology, 12(C), pp. 183–202. doi: 10.1016/0377-8398(87)90020-X.
Wei, K. (1994) 'Allometric heterochrony in the Pliocene-Pleistocene planktic foraminiferal clade Globoconella', Paleobiology, 20(01), pp. 66–84. doi: 10.1017/S0094837300011143.
Wen, L. L., Weaver, J. C. and Lauder, G. V. (2014) 'Biomimetic shark skin: design, fabrication and hydrodynamic function.', The Journal of experimental biology, 217(Pt 10), pp. 1656–66. doi: 10.1242/jeb.097097.
White, C. M. (1946) 'The Drag of Cylinders in Fluids at Slow Speeds', Proceedings of the Royal Society A: Mathematical, Physical and Engineering Sciences, 186(1007), pp. 472–479. doi: 10.1098/rspa.1946.0059.
White, F. M. (1991) Viscous Fluid Flow. Second. New York: McGraw-Hill, Inc.
White Rabbit Corp (2016) 'Molcer'. Tokyo, Japan, Japan: White Rabbit Company Ltd.
Willermet, C. (2016) 'Biological Anthropology in 2015: Open Access, Biocultural Interactions, and Social Change', American Anthropologist, 118(2), pp. 317–329. doi: 10.1111/aman.12529.
Wolf-Gladrow, D. A., Bijma, J. and Zeebe, R. E. (1999) 'Model simulation of the carbonate chemistry in the microenvironment of symbiont bearing foraminifera', Marine Chemistry, 64(3), pp. 181–198. doi: 10.1016/S0304-4203(98)00074-7.
Wolff, N. H. et al. (2018) 'Vulnerability of the Great Barrier Reef to climate change and local pressures', Global Change Biology, 24(September 2017), pp. 1978–1991. doi: 10.1111/gcb.14043.
Wolowicz, C. H. and Bowman, J. S. (1979) NASA Technical Paper 1435 Similitude Requirements and Scaling Relationships as Applied to Model Testing NASA Technical Paper 14-35 Similitude Requirements and Scaling Relationships as Applied to Model Testing, NASA Scientific and Technical Information Branch.
Wong, K. V. and Hernandez, A. (2012) 'A Review of Additive Manufacturing', ISRN Mechanical Engineering, 2012, pp. 1–10. doi: 10.5402/2012/208760.
Wright, G. A. et al. (2013) 'Caffeine in Floral Nectar Enhances a Pollinator's Memory of Reward', Science, 339(6124), pp. 1202–1204. doi: 10.1126/science.1228806.
Yazdi, A. A. et al. (2016) '3D printing: an emerging tool for novel microfluidics and lab-on-a-chip applications', Microfluidics and Nanofluidics. Springer Berlin Heidelberg, 20(3), p. 50. doi: 10.1007/s10404-016-1715-4.
Yoon, W., Kim, S. and Han, K. (2001) 'Morphology and sinking velocities of fecal pellets of copepod, molluscan, euphausiid, and salp taxa in the northeastern tropical Atlantic', Marine Biology, 139(5), pp. 923–928. doi: 10.1007/s002270100630.
Zelditch, M. L. et al. (2004) Geometric Morphometrics for Biologists A Primer. San Diego, CA, CA: Elsevier Academic Press.
Zhang, C. et al. (2013) 'Open-Source 3D-Printable Optics Equipment', PLoS ONE. Edited by A. G. de Brevern, 8(3), p. e59840. doi: 10.1371/journal.pone.0059840.
Zohuri, B. (2015) Dimensional analysis and self-similarity methods for engineers and scientists, Dimensional Analysis and Self-Similarity Methods for Engineers and Scientists. doi: 10.1007/978-3-319-13476-5.

Chapter 9 Appendices

9.1 Chapter 3 Appendices

9.1.1 Calculating distance to reach terminal velocity

An object sinking (in a straight line) with the velocity V can be described using the difference in velocity (ΔV) and difference in time (Δt) between the start- and end-point of the distance λ(with g being gravitational acceleration), thus:

Equation 9-1

$$\frac{\Delta V}{\Delta t} = \frac{1}{\lambda} \cdot V^2 - g$$

Terminal velocity is achieved when the acceleration has stopped, i.e. $\Delta V = 0$ over distance L. Therefore:

Equation 9-2

$$\frac{\Delta V}{\Delta t} = 0$$

Hence:

Equation 9-3

$${V_t}^2 = \lambda \cdot g$$

Therefore, to find ω (i.e. the distance needed to reach V_t) can be found using V_t and g, (where C is the constant of integration) thus:

Equation 9-4

$$\int \frac{\Delta V}{V_t} - \frac{1}{1 - \left(\frac{V}{V_t}\right)^2} = \frac{V_t}{\lambda} \cdot t + C$$

Naturally at terminal velocity $V = V_t$, by inspection:

Equation 9-5

$$u = \frac{t}{\tau} + C;\ v = -V_t\ tanh\ \frac{t - t_0}{\tau}$$

Unfortunately, all this demonstrates is that terminal velocity cannot be reached, i.e. the solution to Equation 9-5 is infinity (∞).

So as technically, it is not possible to achieve terminal velocity. In practice terminal velocity is a theoretical limit which is never reached, but the sinking (or falling) velocity becomes sufficiently close as to be essentially the same (this almost identical velocity is the generally accepted use of terminal velocity). Therefore, the distance required to reach terminal velocity is infinite.

Therefore, for this example 90% of terminal velocity was calculated. The distance to reach 90% of terminal velocity can be calculated using Equation 9-6; where D_{V_t} is the distance to reach terminal

velocity, y_0 is the starting position (i.e. 0 m), t (the time at measurement, i.e. when the particle is at 90% of V_t) is defined in Equation 9-7, t_0 is the starting time (here specified as 0) and τ is defined as per Equation 9-8 and λ is given by Equation 9-9 (where g is acceleration due to gravity: 9.81m·s^{-2})

Equation 9-6

$$D_{V_t} = y_0 - \lambda \cdot \mathrm{In}\left(\cosh\left(\frac{t - t_0}{\tau}\right)\right)$$

Equation 9-7

$$t = \tanh^{-1}(0.9) \cdot \tau$$

Equation 9-8

$$\tau = \frac{\lambda}{V_t \cdot 0.9}$$

Equation 9-9

$$\lambda = \frac{{V_t}^2}{g}$$

9.1.2 Ellipsoid Examples of CSF (Figure 3-6)

Table 9-1: Values for the ellipsoids featured in Figure 3-6. Using the values in the table above, example ellipsoids were modelled in 3D modelling software: AUTODESK® AutoCAD® (Autodesk.com, 2017)*. CSF values were calculated using Equation 3-10.*

CSF	**Top Row**			**Bottom Row**		
	Lengths			Lengths		
	Shortest	Intermediate	Longest	Shortest	Intermediate	Longest
0.1	40	400	400	74.83	400	1400
0.3	120	400	400	207.85	400	1200
0.5	200	400	400	316.23	400	1000
0.7	280	400	400	395.98	400	800
0.9	360	400	400	399.66	400	493
1	400	400	400	400	400	400

9.1.3 Variable Calculation

Table 9-2: The variables used in this study and their derivation. If the value is not given in the original source, then how it was calculated for this study is provided. For the calculation of density, the fluid density (ρ_{fluid}) used is dependent on the fluid used and the temperature reported in the study.

Variable	Unit	Source		
		Takahashi and Bé (1972)	Fok-Pun and Komar (1983)	Caromel *et al.* (2014)
Sinking Speed	$m \cdot s^{-1}$	Calculated sinking times over 0.5 m and Equation 9-10. (Calculated)	Reported values used.	Reported values used.
Corrected Sinking Speed	$m \cdot s^{-1}$	Corrected using Equation 3-14, using $\frac{\emptyset_{max}}{2}$ as particle radius (r) in Equation 3-13. (Calculated)		
Longest length	m	Longest length with aperture orientated upwards. Reported values used.	Longest length. Reported values used.	Longest length (data are reorganized, but reported values used).
Intermediate length	m	Not given. Calculated as average of longest and shortest length, rounded to nearest µm.	Intermediate length. (Reported values used)	Intermediate Length given. (re-ordered, but Reported values used)
Shortest length	m	Shortest perpendicular to length in the same orientation. (Reported values used)	Shortest length. (Reported values used)	Shortest given length. (re-ordered, but reported values used)
Volume	m^3	Calculated from a basic 3D shape, following Caromel *et al.* (2014) Assumes that intermediate length is an average of length and shortest length.	Calculated following Caromel *et al.*'s (2014) methodology, using the 3 measures of length reported	Calculated from a basic 3D shape. (Reported values used)
Density	$Kg \cdot m^{-3}$	For water filled test calculating using Equation 9-11. (Reported values used)	For a water filled test calculated using Equation 3-12 . (Reported values used)	For water filled test, calculated in a similar manner to Takahashi and Bé.
Weight	µg	Foraminifera were ashed and weighed individually. (Reported values used)	None given. Calculated from bulk density and mass	Weighed 5 similar sized foraminifera and divided obtained mass by five. (Reported values used)
$\boldsymbol{Re}$	N/A	Reported, uses Equation 3-2. (Reported values used)	Reported, uses Equation 9-13. (Reported values used)	Not given, calculated using Equation 3-2, assuming a viscosity of 1mPa·s.
Corrected *Re*	N/A	Calculated using Equation 3-2 and corrected sinking velocity.		
$\boldsymbol{C_D}$	N/A	Reported values used.	Reported values used.	Calculated using Equation 3-6, where area (A) is defined by Equation 9-16.
Corrected $\boldsymbol{C_D}$	N/A	All calculated using, Equation 3-6, and corrected sinking velocity and area as per Equation 9-16.		
Morphogroup	N/A	As per (Aze *et al.*, 2011).		

Table 9-3: Equations used to calculate volume for each species.

Species	Volume formula
Globigerina bulloides	$\frac{4}{3} \cdot \pi \cdot \frac{length_{max}}{2} \cdot \frac{length_{inter}}{2} \cdot \frac{length_{min}}{2}$
Globigerinella siphonifera	
Globigerinoides conglobatus	
Globigerinoides ruber	
Globigerinoides sacculifer	
Globigerinoides trilobus	
Globoconella inflata	
Globorotalia tumida	
Hirsutella hirsuta	
Menardella menardii	
Neogloboquadrina dutertrei	
Orbulina universa	
Pulleniatina obliquiloculata	
Truncorotalia truncatulinoides	$\frac{1}{3} \cdot \pi \cdot \frac{length_{max}}{2} \cdot \frac{length_{inter}}{2} \cdot length_{min}$

Velocity can be calculated using the time taken to travel a known distance. Where U is velocity($m \cdot s^{-1}$), D is distance travelled (in metres) and T is time taken (in seconds), thus:

Equation 9-10

$$U = \frac{D}{T}$$

Takahashi and Bé's (1984) formula for finding the bulk density for a water filled test, where $Volume_{test}$ is found using:

Equation 9-11

$$\rho_{bulk} = \frac{weight + \rho_{fluid} \cdot (Volume_{bulk} - Volume_{test})}{Volume_{bulk}}$$

Takahashi and Bé's (1984) calculated test volume using:

Equation 9-12

$$Volume_{test} = \frac{weight\ of\ test}{density\ of\ calcite}$$

Fok-Pun and Komar's (1983) equation for Reynolds number. Note the use of the nominal diameter (Equation 9-14) and kinematic viscosity.

Equation 9-13

$$Re = \frac{w_s \cdot D_n}{\upsilon}$$

Fok-Pun and Komar's (1983) calculation of nominal diameter

Equation 9-14

$$D_n = \sqrt[3]{L_{shortest} \cdot L_{intermediate} \cdot L_{longest}}$$

Kinematic viscosity is can be calculated with Equation 9-15, where μ is dynamic viscosity and ρ_{fluid} is density of the fluid.

Equation 9-15

$$\upsilon = \frac{\rho_{fluid}}{\mu}$$

For this study, area for C_D was calculated using:

Equation 9-16

$$A = \pi \cdot \left(\frac{Longest\ length}{2} \cdot \frac{shortest\ length}{2}\right)$$

9.1.4 Details of historical experiments presented in Chapter 3

Below are further details of the specific methodologies used in the historical experiments discussed in Chapter 3.

9.1.4.1 *Thoulet (1891)*

Thoulet separated the foraminifera tests and fragments into five size categories (see Table 3-4 and Table 3-5) using an early version of a pycnometer (an instrument that uses an upwards flow of water in a tube to measure density). These sizes were then verified under a microscope. The foraminifera were then dropped in small batches in a seawater filled tube. The descent of the first and last foraminifera was then timed between two lines 1750mm apart and an average value obtained. The exact method used to calculate this average is not reported. The measurements were repeated 20 times per sample, Thoulet reported that there was very little variation in these measurements; although provided no numerical quantification of variation. Furthermore, there are a number of uncertainties in the methodology; the diameter of the tube is not reported, Thoulet does not specify the origin or type of sample, nor are any details on how the samples were prepared before sinking. In addition, there are no individual foraminifera sinking speeds reported, only an average value for the size fraction.

9.1.4.2 *Berthois and Le Calvez (1960)*

Berthois and Le Calvez's (1960) use of a pycnometer is possibly the best quantification of density in any of the studies, as it takes measurements directly from the test rather than estimating from bulk volume and bulk mass measurements like most other studies. However, they admit there were issues with the calculation of density, such as the presence of bubbles in the test. These air bubbles would reduce the bulk density of the foraminifera, and therefore slow the sinking velocity in both the pycnometer (affecting the density measurement) and settling tube (affecting the sinking time). Additionally, they then use Stokes' Law (Equation 3-9) to calculate the density. Stokes' law is only applicable for particles with a Re of less than 1, which is not the case for foraminifera (Fok-pun and Komar, 1983) as previously outlined in 3.1.3.

Berthois and Le Calvez (Berthois and Calvez, 1960) are also the first to measure the area of the foraminifera (presumably presented to the fluid, i.e. projected area, A_p). To do this they first, placed the foraminifera in a thin layer of water on a glass slide, which they claim allowed the foraminifera test to orientate itself naturally. The water was then allowed to evaporate, which fixed the foraminifera in position and allowed them to draw an outline using a *camera lucida* on a sheet of paper. From the drawing they could measure the area of the foraminifera that is presented to the fluid.

For mineral particles (i.e. sand) to sink at the same speed as foraminiferal tests, they found the sand must be half the diameter of the foraminifera. They state that as foraminiferal tests descend from

surface waters to 4000m, temperature changes from 14˚C to 2.54˚C will result in slower sinking velocities. It is known that the viscosity and density of water is dependent on temperature (IOC SCOR and IAPSO *et al.*, 2010) and that changes in viscosity of water have a greater effect on sinking velocities than changes in density (Caromel *et al.*, 2014).

9.1.4.3 *Berger and Piper (1972)*

The sediment samples were broken up in a buffered hydrogen peroxide and sodium axalte/sodium carbonate peptizer solution to increase dispersal. The plankton tow specimens were combusted at 550°C to remove organic matter, which could be a high enough temperature to decompose some of the calcium carbonate ($CaCO_3$) to calcium oxide (CaO) (Hills, 1968). Decomposition of $CaCO_3$ is dependent on both temperature and the concentration of carbon dioxide (CO_2) in the air (Hills, 1968). Decomposition would reduce the density of these foraminifera, and thereby sinking velocities. Berger and Piper (1972) then soaked the foraminifera in water with a trace amount of ethyl alcohol to increase wetting and thereby remove air bubbles inside of the test. After wetting, the samples were rinsed with demineralised water to remove trace alcohol. However, unlike Berthois and Le Calvez (Berthois and Calvez, 1960) individual foraminifera were not sunk, but between 100 and 1000 foraminifera were introduced to the top of the settling tube filled with demineralised water. The foraminifera were collected from the bottom of the tube on a glass slide and counted at 15 second intervals. This method does not allow for the sinking speed of individual foraminifera to be measured, only the generation of histograms of sinking velocities grouped in 15, 30 or 60 second intervals.

9.1.4.4 *Fok-Pun and Komar (1983)*

Sinking velocities of individual foraminifera were calculated using the time taken to travel between two lines, separated by 1000mm, in a tube filled with demineralised water. The experiments were conducted at room temperature (22°C) and the water temperature was monitored during the experiments. Unlike earlier studies they state how the sinking time was measured (timed with a pocket calculator) and the timings are precise to within “about 0.1 seconds” (Fok-pun and Komar, 1983).

9.1.4.5 *Takahashi and Bé (1984)*

Measurements of size were made in three orthogonal directions from an apertural view, under a microscope, and with an accuracy of 10µm. The individual foraminifera were weighed and then wetted with methyl alcohol under vacuum to remove air bubbles. The methyl alcohol was sequentially replaced with water and then the specimen was placed under the water surface on a brush and released. The settling tube was contained within an outer jacket which ensured that a temperature of 3°C was maintained throughout the experiments. Sinking was timed over a 500mm distance and these times converted to sinking velocities in metres per day.

9.1.4.6 *Caromel et al (2014)*

Three orthogonal diameter measurements were made, from which the total (bulk) volume of each foraminifera was found using basic 3D shape formulae (i.e. a sphere, spheroid and cone). The volume of calcite was estimated by weighing the foraminifera in groups of five and assuming a density for calcite of 2700 $kg \cdot m^{-3}$. Once measured and weighed, the foraminifera were left in demineralised water for two weeks to allow any air to dissolve. The specimens were recorded during sinking using high speed (100 frames per second) videos. Sinking velocity was then calculated using 20 frames from the lowest 30mm of the settling tube.

9.1.5 Species ANOVA Results

Table 9-4: Results of ANOVA tests for length, mass, density and volume. All are significant results, showing there are differences in the variance of each variable between species.

	Degrees of freedom	Sum Square	Mean Square	F value	p value
Length					
Species	13	16736010	1287385	58.15	<0.001
Residuals	631	13970775	22141	-	-
Mass					
Species	13	1233400	94877	44.74	<0.001
Residuals	631	1338086	2121	-	-
Density					
Species	13	46496354	3576643	70.04	<0.001
Residuals	631	32224460	51069	-	-
Volume					
Species	13	1.792	0.13785	28.1	<0.001
Residuals	631	3.095	0.00491	-	-

9.1.6 Pairwise Comparisons of morphogroups

Table 9-5: Pairwise comparisons of density, mass and volume between morphogroups, significant p values underlined.

Pair-wise comparison	Density				Mass				Volume			
	Difference	Lower CI	Upper CI	Adjusted p value	Difference	Lower CI	Upper CI	Adjusted p value	Difference	Lower CI	Upper CI	Adjusted p value
3-2	305.4	132.2	478.7	<0.001	40.4	10.4	70.3	0.001	0.03	-0.01	0.07	0.296
4-2	171.1	-13.7	355.9	0.091	82.8	50.9	114.8	<0.001	0.082	0.039	0.125	<0.001
6-2	-14.1	-245.4	217.2	>0.99	0.1	-39.9	40.1	>0.99	0.009	-0.045	0.063	0.999
7-2	147.6	-40.8	336	0.237	15.4	-17.2	48	0.803	0.018	-0.026	0.061	0.896
14-2	245.7	58.8	432.5	0.002	114.5	82.2	146.8	<0.001	0.164	0.12	0.207	<0.001
15-2	665.4	472.9	857.9	<0.001	63.9	30.6	97.2	<0.001	0.027	-0.017	0.072	0.541
4-3	-134.3	-241.8	-26.8	0.004	42.5	23.9	61	<0.001	0.052	0.027	0.077	<0.001
6-3	-319.5	-495.3	-143.8	<0.001	-40.3	-70.7	-9.9	0.002	-0.021	-0.062	0.02	0.74
7-3	-157.8	-271.3	-44.4	0.001	-25	-44.6	-5.4	0.003	-0.012	-0.039	0.014	0.814
14-3	-59.8	-170.6	51.1	0.686	74.1	55	93.3	<0.001	0.134	0.108	0.16	<0.001
15-3	360	239.8	480.1	<0.001	23.5	2.7	44.3	0.015	-0.003	-0.03	0.025	>0.99
6-4	-185.2	-372.4	1.9	0.055	-82.8	-115.1	-50.4	<0.001	-0.073	-0.117	-0.03	<0.001
7-4	-23.5	-153.9	106.9	0.998	-67.4	-90	-44.9	<0.001	-0.065	-0.095	-0.034	<0.001
14-4	74.5	-53.6	202.7	0.603	31.7	9.5	53.8	0.001	0.082	0.052	0.111	<0.001
15-4	494.3	358	630.6	<0.001	-19	-42.5	4.6	0.209	-0.055	-0.087	-0.023	<0.001
7-6	161.7	-29	352.4	0.158	15.3	-17.7	48.3	0.816	0.009	-0.036	0.053	0.998
14-6	259.8	70.6	448.9	0.001	114.4	81.7	147.1	<0.001	0.155	0.111	0.199	<0.001
15-6	679.5	484.8	874.2	<0.001	63.8	30.1	97.5	<0.001	0.018	-0.027	0.063	0.897
14-7	98.1	-35.2	231.3	0.31	99.1	76.1	122.2	<0.001	0.146	0.115	0.177	<0.001
15-7	517.8	376.7	658.8	<0.001	48.5	24.1	72.9	<0.001	0.01	-0.023	0.042	0.976
15-14	419.7	280.7	558.7	<0.001	-50.6	-74.7	-26.6	<0.001	-0.136	-0.169	-0.104	<0.001

9.1.7 Linear models by study and by species

Table 9-6: Results of study-specific linear models predicting adjusted sinking velocity from length, volume, density and weight. Adjusted R^2 values are reported here, but for the sake of brevity are referred to only as R^2 in the table and figure below.

Study	Length	Volume	Density	Weight
Fok-Pun and Komar (1983)	$F_{1,107} = 24.65$, $p<0.001$, $R^2 = 0.18$	$F_{1,107} = 121.4$, $p<0.001$, $R^2 = 0.527$	$F_{1,107} = 147.6$, $p<0.001$, $R^2 = 0.576$	$F_{1,107} = 230.7$, $p<0.001$, $R^2 = 0680$
Takahashi and Bé (1984)	$F_{1,285} = 216.1$, $p<0.001$, $R^2 = 0.431$	$F_{1,285} = 232.3$, $p<0.001$, $R^2 = 0.448$	$F_{1,285} = 39.94$, $p<0.001$, $R^2 = 0.12$	$F_{1,285} = 1047$, $p<0.001$, $R^2 = 0.785$
Caromel *et al.* (2014)	$F_{1,247} = 60.69$, $p<0.001$, $R^2 = 0.194$	$F_{1,247} = 69.41$, $p<0.001$, $R^2 = 0.216$	$F_{1,247} = 5.337$, $p = 0.021$, $R^2 = 0.017$	$F_{1,247} = 354.8$, $p<0.001$, $R^2 = 0.588$

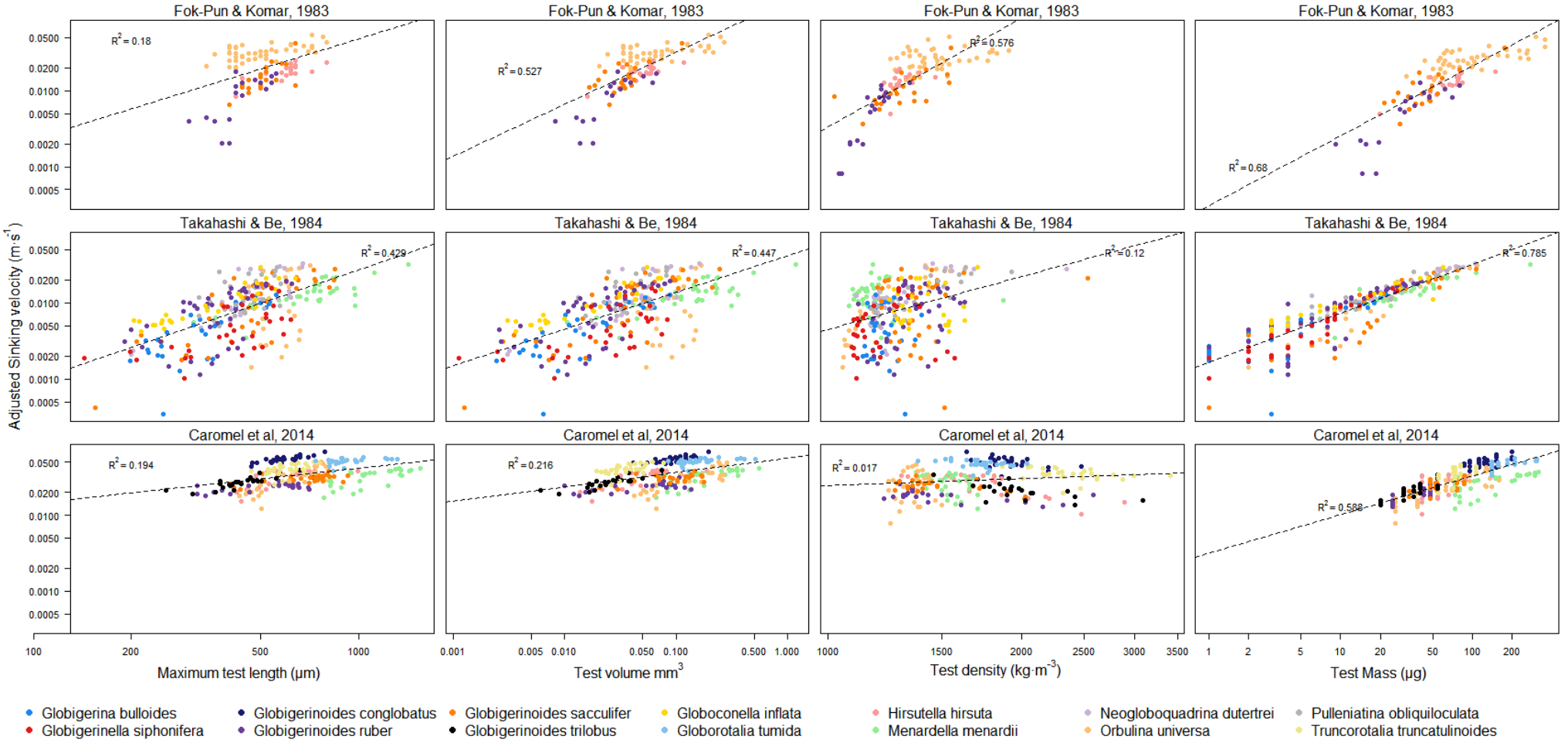

Figure 9-1: Maximum length, test volume and test density have been found to be important parameters in determining sinking velocities of foraminiferal tests. These variables are plotted here using each of the 3 published data sets. The general trends can be seen in all of the studies, but the strength of the trend varies between studies. This may be due to differences between each study. Dashed line is linear model between sinking velocity and variable in question, model statistics reported in Table 3-9. All R^2 values are adjuste

Table 9-7: Linear model results for adjusted sinking velocity predicted by maximum length. See Figure 9-2

Species	***G. bulloides***	***G. siphonifera***	***G. conglobatus***	***G. ruber***
Result	$F_{1,29} = 42.5$, $p<0.001$, $R^2 = 0.580$	$F_{1,28} = 20.1$, $p<0.001$, $R^2 = 0.397$	$F_{1,29} = 42.5$, $p<0.001$, $R^2 = 0.580$	$F_{1,78} = 58.7$, $p<0.001$, $R^2 = 0.422$
Species	***G. tumida***	***H. hirsuta***	***M. menardii***	***N. dutertrei***
Result	$F_{1,28} = 7.01$, $p<0.001$, $R^2 = 0.172$	$F_{1,45} = 19.5$, $p<0.001$, $R^2 = 0.287$	$F_{1,63} = 159$, $p<0.001$, $R^2 = 0.712$	$F_{1,30} = 64.4$, $p<0.001$, $R^2 = 0.672$
Species	***G. trilobus***	***G. inflata***	***G. sacculifer***	
Result	$F_{1,21} = 47.0$, $p<0.001$, $R^2 = 0.676$	$F_{1,25} = 126$, $p<0.001$, $R^2 = 0.828$	$F_{1,84} = 145$, $p<0.001$, $R^2 = 0.629$	

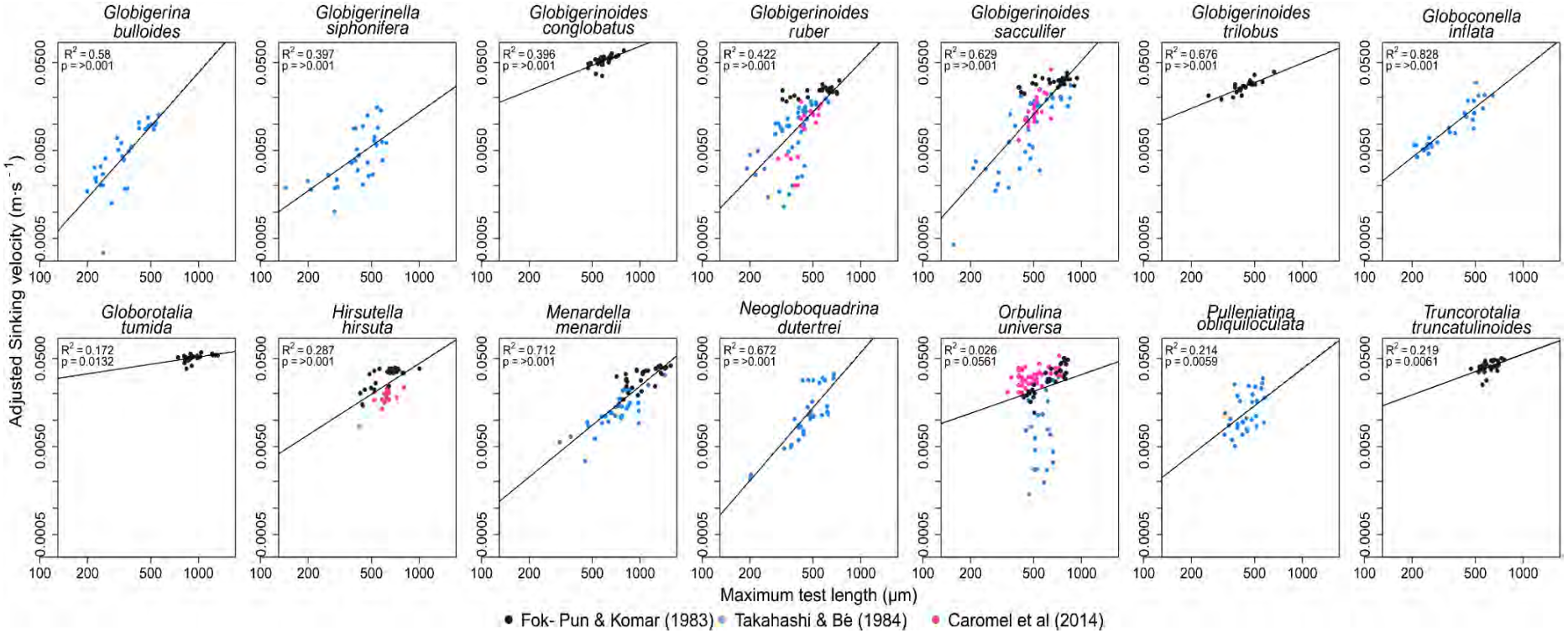

Figure 9-2: Adjusted sinking velocities and maximum test length for each species, coloured by source. The solid line is the linear model predicting reported sinking velocity (U) from maximum test length. A dashed line is also plotted, which is a linear model predicting adjusted sinking velocity (U_{true}) from maximum test length, however for most plots these two lines overlap, showing that the effect of settling tank diameter is minor. Model statistics reported on the graph (R^2 and p values) are for the adjusted sinking velocity linear models (full model results in Table 9-7, above).

9.1.8 Sample types Takahashi & Bé (1984)

When examining the differences, using ANOVA, between sample types in Takahashi and Bé (1984) there are significant differences between the three samples types for all variables (sinking velocity ($F_{2,284}$ = 86.24, p<0.001, see Figure 9-3A), length ($F_{2,284}$= 15.71, p<0.001, Figure 9-3B), mass ($F_{2,284}$ = 67, p<0.001, Figure 9-3C), density ($F_{2,284}$ = 26.86, p<0.001, Figure 9-3D), volume ($F_{2,284}$ = 16.61, p<0.001, Figure 9-3E), Re ($F_{2,284}$ = 62.07, p<0.001, Figure 9-3F) and C_D ($F_{2,284}$ = 50.46, p<0.001, Figure 9-3G)). Tukey HSD *post-hoc* tests found significant differences between all three sample types for sinking velocity and C_D. Planktonic and ashed are not significantly different for length, mass, density and volume, but sediment is significantly different from both planktonic and ashed.

Table 9-8: Pairwise comparisons of sample types (planktonic, ashed and sediment) from Takahashi and Bé (1984) for sinking velocity, length, mass, density, volume, Re and C_D.

Comparison	Difference in means	Lower CI	Upper CI	Adjusted p value
Sinking Velocity				
Planktonic - Ashed	-0.184	-0.279	-0.088	<0.001
Sediment - Ashed	0.374	0.277	0.47	<0.001
Sediment - Planktonic	0.557	0.455	0.659	<0.001
Length				
Planktonic - Ashed	0.025	-0.027	0.077	0.499
Sediment - Ashed	0.121	0.069	0.174	<0.001
Sediment - Planktonic	0.097	0.041	0.152	<0.001
Mass				
Planktonic - Ashed	-0.012	-0.149	0.125	0.975
Sediment - Ashed	0.609	0.47	0.748	<0.001
Sediment - Planktonic	0.621	0.475	0.768	<0.001
Density				
Planktonic - Ashed	-0.01	-0.027	0.006	0.315
Sediment - Ashed	0.043	0.025	0.06	<0.001
Sediment - Planktonic	0.053	0.035	0.071	<0.001
Volume				
Planktonic - Ashed	0.08	-0.08	0.239	0.467
Sediment - Ashed	0.384	0.222	0.546	<0.001
Sediment - Planktonic	0.304	0.134	0.474	<0.001
Reynolds number				
Planktonic - Ashed	-0.159	-0.294	-0.023	0.017
Sediment - Ashed	0.496	0.358	0.634	<0.001
Sediment - Planktonic	0.655	0.51	0.799	<0.001
C_D				
Planktonic - Ashed	0.31	0.154	0.467	<0.001
Sediment - Ashed	-0.401	-0.56	-0.242	<0.001
Sediment - Planktonic	-0.711	-0.878	-0.544	<0.001

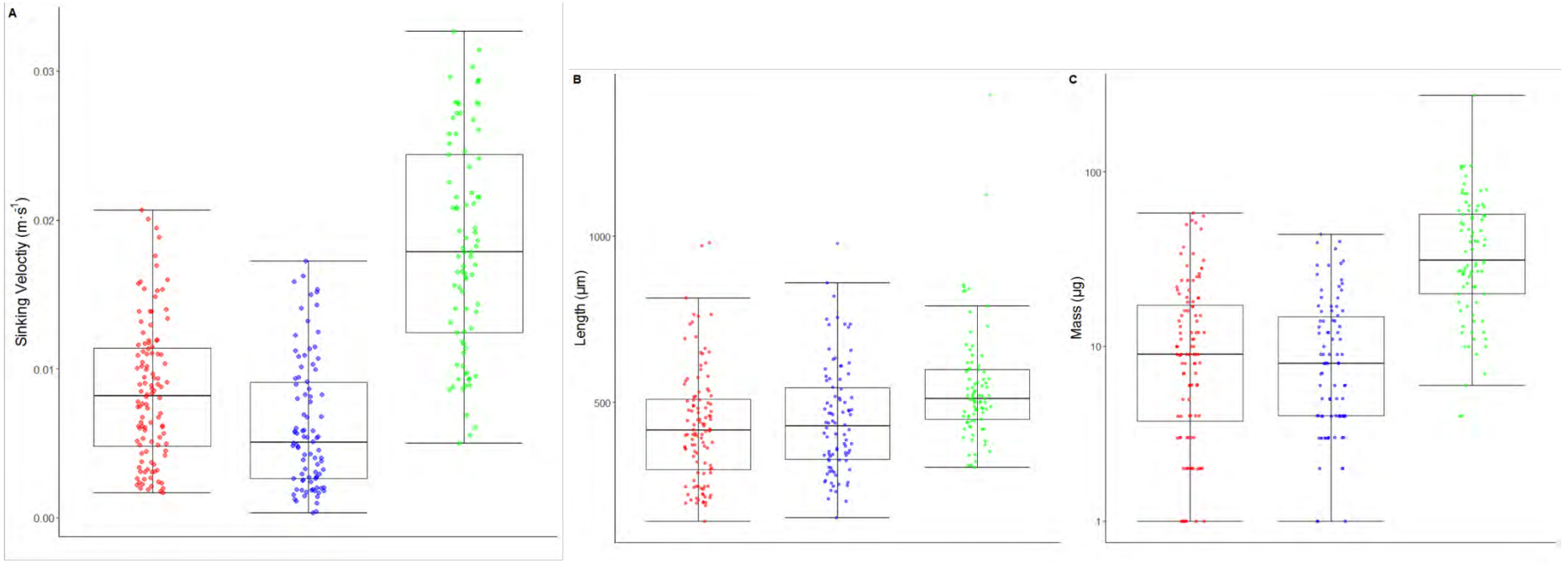

Figure 9-3: Comparison of different sample types (Ashed, red; Planktonic, blue; and sediment, green) from Takahashi and Bé (1984) for sinking velocity (A), length (B), mass (C), density (D), volume (E), Re (F) and C_D (G) (continued over page).

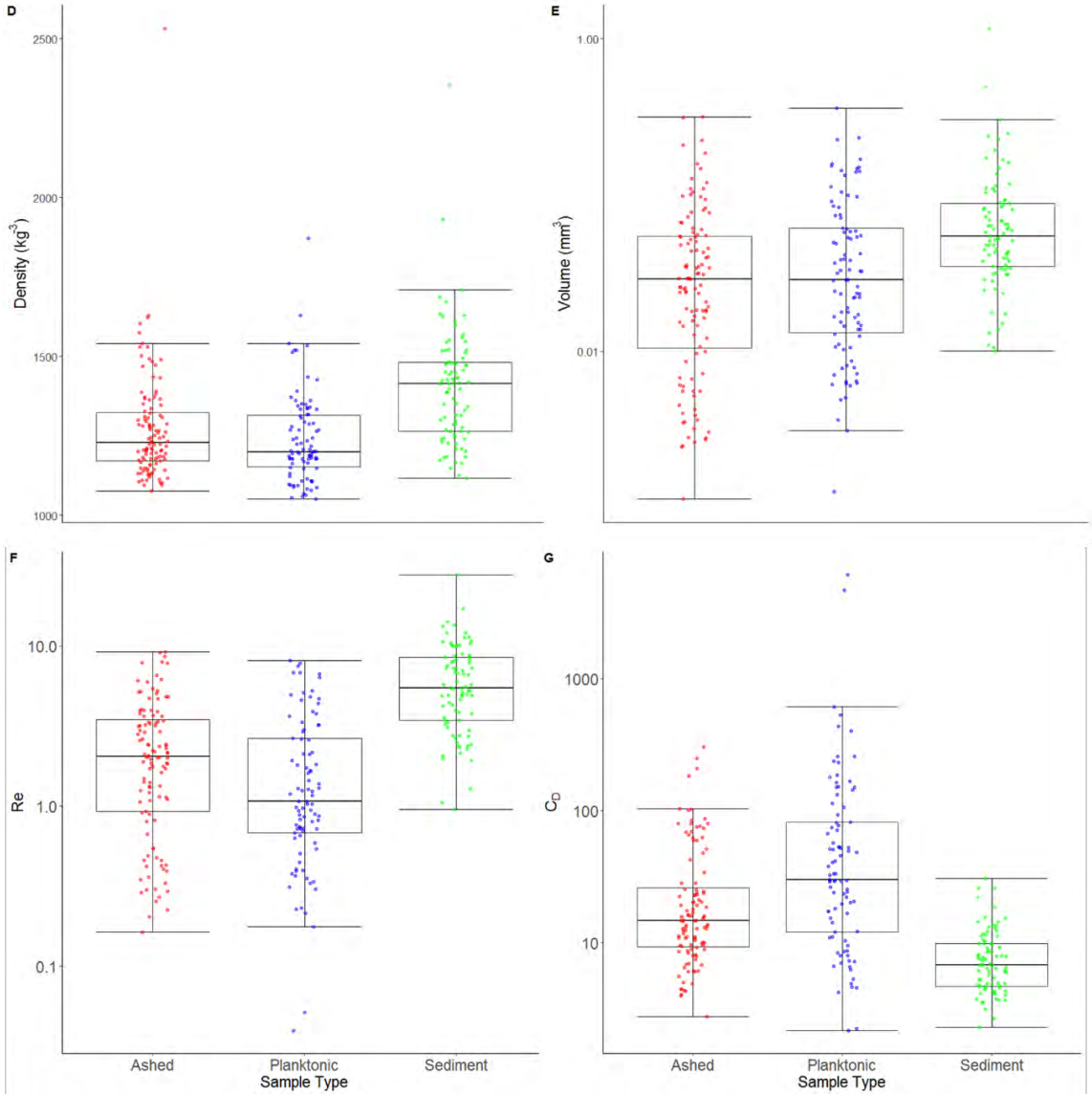

Figure 9-3(cont): Comparison of different sample types (Ashed, red; Planktonic, blue; and sediment, green) from Takahashi and Bé (1984) for sinking velocity (A), length (B), mass (C), density (D), volume (E), Re (F) and C_D (G) (continued from over page).

9.1.9 Sources of Data for Figure 3-33

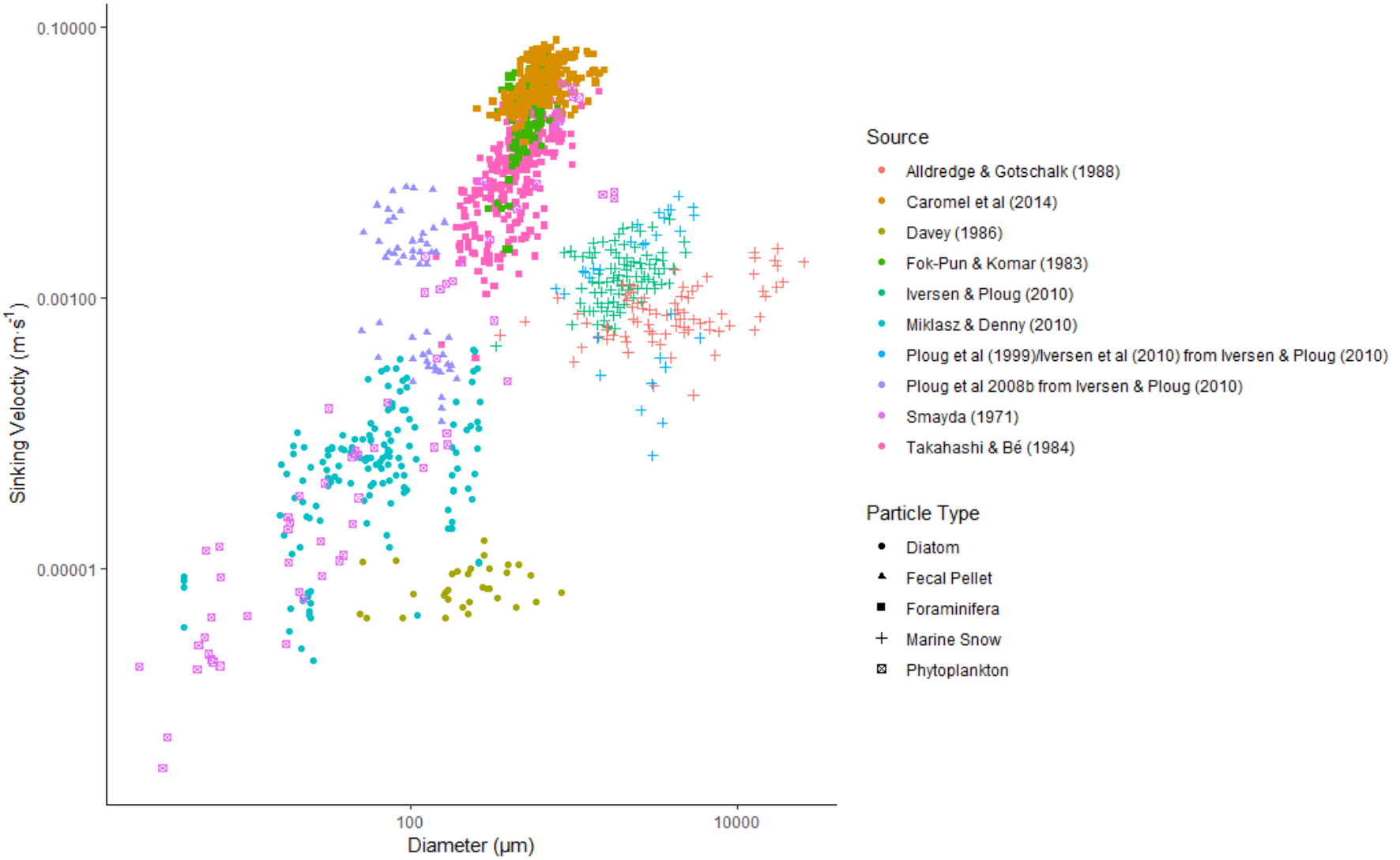

Figure 9-4: Data source and type of specimen, as per Figure 3-33 (Smayda, 1971; Davey, 1986; Alldredge and Gotschalk, 1988; Iversen and Ploug, 2010; Miklasz and Denny, 2010)

9.2 Chapter 4 Appendices

9.2.1 Choice of oil, tank and equipment

9.2.1.1 *3D Printer*

A Formlabs Form1+ 3D printer (Formlabs, Somerville, Massachusetts, USA) was used to print the models required for this study. As discussed in Chapter 2, 3D printing is an additive method of constructing items from many thin layers of material. The Form1+ is a stereolithography 3D printer, which uses a UV sensitive photopolymer resin that forms a solid on exposure to UV light. The liquid resin is poured into a tank with an optically clear base (**9** in Figure 9-5) which is coated with a non-stick layer. A platform (**4** in Figure 9-5) is lowered into the tank, leaving a small gap between the bottom of the tank and the platform surface. The size of this small gap determines the layer thickness (a minimum of 25µm). A UV laser (**5** in Figure 9-5) is directed with two mirror-galvanometers (**6** in Figure 9-5). A galvanometer is an electromechanical device which moves in a precise, pre-determined, and rapid manner when an electrical current is passed through it. The mirror galvanometers direct the laser beam (**8** in Figure 9-5) via the x-y scanning mirror, (**7** in Figure 9-5) across the thin layer of liquid resin between the platform and the bottom of the tank, causing the resin in the beam's path to set and adhere to the platform. The path of the laser is determined by the printer software (Preform, Versions 1.8.2-2.12.3, Formlabs, Somerville, Massachusetts, USA) and the CAD model. Preform adds a series of supporting structures (**2** in Figure 9-5) to the printed part (**1** in Figure 9-5). Once a layer has been formed, the platform moves upwards, allowing a new thin layer of liquid resin to form between the previous layer and the bottom of the tank. Once the printed model was finished, the support structures were removed, and was cleaned by agitation in >99.5% propan-2-ol for two minutes followed by soaking in propan-2-ol for 10 minutes. Once cleaned the printed part was left to air dry. Further curing was achieved by additional exposure to UV light for a minimum of 15 minutes.

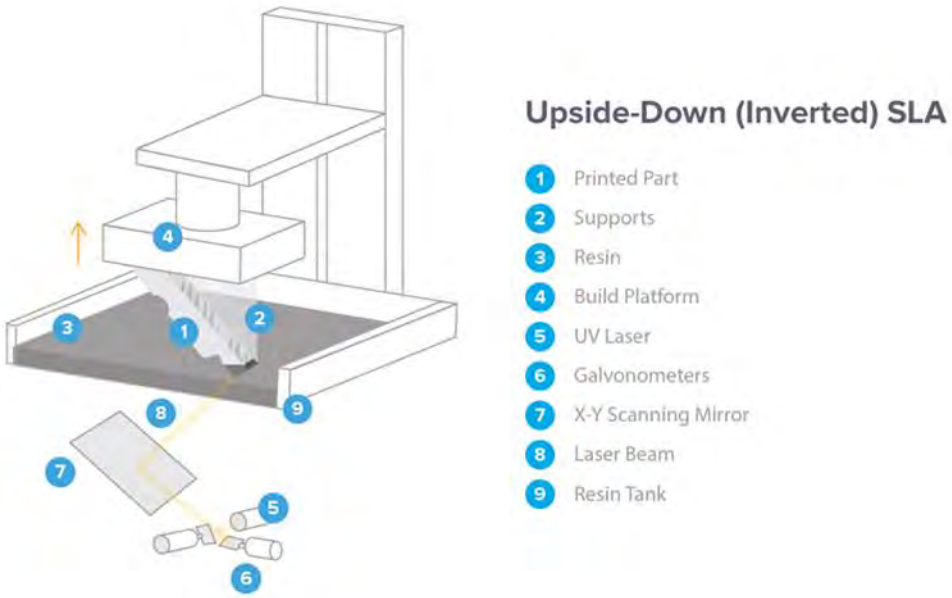

Figure 9-5: A schematic diagram of the Form1+ 3D printer. Courtesy of Formlabs.

Figure 9-6: Formlabs Form1+ 3D printer, with a selection of model foraminifera used for display. Photograph taken by J. Sage.

9.2.1.2 *Fluid Choice*

When making a choice of fluid to use in the experiments a primary list of requirements was made. The fluid chosen needed to:

- Be translucent, but preferably transparent, with a light colour to allow the sinking models to be easily seen
- Not degrade the models, which may need to be stored in fluid for extended periods.
- Be readily available, especially in large quantities
- Have suitable physical properties, in particular viscosity and density. The density of the fluid must be lower than that of the resin used to make the model. For any object to sink the density of the object must be higher than the density of the fluid, i.e. $\Delta\rho$ (density difference between the particle and the fluid) in Equation 9-17 must be positive.

Equation 9-17

$$\Delta\rho = \rho_{particle} - \rho_{fluid}$$

To determine a suitable fluid, a series of calculations and small-scale tests were conducted. Previous dynamic scaling studies have used corn syrup (Furbish and Arnold, 1997; Koehl, 2003), mineral oil (Reidenbach, George and Koehl, 2008), glycerol, and shampoo (Furbish and Arnold, 1997). Shampoo is non-Newtonian (its viscosity is dependent on the rate of force application, Subba Reddy Gorla *et al*. 2014), unlike water (which is Newtonian, its viscosity is not affected by forces being applied). As such shampoo would not behave in a suitable manner for these experiments. Corn syrup is difficult to obtain in the UK and has a high density (Table 9-9). Glycerol is easy to dilute using water to give a range of viscosities but has a high density (See Table 9-9 for a summary of various fluid properties). This leaves oils as possible fluids. Plant-derived oils tend to oxidise during long term storage (Martín-Polvillo, Márquez-Ruiz and Dobarganes, 2004) which may change their properties, so a non-plant based oil would be best, but given the limited choice of suitable fluids, plant based oils may be suitable. Their suitability was dependent on the results of further testing (See section 9.2.1.3).

Small scale testing was first conducted to test the properties of potential oils. Material Safety and Data Sheet (MSDS) information for oils generally only provide dynamic viscosity and density of the oil at a specific temperature, i.e. 20°C. The requirements for the oil needed, in addition to those outlined above, were set out:

- The oil must have a low density and high viscosity to allow the models to sink in the correct Re regime.
- The oil must be stable over long periods of time.
- The oil must have a high flash point and not evaporate or release volatile compounds.

From these requirements a three possible oils were identified: mineral oil, sunflower oil and vegetable oil.

Table 9-9: The possible fluids to sink the models. For comparison, the top two rows contain the 'real life' values for seawater at 20°C (approximate temperature in surface waters) and at 4°C (average ocean temperature). density differences would mean the model would float. Resin density is 1121 kg·m^{-3} (See 9.2.1.4).

Fluid	Density (kg·m^{-3})	Dynamic viscosity (Pa·S)	Density difference (kg·m^{-3})
Seawater (20°C)	1024	0.001072	1676
Seawater (4°C)	997	0.001072	1700
Olive oil	910	0.008	232
Rapeseed oil	920	0.163	242
Corn syrup	1380	1.380	-238
Propylene glyocol	1038	0.056	104
High viscosity Silicon oil	970	4.850	172
93% pure glycerine	1243	0.370	-105
"Carnation" mineral oil	830	0.022	312

9.2.1.3 *Initial Testing - Oil-Resin Interactions*

Once the choice of fluid had been narrowed down to an oil, other tests were needed to ensure the compatibility of the oils with the 3D printing resin. The oil might have a detrimental effect on the structure of the resin, causing it to change its properties. As the photopolymer resin was a recent proprietary invention, and the application unusual, there was no data on the potential effects of oil on the resin.

Methods for Testing Oil-Resin Interactions

Square-cross section beams (3·3·70 mm) were printed in FormLabs' Black Resin Version 1 (Formlabs, Somerville, Massachusetts, USA) with a layer thickness of 50µm. A total of 48 beams were printed and split into four groups of 12. These beams were then stored for six weeks in: mineral oil (Johnson's Baby Oil, Johnson and Johnson, New Brunswick, New Jersey, USA), vegetable oil (Wm Morrison Supermarkets PLC, Bradford, West Yorkshire, UK), sunflower oil (Wm Morrison Supermarkets PLC, Bradford, West Yorkshire, UK), and a control group stored in air. Johnson's Baby Oil uses "Carnation" mineral oil as the base and contains only added perfume, it was used for these tests due to availability compared to "Carnation" mineral oil.

All models were stored in the dark, as light can affect the properties of photosensitive resin, even when cured (Coon *et al.* 2016). After six weeks, the beams were then subjected to a 3-point bending test (Figure 9-7) using an Instron Universal Testing Machine (model 4443, Norwood, Massachusetts, USA) to measure the force required to deform the beam. The beam was placed on two supports, 50mm

apart, and a load applied from above, exactly halfway along the beam. The Young's modulus (*E*, Pascals ($N \cdot m^{-2}$, a measure of stiffness) of the material was calculated using Equation 9-18:

Equation 9-18

$$E = \frac{\delta}{\varepsilon}$$

where δ is stress is calculated using Equation 9-19:

Equation 9-19

$$\delta = \frac{3 \cdot F_{load} \cdot L_{span}}{2 \cdot b \cdot d^2}$$

where F_{load} is load (N), L_{span} is support span (m), b is beam width (m) and d beam thickness (m). While ε is strain, calculated using Equation 9-20:

Equation 9-20

$$\varepsilon = \frac{6 \cdot D \cdot d}{L_{span}^2}$$

where D is the maximum deflection of the beam (m). The Young's moduli of the test groups (mineral, vegetable and sunflower oil) and the control group (air) were compared using an ANOVA with Tukey's HSD *post-hoc* test in R (R Base Statistics Package, version 3.4.2, R Core Team, 2018)).

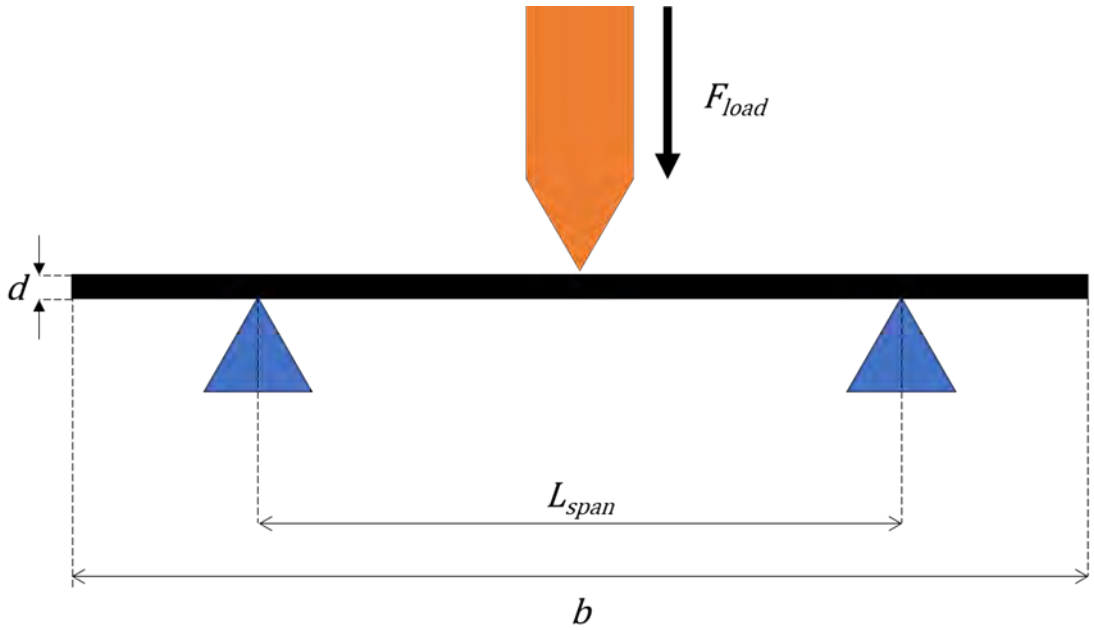

Figure 9-7: Three-point bend test. The beam (in black) is placed on two supports (blue triangles) and a load (F_{load}, thick black arrow) is applied using the crosshead (in orange) across the beam. The amount the beam deflects downwards is recorded (D in Equation 9-20). L_{span} is the length of the span, b is the beam width and d is the beam thickness.

Results

Whilst the mean Young's modulus from the different groups was significantly different ($F_{3,44}$ = 2.886, p = 0.046), there are no significant pairwise differences between any of the oils and the control group, nor between any of the oils (Table 9-10, Figure 9-8).

Table 9-10: Tukey HSD results showing the comparisons between the control (stored in air) and the different oils.

	Difference	**Lower**	**Upper**	**Adjusted p value**
Mineral-Control	326.633	-18.347	671.612	0.069
Sunflower-Control	258.881	-86.099	603.86	0.202
Vegetable-Control	326.039	-18.941	671.018	0.07
Sunflower-Mineral	-67.752	-412.731	277.227	0.953
Vegetable-Mineral	-0.594	-345.574	344.385	>0.99
Vegetable-Sunflower	67.158	-277.822	412.137	0.954

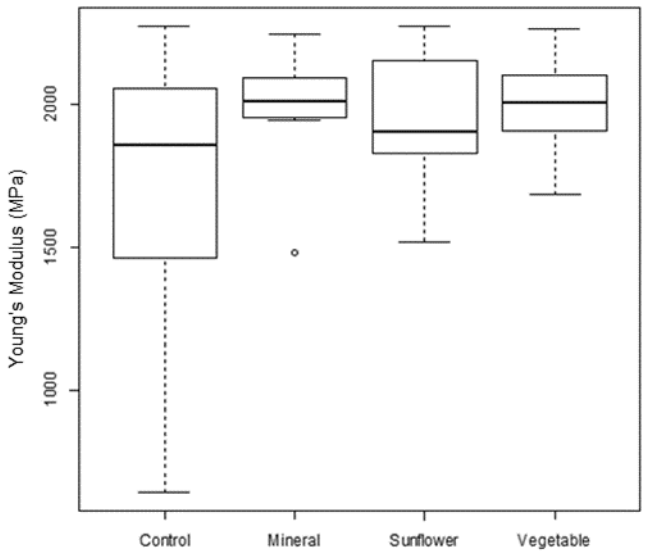

Figure 9-8: Young's modulus of 3D printed beams stored in assorted oils for 6 weeks and control group stored in air.

Therefore, it was concluded that storage of the beams in oil did not significantly affect the mechanical properties of the resin in comparison to storage in air. This would suggest that the choice of oil does not need to be concerned with interactions with the resin. The significant result of the ANOVA is probably due to the two near-significant values for differences between mineral oil group and the control group, and vegetable oil and the control group.

Based on the findings from the beam test and the fact that vegetable oils oxidise over time, "Carnation" mineral oil was chosen as the most suitable oil.

9.2.1.4 *Initial Testing – Resin Choice*

The Formlabs Form1+ can print using a selection of resins, White, Black, Clear and Grey. Initially testing was conducted with black resin (Version 1), which would allow good contrast against a white background for tracking the sinking model. To test the dynamic scaling process, model foraminifera were 3D printed and then sunk in a graduated cylinder. This small-scale test mimicked the planned later full-scale experiments and allowed use of small volumes of oil (up to 1 litre), compared to the several hundred litres for the full-scale experiments. In addition, the small-scale test allowed the method of dynamic scaling to be tested and ensure the initial calculations were correct and the viscosity and density of the oil were suitable.

Measured sinking velocities did not follow the expected trend that sinking velocity increases with size (Figure 9-9) based on both the hydrodynamic equations (see section 3.1.3) and the literature (see Chapter 3).

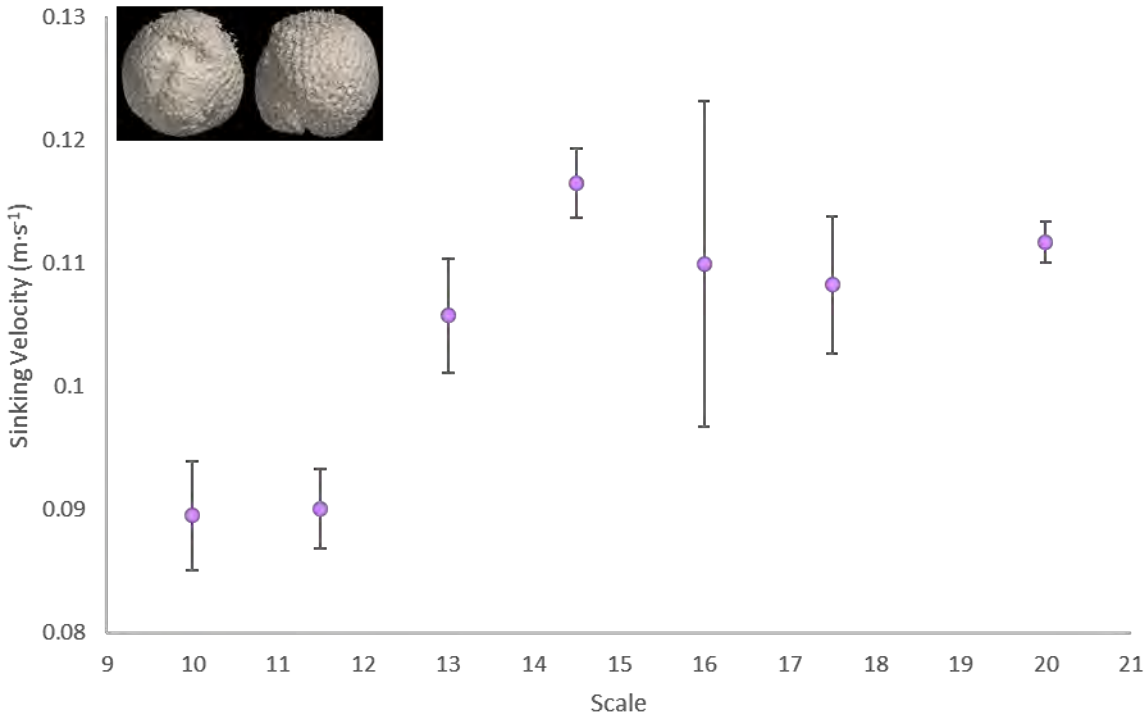

Figure 9-9: Average sinking velocities of preliminary-test model foraminifera (P. curva, inset in top left). Scale is used as an increase in size, a model at scale 10 is 10 times larger than real life. For scale factors 10, 11.5 and 20 the number of models = 3, for all other scales the number of models = 1. All models were sunk 3 times.

Bubbles of air were also observed leaving the model during sinking, as discussed in Chapter 3 the presence of air bubbles inside tests reduce sinking velocities. Thus, the differences sinking velocity was determined to be due to the presence of air within the models' chambers. To ensure that in the full-scale experiments air bubbles could be removed, clear resin was used instead of black resin, so the bubbles would be visible and could be removed. The clear resin has the additional property that it fluoresces under UV light, which was exploited to allow better imaging of the particle.

The most important resin property is density, as discussed above (section 9.2.1.2 and Table 9-9). To measure the density of the resin, three 10 mm^3 cube models were printed at 50µm layer thickness and weighed three times on an electronic balance (model 224-1S, Sartorius Entris, Göttingen, Germany) accurate to 0.001g. Density (ρ) was then calculated by dividing the model's mass by its volume (Equation 9-21). The final average density of the clear resin was 1121.43 ± 13.73 $kg \cdot m^{-3}$ (Table 9-11).

Equation 9-21

$$\rho = \frac{mass}{volume}$$

Table 9-11: Resin cube models used to determine the density of clear resin.

	X axis length (mm)	**Y axis length (mm)**	**Z axis length (mm)**	**Cube volume (mm^3)**	**Average Cube mass (g)**	**Cube density ($kg \cdot m^{-3}$)**
Cube 1	10.16	10.21	10.11	1048.746	1.1644	1110.27
Cube 2	10.25	10.24	10.24	1074.790	1.1965	1113.24
Cube 3	10.19	10.20	9.93	1032.104	1.1774	1140.77
Average	**10.20**	**10.21**	**10.093**	**1051.818**	**1.1794**	**1121.43**

9.2.1.5 *Initial Testing – Air Removal from the Model*

As mentioned above, it became apparent that air removal from the models needed to be performed. Due to the complex internal structure of chambers, trapped air bubbles were difficult to remove. At first manual model reorientation under oil and percussive agitation were used to persuade the air bubbles out. This was a successful method for large models of species with large apertures (e.g.: *Neogloboquadrina acostaensis*, despite the presence of the apertural plate). However, for the species with narrow apertures (e.g.: *Globorotalia flexuosa*) this method did not work. A variety of other methods were tested including: placing the model in oil in a flask, inside a heated laboratory shaker; applying a vacuum to the flask then placing the flask in the shaker; and placing the model in heated oil in a sealed vessel, and applying a high vacuum (low pressure). The application of a vacuum helped to draw some air out of the models, but these methods still proved ineffective at removing all bubbles. Another method tested was using a flask to maintain a vacuum and then passing a 30-gauge needle through the aperture to extract bubbles from the inside of the test (Figure 9-10). This method was moderately successful and was used in conjunction with a syringe and 30-gauge needle which was used to alternate between injecting oil in to the test and sucking air bubbles out.

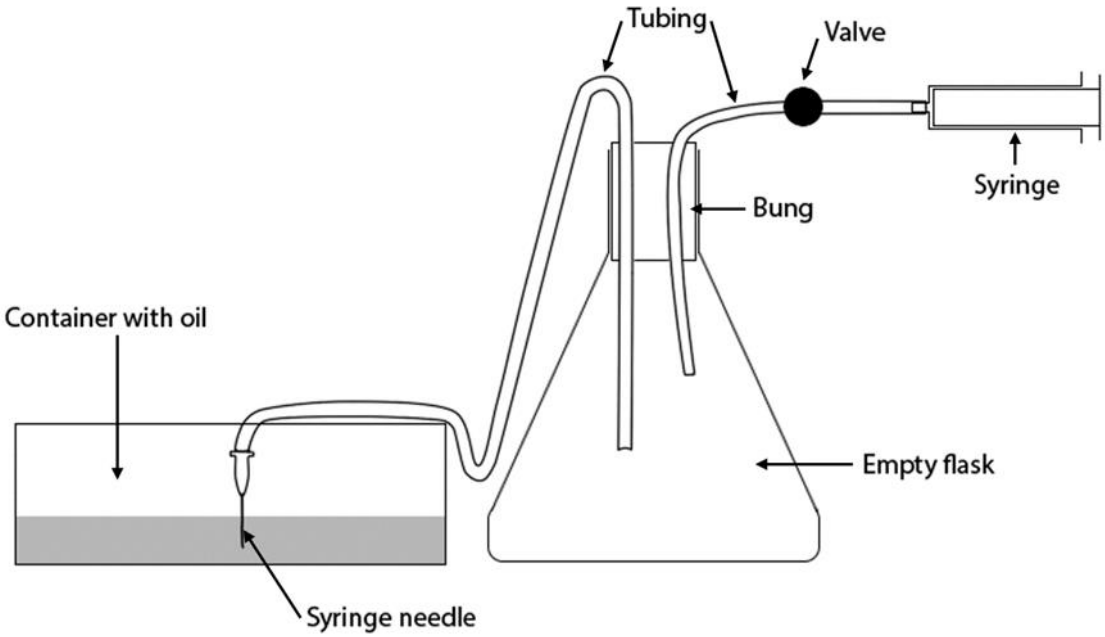

Figure 9-10: A schematic of air removal system, consisting of a 100ml syringe (far right), a 200ml conical flask (centre) and a bath of mineral oil (left) into which the model was placed. The syringe is used to make a partial vacuum in the flask, the valve (black dot) is then closed and the needle (left) is inserted in to the foraminifera model, the vacuum pulls air bubbles out of the model. The vacuum in the flask can be restored by emptying the syringe, reconnecting to the tubing and opening the valve. This apparatus allowed removal of air from multiple models in quick succession with greater ease than using a single hand-held syringe to draw bubbles out of the models.

9.2.1.6 *Initial Testing – Tank*

The primary concern when choosing a tank is its shape, which affects the ability to image the particle. Cuboid tanks have no distortion, as the walls are flat, however cuboid tanks use more material, are weaker, and more expensive, than cylindrical tanks.

Another major factor in the choice of tank was the diameter and height of the tank. The diameter needs to be large enough to reduce wall effects (see Chapter 3) as much as practicable. The tank must be tall enough to allow a sinking model to reach terminal velocity (which occurs in a short distance, less than 2cm) and for the sinking path to be observed (i.e. is the path straight, helical, etc.).

Using the same WECF applied in section 3.3.1.1, the maximum expected model size of 50mm (based on literature values used in the prediction of required scale to achieve similitude), was used as the particle radius (r in Equation 3-14, below). A range of estimated sinking velocities were trialled, and the sinking velocity ($U_{measured}$) was expressed as a percentage of the true sinking velocity (U_{true}, see Figure 9-11). Using Equation 9-22 tank radius (R in Equation 3-14) was then varied between 500mm and 3000mm, and the resulting sinking velocities were then converted to a percentage of the true sinking velocity and graphed (Figure 9-11). This allowed an estimation of a suitable tank diameter that reduced wall effects as much as practicable. For example, a 50mm particle with a true sinking velocity (i.e. sinking in unbounded fluid) of 0.1 m·s^{-1}, would sink at 0.0951 m·s^{-1} in a 900mm diameter tank.

Equation 3-14

$$U_{true} = U_{measured} \cdot \left(1 - \frac{1}{\alpha} \cdot \frac{r}{R}\right)$$

Equation 3-13

$$\alpha = \frac{1 - 0.75857 \cdot \left(\frac{r}{R}\right)^5}{1 - 2.1050 \cdot \left(\frac{r}{R}\right) + 2.0865 \cdot \left(\frac{r}{R}\right)^3 - 0.72603 \cdot \left(\frac{r}{R}\right)^6}$$

Equation 9-22

$$U_{measured} = \frac{U_{true}}{\left(1 - \frac{1}{\alpha} \cdot \frac{r}{R}\right)}$$

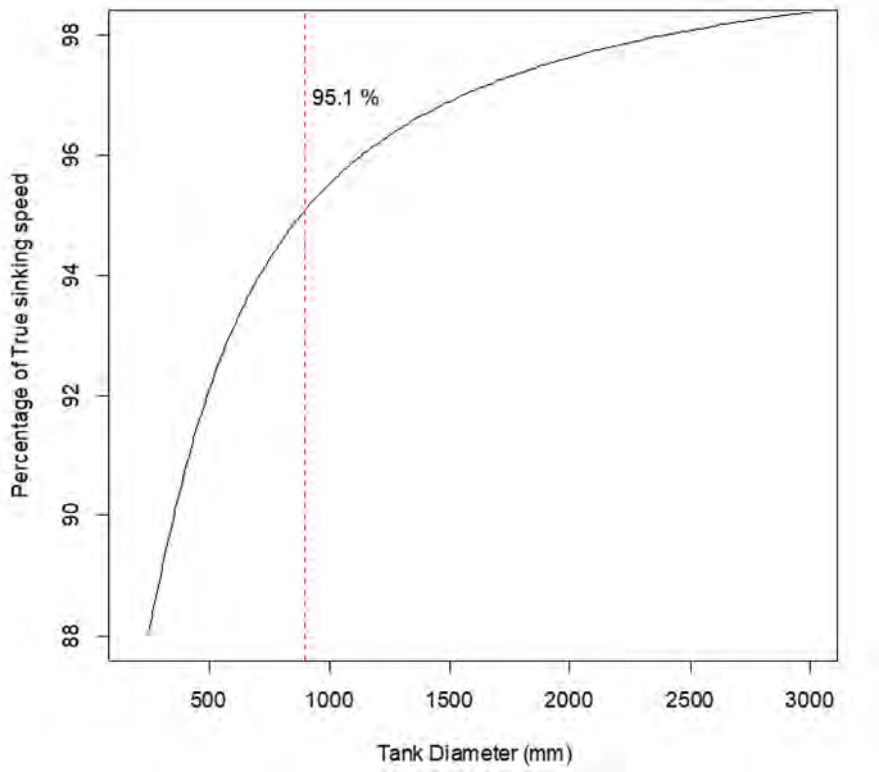

Figure 9-11: Sinking velocity as a function of tank diameter to illustrate wall effects. For a fixed particle diameter (50mm). As the particle diameter was towards the higher expected model size, it was expected that the models would sink closer to their true sinking velocity, than indicated percentage of the sinking velocity, 95.1%. The red dashed line shows the size of tank used in this study. A tank of this size (0.9m) permits 95.1% of the true sinking velocity (U_{true}) to be achieved.

While glass was considered for the tank as it is stronger than acrylic, it is also more brittle and prone to breakage. Taking in to consideration the various points above, a cylindrical acrylic tank was custom built by Complete Aquariums (Hatch End, Borough of Harrow, London, UK), with a diameter of 900mm and a height of 1200mm (See Figure 9-13).

9.2.1.7 *Initial Testing – Particle release, recording, visualisation, image processing, tracking and retrieval*

The initial testing with the full-scale tank was conducted using 3D printed spheres of varying sizes (see section 9.2.1.8). This allowed confirmation of the Re regimes achievable with the oil and allowed initial predictions of the foraminifera model size required to match the Re for the model to those of real foraminifera (based on values from previous studies). Once these initial tests had been completed a second set were conducted using examples species (*N. acostaensis* and *P. curva*) to examine sinking orientation and to highlight any potential problems that were not evident from the sphere tests. *P. curva* was chosen as it is approximately spherical providing a good comparison to the theoretical predictions made using equations developed for spheres. *N. acostaensis* was chosen as it is a flattened disc-like shape and provided an example of how non-spherical species might perform whilst sinking. However, before sinking the models of the spheres the various methods of particle release, recording, visualisation, image processing, particle tracking, and model retrieval had to be developed. A brief outline of these methods follows with more specific details with regard to the foraminifera models being given in Section 4.4.

Particle Release

The release of the model in the tank needs to be consistent and easily achieved. To do this a "Pickle and Ice Cube Grabber" (BarCraft) was modified to fit inside a custom 3D printed holder and weighted quick release mechanism (Figure 9-12). The grabber was chosen as it has three mechanically linked 'prongs' to hold the model and ensure that it was released consistently, without one prong releasing at a slightly different time, which would potentially induce rotation of the particle.

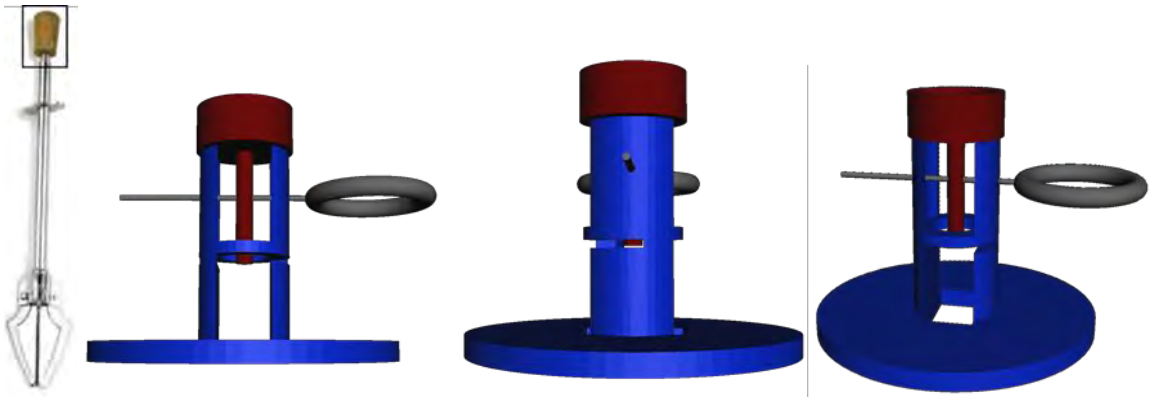

Figure 9-12: From left to right: the Pickle and Ice Cube Grabber (BarCraft), used to release the models; front view of CAD model of the release mechanism that was 3D printed for use; side view of the model; finally a perspective view of the release mechanism. The red section, held a small weight and was threaded to accept the grabber. The grabber handle (highlighted on the image of the Grabber (left)) was replaced by this weight-holder, while the larger (blue) section of the release mechanism held the grabber. The pin (in grey) held the grabber in the closed position and when it was removed the weight caused the jaws (prongs) to open at the same time.

Particle Retrieval

Once the particle has been sunk it is necessary to retrieve it for re-sinking, to obtain replicated data (see section 4.4.6, below). To retrieve the models from the bottom of the tank a custom system was

designed and built from clear acrylic (Figure 9-13). The system was designed to also hold the release mechanism. The armature and pulley wheels supported lengths of clear nylon monofilament to which a galvanised steel wire net support structure was fastened. A nylon net (mesh size: 5 × 5 mm) was attached to the support structure with nylon monofilament. The use of very small models for some species meant a fine mesh was also placed on top of the central area of the net. The nylon monofilament was attached to a medium density polyethylene hoop, so lowering the hoop raised the net from the bottom of the tank. The hoop was then secured, and the model could be retrieved from the net by hand. During the times when experiments were not running the model retrieval system supported four acrylic panels which covered the tank, to prevent the ingress of dust.

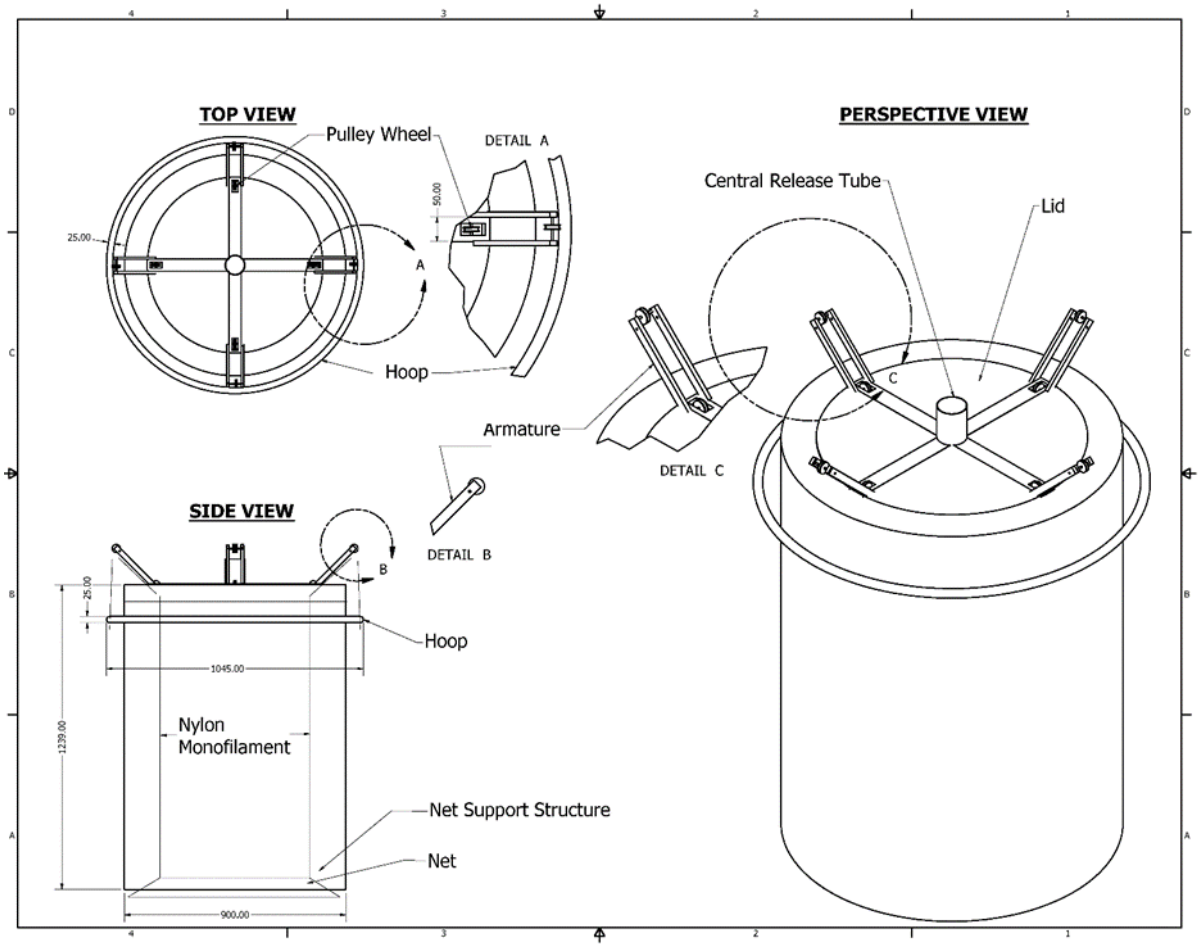

Figure 9-13: Schematic of the tank and model retrieval system. All measurements in mm.

Particle Recording

There is anecdotal evidence of rotation of foraminifera during sinking (Takahashi and Bé, 1984), along with expectations from theory that they may have gliding paths rather than falling only vertically (Albertson, 1953). In order to visualise the orientation and path accurately, the models were recorded using two Logitech C920 HD webcams (Logitech, Lausanne, Switzerland, recording at 960 pixels x 720 pixels and ~30 frames per second), placed at 90° to each other (Figure 9-14), allowing monitoring of

the position and movement of the particle in 3D as it fell. Knowing the time difference between the frames is vital to calculating sinking velocity. However, the webcams used a variable frame-rate system and so a custom MATLAB script was used to initiate camera recording and allow frames and the exact time at which the frame was taken to be recorded. Videos were recorded for 500 frames or approximately 16.667 seconds (at ~30 frames per second (fps)), this was sufficient for all but the smallest models to be recorded travelling the full length of the tank, although sinking velocity was only calculated over a central 0.8m (see section 4.4.7).

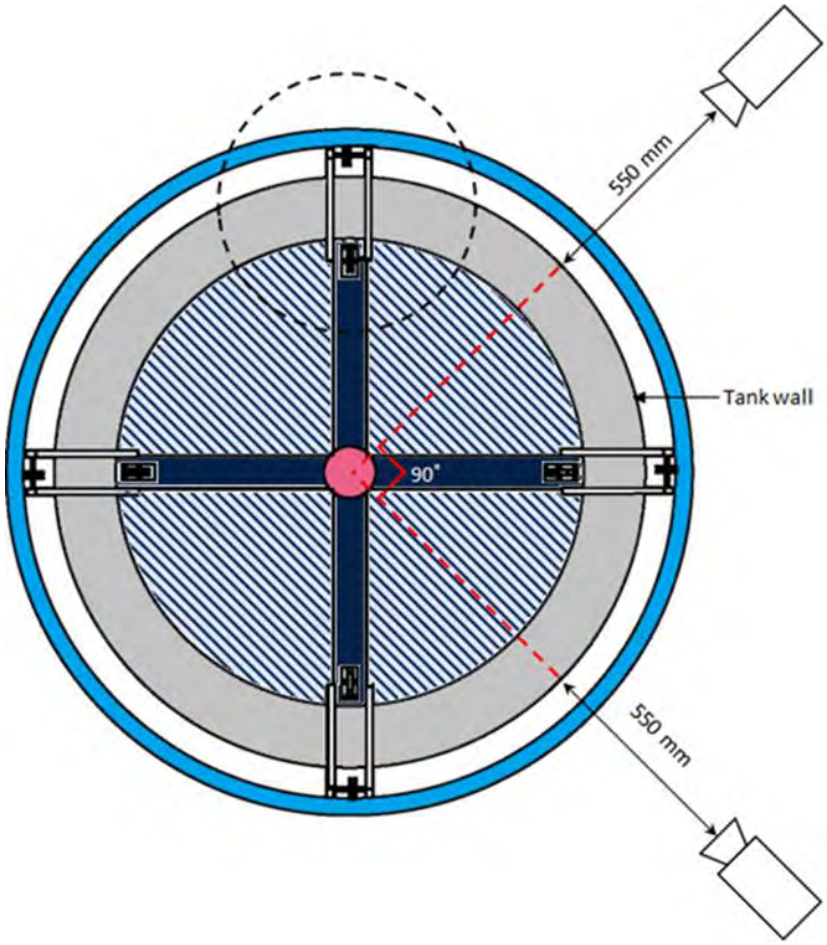

Figure 9-14: A top down view of the tank and camera position. An external hoop (light blue) was used to raise the net from the bottom of the tank, via the system of pulleys and nylon monofilament mounted on the armatures (circled with black dashed line). The support arms (dark blue) held a central tube (pink) where the release mechanism was mounted. A ledge (grey) around the top of the tank was used to support the armatures, support arms and cover for when the tank was not in use. The open part of the tank is shown with dark blue hatching.

Particle Visualisation

Small-scale testing of the sinking clear resin models indicated that the resin and the mineral oil have a similar refractive index, meaning that the model is very difficult to see in mineral oil (Figure 9-15). Various methods to help visualise the model were tested, including patterned backgrounds which are distorted by the sinking particle (Figure 9-15), and a solid black background. The best method was found to be a bright illumination from above or below with a black background. It later became apparent that

the clear resin fluoresces blue under UV light, further enhancing contrast with the black background. To take advantage of the fluorescence, in the full-size tank a single 200W equivalent LED spotlight was placed underneath the tank and two 20W “Blacklight” UV fluorescent tubes were placed above the tank.

To reduce ambient light levels and minimise reflections on the curved walls of the tank it was surrounded by a black-out sheet on a frame and all the experiments were conducted in a darkened room.

Figure 9-15: Small scale experiments examining visualisation of the sinking models. Left: plain background, right: patterned background, model highlighted in red in both images. These images are examples of methods of particle visualisation (see text for details).

Image Processing and particle tracking

In addition to the use of lighting and reducing reflections it also became apparent that the visual distortion introduced by curvature of the tank would have to be removed, or reduced, to enable accurate measurements to be taken. Firstly, the cameras were fixed in their relative positions, both placed 550mm away from the tank wall (Figure 9-14) and not moved once calibration images had been acquired.

The walls of the tank introduced ‘barrel’ distortion to the images, i.e. the vertical edges of the image appeared to be curved and compressed, whilst the top and bottom also had some curved distortion. In addition to this distortion from the tank, all camera lenses introduce small amount of distortion unique to that lens. To remove distortion (see Figure 9-16) the MATLAB toolbox “Camera Calibrator” (The

Mathworks, 2016) was used. The calibration images placed into the tank consisted of a checkerboard, with black and white squares 25 × 25 mm, in 25 different positions and orientations. Distortion in the images is computed by locating the edges of each check on the checkerboard and finding a transformation that produces a square from the distorted image.

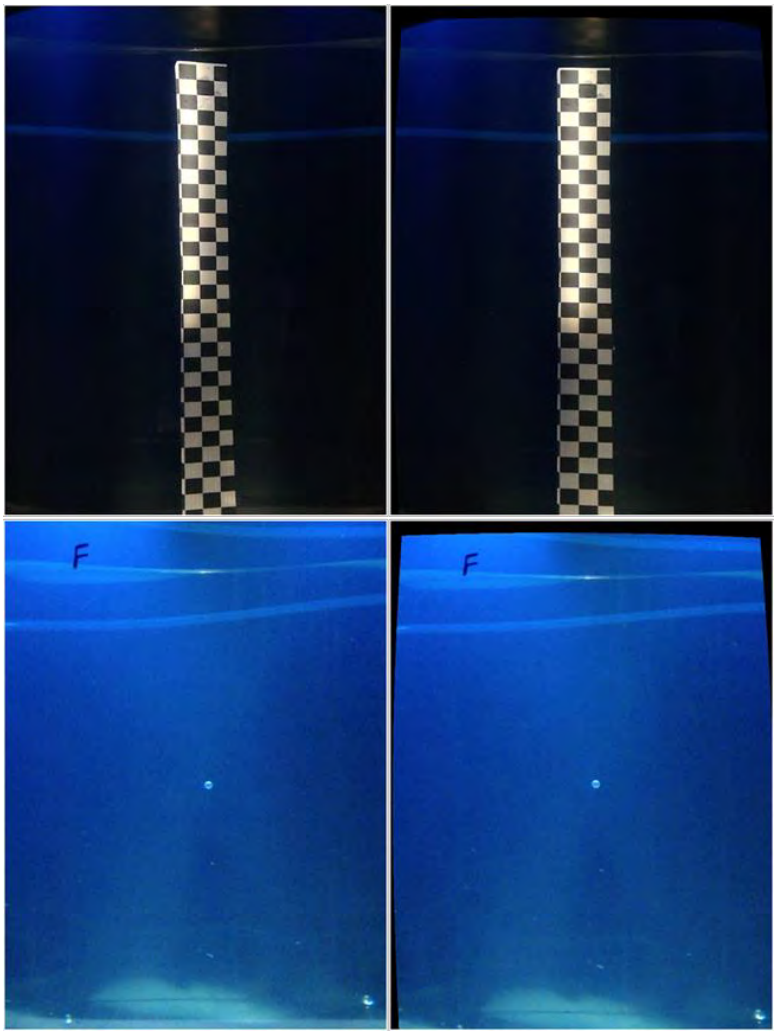

Figure 9-16: Top left original image of the checkerboard in the tank, the apparent angle of the checkerboard is caused by the distortion of the tank. Top right: the undistorted checkerboard. Bottom left: an example frame of a sinking sphere before distortion correction. Bottom right: the same frame undistorted. The "F" visible in the lower images provided a visual check for which camera the image was being taken from, i.e. the front camera.

Distortion could only be removed accurately from a section in the centre of the tank, most likely due to the curvature of the tank generating complex non-symmetrical distortions. A mathematical algorithm generated by the MATLAB toolbox was then applied to all frames of each video, resulting in an undistorted image. The undistorted checkerboard (Figure 9-16) was also used to find the pixel-to-mm scaling for the cameras, to allow the distance a particle travels to be measured. This was achieved by measuring a checkerboard square in FIJI (Schindelin *et al.*, 2012), as the size of the square (in mm) is known the distance per pixel can be calculated. For camera one, scale is 1.08 pixels per millimetre

with a reprojection error (from undistorting the image) of 0.48 pixels; for camera two, the scale is 1.04 pixels per millimetre with a reprojection error of 0.51 pixels.

The rest of the image processing, and particle tracking, was performed using a modified version of Trackbac (Guadayol, 2016), a MATLAB-code based tracking system developed for bacteria. Before the particle could be tracked the frames were submitted to a thresholding process to maximise the contrast between the particle and the background of the image. The first step in this process was to isolate the green channel, which had the best initial contrast between the particle and the background (Figure 9-17). The background image was then subtracted from the image and a thresholding process was then applied for the boundary of the particle, to determine the edges of the particle, and the particle itself. A standard threshold limit was applied (boundary = 220, particle = 188, values in greyscale brightness). For those images on which this automated thresholding did not work, a manual process to find the particle thresholding was performed. This process was repeated for all frames, in all videos.

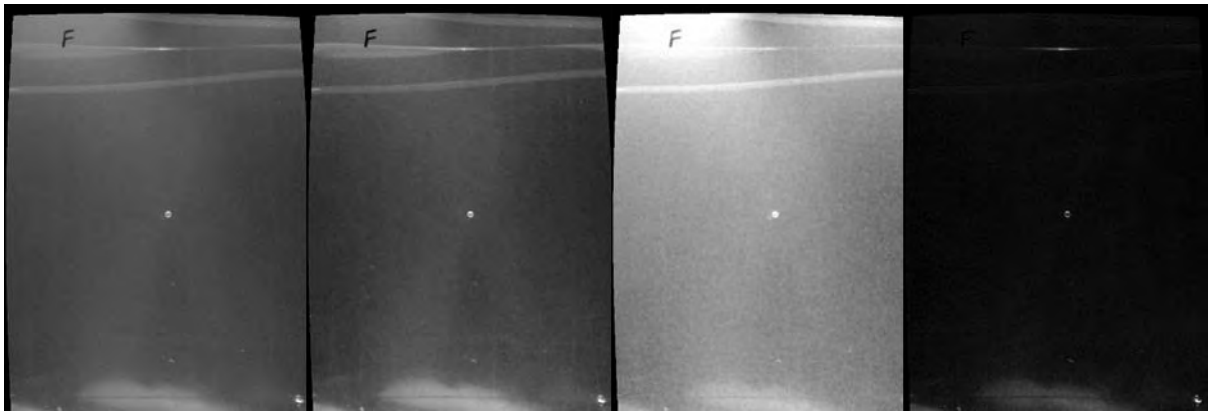

Figure 9-17. The same frame as in Figure 9-16 bottom right, but in greyscale (left), green channel (centre left), blue channel (centre right) and red channel (right). The green channel was used to track the sinking particles, as it provides the greatest contrast between the background and the sinking particle.

The use of fluorescent UV lighting resulted in a further complication; the light emittance of fluorescent lights occurs in high frequency waves (100-5000 cycles per second) which to human vision appears to be a continuous light source. However, when recorded this resulted in light and dark bands moving across the image (bands are evident in Figure 9-16), which resulted in the particle being more difficult to track, and so a secondary "data sorting" script was used to identify particles from these noisy images.

Before data sorting, the Trackbac code provided a centroid position of the particle in each frame. Centroid position was converted from pixels to mm by multiplying the camera scale by the number of pixels. Once converted into a 'real-world' distance, data sorting was carried out in MATLAB using a custom script, which used the centroid position, frame number and frame rate and paired these data with the time at which each frame was recorded. This script took specified starting and end positions, estimated maximum and minimum sinking velocities, and expected size range (measured as area). The starting and end points could differ as the model was not always clearly imaged during the entire

descent due to lighting issues. Using these parameters, the script interrogated each frame for particles which fit within these criteria and moved consistently downwards through the frames. Once possible particles were identified, their position was plotted on a graph of time and position (see Figure 9-18), then a straight line was fitted through the data points (Equation 9-23, where *m* is the gradient or slope of the line, *b* is the y-intercept and *x* and *y* are the x and y coordinates respectively). Any potential particles with a distance from this fitted line greater than the 99th percentile of all particles in the frame sequence were then removed, and the line refitted until the R^2 value was greater than or equal to 0.99. (Figure 9-18 for an example). The slope of this line (i.e. *m* in Equation 9-23) is the velocity of the particle over the entire sinking path. The vertical and horizontal sinking velocities from each camera were combined into a 3D sinking velocity (see Section 4.4.7 for a more detailed explanation).

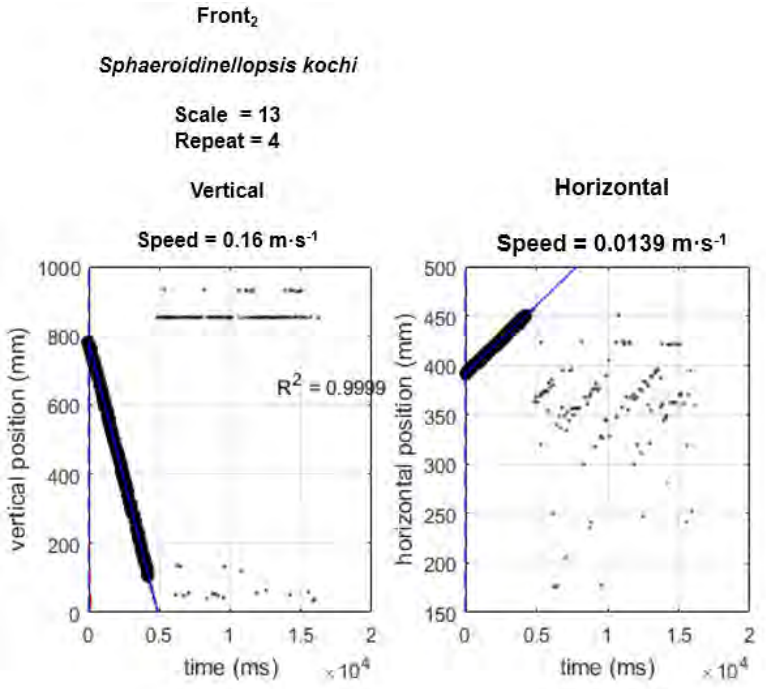

Figure 9-18: an example of the data sorting script output.

Equation 9-23

$$y = mx + b$$

9.2.1.8 *Initial testing – checking Reynolds number regime*

To test that the Reynolds number regime of the tank conditions matched the expectations of theory, a series of spheres were sunk.

Methods

A series of hollow spheres were designed and printed to provide a range of Re values from 10 to 55, by varying the diameter and wall thickness, determined by re-arranging the equation for Re Equation 3-2. Once the outside had been cleaned, the interiors of the spheres were flushed with propan-2-ol using a 30-gauge needle and syringe before they were weighed (Sartorius Entris 224-1S electronic

balance) and filled with mineral oil using a 30-gauge needle and syringe. The sinking velocity of the spheres was then measured as described above. A comparison was then made between the Re and C_D values of the sphere in the tank and the predictions using Morrison's equation (Equation 3-8). To test how divergent the experimental results were from theory an R^2 value was calculated. To calculate the R^2 value, a C_D value for each model sphere was calculated using the measured Re and Equation 3-8, this provides an expected C_D value. Then an R^2 value was calculated using Equation 9-24a, where SS_{res} is the sum of squares of residuals, calculated using Equation 9-24b using the observed C_D (y) the calculated C_D (f). SS_{tot} is the total sum of squares calculated with Equation 9-24c, again using the observed value (y) and mean of the observed values ($\bar{y}$).

Equation 3-8

$$C_D = \frac{24}{Re} + \frac{2.6 \cdot \left(\frac{Re}{5.0}\right)}{1 + \left(\frac{Re}{5.0}\right)^{1.52}} + \frac{0.411 \cdot \left(\frac{Re}{263{,}000}\right)^{-7.94}}{1 + \left(\frac{Re}{263{,}000}\right)^{-8.00}} + \left(\frac{Re^{0.80}}{461{,}000}\right)$$

Equation 9-24a

$$R^2 = 1 - \frac{SS_{res}}{SS_{tot}}$$

Equation 9-24b

$$SS_{res} = \sum_i (y_i - f_i)^2$$

Equation 9-24c

$$SS_{tot} = \sum_i (y_i - \bar{y})^2$$

Results

The Re and C_D values obtained are in close agreement with the theoretical results (Figure 9-19), providing strong evidence that the experimental method was valid and could be extended to the model foraminifera. C_D for a given Re was slightly higher than predicted, but within acceptable limits to errors.

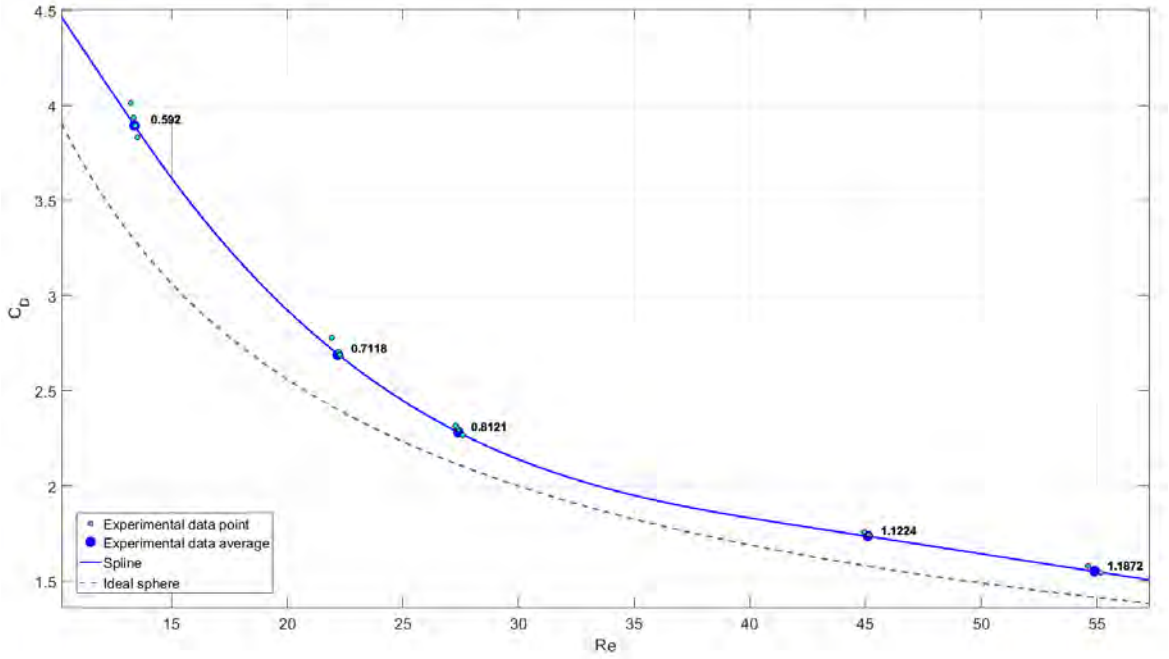

Figure 9-19: Confirmation of Reynolds number and therefore scaling of objects using spheres. Theoretical values derived from Equation 3-8 are shown as a grey dashed line. This experiment shows that the sinking regime (i.e. the Re and C_D values) fall approximately in line with the line predicted by theory (R^2 = 0.851), thereby validating the method.

Using the initial testing results above, it is possible to revisit and update Table 4-1 with some of the previously unknown values (Table 9-12). The exact scale of the model is still unknown and is solved for during the experiments (See 4.4.8).

Table 9-12: Table 4-1 updated with the potential values under the tank conditions. The variables in Equation 4-1 and Equation 3-2 and their values for a real foraminifera test (N. acostaensis). Values that are still to be determined are marked as TBD.

Variable		**Real Life**	**Tank**
Foraminifera & Foraminifera model	Density	Calcite: 2700 kg·m^3	Resin: 1121 kg·m^3
	Volume$_{wall}$	1.6 · 10^7 µm^3	Adjustable: Dependent on scale
	Length (longest)	543 µm	Adjustable: Dependent on scale
	Projected Area	Unknown	Adjustable: Dependent on scale
	Sinking Velocity	Unknown	TBD: dependent on other variables
Acceleration due to gravity		Fixed: 9.81 m·s^{-1}	Fixed: 9.81 m·s^{-1}
Fluid	Density	Seawater: 1024 kg·m^3	Carnation Mineral Oil: 830 kg·m^3
	Viscosity	Seawater: 0.001072 Pa·S	Carnation Mineral Oil: 0.022 Pa·S

9.2.2Comparisons between morphogroups

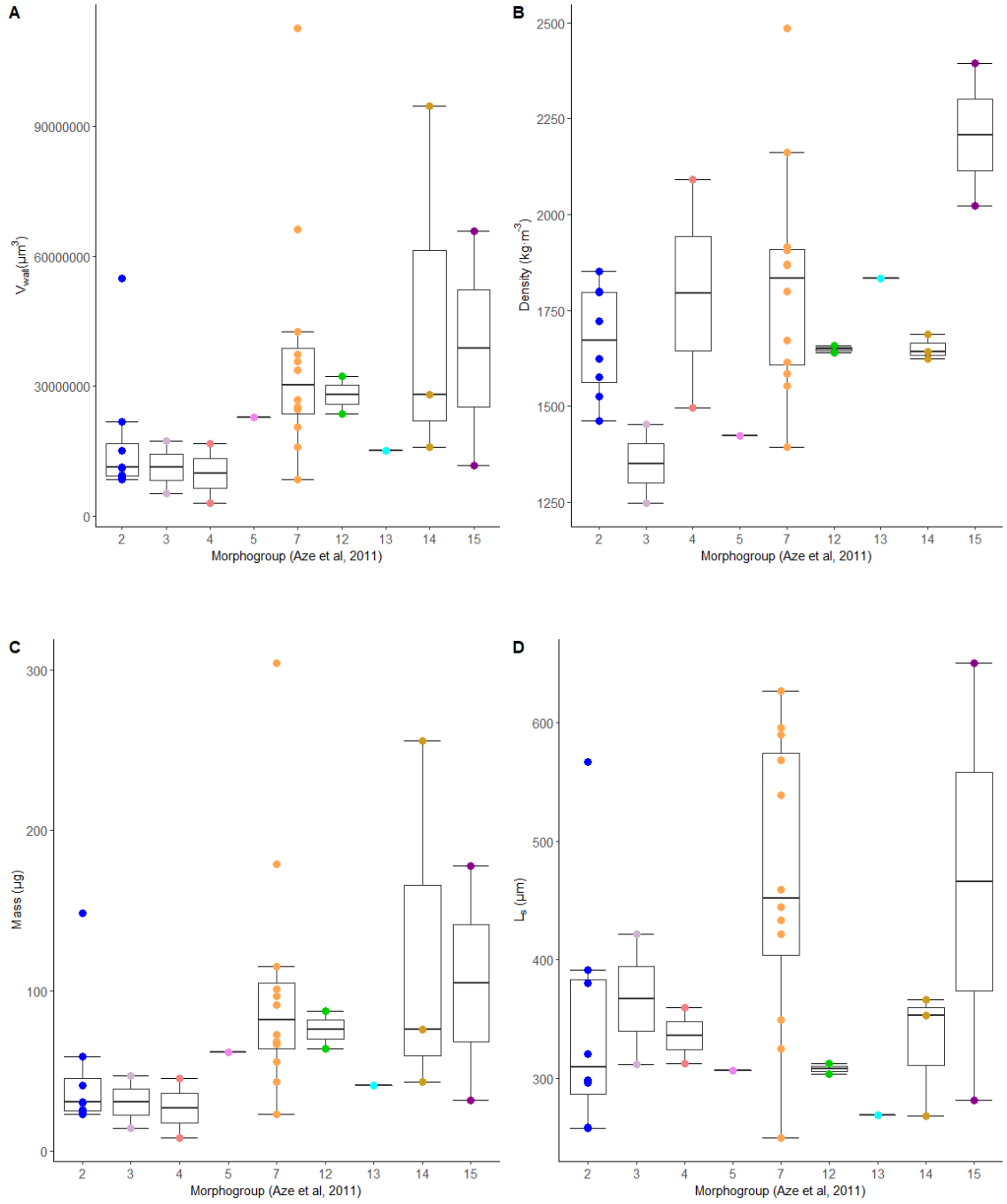

Figure 9-20: There are no significant differences when comparing the variance of: A) V_{wall} ($F_{8,24}$= 0.882, P= 0.546) B) Density ($F_{8,24}$= 2.212, P= 0.0634), C) Mass ($F_{8,24}$= 0.882, P= 0.546), D) L_s ($F_{8,24}$= 1.455, P= 0.225) between morphogroups.

There is no significant relationship between sinking velocity and CSF ($F_{1,31}$= 0.1617, P= 0.6904, adjusted R^2= -0.03, Figure 9-21A), nor between U_{mass} and CSF ($F_{1,31}$= 0.5639, P= 0.4583, adjusted R^2= -0.01382, Figure 9-21B).

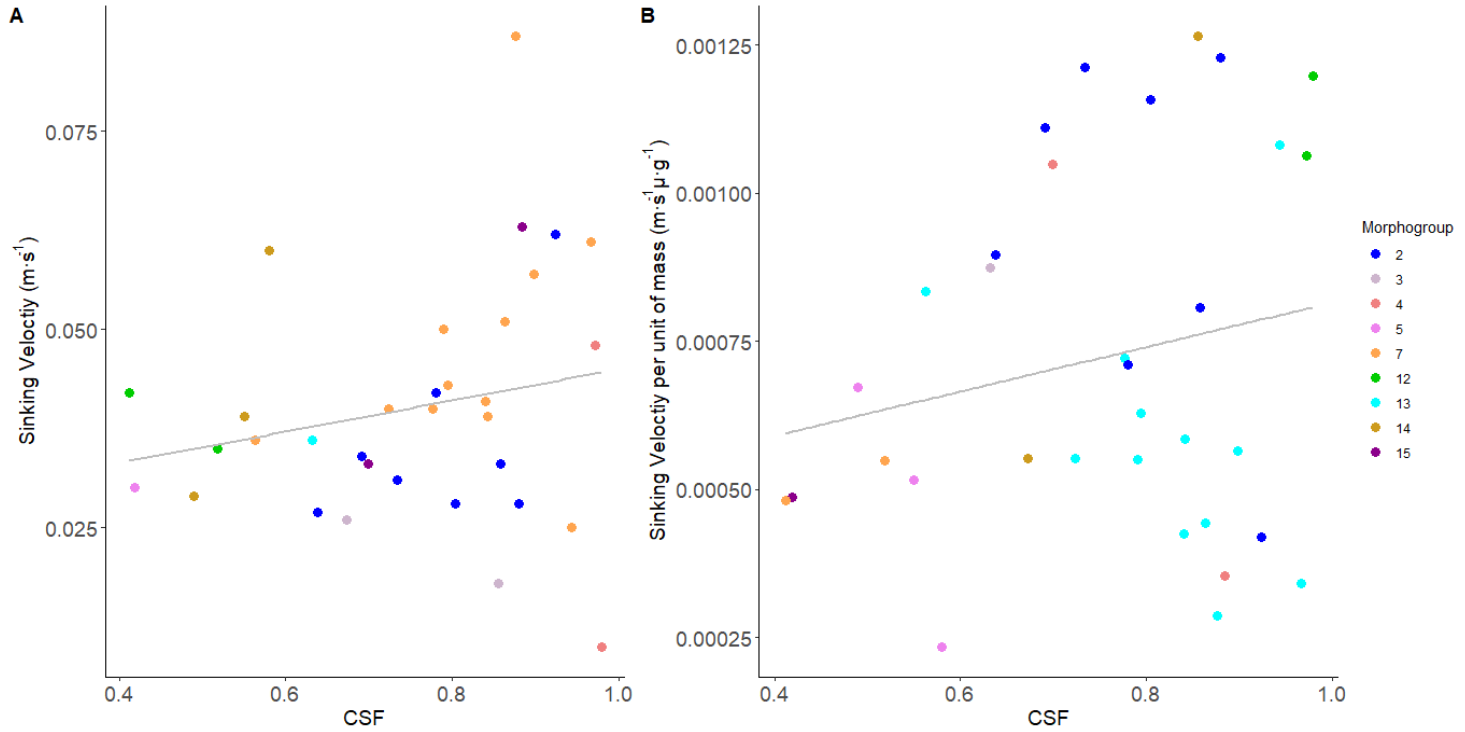

Figure 9-21: Sinking velocity and sinking velocity per unit of mass (U_{mass}) with CSF, coloured by morphogroup.

Table 9-13: Pairwise comparison results from Tukey HSD test comparing U_{mass} between morphogroups.

Morpho-group pair	Sinking velocity per unit of mass ($m \cdot s^{-1} \cdot \mu g^{-1}$)			
	Difference in means	Lower CI	Upper CI	Adjusted P value
3-2	-0.00003	-0.00075	0.00068	>0.99
4-2	0.00019	-0.00053	0.0009	0.991
5-2	-0.00046	-0.00142	0.00051	0.788
7-2	-0.00036	-0.00077	0.00006	0.128
12-2	-0.00043	-0.00114	0.00029	0.54
13-2	-0.00007	-0.00103	0.00089	>0.99
14-2	-0.00047	-0.00108	0.00015	0.24
15-2	-0.00024	-0.00096	0.00048	0.961
4-3	0.00022	-0.00068	0.00113	0.995
5-3	-0.00042	-0.00153	0.00069	0.924
7-3	-0.00032	-0.00102	0.00037	0.8
12-3	-0.00039	-0.0013	0.00051	0.856
13-3	-0.00003	-0.00114	0.00108	>0.99
14-3	-0.00043	-0.00126	0.00039	0.692
15-3	-0.00021	-0.00111	0.0007	0.997
5-4	-0.00064	-0.00176	0.00047	0.575
7-4	-0.00055	-0.00124	0.00015	0.207
12-4	-0.00062	-0.00152	0.00029	0.376
13-4	-0.00026	-0.00137	0.00085	0.996
14-4	-0.00066	-0.00148	0.00017	0.202
15-4	-0.00043	-0.00134	0.00048	0.792
7-5	0.0001	-0.00085	0.00104	>0.99
12-5	0.00003	-0.00108	0.00114	>0.99
13-5	0.00039	-0.00089	0.00167	0.979
14-5	-0.00001	-0.00106	0.00104	>0.99
15-5	0.00022	-0.00089	0.00133	0.999
12-7	-0.00007	-0.00076	0.00062	>0.99
13-7	0.00029	-0.00065	0.00123	0.977
14-7	-0.00011	-0.0007	0.00048	0.999
15-7	0.00012	-0.00058	0.00081	>0.99
13-12	0.00036	-0.00075	0.00147	0.969
14-12	-0.00004	-0.00087	0.00079	>0.99
15-12	0.00019	-0.00072	0.00109	0.998
14-13	-0.0004	-0.00145	0.00065	0.922
15-13	-0.00017	-0.00128	0.00094	>0.99
15-14	0.00023	-0.0006	0.00106	0.988

9.3Chapter 5 Appendices

9.3.1 GM morphospace plots

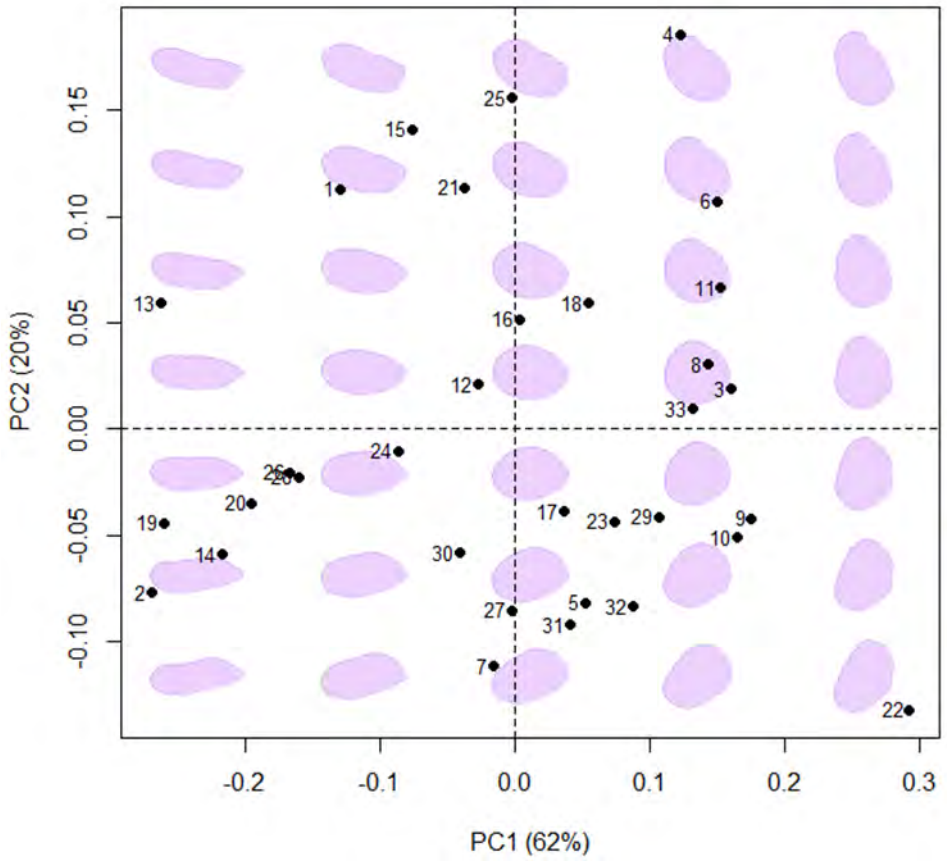

Figure 9-22: PC1 and PC2 scores in the aperture orientation, with representative shapes in purple. Percentage of shape variation (rounded to the nearest one percent) explained by each axis is included. Numbering as per Table 5-1, below.

Table 5-1: The 32 species of planktonic foraminifera whose shape was quantified in this study. The numbering provided is used throughout this chapter in figures to identify species.

Nº	Species	Nº	Species	Nº	Species	Nº	Species	Nº	Species
1	*Neogloboquadrina acostaensis*	**8**	*Praeorbulina curva*	**15**	*Globorotaloides hexagonus*	**22**	*Globoturborotalita nepenthes*	**29**	*Dentoglobigerina rohri*
2	*Globigerinella adamsi*	**9**	*Sphaeroidinella dehiscens*	**16**	*Neogloboquadrina humerosa*	**23**	*Pulleniatina obliquiloculata*	**30**	*Paragloborotalia siakensis*
3	*Dentoglobigerina altispira*	**10**	*Sphaeroidinella dehiscens (HR)*	**17**	*Globoconella inflata*	**24**	*Fohsella peripheroronda*	**31**	*Globoconella sphericomiozea*
4	*Globoturborotalita apertura*	**11**	*Catapsydrax dissimilis*	**18**	*Sphaeroidinellopsis kochi*	**25**	*Globigerina praebulloides*	**32**	*Truncorotalia truncatulinoides*
5	*Globigerina bulloides*	**12**	*Neogloboquadrina dutertrei*	**19**	*Fohsella lobata*	**26**	*Menardella praemenardii*	**33**	*Orbulina universa*
6	*Globigerinoides conglobatus*	**13**	*Globigerinoides fistulosus*	**20**	*Hirsutella margaritae*	**27**	*Globoconella puncticulata*		
7	*Truncorotalia crassaformis*	**14**	*Globorotalia flexuosa*	**21**	*Paragloborotalia mayeri*	**28**	*Fohsella robusta*		

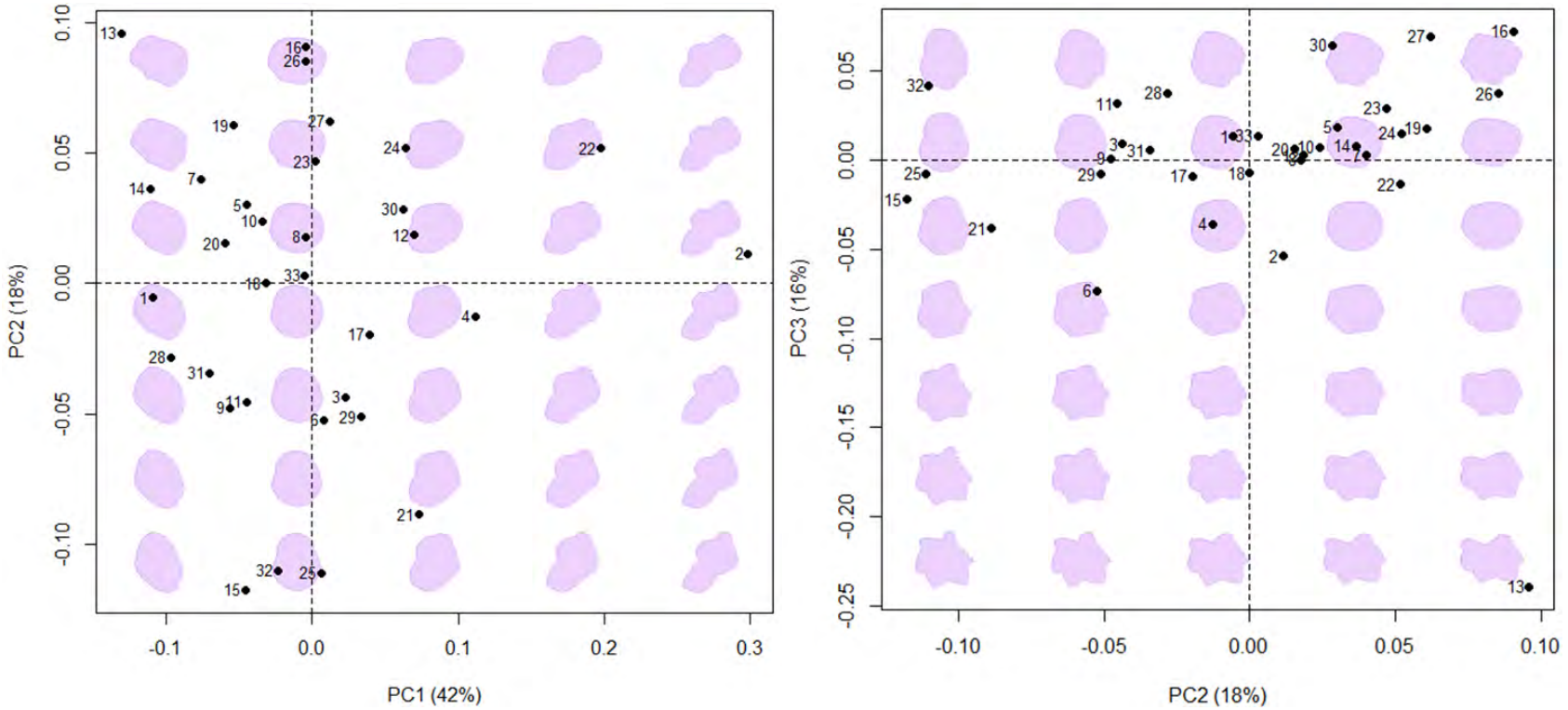

Figure 9-23: PC scores in sinking orientation underneath view, with representative shapes in purple. Percentage of shape variation (rounded to the nearest one percent) explained by each axis is included. Numbering as per Table 5-1, below.

Table 5-1: The 32 species of planktonic foraminifera whose shape was quantified in this study. The numbering provided is used throughout this chapter in figures to identify species.

Nº	Species	Nº	Species	Nº	Species	Nº	Species	Nº	Species	Nº	Species
1	*Neogloboquadrina acostaensis*	**7**	*Truncorotalia crassaformis*	**13**	*Globigerinoides fistulosus*	**19**	*Fohsella lobata*	**25**	*Globigerina praebulloides*	**31**	*Globoconella sphericomiozea*
2	*Globigerinella adamsi*	**8**	*Praeorbulina curva*	**14**	*Globorotalia flexuosa*	**20**	*Hirsutella margaritae*	**26**	*Menardella praemenardii*	**32**	*Truncorotalia truncatulinoides*
3	*Dentoglobigerina altispira*	**9**	*Sphaeroidinella dehiscens*	**15**	*Globorotaloides hexagonus*	**21**	*Paragloborotalia mayeri*	**27**	*Globoconella puncticulata*	**33**	*Orbulina universa*
4	*Globoturborotalita apertura*	**10**	*Sphaeroidinella dehiscens (HR)*	**16**	*Neogloboquadrina humerosa*	**22**	*Globoturborotalita nepenthes*	**28**	*Fohsella robusta*		
5	*Globigerina bulloides*	**11**	*Catapsydrax dissimilis*	**17**	*Globoconella inflata*	**23**	*Pulleniatina obliquiloculata*	**29**	*Dentoglobigerina rohri*		
6	*Globigerinoides conglobatus*	**12**	*Neogloboquadrina dutertrei*	**18**	*Sphaeroidinellopsis kochi*	**24**	*Fohsella peripheroronda*	**30**	*Paragloborotalia siakensis*		

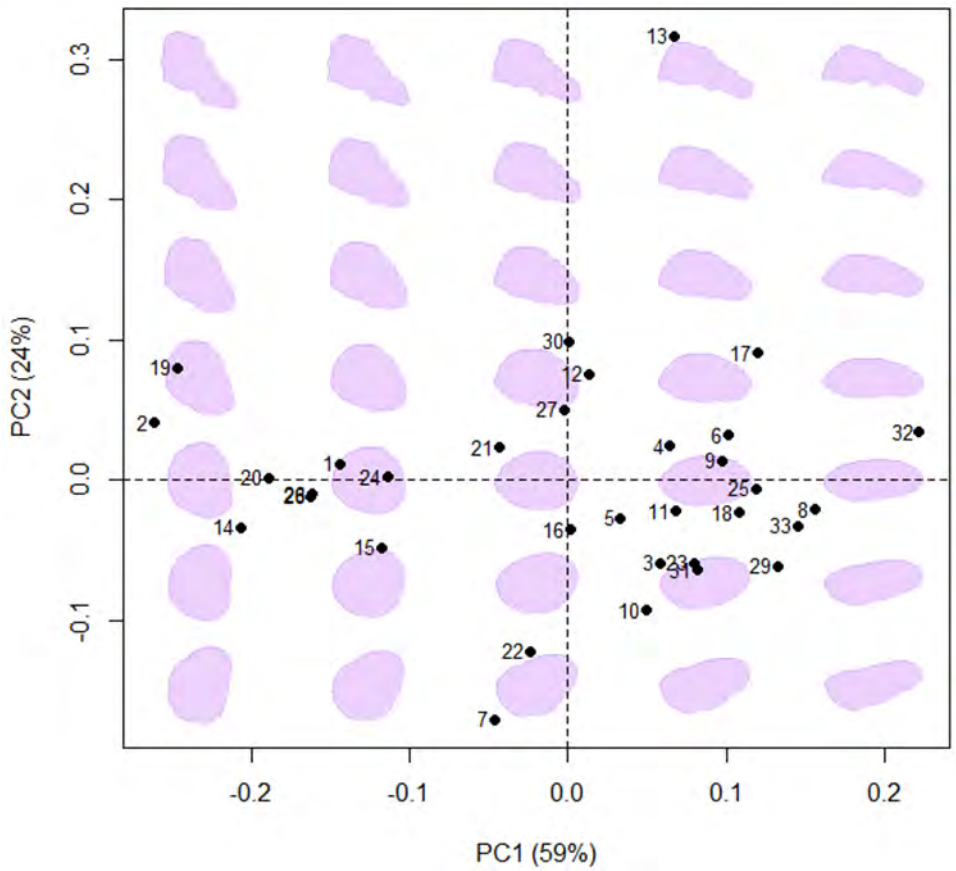

Figure 9-24: PC1 & 2 in a side orientation, with representative shapes in purple. Percentage of shape variation (rounded to the nearest one percent) explained by each axis is included. Numbering as per table below.

Nº	Species	Nº	Species	Nº	Species	Nº	Species	Nº	Species
1	*Neogloboquadrina acostaensis*	**8**	*Praeorbulina curva*	**15**	*Globorotaloides hexagonus*	**22**	*Globoturborotalita nepenthes*	**29**	*Dentoglobigerina rohri*
2	*Globigerinella adamsi*	**9**	*Sphaeroidinella dehiscens*	**16**	*Neogloboquadrina humerosa*	**23**	*Pulleniatina obliquiloculata*	**30**	*Paragloborotalia siakensis*
3	*Dentoglobigerina altispira*	**10**	*Sphaeroidinella dehiscens (HR)*	**17**	*Globoconella inflata*	**24**	*Fohsella peripheroronda*	**31**	*Globoconella sphericomiozea*
4	*Globoturborotalita apertura*	**11**	*Catapsydrax dissimilis*	**18**	*Sphaeroidinellopsis kochi*	**25**	*Globigerina praebulloides*	**32**	*Truncorotalia truncatulinoides*
5	*Globigerina bulloides*	**12**	*Neogloboquadrina dutertrei*	**19**	*Fohsella lobata*	**26**	*Menardella praemenardii*	**33**	*Orbulina universa*
6	*Globigerinoides conglobatus*	**13**	*Globigerinoides fistulosus*	**20**	*Hirsutella margaritae*	**27**	*Globoconella puncticulata*		
7	*Truncorotalia crassaformis*	**14**	*Globorotalia flexuosa*	**21**	*Paragloborotalia mayeri*	**28**	*Fohsella robusta*		

9.3.2 Phylomorphospace plots

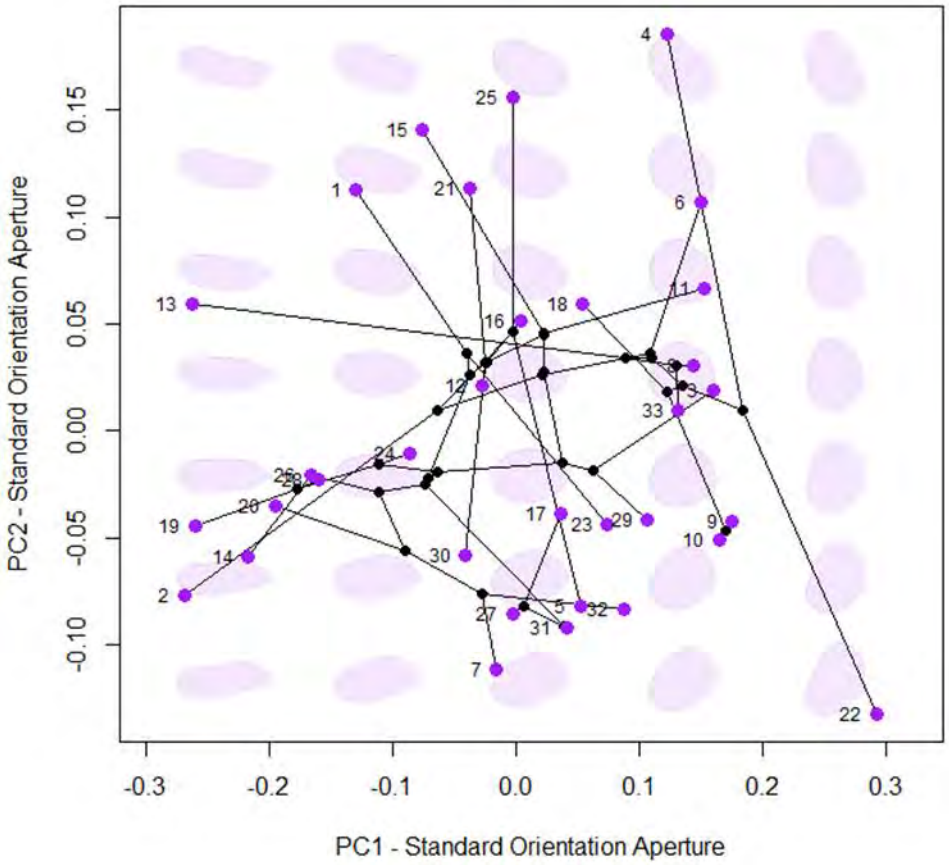

*Figure 9-25:Phylomorphospace using PC axes 1 & 2 in the aperture view. Note the closely positioned 9 (*S. dehiscens*) and 10 (*S. dehiscens *(HR)). In these plots the terminal taxa are shown in purple and numbered in accordance with table below. Nodes are coloured black; their position being calculated using ASR.*

Nº	Species	Nº	Species	Nº	Species	Nº	Species	Nº	Species
1	*Neogloboquadrina acostaensis*	**8**	*Praeorbulina curva*	**15**	*Globorotaloides hexagonus*	**22**	*Globoturborotalita nepenthes*	**29**	*Dentoglobigerina rohri*
2	*Globigerinella adamsi*	**9**	*Sphaeroidinella dehiscens*	**16**	*Neogloboquadrina humerosa*	**23**	*Pulleniatina obliquiloculata*	**30**	*Paragloborotalia siakensis*
3	*Dentoglobigerina altispira*	**10**	*Sphaeroidinella dehiscens (HR)*	**17**	*Globoconella inflata*	**24**	*Fohsella peripheroronda*	**31**	*Globoconella sphericomiozea*
4	*Globoturborotalita apertura*	**11**	*Catapsydrax dissimilis*	**18**	*Sphaeroidinellopsis kochi*	**25**	*Globigerina praebulloides*	**32**	*Truncorotalia truncatulinoides*
5	*Globigerina bulloides*	**12**	*Neogloboquadrina dutertrei*	**19**	*Fohsella lobata*	**26**	*Menardella praemenardii*	**33**	*Orbulina universa*
6	*Globigerinoides conglobatus*	**13**	*Globigerinoides fistulosus*	**20**	*Hirsutella margaritae*	**27**	*Globoconella puncticulata*		
7	*Truncorotalia crassaformis*	**14**	*Globorotalia flexuosa*	**21**	*Paragloborotalia mayeri*	**28**	*Fohsella robusta*		

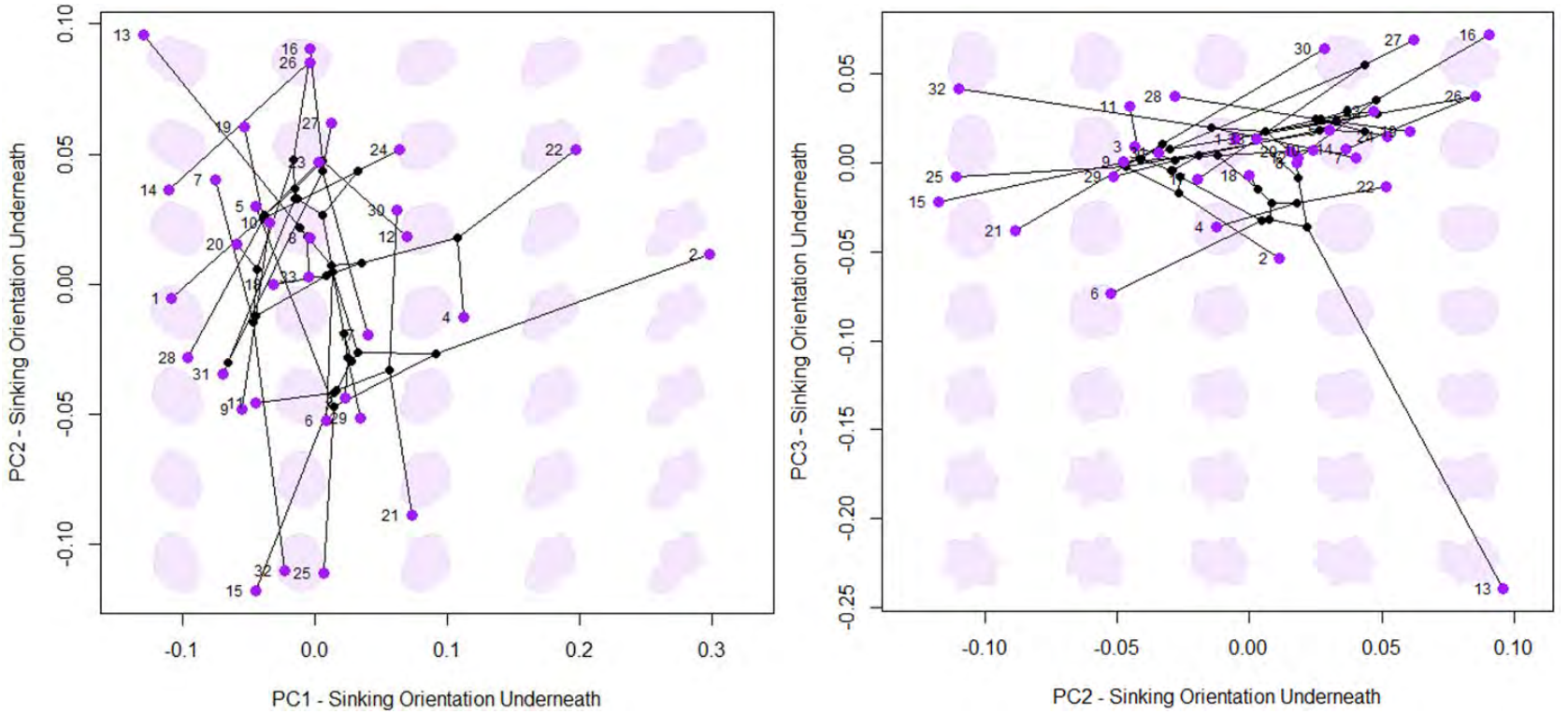

Figure 9-26: Phylomorphospace using PC axes 1, 2 & 3 in the sinking orientation. In these plots the terminal taxa are shown in purple and numbered in accordance with table below. Nodes are coloured black; their position being calculated using ASR.

Nº	Species	Nº	Species	Nº	Species	Nº	Species	Nº	Species	Nº	Species
1	*Neogloboquadrina acostaensis*	**7**	*Truncorotalia crassaformis*	**13**	*Globigerinoides fistulosus*	**19**	*Fohsella lobata*	**25**	*Globigerina praebulloides*	**31**	*Globoconella sphericomiozea*
2	*Globigerinella adamsi*	**8**	*Praeorbulina curva*	**14**	*Globorotalia flexuosa*	**20**	*Hirsutella margaritae*	**26**	*Menardella praemenardii*	**32**	*Truncorotalia truncatulinoides*
3	*Dentoglobigerina altispira*	**9**	*Sphaeroidinella dehiscens*	**15**	*Globorotaloides hexagonus*	**21**	*Paragloborotalia mayeri*	**27**	*Globoconella puncticulata*	**33**	*Orbulina universa*
4	*Globoturborotalita apertura*	**10**	*Sphaeroidinella dehiscens (HR)*	**16**	*Neogloboquadrina humerosa*	**22**	*Globoturborotalita nepenthes*	**28**	*Fohsella robusta*		
5	*Globigerina bulloides*	**11**	*Catapsydrax dissimilis*	**17**	*Globoconella inflata*	**23**	*Pulleniatina obliquiloculata*	**29**	*Dentoglobigerina rohri*		
6	*Globigerinoides conglobatus*	**12**	*Neogloboquadrina dutertrei*	**18**	*Sphaeroidinellopsis kochi*	**24**	*Fohsella peripheroronda*	**30**	*Paragloborotalia siakensis*		

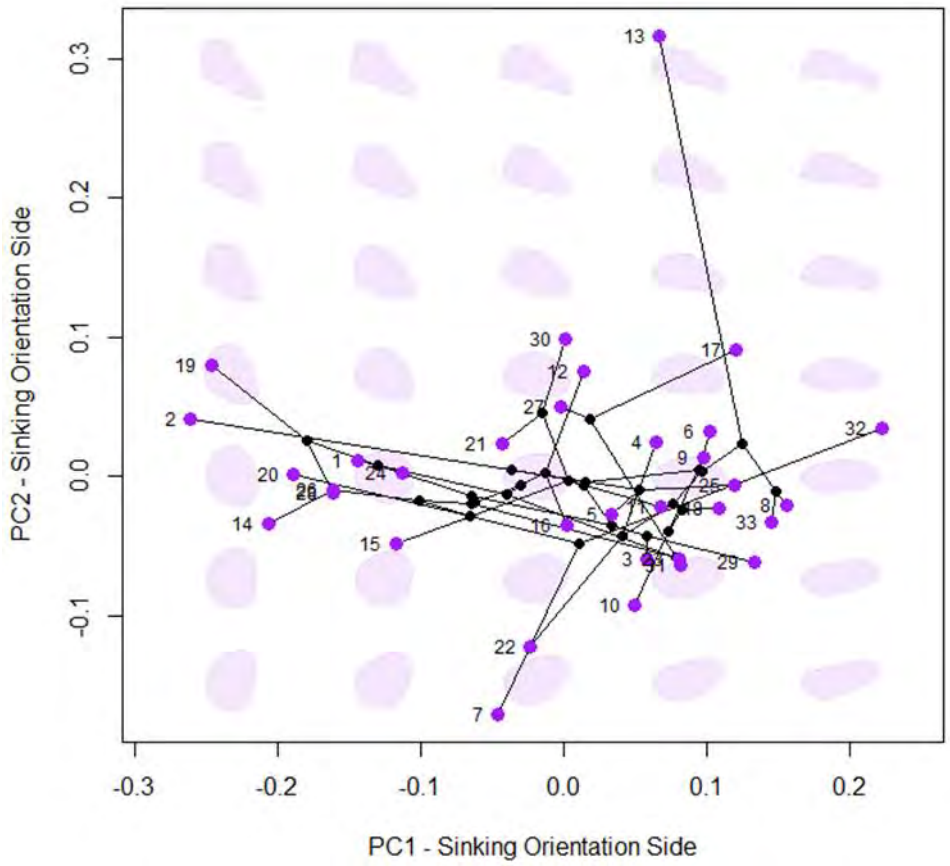

Figure 9-27: Phylomorphospace using PC axes 1 and 2 in the sinking orientation side view. In these plots the terminal taxa are shown in purple and numbered in accordance with table below. Nodes are coloured black; their position being calculated using ASR.

Nº	Species	Nº	Species	Nº	Species	Nº	Species	Nº	Species
1	*Neogloboquadrina acostaensis*	**8**	*Praeorbulina curva*	**15**	*Globorotaloides hexagonus*	**22**	*Globoturborotalita nepenthes*	**29**	*Dentoglobigerina rohri*
2	*Globigerinella adamsi*	**9**	*Sphaeroidinella dehiscens*	**16**	*Neogloboquadrina humerosa*	**23**	*Pulleniatina obliquiloculata*	**30**	*Paragloborotalia siakensis*
3	*Dentoglobigerina altispira*	**10**	*Sphaeroidinella dehiscens (HR)*	**17**	*Globoconella inflata*	**24**	*Fohsella peripheroronda*	**31**	*Globoconella sphericomiozea*
4	*Globoturborotalita apertura*	**11**	*Catapsydrax dissimilis*	**18**	*Sphaeroidinellopsis kochi*	**25**	*Globigerina praebulloides*	**32**	*Truncorotalia truncatulinoides*
5	*Globigerina bulloides*	**12**	*Neogloboquadrina dutertrei*	**19**	*Fohsella lobata*	**26**	*Menardella praemenardii*	**33**	*Orbulina universa*
6	*Globigerinoides conglobatus*	**13**	*Globigerinoides fistulosus*	**20**	*Hirsutella margaritae*	**27**	*Globoconella puncticulata*		
7	*Truncorotalia crassaformis*	**14**	*Globorotalia flexuosa*	**21**	*Paragloborotalia mayeri*	**28**	*Fohsella robusta*		

9.3.3Comparison of GM and EFA

There is a significant positive correlation between GM and EFA in PC1 for spiral (r_s=0.793, N=33, p<0.001), aperture (r_s=-0.887, N=33, p<0.001) and side view (r_s=0.904, N=33, p<0.001). There is no significant correlation between GM PC1 and EFA PC1 in the underneath view (r_s= -0.109, N=33, p=0.545). For PC2 there is no significant correlation between GM and EFA in spiral (r_s= 0.037, N=33, p=0.837), underneath view (r_s= 0.007, N=33, p=0.967) and side view (r_s= -0.1638, N=33, p=0.361). There is a significant correlation for PC2 in the aperture orientation (r_s= -0.633, N=33, p<0.001)..

Whilst both GM and EFA quantify shape to give similar results, especially in the first PC axis. EFA has the advantage that it does not require a homologous starting point between all specimens (as mentioned above), which could be advantageous with outlining, for example views that do not have homologous points between specimens, this may explain some of the differences between EFA and GM PC scores. In the same orientation the PC axes explain a similar amount of variance (e.g.: spiral view GM PC1 explains 32.6%, the EFA PC1 explains 39.9%). In the second axes the amount of variance explained differs more, and the PC values differ significantly, this suggests that a different element of shape variance is captured using the different methods. Here, the differences between GM and EFA (see Appendix 9.3.3 for comparison) are small in most views. For the underneath view GM PC scores have a larger spread in PC1 and PC2 compared to EFA PC1 and 2, suggesting that GM allows better separation of species in this view.

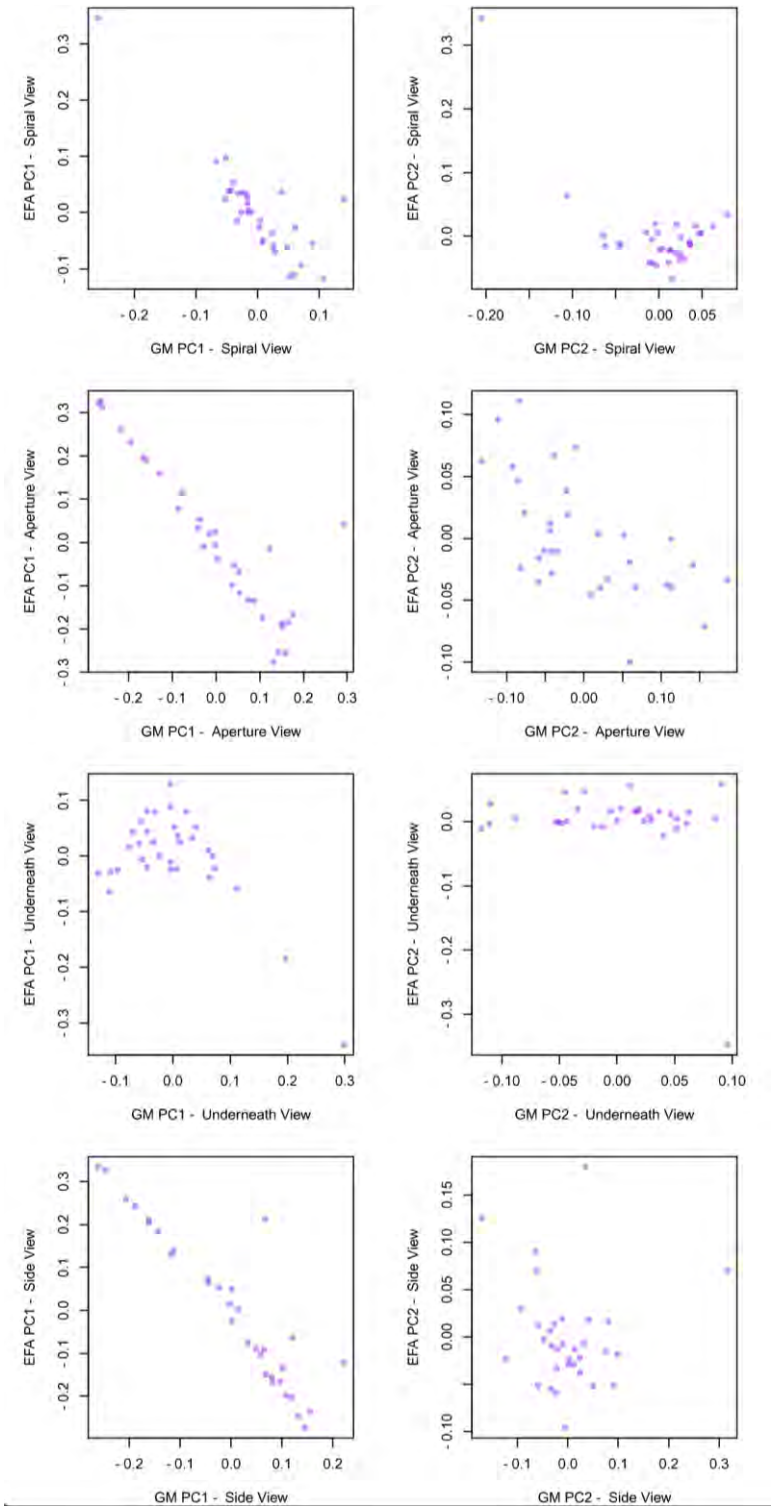

Figure 9-28: PC1 & 2 scores for GM (x) and EFA (y). Spearman's rank correlation tests are reported in text, but in general PC1 shows positive correlations in all views apart from underneath view PC1. This suggests that species with high GM PC1 scores are likely to have high EFA PC1 values and would indicate similar variation in shape is determined as being the most important, irrespective of the method used to captured shape. Comparisons of PC2 show was only significant for aperture view, suggesting the second most important aspect of shape (i.e. PC2) differs between EFA and GM methods.

9.3.4 Comparison of GM to CSF

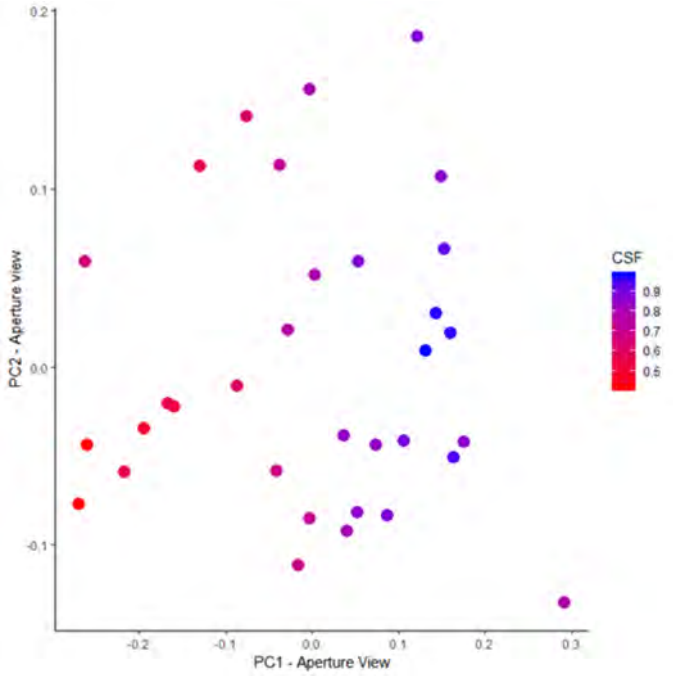

Figure 9-29: PC1 & 2 in aperture view, with points coloured by CSF value, with bluer colours being more spherical shapes and the redder the colour the less spherical.

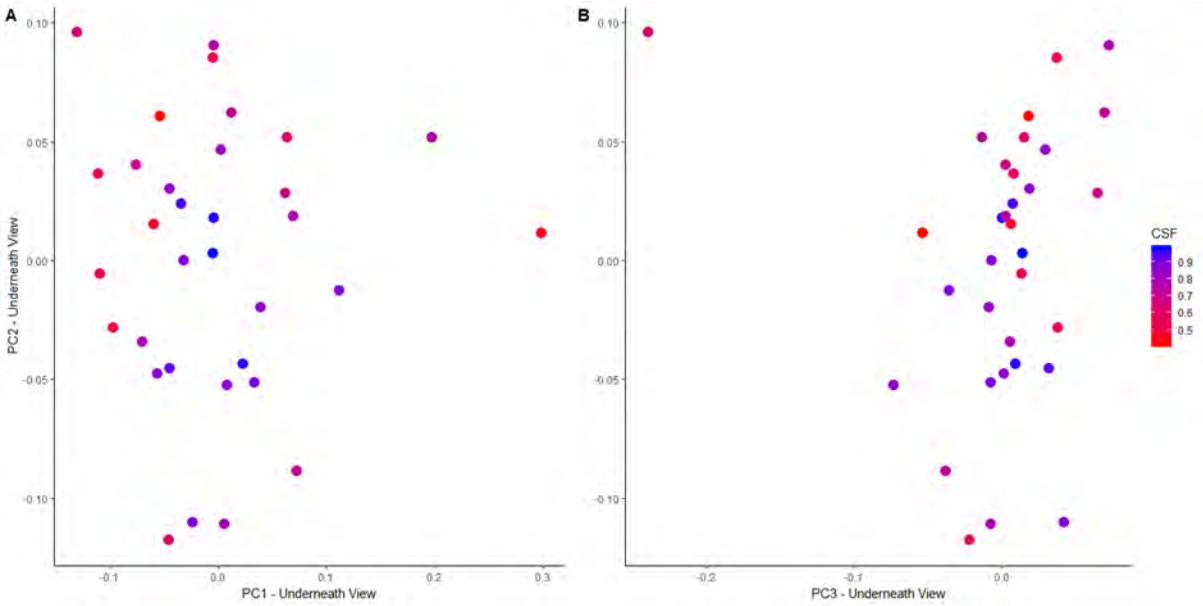

Figure 9-30: PC1, 2, & 3 in underneath view, with the data points coloured by CSF value, with bluer colours being more spherical shapes and the redder the colour the less spherical.

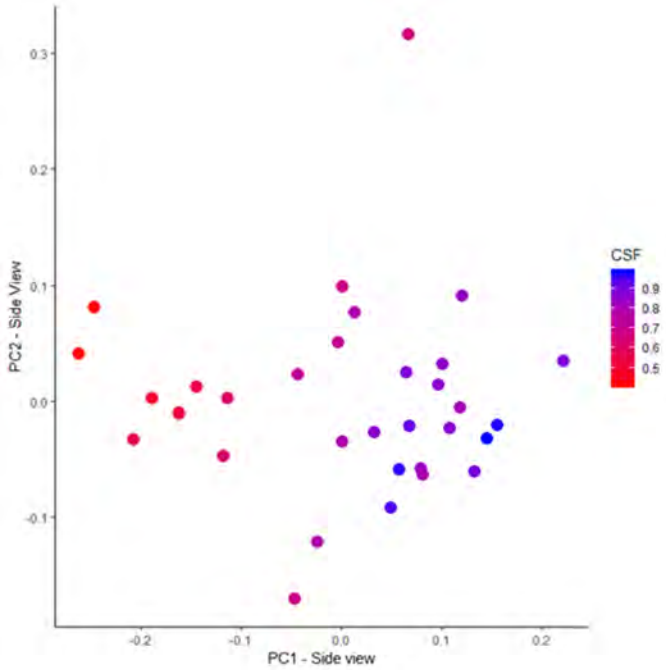

Figure 9-31: PC1 & 2 in the side view of sinking orientation, with the data points coloured by CSF value, with bluer colours being more spherical shapes and the redder the colour the less spherical.

9.3.5 Elliptical Fourier Analysis

The most popular method of outline analysis is Elliptical Fourier Analysis (EFA, MacLeod, 2012). This method does not require homologous features (i.e. a point at which to start outlining that is shared between different specimens) but, similarly to geometric morphometrics, is performed on outlines of a shape.

To describe the outline of a circle, whose radius is one, imagine a point moving around the outside of the circle at a constant speed. The x and y co-ordinates of this point can be plotted as a time series, with the x-coordinates generating a cosine wave and y-coordinates generating a sine wave. These two simple waves can be summed together, forming a more complex wave which encompasses both x- and y-positions. This complex wave can be described by partial differential equations, which contain two terms that equate to the sine and cosine waves. For the circle example (Figure 9-32), it is described perfectly by one sine and one cosine term. However, more complex shapes require more cosine and sine terms, or harmonics.

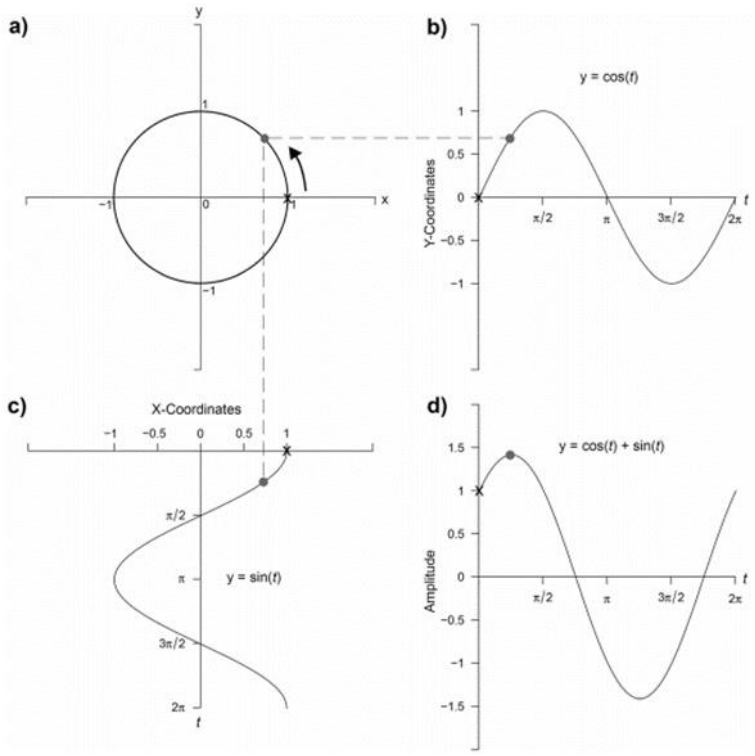

Figure 9-32: a) The example circle (of radius one) and the point moving around the perimeter, with the arrow denoting direction of travel. In b) and c) the projection of the point's y and x coordinates respectively. In d) the complex wave produced by summing the cosine and sine waves from b) and c). Image from (Caple, Byrd and Stephan, 2017)

When applying Fourier analysis to shape quantification, harmonics are fitted until the shape is adequately described (Figure 9-33 and Figure 9-34). Elliptical Fourier analysis, as the name suggests, use ellipses rather than circles. This means that for each harmonic there are two sets of partial differential equations, as opposed to the one used by Fourier Analysis. The manner in which these mechanics work is best illustrated by animation (such as the Supplementary Videos 1-3 by Caple *et al.*, 2017).

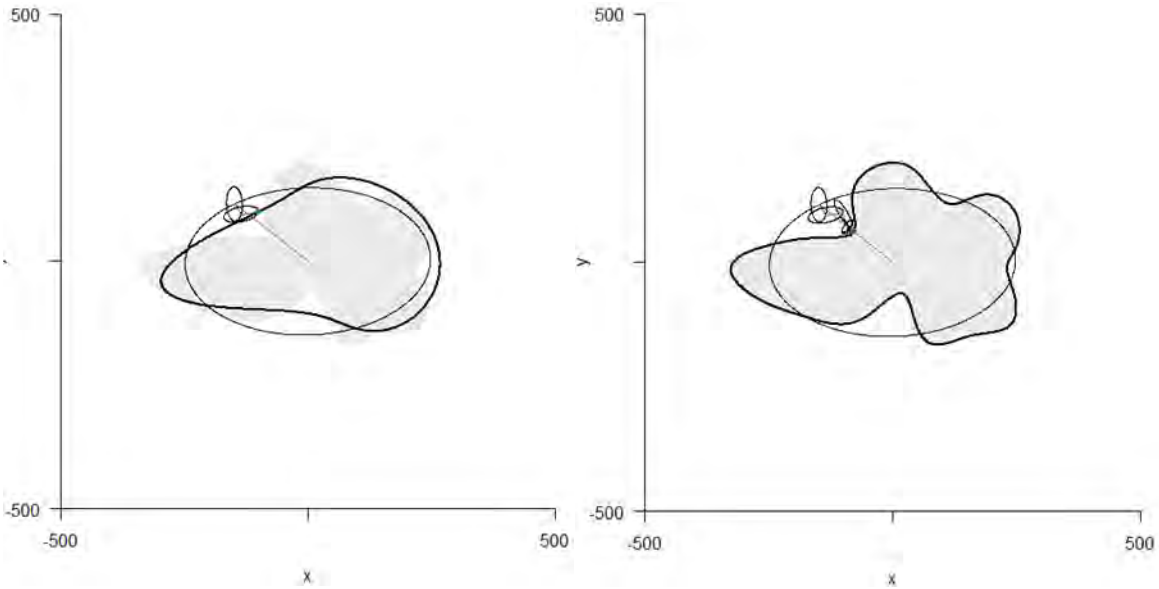

Figure 9-33: An example of EFA, the bold black outline shows the final shape described using (on the left) 3 harmonics and (on the right) 10 harmonics. The example uses an outline of G.adamsi *(in grey). Units are non-dimensional space. Generated using R code from Capel (2017).*

9.3.5.1 *EFA Method*

The same thresholded images that were used in the GM analyses, were subjected to EFA using the R package "Momocs" (Version 1.2.9, Bonhomme *et al*., 2013). Closed outlines were created and resampled to 100 points before being subjected to a Procrustes fit and EFA. The number of harmonics were automatically estimated, along with the deviations from the original shape and the reconstructed shape. The EFA values were then passed to a PCA, giving each species a unique PC score that was then plotted in a morphospace. Visualisations of morphospace were produced using "Momocs", including the back-transformed shapes.

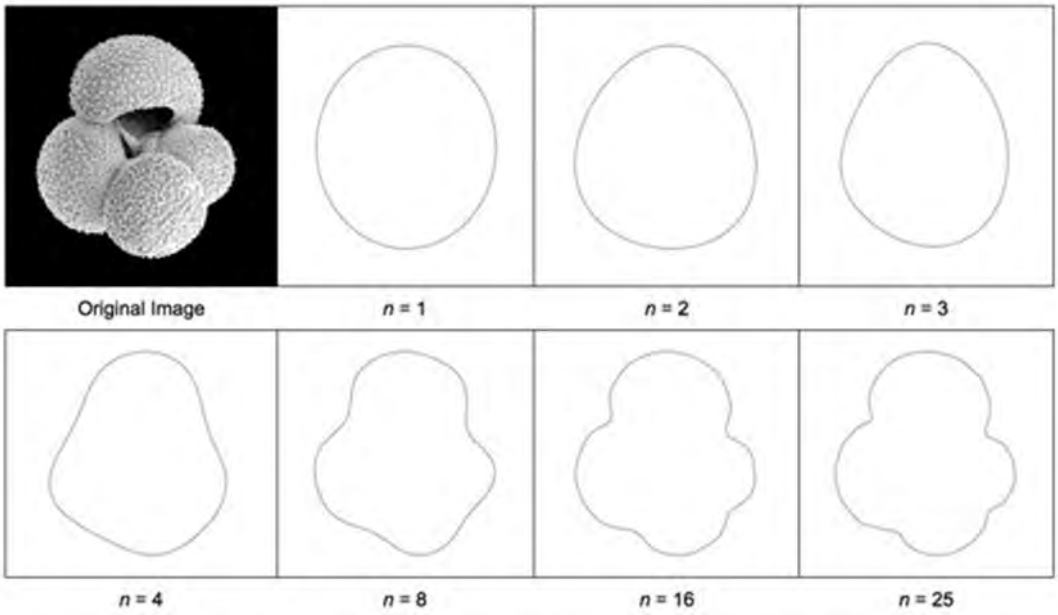

Figure 9-34: EFA example of Globigerina bulloides, *the outlines shown in each panel are the shapes described by n number of harmonics. from* (MacLeod, 2012)*, used with permission.*

The sum of these harmonics can then be used as a shape descriptor, upon which Principle Component Analysis (PCA) can be performed. EFA has been used extensively in the comparisons of shape within planktonic foraminifera species (e.g.: Healy-Williams & Williams, 1981; De Vargas *et al*., 2001). Therefore, EFA will be used here to serve as a comparison with the GM techniques used.

9.3.5.2 *EFA Morphospace*

The results from the EFA in each orientation show similar overall patterns in grouping of species, with the PC1 in the aperture view and side view explaining a large amount of the shape variation (80% and 79.5% respectively) from a side view. The majority of the species are found in close proximity to the origin, with the exception of *G. adamsi* and *G. fistulosus*. Specific locations of the species within the EFA morphospace differ from the GM, but the same species (*G. adamsi* and *G. fistulosus*) lie at the extreme points in the spiral and view from underneath. The spiral and side views have similar amount of shape variation explained by PC1 and PC2.

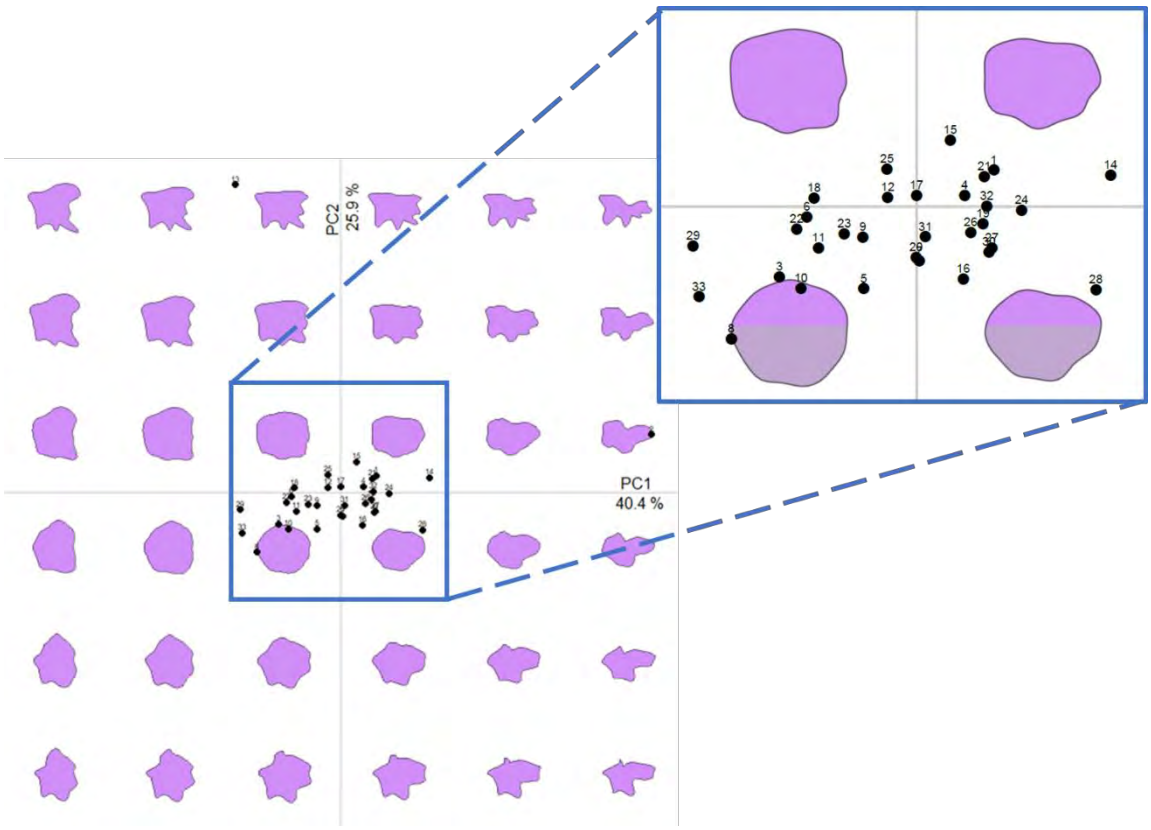

Figure 9-35: EFA PC1 and 2 (explaining 40.4% and 25.9% of shape variation, respectively) for spiral view. Back-transformed shapes are shown in purple for reference. As with GM, these are the shapes a species would be if they occurred at that point in morphospace. Note G. adamsi *lies to the far right of the x-axis (PC1).Species numbered as in table below, outliers on the graph are underlined in the table.*

Nº	Species	Nº	Species	Nº	Species	Nº	Species	Nº	Species
1	*Neogloboquadrina acostaensis*	**8**	*Praeorbulina curva*	**15**	*Globorotaloides hexagonus*	**22**	*Globoturborotalita nepenthes*	**29**	*Dentoglobigerina rohri*
2	*Globigerinella adamsi*	**9**	*Sphaeroidinella dehiscens*	**16**	*Neogloboquadrina humerosa*	**23**	*Pulleniatina obliquiloculata*	**30**	*Paragloborotalia siakensis*
3	*Dentoglobigerina altispira*	**10**	*Sphaeroidinella dehiscens (HR)*	**17**	*Globoconella inflata*	**24**	*Fohsella peripheroronda*	**31**	*Globoconella sphericomiozea*
4	*Globoturborotalita apertura*	**11**	*Catapsydrax dissimilis*	**18**	*Sphaeroidinellopsis kochi*	**25**	*Globigerina praebulloides*	**32**	*Truncorotalia truncatulinoides*
5	*Globigerina bulloides*	**12**	*Neogloboquadrina dutertrei*	**19**	*Fohsella lobata*	**26**	*Menardella praemenardii*	**33**	*Orbulina universa*
6	*Globigerinoides conglobatus*	**13**	*Globigerinoides fistulosus*	**20**	*Hirsutella margaritae*	**27**	*Globoconella puncticulata*		
7	*Truncorotalia crassaformis*	**14**	*Globorotalia flexuosa*	**21**	*Paragloborotalia mayeri*	**28**	*Fohsella robusta*		

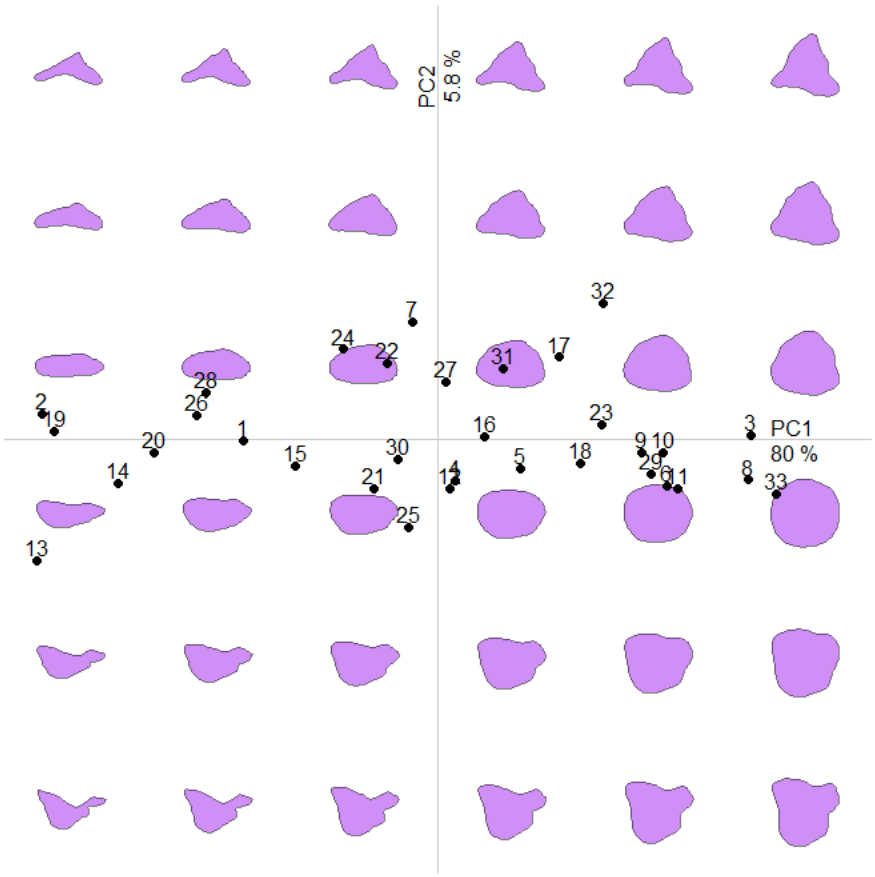

Figure 9-36: EFA PC1 & 2 (explaining 80% and 5.8% of shape variance) in the aperture view. Back-transformed shapes are shown in purple for reference. Note how extrapolations beyond the data (i.e. bottom right) result in not-seen-in-nature shapes. Species numbered as in table below.

Nº	Species	Nº	Species	Nº	Species	Nº	Species	Nº	Species
1	*Neogloboquadrina acostaensis*	**8**	*Praeorbulina curva*	**15**	*Globorotaloides hexagonus*	**22**	*Globoturborotalita nepenthes*	**29**	*Dentoglobigerina rohri*
2	*Globigerinella adamsi*	**9**	*Sphaeroidinella dehiscens*	**16**	*Neogloboquadrina humerosa*	**23**	*Pulleniatina obliquiloculata*	**30**	*Paragloborotalia siakensis*
3	*Dentoglobigerina altispira*	**10**	*Sphaeroidinella dehiscens (HR)*	**17**	*Globoconella inflata*	**24**	*Fohsella peripheroronda*	**31**	*Globoconella sphericomiozea*
4	*Globoturborotalita apertura*	**11**	*Catapsydrax dissimilis*	**18**	*Sphaeroidinellopsis kochi*	**25**	*Globigerina praebulloides*	**32**	*Truncorotalia truncatulinoides*
5	*Globigerina bulloides*	**12**	*Neogloboquadrina dutertrei*	**19**	*Fohsella lobata*	**26**	*Menardella praemenardii*	**33**	*Orbulina universa*
6	*Globigerinoides conglobatus*	**13**	*Globigerinoides fistulosus*	**20**	*Hirsutella margaritae*	**27**	*Globoconella puncticulata*		
7	*Truncorotalia crassaformis*	**14**	*Globorotalia flexuosa*	**21**	*Paragloborotalia mayeri*	**28**	*Fohsella robusta*		

As with GM morphospaces, the changes in shape in the first PC of the spiral view (Figure 9-35) can be explained by the changes in the outline due to the spiral pattern of growth which is seen in foraminifera. However, PC2 in the spiral view accounts for more of the variability in curvature of the outlines, i.e. the presence or absence of protrusions.

Once again there are similarities between GM and EFA in the aperture view. The changes in PC scores reflect the relative circularity of the foraminifera in a side view (Figure 9-36), which is probably accounted for by the spiral angle. With the aperture orientation PC2, there is even clearer demonstration of the trochospiral coiling pattern.

The patterns seen in the sinking orientation underneath view (Figure 9-37) is similar to the spiral orientation and so is the likely explanation for the patterns seen. Likewise, the reasons for the distribution of species in the side view of the sinking orientation (Figure 9-38) is very similar in overall trends to the aperture orientation.

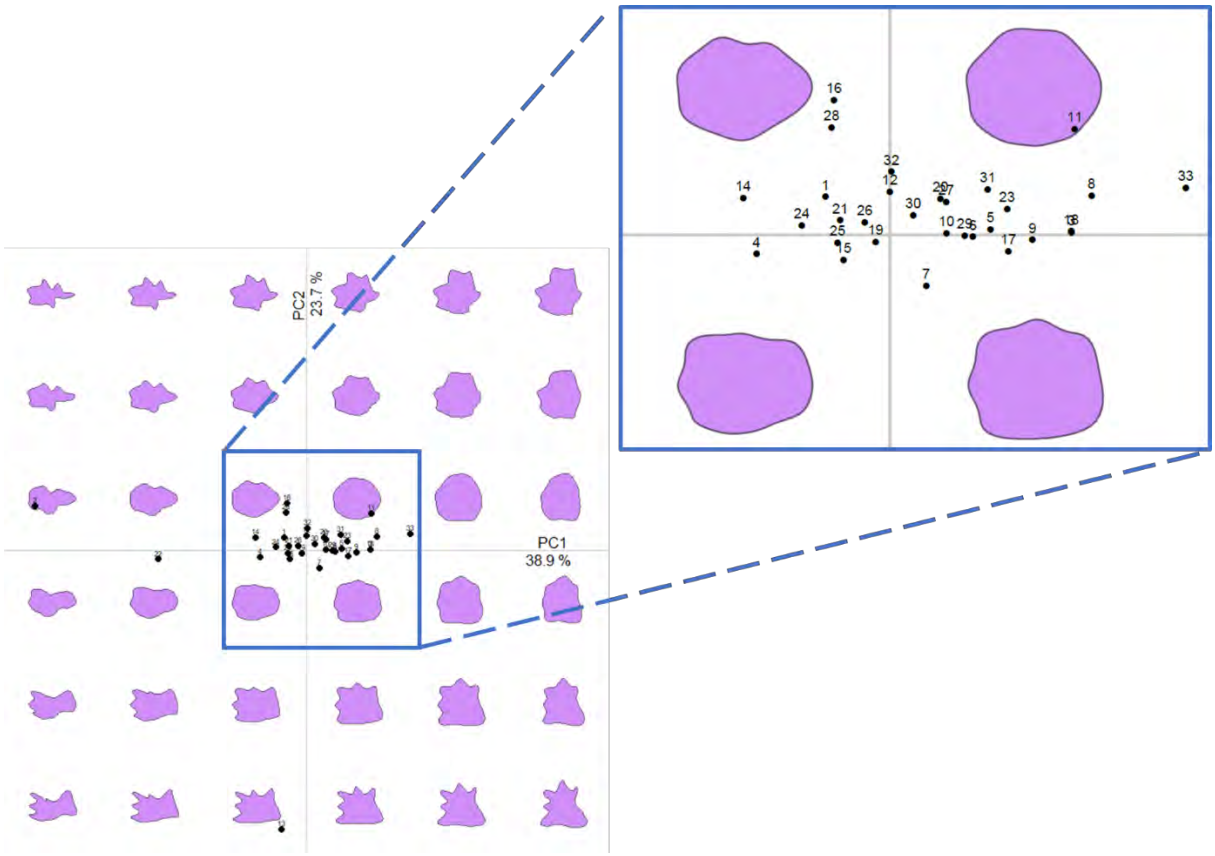

Figure 9-37: EFA PC1 & 2 (explaining 38.9% and 23.7 % of shape variance) in the underneath view. Back-transformed shapes are shown in purple for reference. Species numbered as per table below, with the outliers (not present in insert) underlined in the table.

Nº	Species	Nº	Species	Nº	Species	Nº	Species	Nº	Species
1	*Neogloboquadrina acostaensis*	**8**	*Praeorbulina curva*	**15**	*Globorotaloides hexagonus*	**22**	*Globoturborotalita nepenthes*	**29**	*Dentoglobigerina rohri*
2	*Globigerinella adamsi*	**9**	*Sphaeroidinella dehiscens*	**16**	*Neogloboquadrina humerosa*	**23**	*Pulleniatina obliquiloculata*	**30**	*Paragloborotalia siakensis*
3	*Dentoglobigerina altispira*	**10**	*Sphaeroidinella dehiscens (HR)*	**17**	*Globoconella inflata*	**24**	*Fohsella peripheroronda*	**31**	*Globoconella sphericomiozea*
4	*Globoturborotalita apertura*	**11**	*Catapsydrax dissimilis*	**18**	*Sphaeroidinellopsis kochi*	**25**	*Globigerina praebulloides*	**32**	*Truncorotalia truncatulinoides*
5	*Globigerina bulloides*	**12**	*Neogloboquadrina dutertrei*	**19**	*Fohsella lobata*	**26**	*Menardella praemenardii*	**33**	*Orbulina universa*
6	*Globigerinoides conglobatus*	**13**	*Globigerinoides fistulosus*	**20**	*Hirsutella margaritae*	**27**	*Globoconella puncticulata*		
7	*Truncorotalia crassaformis*	**14**	*Globorotalia flexuosa*	**21**	*Paragloborotalia mayeri*	**28**	*Fohsella robusta*		

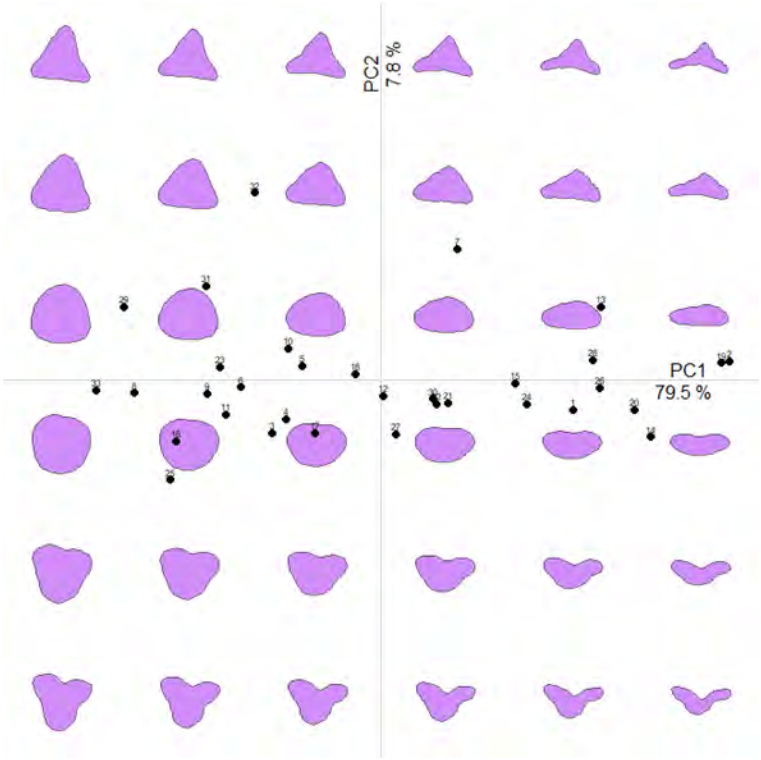

Figure 9-38: EFA PC1 & 2 (explaining 79.5% and 7.8 % of shape variance) side view. Back-transformed shapes are shown in purple for reference. Species numbered as per table below.

Nº	Species	Nº	Species	Nº	Species	Nº	Species	Nº	Species
1	*Neogloboquadrina acostaensis*	**8**	*Praeorbulina curva*	**15**	*Globorotaloides hexagonus*	**22**	*Globoturborotalita nepenthes*	**29**	*Dentoglobigerina rohri*
2	*Globigerinella adamsi*	**9**	*Sphaeroidinella dehiscens*	**16**	*Neogloboquadrina humerosa*	**23**	*Pulleniatina obliquiloculata*	**30**	*Paragloborotalia siakensis*
3	*Dentoglobigerina altispira*	**10**	*Sphaeroidinella dehiscens (HR)*	**17**	*Globoconella inflata*	**24**	*Fohsella peripheroronda*	**31**	*Globoconella sphericomiozea*
4	*Globoturborotalita apertura*	**11**	*Catapsydrax dissimilis*	**18**	*Sphaeroidinellopsis kochi*	**25**	*Globigerina praebulloides*	**32**	*Truncorotalia truncatulinoides*
5	*Globigerina bulloides*	**12**	*Neogloboquadrina dutertrei*	**19**	*Fohsella lobata*	**26**	*Menardella praemenardii*	**33**	*Orbulina universa*
6	*Globigerinoides conglobatus*	**13**	*Globigerinoides fistulosus*	**20**	*Hirsutella margaritae*	**27**	*Globoconella puncticulata*		
7	*Truncorotalia crassaformis*	**14**	*Globorotalia flexuosa*	**21**	*Paragloborotalia mayeri*	**28**	*Fohsella robusta*		

9.3.5.3 *EFA Phylomorphospace*

As with GM phylomorphospace closely related species are generally not close in morphospace in any of the orientations (Figure 9-39 to Figure 9-42). However, some species are close to sister species (e.g.: *G. puncticulata*, 27; and *N. acostaensis*, 1 in sinking orientation from a side, Figure 9-42). Using a Mantel test, species are significantly more separated in morphospace in PC1 of the spiral view compared to branch length (R^2 = 0.22, p = 0.008), PC2 spiral (R^2 = 0.22, p = 0.012), PC2 aperture (R^2 = 0.12, p = 0.087), and PC2 underneath (R^2 = 0.22, p = 0.01). This is not the case for, PC1 aperture (R^2 = 0.03, p = 0.30), PC1 underneath view (R^2 = 0.11, p = 0.10), PC1 side view (R^2 = 0.08, p = 0.31) and PC2 side view (R^2 = -0.001, p = 0.48), where branch length and distance in morphospace are not significantly different.

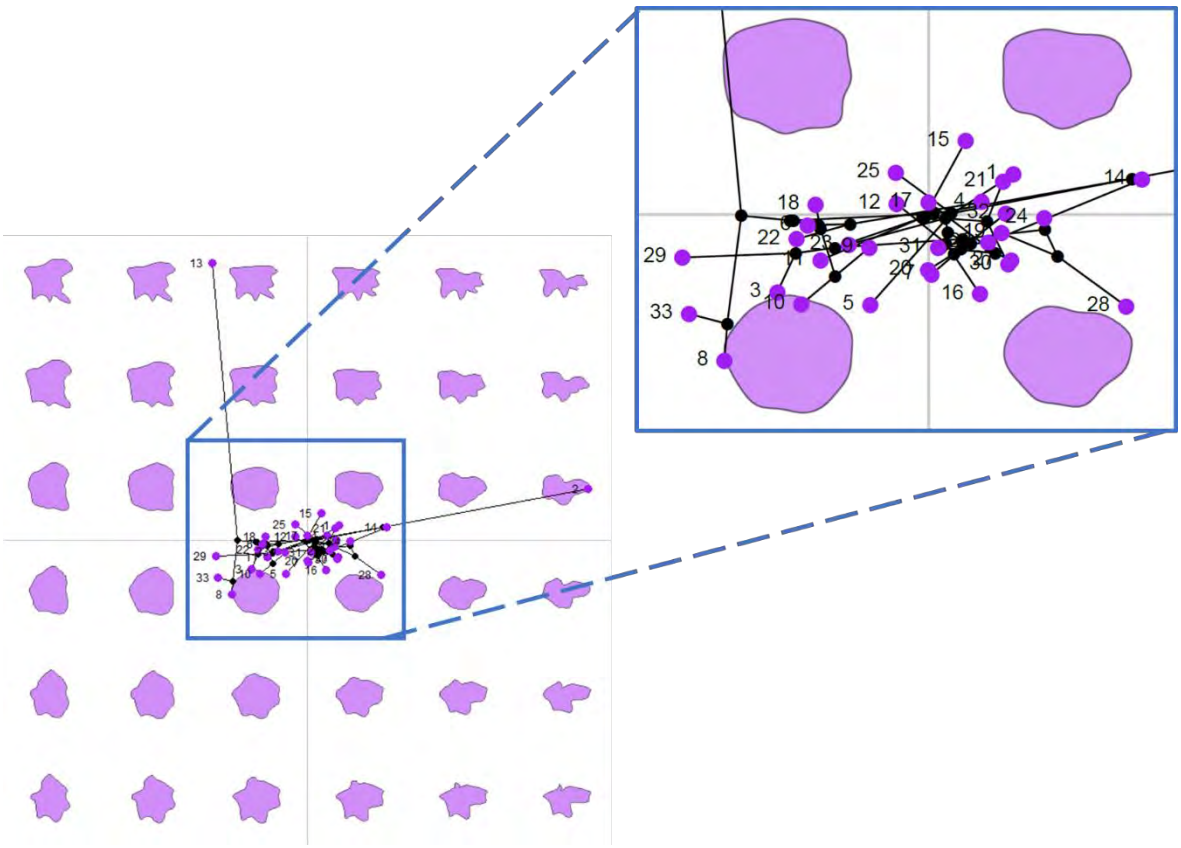

Figure 9-39: Phylomorphospace for EFA PC scores in spiral view of the standard orientation. Species number as per table below, in which the outliers are underlined.

Nº	Species	Nº	Species	Nº	Species	Nº	Species	Nº	Species
1	*Neogloboquadrina acostaensis*	**8**	*Praeorbulina curva*	**15**	*Globorotaloides hexagonus*	**22**	*Globoturborotalita nepenthes*	**29**	*Dentoglobigerina rohri*
2	*Globigerinella adamsi*	**9**	*Sphaeroidinella dehiscens*	**16**	*Neogloboquadrina humerosa*	**23**	*Pulleniatina obliquiloculata*	**30**	*Paragloborotalia siakensis*
3	*Dentoglobigerina altispira*	**10**	*Sphaeroidinella dehiscens (HR)*	**17**	*Globoconella inflata*	**24**	*Fohsella peripheroronda*	**31**	*Globoconella sphericomiozea*
4	*Globoturborotalita apertura*	**11**	*Catapsydrax dissimilis*	**18**	*Sphaeroidinellopsis kochi*	**25**	*Globigerina praebulloides*	**32**	*Truncorotalia truncatulinoides*
5	*Globigerina bulloides*	**12**	*Neogloboquadrina dutertrei*	**19**	*Fohsella lobata*	**26**	*Menardella praemenardii*	**33**	*Orbulina universa*
6	*Globigerinoides conglobatus*	**13**	*Globigerinoides fistulosus*	**20**	*Hirsutella margaritae*	**27**	*Globoconella puncticulata*		
7	*Truncorotalia crassaformis*	**14**	*Globorotalia flexuosa*	**21**	*Paragloborotalia mayeri*	**28**	*Fohsella robusta*		

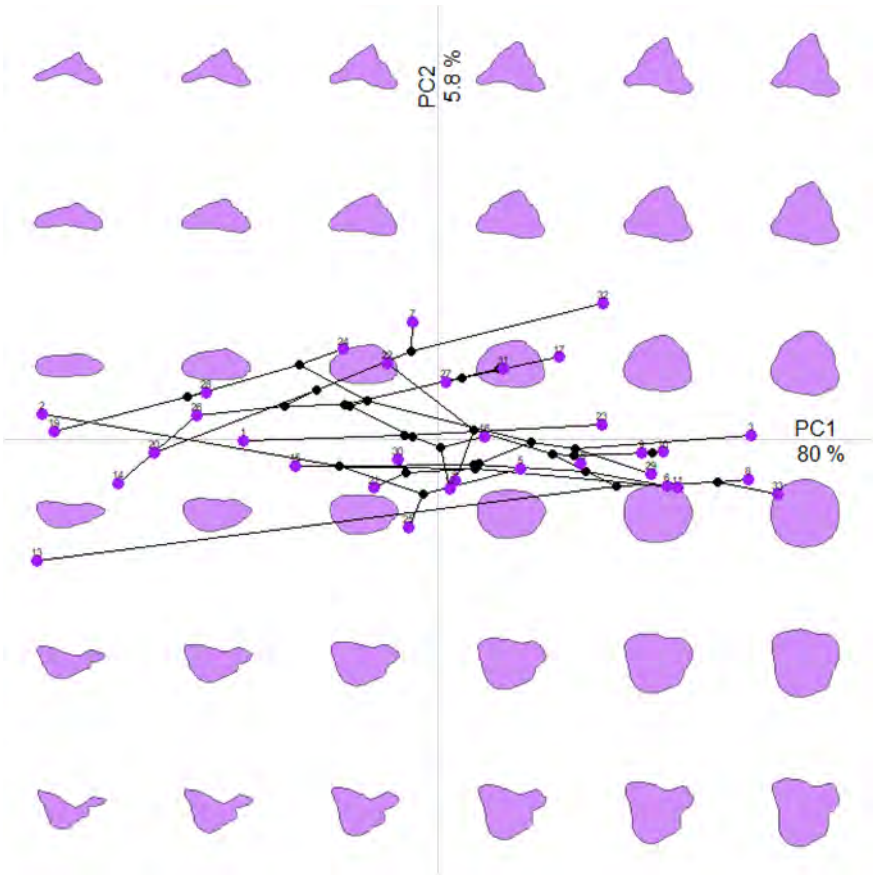

Figure 9-40: Phylomorphospace for EFA PC scores in aperture view of the standard orientation.

Nº	Species	Nº	Species	Nº	Species	Nº	Species	Nº	Species
1	*Neogloboquadrina acostaensis*	**8**	*Praeorbulina curva*	**15**	*Globorotaloides hexagonus*	**22**	*Globoturborotalita nepenthes*	**29**	*Dentoglobigerina rohri*
2	*Globigerinella adamsi*	**9**	*Sphaeroidinella dehiscens*	**16**	*Neogloboquadrina humerosa*	**23**	*Pulleniatina obliquiloculata*	**30**	*Paragloborotalia siakensis*
3	*Dentoglobigerina altispira*	**10**	*Sphaeroidinella dehiscens (HR)*	**17**	*Globoconella inflata*	**24**	*Fohsella peripheroronda*	**31**	*Globoconella sphericomiozea*
4	*Globoturborotalita apertura*	**11**	*Catapsydrax dissimilis*	**18**	*Sphaeroidinellopsis kochi*	**25**	*Globigerina praebulloides*	**32**	*Truncorotalia truncatulinoides*
5	*Globigerina bulloides*	**12**	*Neogloboquadrina dutertrei*	**19**	*Fohsella lobata*	**26**	*Menardella praemenardii*	**33**	*Orbulina universa*
6	*Globigerinoides conglobatus*	**13**	*Globigerinoides fistulosus*	**20**	*Hirsutella margaritae*	**27**	*Globoconella puncticulata*		
7	*Truncorotalia crassaformis*	**14**	*Globorotalia flexuosa*	**21**	*Paragloborotalia mayeri*	**28**	*Fohsella robusta*		

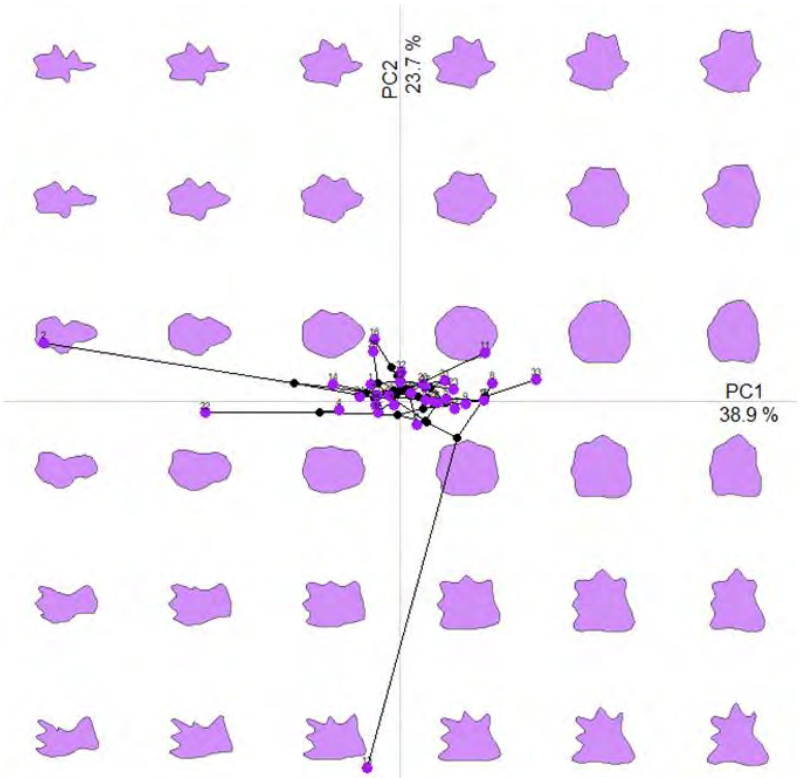

Figure 9-41: Phylomorphospace for EFA PC scores in underneath view of the sinking orientation.

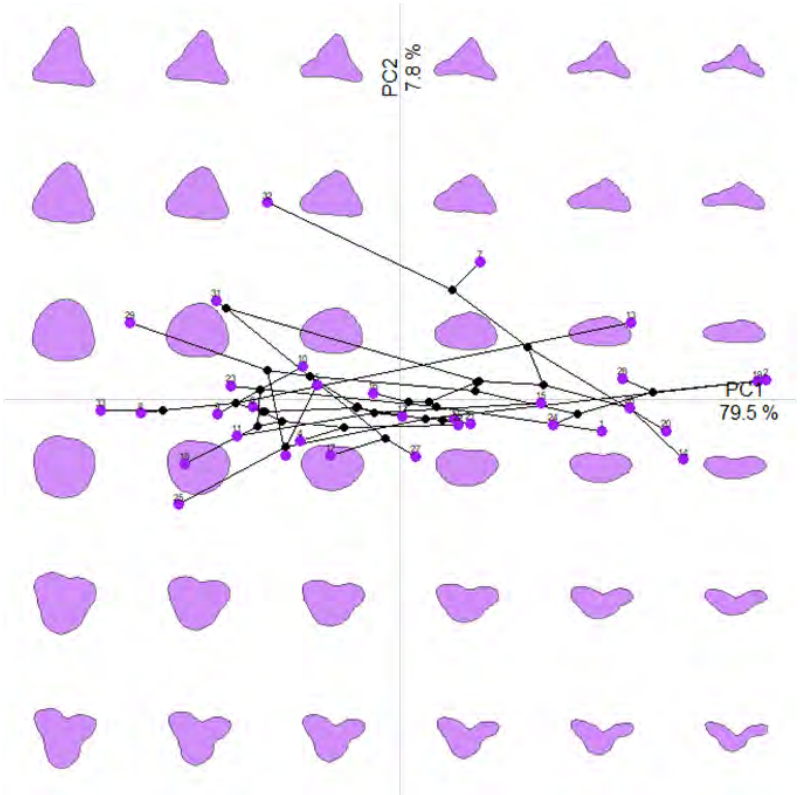

Figure 9-42: Phylomorphospace for EFA PC scores in side view of the sinking orientation.

9.3.6 Comparison of EFA and CSF

The same general trends, present above, are present in the EFA PC scores with CSF values. The more spherical species (i.e. those with higher CSF values) are found with more positive PC1 values in all orientations (Figure 9-45). There is less of an effect with PC2, but as PC value deviates from zero, CSF values increase. The relationship between EFA PC scores and CSF is significant in all views, but the strength of the correlation differs: spiral view ($F_{3,29}$= 13.7, p<0.001, adjusted R^2= 0.54); aperture view ($F_{3,29}$=175.1, p<0.001, adjusted R^2= 0.94); underneath view ($F_{3,29}$= 13.7, p<0.001, adjusted R^2= 0.54) and side view ($F_{3,29}$= 5.022, p<0.001, adjusted R^2= 0.27).

9.3.7 Comparison of EFA and Morphogroups

As with GM PC scores and morphogroup there are no trends between these two measures of shape. In the spiral view 49% of variation in morphogroup is explained by the interaction of EFA PC1 and PC2 scores (Figure 9-43A, McFadden R^2=0.41, X^2=49.52, *p*< 0.001). ANOVA comparison of morphogroup and EFA PC scores found significant differences between morphogroups for PC1 ($F_{8,24}$ = 12.33, *p*<0.001) and for PC2 ($F_{8,24}$ = 3.022, p =0.017). Significant Tukey HSD results for pairwise comparisons of morphogroups for both PC axes can be found in Table 9-14.

Table 9-14: Significant results from the Tukey HSD pairwise comparison between morphogroups for EFA spiral view.

	Morphogroup pair	Difference	Lower Interval	Upper Interval	Adjusted p value
PC1	3-12	0.149	0.004	0.293	0.04
	12-4	0.164	0.02	0.309	0.018
	14-4	0.144	0.012	0.276	0.026
	5-2	0.351	0.198	0.505	<0.001
	5-3	0.433	0.256	0.61	<0.001
	5-4	0.448	0.271	0.625	<0.001
	5-7	-0.369	-0.519	-0.218	<0.001
	5-12	-0.284	-0.461	-0.107	<0.001
	5-13	-0.293	-0.498	-0.089	0.002
	5-14	-0.305	-0.471	-0.138	<0.001
	5-15	-0.328	-0.505	-0.151	<0.001
PC2	3-2	0.171	0.025	0.317	0.013
	3-4	0.225	0.04	0.41	0.009
	3-7	-0.182	-0.323	-0.041	0.005
	3-12	-0.194	-0.378	-0.009	0.035
	3-14	-0.176	-0.345	-0.007	0.036

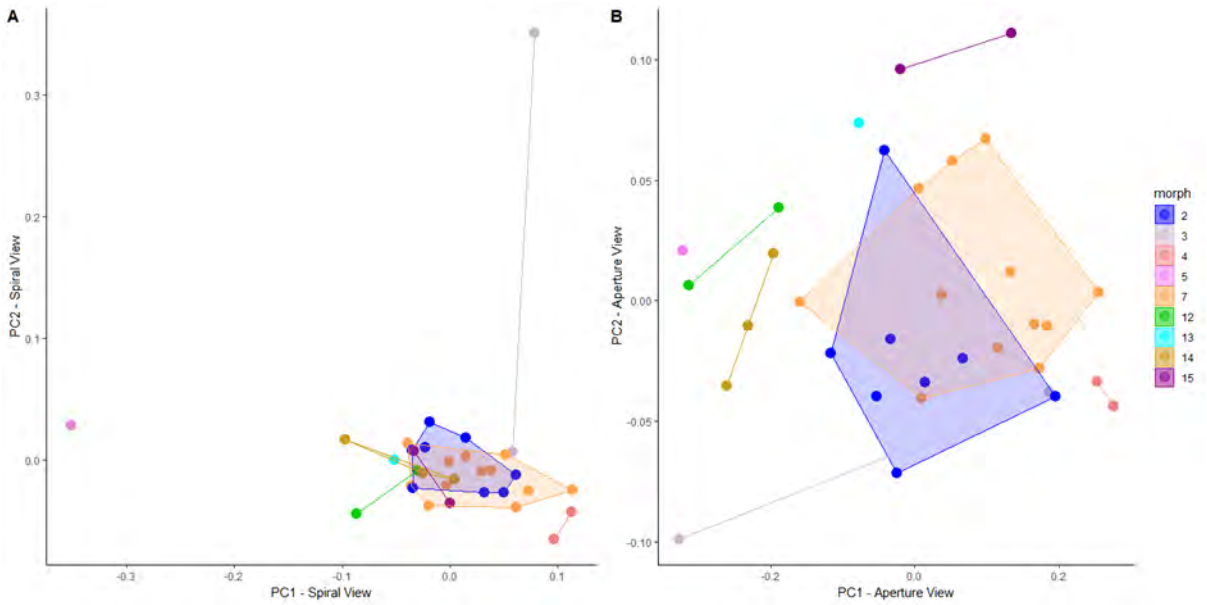

Figure 9-43: EFA PC scores in spiral (A) and aperture (B) views, coloured by morphogroup.

In the aperture view, the MLR formula had to be specified differently due to reaching a singularity in the calculations. For this view two models were constructed, PC1 and PC2 (with no interaction), and secondly only the interaction between PC1 and PC2 was calculated. For PC1 and PC2 77% of the variance in morphogroup is explained by PC scores (McFadden R^2=0.77, X^2=92.52, p<0.001), and for the interaction between PC1 and PC2 24% of the variance is explained by PC scores (Figure 9-43B, McFadden R^2=0.24, X^2=28.81, p<0.001). ANOVA found differences in the PC score variance between morphogroups for PC1 ($F_{8,24}$ = 5.586, p<0.001) and for PC2 ($F_{8,24}$ = 5.06, p<0.001). Significant Tukey HSD pairwise comparisons can be found in Table 9-15.

Table 9-15: Significant results from the Tukey HSD pairwise comparison between morphogroups for EFA aperture view.

	Morphogroup pair	Difference	Lower Interval	Upper Interval	Adjusted p value
PC1	4-5	0.587	0.086	1.088	0.013
	4-12	0.516	0.107	0.925	0.007
	4-14	0.494	0.121	0.868	0.004
	7-12	0.341	0.028	0.653	0.025
	7-14	0.319	0.055	0.583	0.01
PC2	15-2	0.126	0.036	0.217	0.002
	15-3	0.172	0.058	0.286	0.001
	15-4	0.143	0.029	0.257	0.007
	15-7	0.097	0.01	0.184	0.022
	15-14	0.112	0.008	0.217	0.028
	13-3	0.142	0.003	0.282	0.044

There is overlap of morphogroups in EFA sinking orientation morphospaces (see Figure 9-44). In the underneath view 51% of variance in morphogroup is explained by PC1 and 2 (McFadden R^2=0.51, X^2=61.25, p<0.001), which increases to 73% for sinking orientation side view (McFadden R^2=0.73, X^2=87.23, p<0.001). There are significant differences in the variance of PC scores between morphogroups for underneath view PC1 ($F_{8,24}$ = 7.269, p<0.001), and PC2 ($F_{8,24}$ = 2.957, p =0.0188). Significant Tukey HSD pairwise comparisons for PC1 and PC2 are shown in Table 9-16.

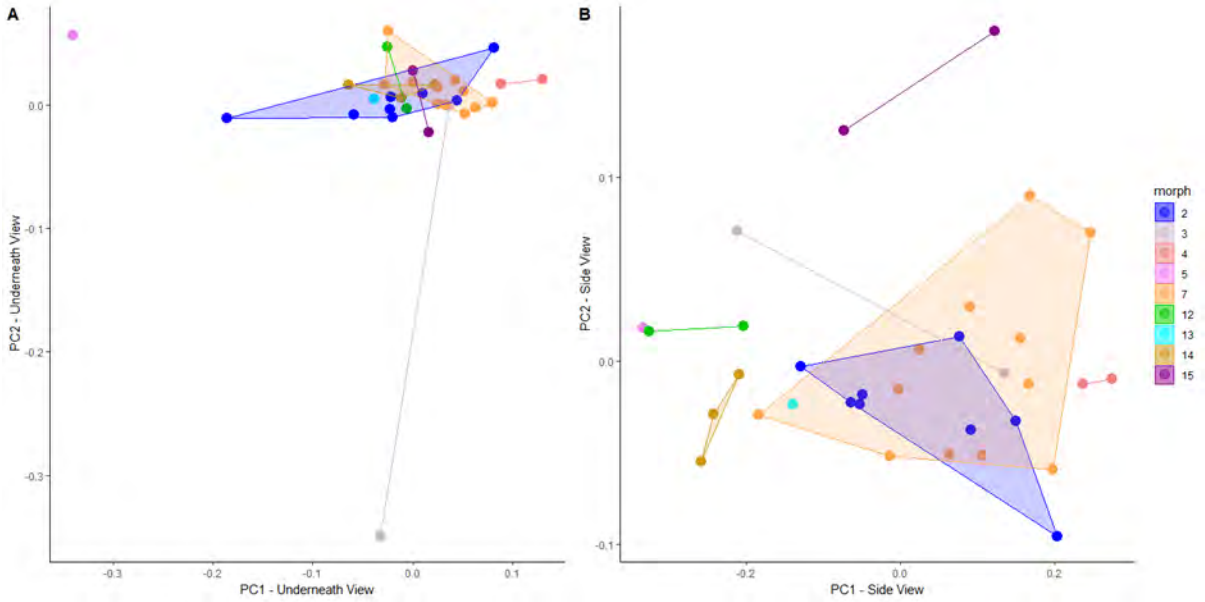

Figure 9-44: EFA PC scores in underneath view (A) and side view (B), coloured by morphogroup.

Table 9-16: Significant results from the Tukey HSD pairwise comparison between morphogroups for EFA underneath view.

	Morphogroup pair	Difference	Lower Interval	Upper Interval	Adjusted p value
PC1	5-2	-0.318	-0.506	-0.129	<0.001
	5-3	-0.342	-0.56	-0.124	0.001
	5-4	-0.449	-0.666	-0.231	<0.001
	7-5	0.373	0.188	0.558	<0.001
	5-12	0.324	0.106	0.541	0.001
	5-13	0.301	0.05	0.552	0.011
	5-14	0.322	0.117	0.527	0.001
	5-15	0.348	0.13	0.566	<0.001
PC2	3-2	-0.178	-0.322	-0.034	0.008
	3-4	-0.193	-0.375	-0.011	0.031
	3-5	0.23	0.008	0.453	0.039
	3-7	0.186	0.047	0.325	0.004
	3-12	0.197	0.015	0.379	0.027
	3-14	0.187	0.021	0.353	0.019

ANOVA comparisons of PC scores between morphogroups in side view show significant differences in PC scores variance between morphogroups for PC1 ($F_{8,24}$ = 5.925, p<0.001) and for PC2 ($F_{8,24}$ = 4.548, p =0.002). Significant results from a pairwise comparison using Tukey HSD are presented in Table 9-17 for both PC1 and PC2.

Table 9-17: Significant results from the Tukey HSD pairwise comparison between morphogroups for EFA side view.

	Morphogroup pair	Difference	Lower Interval	Upper Interval	Adjusted p value
PC1	4-5	0.589	0.095	1.082	0.011
	4-12	0.52	0.117	0.923	0.005
	4-14	0.492	0.124	0.86	0.003
	7-12	0.349	0.042	0.657	0.018
	7-14	0.322	0.062	0.582	0.008
PC2	15-2	0.18	0.071	0.289	<0.001
	15-4	0.164	0.026	0.301	0.011
	15-7	0.158	0.053	0.263	0.001
	15-13	0.176	0.008	0.345	0.035
	15-14	0.183	0.058	0.308	0.001

Morphogroups cannot be significantly predicted using any PC score, in any orientation, compared to morphogroup 4 (i.e. spherical).

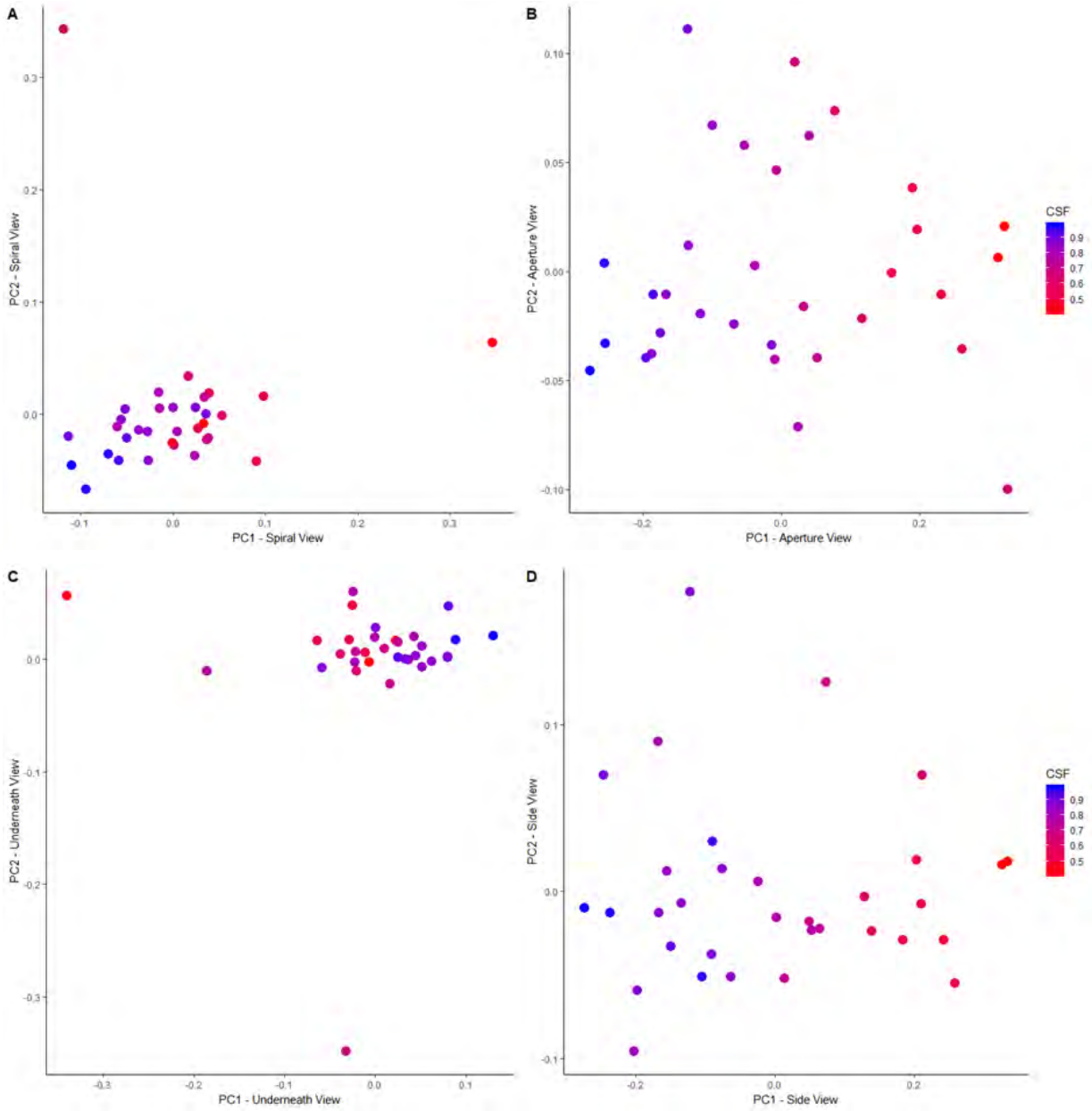

Figure 9-45: EFA PC1 and 2 in the spiral view (A), aperture view (B), underneath view(C) and side view (D), with CSF represented with colour gradient from blue (high CSF, more spherical) to red (low CSF, less spherical).

9.3.8 Outlines used for GM and EFA

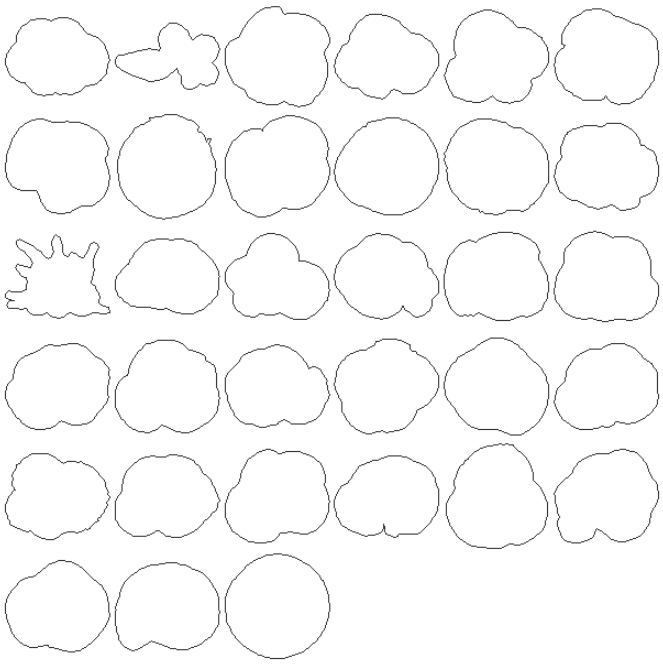

Figure 9-46: Outlines of the 33 species used in this study, for the spiral view (standard orientation).

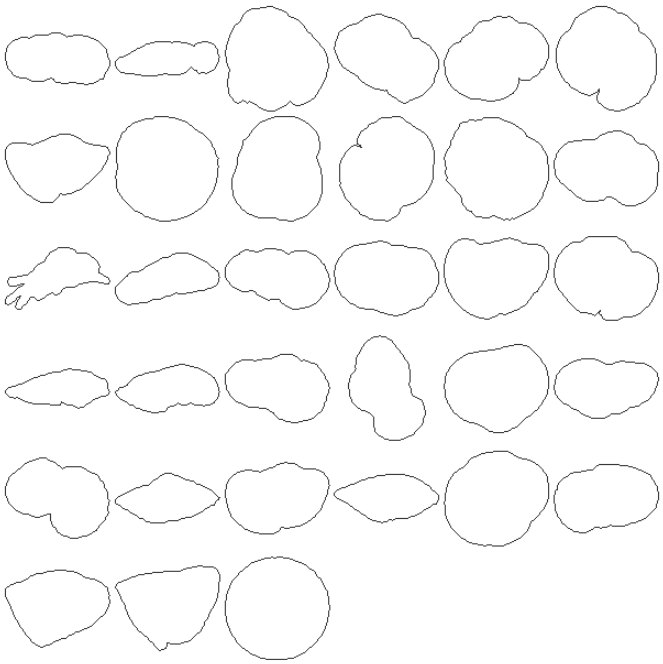

Figure 9-47: Outlines of the 33 species used in this study, aperture view (standard orientation).

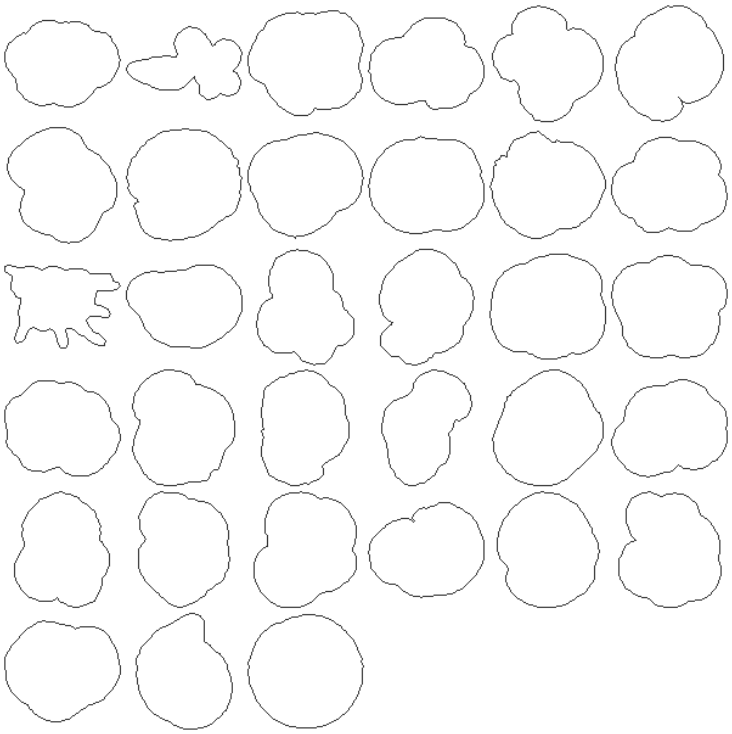

Figure 9-48: Outlines of the 33 species used in this study, underneath view (sinking orientation).

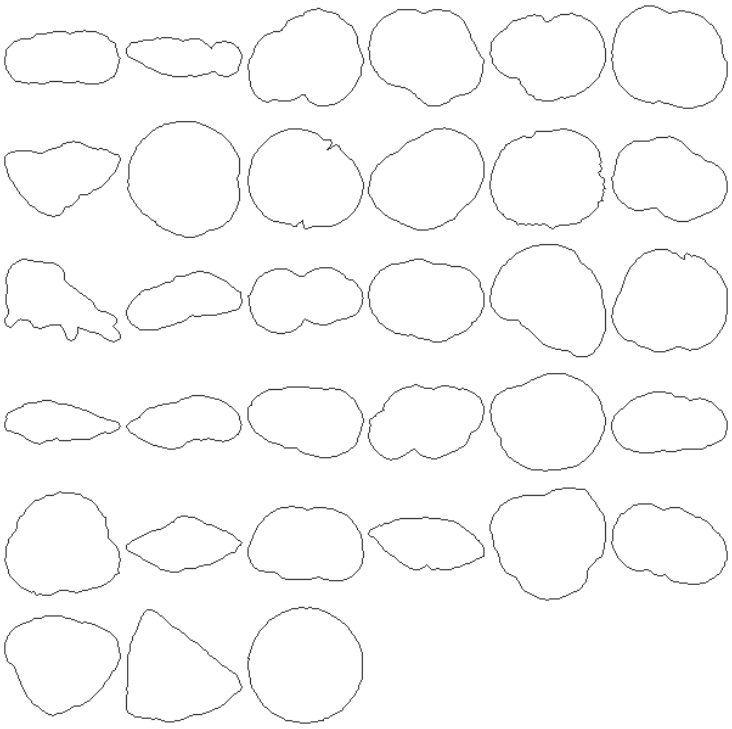

Figure 9-49: Outlines of the 33 species used in this study, side view (sinking orientation).

9.4 Chapter 7 Appendices

9.4.1MCMCglmm traces from Standard Orientation

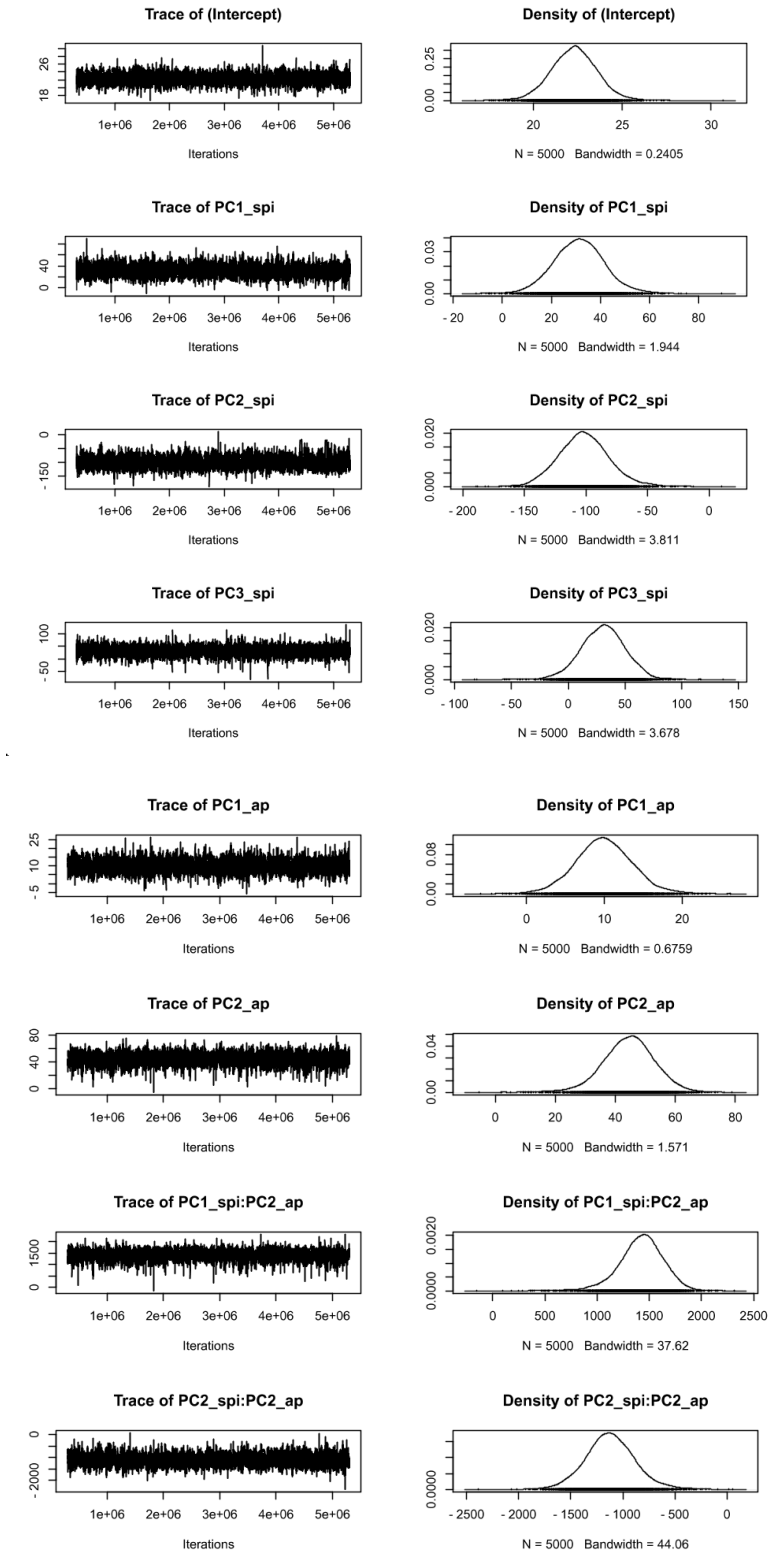

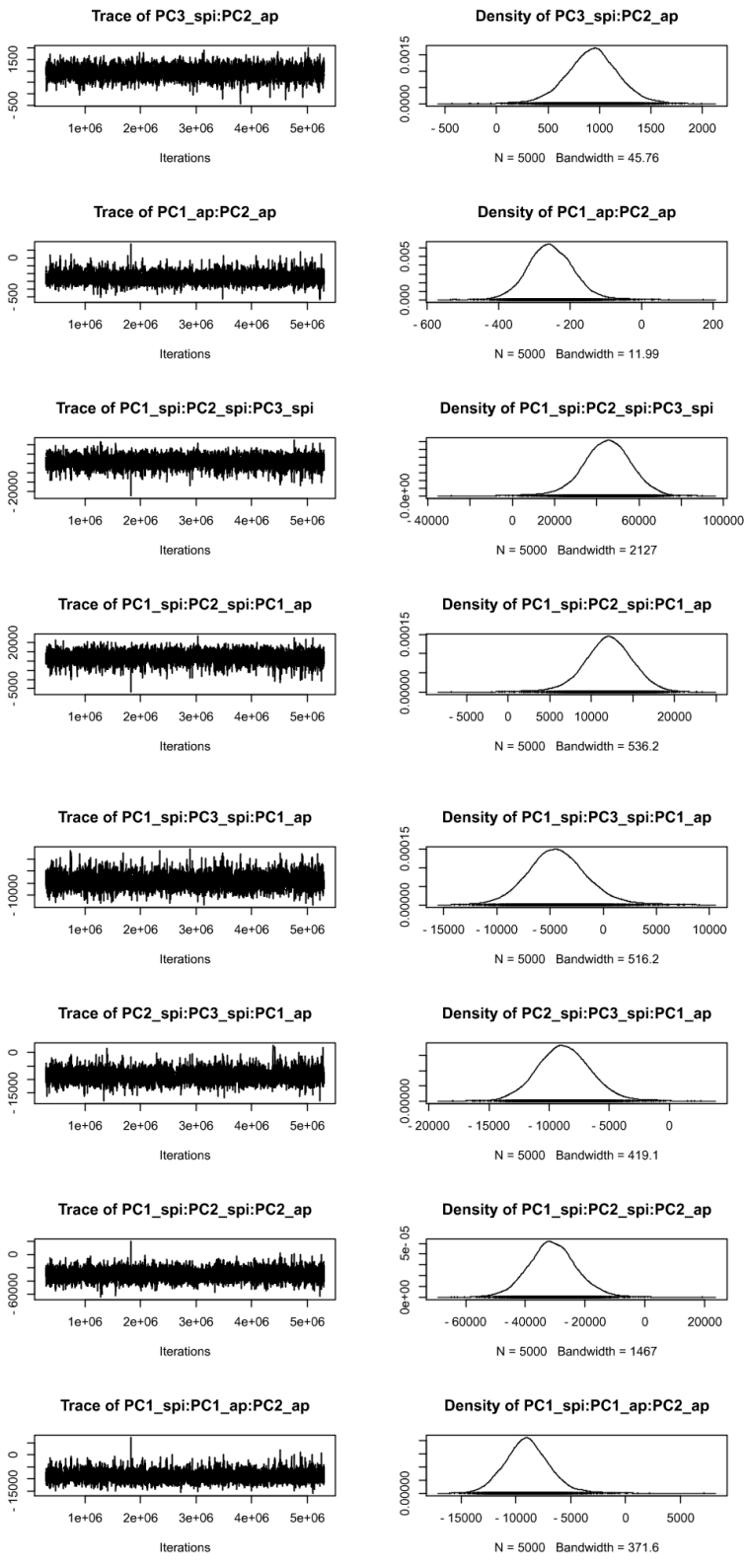
Trace of PC3_spi:PC2_ap
Density of PC3_spi:PC2_ap
Iterations
N = 5000 Bandwidth = 45.76
Trace of PC1_ap:PC2_ap
Density of PC1_ap:PC2_ap
Iterations
N = 5000 Bandwidth = 11.99
Trace of PC1_spi:PC2_spi:PC3_spi
Density of PC1_spi:PC2_spi:PC3_spi
Iterations
N = 5000 Bandwidth = 2127
Trace of PC1_spi:PC2_spi:PC1_ap
Density of PC1_spi:PC2_spi:PC1_ap
Iterations
N = 5000 Bandwidth = 536.2
Trace of PC1_spi:PC3_spi:PC1_ap
Density of PC1_spi:PC3_spi:PC1_ap
Iterations
N = 5000 Bandwidth = 516.2
Trace of PC2_spi:PC3_spi:PC1_ap
Density of PC2_spi:PC3_spi:PC1_ap
Iterations
N = 5000 Bandwidth = 419.1
Trace of PC1_spi:PC2_spi:PC2_ap
Density of PC1_spi:PC2_spi:PC2_ap
Iterations
N = 5000 Bandwidth = 1467
Trace of PC1_spi:PC1_ap:PC2_ap
Density of PC1_spi:PC1_ap:PC2_ap
Iterations
N = 5000 Bandwidth = 371.6

9.4.2MCMCglmm traces from Sinking Orientation

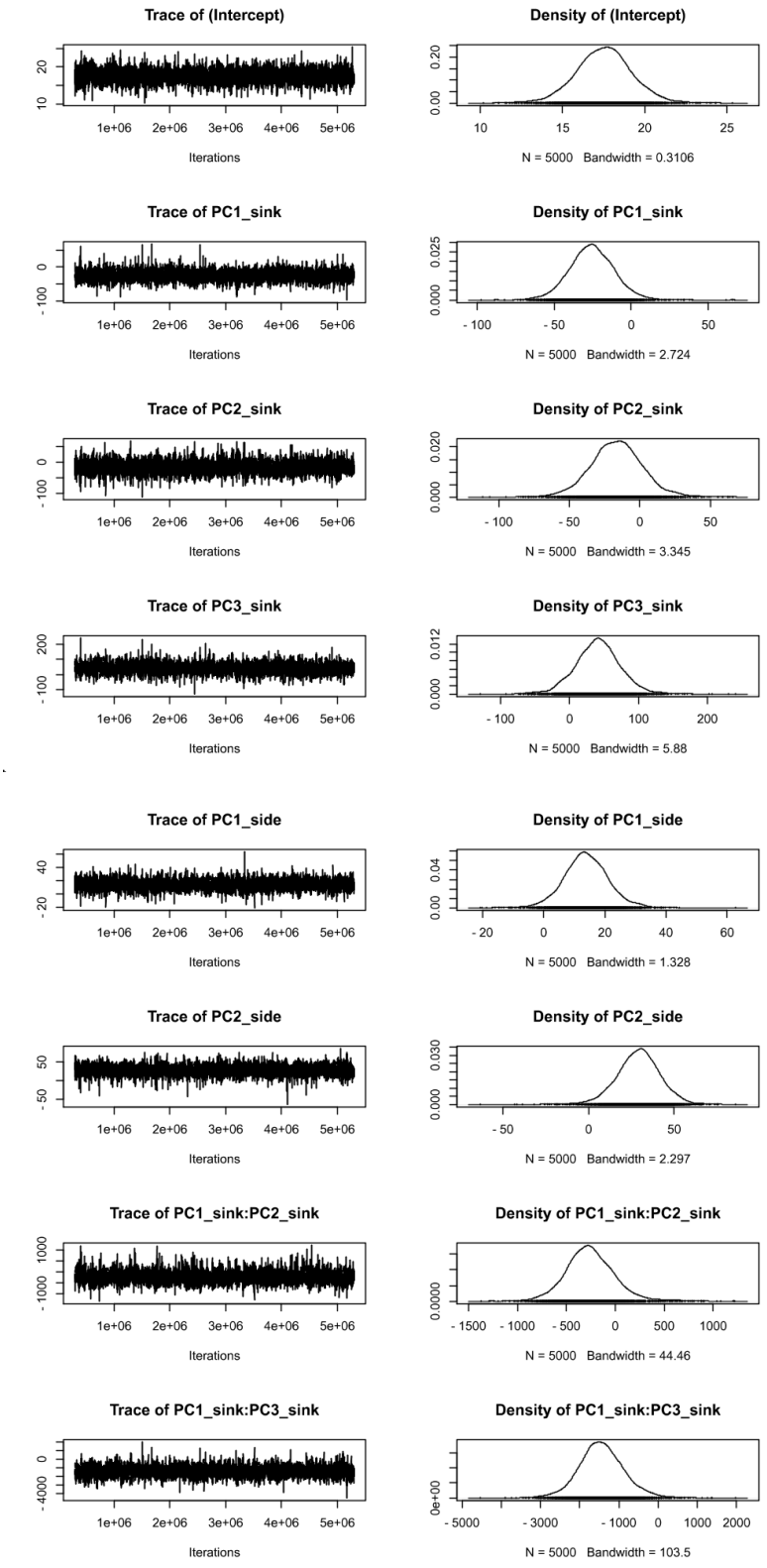

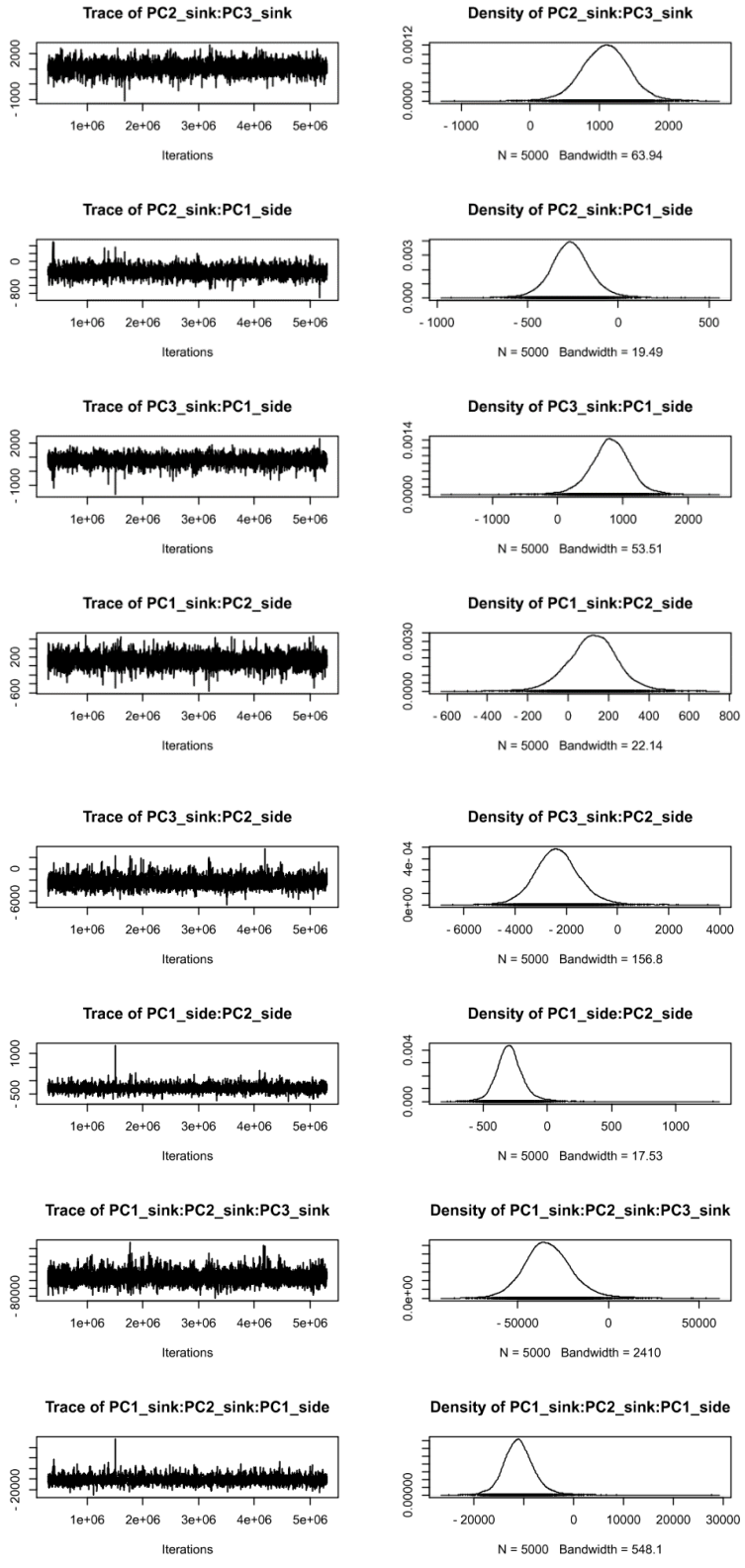
Trace of PC2_sink:PC3_sink
Density of PC2_sink:PC3_sink
N = 5000 Bandwidth = 63.94
Trace of PC2_sink:PC1_side
Density of PC2_sink:PC1_side
N = 5000 Bandwidth = 19.49
Trace of PC3_sink:PC1_side
Density of PC3_sink:PC1_side
N = 5000 Bandwidth = 53.51
Trace of PC1_sink:PC2_side
Density of PC1_sink:PC2_side
N = 5000 Bandwidth = 22.14
Trace of PC3_sink:PC2_side
Density of PC3_sink:PC2_side
N = 5000 Bandwidth = 156.8
Trace of PC1_side:PC2_side
Density of PC1_side:PC2_side
N = 5000 Bandwidth = 17.53
Trace of PC1_sink:PC2_sink:PC3_sink
Density of PC1_sink:PC2_sink:PC3_sink
N = 5000 Bandwidth = 2410
Trace of PC1_sink:PC2_sink:PC1_side
Density of PC1_sink:PC2_sink:PC1_side
N = 5000 Bandwidth = 548.1
Iterations

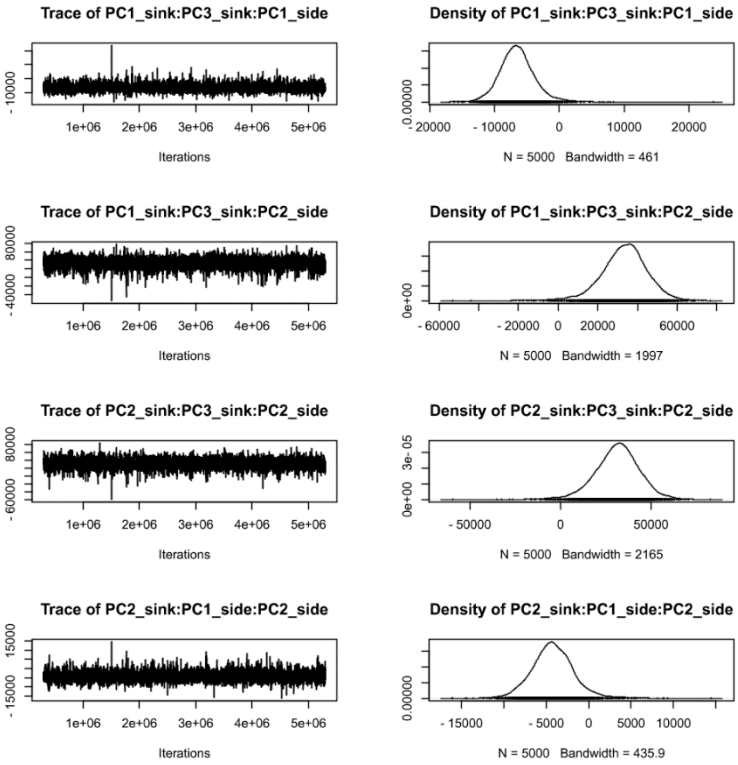
Trace of PC1_sink:PC3_sink:PC1_side
- 10000
1e+06 2e+06 3e+06 4e+06 5e+06
Iterations
Density of PC1_sink:PC3_sink:PC1_side
0.00000
- 20000 - 10000 0 10000 20000
N = 5000 Bandwidth = 461
Trace of PC1_sink:PC3_sink:PC2_side
- 40000 80000
1e+06 2e+06 3e+06 4e+06 5e+06
Iterations
Density of PC1_sink:PC3_sink:PC2_side
0e+00
- 60000 - 20000 0 20000 60000
N = 5000 Bandwidth = 1997
Trace of PC2_sink:PC3_sink:PC2_side
- 60000 80000
1e+06 2e+06 3e+06 4e+06 5e+06
Iterations
Density of PC2_sink:PC3_sink:PC2_side
0e+00 3e- 05
- 50000 0 50000
N = 5000 Bandwidth = 2165
Trace of PC2_sink:PC1_side:PC2_side
- 15000 15000
1e+06 2e+06 3e+06 4e+06 5e+06
Iterations
Density of PC2_sink:PC1_side:PC2_side
0.00000
- 15000 - 5000 0 5000 10000
N = 5000 Bandwidth = 435.9